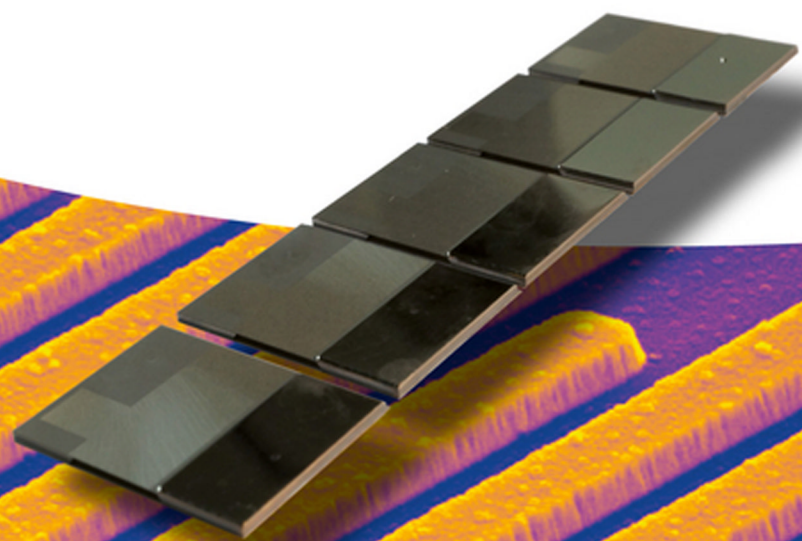


Danick Briand, Eric Yeatman, Shad Roundy (Eds.)

# Micro Energy Harvesting

Series Editors:  
Brand, Fedder, Hierold,  
Korvink, Tabata





*Edited by  
Danick Briand, Eric Yeatman,  
and Shad Roundy*

**Micro Energy Harvesting**

## *Related Titles*

Tabata, O., Tsuchiya, T. (eds.)

### **Reliability of MEMS Testing of Materials and Devices**

2008  
Print ISBN: 978-3-527-31494-2;  
also available in electronic formats

Saile, V., Wallrabe, U., Tabata, O., Korvink,  
J.G. (eds.)

### **LIGA and its Applications**

2009  
Print ISBN: 978-3-527-31698-4;  
also available in electronic formats

Hierold, C. (ed.)

### **Carbon Nanotube Devices Properties, Modeling, Integration and Applications**

2008  
Print ISBN: 978-3-527-31720-2;  
also available in electronic formats

Krüger, A.

### **Carbon Materials and Nanotechnology**

2010  
Print ISBN: 978-3-527-31803-2;  
also available in electronic formats

Bechtold, T., Schrag, G., Feng, L. (eds.)

### **System-level Modeling of MEMS**

2013  
Print ISBN: 978-3-527-31903-9;  
also available in electronic formats

Korvink, J.G., Smith, P.J., Shin, D. (eds.)

### **Inkjet-based Micromanufacturing**

2012  
Print ISBN: 978-3-527-31904-6;  
also available in electronic formats  
ISBN: 978-3-527-64710-1

Brand, O., Dufour, I., Heinrich, S.M., Josse, F.  
(eds.)

### **Resonant MEMS Principles, Modeling, Implementation and Applications**

2014  
Print ISBN: 978-3-527-33545-9;  
also available in electronic formats  
ISBN: 978-3-527-67633-0

*Edited by Danick Briand, Eric Yeatman,  
and Shad Roundy*

## **Micro Energy Harvesting**

**WILEY-VCH**  
Verlag GmbH & Co. KGaA

## Volume Editors

**Dr. Danick Briand**  
EPFL-IMT SAMLAB  
Rue Jaquet-Droz 1  
2000 NEUCHÂTEL  
Switzerland

**Prof. Eric Yeatman**  
Imperial College London  
Dep. of Electr. & Electron. Engin.  
South Kensington Campus  
London SW7 2AZ  
United Kingdom

**Prof. Shad Roundy**  
University of Utah  
Dept. of Mech. Engineering  
50 S. Central Campus Drive  
United States

## Series Editors

**Oliver Brand**  
School Electrical/Comp. Eng.  
Georgia Inst. of Technology  
777 Atlantic Drive  
United States

**Gary K. Fedder**  
ECE Department & Robotics Inst  
Carnegie Mellon University  
United States

**Prof. Christofer Hierold**  
ETH Zürich  
ETH-Zentrum, CLA H9  
Tannenstr. 3  
8092 Zürich  
Switzerland

**Jan G. Korvink**  
Inst. f. Mikrosystemtechnik  
Albert-Ludwigs-Univ. Freiburg  
Georges-Köhler-Allee 103  
79110 Freiburg  
Germany

**Osamu Tabata**  
Dept. of Mech. Eng./Kyoto Univ.  
Faculty of Engineering  
Yoshida Honmachi Sakyo-ku  
606-8501 Kyoto  
Japan

All books published by **Wiley-VCH** are carefully produced. Nevertheless, authors, editors, and publisher do not warrant the information contained in these books, including this book, to be free of errors. Readers are advised to keep in mind that statements, data, illustrations, procedural details or other items may inadvertently be inaccurate.

**Library of Congress Card No.:** applied for

## British Library Cataloguing-in-Publication Data

A catalogue record for this book is available from the British Library.

## Bibliographic information published by the Deutsche Nationalbibliothek

The Deutsche Nationalbibliothek lists this publication in the Deutsche Nationalbibliografie; detailed bibliographic data are available on the Internet at <<http://dnb.d-nb.de>>.

© 2015 Wiley-VCH Verlag GmbH & Co. KGaA, Boschstr. 12, 69469 Weinheim, Germany

All rights reserved (including those of translation into other languages). No part of this book may be reproduced in any form – by photoprinting, microfilm, or any other means - nor transmitted or translated into a machine language without written permission from the publishers. Registered names, trademarks, etc. used in this book, even when not specifically marked as such, are not to be considered unprotected by law.

**Print ISBN:** 978-3-527-31902-2  
**ePDF ISBN:** 978-3-527-67293-6  
**ePub ISBN:** 978-3-527-67292-9  
**Mobi ISBN:** 978-3-527-67291-2  
**oBook ISBN:** 978-3-527-67294-3

**Cover Design** Schulz Grafik-Design,  
Fußgönningheim, Germany  
**Typesetting** Laserwords Private Limited,  
Chennai, India  
**Printing and Binding** Strauss GmbH,  
Mörlenbach, Germany

Printed on acid-free paper

## Contents

**About the Volume Editors** *XVII*

**List of Contributors** *XIX*

<b>1</b>	<b>Introduction to Micro Energy Harvesting</b>	<b>1</b>
	<i>Danick Briand, Eric Yeatman, and Shad Roundy</i>	
1.1	Introduction to the Topic	1
1.2	Current Status and Trends	3
1.3	Book Content and Structure	4
<b>2</b>	<b>Fundamentals of Mechanics and Dynamics</b>	<b>7</b>
	<i>Helios Vocca and Luca Gammaitoni</i>	
2.1	Introduction	7
2.2	Strategies for Micro Vibration Energy Harvesting	8
2.2.1	Piezoelectric	9
2.2.2	Electromagnetic	10
2.2.3	Electrostatic	11
2.2.4	From Macro to Micro to Nano	11
2.3	Dynamical Models for Vibration Energy Harvesters	12
2.3.1	Stochastic Character of Ambient Vibrations	14
2.3.2	Linear Case 1: Piezoelectric Cantilever Generator	14
2.3.3	Linear Case 2: Electromagnetic Generator	15
2.3.4	Transfer Function	15
2.4	Beyond Linear Micro-Vibration Harvesting	16
2.4.1	Frequency Tuning	16
2.4.2	Multimodal Harvesting	17
2.4.3	Up-Conversion Techniques	17
2.5	Nonlinear Micro-Vibration Energy Harvesting	18
2.5.1	Bistable Oscillators: Cantilever	19
2.5.2	Bistable Oscillators: Buckled Beam	21
2.5.3	Monostable Oscillators	23
2.6	Conclusions	24
	Acknowledgments	24
	References	24

<b>3</b>	<b>Electromechanical Transducers</b>	<b>27</b>
	<i>Adrien Badel, Fabien Formosa, and Mickaël Lallart</i>	
3.1	Introduction	27
3.2	Electromagnetic Transducers	27
3.2.1	Basic Principle	27
3.2.1.1	Induced Voltage	28
3.2.1.2	Self-Induction	28
3.2.1.3	Mechanical Aspect	29
3.2.2	Typical Architectures	30
3.2.2.1	Case Study	30
3.2.2.2	General Case	33
3.2.3	Energy Extraction Cycle	33
3.2.3.1	Resistive Cycle	34
3.2.3.2	Self-Inductance Cancelation	34
3.2.3.3	Cycle with Rectification	35
3.2.3.4	Active Cycle	36
3.2.4	Figures of Merit and Limitations	36
3.3	Piezoelectric Transducers	37
3.3.1	Basic Principles and Constitutive Equations	37
3.3.1.1	Physical Origin of Piezoelectricity in Ceramics and Crystals	37
3.3.1.2	Constitutive Equations	38
3.3.2	Typical Architectures for Energy Harvesting	39
3.3.2.1	Modeling	39
3.3.2.2	Application to Typical Configurations	40
3.3.3	Energy Extraction Cycles	41
3.3.3.1	Resistive Cycles	41
3.3.3.2	Cycles with Rectification	43
3.3.3.3	Active Cycles	43
3.3.3.4	Comparison	43
3.3.4	Maximal Power Density and Figure of Merit	44
3.4	Electrostatic Transducers	45
3.4.1	Basic Principles	45
3.4.1.1	Gauss's Law	45
3.4.1.2	Capacitance $C_0$	45
3.4.1.3	Electric Potential	46
3.4.1.4	Energy	46
3.4.1.5	Force	47
3.4.2	Design Parameters for a Capacitor	47
3.4.2.1	Architecture	47
3.4.2.2	Dielectric	48
3.4.3	Energy Extraction Cycles	48
3.4.3.1	Charge-Constrained Cycle	49
3.4.3.2	Voltage-Constrained Cycle	50
3.4.3.3	Electret Cycle	51
3.4.4	Limits	51



3.4.4.1	Parasitic Capacitors	51
3.4.4.2	Breakdown Voltage	53
3.4.4.3	Pull-In Force	53
3.5	Other Electromechanical Transduction Principles	53
3.5.1	Electrostrictive Materials	53
3.5.1.1	Physical Origin and Constitutive Equations	53
3.5.1.2	Energy Harvesting Strategies	54
3.5.2	Magnetostrictive Materials	55
3.5.2.1	Physical Origin	55
3.5.2.2	Constitutive Equations	56
3.6	Effect of the Vibration Energy Harvester Mechanical Structure	56
3.7	Summary	58
	References	59
<b>4</b>	<b>Thermal Fundamentals</b>	<b>61</b>
	<i>Mathieu Francoeur</i>	
4.1	Introduction	61
4.2	Fundamentals of Thermoelectric Power Generation	62
4.2.1	Overview of Nanoscale Heat Conduction and the Seebeck Effect	62
4.2.2	Heat Transfer Analysis of Thermoelectric Power Generation	64
4.3	Near-Field Thermal Radiation and Thermophotovoltaic Power Generation	66
4.3.1	Introduction	66
4.3.2	Theoretical Framework: Fluctuational Electrodynamics	67
4.3.3	Introduction to Thermophotovoltaic Power Generation and Physics of Near-Field Radiative Heat Transfer between Two Bulk Materials Separated by a Subwavelength Vacuum Gap	70
4.3.4	Nanoscale-Gap Thermophotovoltaic Power Generation	76
4.4	Conclusions	80
	Acknowledgments	80
	References	81
<b>5</b>	<b>Power Conditioning for Energy Harvesting – Theory and Architecture</b>	<b>85</b>
	<i>Stephen G. Burrow and Paul D. Mitcheson</i>	
5.1	Introduction	85
5.2	The Function of Power Conditioning	85
5.2.1	Interface to the Harvester	86
5.2.2	Circuits with Resistive Input Impedance	87
5.2.3	Circuits with Reactive Input Impedance	89
5.2.4	Circuits with Nonlinear Input Impedance	90
5.2.5	Peak Rectifiers	90
5.2.6	Piezoelectric Pre-biasing	92
5.2.7	Control	94
5.2.7.1	Voltage Regulation	94

5.2.7.2	Peak Power Controllers	96
5.2.8	System Architectures	97
5.2.8.1	Start-Up	97
5.2.9	Highly Dynamic Load Power	98
5.3	Summary	100
	References	100
<b>6</b>	<b>Thermoelectric Materials for Energy Harvesting</b>	<b>103</b>
	<i>Andrew C. Miner</i>	
6.1	Introduction	103
6.2	Performance Considerations in Materials Selection: $zT$	103
6.2.1	Properties of Chalcogenides (Group 16)	106
6.2.2	Properties of Crystallogens (Group 14)	106
6.2.3	Properties of Pnictides (Group 15)	107
6.2.4	Properties of Skutterudites	108
6.3	Influence of Scale on Material Selection and Synthesis	110
6.3.1	Thermal Conductance Mismatch	111
6.3.2	Domination of Electrical Contact Resistances	112
6.3.3	Domination of Bypass Heat Flow	113
6.3.4	Challenges in Thermoelectric Property Measurement	113
6.4	Low Dimensionality: Internal Micro/Nanostructure and Related Approaches	114
6.5	Thermal Expansion and Its Role in Materials Selection	115
6.6	Raw Material Cost Considerations	116
6.7	Material Synthesis with Particular Relevance to Micro Energy Harvesting	116
6.7.1	Electroplating, Electrophoresis, Dielectrophoresis	117
6.7.2	Thin and Thick Film Deposition	118
6.8	Summary	118
	References	119
<b>7</b>	<b>Piezoelectric Materials for Energy Harvesting</b>	<b>123</b>
	<i>Emmanuel Defay, Sébastien Boisseau, and Ghislain Despesse</i>	
7.1	Introduction	123
7.2	What Is Piezoelectricity?	123
7.3	Thermodynamics: the Right Way to Describe Piezoelectricity	125
7.4	Material Figure of Merit: the Electromechanical Coupling Factor	126
7.4.1	Special Considerations for Energy Harvesting	128
7.5	Perovskite Materials	129
7.5.1	Structure	129
7.5.1.1	Ferroelectricity in Perovskites	129
7.5.1.2	Piezoelectricity in Perovskites: Poling Required	131
7.5.2	PZT Phase Diagram	131
7.5.3	Ceramics	132

7.5.3.1	Fabrication Process	132
7.5.3.2	Typical Examples for Energy Harvesting	134
7.5.4	Bulk Single Crystals	135
7.5.4.1	Perovskites	135
7.5.4.2	Energy Harvesting with Perovskites Bulk Single Crystals	135
7.5.5	Polycrystalline Perovskites Thin Films	136
7.5.5.1	Fabrication Processes	136
7.5.5.2	Energy Harvesting with Poly-PZT Films	136
7.5.6	Single-Crystal Thin Films	137
7.5.6.1	Fabrication Process	137
7.5.6.2	Energy Harvesting with SC Perovskite Films	137
7.5.7	Lead-Free	138
7.5.7.1	Energy Harvesting with Lead-Free Materials	139
7.6	Wurtzites	139
7.6.1	Structure	139
7.6.2	Thin Films and Energy Harvesting	140
7.6.3	Doping	141
7.7	PVDFs	141
7.7.1	Structure	141
7.7.2	Synthesis	143
7.7.3	Energy Harvesters with PVDF	143
7.8	Nanomaterials	143
7.9	Typical Values for the Main Piezoelectric Materials	144
7.10	Summary	145
	References	145
<b>8</b>	<b>Electrostatic/Electret-Based Harvesters</b>	<b>149</b>
	<i>Yuji Suzuki</i>	
8.1	Introduction	149
8.2	Electrostatic/Electret Conversion Cycle	149
8.3	Electrostatic/Electret Generator Models	151
8.3.1	Configuration of Electrostatic/Electret Generator	151
8.3.2	Electrode Design for Electrostatic/Electret Generator	153
8.4	Electrostatic Generators	156
8.4.1	Design and Fabrication Methods	156
8.4.2	Generator Examples	158
8.5	Electrets and Electret Generator Model	160
8.5.1	Electrets	160
8.5.2	Electret Materials	161
8.5.3	Charging Technologies	162
8.5.4	Electret Generator Model	163
8.6	Electret Generators	168
8.7	Summary	171
	References	171

<b>9</b>	<b>Electrodynamic Vibrational Energy Harvesting</b>	<b>175</b>
	<i>Shuo Cheng, Clemens Cepnik, and David P. Arnold</i>	
9.1	Introduction	175
9.2	Theoretical Background	178
9.2.1	Energy Storage, Dissipation, and Conversion	178
9.2.2	Electrodynamic Physics	179
9.2.2.1	Faraday's Law	179
9.2.2.2	Lorentz Force	180
9.2.3	Simplified Electrodynamic Equations	180
9.3	Electrodynamic Harvester Architectures	181
9.4	Modeling and Optimization	183
9.4.1	Modeling	184
9.4.1.1	Lumped Element Method	184
9.4.1.2	Finite Element Method	188
9.4.1.3	Combination of Lumped Element Model and Finite Element Model	189
9.4.2	Optimization	190
9.5	Design and Fabrication	191
9.5.1	Design of Electrodynamic Harvesters	192
9.5.2	Fabrication of Electrodynamic Harvesters	194
9.6	Summary	196
	References	197
<b>10</b>	<b>Piezoelectric MEMS Energy Harvesters</b>	<b>201</b>
	<i>Jae Yeong Park</i>	
10.1	Introduction	201
10.1.1	The General Governing Equation	202
10.1.2	Design Consideration	203
10.2	Development of Piezoelectric MEMS Energy Harvesters	204
10.2.1	Overview	204
10.2.2	Fabrication Technologies	205
10.2.3	Characterization	211
10.2.3.1	Frequency Response	211
10.2.3.2	Output Power of Piezoelectric MEMS Energy Harvesters	211
10.3	Challenging Issues in Piezoelectric MEMS Energy Harvesters	213
10.3.1	Output Power	213
10.3.2	Frequency Response	215
10.3.3	Piezoelectric Material	217
10.4	Summary	218
	References	218
<b>11</b>	<b>Vibration Energy Harvesting from Wideband and Time-Varying Frequencies</b>	<b>223</b>
	<i>Lindsay M. Miller</i>	
11.1	Introduction	223

11.1.1	Motivation	223
11.1.2	Classification of Devices	223
11.1.3	General Comments	225
11.2	Active Schemes for Tunable Resonant Devices	225
11.2.1	Stiffness Modification for Frequency Tuning	226
11.2.1.1	Modify $L$	226
11.2.1.2	Modify $E$	227
11.2.1.3	Modify $k_{\text{eff}}$ Using Axial Force	227
11.2.1.4	Modify $k_{\text{eff}}$ Using an External Spring	229
11.2.1.5	Modify $k_{\text{eff}}$ Using an Electrical External Spring	231
11.2.2	Mass Modification for Frequency Tuning	232
11.3	Passive Schemes for Tunable Resonant Devices	232
11.3.1	Modify $m_{\text{eff}}$ by Coupling Mass Position with Beam Excitation	233
11.3.2	Modify $k_{\text{eff}}$ by Coupling Axial Force with Centrifugal Force from Rotation	234
11.3.3	Modify $L$ by Using Centrifugal Force to Toggle Beam Clamp Position	234
11.4	Wideband Devices	235
11.4.1	Multimodal Designs	236
11.4.2	Nonlinear Designs	237
11.5	Summary and Future Research Directions	240
11.5.1	Summary of Tunable and Wideband Strategies	240
11.5.2	Areas for Future Improvement in Tunable and Wideband Strategies	241
11.5.2.1	Tuning range and resolution	241
11.5.2.2	Tuning sensitivity to driving vibrations	242
11.5.2.3	System Size considerations	242
	References	243
<b>12</b>	<b>Micro Thermoelectric Generators</b>	<b>245</b>
	<i>Ingo Stark</i>	
12.1	Introduction	245
12.2	Classification of Micro Thermoelectric Generators	247
12.3	General Considerations for MicroTEGs	250
12.4	Micro Device Technologies	252
12.4.1	Research and Development	253
12.4.1.1	Electrodeposition	253
12.4.1.2	Silicon-MEMS Technology	253
12.4.1.3	CMOS-MEMS Technology	254
12.4.1.4	Other	255
12.4.2	Commercialized Micro Technologies	257
12.4.2.1	Micropelt Technology	257
12.4.2.2	Nextreme/Laird Technology	258
12.4.2.3	Thermogen Technology	259
12.5	Applications of Complete Systems	260

12.5.1	Energy-Autonomous Sensor for Air Flow Temperature	261
12.5.2	Wireless Pulse Oximeter SpO <sub>2</sub> Sensor	261
12.5.3	Intelligent Thermostatic Radiator Valve (iTRV)	262
12.5.4	Wireless Power Generator Evaluation Kit	263
12.5.5	Jacket-Integrated Wireless Temperature Sensor	263
12.6	Summary	264
	References	265
<b>13</b>	<b>Micromachined Acoustic Energy Harvesters</b>	<b>271</b>
	<i>Stephen Horowitz and Mark Sheplak</i>	
13.1	Introduction	271
13.2	Historical Overview	272
13.2.1	A Brief History	272
13.2.2	Survey of Reported Performance	274
13.3	Acoustics Background	276
13.3.1	Principles and Concepts	276
13.3.2	Fundamentals of Acoustics	276
13.3.3	Challenges of Acoustic Energy Harvesting	277
13.4	Electroacoustic Transduction	277
13.4.1	Modeling	278
13.4.1.1	Lumped Element Modeling (LEM)	278
13.4.1.2	Equivalent Circuits	279
13.4.1.3	Transduction	280
13.4.1.4	Numerical Approaches	281
13.4.2	Impedance Matching and Energy Focusing	281
13.4.3	Transduction Methods	281
13.4.3.1	Piezoelectric Transduction	281
13.4.3.2	Electromagnetic Transduction	282
13.4.3.3	Electrostatic Transduction	282
13.4.3.4	Comparative Analysis	283
13.4.4	Transduction Structures	284
13.4.4.1	Structures for Impedance Matching	284
13.4.4.2	Structures for Acoustical to Mechanical Transduction	286
13.5	Fabrication Methods	288
13.5.1	Materials	288
13.5.2	Processes	289
13.6	Testing and Characterization	289
13.7	Summary	290
	Acknowledgments	290
	References	290
<b>14</b>	<b>Energy Harvesting from Fluid Flows</b>	<b>297</b>
	<i>Andrew S. Holmes</i>	
14.1	Introduction	297
14.2	Fundamental and Practical Limits	298

14.3	Miniature Wind Turbines	301
14.3.1	Scaling Effects in Miniature Wind Turbines	302
14.3.1.1	Turbine Performance	302
14.3.1.2	Generator and Bearing Losses	305
14.4	Energy Harvesters Based on Flow Instability	306
14.4.1	Vortex Shedding Devices	307
14.4.2	Devices Based on Galloping and Flutter	310
14.5	Performance Comparison	316
14.6	Summary	317
	References	317
<b>15</b>	<b>Far-Field RF Energy Transfer and Harvesting</b>	<b>321</b>
	<i>Hubregt J. Visser and Ruud Vullers</i>	
15.1	Introduction	321
15.2	Nonradiative and Radiative (Far-Field) RF Energy Transfer	322
15.2.1	Nonradiative Transfer	322
15.2.2	Radiative Transfer	323
15.2.3	Harvesting versus Transfer	324
15.3	Receiving Rectifying Antenna	326
15.3.1	Antenna–Rectifier Matching	326
15.3.1.1	Voltage Boosting Technique	327
15.3.1.2	Antenna Matched to Rectifier	328
15.3.1.3	Antenna Not Matched to the Rectifier/Multiplier	329
15.3.1.4	Consequences for the Rectifier and the Antenna Design	330
15.4	Rectifier	330
15.4.1	RF Input Impedance	331
15.4.2	DC Output Voltage	332
15.4.3	Antenna	334
15.4.3.1	50 $\Omega$ Antenna	335
15.4.3.2	Complex Conjugately Matched Antenna	335
15.4.4	Rectenna Results	336
15.4.5	Voltage Up-Conversion	339
15.5	Transmission	340
15.6	Examples and Future Perspectives	341
15.7	Conclusions	344
	References	344
<b>16</b>	<b>Microfabricated Microbial Fuel Cells</b>	<b>347</b>
	<i>Hao Ren and Junseok Chae</i>	
16.1	Introduction	347
16.2	Fundamentals of MEMS MFC	348
16.2.1	Operation Principle	348
16.2.1.1	Structure	348
16.2.1.2	Materials	350
16.2.2	Critical Parameters for Testing	350

16.2.2.1	Anode and Cathode Potential, the Total Cell Potential	350
16.2.2.2	Open Circuit Voltage ( $E_{OCV}$ )	351
16.2.2.3	Areal/Volumetric Current Density and Areal/Volumetric Power Density	351
16.2.2.4	Internal Resistance and Areal Resistivity	352
16.2.2.5	Efficiency	353
16.3	Prior Art MEMS MFCS	354
16.4	Future Work	355
16.4.1	Reducing Areal Resistivity	355
16.4.1.1	Applying Materials with High Surface-Area-to-Volume Ratio	355
16.4.1.2	Mitigating Oxygen Intrusion	358
16.4.2	Autonomous Running	359
16.4.3	Elucidating the EET Mechanism	359
	References	359
<b>17</b>	<b>Micro Photovoltaic Module Energy Harvesting</b>	<b>363</b>
	<i>Shunpu Li, Wensi Wang, Ningning Wang, Cian O'Mathuna, and Saibal Roy</i>	
17.1	Introduction	363
17.1.1	p-n Junction and Crystalline Si Solar Cells	363
17.1.2	Amorphous Silicon Solar Cell	366
17.1.3	CIGS and CdTe Solar Cell Development	367
17.1.4	Polymer Solar Cell	370
17.1.5	Dye-Sensitized Solar Cells (DSSC)	373
17.2	Monolithically Integration of Solar Cells with IC	375
17.3	Low-Power Micro Photovoltaic Systems	376
17.3.1	Maximum Power Point Tracking	376
17.3.2	Output Voltage Regulation	379
17.3.3	Indoor-Light-Powered Wireless Sensor Networks – a Case Study	380
17.4	Summary	382
	References	383
<b>18</b>	<b>Power Conditioning for Energy Harvesting – Case Studies and Commercial Products</b>	<b>385</b>
	<i>Paul D. Mitcheson and Stephen G. Burrow</i>	
18.1	Introduction	385
18.2	Submilliwatt Electromagnetic Harvester Circuit Example	386
18.3	Single-Supply Pre-biasing for Piezoelectric Harvesters	388
18.4	Ultra-Low-Power Rectifier and MPPT for Thermoelectric Harvesters	392
18.5	Frequency Tuning of an Electromagnetic Harvester	393
18.6	Examples of Converters for Ultra-Low-Output Transducers	396
18.7	Power Processing for Electrostatic Devices	397
18.8	Commercial Products	397



18.9	Conclusions	398
	References	399
<b>19</b>	<b>Micro Energy Storage: Considerations</b>	<b>401</b>
	<i>Dan Steingart</i>	
19.1	Introduction	401
19.2	Boundary Conditions	401
19.2.1	Microbatteries	404
19.2.2	Supercapacitors	405
19.3	Primary Energy Storage Approaches	405
19.3.1	Volume-Constrained versus Conformally Demanding Approaches	408
19.3.2	Caveat Emptor	409
19.3.3	Future Work and First-Order Problems	409
	References	410
<b>20</b>	<b>Thermoelectric Energy Harvesting in Aircraft</b>	<b>415</b>
	<i>Thomas Becker, Alexandros Elefsiniotis, and Michail E. Kiziroglou</i>	
20.1	Introduction	415
20.2	Aircraft Standardization	416
20.3	Autonomous Wireless Sensor Systems	417
20.4	Thermoelectric Energy Harvesting in Aircraft	419
20.4.1	Efficiency of a Thermoelectric Energy Harvesting Device	420
20.4.2	Static Thermoelectric Energy Harvester	421
20.4.3	Dynamic Thermoelectric Energy Harvester	423
20.5	Design Considerations	425
20.6	Applications	427
20.6.1	Static Thermoelectric Harvester for Aircraft Seat Sensors	427
20.6.2	The Dynamic Thermoelectric Harvesting Prototype	428
20.6.3	Heat Storage Thermoelectric Harvester for Aircraft Strain Sensors	428
20.6.4	Outlook	430
20.7	Conclusions	432
	References	433
<b>21</b>	<b>Powering Pacemakers with Heartbeat Vibrations</b>	<b>435</b>
	<i>M. Amin Karami and Daniel J. Inman</i>	
21.1	Introduction	435
21.2	Design Specifications	436
21.3	Estimation of Heartbeat Oscillations	437
21.4	Linear Energy Harvesters	438
21.5	Monostable Nonlinear Harvesters	441
21.6	Bistable Harvesters	446
21.7	Experimental Investigations	450
21.8	Heart Motion Characterization	450

21.9	Conclusions	456
	Acknowledgment	457
	References	457

	<b>Index</b>	<b>459</b>
--	--------------	------------

## About the Volume Editors



Danick Briand obtained his PhD degree in the field of microchemical systems from the Institute of Microtechnology (IMT), University of Neuchâtel, Switzerland, in 2001. He is currently a team leader at EPFL IMT Samlab in the field of EnviroMEMS, Energy and Environmental MEMS. He has been awarded the Eurosenors Fellowship in 2010. He has been author or co-author of more than 150 papers published in scientific journals and conference proceedings. He is a member of several scientific and technical conference committees in the field of sensors and MEMS, participating also in the organization of workshop and conferences. His research interests in the field of sensors and microsystems include environmental and energy MEMS.



Eric M. Yeatman has been a member of academic staff in Imperial College London since 1989 and Professor of Microengineering since 2005. He is Deputy Head of the Department of Electrical and Electronic Engineering, and has published more than 200 papers and patents, primarily on optical devices and materials and on microelectromechanical systems (MEMS). He is a Fellow and Silver Medalist of the Royal Academy of Engineering, and a Fellow of the IEEE. Prof. Yeatman is also co-founder and director of Microsaic Systems plc, which develops and markets miniature mass spectrometers for portable chemical analysis. His current research interests are in energy sources for wireless devices (particularly energy harvesting), radio frequency and photonic MEMS devices, pervasive sensing, and sensor networks.

*[www.imperial.ac.uk/people/e.yeatman](http://www.imperial.ac.uk/people/e.yeatman)*



Shad Roundy received his PhD in Mechanical Engineering from the University of California, Berkeley, in 2003. From there he moved to the Australian National University where he was a senior lecturer for 2 years. He spent the next several years working with start-up companies LV Sensors and EcoHarvester developing MEMS pressure sensors, accelerometers, gyroscopes, and energy-harvesting devices. He recently re-entered academia joining the mechanical engineering faculty at the University of Utah in 2012. Dr. Roundy is the recipient of the DoE Integrated Manufacturing Fellowship, the Intel Noyce Fellowship, and was named by *MIT Technology Review* as one of the world's top 100 young innovators for 2004. His current research interests are in harvesting energy for wireless sensors, particularly from vibrations, acoustics, and human motion, and in MEMS inertial sensing.

## List of Contributors

### ***M. Amin Karami***

University of Michigan  
 Department of Aerospace  
 Engineering  
 3064 Francois-Xavier Bagnoud  
 Building  
 1320 Beal Avenue  
 Ann Arbor, MI 48109-2140  
 USA

### ***David P. Arnold***

University of Florida  
 Department of Electrical and  
 Computer Engineering  
 213 Larsen Hall  
 Gainesville, FL 32611  
 USA

### ***Adrien Badel***

Université de Savoie  
 SYMME  
 74000 Annecy  
 France

### ***Thomas Becker***

Airbus Group Innovations  
 The Netherlands

*and*

EADS Innovation Works  
 EADS Deutschland GmbH  
 81663 Munich  
 Germany

### ***Sébastien Boisseau***

CEA-LETI  
 38054 Grenoble Cedex  
 France

### ***Danick Briand***

EPFL-IMT SAMLAB  
 Rue Jaquet-Droz 1  
 2000 NEUCHÂTEL  
 Switzerland

### ***Stephen G. Burrow***

University of Bristol  
 Faculty of Engineering  
 Queen's Building  
 Clifton BS8 1TR  
 UK

### ***Clemens Cepnik***

Robert Bosch GmbH  
 Automotive Electronics  
 Tübinger Str. 123  
 72762 Reutlingen  
 Germany

### ***Junseok Chae***

Arizona State University  
 School of Electrical  
 Computer, and Energy  
 Engineering  
 650 E. Tyler Mall  
 Tempe, AZ 85287  
 USA

***Shuo Cheng***

Stellarray Incorporated  
9210 Cameron Rd Ste 300  
Austin, TX 78754  
USA

***Emmanuel Defay***

CEA-LETI  
38054 Grenoble Cedex  
France

*and*

Luxembourg Institute of Science  
and Technology  
4422 Belvaux  
Luxembourg

***Ghislain Despesse***

CEA-LETI  
38054 Grenoble Cedex  
France

***Alexandros Elefsiniotis***

Airbus Group Innovations  
The Netherlands

***Fabien Formosa***

Université de Savoie  
SYMME  
74000 Annecy  
France

***Mathieu Francoeur***

University of Utah  
Department of Mechanical  
Engineering  
Radiative Energy Transfer Lab  
Salt Lake City, UT 84112  
USA

***Luca Gammaitoni***

University of Perugia  
INFN Perugia and Wisepower srl  
NiPS Laboratory  
Department of Physics  
via A. Pascoli, 1  
06123 Perugia  
Italy

***Andrew S. Holmes***

Imperial College  
Electrical and Electronic  
Engineering  
South Kensington Campus  
London SW7 1AZ  
UK

***Stephen Horowitz***

Interdisciplinary Consulting  
Corporation (IC2)  
5745 SW 75th St, #364  
Gainesville, FL 32608-5508  
USA

***Daniel J. Inman***

University of Michigan  
Department of Aerospace  
Engineering  
3064 Francois-Xavier Bagnoud  
Building  
1320 Beal Avenue  
Ann Arbor, MI 48109-2140  
USA

***Michail E. Kiziroglou***

Imperial College London  
South Kensington Campus  
London SW7 2AZ  
UK

**Mickaël Lallart**

LGEF INSA Lyon  
8 rue de la Physique  
69621 Villeurbanne Cedex  
France

**Shunpu Li**

University of Cambridge  
Electrical Engineering Division  
Cambridge CB3 0FA  
UK

**Lindsay M. Miller**

University of California Berkeley  
Mechanical Engineering  
Etcheverry  
Berkeley, CA 94720  
USA

**Andrew C. Miner**

Romny Scientific, Inc.  
1192 Cherry Avenue  
San Bruno, CA 94066  
USA

**Paul D. Mitcheson**

Imperial College  
Electrical and Electronic  
Engineering  
South Kensington Campus  
London SW7 1AZ  
UK

**Cian O'Mathuna**

Microsystems Group  
Tyndall National Institute  
Dyke Parade  
Cork  
Ireland

**Jae Yeong Park**

Kwangwoon University  
Department of Electronic  
Engineering  
447-1, Wolgye-Dong  
Nowon-Gu  
Seoul 139-701  
Korea

**Hao Ren**

Arizona State University  
School of Electrical  
Computer, and Energy  
Engineering  
650 E. Tyler Mall  
Tempe, AZ 85287  
USA

**Shad Roundy**

University of Utah  
Dept. of Mech. Engineering  
50 S. Central Campus Drive  
Salt Lake City, UT 84112  
USA

**Saibal Roy**

Microsystems Group  
Tyndall National Institute  
Dyke Parade  
Cork  
Ireland

**Mark Sheplak**

University of Florida  
Interdisciplinary Microsystems  
Group  
Department of Mechanical and  
Aerospace Engineering  
Department of Electrical and  
Computer Engineering  
P. O. Box 116200  
215 Larsen Hall  
Gainesville, FL 32611-6200  
USA

***Ingo Stark***

Perpetua Power Source  
Technologies, Inc.  
1749 SW Airport Avenue  
Corvallis, OR 97333  
USA

***Dan Steingart***

Princeton University  
Department of Mechanical and  
Aerospace Engineering and the  
Andlinger Center for Energy and  
The Environment  
D428 Engineering Quadrangle  
Princeton, NJ 08544  
USA

***Yuji Suzuki***

The University of Tokyo  
Department of Mechanical  
Engineering  
Hongo 7-3-1  
Bukyo-ku  
Tokyo 113-8656  
Japan

***Hubregt J. Visser***

IMEC/Holst Centre  
Sensors & Energy Harvesters  
Department  
High Tech Campus 31  
PO Box 8550  
5605 KN Eindhoven  
The Netherlands

***Helios Vocca***

University of Perugia  
INFN Perugia and Wisepower srl  
NiPS Laboratory  
Department of Physics  
via A. Pascoli, 1  
06123 Perugia  
Italy

***Ruud Vullers***

IMEC/Holst Centre  
Sensors & Energy Harvesters  
Department  
High Tech Campus 31  
PO Box 8550  
5605 KN Eindhoven  
The Netherlands

***Ningning Wang***

Microsystems Group  
Tyndall National Institute  
Dyke Parade  
Cork  
Ireland

***Wensi Wang***

Microsystems Group  
Tyndall National Institute  
Dyke Parade  
Cork  
Ireland

***Eric Yeatman***

Imperial College London  
Dep. of Electr. & Electron. Engin.  
South Kensington Campus  
London SW7 2AZ  
UK



# 1

## Introduction to Micro Energy Harvesting

*Danick Briand, Eric Yeatman, and Shad Roundy*

### 1.1

#### Introduction to the Topic

We are living in an increasingly intelligent world where countless numbers of autonomous wireless sensing devices continuously monitor, provide information on, and manipulate the environments in which we live. This trend is growing fast and will undoubtedly continue. The vision of this intelligent world has gone by many names including “wireless sensor networks,” “ambient intelligence,” and, more recently, “the Internet of Things (IoT).” Regardless of the current buzzwords, this vision will continue to take shape. We are now realistically talking about a trillion or more connected sensors populating the world. Almost all of these wireless connected devices are currently powered by batteries that have to be periodically recharged or replaced. This state of affairs is simply not practical if we are to have many hundreds of sensors per person on the planet. Alternative autonomous power supplies are becoming more and more critical. Furthermore, these power sources must be small, inexpensive, and highly reliable. This need has given rise to a new field of research, study, and engineering practice, usually referred to as Energy Harvesting. This book is intended to cover the engineering fundamentals and current state of the art associated with energy harvesting at the small scale, or Micro Energy Harvesting.

The term “Energy Harvesting” usually refers to devices or systems that capture (or harvest) ambient energy in the environment and convert it into a useful form, which is usually electricity. Large-scale renewable power generation such as solar arrays, wind farms, and ocean wave generators can be considered forms of energy harvesting. However, for the purposes of this book, we define the term somewhat more narrowly. We define energy harvesting as technologies, devices, and systems that capture ambient energy to replace or augment the batteries in wireless devices. The title of this book is “*Micro Energy Harvesting*”. In the energy harvesting literature, the word “micro” sometimes refers to different aspects of the system. The first is the power level. Micro energy harvesting systems generally produce power best described by microwatts, usually 10–100s of microwatts. Sometimes, “micro” refers to the scale of the energy harvesting device, that is,

micrometers. While the overall dimensions of micro energy harvesters are usually in the millimeter or centimeter range, the key features of the transducers are usually microscale. Finally, “micro” sometimes refers more to the fabrication method, using highly parallel fabrication techniques common to the semiconductor and MEMS industries. While many of the techniques covered in this book can be applied across different size scales, we are generally concerned with energy harvesters that can be mass produced at microscales using microfabrication techniques. In practice, some of the devices will be macroscale devices that are moving toward microscale implementations.

Micro energy harvesting covers a broad range of technologies and relies on quite a broad range of fundamental science. A typical engineer or scientist working in the field will most likely be an expert in only a few areas. However, in order to make good engineering decisions, it is important to be well grounded in the entire breadth of the field. This book is intended, in part, to provide a solid foundation in a broad range of technologies that comprise the field of micro energy harvesting.

An energy harvesting system is comprised of four different components as depicted in Figure 1.1. Some form of environmental energy is available (e.g., thermal, solar, vibration, RF, wind). A device or subsystem captures that energy and presents it to an energy converting transducer (e.g., thermoelectric stack, piezoelectric element, photovoltaic cell). In some systems, such as most PV systems, the capture device and transducer are one element. The transducer outputs an electrical current. This current can be unpredictable and requires conditioning before being stored or used by an electronic load. The role of the power electronics is not only to condition the signal for use but also to optimize the power flow from the transducer.

Let’s use a vibration energy harvester as a simple example. The capture mechanism is usually a mechanical oscillator of some sort. This oscillator may be a simple linear oscillator or may have more complex modes and/or nonlinearities. The proof mass of this oscillator transfers the energy from the environmental vibrations to a transducer. If the transducer is a piezoelectric element, it will usually form part of the spring and will create some of the damping that characterizes the behavior of the mechanical oscillator. The output of the piezoelectric device will be a high-impedance AC voltage of unpredictable magnitude. The power electronics must condition this output to a stable DC voltage. However, the power electronics also play a role in influencing the power flow from the transducer, which can affect the apparent level of damping and even the natural oscillation frequency of

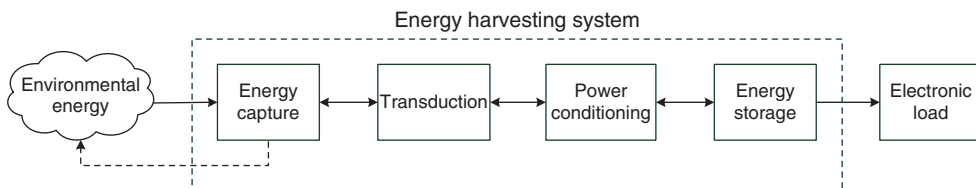


Figure 1.1 General energy harvesting system architecture.

the oscillator. Thus, the arrows shown in Figure 1.1 are bidirectional to indicate that each component of the harvesting system affects the upstream components. While not usually the case, the harvester can even affect the environment in some situations. For example, if the energy harvester is large enough compared to the vibrating body to which it is coupled, it can actually affect the incoming vibrations. A similar breakdown of other types of harvesters could also be made. It is important to recognize that a well-performing harvester needs to be designed with the entire system in mind.

The block diagram of Figure 1.1 is similar to that of a sensor or detector, and, indeed, energy harvesters share many characteristics with these, including the transduction methods employed. However, there are also important differences. In sensor and detector systems, additional power is typically added to the signal at the first stage of conditioning (e.g., in amplification) in order to reduce degradation of the signal fidelity (e.g., by additive noise) in subsequent stages, and this power level is often much larger than that of the received signal. In an energy harvester, of course, any added power for signal conditioning and control functions must be minimized and constitutes a penalty against the power harvested. On the other hand, there is no need to preserve the received waveform characteristics. Within these different constraints, both harvesting and detection/sensing systems generally aim at maximizing the power extracted from the source.

## 1.2

### Current Status and Trends

Of the main types of energy harvesting for small-scale applications, solar (or photovoltaic (PV)) cells are the most mature and long established, with devices such as PV-powered pocket calculators having been available for over 30 years. Further PV development in the last few decades has focused on conversion efficiency and cost, the latter being particularly critical in large-scale applications. Major advances have been made in these metrics. Another area of PV research is the development of devices based on organic materials, which are enabling new integration possibilities such as flexible substrates. Thermoelectric devices for power generation are also long established, but less extensively commercialized than PV systems, although this is beginning to change. In recent years, major research efforts have been witnessed in this field, using a wide range of materials systems, with a strong emphasis on increasing conversion efficiency, but with developments in size, weight and cost reduction, and use of more sustainable materials as well. Nanostructured materials have shown particular promise in recent years for increasing efficiency.

Motion-based energy harvesting has seen major international research efforts for the past 10–15 years, with particular emphasis on inertial devices, that is, devices that extract power from the relative motion of an internal proof mass. The fundamental theory is now well established, and recent developments have concentrated on improved conversion circuits, broadband operation, and application-specific implementations. Some commercial devices have been launched, and this

looks set to be a growing business opportunity. Devices based on fluid flow, such as microturbines, have also made impressive advances. A further harvesting method that is attracting attention is the extraction of power from human-made radiation, that is, radio signals from various systems such as cellular communications, WiFi, and others. With the increasing use of wireless communications, opportunities for radio frequency harvesting are growing. One key challenge, as also found in some motion harvesting methods, is to produce DC power from AC sources with voltages below those required for conventional rectification. Promising advances are being made in tackling this problem. Among other harvesting methods, fuel cells using biological sources are also attracting interest.

As discussed above, a key driver for small-scale energy harvesting is the proliferation of electronic devices, particularly sensors, which are not connected to mains power. This includes mobile devices, but also fixed devices where mains connection would be impractical or involve excessive installation costs. Because in most such applications, harvesters will be considered an alternative to batteries, for large-scale adoption they will need to be an attractive alternative. This means they must provide their theoretical promise of perpetual, maintenance-free power by having long lifetimes and high reliability. They must also be competitive on size and cost. An important challenge to achieving low cost is that harvesters tend to need to be designed with specific applications in mind, and so they do not achieve the economies of scale in production that batteries do. Thus, identifying high-volume applications, or harvesters suitable for wide ranges of application without customization, will be critical aims in coming years. On the other hand, the power requirements of key electronic functions, including computation and wireless communication, continue to drop, so the further growth of both the number of wireless devices and the opportunities for micro energy harvesters can be predicted with confidence.

### 1.3

#### **Book Content and Structure**

Micro energy harvesting covers a broad range of technologies and relies on quite a broad range of fundamental science. A typical engineer or scientist working in the field will most likely be an expert in only a few areas. However, in order to make good engineering decisions, it is important to be well grounded in the entire breadth of the field. This book is intended, in part, to provide a solid foundation in the broad range of technologies that comprise the field of micro energy harvesting, and in another part, to cover the state of the art and trends in the field. We consider the book to be valuable for engineers who would like to get an introduction to the topic. Moreover, its structure and large coverage of the topic are intended to support graduate courses and lectures. The book would also be an excellent reference to early stage researchers who consider to research in this field or to apply part of the knowledge and technology available to their research. The topic of energy harvesting is broad. So, hopefully there is something valuable to learn here for readers from diverse backgrounds. We believe that the content of this book is sufficiently

broad, yet detailed and deep enough that even those readers who are familiar with the topic will profit from reading and studying its contents.

This book covers fundamentals and devices for harvesting energy from vibrations, fluid flow, acoustics, heat, light, RF radiation, and chemicals. An emphasis is especially given on the topics of kinetic and thermal energy harvesting for which microscale technologies have been readily developed. In addition, it covers topics applicable to any energy source, such as power electronics, and micro energy storage devices, and it gives some insights into few selected applications and the trends in the field. These topics are divided into three specific sections: Fundamentals and Theory, Materials and Devices, and Systems and Applications. The section on Fundamentals addresses all the aspects related to the basics and theory of power electronics as well as micro harvesting from thermal and mechanical energy, such as heat transfer, thermophotovoltaics, mechanics and dynamics, and transduction principles. In the section on Materials and Devices, thermoelectric and piezoelectric materials and harvesting devices are thoroughly reviewed in a set of chapters. The topic of vibration energy harvesting also includes chapters on electrostatic, electromagnetic, and wideband energy harvesters. These are also complemented by contributions on fluid flow and acoustics energy harvesting. This section is finally completed with chapters on harvesting energy from RF radiation, light and chemical energy sources, addressing rectennas, solar cells and microbial fuel cells, respectively. In the last section on Systems and Applications, electronics for energy conversion and power management as well as energy storage devices are addressed. Applicative chapters focusing on kinetic and heat energy harvesting are concluding the book.

Finally, we would like to take the opportunity to warmly thank all the authors who contributed with an outstanding chapter in their field of expertise, which, by their quality, will hopefully make this book become a standard reference in the field.



## 2

# Fundamentals of Mechanics and Dynamics

*Helios Vocca and Luca Gammaitoni*

### 2.1

#### Introduction

Among various sources of renewable energy present in the environment such, as solar, radio frequency (RF), temperature difference, and biochemical, kinetic energy in the form of mechanical vibrations is deemed to be the most attractive, in the microscale domain because of its power density, versatility, and abundance [1]. This type of energy source is ubiquitous indeed. Vibrations potentially suitable for energy harvesting can be found in numerous aspects of human experience, including natural events (seismic motion, wind, water tides), common household goods (fridges, fans, washing machines, microwave ovens, etc.), industrial plant equipment, moving structures such as automobiles and airplanes, and structures such as buildings and bridges. In addition, human and animal bodies are considered interesting sites for vibration harvesting. The amount of available power clearly varies significantly from one source to the other.

On the other hand, the power consumption of wireless sensors has been largely reduced in the last years thanks to the ultra-low-power electronics [2]. Typical power needs of mobile devices can range from a few microwatts for wristwatches, RFID, MEMS (micro-electro-mechanical system) sensors, and actuators up to hundreds of milliwatts for MP3, mobile phone, and GPS applications. They are usually in a sleep state for 99.9% of their operation time, waking up for a few milliseconds only to communicate data. Consequently, their average power consumption has been reduced to below  $10\ \mu\text{W}$  in order to match the power density capability of current generators ( $100\text{--}300\ \mu\text{W cm}^{-3}$ ). For comparison, a lithium battery can provide  $30\ \mu\text{W cc}^{-1}$  for 1 year or  $30\ \text{mW cc}^{-1}$  for just 10 h, while a vibration-driven generator could last for at least 50 years with the same power level [3]. Along with virtually infinite operational life, many other benefits come from motion-driven energy harvesting: no chemical disposal, zero wiring cost, maintenance-free, no charging points, capability for deployment in dangerous and inaccessible sites, low cost of retrofitting, inherent safety, and high reliability.

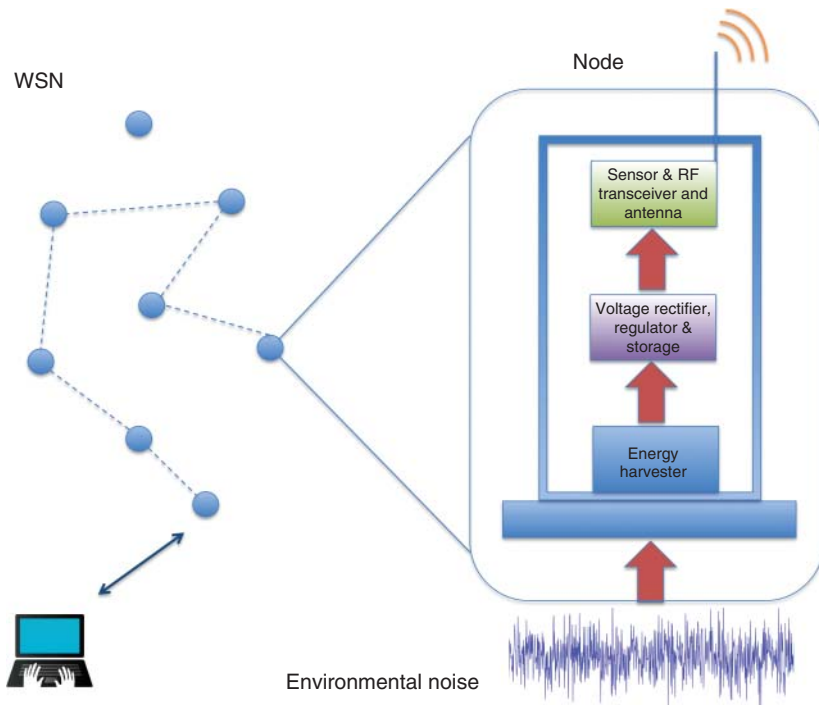


**Figure 2.1** A wireless sensor network made by vibration-driven wireless nodes. Inset: schematic of the power management in the node.

A typical application for microscale vibration harvesting is represented by integrated vibration-powered wireless sensor nodes. This includes an embedded vibration energy harvester (VEH), multiple-sensor module, microcontroller, and a transceiver for communication (Figure 2.1).

The VEH module is often tailored for the specific application and vibration spectrum of the source: harmonic excitation, random noise, or pulsed movement.

In the following, we will address the various aspects of micro vibration energy harvesting.

## 2.2

### Strategies for Micro Vibration Energy Harvesting

An important question that must be addressed by any energy harvesting technology is related to the characteristics of the vibrational energy available. As a matter of fact, kinetic energy harvesting requires a transduction mechanism to generate electrical energy from motion and the generator requires a mechanical system that couples environmental displacements to the transduction mechanism. The



design of the mechanical system is realized with the aim of maximizing the coupling between the kinetic energy source and the transduction mechanism and depends entirely upon the characteristics of the kinetic energy source under consideration.

At micro- and nanoscale, kinetic energy is usually available as random vibrations or displacement noise. In order to explore the wide panorama of available vibrations, our laboratory has started the construction of a general database of ambient vibrations [4]. In this database, one can find a vast variety of vibration sources [5]. All these different sources produce vibrations that vary largely in amplitude and spectral characteristics. Generally speaking, the human motion is classified among the high-amplitude/low-frequency sources. An interesting limiting case of small-scale kinetic energy is represented by the thermal fluctuations at micro- and nanoscale. This very special environment represents also an important link between the two most promising sources of energy at the nanoscale: thermal gradients and thermal nonequilibrium fluctuations [3].

A second aspect that is no less important is associated with the available physical principles for energy transduction. In fact, there are three main categories of kinetic-to-electrical energy conversion systems: piezoelectric, electromagnetic, and electrostatic. In addition, there is the magnetostrictive branch as a variant of piezoelectric except for the use of magnetically polarized materials [6]. Each technique presents advantages and drawbacks and the optimal choice depends on the spectral characteristics of the available vibrations and the specific application.

### 2.2.1

#### Piezoelectric

The direct piezoelectric effect was discovered in 1880 by Jacques and Pierre Curie. This is a phenomenon where an electric charge is generated within a material in response to applied mechanical stress (Figure 2.2b). The strain and coupling coefficients in the fundamental piezoelectric equations are in general higher in 33 mode than in 31 (Figure 2.2a) [7]. The 33 mode of bulk crystal corresponds to very high natural frequencies ( $\sim 1$  to 100 kHz), while longitudinal strain is easily produced within a cantilever beam that resonates at lower frequencies ( $\sim 100$  Hz) (Figure 2.2c). Typical piezoelectric materials are barium titanate ( $\text{BaTiO}_3$ ), zinc oxide ( $\text{ZnO}$ ), and lead zirconate titanate ( $\text{Pb}[\text{Zr}_x\text{Ti}_{1-x}]\text{O}_3$ ) or PZT, considered one of the best candidates because it shows an high electromechanical coupling.

Piezoelectric systems are good candidates for small-scale vibration harvesters although the coupling strength decreases very fast at micrometric scale and relatively large load impedances are required to reach the optimal working point [8]. Other drawbacks are represented by aging phenomena that imply depolarization and brittleness. For low-frequency applications, such as those related to wearable sensors, polymer-based materials (e.g., dielectric elastomers) constitute a valid alternative to ceramics because of their flexibility, inexpensiveness, and durability

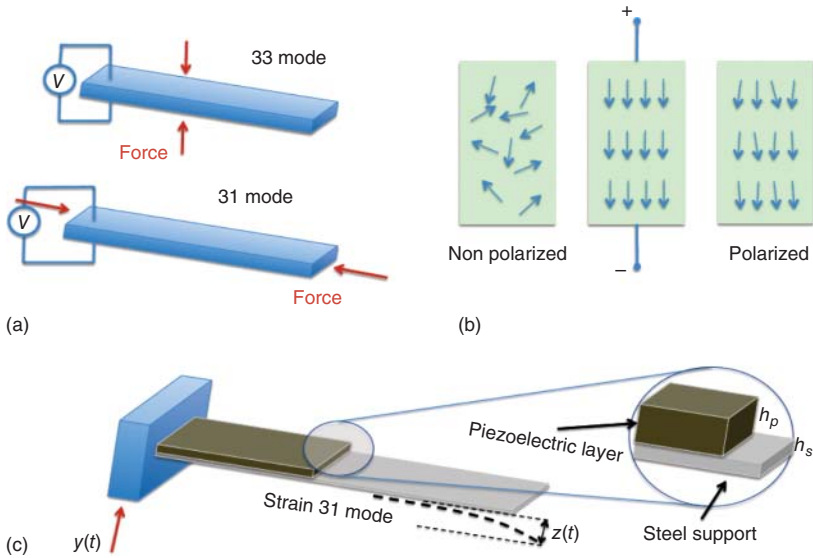


**Figure 2.2** Piezoelectric effect in a beam. (a) 33 and 31 modes that couple strain to charge generation. (b) Piezoelectric principle: microscopic polarization process scheme. (c) Drawing of bimorph piezoelectric cantilever beam.

[9]. Piezoelectric materials and harvesting devices are reviewed in more detail in Chapters 13 and 5 respectively.

### 2.2.2

#### Electromagnetic

The electromagnetic harvester is based on the *electromagnetic induction* phenomena, that is, the production of a voltage across a conductor when it is exposed to a varying magnetic field. The inductive technique is usually realized by coupling a permanent magnet and a solenoid in motion relative to each other (Figure 2.3). These systems show complementary behavior in terms of frequency

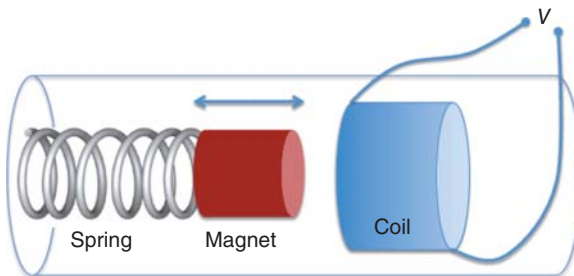


**Figure 2.3** Basic scheme of an electromagnetic vibration harvester where a moving magnet oscillates with respect to a fixed coil.

bandwidth and optimal load in relation to piezoelectric techniques. They are recommended for low frequencies (2–20 Hz), small impedance, and medium size [10]. Drawbacks are represented by the difficulties in the integration of electromagnetic harvesters into MEMSs [11–13]. Electromagnetic harvesting devices are reviewed in more detail in Chapter 2.

### 2.2.3

#### Electrostatic

Electrostatic harvesters are based on the principle of variable capacitance. The voltage across a capacitor changes with the capacitance. This is usually accomplished by keeping one plate fixed, while the other is attached to an oscillating mass. The change in the capacitance is realized by varying either the distance or the overlap between the plates. The first occurrence is usually addressed as an in-plane gap-closing converter, while the second case represents an overlap-varying converter. The most relevant drawback of the electrostatic harvester is represented by the necessity for an external voltage source to charge the plates [12, 13]. Some designs overcome this problem by using electrets to provide the precharge bias voltage [14, 15]. On the other hand, electrostatic technology is very well suited for MEMS manufacturing as it employs the same technology behind micro-accelerometers [16–18]. In comparison with the two previous techniques (piezoelectric and electromagnetic), the power generated by an electrostatic energy harvester is significantly smaller [4, 19]. Electrostatic harvesting devices are reviewed in more detail in Chapter 11.

### 2.2.4

#### From Macro to Micro to Nano

Nowadays, VEHs are commercially available from a number of companies such as Perpetuum Ltd, Ferro Solution, Mide Vulture, and Wisepower srl. All the products however are larger than a few centimeters and show a power density that ranges from 10 to 300  $\mu\text{W cc}^{-1}$  relative to acceleration levels of 0.01–1 g rms. On-going research studies at universities and research institutes have demonstrated prototypes of MEMS-based harvesters; however, they are still at a prototypal stage. Beeby *et al.* have implemented a vibration-powered wireless sensor node with embedded micro-electromagnetic generator [11]. Millimeter-sized electrostatic generators were formerly proposed by Roundy *et al.* [20]. Miao implemented a parametric generator for biomedical applications [21] and examples of piezoelectric nanomechanical generators are also emerging [22]. Paracha and Basset have successfully built and tested an efficient MEMS-based electrostatic harvester [17, 23]. Improved versions with wideband feature have also been recently demonstrated [18, 24].

On the nanoscale side, results have been reported in the framework of the EC-funded project NANOPOWER [25] where piezoelectric nano-membranes [26] have been investigated (Figure 2.4). Furthermore, nanowire-powered

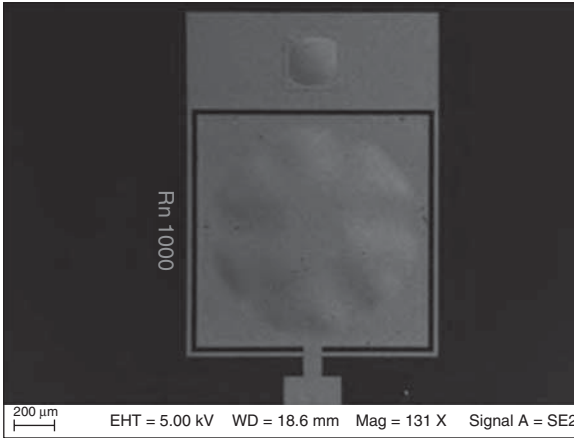


**Figure 2.4** Piezoelectric vibrational membrane harvester based on freestanding Mo–AlN–Mo film stack (100 nm thick). The membrane is produced by VTT Technical Research Centre of Finland. Picture: courtesy of LUNA, University of Perugia.

vibration harvesters that exploit the triboelectric effect have been recently proposed [27].

### 2.3

#### Dynamical Models for Vibration Energy Harvesters

In this section, we discuss the dynamical description of vibration harvesters. This is largely independent of the transduction technique and specific cases are discussed in the following. Under a general perspective, VEHS can be organized into two main classes: those that utilize direct application of force (Figure 2.5a) and those that make use of the inertial force associated to a moving mass  $m$  (Figure 2.5b). For micro-harvesting the class of inertial harvesters is geometrically more viable because they only need one point of attachment to a vibrating structure.

We will adopt the following notation:  $F(t)$  is the driving force (in the inertial case is equal to  $-m\ddot{y}$ ), the vibrations are represented as  $y(t)$  and over-dot stands for the derivative with respect to time.  $z(t)$  is the relative motion between the reference frame and proof mass,  $U(z)$  is the potential energy that reduces to  $\frac{1}{2}kz^2$  when the system is linear ( $k$  is the spring stiffness).  $d$  is the parasitic damping,  $f_e$  represents the electrical restoring force due to the transduction mechanism.  $R_L$  is the electrical resistive load through which flows the generated current  $i$ .

According to the model proposed by Williams and Yates [28], the conversion force  $f_e$  is considered an electrical damping force proportional to the velocity  $f_e = -d_e\dot{z}$ , thus mimicking a viscous damping effect. However, the electrical restoring force can in general be a complex function of the mass displacement, velocity, and acceleration. In addition, such an approximation does not take

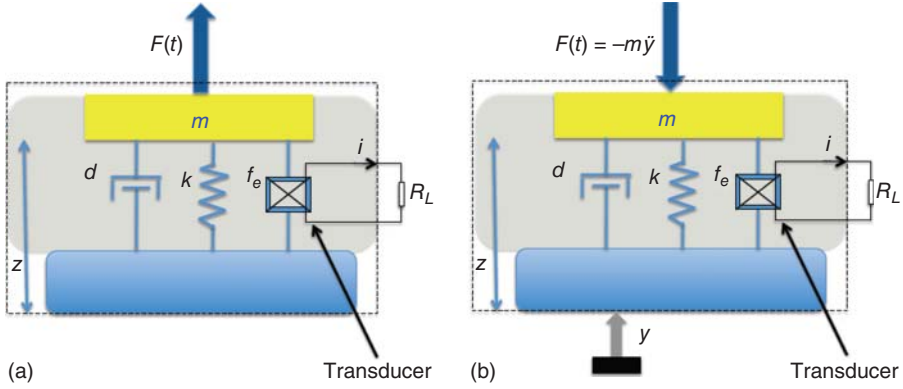


**Figure 2.5** Dynamical model of vibration harvesters: (a) direct force and (b) inertial force.

into account the effect of the electrical branch coupled to the mechanical system.

In the following, we describe the lumped parameters model of the vibration harvester by including the electrical domain as sketched in Figure 2.5b. This can be then applied to different types of conversion systems. The coupled governing equations of a generic single degree of freedom vibration-driven generator are derived from the second Newton's law and Kirchhoff's law as follows:

$$m\ddot{z} + d\dot{z} + \frac{dU(z)}{dz} + \alpha V = -m\ddot{y}, \quad (2.1)$$

$$\dot{V} + (\omega_c + \omega_i)V = \omega_c \lambda \cdot z, \quad (2.2)$$

Equation (2.1) describes the dynamics of the inertial mass and Eq. (2.2) accounts for the coupled electrical circuit.  $V$  is the voltage produced across the electrical resistance, and  $\alpha$  is the electromechanical coupling factor;  $\omega_c$  represents the characteristic cutoff frequencies of the electrical circuit of the system operating as high-pass filter due to the specific transduction technique. This parameter is the inverse to the characteristic time  $\tau$  of the electrical branch, that is  $\omega_c = 1/\tau$ .  $\omega_i$  has the same meaning but corresponds to the internal resistance  $R_i$  of the system. Finally,  $\lambda$  is the electromechanical conversion factor. These characteristic parameters are derived from the harvester design depending on the specific conversion method and architecture as explained in the following examples. In the rest of this paragraph we will focus on the linear case. This is characterized by

$$U(z) = \frac{1}{2}kz^2 \quad (2.3)$$

Moreover, we will only treat here the piezoelectric and electromagnetic cases, as the electrostatic case is inherently nonlinear when considering the electrical force between close electrostatic plates.

## 2.3.1

**Stochastic Character of Ambient Vibrations**

The vibrational force that acts on the harvester is represented in Eq. (2.1) by the quantity  $-m\ddot{y}$  where  $\ddot{y}$  represents the vibration acceleration. In Figure 2.6 we show a real time series of the quantity  $\ddot{y}(t)$  (in arbitrary units) taken from a car hood with an accelerometer. What is apparent from this time series is the random character of the vibrational force.

In general, this is a stochastic quantity due to the random character of most, if not all, practically available vibrations and the set of equations becomes a stochastic differential equation set, also known as the *Langevin equation* set, by the name of the French physicist who introduced it in 1908 in order to describe Brownian motion. By the moment that the force term is random, the solution of this equation can be attained only in statistical terms, provided we have information on the statistical quantities that characterize the stochastic force, such as momenta and probability densities. In general, the treatment of stochastic differential equations requires the methods of the theory of stochastic processes [29]. In what follows, the relevant quantities of interest, such as the harvester electric power, have to be taken as averages of the respective quantities obtained by time averaging the solutions of the dynamic equations.

## 2.3.2

**Linear Case 1: Piezoelectric Cantilever Generator**

Equations (2.1) and (2.2) have parameters such as  $\alpha, \lambda, \dots$  that need to be specified according to the physical principles involved in the transduction mechanism. For bimorph piezoelectric cantilevers such as the one shown in Figure 2.2, with active layers wired in parallel, the characteristic parameters are

$$\alpha = kd_{31}/h_p k_2, \quad \lambda = \alpha R_L, \quad \omega_c = 1/R_L C_p, \quad \omega_i = 1/R_i C_p$$

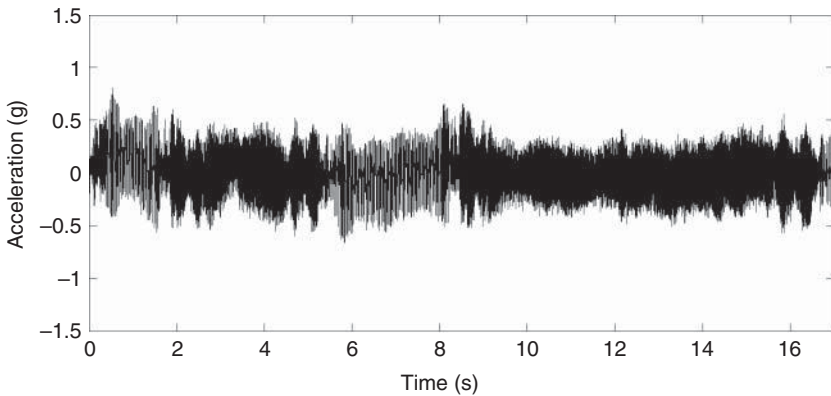


**Figure 2.6** Acceleration time series from a car hood during urban motion.

where  $h_p$  and  $h_s$  are the thickness of piezoelectric and support layer respectively;  $d_{31}$ ,  $E_p$ ,  $\epsilon_o$ ,  $\epsilon_r$ , and  $C_p$  are respectively piezoelectric strain factor, Young's modulus, vacuum, and relative dielectric permittivity, and equivalent capacitance of piezoelectric beam which is equal to half the capacitance of a single piezoelectric layer in case of series connection. These constants can be connected to the system structural parameters [26]. Usually, the internal resistance  $R_i$  of a piezoelectric crystal is very high, hence  $\omega_i$  is negligible.

### 2.3.3

#### Linear Case 2: Electromagnetic Generator

For the simple "magnet in-line coil" electromagnetic generator configuration shown schematically in Figure 2.3, the characteristic parameters are

$$\alpha = Bl/R_L, \quad \lambda = Bl = \alpha R_L, \quad \omega_c = R_L/L_e, \quad \omega_i = R_i/L_e,$$

with  $B$  representing the magnetic field across a coil of length  $l$  and self-inductance  $L_e$ . As before, by assuming an internal resistance of the coil  $R_i$  to be small with respect to the external load ( $R_o \ll R_L$ ),  $\omega_i$  becomes negligible.

### 2.3.4

#### Transfer Function

According to the linear response theory principles, we write in the spectral domain the governing equation our dynamic system (2.1) and (2.2) as

$$\begin{pmatrix} ms^2 + ds + k & \alpha \\ -\lambda\omega_c s & s + \omega_c \end{pmatrix} \begin{pmatrix} Z \\ V \end{pmatrix} = \begin{pmatrix} -mY \\ 0 \end{pmatrix} \quad (2.4)$$

where  $s = j\omega$  and we have taken the Laplace transform ( $j$  being the imaginary unit). The functions  $Y(s)$ ,  $Z(s)$ , and  $V(s)$  are the acceleration amplitude, mass displacement, and output voltage *transforms*. The  $2 \times 2$  matrix on the left side,  $A$ , is the generalized impedance. The system solution provides

$$Z(s) = \frac{-mY}{\det A} (s + \omega_c) = \frac{-mY \cdot (s + \omega_c)}{ms^3 + (m\omega_c + d)s^2 + (k + \alpha\lambda\omega_c + d\omega_c)s + k\omega_c} \quad (2.5)$$

$$V(s) = \frac{-mY}{\det A} \lambda\omega_c s = \frac{-mY \cdot \lambda\omega_c s}{ms^3 + (m\omega_c + d)s^2 + (k + \alpha\lambda\omega_c + d\omega_c)s + k\omega_c}. \quad (2.6)$$

Accordingly, the transfer functions between displacement and voltage over input acceleration are given by

$$H_{ZY}(s) = \frac{Z}{Y} \quad (2.7)$$

$$H_{VY}(s) = \frac{V}{Y} \quad (2.8)$$

By substituting  $s = j\omega$  in Eq. (2.6), we obtain the electrical power across the resistive load as

$$P_e(\omega) = \frac{|V(j\omega)|^2}{2R_L} = \frac{Y_0^2}{2R_L} \left| \frac{-\lambda\omega_j\omega}{(\omega_c + j\omega)(\omega_n^2 - \omega^2 + 2\zeta\omega_n j\omega) + \alpha\lambda\omega_j\omega/m} \right|^2 \quad (2.9)$$

where we have used  $\omega_n = \sqrt{k/m}$  and the normalized damping factor  $\zeta = d/2m\omega_n$ . As expected, for the underdamped oscillator, the electrical power peaks at the resonance frequency  $\omega = \omega_n$ . As a consequence, the linear oscillator approach performs well when the vibration acceleration spectrum is concentrated around the system resonance frequency, while it performs poorly when far from it, as in most cases, on ambient vibrations. Most importantly, at microscale, the typical resonance frequencies of mechanical oscillatory systems are characterized by values that easily exceed a few kilohertz, making the harvesting of low-frequency ambient vibrations difficult.

## 2.4 Beyond Linear Micro-Vibration Harvesting

As we have discussed [4], ambient vibrations come in the form of random, that is, broad spectrum signals. For this class of driving forces, the linear harvester, characterized by a sharp frequency response at the resonance frequency, is not the ideal solution. Various strategies have been investigated to overcome this difficulty and increase the bandwidth of vibration-based harvesters [19, 30]. Among these “resonance frequency tuning,” “multimodal oscillators,” and “frequency up-conversion” are the most common.

### 2.4.1 Frequency Tuning

The main idea behind frequency tuning is the adjustment of some of the oscillator parameters in order to change the resonance frequency to move it closer to where the vibration spectrum is higher [31]. There are two possible approaches to this task: external tuning and on-board tuning. External tuning requires an occasional intervention where some energy is spent from outside the harvester in order to tune the system parameters. The active mode is more power demanding because a continuous power is needed to tune the system. In this case, the energy is usually provided by the harvester itself.

The tuning mechanisms can be realized using springs or screws, with magnets, or using a piezoelectric material, and are aimed at changing the system stiffness and/or the mass distribution. Examples in the literature cover mechanical [32], magnetic [33], and piezoelectric [34] actuators to mention the most common. The advantage of frequency tuning is apparent when the driving vibration is characterized by sharp spectral peaks that tend to move with time.



## 2.4.2

**Multimodal Harvesting**

Multimodal harvesting is based on the exploitation of a simple combination of different oscillators, each characterized by its own resonance frequency. In this way, useful power can be harvested over broadband vibration spectra, by using the resonance window of each oscillator. In the literature, piezoelectric cantilever arrays with various lengths and tip masses [35] and the same cantilevers with different tip masses [36] have been presented (Figure 2.7).

In [37], a hybrid scenario is presented by Tadesse *et al.* The harvester consists of a cantilever beam with piezoelectric crystal plates bonded on it at a fixed distance from each other; a permanent magnet is attached at the cantilever tip oscillating within a coil fixed to the housing structure. In this configuration, the electromagnetic transducer generates high output power at the cantilever's first mode (at 20 Hz), while the piezoelectric transducer generates higher power at the cantilever's second mode (at 300 Hz). The combination of the two schemes in one device is able to significantly improve the harvester response covering two frequency ranges. The drawback of this solution is the difficulty in combining the output power from two different mechanisms, thus requiring two separate converting circuits. As a matter of fact, the multimodal approach increases the bandwidth, increasing the volume or the weight of the harvester, thus reducing the energy density.

## 2.4.3

**Up-Conversion Techniques**

As we have observed in many practical situations, the ambient vibrations suitable for energy harvesting have an energy content that is mainly present in the low-frequency range, that is, below a few hundred hertz. On the other hand, as we noticed, micro-energy harvester oscillators tend to have their

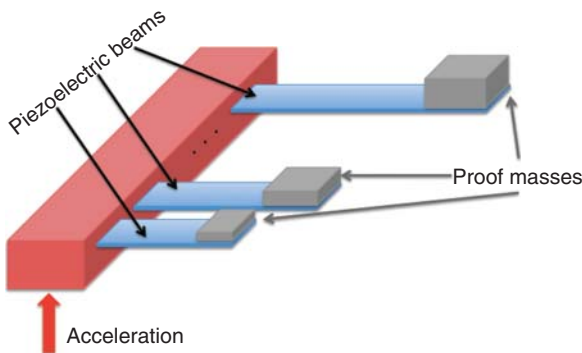


**Figure 2.7** Simple scheme of multimode harvester realized with multiple oscillators of different lengths and tip masses.

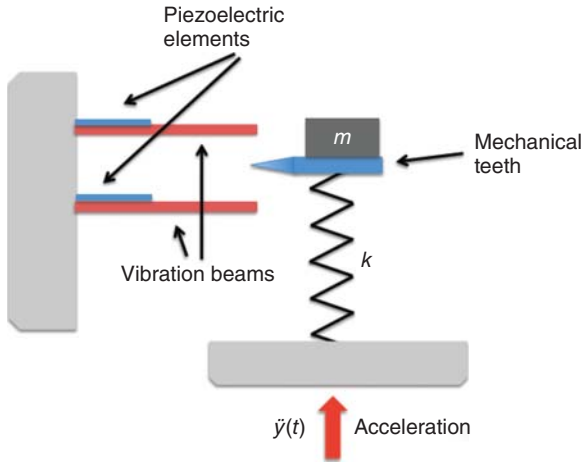


**Figure 2.8** Schematic of an up-conversion mechanism.

resonance frequency in a range of frequencies much higher than these. The idea behind up-conversion techniques is to operate in order to transform the input vibrations so that the low-frequency energy content is transferred to higher frequencies, possibly in the range of the resonance frequencies available in the harvester.

Figure 2.8 presents a possible up-conversion scheme: the oscillator with elastic constant  $k$  has a resonant frequency in a lower region with respect to the resonant frequencies of the piezoelectric cantilevers (left). When the tooth hits the cantilever tips, they start to oscillate at their natural frequency. Thus the low-frequency vibration of the primary vibrating unit (i.e., the oscillating mass  $m$ ) is transferred to the high-frequency vibration of the secondary units (i.e., the piezoelectric cantilevers).

This frequency up-conversion principle has been realized in different implementations [38]. Most often, the main drawback is that the “first unit” resonance frequency needs to be tuned to the main frequency of the vibration source: this is of little use when the vibration frequency spectrum is very broad.

## 2.5 Nonlinear Micro-Vibration Energy Harvesting

All the above-mentioned strategies to harvest vibration energy from the environment belong to the category of harvesting techniques based on the use of linear oscillators. As we have discussed, the linear oscillator system presents some limitations that prevent its wide applicability. The following are the two most important limitations:

- 1) The frequency spectrum of available vibrations instead of being sharply peaked at some frequency is usually very broad compared to the narrow band of the linear oscillator transfer function.
- 2) The frequency spectrum of available vibrations is particularly rich in energy in the low-frequency range, and it is very difficult, if not impossible, to build small, low-frequency resonant systems.

On the basis of these considerations, we are now interested in exploring nonresonant, that is, nonlinear oscillators in order to inspect their dynamical behavior and see if the limitations shown by linear systems can be somehow overcome by their implementation as VEHs.

The starting point is still represented by Eqs. (2.1) and (2.2). As before,  $U(z)$  plays the role of dynamical energy storage facility (before transduction) for our mechanical oscillator and thus it is here that we should focus our attention. A nonlinear oscillator is characterized by the condition

$$U(z) \neq \frac{1}{2}kz^2 \quad (2.10)$$

indicating that the potential energy of the oscillator is not quadratically dependent on the relevant displacement variable. In recent years, few possible candidates have been explored [39–46].

In the following section, two of these nonlinear potential cases will be briefly addressed: bistable oscillators and monostable oscillators.

### 2.5.1

#### Bistable Oscillators: Cantilever

The first case studied in the literature for nonlinear energy harvesting [39] was represented by a bistable potential. This was considered a good candidate example for illustrating the potential advantages of nonlinear versus linear oscillators. This can be realized with a slightly modified version of the vibration harvester cantilever analyzed above (Figure 2.9).

This is a common piezoelectric cantilever with a small magnet added to the tip of the beam. The dynamics of the oscillator is controlled with the introduction of

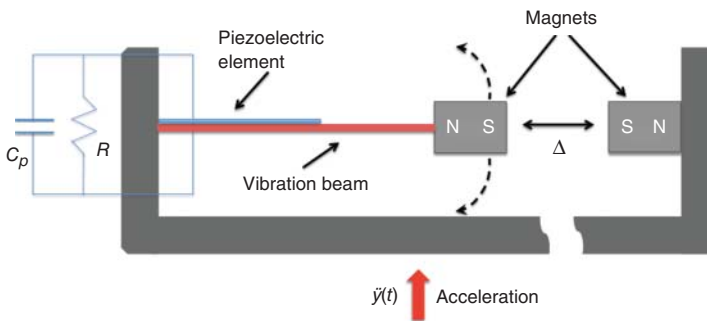


**Figure 2.9** Schematic of the bistable energy harvester.

an external magnet conveniently placed at a certain distance  $\Delta$  and with polarities opposed to those of the tip magnet. The interaction between the two magnets generates a force dependent on  $\Delta$  that opposes the elastic restoring force of the bended beam. As a result, the oscillator dynamics shows three different behaviors as a function of  $\Delta$ :

- 1) When  $\Delta$  is large ( $\Delta \gg \Delta_o$ ), it behaves like a linear oscillator.
- 2) If  $\Delta$  is small ( $\Delta \ll \Delta_o$ ), the oscillator is confined to the left or to the right of the vertical. In the limit of small oscillations, this can still be described in terms of a linear oscillator but with a resonant frequency higher than in the previous case.
- 3) In between, there exists an intermediate condition ( $\Delta \cong \Delta_o$ ) where the cantilever swings in a more complex way with small oscillations around each of the two equilibrium positions (left and right of the vertical) and large excursions from one to the other.

The dynamics of the oscillator in Figure 2.9 can be described by Eqs. (2.1) and (2.2) with nonlinear potential [39]:

$$U(z) = \frac{1}{2}k_e z^2 + (Az^2 + B\Delta^2)^{-\frac{3}{2}} \quad (2.11)$$

with  $k_e$ ,  $A$ , and  $B$  representing constants related to the physical parameters of the cantilever. When the distance  $\Delta$  between the magnets is very large, the second term in Eq. (2.11) becomes negligible and the potential tends to the harmonic potential of the linear case, typical of the simple cantilever harvester. In Figure 2.10, we show the potential  $U(z)$  for different values of  $\Delta$ . As can be easily seen when  $\Delta \rightarrow 0$ , the potential develops two distinct minima that correspond to two distinct equilibrium oscillation conditions.

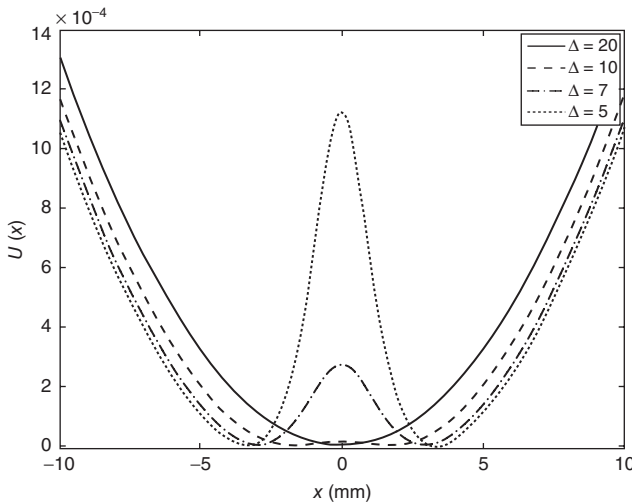


**Figure 2.10** Potential energy  $U(z)$  in Eq. (2.11) for different values of  $\Delta$ .

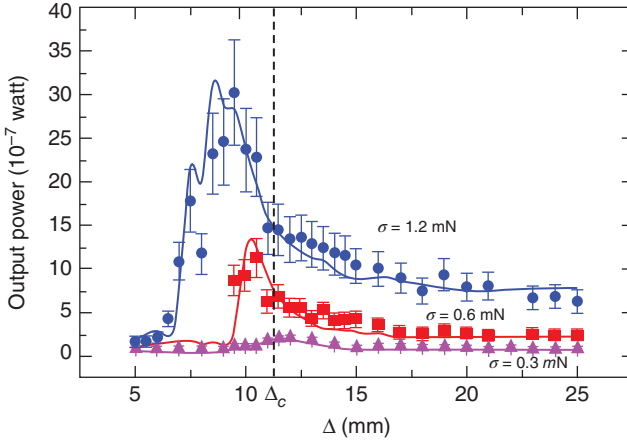


**Figure 2.11** Piezoelectric nonlinear vibration harvester mean electrical power versus distance  $\Delta$  between the two magnets (see scheme in Figure 2.9) for three different vibration intensities. For  $\Delta < \Delta_c$  the potential is bistable. For further details see [39].

The system dynamics, in the presence of stochastic force mimicking the random vibration can be solved numerically and the average output power computed according to Eq. (2.9):  $P_{\text{avg}} = V_{\text{rms}}^2/R$ .

In Figure 2.11 we show  $P_{\text{avg}}$  as a function of  $\Delta$  for three different values of the standard deviation of the random vibration (assumed exponentially correlated, Gaussian distributed, and with zero mean) [39]. Together with the numerical solution (continuous line), the results of experimental measurements made on a prototype [39] of the system in Figure 2.9 are also shown. As is well evident, there is an optimal distance  $\Delta_o$  where the power peaks to a maximum. Most remarkably, such a maximum condition is reached when the potential is in the bistable configuration [45].

### 2.5.2

#### Bistable Oscillators: Buckled Beam

Another possible configuration that realizes a bistable oscillator is presented in Figure 2.12. This is a buckled beam obtained by clamping a piezoelectric beam at both ends and applying a longitudinal compression strain [46].

If  $x$  is the vertical mass displacement, the buckled beam dynamics can be described [46] according to

$$m\ddot{x} + \gamma\dot{x} + k_3x^3 + (k_2 - k_1V)x + k_0V = \xi(t) \quad (2.12)$$

$$\frac{1}{2}C\dot{V} + \frac{V}{R_L} = k_0\dot{x} - k_1x\dot{x} \quad (2.13)$$

where  $m$ ,  $\gamma$ ,  $C$ , and  $R_L$  are the equivalent mass, the viscous parameter, the coupling capacitance, and the resistive load respectively.  $\xi(t)$  represents the random

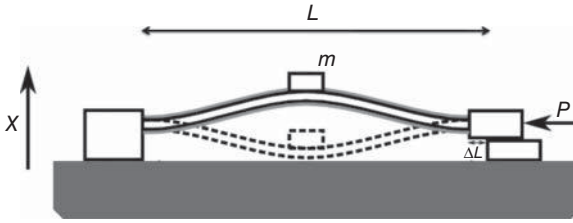


Figure 2.12 Schematic of a piezoelectric buckled beam. (Source: Vocca *et al.* 2013 [47].)

vibration force that drives the beam. The term  $k_3$  is the third-order stiffness coefficient of the beam;  $k_0$  and  $k_1$  are the piezoelectric coupling terms due to the bending and to the axial strain of the beam respectively. The term  $k_2 = k_a - k_b \Delta L$  is the stiffness parameter, where  $k_a$  and  $k_b$  are constants depending on the physical parameters of the beam. When the beam is compressed by increasing  $\Delta L$  the stiffness becomes negative and the system becomes bistable. For  $\Delta L = 0$  we recover linear behavior. The buckled model in Eqs. (2.12) and (2.13) is valid for small compressions  $\Delta L$ .

In Figure 2.13, we show the harvester output as a function of the compression  $\Delta L$ . In Figure 2.13, the average electrical power versus compression length ratio for the experimental (on the left) and numerical models (on the right) are shown for three noise amplitudes.

In Ref. [47], the authors present a comparison between the cantilever bistable configuration and the buckled beam, the same piezoelectric element subjected to a fixed vibrating body in both configurations has been simulated. The cantilever

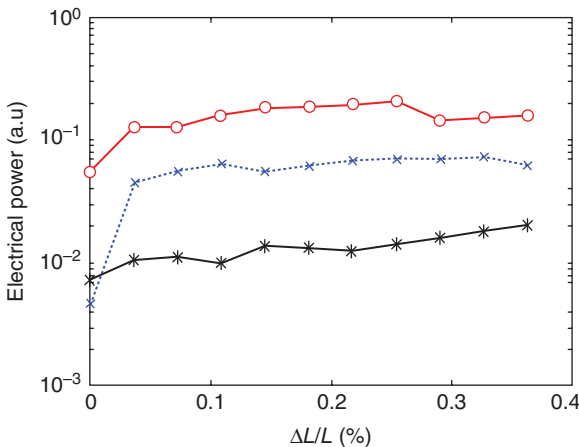


Figure 2.13 Average electrical power versus relative compression  $\Delta L/L$  (%) for the dynamic system Eqs. (2.12) and (2.13) after [45]. The random vibration standard deviation are (from top to bottom):  $\sigma = 3, \sigma = 2, \sigma = 1$ .

configuration appears to perform better than the beam configuration in all the simulated conditions.

### 2.5.3

#### Monostable Oscillators

Nonlinear oscillators for random vibration harvesting can be found also in the wide class of dynamic systems characterized by monostable potentials. As an example, we consider the following class of potential functions:

$$U(z) = az^{2n} \quad (2.14)$$

with  $a > 0$  and  $n = 1, 2, \dots$  where  $n = 1$  corresponds to the linear case explored in Eq. (2.14). For  $n > 1$ , we still have a monostable potential but the dynamics is not linear anymore. In Figure 2.14, we show [40] the rms voltage  $V_{\text{rms}}$  as a function of  $a$  and  $n$ . If the stiffness parameter  $a$  is larger than a certain threshold  $a_{\text{th}}$  then  $V_{\text{rms}}$  increases with  $n$  and a nonlinear potential outperforms a linear one, thus extending the main finding of the bistable potentials also to the monostable case. On the other hand if  $a < a_{\text{th}}$ , then  $V_{\text{rms}}$  decreases with  $n$  and the linear case performs better than the nonlinear one. The value  $a_{\text{th}}$  is linearly dependent on the random vibration intensity [40].

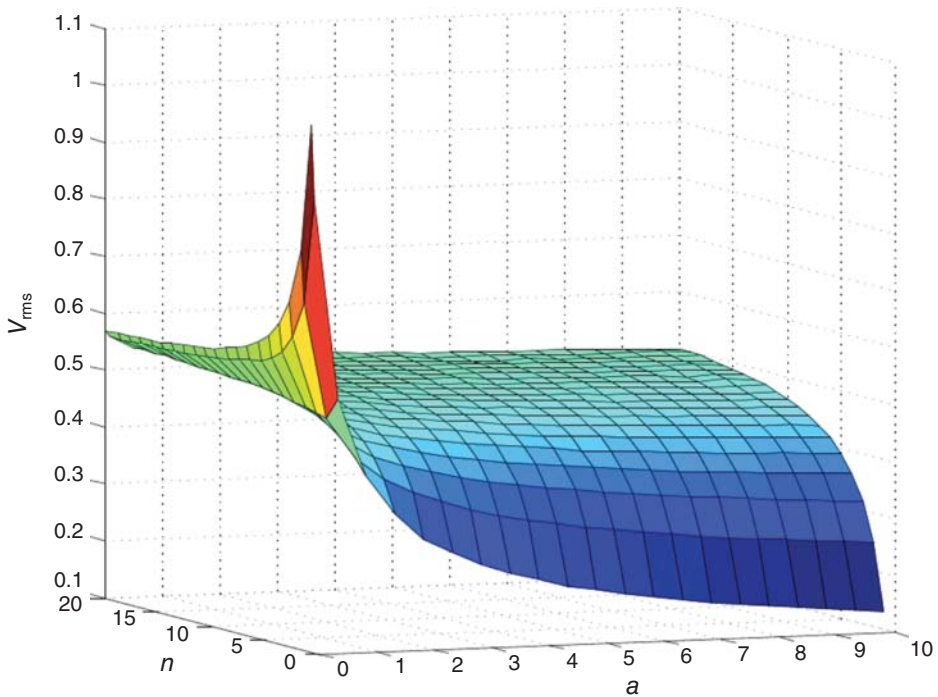


**Figure 2.14** 3D plot of the average electrical voltage  $V_{\text{rms}}$  (in arbitrary units) as a function of  $a$  and  $n$ .

## 2.6

## Conclusions

In this chapter, we discussed the fundamental dynamic aspects of vibration energy harvesting at microscale. Specific attention has been devoted to the discussion of the various strategies presently employed in the selection of the mechanical structures, starting with the widely spread linear oscillators. Owing to the limitations in the performances of linear oscillators in the presence of wideband vibrations, most recently, a novel class of nonlinear mechanical oscillators has gained popularity. We have briefly analyzed the bistable oscillators (modified cantilever and buckled beam configuration) and the general “power-law” monostable nonlinear oscillators. This novel class has shown potential advantages over the more traditional linear ones [48–50]. Other strategies in kinetic energy harvesting at small scale involve more complex dynamics, such as the use of rotating and gyroscopic proof masses [51] or piezomagnetoelastic structures [52] but these could not be addressed here.

## Acknowledgments

The authors gratefully acknowledge useful discussions with the members of NiPS Laboratory and in particular with I. Neri, F. Cottone, F. Orfei, F. Travasso, and the members of NANOPOWER project and specifically the group leaders of the participating laboratories: L. Worschech, J. Ahopelto, C. Sotomayor-Torres, M. Buttiker, and F. Marchesoni. The results presented here have been obtained thanks to the financial support from European Commission (FPVII, Grant agreement no: 256959, NANOPOWER and Grant agreement no: 270005, ZEROPOWER), Ministero Italiano della Ricerca Scientifica (PRIN 2009), the Fondazione Cassa di Risparmio di Perugia (Bando a tema – Ricerca di Base 2009 and 2010, Microgeneratori di energia di nuova concezione per l’alimentazione di dispositivi elettronici mobili) and ONRG Grant N00014-11-1-0695: *Novel techniques for the realization of energy harvesting systems capable of substituting/integrating existing batteries for the powering of autonomous electronic devices.*

## References

1. Mitcheson, P.D. *et al.* (2008) Energy harvesting from human and machine motion for wireless electronic devices. *Proc. IEEE*, **96**, 1457–1486.
2. Bilbao, A. *et al.* (2011) Ultra-low power wireless sensing for long-term structural health monitoring. *Proc. SPIE* (Sensors and Smart Structures Technologies for Civil, Mechanical, and Aerospace Systems, 2011), **7981**, 798109–798109-14.
3. Gammaitoni, L. (2012) There’s plenty of energy at the bottom (Micro and nano scale nonlinear noise harvesting). *Contemp. Phys.*, **53** (2), 119–135.
4. Neri, I., Travasso, F., Mincigrucci, R., Vocca, H., Orfei, F., and Gammaitoni, L. (2012) A real vibration database



- for kinetic energy harvesting application. *J. Intell. Mater. Syst. Struct.* doi: 10.1177/1045389X12444488
5. NiPS Laboratory Data Sets [www.nipslab.org/realvibrations](http://www.nipslab.org/realvibrations) (accessed 7 November 2114).
  6. Wang, L. and Yuan, F.G. (2007) Energy harvesting by magnetostrictive material (MsM) for powering wireless sensors in SHM. *Proc. SPIE (Sensors and Smart Structures Technologies for Civil, Mechanical, and Aerospace Systems, 2007)*, **6529**, 652941–652941-11.
  7. Ikeda, T. (1996) *Fundamentals of Piezoelectricity*, Oxford University Press, Walton St, Oxford.
  8. Lefevre, A.b.E., Richard, C., Petit, L., and Guyomar, D. (2005) A comparison between several approaches of piezoelectric energy harvesting. *J. Phys. IV France*, **128**, 177–186.
  9. McKay, T.G. *et al.* (2011) Soft generators using dielectric elastomers. *Appl. Phys. Lett.*, **98**, 142903–142903-3.
  10. Poulin, G. *et al.* (2004) Generation of electrical energy for portable devices comparative study of an electromagnetic and a piezoelectric system. *Sens. Actuators, A*, **116**, 461–471.
  11. Beeby, S.P. *et al.* (2007) A micro electromagnetic generator for vibration energy harvesting. *J. Micromech. Microeng.*, **17**, 1257.
  12. Wang, P. *et al.* (2009) A micro electromagnetic low level vibration energy harvester based on MEMS technology. *Microsyst. Technol.*, **15**, 941–951.
  13. Sari, I. *et al.* (2008) An electromagnetic micro power generator for wideband environmental vibrations. *Sens. Actuators, A*, **145**, 405–413.
  14. Boisseau, S. *et al.* (2011) Cantilever-based electret energy harvesters. *Smart Mater. Struct.*, **20**, 105013.
  15. Peano, F. and Tambosso, T. (2005) Design and optimization of a MEMS electret-based capacitive energy scavenger. *J. Microelectromech. Syst.*, **14**, 429–435.
  16. Meninger, S. *et al.* (2001) Vibration-to-electric energy conversion. *IEEE Trans. Very Large Scale Integr. VLSI Syst.*, **9**, 64–76.
  17. Basset, P. *et al.* (2009) A batch-fabricated and electret-free silicon electrostatic vibration energy harvester. *J. Micromech. Microeng.*, **19**, 115025.
  18. Cottone, F. *et al.* (2013) Non-linear mems electrostatic kinetic energy harvester with a tunable multistable potential for stochastic vibrations. IEEE 17th International Conference on Solid-State Sensors, Actuators and Microsystems, 2013.
  19. Zhu, D. *et al.* (2010) Strategies for increasing the operating frequency range of vibration energy harvesters: a review. *Meas. Sci. Technol.*, **21**, 022001.
  20. Roundy, S. (2003) Energy scavenging for wireless sensor nodes. PhD thesis, University of California, Berkley.
  21. Miao, P. *et al.* (2006) MEMS inertial power generators for biomedical applications. *Microsyst. Technol.*, **12**, 1079–1083.
  22. Wang, X. *et al.* (2007) Direct-current nanogenerator driven by ultrasonic waves. *Science*, **316**, 102–105.
  23. Paracha, A.M. *et al.* (2009) A silicon MEMS DC/DC converter for autonomous vibration-to-electrical-energy scavenger. *IEEE Electron Device Lett.*, **30**, 481–483.
  24. Guillemet, R., *et al.* (2013) Wideband MEMS electrostatic vibration energy harvesters based on gap-closing interdigitated combs with a trapezoidal section. IEEE 26th International Conference on MEMS, Taipei, Taiwan, 2013.
  25. NANO POWER For info and documents from the EC project NANOPOWER (G.A. 256959), [www.nanopwr.eu](http://www.nanopwr.eu) (accessed 7 November 2014).
  26. NANOPOWER Final Publishable Summary Results, <http://www.nanopwr.eu/node/462> (accessed 7 November 2014).
  27. Yang, W., Chen, J., Zhu, G., Wen, X., Bai, P., Yuanjie, S., Lin, Y., and Wang, Z. (2013) Harvesting vibration energy by a triple-cantilever based triboelectric nanogenerator. *Nano Res.*, **6** (12), 880–886.
  28. Williams, C.B. and Yates, R.B. (1995) Analysis of a micro-electric generator for microsystems. The 8th International Conference on Solid-State Sensors and

- Actuators, 1995 and Eurosensors IX. Transducers' 95, 1995, Vol. 1.
29. Gardiner, C. (2009) *Stochastic Methods. A Handbook for the Natural and Social Sciences*, 4th edn, Springer.
  30. Roundy, S. and Wright, P.K. (2004) A piezoelectric vibration based generator for wireless electronics. *Smart Mater. Struct.*, **13**, 1131.
  31. Tang, L. *et al.* (2010) Toward broadband vibration-based energy harvesting. *J. Intell. Mater. Syst. Struct.*, **21**, 1867–1897.
  32. Miller, L.M., Pillatsch, P., Halvorsen, E. *et al.* (2013) Experimental passive self-tuning behavior of a beam resonator with sliding proof mass. *J. Sound Vib.*, **332**, 7142–7152, ISSN:0022-460X.
  33. (a) Challa, V.R. *et al.* (2009) A coupled piezoelectric–electromagnetic energy harvesting technique for achieving increased power output through damping matching. *Smart Mater. Struct.*, **18**, 095029; See also (b) Ayala-Garcia, N., Mitcheson, P.D., Yeatman, E.M., Zhu, D., Tudor, M.J., and Beeby, S.P. (2013) Magnetic tuning of a kinetic energy harvester using variable reluctance. *Sens. Actuators, A*, **189**, 0924–4247.
  34. Roundy, S. and Zhang, Y. (2004) Toward self-tuning adaptive vibration-based microgenerators. *Proc. SPIE*, **5649**, 373–384.
  35. Shahruz, S. (2006) Design of mechanical band-pass filters for energy scavenging. *J. Sound Vib.*, **292**, 987–998.
  36. Ferrari, M. *et al.* (2008) Piezoelectric multifrequency energy converter for power harvesting in autonomous microsystems. *Sens. Actuators, A*, **142**, 329–335.
  37. Tadesse, Y. *et al.* (2009) Multimodal energy harvesting system: piezoelectric and electromagnetic. *J. Intell. Mater. Syst. Struct.*, **20**, 625–632.
  38. Le, C.P., Halvorsen, E., Sorasen, O., and Yeatman, E.M. (2012) Microscale electrostatic energy harvester using internal impacts. *J. Intell. Mater. Syst. Struct.*, **23**, 1409–1421, ISSN:1045-389X.
  39. Cottone, F., Vocca, H., and Gammaitoni, L. (2009) Nonlinear energy harvesting. *Phys. Rev. Lett.*, **102**, 080601.
  40. Gammaitoni, L. *et al.* (2009) Nonlinear oscillators for vibration energy harvesting. *Appl. Phys. Lett.*, **94**, 164102–164102-3.
  41. Arrieta, A. *et al.* (2010) A piezoelectric bistable plate for nonlinear broadband energy harvesting. *Appl. Phys. Lett.*, **97**, 104102.
  42. Andò, B. *et al.* (2010) Nonlinear mechanism in MEMS devices for energy harvesting applications. *J. Micromech. Microeng.*, **20**, 125020.
  43. Barton, D.A.W., Burrow, S.G., and Clare, L.R. (2010) Energy harvesting from vibrations with a nonlinear oscillator. *J. Vib. Acoust.*, **132**, 021009.
  44. Stanton, S.C. *et al.* (2010) Nonlinear dynamics for broadband energy harvesting: investigation of a bistable piezoelectric inertial generator. *Physica D*, **239**, 640–653.
  45. Vocca, H. *et al.* (2012) Kinetic energy harvesting with bistable oscillators. *Appl. Energy*, **97**, 771–776.
  46. Cottone, F. *et al.* (2012) Piezoelectric buckled beams for random vibration energy harvesting. *Smart Mater. Struct.*, **21**, 035021.
  47. Vocca, H. *et al.* (2013) A comparison between nonlinear cantilever and buckled beam for energy harvesting. *Eur. Phys. J. Spec. Top.*, **222**, 1699–1705.
  48. Gammaitoni, L. *et al.* (2010) The benefits of noise and nonlinearity: extracting energy from random vibrations. *Chem. Phys.*, **375**, 435–438.
  49. Ferrari, M. *et al.* (2010) Improved energy harvesting from wideband vibrations by nonlinear piezoelectric converters. *Sens. Actuators, A*, **162**, 425–431.
  50. Erturk, A. and Inman, D.J. (2011) Broadband piezoelectric power generation on high-energy orbits of the bistable Duffing oscillator with electromechanical coupling. *J. Sound Vib.*, **330**, 2339–53.
  51. Yeatman, E. (2008) Energy harvesting from motion using rotating and gyroscopic proof masses. *J. Mech. Eng. Sci.*, **222**, 27–36, ISSN: 0954–4062.
  52. Erturk, A., Hoffmann, J., and Inman, D.J. (2009) A piezomagnetoelastic structure for broadband vibration energy harvesting. *Appl. Phys. Lett.*, **94**, 254102.

## 3

### Electromechanical Transducers

*Adrien Badel, Fabien Formosa, and Mickaël Lallart*

#### 3.1

##### Introduction

This chapter presents five electromechanical transduction mechanisms used for vibration energy harvesting. Electromagnetic, piezoelectric, and electrostatic transducers are by far the most commonly used technologies. They are presented in Sections 3.2–3.4, respectively. Physical principles, typical architectures, energy cycles, figures of merits, and limitations are presented for each of them.

Electrostrictive and magnetostrictive transducers are briefly presented in Sections 3.5.1 and 3.5.2, where their physical principles and constitutive equations are presented.

A discussion on the effect of the mechanical structure of a vibration energy harvester on the harvested power is given in Section 3.6. Finally, a summary on the selection of the conversion effect, design rules, and implementation is given in Section 3.7.

#### 3.2

##### Electromagnetic Transducers

##### 3.2.1

###### Basic Principle

Electromagnetic vibration energy harvesters (EVEHs) are based on Faraday's law of induction, which states that a change in the magnetic flux through a conductive loop will cause a voltage to be induced in that loop. They are made with at least one coil, which is moving relatively to at least one magnet.

A simple system with only one coil and one magnet is first considered, as shown in Figure 3.1. The relative displacement between the coil and the magnet is  $u$ . The coil is supposed to have  $N$  turns, a cylindrical shape along the  $\vec{x}$  axis, a section  $S$  and a height  $h$ .

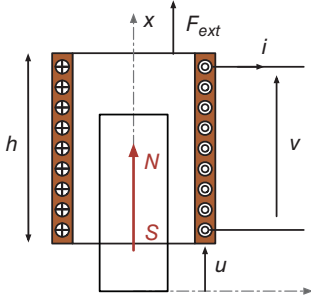


Figure 3.1 Schematic of electromagnetic transducer.

### 3.2.1.1 Induced Voltage

The magnetic flux generated by the magnet and seen by a simple loop at the position  $x$  is defined by Eq. (3.1), where  $S$  indicates the area enclosed by the wire loop and  $\vec{B}$  is the magnetic field.

$$\varphi_{\text{CM}}(x) = \int_S \vec{B} \cdot d\vec{S} \quad (3.1)$$

The total flux  $\phi_{\text{CM}}$  seen by the coil is

$$\phi_{\text{CM}}(u) = \int_u^{u+h} \varphi_{\text{CM}}(x) \frac{N}{h} dx \quad (3.2)$$

Faraday's law leads to a voltage induced across the coil, which is also called electromotive force (emf) and is given by Eq. (3.3).

$$v_{\text{CM}}(t) = -\frac{d\phi_{\text{CM}}}{dt} = -\frac{d\phi_{\text{CM}}}{du} \frac{du}{dt} \quad (3.3)$$

It is then clear that a voltage will be generated provided that

- a relative displacement between the coil and the magnet occurs;
- the total flux seen by the coil varies with the relative position of the magnet and the coil.

The EVEH electromechanical coefficient  $\beta$  is then given by Eq. (3.4). It is defined as the proportionality coefficient between the induced voltage and the speed of the relative motion between the coil and the magnet. It is a key parameter for the design of EVEH.

$$\beta = -\frac{d\phi_{\text{CM}}}{du} \quad (3.4)$$

### 3.2.1.2 Self-Induction

If the EVEH is connected to a load, a current  $i$  will naturally flow into the coil. The current in the coil in turn creates a magnetic field. The self-inductance  $L$  is defined, as shown by Eq. (3.5), as the proportionality coefficient between the flux  $\phi_{\text{CC}}$  generated by the current flowing the coil and seen by the coil itself.

$$\phi_{\text{CC}} = Li \quad (3.5)$$

Following Faraday's law, variations of the current will induce a voltage across the coil:

$$v_{CC} = -\frac{d\phi_{CC}}{dt} = -L\frac{di}{dt} \quad (3.6)$$

Following Ohm's law, the resistance  $r_L$  of the coil also leads to a voltage drop. Finally, the electrical governing equation for an EVEH is

$$v(t) = \beta\frac{du(t)}{dt} - L\frac{di(t)}{dt} - r_L i(t) \quad (3.7)$$

### 3.2.1.3 Mechanical Aspect

From a mechanical point of view, when a wire element  $dl$  carrying an electrical current is placed in a magnetic field, Lorentz's law states that an elementary force given by (Eq. (3.8)) will be generated on the wire element.

$$\vec{dF} = i\vec{dl} \wedge \vec{B} \quad (3.8)$$

Following Lenz's law, which states that an induced emf always gives rise to a current whose effect opposes the original change in magnetic flux, it can be inferred that the combination of the elementary forces generated on the coil will generate a macroscopic force along the axis that opposes the relative motion between the magnet and the coil.

From Eq. (3.8), this force magnitude  $F$  is proportional to the current  $i$ . It is then given by Eq. (3.9), where  $\beta'$  is called *force factor*.

$$F(t) = \beta' i(t) \quad (3.9)$$

It is considered that the coil is moving at a constant speed relatively to the magnet. In these conditions, the current and voltage are constants and an external force  $F_{\text{ext}} = -F$  has to be applied on the coil. Multiplying Eq. (3.9) by the speed and integrating over time leads to the mechanical energy balance Eq. (3.10), where the first term represents the mechanical energy provided to the EVEH. Multiplying Eq. (3.7) by the current and integrating over time leads to the electrical energy Eq. (3.11), where the first term corresponds to the electrical energy provided by the EVEH to the load.

$$\int F_{\text{ext}} \frac{du}{dt} dt = -\beta' \int i \frac{du}{dt} dt \quad (3.10)$$

$$\int v i dt = \beta \int \frac{du}{dt} i dt - \frac{1}{2} L i^2 - \int r_L i^2 dt \quad (3.11)$$

Considering the energy balance in the EVEH, the mechanical energy provided to the EVEH has to be equal to the summation of the electrical energy provided by the EVEH to the load, the energy lost in the resistance  $r_L$  and the energy stored in the inductance  $L$ , which gives the following expression:

$$\int F_{\text{ext}} \frac{du}{dt} dt = \int v i dt + \frac{1}{2} L i^2 + \int r_L i^2 dt \quad (3.12)$$

From Eqs. (3.10)–(3.12), it is clear that  $\beta' = -\beta$ , and the constitutive equations of an EVEH can finally be given as follows:

$$\begin{cases} v(t) = \beta \frac{du(t)}{dt} - L \frac{di(t)}{dt} - r_L i(t) \\ F(t) = -\beta i(t) \end{cases} \quad (3.13)$$

### 3.2.2

#### Typical Architectures

Spreemann and Manoli [1] proposed to classify EVEHs in two categories:

- Magnet in line, where the central axis of the magnet and the coil is congruent with the relative displacement direction
- Magnet across coil, where the central axis of the magnet and the coil is perpendicular to the relative displacement direction

In their work, Spreeman and Manoli also described the most common architectures belonging to these two categories. They are given in Figure 3.2, which is taken from their work. In all considered cases, the relative displacement of the coil and the magnet induces a variation in the magnetic flux seen by the coil, which leads to the generation of an induced voltage.

Some of the classical architectures implement back iron. Back iron concentrates and guides the magnetic lines, which allows increasing the magnetic flux seen by the coil. Proper optimization of the magnetic circuit using back iron is then a way to increase the electromechanical factor  $\beta$ . The main limitation of using back iron is that it exhibits a saturation magnetic field that should not be exceeded otherwise the expected performances will not be reached.

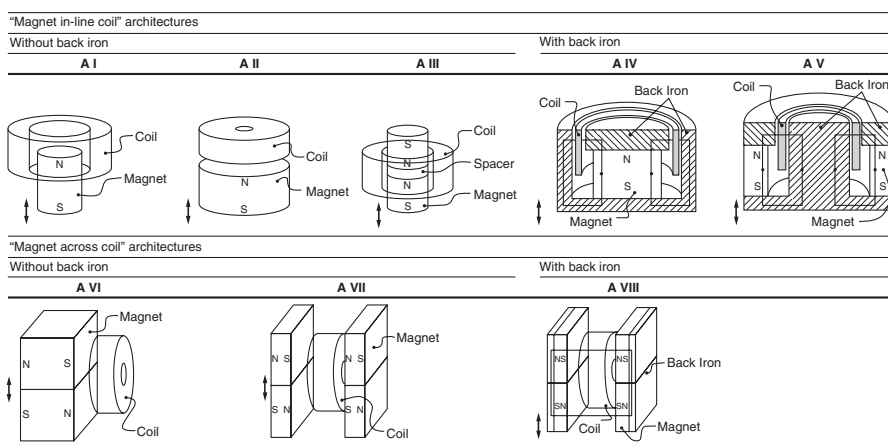
#### 3.2.2.1 Case Study

A simple example is chosen in this section to explain how the parameters used in Eq. (3.13) can be obtained from the EVEH architecture. The studied structure is shown in Figure 3.3. It is composed of two magnets, a squared section coil and back iron with an air gap.

To calculate the EVEH electromechanical coefficient  $\beta$ , the flux generated by the magnets into the coil has to be calculated, and it is considered that no current is flowing through the coil (open-circuit condition).

The relation between the magnetic field  $\vec{B}$  and the magnetic field strength  $\vec{H}$  in a different material is given in Eq. (3.14), where the subscript  $A$  refers to air,  $M$  to the magnet, and  $I$  to back iron.  $B_0$  is the magnetic remnant field of the magnet. The relation between  $B_M$ ,  $B_0$ , and  $H_M$  is an approximation of the magnetization curve, which is accurate for rare earth and ferrite magnets.

$$\begin{cases} \vec{B}_A = \mu_0 \vec{H}_A \\ \vec{B}_M = \vec{B}_0 + \mu_M \vec{H}_M \\ \vec{B}_I = \mu_I \vec{H}_I \end{cases} \quad (3.14)$$



The architectures are classified into "Magnet in-line coil" (A I – A V) and "Magnet across coil" architectures (A VI – A VIII). Further separation takes the existence of back iron components into account

Figure 3.2 EVEH architecture considered in the study by Spreemann and Manoli [1].

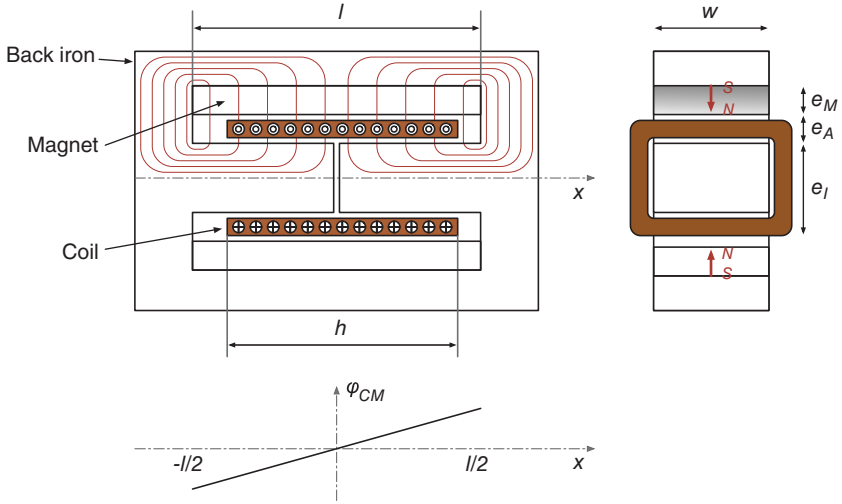


Figure 3.3 Simple EVEH structure.

Considering that the magnetic permeability in back iron  $\mu_I$  is much larger than those in air and in the magnet ( $\mu_0$  and  $\mu_M$ ), that the magnetic lines are all perpendicular to the magnet poling direction (side effects are neglected), and applying Ampère's circuital law lead to<sup>1)</sup> Eq. (3.15).

$$\oint \vec{H} \cdot d\vec{l} = 0 = H_M e_M + H_A e_A \quad (3.15)$$

From the magnetic flux conservation law, it can be inferred that the magnetic field  $B_M$  in the magnet and  $B_A$  in air are equivalent and that their values are given by

$$B_A = B_M = B_0 \frac{\frac{e_M}{\mu_M}}{\frac{e_A}{\mu_0} + \frac{e_M}{\mu_M}} \quad (3.16)$$

From Eq. (3.16), it is clear that the magnetic field generated by the magnet is lower than or equal to the remnant field  $B_0$  and that the space for the coil has to be limited to increase the magnetic field.

The magnetic flux generated by the magnets in the central rod of the structure along the  $\vec{x}$  axis can then be expressed as follows:

$$\varphi_{CM}(x) = 2B_M w x \quad (3.17)$$

1) This is a good assumption provided that the ratio of the path length of the magnetic strength field in back iron by  $\mu_I$  is much lower than  $e_A/\mu_0$  and  $e_M/\mu_M$ .



The total flux  $\phi_{CM}$  seen by the coil can then be calculated from Eq. (3.2), which leads to

$$\phi_{CM}(u) = B_M N \frac{W}{l} (2uh - h^2) \quad (3.18)$$

The EVEH electromechanical coefficient  $\beta$  can then be calculated from Eq. (3.4), which gives Eq. (3.19). In this particular case,  $\beta$  is constant because  $\phi_{CM}$  is linear with respect to the relative position on the coil and magnets. In the general case,  $\beta$  is a function of  $u$ .

$$\beta = -2B_M N \frac{wh}{l} \quad (3.19)$$

To calculate the EVEH self-inductance  $L$ , the flux  $\phi_{CC}$  generated by the current flowing through the coil and seen by the coil itself has to be calculated.

Considering that  $\mu_I$  is much larger than  $\mu_0$  and the magnetic lines are all perpendicular to the back iron section and applying Ampère's circuital law lead to Eq. (3.20), where  $l_A$  is the length of the air gap.

$$\oint \vec{H} \cdot d\vec{l} = NI = H_A l_A \quad (3.20)$$

The flux  $\phi_{CC}$  generated by the current flowing through the coil and seen by the coil itself can then be calculated as (Eq. (3.21)), and  $L$  can be deduced from Eq. (3.5) and is finally given by (Eq. (3.22))

$$\phi_{CC} = N \mu_0 H_A w e_I = I \mu_0 N^2 \frac{w e_I}{l_A} \quad (3.21)$$

$$L = \mu_0 N^2 \frac{w e_I}{l_A} \quad (3.22)$$

The last parameter to be calculated is the coil resistance  $r_L$ . It can be easily estimated from the coil volume and the number of turns. In the considered example, it is given by Eq. (3.23), where  $k_F$  is the coil filling factor (usually taken as  $\pi/4$ ) and  $\rho$  is resistivity of the material used for the coil winding.

$$r_L = 4\rho N^2 \frac{e_A + e_I}{k_F e_A h} \quad (3.23)$$

### 3.2.2.2 General Case

The case previously studied is a textbook case, where all parameters can be derived from analytical calculation. In most of real cases, the parameters  $L$  and  $\beta$  are obtained from the finite element calculation of the flux  $\phi_{CM}$  and  $\phi_{CC}$  (see Refs. [2, 3] for instance).

### 3.2.3

#### Energy Extraction Cycle

For a given architecture, this section aims at describing the typical energy cycles that can be used for harvesting electrical energy. For the sake of simplicity, it will be considered a given harmonic relative displacement between the coil and the magnets, with a magnitude  $u_M$ .

### 3.2.3.1 Resistive Cycle

The simplest way for harvesting energy lies in directly connecting a load  $R$  to the terminal of the device, as shown in Figure 3.4a. In this case, the voltage and displacement are linked in the frequency domain by

$$V = RI \Rightarrow V = j\omega\beta u \frac{R}{R + jL\omega + r_L} \quad (3.24)$$

where  $j = \sqrt{-1}$  and  $\omega$  is the angular frequency. The output energy per cycle can then be obtained from the power harvested in the load  $R$  (Eq. (3.25)). Its maximal value is obtained for an optimal value  $R_{\text{opt}}$  of the load, given by Eq. (3.26).

$$E_{\text{res}} = \frac{V_M^2}{2R} \frac{2\pi}{\omega} = \frac{\beta^2 u_M^2 \pi \omega R}{(R + r_L)^2 + L^2 \omega^2} \quad (3.25)$$

$$R_{\text{opt}} = \sqrt{L^2 \omega^2 + r_L^2} \quad (3.26)$$

From the mechanical point of view, the mechanical energy converted into electrical energy can be represented as the area of the  $(\beta i, u)$  cycle, because work of the electromagnetic force during a cycle is given by Eq. (3.27). This cycle is shown in Figure 3.5a. It can be noticed that, because of the resistive losses in  $r_L$ , the harvested energy is lower than the mechanical energy converted into electricity.

$$E_{\text{mech}} = - \int_T F du = -\beta \int_T I du \quad (3.27)$$

### 3.2.3.2 Self-Inductance Cancellation

It is clear from Eq. (3.25) that self-inductance  $L$  should be as small as possible to maximize the harvested power. In many cases, because of low operating frequencies of EVEH,  $L\omega$  is much smaller than  $r_L$ . If necessary, a capacitance  $C$ , whose

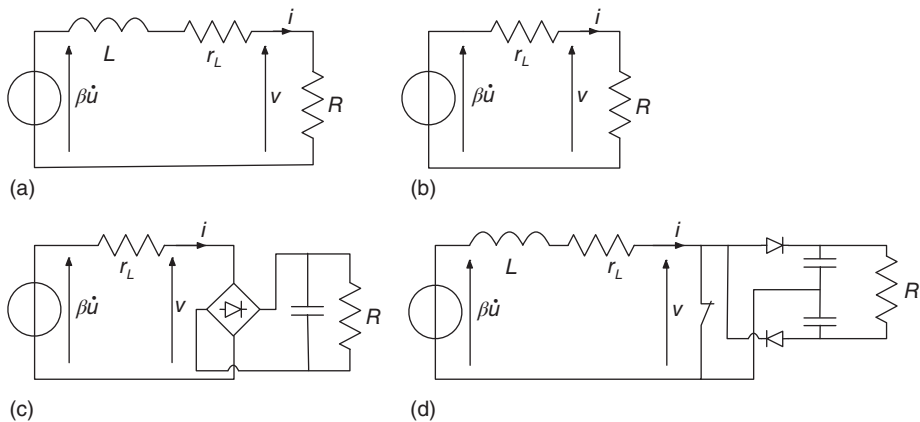


**Figure 3.4** Electrical interface: (a) resistive, (b) inductance compensation, (c) rectification, and (d) SMFE interface.

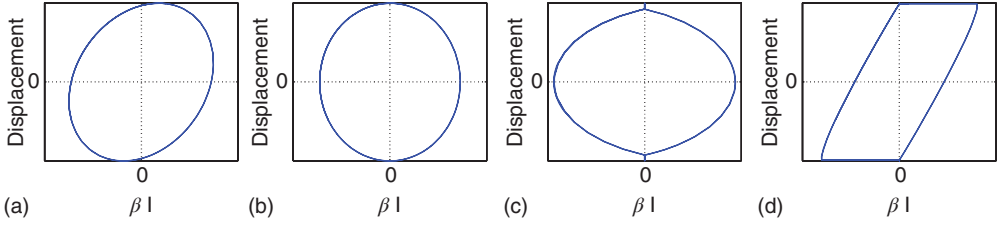


**Figure 3.5** Energy cycles: (a) resistive, (b) inductance compensation, (c) rectification, and (d) SMFE interface.

value is given by (Eq. (3.28)), can be added in series with the EVEH to cancel the inductive reactance. However, it can be noted that such an impedance adaptation works only for a given frequency.

$$C = \frac{1}{L\omega^2} \quad (3.28)$$

The output energy per cycle can then be obtained from Eq. (3.25) with  $L = 0$ . Its maximal value is obtained at the optimal value  $R_{\text{opt}} = r_L$  and is given by Eq. (3.29). This energy is a physical limit that cannot be exceeded whatever the energy harvesting circuit. This limitation is due to the output resistance  $r_L$  of the EVEH.

$$E_{\text{res max}} = \frac{\beta^2 u_M^2 \pi \omega}{4r_L} \quad (3.29)$$

The mechanical energy converted into electricity is then given by Eq. (3.30). The corresponding energy cycle is shown in Figure 3.5b. This result shows that to maximize the harvested energy, half of the converted energy is lost in the coil resistance.

$$E_{\text{mech opt}} = \frac{\beta^2 u_M^2 \pi \omega}{2r_L} \quad (3.30)$$

### 3.2.3.3 Cycle with Rectification

Although simple, resistive energy harvesting is not realistic as most of electronic devices require DC input voltage. Rectification can be done using a standard full bridge passive rectifier, as shown in Figure 3.4c. The rectifier electrically connects the EVEH to the circuit when its absolute voltage is greater than the output voltage (the latter being held constant by a smoothing capacitor), yielding the energy cycle shown in Figure 3.5c.

The expressions of the harvested energy and of the optimal value of the load cannot be given as simple analytical equations. However, considering perfect diodes (no on-resistance, no threshold voltage, and no leakage current), it can be shown that the maximal harvested energy can reach 92% of  $E_{\text{res max}}$  for an optimal load equal to  $1.35r_L$  (when  $L\omega \ll r_L$ ).

The main problem in using a standard full bridge rectifier is that a large amount of energy can be lost in the diodes if the EVEH open-circuit voltage amplitude ( $\beta\omega u_M$ ) is not much larger than the diode threshold voltage (which is typical for many electromagnetic systems).

### 3.2.3.4 Active Cycle

A nonlinear circuit called Synchronized Magnetic Flux Extraction (SMFE) has also been developed for EVEH, as an alternative to the standard rectification approach. It realizes the rectification and the amplification of the voltages as well as the optimization of the energy transfer whatever the load impedance [4]. Its principle is as follows: the coil remains short-circuited while the induced current  $i$  increases (or decreases). When the current reaches a maximum (or minimum) value, the switch is briefly opened and the current charges one or the other storage capacitance, yielding a cancelation of the current. This mechanism allows to strongly reduce the losses due to diode threshold voltages. Figure 3.4d shows a schematic of the circuit, and Figure 3.5d the corresponding energy extraction cycle.

Contrary to the previous approaches, the SMFE technique requires that  $L\omega \gg r_L$ . In many cases, adding an inductance in series with the EVEH is then mandatory to use the SMFE approach (which however decreases the coupling coefficient). Dedicated generators with high reactance can also be specifically designed, such as in Ref. [3].

In any case however, the maximal harvested energy cannot exceed the one given by Eq. (3.29).

## 3.2.4

### Figures of Merit and Limitations

Equation (3.29) gives the maximal energy that can be provided by an EVEH. It is proportional to the operating frequency, the squared displacement amplitude, and  $\beta^2/r_L$ . The operating frequency is strongly dependent on the ambient vibrations, and the displacement amplitude may be limited by the EVEH geometry itself.

Dividing  $\beta^2/r_L$  by the volume  $V_{\text{EVEH}}$  of the generator gives a figure of merit  $\text{FoM}_{\text{EM}}$  of the energy density of an EVEH. It is given by Eq. (3.31), and its physical dimension is the same as a damper per unit of volume. It demonstrates that an ideal EVEH exhibits a high electromechanical coefficient  $\beta$ , together with a low coil resistance  $r_L$ .

$$\text{FoM}_{\text{EM}} = \frac{\beta^2}{V_{\text{EVEH}} r_L} = \alpha \frac{B_0^2}{\rho} \quad \text{with } \alpha < 1 \quad (3.31)$$

It can be shown that  $\text{FoM}_{\text{EM}}$  is the product of a dimensionless coefficient  $\alpha < 1$ , which is only function of the EVEH geometry and  $B_0^2/\rho$ . The latter term is then the physical limit of the figure of merit. Its value for a Ne–Fe–B magnet and a copper coil is  $8.5e7 \text{ Nm}^{-4} \text{ s}$ . It is worthy of note that it is not dependent on the EVEH volume. From the physics point of view, the maximal power density of an EVEH is then not a function of volume. However, in practical implementation, technical issues usually make  $\alpha$  decreases with volume.

Considering the previous case study, the corresponding figure of merit can be obtained from Eqs. (3.16), (3.19), and (3.23). It is given by Eq. (3.32), as a function of the material properties and geometry of the EVEH. The ways to maximize the

**Table 3.1** Optimization of the figure of merit.

Term	How to maximize
$B_0^2$	The remnant field of magnets should be as high as possible
$\frac{e_M e_A}{(e_A \cdot \mu_M / \mu_0 + e_M)^2}$	There is an optimal ratio between $e_A$ and $e_M$ : $e_{Aopt} = e_M \frac{\mu_0}{2\mu_0 - \mu_M}$
$\frac{k_f}{\rho}$	The coil should have an optimal filling factor and a low resistivity
$\frac{e_M h w}{V_{EVEH}}$	Volume of the magnet should be as large as possible compared to that of the generator
$\frac{w}{e_A + e_f}$	The flux generated by the magnet and seen by the coil should be maximized
$\frac{h^2}{L^2}$	The coil should be as long as possible

EVEH performances are detailed in Table 3.1.

$$FoM_{EM} = B_0^2 \frac{e_M e_A}{\left(\frac{e_A \cdot \mu_M}{\mu_0} + e_M\right)^2} \frac{k_f}{\rho} \frac{e_M h w}{V_{EVEH}} \frac{w}{e_A + e_f} \frac{h^2}{L^2} \quad (3.32)$$

### 3.3

#### Piezoelectric Transducers

Piezoelectricity is the ability of particular materials to convert mechanical energy into electrical energy and vice versa. The word “piezoelectricity” derives from the Greek term *piezein* (to press) and *electricity*. Although piezoelectricity has been known for centuries, its thorough analysis is attributed to Pierre and Jacques Curie who investigated these materials in the nineteenth century. Piezoelectric elements are the most commonly used materials for small-scale energy harvesting devices. Such an interest lies in their compactness and integrability, as well as in their good power density. Hence, this section exposes the principles of piezoelectricity, material aspects, typical architectures used in energy harvesting systems, and finally techniques for interfacing such elements for energy harvesting purposes.

#### 3.3.1

##### Basic Principles and Constitutive Equations

##### 3.3.1.1 Physical Origin of Piezoelectricity in Ceramics and Crystals

Not all the materials feature piezoelectric effects. Material configuration showing high asymmetry is required in order to be able to show the piezoelectric behavior. This asymmetry leads to a noncoincidence of the positive and negative charge barycenters. Hence, under no mechanical solicitation, the system is electrically at equilibrium. However, if a material is submitted to a mechanical stress or strain, the crystalline structure is deformed and the distance between the charge

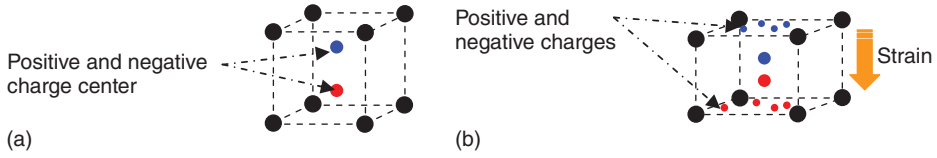


**Figure 3.6** Piezoelectric effect in ceramics and crystals (a) at rest and (b) under mechanical strain.

barycenters changes. Therefore, in order to keep the electrical neutrality, charges appear at the surface of the crystal (Figure 3.6). The converse effect, that is, modification of the mechanical structure due to the change in the distance between the barycenters of the charge (e.g., caused by the application of an electric field), also exists. However, in order to get a macroscopic remnant polarization, first poling process of the piezoelectric material has to be applied, which allows the orientation of the domains within the material.

### 3.3.1.2 Constitutive Equations

Hence, through the piezoelectric effect, a direct link between the strain, stress, electric field, and electric displacement can be found, allowing deriving the constitutive tensorial equations of piezoelectricity (e.g., using phenomenological analyses using Gibb's free energy – [5–7]). For example, considering that the independent parameters are the electric displacement  $D$  and the stress  $T$ , the constitutive equations yield [8, 9]

$$\begin{aligned} [S] &= [s^D][T] + [g]^t[D] \\ [E] &= [\beta^T][D] - [g][T] \end{aligned} \quad (3.33)$$

where  $S$  is the strain,  $E$  is the electrical field,  $s$  denotes the mechanical compliance,  $\beta$  is the dielectric stiffness (inverse of the permittivity), and  $g$  is the piezoelectric constant. The superscripts denote the constant quantity and  $^t$  is the transpose operator.

As piezoelectric materials can convert energy from the mechanical to electrical domain and vice versa, this quantity of converted energy is a significant parameter to characterize the piezoelectric effect. Hence, the coupling coefficient  $k$ , which relates the converted energy to the total energy, can be introduced as follows,<sup>2)</sup> considering the direct effect that is used in energy harvesting:

$$k^2 = \frac{\text{electrostatic potential energy}}{\text{total input energy}} \quad (3.34)$$

2) Other definitions, for example, considering mechanical and electrical cycles, can also be used for  $k^2$ .

## 3.3.2

**Typical Architectures for Energy Harvesting**

Once the constitutive equations of piezoelectricity are obtained, it is possible to investigate the typical configurations used for harvesting mechanical energy into electricity. Here, for the sake of simplicity, it will be considered that the piezoelectric element is submitted to a given unidimensional stress (which corresponds, in a macroscopic view, to an imposed force along one axis). The stress direction will be given by the considered architecture, as shown in Figure 3.7.

## 3.3.2.1 Modeling

Whatever the considered architecture, the electrical quantities are along the polarization axis 3. Hence, considering open-circuit operations (i.e.,  $D = 0$ ) and stress-free samples along axes other than the applied stress direction  $i$ , the constitutive equations can be reduced to

$$\begin{aligned} S_i &= s_{ii}^D T_i + g_{3i} D_3 \\ E_3 &= \beta_{33}^T D_3 - g_{3i} T_i \end{aligned} \quad (3.35)$$

The coupling coefficient may also be obtained as follows:

$$k_{3i}^2 = \frac{\epsilon_{33}^S E_i^2}{s_{ii}^D T_i^2} = \frac{\epsilon_{33}^S g_{3i}^2}{s_{ii}^D} = \frac{d_{3i} g_{3i}}{s_{ii}^E} \quad (3.36)$$

where  $\epsilon^S$  and  $d$  refer to the strain-free electrical permittivity and piezoelectric charge constant. As proposed in Ref. [10], electrical losses, represented by the loss tangent  $\tan \delta$  can also be taken into account to define the figure of merit of an energy harvester given as  $(d_{3i} g_{3i}) / (s_{ii}^E \tan \delta)$ . However, these losses are usually quite low and can thus be neglected.

Instead of using local parameters, it is also possible to express the macroscopic relationships between voltage  $V$ , outgoing current  $I$ , applied force  $F$  on the piezoelectric element, and displacement  $u$  under small signal operations as

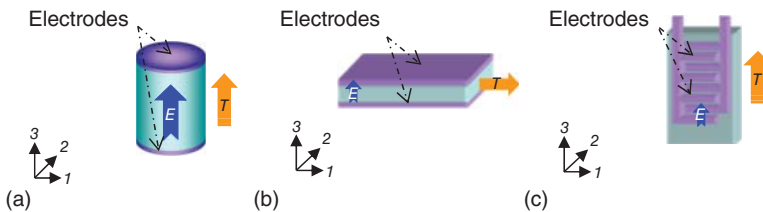


**Figure 3.7** Typical configurations for energy harvesting: (a) longitudinal; (b) transverse; and (c) interdigitated electrodes.

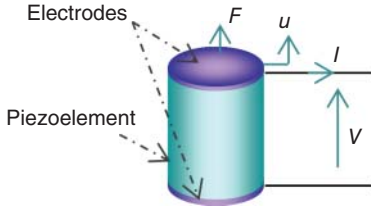


**Figure 3.8** Macroscopic model parameter definition for piezoelectric device.

follows (Figure 3.8):

$$\begin{aligned}
 I &= \alpha \dot{u} - C_0 \dot{V} \\
 F &= K^E u + \alpha V \quad \text{with} \quad \alpha = -\frac{g_{3i} A}{(\beta_{33}^T s_{ii}^D + g_{3i}^2) l}; \\
 C_0 &= \frac{A}{\left(\beta_{33}^T + \frac{g_{3i}^2}{s_{ii}^D}\right) l}; \quad K^E = \frac{A}{\left(s_{ii}^D + \frac{g_{3i}^2}{\beta_{33}^T}\right) l}
 \end{aligned} \tag{3.37}$$

where  $\alpha$  refers to the electromechanical force factor,  $C_0$  is the clamped capacitance, and  $K^E$  is the short-circuit stiffness, and  $A$  and  $l$  are the cross-sectional area and thickness of the material, respectively.

### 3.3.2.2 Application to Typical Configurations

The basic method for converting mechanical energy into electricity consists of directly applying the strain in the same direction than the electric field (axis 3 – Figure 3.7a), yielding a longitudinal response. However, although very simple and straightforward to use, longitudinal architecture is not suitable for energy harvesting, as the high stiffness leads to limited strain and high-frequency operations that are not compatible with typical vibration spectra of realistic excitations.

In order to dispose of harvesters able to work at lower frequencies, transverse operation, using the 31 mode (strain along the axis 1 and electric field along the axis 3) can be considered (Figure 3.7b). This is the typical mode used in unimorph and bimorph harvesters, operating under flexural solicitation. Such an architecture therefore permits benefiting of lower resonance frequencies of bending structures, hence allowing a better match between the input excitation frequency and the harvester natural frequency. Nevertheless, in this case, strain is still limited to less than a few percent.

The last architecture commonly used, allowing high-strain and low-frequency operations, consists of using interdigitated electrodes within the material (Figure 3.7c). As in this case, the piezoelectric material is made of fibers (MFC – macro fiber composite), the structure is very easy to bend, making it very flexible and thus able to operate at low frequencies. It can also be noted that some MFC configurations work under 31 mode, allowing their use as flexible bender. However, the coupling coefficient of fibers is usually lower than that of bulk ceramics.



**Table 3.2** Parameters of typical materials.

Material type	Operation	Piezoelectric coefficients		Mechanical compliance ( $10^{-12} \text{ m}^2 \text{ N}^{-1}$ )	Squared coupling coefficient
		$g_{ij}$ ( $10^{-3} \text{ V m N}^{-1}$ )	$d_{ij}$ ( $10^{-12} \text{ m V}^{-1}$ or $\text{C N}^{-1}$ )		
Piezoelectric ceramic (NAVY-III type – P1-89 [11])	33 mode	$g_{33} = 26$	$d_{33} = 425$	$s_{33}^E = 20.09$	$k_{33}^2 = 55\%$
PVDF film [12]	31 mode	$g_{31} = -11.4$	$d_{31} = -186$	$s_{11}^E = 15.44$	$k_{31}^2 = 14\%$
	33 mode	$g_{33} = 200$	$d_{33} = 20$	$s_{33}^E \approx 1800^{\text{a}}$	$k_{33}^2 = 2.2\%$
Piezoelectric fibers of MFC	31 mode	$g_{31} = -90^{\text{b}}$	$d_{31} = -8$	$s_{11}^E \approx 1800^{\text{c}}$	$k_{31}^2 = 0.4\%$
	33 mode	$g_{33} = 26.4^{\text{d}}$	$d_{33} = 400$ ( <a href="http://www.smart-material.com/MFC-product-main.html">http://www.smart-material.com/MFC-product-main.html</a> )	$s_{33}^E = 32.96$ ( <a href="http://www.smart-material.com/MFC-product-main.html">http://www.smart-material.com/MFC-product-main.html</a> )	$k_{33}^2 = 32\%$ [13]

a) Estimated from  $d_{31}$ ,  $g_{31}$ , and  $k_{33}$ .

b) Estimated from  $d_{31}$  and permittivity.

c) Considering that PVDF is isotropic.

d) Estimated from  $d_{33}$ ,  $s_{33}^E$ , and  $k_{33}$ .

Comparing the performance of the considered materials and architectures (Table 3.2) shows that the longitudinal mode (33) features a much higher coupling, yielding a higher energy output for the same input mechanical energy. However, for ceramics, the low value of compliance makes the material quite stiff and thus very difficult to exploit in realistic applications, while the transverse mode can easily take advantage of bending. To overcome this, PVDF (Poly(Vinylidene Fluoride)) polymers allow benefiting of much higher flexibility, but also feature a dramatically decreased conversion ability. Finally, the MFC composite is a trade-off between flexibility and coupling, but also has a much higher cost.

### 3.3.3

#### Energy Extraction Cycles

For a given architecture, this section aims at describing the typical energy cycles that can be used for harvesting electrical energy. For the sake of simplicity, it will be considered that the device is submitted to a given input displacement with a magnitude  $u_M$  and that all considered parameters are unidimensional, allowing the use of the macroscopic model previously established.

##### 3.3.3.1 Resistive Cycles

The simplest way for harvesting energy lies in directly connecting a load  $R$  to the electrical terminal of the device (Figures 3.9a and 3.10b). In this case, the voltage

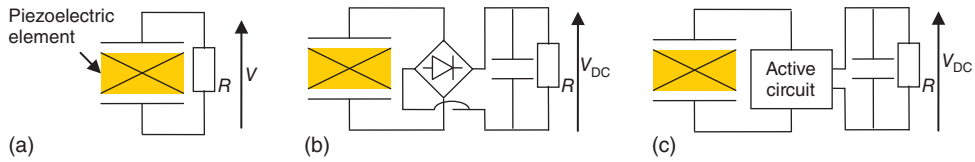


Figure 3.9 Energy harvesting interfaces: (a) resistive; (b) rectification; and (c) active.

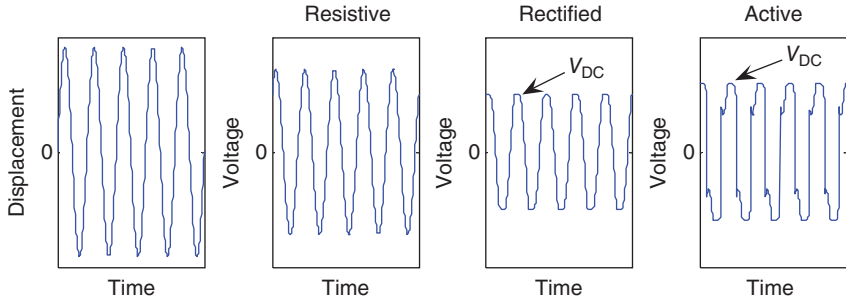


Figure 3.10 Voltage waveforms with several harvesting interfaces: (a) open-circuit; (b) resistive; (c) rectification; and (d) active.

and displacement are linked in the frequency domain (with  $\omega$  the angular frequency) through (Figure 3.10) the following relation:

$$V = RI \Rightarrow V = \frac{j\omega R\alpha}{1 + j\omega RC_0} u \tag{3.38}$$

yielding the output energy per cycle and its maximal value:

$$E_{\text{res}} = \pi \frac{R(\alpha)^2 \omega}{1 + (\omega RC_0)^2} u_M^2; \quad E_{\text{res}}|_{\text{max}} = \frac{\pi}{2} \frac{\alpha^2}{C_0} u_M^2 \tag{3.39}$$

Associated energy cycles are depicted in Figure 3.11a.

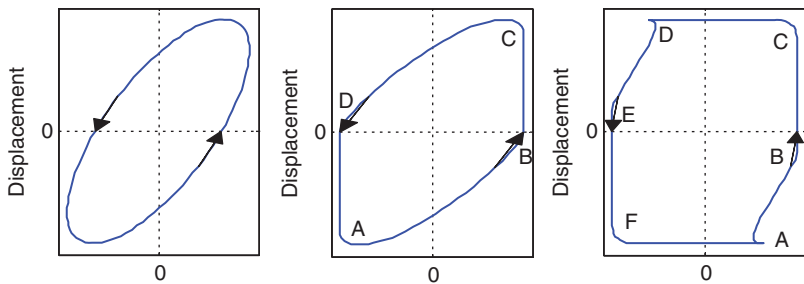


Figure 3.11 Electromechanical energy cycles with: (a) pure resistive interface; (b) rectification; and (c) active cycle ( $\gamma = 0.8$ ).

### 3.3.3.2 Cycles with Rectification

Although simple, resistive energy harvesting is not very realistic as most electronic devices require DC input voltage. Hence, means of rectification are necessary. Simply speaking, this can be done using standard full bridge passive rectifiers (Figure 3.9b) that consist of electrically connecting the harvester to the circuit when its absolute voltage is greater than the output voltage (the latter being held constant by a smoothing capacitor – Figure 3.10c), yielding the energy cycle shown in Figure 3.11b. Under these conditions, considering the piezoelectric voltage, rectified voltage  $V_{DC}$ , displacement at conduction  $u_1$ , and maximum displacement:

$$-V_{DC} = -\frac{\alpha}{C_0}u_M + K ; V_{DC} = \frac{\alpha}{C_0}u_1 + K \quad (3.40)$$

with  $K$  an integration constant, the expression of the energy for one cycle and its maximal value are given as follows:

$$E_{\text{rec}} = 2 \int_{u_1}^{u_M} \alpha V_{DC} du = \frac{V_{DC}^2}{Rf} \Rightarrow E_{\text{rec}} = \frac{(4\alpha)^2 Rf}{(1 + 4fRC_0)^2} u_M^2 ; E_{\text{rec}}|_{\text{max}} = \frac{\alpha^2}{C_0} u_M^2 \quad (3.41)$$

### 3.3.3.3 Active Cycles

Previously considered cycles consisted of purely passive interfaces. However, considering the converted energy between time instants  $t_0$  and  $t_0 + \Delta t$ , given as  $E_{\text{conv}} = \alpha \int_{t_0}^{t_0 + \Delta t} V \dot{u} dt$ , it can be inferred that, in order to have the highest available electrical energy, the voltage should be as large as possible and in phase with the speed. To do so, active cycles have been proposed (Figure 3.9c), relying on actively changing the piezoelectric element voltage [14, 15]. As an example, taking the technique called parallel SSHI (Synchronized Switch Harvesting on Inductor – [14]), whose typical waveforms are depicted in Figure 3.10d, the cycle is greatly increased and more energy can be harvested due to the semi-active process (Figure 3.11c). In this case, the expression for energy per cycle and its maximal value yield (using a similar analysis to that in the rectified case) is

$$E_{\text{act}} = \frac{(4\alpha)^2 Rf}{[1 + 2(1 - \gamma)fRC_0]^2} u_M^2 ; E_{\text{act}}|_{\text{max}} = \frac{2}{1 - \gamma} \frac{\alpha^2}{C_0} u_M^2 \quad (3.42)$$

where  $\gamma$  is a parameter reflecting the efficiency of the active treatment ( $0 \leq \gamma \leq 1$ ).

### 3.3.3.4 Comparison

When considering the input energy  $E_p$  given as the elastic potential energy of the structure plus the converted energy, the expression of the normalized harvested energy per period for each cycle can be obtained and is given in Table 3.3. When comparing the energies, it can be shown that, for low coupling values, active techniques are very interesting while classical approaches (resistive and rectified) are more efficient for high coupling values, as losses occur in the active branch.

**Table 3.3** Normalized energy for each type of cycle ( $k^2$  is the global squared coupling coefficient given as  $k^2 = \alpha^2 / (C_0 K_E + \alpha^2)$ ).

	Resistive cycle	Cycle with rectification	Active cycle
Normalized energy	$\frac{E_{res} _{max}}{E_p} = \frac{\pi k^2}{1+(\pi-1)k^2}$	$\frac{E_{rec} _{max}}{E_p} = \frac{2k^2}{1+k^2}$	$\frac{E_{act} _{max}}{E_p} = \frac{4k^2}{(1-\gamma)+(5+3\gamma)k^2}$

## 3.3.4

**Maximal Power Density and Figure of Merit**

Now the local and macroscopic aspects of piezoelectric energy transducers for energy harvesting exposed, the aim of this section is to give some ideas on the maximum admissible quantities before failure and thus the absolute maximum energy that can be harvested. This section mainly compares bulk ceramics with MFC, in the second part. In the case of bulk ceramics, the maximum static stress is basically given by the depoling stress and the maximum electric field by the coercive field (both with a security coefficient), leading to the data given in Table 3.4. Therefore, the expression of the maximal converted energy density for the given maximal input stress given as follows:

$$W_{max} = \frac{1}{2} k_{3i}^2 s_{ii}^D (T_{ii})_{max}^2 \quad (3.43)$$

yields the values reported in Table 3.5. This table shows that, although working in 33 mode that allows relatively high coupling coefficients, the MFC has the lowest energy density because of its limited stress. Also, although the squared coupling coefficient in the transverse mode is lower than in the longitudinal mode

**Table 3.4** Maximum operating conditions.

Material type	Max stress (Mpa)	Max field (kV mm <sup>-1</sup> )	Max strain (%)
Piezoelectric ceramic (NAVY-III type – P1-89 – [11])	50	1.5	0.05
PVDF film [12]	30	100	5
MFC	30 [16]	1.5	0.2 [16]

**Table 3.5** Maximum converted energy density.

Material type	Longitudinal 33 mode (mJ cm <sup>-3</sup> )	Transverse 31 mode (mJ K cm <sup>-3</sup> )
Piezoelectric ceramic (NAVY-III type – P1-89)	$W_{max} = 5$	$W_{max} = 2.3$
PVDF film [12]	$W_{max} = 18$	$W_{max} = 3$
MFC	$W_{max} = 1$	—

for the piezoelectric ceramic (by a factor 4), the higher value of compliance in the transverse mode permits reducing the difference in terms of harvested energy. The highest energy density is obtained in the case of PVDF working in 33 mode. However, it should be kept in mind that the film nature of such a material makes such an application uneasy and complex.

Furthermore, Eq. (3.43) shows, for a given input stress, that the figure of merit in terms of material and mode selection is given by the following expression:

$$\frac{E_{\text{res}}|_{\text{max}}}{E_p} = \frac{\pi k^2}{1 + (\pi - 1)k^2} \quad (3.44)$$

### 3.4

#### Electrostatic Transducers

##### 3.4.1

##### Basic Principles

Electrostatic vibration energy harvesters are based on the variation of the capacitance of a charged capacitor. They are made with at least one capacitor, whose one electrode is moving relatively to the other one. A simple planar capacitor system is first considered, as shown in Figure 3.12. The relative displacement along the  $\vec{x}$  axis between the electrodes is  $u$ . The electrode surface is  $S_f$ .

##### 3.4.1.1 Gauss's Law

This fundamental law in electrostatic, given in Eq. (3.45), states that the net outward normal electric flux through any closed surface  $S$  is proportional to the total electric charge enclosed within that surface.

$$\oint_S \epsilon_0 \vec{E} \cdot \vec{n} dS = \sum_S q' \quad (3.45)$$

where  $q'$  is any elementary charge within the volume bounded by  $S$ .

##### 3.4.1.2 Capacitance $C_0$

For an isolated conductive material structure, carrying  $Q$  electric charges, its capacitance  $C_0$  is defined as the ratio of its total charges to its electric potential

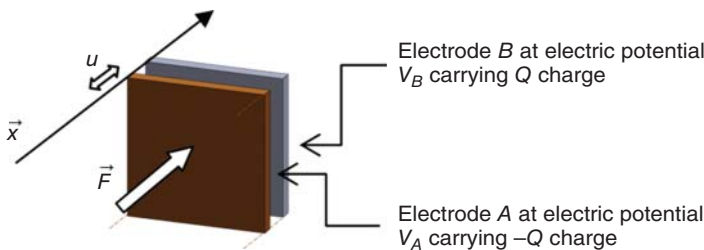


Figure 3.12 Simple arrangement for a variable capacitance.

$V = |V_A - V_B|$ . Therefore,

$$C_0 = \frac{Q}{V} \quad (3.46)$$

This capacitance is a function of the structure geometry, dimensions, and position with respect to other conductors (electric mass especially). A large value of capacitance shows the good capability of the structure to store electrical charges. Common values of capacitance are a few picofarads ( $\text{pF} = 10^{-12} \text{ F}$ ) or nanofarads ( $\text{nF} = 10^{-9} \text{ F}$ ). It is worthy of note that the current  $i = dQ/dt$ .

The simplest capacitor is a parallel plane (= electrodes) arrangement (Figure 3.12) for which the electric field is assumed to be uniform between the electrodes (in other words, the thickness is far less than the lateral dimensions). In this case, capacitance is defined as

$$C_0(u) = \frac{\epsilon_0 S_f}{u_0 + u} \quad (3.47)$$

here  $\epsilon_0 = \frac{1}{36\pi} 10^{-9} \text{ F m}^{-1}$  is the vacuum permittivity and  $u_0$  is the distance (gap) between the electrodes at the static equilibrium position. Because capacitance is a function of the distance  $u$ , the latter is underlined in the definition of  $C_0$ .

Equation (3.47) can be demonstrated from Eqs. (3.45), (3.46), and, (3.48) for which the electric field is assumed to be constant and no fringe effect is considered.

### 3.4.1.3 Electric Potential

The electric potential is defined as the energy of a capacitor for a unit electric charge. The elementary potential variation is  $dV = -Edu$  and  $E = |\vec{E}|$  is the electric field.

From a point A of the corresponding electrode to a point B, one can set

$$V_B - V_A = - \int_A^B E dx$$

Finally, in the common practical case where  $E$  is constant and the distance between the electrodes is  $u_0 + u = AB$ ,

$$E = \frac{V_A - V_B}{u_0 + u} \quad (3.48)$$

One of the two potentials is usually the reference potential for which one can set, for example,  $V_A = 0$ .

### 3.4.1.4 Energy

The energy for a capacity  $C_0$  is defined as the total work needed to store  $Q$  charges. For one elementary charge  $\delta q$ . This work is  $\delta W = V(q)\delta q$ . Finally, summing the

electric charges, one can write  $W = \sum_0^Q V \delta q = \sum_0^Q \frac{q}{C_0(u)} \delta q = \frac{1}{2} \frac{Q^2}{C_0(u)}$ .

Using Eq. (3.47), the energy can be written alternatively such as

$$W = \frac{1}{2}QV = \frac{1}{2}C_0(u)V^2 = \frac{1}{2} \frac{Q^2}{C_0(u)} \quad (3.49)$$

#### 3.4.1.5 Force

The force  $\vec{F}$  is defined as the force applied by electrode *A* on electrode *B*. The relationship between the force and the electric field is given as follows:

$$\vec{F} = Q\vec{E} \quad (3.50)$$

At electrical equilibrium, the charge of the electrodes are opposite in sign and equal in quantities. Therefore, an attractive force is generated between the electrodes.

The force can be expressed from the energy stored within the capacitor. The electrical energy is equal to the mechanical work. Therefore, we can set  $F\delta u = \delta W = V(q)\delta q$ .

For *Q* charges, it can be inferred that

$$F = \sum \frac{d(V\delta q)}{du} = \frac{d}{du} \sum V\delta q = \frac{d}{du} W = \frac{d}{du} \left( \frac{1}{2} \frac{Q^2}{C_0(u)} \right) = \frac{d}{du} \left( \frac{1}{2} C_0(u) V^2 \right) \quad (3.51)$$

The last two terms of Eq. (3.51) can be read as the charge constant case  $\frac{d}{du} W|_{Q=\text{cste}}$  or the potential constant case  $\frac{d}{du} W|_{V=\text{cste}}$ , respectively.

From the definition of the energy, the electric charge can be seen as the energy variation for an elementary potential change as

$$Q = \frac{d}{dV} \left( \frac{1}{2} C_0(u) V^2 \right) \quad (3.52)$$

Equations (3.51) and (3.52) can be considered as the constitutive relations for the electrostatic conversion.

### 3.4.2

#### Design Parameters for a Capacitor

Generally, the capacitance value is a function of two geometrical parameters and a “material” parameter. One can write it as follows:

$$C = C(u, S_f, \epsilon_r) \quad (3.53)$$

where  $\epsilon_r$  is the relative electric permittivity, which depends on the material (gas, fluid, or solid) within the gap.

Geometrical parameters can be optimized using various usual architectures, whereas capacitance can be increased through the addition of a dielectric material.

#### 3.4.2.1 Architecture

The basic structure comprises two surfaces (electrodes). The whole or only a part of each structure presents a facing arrangement. The main usual geometries are given in Figure 3.13.

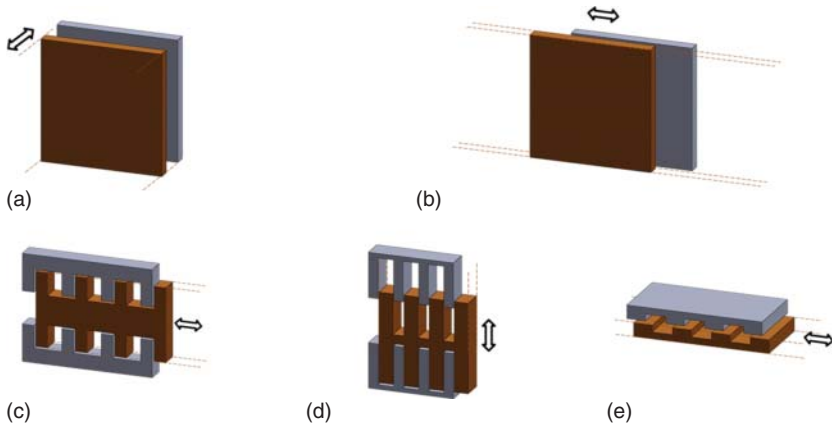


**Figure 3.13** Main arrangements for variable capacitors and their respective derived structures. (a) Out-of-plane gap closing (OP), (b) in plane variable overlap surfaces (IP), (c) OP finger type, (d) IP finger type, and (e) IP boss type.

Two types of variable capacitor are used: out-of-plane gap closing (Figure 3.13 a,c), which allows a large capacitance variation but requires mechanical stoppers, and in-plane gap closing (Figure 3.13b–e), which presents a smaller capacitance variation but can be used without stoppers (Figure 3.13b,e), and mechanical stability issues can occur for large displacements.

It is worthy to note that the out-of-plane finger type in Figure 3.13c is usually called in-plane gap closing because of the nature of the displacement [17]. Considering the relative motion of the electrode surfaces, the out-of-plane type appears to be more relevant here.

The boss type is well suited for variable amplitude displacement as the maximum capacitance variation is obtained for a given pitch of bumps.

#### 3.4.2.2 Dielectric

If an insulated material is introduced within the gap of a capacitor, capacitance is modified as follows:

$$C(u) = \epsilon_r C_0(u) = \epsilon_r \frac{\epsilon_0 S_f}{u_0 + u} \quad (3.54)$$

$\epsilon_r$  is the dielectric constant or relative permittivity.

Dielectric constant of vacuum is equal to 1 ( $\epsilon_r = 1$ ), whereas it is about 1 for gas (e.g.,  $\epsilon_r = 1.00059$  for air). For most insulated liquids or solids,  $2 < \epsilon_r < 12$  [18].

#### 3.4.3

##### Energy Extraction Cycles

An energy cycle has to be established to convert mechanical energy into electrical energy.



With no mechanical or electrical losses, the elementary mechanical work generated on the capacitor ( $dW = Fdu$ ) equals the elementary electric energy ( $dW = Vdq$ ).

Two common cycles are used: the charge-constrained cycle and the voltage-constrained cycle [19]. For the sake of clarity, a parallel plate capacitor will be used hereafter to detail the two cycles. The principle and methodology can be easily extended to other architectures.

### 3.4.3.1 Charge-Constrained Cycle

Figure 3.14 describes the cycle in the  $(Q, V)$  and  $(F, u)$  spaces and gives the equivalent electrical scheme. Let the cycle start at point 1 when the capacitor is at its maximum capacitance  $C_{\text{Max}}$  obtained at the minimal position  $u_0 + u_{\text{min}}$  (note that  $u_{\text{min}}$  can be negative). From points 1 to 2, the structure is charged to a constant electric charge  $Q_c$  using an external polarization source. The associated voltage is  $V_{\text{min}} = Q_c / C_{\text{Max}}$ . Then, the capacitor is set in open-circuit condition. The energy stored in the capacitor is  $E_{Q2} = \frac{1}{2} \frac{Q_c^2}{C_{\text{Max}}}$ . The transfer time  $1 \rightarrow 2$  is supposed to be very small compared to the mechanical period assuming a given harmonic displacement. According to Eq. (3.51), an electrostatic force appears. Under the external excitation, the moving part of the structure proceeds to position  $u_0 + u_{\text{Max}}$  (point 3). By doing this, capacitance is now minimal and equals  $C_{\text{min}}$ . The corresponding mechanical work is provided by the external excitation. The energy stored in the capacitor at point 3 is  $E_{Q3} = \frac{1}{2} \frac{Q_c^2}{C_{\text{min}}}$ . Because of the capacitance variation, one gets  $E_{Q3} > E_{Q2}$ . Electric charges are then removed from the structure and the voltage decreases accordingly ( $3 \rightarrow 4$ ). The transfer time  $3 \rightarrow 4$  is supposed to be very small compared to the mechanical period. The electrostatic force is zero, and the alternative motion of the moving part makes the minimal position  $u_0 + u_{\text{min}}$  to be reached again.

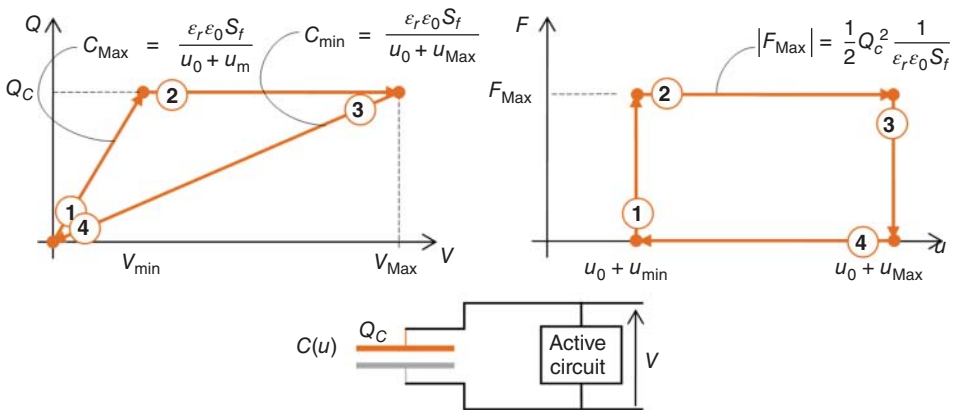


**Figure 3.14** Charge-constrained cycle (a) cycle in the  $(Q, V)$  space; (b) cycle in the  $(F, u)$  space; (c) circuit.

The theoretical extracted energy over a cycle is then given as follows:

$$E_{Q_{\text{cycle}}} = E_{Q_3} - E_{Q_2} = \frac{1}{2} Q_c^2 \left( \frac{1}{C_{\text{min}}} - \frac{1}{C_{\text{Max}}} \right) \quad (3.55)$$

Normalizing with respect to the added energy  $E_a = \frac{1}{2} \frac{Q_c^2}{C_{\text{Max}}}$  yields

$$\bar{E}_{Q_{\text{cycle}}} = \left( \frac{C_{\text{Max}}}{C_{\text{min}}} - 1 \right) \quad (3.56)$$

### 3.4.3.2 Voltage-Constrained Cycle

The description of the voltage constant cycle is similar to the constant charge cycle. Let the cycle start at point 1 in Figure 3.15, when the capacitor is at its maximum capacitance  $C_{\text{Max}}$  obtained at the minimal position  $u_0 + u_{\text{min}}$ . A constant voltage  $V_c$  is applied to the capacitor so that its charges raise to add up to  $Q_{\text{Max}} = C_{\text{Max}} V_c$  (1 → 2). The energy stored in the capacitor is  $E_{V_2} = \frac{1}{2} C_{\text{Max}} V_c^2$ . According to Eq. (3.51), an electrostatic force appears. The moving part of the structure proceeds to position  $u_0 + u_{\text{Max}}$  at point 3, for which the distance is minimal, and capacitance equals  $C_{\text{min}}$ . The corresponding mechanical work is provided by the external excitation. The energy stored in the capacitor at point 3 is  $E_{V_3} = \frac{1}{2} C_{\text{min}} V_c^2$ , and because of the capacitance variation, one gets  $E_{V_3} > E_{V_2}$ . The remaining electric charges ( $Q_{\text{min}} = C_{\text{min}} V_c$ ) are then removed from the structure and the voltage decreases to zero (3 → 4). The electrostatic force is zero, and the alternative motion of the moving part makes the minimal position  $u_0 + u_{\text{min}}$  to be reached again.

It can be pointed out that energy is extracted during the plate movement for the voltage-constrained cycle, contrary to charge-constrained cycle where electrical energy is only harvested during the discharge.

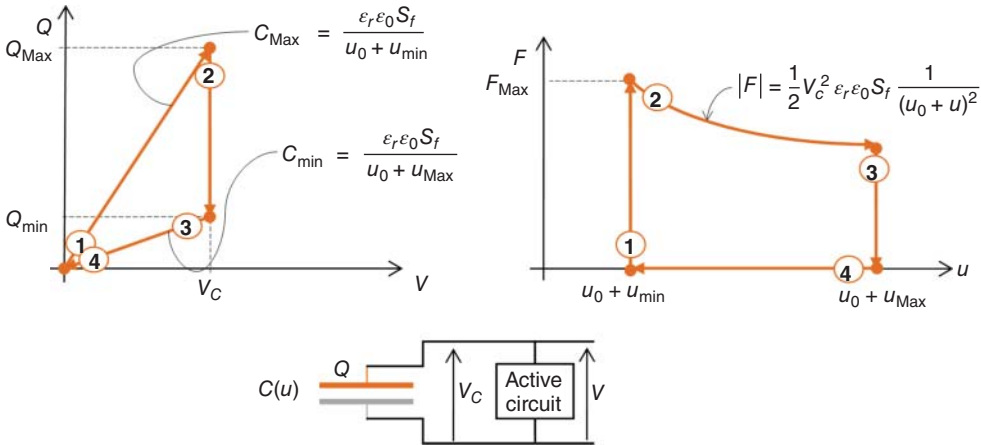


Figure 3.15 Voltage-constrained cycle (a) cycle in the (Q,V) space; (b) cycle in the (F,u) space; (c) circuit.

The theoretical extracted energy over a cycle is then given as follows:

$$E_{V_{\text{cycle}}} = E_{V_3} - E_{V_2} = \frac{1}{2} V_c^2 (C_{\text{Max}} - C_{\text{min}}) \quad (3.57)$$

The extracted electrical energy equals the absorbed mechanical energy and could be obtained using the  $(F, u)$  variables as can be seen in Figure 3.15.

Normalizing with respect to the added energy  $E_a = \frac{1}{2} C_{\text{Max}} V_c^2$  yields

$$\bar{E}_{V_{\text{cycle}}} = \left( 1 - \frac{C_{\text{min}}}{C_{\text{Max}}} \right) \quad (3.58)$$

Comparing Eqs. (3.56) and (3.58), the added energy required to perform the cycle and generate the same amount of energy is greater in the case of the voltage-constrained cycle.

### 3.4.3.3 Electret Cycle

The required high voltage to drive a capacitor is a major drawback of this approach requiring alternative synchronized injection and extraction of charges on the electrode. Electrets are dielectric materials having the ability to keep internal charges. They can be compared with magnets in the electromagnetic approach. The use of electrets allows the aforementioned cycles to be performed without complex driving electronics.

For example,  $\text{SiO}_2/\text{Si}_3\text{N}_4$  layers of a few hundreds of nanometer thickness can hold a 100 V voltage for more than 3 years [20].

The electret material is fixed on one surface between the facing areas of a capacitor. The electret charges  $Q_e$  enforce opposite charges to appear at the electret free electrode so that  $Q_e = Q_{\text{top}} + Q_{\text{bot}}$ , where  $Q_{\text{top}}$  ( $Q_{\text{bot}}$ ) is the amount of charges on the top (bottom) electrode.

The electret can be viewed as a constant capacitor in series with a voltage source  $V_e$  such as  $V_e = Q_e/C_e$ , where  $C_e$  is the electret's capacitance.

The electrical behavior of an electret-based system is governed by the following equation:

$$R \frac{dQ_{\text{top}}(t)}{dt} = V_e - \frac{Q_{\text{top}}(t)}{C(u(t))} \quad (3.59)$$

where  $R$  is the electric load as can be seen in Figure 3.16.

## 3.4.4

### Limits

From Eqs. (3.55) and (3.57), optimization of the energy over a cycle requires that the capacitance variation is maximized, whereas high-voltage sources have to be used to increase the constant charge or voltage.

### 3.4.4.1 Parasitic Capacitors

In practical applications, additional unintended parallel capacitors associated with the fixed parts of a device have to be taken into account.

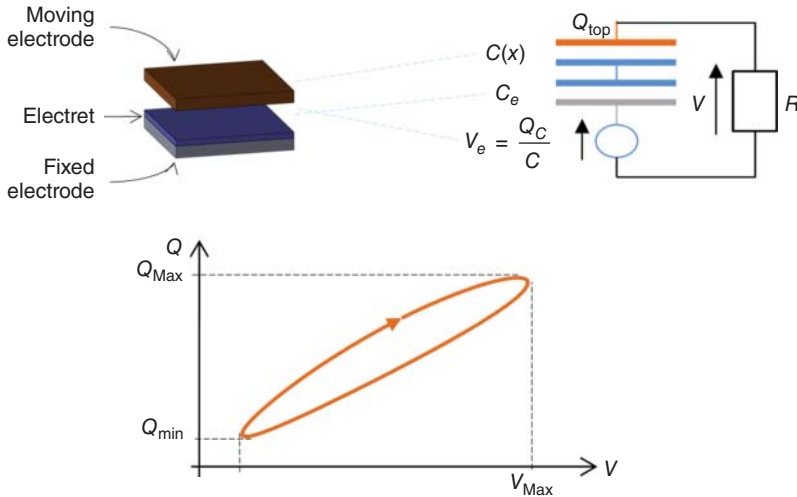


Figure 3.16 Electret-based converter.

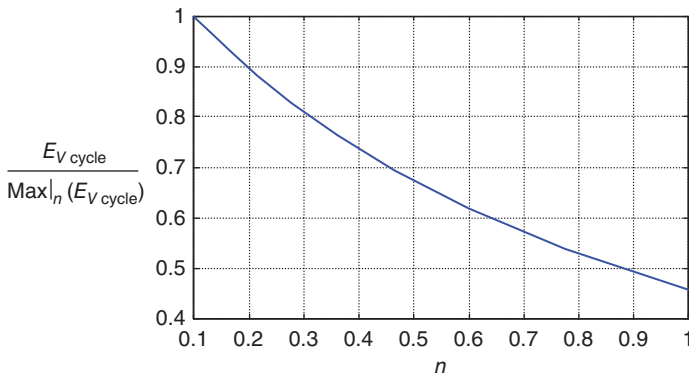


Figure 3.17 Evolution of the voltage-constrained cycle energy with respect to the parasitic capacitance.

The effect of a parasitic capacity  $C_p = nC_{\min}$  on the charge-constrained cycle energy is plotted in Figure 3.17. It can be shown that for a parasitic capacitor that amounts to 30% of the minimal capacitor, the theoretical maximal harvested energy is reduced to approximately 80%.

Capacitance can be increased by using an additional dielectric material. This would reduce the effect of the parasitic capacitance. However, the relative motion of the structures and the detrimental effect of any mechanical damping prevent the practical application of dielectric materials (liquids or polymers).

Moreover, because of the nonideal behavior of dielectric materials, the associated electrical resistance may not be infinite, which induces electrical losses.

#### 3.4.4.2 Breakdown Voltage

Electrical voltage cannot be increased higher than the breakdown voltage. At this value, any free electron would gain sufficient energy for the atoms of a dielectric material to be ionized so that more electrons are released and induce more ionization. The resulting avalanche leads to an electric spark. In gas, this behavior is represented by the Paschen curve. It relates the breakdown characteristics of a gap as a function of the product of the gas pressure  $p$  and the gap length  $u_0 + u$ :  $V_{\text{Max}} = f(p(u_0 + u))$ .

#### 3.4.4.3 Pull-In Force

From Eq. (3.51) the force acting on the electrodes can be established. In classical energy harvesting devices, one electrode is connected to a spring such as the spring force is proportional to the gap. As a result, in the case of a constant voltage cycle, the static equilibrium is given as follows:

$$k(u_{\text{Max}} - u) = -\frac{1}{2} V_c^2 \epsilon_r \epsilon_0 S_f \frac{1}{(u_0 + u)^2} \quad (3.60)$$

Depending on the applied voltage, the balance of the system may be broken to lead to instability for which the two electrodes stick together. With no parasitic capacitors, instability appears at  $u_0 + u_{\text{pi}} = 2/3 (u_0 + u_{\text{Max}})$  and the pull-in voltage is

$$V_{\text{pi}} = \sqrt{\frac{8}{27} \frac{u_0 + u_{\text{Max}}^2}{C_{\text{min}}}} \quad (3.61)$$

### 3.5

#### Other Electromechanical Transduction Principles

Although not as widely used as the previously exposed transduction mechanisms, this part aims at presenting other physical effects for converting mechanical energy into electricity for harvesting purposes.

#### 3.5.1

##### Electrostrictive Materials

Electrostrictive materials, and more particularly electrostrictive polymers, are very suitable for low-frequency, high-strain excitation owing to their flexibility. Hence, contrary to piezoelectric materials, for example, which are very stiff, electrostrictive polymers can be advantageously used for instance in human motion or fluidic energy harvesting.

##### 3.5.1.1 Physical Origin and Constitutive Equations

There are mainly two kinds of dielectric polymers: ionic and dielectric. Ionic electrostrictive polymers are based on the migration of positive and negative ions to the upper and lower electrodes when a voltage is applied. However, such a

phenomenon cannot be successfully applied to energy harvesting, because of high electrical losses. On the other hand, dielectric polymers are based on the dipolar orientation within the polymer matrix [21]. This dielectric nature therefore yields low losses and can be used for energy harvesting purposes. For electrical to mechanical conversion, it can be shown that applying an electric field leads to charges appearing on the electrodes, yielding a Maxwell stress on the sample [22], while in the converse effect, the conversion mechanism is explained by a better orientability of the dipoles due to the application of strain [21]. Hence, it can be shown that, for low regime, electrostriction is defined by a quadratic coupling between the electric field  $E$  and generated strain  $S$ , and by an electric-field activated electromechanical electric displacement [21, 22]:

$$\begin{aligned} S_i &= s_{ii}^E T_i + M_{3i} E_3^2 \\ D_3 &= \epsilon_{33} E_3 + 2M_{3i} E_3 T_i \end{aligned} \quad (3.62)$$

where  $M$  is defined as the electrostrictive coefficient. From a macroscopic point of view, it is also possible to show that the link between the applied force  $F$ , displacement  $u$ , voltage  $V$ , and outgoing current  $I$  is given by (Figure 3.18):

$$\begin{aligned} F &= K^E u + \frac{1}{2} \alpha V^2 \\ I &= \alpha V \dot{u} - C_0 \dot{V} \end{aligned} \quad (3.63)$$

where  $K^E$  denotes the short-circuit stiffness,  $C_0$  is the strain-free capacitance, and  $\alpha$  is the electrostrictive coupling factor.

### 3.5.1.2 Energy Harvesting Strategies

Because of the capacitive nature of dielectric electrostrictive polymers, it is possible to directly apply electrostatic cycles for harvesting energy [23], except that, because in this case the transduction mechanism is intrinsically linked to the material, the stiffness is taken into account when using electrostrictive materials. Another possible way, dispensing the necessity of using controllable voltage sources, consists of using two constant voltage sources, one charging the polymer and the other one used for harvesting the energy [23]. However, from the macroscopic constitutive equations, it can be shown that applying a bias electric field permits disposing of a pseudo-piezoelectric behavior. Indeed, applying a constant bias voltage  $V_{DC}$  and considering that the global voltage on the polymer is this constant voltage plus a varying voltage  $V_{AC}$  (which can be obtained, for example, by using a resistance between the constant voltage source and the electrostrictive material – [24]), with  $V_{AC} \ll V_{DC}$ , the macroscopic

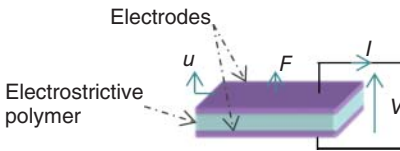


**Figure 3.18** Macroscopic model parameter definition for electrostrictive device.

equations can be rewritten as<sup>3)</sup> follows:

$$\begin{aligned} F &= K^E u + \alpha V_{DC} V_{AC} \\ I &= \alpha V_{DC} \dot{u} - C_0 \dot{V}_{AC} \end{aligned} \quad (3.64)$$

which is similar to the one obtained for piezoelectric element with an equivalent force factor equal to  $\alpha V_{DC}$ . Therefore, applying such a bias voltage allows applying all of the existing techniques for piezoelectric energy harvesting to electrostrictive polymers in a dynamic manner [24].

### 3.5.2

#### Magnetostrictive Materials

The second type of other possible effect lies in magnetostriction. This conversion effect is actually the dual effect of electrostriction, because of the magnetic-based transduction instead of electrostatic.

##### 3.5.2.1 Physical Origin

The physical origin of magnetostriction lies in the orientation of magnetic domains in the material (Villari effect). Hence, constitutive equations similar to those of electrostriction, linking strain to the square of the magnetic strength field  $H$  and showing a strain-activated electromechanical magnetic field  $B$ , can be found (low-field region in Figure 3.19):

$$\begin{aligned} S &= s^H T + mH^2 \\ B &= \mu^T H + 2mHT \end{aligned} \quad (3.65)$$

with  $s^H$  is compliance at constant magnetic strength field,  $\mu^T$  is the stress-free permeability, and  $m$  is the magnetostrictive coefficient.

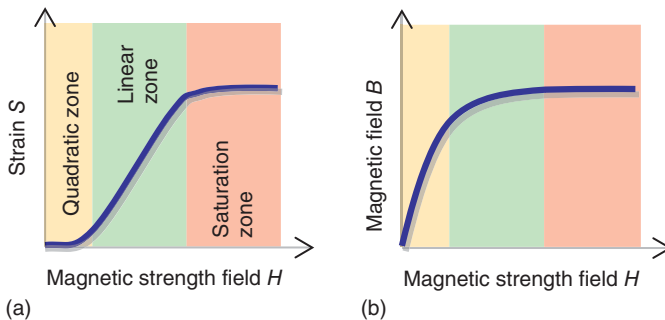


**Figure 3.19** Saturation of magnetostrictive materials: (a) magnetomechanic curve; (b) magnetic curve.

3) The differentiation term, which applies for all the quantities, is omitted here for the sake of simplicity.

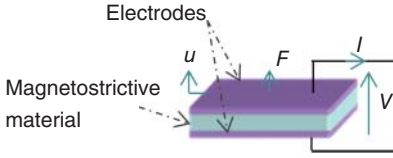


Figure 3.20 Macroscopic model parameter definition for magnetostrictive device.

### 3.5.2.2 Constitutive Equations

However, because of a very early saturation of magnetization (medium-field zone in Figure 3.19b), magnetostrictive materials are typically used in a linear field-induced strain zone (medium-field zone in Figure 3.19a), for example, by the application of a bias magnetic strength field  $H_{DC}$ , yielding linear relationships [25]<sup>4)</sup>:

$$\begin{aligned} S &= s^H T + d(H_{DC})H \\ B &= \mu^T H + d(H_{DC})T \end{aligned} \quad (3.66)$$

with  $d(H_{DC})$  the linearized, bias magnetic strength field-dependent magnetostrictive coefficient.

In a macroscopic point of view, the constitutive equation may be written in terms of  $F$ , the applied force to the material;  $u$ , its displacement;  $V$ , the voltage across the electrodes; and  $I$ , the outgoing current (Figure 3.20):

$$\begin{aligned} F &= K^H u - \beta I \\ V &= \beta \dot{u} - L \dot{I} \end{aligned} \quad (3.67)$$

with  $K^H$ ,  $L$ , and  $b$  referring to the constant magnetic strength field stiffness, strain-free inductance, and magnetostrictive macroscopic coefficient. Therefore, in a macroscopic point of view and in dynamic operations (because of the differentiation term), magnetostrictive materials are similar to electromagnetic materials (with the addition of stiffness because of the material intrinsic electromechanical coupling), allowing the use of all previously exposed strategies for electromagnetic devices.

## 3.6

### Effect of the Vibration Energy Harvester Mechanical Structure

The power generated by a vibration energy harvester does not depend only on the transducer used for electromechanical energy conversion but also on the way the transducer is implemented in a mechanical structure that is suitable to capture ambient mechanical energy.

In most vibration energy harvesters, an inertial mass driven by the ambient acceleration is used to act on the electromechanical transducer. A simple mass–spring–damper system, initially proposed by Williams and Yates [26], can be used to model this behavior. A schematic of such an inertial vibration energy

4) The differentiation term, which applies for all the quantities, is omitted here for the sake of simplicity.



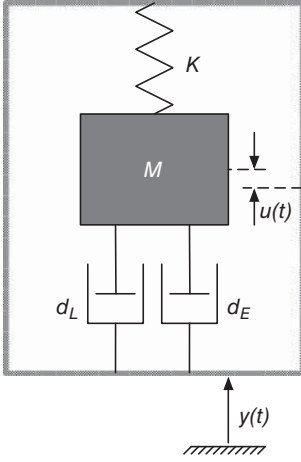


Figure 3.21 Inertial vibration energy harvester.

harvester is shown in Figure 3.21, where  $d_L$  is a damper that embodies mechanical and electrical losses and  $d_E$  is a damper that corresponds to the electromechanical transducer. The assumption of modeling a transducer by a simple damper is valid in the case of sinusoidal ambient acceleration, choosing the value of  $d_E$  such as the energy dissipated into the damper during one mechanical cycle corresponds to the harvested energy.

In this case, the equation governing the motion of the inertial mass is given by Eq. (3.68), where  $\gamma = \ddot{y}$  is the ambient acceleration.

$$M\ddot{u} + (d_E + d_L)\dot{u} + Ku = -M\gamma \quad (3.68)$$

The relative motion  $u$  of the mass with respect to the housing can then be expressed in the frequency domain as follows:

$$\underline{u} = -\frac{\underline{\gamma}}{(\omega_0^2 - \omega^2) + 2j\omega\omega_0(\xi_L + \xi_E)} \quad \text{with} \quad \begin{cases} \omega_0 = \sqrt{\frac{K}{M}} \\ \xi_L = \frac{d_L}{2} \sqrt{\frac{1}{KM}} \\ \xi_E = \frac{d_E}{2} \sqrt{\frac{1}{KM}} \end{cases} \quad (3.69)$$

The harvested power, calculated as the power dissipated in the damper  $d_E$ , is then:

$$P = d_E \omega^2 z_{\text{RMS}}^2 = \frac{2\xi_E M \omega_0 \omega^2 \gamma_{\text{RMS}}^2}{(\omega_0^2 - \omega^2)^2 + 4\omega^2 \omega_0^2 (\xi_L + \xi_E)^2} \quad (3.70)$$

This power reaches a maximum at the resonance frequency ( $\omega = \omega_0$ ) and when the damping ratios equal ( $\xi_E = \xi_L$ ):

$$P_{\text{max}} = d_E \omega^2 u_{\text{RMS}}^2 = \frac{M \gamma_{\text{RMS}}^2}{8\omega_0 \xi_L} \quad (3.71)$$

Finally, the maximal power that can be harvested is proportional to the inertial mass and to the square of the root mean square (RMS) ambient acceleration value.

It is also inversely proportional to the losses (mechanical and electrical) in the harvester and the resonance angular frequency.

This power limit is independent of the transduction principle itself. This means that whatever the transduction mechanism, the maximal power can be harvested provided that the electromechanical coupling is high enough [27] to reach the intrinsic damping ratio.

It is worthy of note that this final result is only valid for inertial linear vibration energy harvesters driven around their resonance frequencies by sinusoidal vibrations. It, however, demonstrates that, in order to evaluate and compare different energy harvesters, it is mandatory to take into account the mechanical structure used to capture the ambient mechanical energy and to drive the electromechanical transducers.

### 3.7

#### Summary

Electrical energy extracted per mechanical cycle has been calculated for electromagnetic, piezoelectric, and electrostatic transducers, in Sections 3.2–3.4 respectively, and figure of merits have been proposed.

From these results, it is, however, impossible to give a clear and definitive comparison of power density of these different transducers. As mentioned in Section 3.6, the harvested power also depends on the mechanical structure of a vibration energy harvester. In the conditions described in Section 3.6, the harvested power theoretically tends to a limit that is not dependent on the transduction mechanism. In fact, technological issues rather than physical limitations usually limit the generated power. For instance, power densities are theoretically not dependent on volume, whereas for practical energy harvesters, they clearly decrease with volume. More precisely, electromagnetic transducers are known to be less effective than piezoelectric and electrostatic transducers for volumes lower than a few cubic centimeters [27, 28].

Moreover, the volume considered when defining the power density is the volume of the transducer itself. It does not take into account the volume of other mechanical and/or electrical parts that are mandatory to realize a vibration energy harvester. For instance, for piezoelectric energy harvesters, a piezoelectric material is usually bonded on a clamped free cantilever beam with an inertial mass at the free end (see Ref. [29] for instance). In a similar way, external voltage source is required for electrostatic systems (without electrets). In this case, volume of the generator is much larger than that of the piezoelectric material.

Finally, the transduction principle has to be chosen according to the targeted application. A rule of thumb is that electrostatic transducers are good for micrometer to millimeter scale applications, piezoelectric transducers are suitable for millimeter to centimeter scale, small strain applications, and electromagnetic transducers are better for large displacement, centimeter to decimeter scale applications.

## References

1. Spreemann, D. and Manoli, Y. (2012) *Electromagnetic Vibration Energy Harvesting Devices*, Springer.
2. von Büren, T. and Tröster, G. (2007) Design and optimization of a linear vibration-driven electromagnetic micro-power generator. *Sens. Actuators, A*, **135** (2), 765–775. doi: 10.1016/j.sna.2006.08.009
3. Arroyo, E., Badel, A., and Formosa, F. (2013) Energy harvesting from ambient vibrations: electromagnetic device and synchronous extraction circuit. *J. Intell. Mater. Syst. Struct.*, **24** (16), 2023–2035. doi: 10.1177/1045389X13488254
4. Arroyo, E. and Badel, A. (2011) Electromagnetic vibration energy harvesting device optimization by synchronous energy extraction. *Sens. Actuators, A*, **171** (2), 266–273. doi: 10.1016/j.sna.2011.06.024
5. Devonshire, A.F. (1949) Theory of barium titanate PART I. *Philos. Mag.*, **40**, 1040.
6. Devonshire, A.F. (1951) Theory of barium titanate PART II. *Philos. Mag.*, **42**, 1065.
7. Landau, L.D. and Lifshitz, E.M. (1980) Statistical physics, in *Course of Theoretical Physics*, vol. 5, Part 1, Elsevier Science Ltd.
8. ANSI/IEEE ANSI/IEEE Std 176-1987. (1988) *IEEE Standard on Piezoelectricity*, IEEE Ultrasonics, Ferroelectrics, and Frequency Control Society. doi: 10.1109/IEEESTD.1988.79638
9. IEEE (1996) Publication and Proposed Revision of ANSI/IEEE Standard 176-1987 “ANSI/IEEE Standard on Piezoelectricity”. *IEEE Trans. Ultrason. Ferroelectr. Freq. Control*, **43** (5), 717. doi: 10.1109/TUFFC.1996.535477
10. Pryia, S. (2010) Criterion for material selection in design of bulk piezoelectric energy harvesters. *IEEE Trans. Ultrason. Ferroelectr. Freq. Control*, **57** (12), 2610.
11. Saint-Gobain Quartz Technical Note and Datasheet, [http://www.ocsimize.fr/download/download\\_doc/materiaux/piezoceramiques.pdf](http://www.ocsimize.fr/download/download_doc/materiaux/piezoceramiques.pdf) (accessed 13 January 2014).
12. Piezotech Piezotech Datasheet, <http://www.piezotech.fr/fr/2-products-piezoelectric-polymers/news/news-31-p-vdf-trfe-piezoelectric-films.html> (accessed 24 January 2014).
13. Li, K.-A. (2009) Modeling time-dependent responses of piezoelectric fiber composite. MSc thesis. Texas A&M University, <http://repository.tamu.edu/handle/1969.1/ETD-TAMU-2009-12-7437> (accessed 13 January 2014)
14. Guyomar, D., Badel, A., Lefeuvre, E., and Richard, C. (2005) Towards energy harvesting using active materials and conversion improvement by nonlinear processing. *IEEE Trans. Ultrason. Ferroelectr. Freq. Control*, **52**, 584.
15. Liu, Y., Tian, G., Wang, Y., Lin, J., Zhang, Q., and Hofmann, H.F. (2009) Active piezoelectric energy harvesting: general principle and experimental demonstration. *J. Intell. Mater. Syst. Struct.*, **20** (5), 575.
16. Williams, R.B. (2004) Nonlinear mechanical and actuation characterization of piezoceramic fiber composites. PhD thesis. Virginia Polytechnic Institute and State University, <http://vtechworks.lib.vt.edu/handle/10919/11141> (accessed 13 January 2014).
17. Roundy, S., Wright, P.K., and Rabaey, J. (2003) A study of low level vibrations as a power source for wireless sensor nodes. *Comput. Commun.*, **26**, 1131–1144.
18. Menguy, C. (1993) Électricité statique – Principes. Problèmes. Applications. Techniques de l’Ingénieurs, p. D1035.
19. Boisseau, S., Despesse, G., Chaillout, J.-J., and Sylvester, A. (2010) Microstructures électrostatiques de récupération d’énergie vibratoire pour les microsystèmes, Techniques de l’Ingénieurs, p. RE160.
20. Amjadi, H. (1999) Charge storage in double layers of thermally grown silicon dioxide and APCVD silicon nitride. *IEEE Trans. Dielectr. Electr. Insul.*, **6** (6), 852–857.

21. Lallart, M., Capsal, J.-F., Sébald, G., Cottinet, P.-J., and Guyomar, D. (2014) Converse electrostrictive effect in dielectric polymers. *Sens. Actuators, B*, **190**, 259.
22. Capsal, J.-F., Lallart, M., Cottinet, P.-J., Galineau, J., Sébald, G., and Guyomar, D. (2012) Evaluation of macroscopic polarization and actuation abilities of electrostrictive dipolar polymers using microscopic Debye/Langevin formalism. *J. Phys. D Appl. Phys.*, **45** (20), 205401.
23. Liu, Y., Ren, K.L., Hofmann, H.F., and Zhang, Q. (2005) Investigation of electrostrictive polymers for energy harvesting. *IEEE Trans. Ultrason. Ferroelectr. Freq. Control*, **12**, 2411.
24. Lallart, M., Cottinet, P.-J., Lebrun, L., and Guyomar, D. (2012) Review: electrostrictive polymer for mechanical energy harvesting. *J. Polym. Sci., Part B: Polym. Phys.*, **50** (8), 523.
25. Wang, L. and Yuan, F.G. (2008) Vibration energy harvesting by magnetostrictive material. *Smart Mater. Struct.*, **17**, 045009.
26. Williams, C.B. and Yates, R.B. (1996) Analysis of a micro-electric generator for microsystems. *Sens. Actuators, A*, **52** (1-3), 8–11. doi: 10.1016/0924-4247(96)80118-X
27. Arroyo, E., Badel, A., Formosa, F., Wu, Y., and Qiu, J. (2012) Comparison of electromagnetic and piezoelectric vibration energy harvesters: model and experiments. *Sens. Actuators, A*, **183**, 148–156. doi: 10.1016/j.sna.2012.04.033
28. Poulin, G., Sarraute, E., and Costa, F. (2004) Generation of electrical energy for portable devices. *Sens. Actuators, A*, **116** (3), 461–471. doi: 10.1016/j.sna.2004.05.013
29. Marzencki, M., Ammar, Y., and Basrour, S. (2008) Integrated power harvesting system including a MEMS generator and a power management circuit. *Sens. Actuators, A*, **145-146**, 363–370. doi: 10.1016/j.sna.2007.10.073

## 4

# Thermal Fundamentals

*Mathieu Francoeur*

### 4.1

#### Introduction

Approximately 60% of the energy consumed in the United States is lost to heat [1, 2]. There is therefore an urgent need for developing devices recycling both low- and high-grade waste heat. The conversion of heat into useful work requires a heat engine. A heat engine produces work by absorbing heat from a high-temperature source and by rejecting heat toward a low-temperature sink. Heat to work conversion is traditionally done via heat engines operating with a working fluid. Alternative technologies such as thermoelectric (TE) and thermophotovoltaic (TPV) power generation can also be employed for converting heat directly into electricity. The potential advantages of these solid-state heat engines come from the fact that they do not require any working fluid and they do not involve any moving parts. For both technologies, micro/nanoscale engineering could positively impact their performances significantly and thus accelerate their implementation [1].

The general objective of this chapter is to provide the fundamental aspects of heat conduction and thermal radiation at the micro/nanoscale necessary to understand TE and TPV power generation. In the next section, the Seebeck effect, which is the basis of TE power generation, is theoretically demonstrated starting from the Boltzmann transport equation (BTE). The efficiency and figure of merit of TE power generators are then discussed using a steady-state, one-dimensional heat transfer analysis. The benefits of using micro/nanostructures and the materials optimizing TE performance are intentionally not addressed here, as they are discussed in Chapters 19 and 14, respectively. Most of the chapter focuses on describing the fundamentals of near-field thermal radiation, both from physical and mathematical standpoints, and their potential application to TPV power generation.

## 4.2

## Fundamentals of Thermoelectric Power Generation

## 4.2.1

## Overview of Nanoscale Heat Conduction and the Seebeck Effect

Conduction is defined as heat transfer through a macroscopically stationary medium caused by a temperature gradient. At the macroscale, conduction heat transfer is considered as a diffusive process and is modeled using Fourier's law  $\mathbf{q} = -k\nabla T$ , where  $\mathbf{q}$  is the heat flux vector ( $\text{W m}^{-2}$ ),  $k$  is the thermal conductivity ( $\text{W m}^{-1} \text{K}^{-1}$ ), and  $\nabla T$  is the temperature gradient ( $\text{K m}^{-1}$ ). Physically, heat is carried by conduction due to the random motion and collisions of the energy carriers. In solids, these energy carriers are electrons and phonons (lattice vibrations). The thermal conductivities of metals and insulators are dominated by electrons and phonons, respectively, while phonons are dominant in semiconductors except in the case of heavily doped materials. The objective of this section is to theoretically demonstrate the Seebeck effect on which TE power generation is based. For that purpose, the BTE, describing transport of energy carriers in nonequilibrium processes, is introduced. Note that detailed discussions of the BTE can be found in Refs [3–5].

At short time and length scales, phonon and electron transport can be described by the BTE given by [3]

$$\frac{\partial f}{\partial t} + \mathbf{v} \cdot \nabla_{\mathbf{r}} f + \frac{\mathbf{F}}{m} \cdot \nabla_{\mathbf{v}} f = \left( \frac{\partial f}{\partial t} \right)_{\text{coll}} \quad (4.1)$$

where  $f$  is the particle distribution function,  $\mathbf{v}$  is the velocity,  $\mathbf{F}$  is an external force acting on the particles,  $m$  is the mass while  $\nabla_{\mathbf{r}}$  and  $\nabla_{\mathbf{v}}$  are the gradients with respect to space and velocity, respectively. The right-hand side of Eq. (4.1) is the scattering term describing particle collisions. The steady-state form of the BTE can be greatly simplified by applying the relaxation time approximation and by assuming local equilibrium [3]:

$$f = f_0 - \tau \left( \mathbf{v} \cdot \nabla_{\mathbf{r}} f_0 + \frac{\mathbf{F}}{m} \cdot \nabla_{\mathbf{v}} f_0 \right) \quad (4.2)$$

where  $\tau$  is the relaxation time, defined as the average time between two successive collisions, and  $f_0$  is the equilibrium distribution function. For electrons and phonons,  $f_0$  is given by the Fermi–Dirac and Bose–Einstein distributions, respectively [4]:

$$f_0 = f_{\text{FD}} = \frac{1}{\exp \left[ \frac{(\varepsilon - \mu)}{k_B T} \right] + 1} \quad (4.3a)$$

$$f_0 = f_{\text{BE}} = \frac{1}{\exp \left[ \frac{\hbar \omega}{k_B T} \right] - 1} \quad (4.3b)$$

where  $\varepsilon$  is the energy of an electron,  $\mu$  is the chemical potential,  $\hbar$  ( $=1.055 \times 10^{-34} \text{ J} \cdot \text{s}$ ) is the Planck constant normalized by  $2\pi$ ,  $k_B$  ( $=1.381 \times 10^{-23} \text{ J K}^{-1}$ ) is the

Boltzmann constant and  $\omega$  is the angular frequency. Note that classical constitutive relations such as Ohm's law and Fourier's law can be derived starting from Eq. (4.2) [3, 4].

The Seebeck effect is demonstrated hereafter by analyzing electron transport under the combined effects of a temperature gradient and an electric field. Without loss of generality, it is assumed that both the temperature gradient and the electric field are along the  $z$ -direction only. The force resulting from the electric field  $E$  is thus given by  $F = -eE$ , where  $-e$  is the charge of an electron. Under these conditions, the simplified BTE can be written as follows:

$$f = f_0 - \tau \left( v_z \frac{\partial f_0}{\partial z} - \frac{eE}{m_e} \frac{\partial f_0}{\partial v_z} \right) \quad (4.4)$$

where  $m_e$  is the electron mass ( $= 9.109 \times 10^{-31}$  kg). The derivatives of the equilibrium distribution function with respect to  $z$  and  $v_z$  can be transformed into derivatives with respect to  $\epsilon$  as follows:

$$\frac{\partial f_0}{\partial z} = -\frac{\partial f_0}{\partial \epsilon} \frac{d\mu}{dz} - \frac{\epsilon - \mu}{T} \frac{\partial f_0}{\partial \epsilon} \frac{dT}{dz} \quad (4.5a)$$

$$\frac{\partial f_0}{\partial v_z} = m_e v_z \frac{\partial f_0}{\partial \epsilon} \quad (4.5b)$$

Substitution of Eqs. (4.5a) and (4.5b) into Eq. (4.4) leads to

$$f = f_0 + \tau v_z \frac{\partial f_0}{\partial \epsilon} \left( \frac{d\mu}{dz} + \frac{\epsilon - \mu}{T} \frac{dT}{dz} + eE \right) \quad (4.6)$$

The current density  $J_e$  ( $\text{Am}^{-2}$ ) is calculated by multiplying the particle flux by the electron charge. The general expression for the current density is given by [4]

$$J_e = -e \int_0^\infty f v_z D(\epsilon) d\epsilon \quad (4.7)$$

where  $D(\epsilon)$  is the density of states. Substitution of the distribution function given by Eq. (4.6) into Eq. (4.7) leads to the following expression for the current density:

$$J_e = -\frac{d\Phi}{dz} L_{11} - \frac{dT}{dz} L_{12} \quad (4.8)$$

The electrochemical potential  $d\Phi/dz$ , and the terms  $L_{11}$  and  $L_{12}$  are given by

$$\frac{d\Phi}{dz} = -\left( \frac{1}{e} \frac{d\mu}{dz} + E \right) \quad (4.9a)$$

$$L_{11} = \frac{-e^2}{3} \int_0^\infty \tau v^2 \frac{\partial f_0}{\partial \epsilon} D(\epsilon) d\epsilon \quad (4.9b)$$

$$L_{12} = \frac{e}{3T} \int_0^\infty \tau v^2 (\epsilon - \mu) \frac{\partial f_0}{\partial \epsilon} D(\epsilon) d\epsilon \quad (4.9c)$$

where  $v_z^2$  has been substituted by  $(1/3)v^2$ . Note that the term  $L_{11}$  is equal to the electrical conductivity  $\sigma_e$  [3]. Physically, Eq. (4.8) can be interpreted as follows.

The first term on the right-hand side represents electrical conduction due to an electrochemical potential gradient, which is a combination of an electrostatic and a chemical potential. The second term on the right-hand side represents the current contribution due to diffusion of electrons induced by a temperature gradient. In open-circuit condition (i.e.,  $J_e = 0$ ), Eq. (4.8) can be reorganized as

$$\frac{d\Phi}{dz} = -\frac{L_{12}}{L_{11}} \frac{dT}{dz} \quad (4.10)$$

where the ratio  $L_{12}/L_{11}$ , usually denoted by  $S$ , is a material property called the *Seebeck coefficient* with units of  $\text{V K}^{-1}$ . Equation (4.10) describes the Seebeck effect and shows that a voltage can be induced across a material by maintaining a temperature gradient. TE power generation is based on the Seebeck effect, where electrical power is produced by a temperature difference.

In the next section, the efficiency of TE power generators is derived by performing a steady-state, one-dimensional heat transfer analysis.

#### 4.2.2

##### Heat Transfer Analysis of Thermoelectric Power Generation

TE power generators are solid-state heat engines. The thermal efficiency of a heat engine is given by

$$\eta = \frac{W_e}{Q_H} \quad (4.11)$$

where  $W_e$  is the electrical power output while  $Q_H$  is the heat supplied by a high-temperature source at temperature  $T_H$ . These two quantities are related to each other via an energy balance,  $W_e = Q_H - Q_L$ , where  $Q_L$  is the amount of heat released to a low-temperature sink at temperature  $T_L$ .

A single-junction TE power generator consisting of two semiconducting legs, one with negative charge carriers (n-doped) and one with positive charge carriers (p-doped) is shown in Figure 4.1. The heat flows in parallel in the legs while the current  $I_e$  flows in series. Thin metallic conductors are used to connect the TE legs to an external load denoted by  $R_L$ . Heat  $Q_H$  from the high-temperature source is supplied on the top portion of the TE device. The current and heat flow in opposite direction in the n-doped material (Seebeck coefficient  $S_n$ ) while the current and heat flow along the same direction in the p-doped material (Seebeck coefficient  $S_p$ ). The electrical power generated by the TE is given by  $W_e = Q_H - Q_L = I_e^2 R_L$ .

The efficiency of TE power generation is derived hereafter using a simple steady-state, one-dimensional heat transfer analysis. Note that only the main equations are presented here; an in-depth discussion of one-dimensional, steady-state conduction in TE devices has been provided by Hodes [6]. The heat supplied to the hot side of the TE device is determined by performing a surface energy balance at  $z = 0$ . The resulting expression can be written as

$$Q_H = \frac{(T_H - T_L)}{R_t} + I_e(S_p - S_n)T_H - \frac{1}{2}I_e^2 R_e \quad (4.12)$$



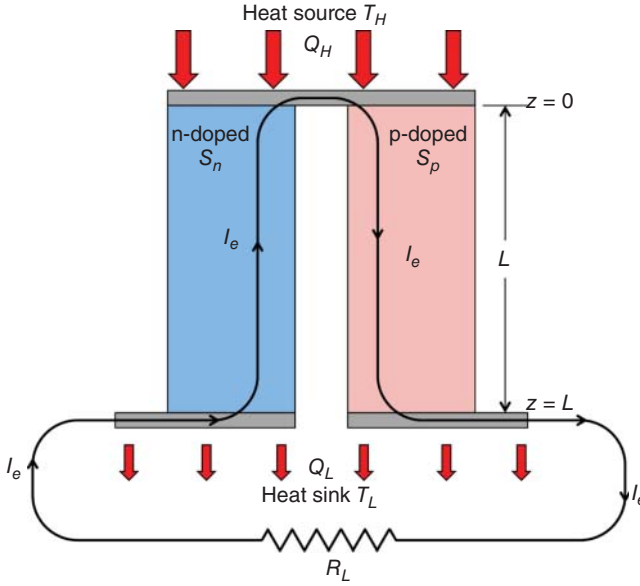


**Figure 4.1** Schematic representation of a single-junction TE power generator. Heat  $Q_H$  is provided by a high-temperature source at  $T_H$  while an amount of heat  $Q_L$  is rejected to a low-temperature sink at  $T_L$ . The temperature gradient established in the TE device induces diffusion of both electrons and holes

along the temperature gradient. The current  $I_e$  flow is opposite to the electron diffusion in the n-doped leg while the current flow is along the same direction as the holes in the p-doped leg. The power produced by the TE device is  $W_e = I_e^2 R_L$ .

where  $R_e$  and  $R_t$  are respectively the electrical and thermal resistances of the two legs [2]. Similarly, the heat output  $Q_L$  can be derived by performing a surface energy balance at  $z = L$ :

$$Q_L = \frac{(T_H - T_L)}{R_t} + I_e(S_n - S_p)T_L + \frac{1}{2}I_e^2 R_e \quad (4.13)$$

The power generated by the TE junction is determined by subtracting Eq. (4.13) from Eq. (4.12):

$$W_e = I_e(S_p - S_n)(T_H - T_L) - I_e^2 R_e \quad (4.14)$$

The current can be expressed as a function of the load resistance by combining Eq. (4.14) with  $W_e = I_e^2 R_L$ :

$$I_e = \frac{(S_p - S_n)(T_H - T_L)}{R_e + R_L} \quad (4.15)$$

The thermal efficiency of the TE power generator is determined by substituting Eqs. (4.12) and (4.14) into Eq. (4.11):

$$\eta = \frac{I_e^2 R_L}{\frac{(T_H - T_L)}{R_t} + I_e(S_p - S_n)T_H - \frac{1}{2}I_e^2 R_e} \quad (4.16)$$

The maximum efficiency is found by taking the derivative of Eq. (4.16) with respect to  $R_L$ , and by setting the resulting expression equal to zero [3]. After some algebraic manipulations, the maximum thermal efficiency is given by

$$\eta_{\max} = \left(1 - \frac{T_L}{T_H}\right) \frac{\sqrt{1 + Z\bar{T}} - 1}{\sqrt{1 + Z\bar{T}} + T_L/T_H} \quad (4.17)$$

where  $\bar{T}$  is an average temperature defined as  $(T_H + T_L)/2$ . Note that the maximum efficiency point is not exactly the same as the maximum power delivery point. Please refer to Chapter 20 for a description of the distinction between maximum efficiency and maximum power delivery. The variable  $Z$  in Eq. (4.17) is called the *figure of merit*. For a given material, the figure of merit is given by [3]:

$$Z = \frac{S^2 \sigma_e}{k} \quad (4.18)$$

In practice,  $Z\bar{T}$  is usually considered as a dimensionless figure of merit. As  $Z\bar{T} \rightarrow \infty$ ,  $\eta_{\max} \rightarrow (1 - T_L/T_H)$  which corresponds to the Carnot efficiency. Materials optimizing TE power generation should have a large Seebeck coefficient  $S$ , a large electrical conductivity  $\sigma_e$  and a small thermal conductivity  $k$ . These properties are not independent of each other, such that maximizing  $Z\bar{T}$  is not a trivial task. Doped semiconductors are typically employed for TE devices as metals have a low  $S$ , while insulators have a small  $\sigma_e$  [1, 3]. Both phonons and electrons contribute to the thermal conductivity of semiconductors. Significant efforts have been devoted to reducing the phonon contribution of thermal conductivity via nanostructures without compromising electron transport [1]. More information about materials suitable for TE power generation is provided in Chapter 6.

### 4.3

#### Near-Field Thermal Radiation and Thermophotovoltaic Power Generation

##### 4.3.1

###### Introduction

Radiation heat transfer is defined as energy transfer by electromagnetic waves due to a temperature gradient. The classical theory of thermal radiation is based on the blackbody concept. A blackbody is defined as an ideal body absorbing and emitting the maximum amount of radiation irrespective of the direction and the wavelength [7–9]. By comparison against the blackbody, surface properties such as emissivity, absorptivity, and reflectivity, that are in general spectral and directional, can be defined. The blackbody concept is, however, based on a fundamental assumption given in Chapter 1 of Planck's book *The Theory of Heat Radiation* [7]: "Throughout the following discussion it will be assumed that the linear dimensions of all parts of space considered, as well as the radii of curvature of all surfaces under consideration, are large compared with the wavelengths

of the rays considered.” This assumption implies that the wave characteristic of the energy carriers is neglected (“neglect the influence of diffraction” [7]), and that radiative transport is considered as incoherent. The key element of Planck’s assumption is that the dimension of the bodies and their separation distances must be larger than the wavelength in order to neglect the wave nature of radiation. This is reasonable because the coherence length of a blackbody is of the same order of magnitude as the dominant wavelength emitted as predicted by Wien’s law ( $\lambda_w T = 2898 \mu\text{m K}$ ) [3].

Progress in nanotechnology has enabled fabrication of engineering devices with micro/nanosize features separated by micro/nanosize distances comparable to, or smaller than, the radiation wavelength. In such devices, the classical theory of thermal radiation ceases to be valid and the wave nature of the energy carriers cannot be neglected. In this so-called near-field regime, radiation heat transfer can exceed by several orders of magnitude the blackbody predictions and the energy carriers may experience constructive and destructive interferences. Enhanced radiation heat transfer between two half-spaces separated by a sub-wavelength vacuum gap has been demonstrated theoretically for the first time by Polder and Van Hove [10] using Rytov’s formalism [11]. Experimental evidence of this phenomenon in the extreme near field (i.e., gaps below 100 nm) has been achieved by measuring radiative heat transfer between a microsphere and a surface [12, 13]. Physically, the enhancement is due to the extraneous contribution to energy transport by waves evanescently confined within a distance of about a wavelength normal to the surface of a thermal source.

The objective of this section is to provide the physical and theoretical background necessary to understand and to predict radiative heat transfer in micro/nanoscale engineering devices where near-field effects play a key role. Additionally, the potential application of near-field thermal radiation to TPV power generation is discussed.

#### 4.3.2

##### Theoretical Framework: Fluctuational Electrodynamics

Near-field thermal radiation is modeled using fluctuational electrodynamics, where stochastic currents representing thermal emission are added to Maxwell’s equations [11]:

$$\nabla \times \mathbf{E}(\mathbf{r}, \omega) = i\omega\mu_0\mu\mathbf{H}(\mathbf{r}, \omega) - \mathbf{J}^{r,m}(\mathbf{r}, \omega) \quad (\text{Faraday’s law}) \quad (4.19a)$$

$$\nabla \times \mathbf{H}(\mathbf{r}, \omega) = -i\omega\varepsilon_0\varepsilon\mathbf{E}(\mathbf{r}, \omega) + \mathbf{J}^{r,e}(\mathbf{r}, \omega) \quad (\text{Ampère’s law}) \quad (4.19b)$$

where  $\mathbf{E}$  and  $\mathbf{H}$  are the electric and magnetic field vectors,  $\varepsilon$  is the relative electric permittivity (dielectric function),  $\mu$  is the relative magnetic permeability,  $\varepsilon_0$  and  $\mu_0$  are respectively the permittivity and permeability of vacuum,  $i$  is the complex constant and  $\mathbf{r}$  is the spatial location. The terms  $\mathbf{J}^{r,m}(\mathbf{r}, \omega)$  and  $\mathbf{J}^{r,e}(\mathbf{r}, \omega)$  are the stochastic currents generating a thermal field due to fluctuating magnetic and electric dipoles, respectively. In the thermal radiation spectral band, most

materials are nonmagnetic such that emission due to magnetic dipole oscillations does not need to be included in Faraday's law. It is worth noting that effectively magnetic materials can be engineered in the thermal spectral band via metamaterials. A few studies have analyzed the effect of magnetic dipole oscillations on near-field radiative heat exchange [14–22]. In the remainder of this section, it is assumed that materials are nonmagnetic ( $\mu = \mu_0$ ) such that the stochastic current due to electric dipole oscillations is denoted by  $\mathbf{J}'(\mathbf{r}', \omega)$  for simplicity. In addition, Eqs. (4.19a) and (4.19b) are valid under the assumptions that the media are homogeneous, isotropic, and described by frequency-dependent dielectric functions local in space.

The electric and magnetic fields observed at  $\mathbf{r}$  due to emission by a source located at  $\mathbf{r}'$  are expressed as a function of the stochastic current using electric and magnetic dyadic Green's functions (DGFs) [23]:

$$\mathbf{E}(\mathbf{r}, \omega) = i\omega\mu_0 \int_V dV' \overline{\overline{\mathbf{G}}}^E(\mathbf{r}, \mathbf{r}', \omega) \cdot \mathbf{J}'(\mathbf{r}', \omega) \quad (4.20a)$$

$$\mathbf{H}(\mathbf{r}, \omega) = \int_V dV' \overline{\overline{\mathbf{G}}}^H(\mathbf{r}, \mathbf{r}', \omega) \cdot \mathbf{J}'(\mathbf{r}', \omega) \quad (4.20b)$$

where  $V$  is the volume of the emitter and  $\overline{\overline{\mathbf{G}}}$  represents the DGF due to electric dipole oscillations, relating a field with frequency  $\omega$  at location  $\mathbf{r}$  to a source located at  $\mathbf{r}'$ . The superscripts  $E$  and  $H$  indicate that an electric ( $E$ ) and a magnetic field ( $H$ ) are generated owing to electric dipole oscillations. The electric and magnetic DGFs are related to each other via the relation  $\overline{\overline{\mathbf{G}}}^H = \nabla \times \overline{\overline{\mathbf{G}}}^E$  [24]. In heat transfer analysis, the quantity of interest is usually the radiative heat flux which is calculated via the time-averaged Poynting vector [4]:

$$\langle \mathbf{S}(\mathbf{r}, \omega) \rangle = 2\text{Re} \{ \langle \mathbf{E}(\mathbf{r}, \omega) \times \mathbf{H}^*(\mathbf{r}, \omega) \rangle \} \quad (4.21)$$

where the superscript\* denotes the complex conjugate and  $\text{Re}$  refers to the real part. Here, the Poynting vector is four times larger than its customary definition, because only positive frequencies are considered in the Fourier decomposition of the time-dependent fields into frequency-dependent fields. The evaluation of the Poynting vector requires computation of terms  $\langle E_m(\mathbf{r}, \omega) H_n^*(\mathbf{r}, \omega) \rangle$  expressed as a function of the stochastic current using Eqs. (4.20a) and (4.20b):

$$\begin{aligned} \langle E_m(\mathbf{r}, \omega) H_n^*(\mathbf{r}, \omega) \rangle &= i\omega\mu_0 \int_V dV' \int_V dV'' G_{m\alpha}^E(\mathbf{r}, \mathbf{r}', \omega) G_{n\beta}^{H*}(\mathbf{r}, \mathbf{r}'', \omega) \\ &\quad \langle J'_\alpha(\mathbf{r}', \omega) J''_\beta{}^*(\mathbf{r}'', \omega) \rangle \end{aligned} \quad (4.22)$$

where  $m$  and  $n$  are orthogonal components representing the state of polarization of the fields ( $m \neq n$ ) while  $\alpha$  and  $\beta$  refer to orthogonal components indicating the state of polarization of the source. Indices  $m\alpha$  and  $n\beta$  imply that a summation is performed over all components. Equation (4.22) shows that the radiative heat flux is proportional to the ensemble average of the spatial correlation function of currents. Note that other quantities of interest in near-field thermal radiation

include the energy density and the local density of electromagnetic states that are also proportional to the spatial correlation function of currents [4, 25].

Radiant energy exchange can be computed in the near field by specifying the moments of the stochastic current. The first moment of the stochastic current is zero, thus implying that the mean thermally radiated electric and magnetic fields are also equal to zero [11]. The radiative flux is proportional to the ensemble average of the spatial correlation function of currents (second moment) which is given by the fluctuation-dissipation theorem [11]:

$$\langle J_\alpha^r(\mathbf{r}', \omega) J_\beta^{r*}(\mathbf{r}'', \omega) \rangle = \frac{\omega \epsilon_0 \epsilon''}{\pi} \Theta(\omega, T) \delta(\mathbf{r}' - \mathbf{r}'') \delta_{\alpha\beta} \quad (4.23)$$

where  $\epsilon''$  is the imaginary part of the dielectric function ( $\epsilon = \epsilon' + i\epsilon''$ ) of the emitting material and  $\Theta$  is the mean energy of an electromagnetic state given by [4]

$$\Theta(\omega, T) = \frac{\hbar\omega}{\exp(\hbar\omega/k_B T) - 1} \quad (4.24)$$

The fluctuation-dissipation theorem is the key for solving near-field thermal radiation problems as it relates the stochastic current due to electric dipole oscillations to the local temperature of the thermal source. The fluctuation-dissipation theorem is applicable to media in local thermodynamic equilibrium where a temperature can be defined [11].

An expression for the monochromatic radiative heat flux along a given orthogonal direction (e.g.,  $z$ -direction) as a function of the source temperature is obtained by substituting Eq. (4.22) into Eq. (4.21) after application of the fluctuation-dissipation theorem and by applying the ergodic hypothesis [26]:

$$\begin{aligned} q_{\omega,z}(\mathbf{r}) &\equiv \langle S_z(\mathbf{r}, \omega) \rangle \\ &= \frac{2k_0^2 \Theta(\omega, T)}{\pi} \operatorname{Re} \left\{ i\epsilon'' \int_V dV' \left[ G_{x\alpha}^E(\mathbf{r}, \mathbf{r}', \omega) G_{y\alpha}^{H*}(\mathbf{r}, \mathbf{r}', \omega) \right. \right. \\ &\quad \left. \left. - G_{y\alpha}^E(\mathbf{r}, \mathbf{r}', \omega) G_{x\alpha}^{H*}(\mathbf{r}, \mathbf{r}', \omega) \right] \right\} \end{aligned} \quad (4.25)$$

where  $k_0$  is the magnitude of the wavevector in vacuum ( $k_0 = \omega/c_0$ , where  $c_0$  is the speed of light in vacuum). The radiative heat flux  $q_{\omega,z}$  has units of  $\text{W m}^{-2} (\text{rad/s})^{-1}$ ; the total radiative heat flux in  $\text{W m}^{-2}$  is calculated by integrating Eq. (4.25) over the entire spectrum:  $q_z(\mathbf{r}) = \int_0^\infty q_{\omega,z}(\mathbf{r}) d\omega$ .

It can be seen from Eq. (4.25) that calculation of the radiative heat flux reduces to determining the appropriate DGFs for a given set of boundary conditions [27, 28]. The majority of near-field thermal radiation problems have been solved by deriving closed-form expressions for the DGFs. This approach has the advantage of providing an exact solution but has the drawback of limiting the analysis to relatively simple geometries such as one-dimensional layered medium [29] and two spheres [30]. Recently, a few discretization-based methods have been proposed for solving near-field thermal radiation problems in complex three-dimensional geometries [21, 31–34]. One of the bottlenecks in modeling near-field thermal radiation problems is the large computational time associated

with solving stochastic equations. In addition, multiscale problems involving, for instance, a large surface and micro/nanoscale objects, as in thermal microscopy where an arbitrarily shaped probe interacts with the near field of a substrate [35, 36], are quite challenging [37, 38]. For these reasons, large-scale computation of near-field radiative heat transfer and coupling with other energy transfer modes is still an open research area.

In the following section, TPV power generation is introduced and the physical details underlying near-field thermal radiation are explained by solving a relatively simple problem involving two half-spaces of silicon carbide (SiC) separated by a vacuum gap.

#### 4.3.3

##### Introduction to Thermophotovoltaic Power Generation and Physics of Near-Field Radiative Heat Transfer between Two Bulk Materials Separated by a Subwavelength Vacuum Gap

A schematic of a TPV power generator is shown in Figure 4.2.

The working principle of TPV power generation is the same as for solar photovoltaic energy conversion. A cell consisting of a p–n junction absorbs thermal radiation and generates electricity with waves having energy  $E$  equal or larger than its absorption bandgap  $E_g$ . The particularity of TPV systems comes from the fact that radiation is provided by a terrestrial source (“radiator”) maintained at some constant and uniform temperature via an external heat input [39]. TPV power generation is an attractive technology for recycling waste heat generated in diverse

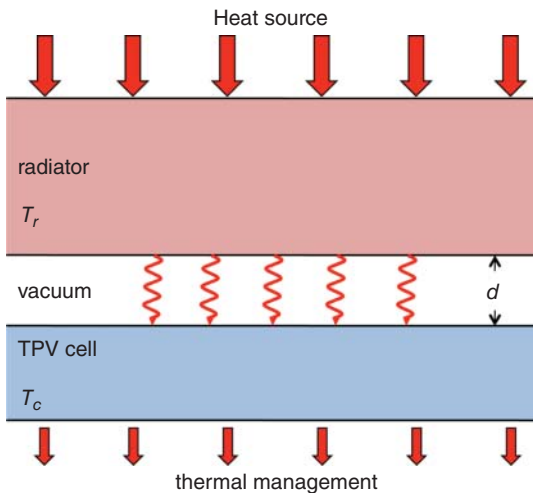


**Figure 4.2** Schematic representation of a TPV power generator. A radiator is maintained at a constant and uniform temperature  $T_r$  via an external heat source, while the

cell is maintained at  $T_c$  using a thermal management device. The radiator and the cell are separated by a vacuum gap of thickness  $d$  in order to avoid heat transfer by conduction.

processes. In addition, there is a growing interest in applying TPV systems for solar energy conversion as the thermal spectrum emitted by the source can be tuned above the cell absorption bandgap by micro/nanostructuring the radiator. Solar TPV power generation has a maximum efficiency of 85.4%, which is similar to the maximum efficiency of 86.8% for infinite multi-junction photovoltaic cells [1]. The potential advantage of TPV devices is that a single-junction cell can be used to achieve the efficiency of multi-junctions. A solar TPV radiator must maximize broadband solar radiation absorption, must minimize reemission to the atmosphere and must optimize reemission toward the cell in order to minimize radiative, electrical, and thermal losses in the p–n junction [40]. Note that Lenert *et al.* [41] recently reported a record efficiency of 3.2% for a solar TPV system, where solar absorption was maximized using multiwalled carbon nanotubes and where selective thermal emission was achieved via a one-dimensional Si/SiO<sub>2</sub> photonic crystal.

Conventional TPV power generators are limited by Planck's blackbody distribution. Whale and Cravalho [42, 43] hypothesized that enhanced power generation and conversion efficiency could be achieved in TPV devices by separating the radiator and the cell by a subwavelength vacuum gap. In other words, the idea is to convert evanescent modes, not playing any role in far-field radiative transfer, into electricity in order to improve TPV performance. Since the near-field effects are dominant at nanoscale gaps for typical thermal radiation temperatures, TPV systems capitalizing on evanescent modes are referred to as *nanoscale-gap TPV power generators* or simply *nano-TPV power generators*. In order to understand the physics underlying nano-TPV power generation, a relatively simple near-field radiative heat transfer problem involving two bulks of SiC, modeled as planar half-spaces and separated by a vacuum gap of thickness  $d$ , is discussed in the rest of this section. Section 4.3.4 is devoted to nano-TPV power generation.

Near-field radiative heat transfer between two SiC half-spaces was analyzed for the first time by Mulet *et al.* [23]. As shown in Figure 4.3, the two half-spaces, labeled as media 1 and 2, are maintained at constant and uniform temperatures  $T_1 = 300$  K and  $T_2 = 0$  K (heat sink). The vacuum separating the SiC slabs is denoted as medium 0. Only the variations of the flux along the  $z$ -axis are considered, because the geometry is azimuthally symmetric and infinite in the  $\rho$ -direction.

As mentioned in Section 4.3.1, radiative energy is transferred in the near field via propagating and evanescent waves. The modes contributing to heat exchange in the near field are schematically illustrated in Figure 4.4.

In Figure 4.4a, a thermally generated wave is propagating within the source medium. At the emitter–vacuum interface, the wave incident at an angle  $\theta_1$  is refracted at an angle  $\theta_0$  in vacuum as predicted by Snell's law [24]. Owing to the propagative nature of the wave refracted in vacuum, heat is carried away from the emitter. Emission of propagating waves a few wavelengths away from the source is correctly described by Planck's blackbody distribution. In the near field, the wave characteristic of propagating modes cannot be ignored owing to potential constructive and destructive interferences. Additionally, Planck's theory assumes that

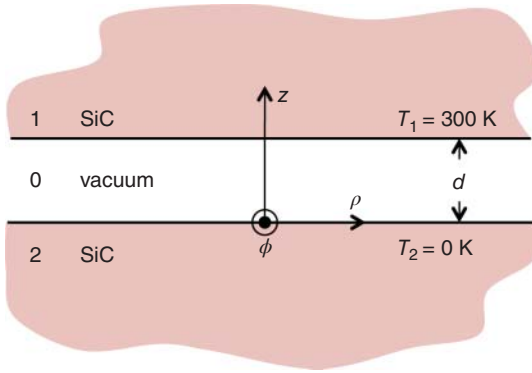


**Figure 4.3** Schematic representation of the geometry considered: two half-spaces of SiC (media 1 and 2) maintained at constant and uniform temperatures  $T_1$  and  $T_2$  are separated by a vacuum gap of thickness  $d$  (medium 0).

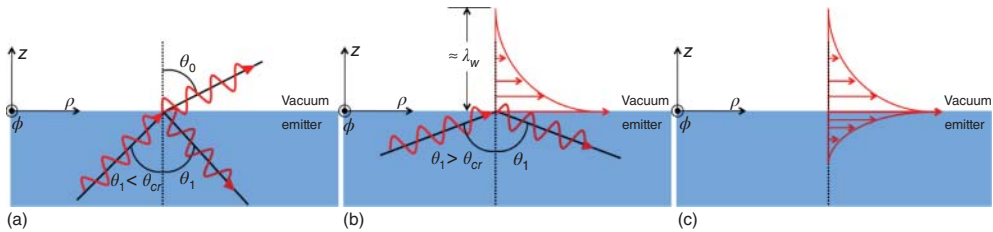


**Figure 4.4** Schematic representation of the modes contributing to near-field radiative heat transfer: (a) propagating wave, (b) evanescent wave generated by total internal reflection, and (c) surface polariton.

thermal emission is a surface process, while fluctuational electrodynamics treats emission as a volumetric phenomenon in accordance with Figure 4.4a. Indeed, Eq. (4.22) shows explicitly that the flux at  $\mathbf{r}$  is the result of sources  $\mathbf{r}'$  contained within a volume  $V$ . This implies that Planck's theory cannot be applied for predicting thermal emission by features with characteristic dimensions of the same order of magnitude as, or less than, the dominant wavelength emitted. The size effect on the emissivity of thin films was analyzed by Edalatpour and Francoeur [44] using fluctuational electrodynamics.

Figure 4.4b depicts a thermally generated wave propagating in the source medium. The wave reaches the emitter–vacuum interface at an angle  $\theta_1$  larger than the critical angle for total internal reflection  $\theta_{cr}$  [24]. Despite the wave being totally reflected back in medium 1, solution of Maxwell's equations at the emitter–vacuum interface predicts the presence of an evanescent wave field decaying exponentially over a distance of about a wavelength in vacuum [24]. Evanescent waves do not play any role in far-field radiation heat transfer (i.e.,  $d \gg \lambda_w$ ) because these modes do not propagate away from the thermal source. However, when a dissipative body is brought within the evanescent wave field of the source, a net energy transfer occurs owing to radiation tunneling [4].



Figure 4.4c shows a schematic representation of a surface polariton, where the field is evanescent both in the emitter and the vacuum. Surface polaritons are different from evanescent waves owing to total internal reflection as they are induced by mechanical oscillations within the emitting medium. In metals and doped semiconductors, the out-of-phase longitudinal oscillations of free electrons relative to the positive ion cores generate an electromagnetic field, and its evanescent component is a surface plasmon–polariton [45]. Similarly, oscillations of transverse optical phonons in polar crystals generate an electromagnetic field and its evanescent component is a surface phonon–polariton [45, 46]. When surface polaritons are excited at their resonant frequency, near-field radiant energy exchange can become quasi-monochromatic owing to a large number of electromagnetic states contained within a narrow spectral band [23, 46–48]. Surface polaritons do not contribute to heat transfer in the far field due to their confinements at an interface; they contribute to radiant energy exchange in the near field by tunneling.

In order to account for all aforementioned modes, the near-field radiative heat flux between media 1 and 2 is calculated using Eq. (4.25) derived from fluctuational electrodynamics. After substitution of the appropriate DGFs for two plane interfaces [46], the net total radiative heat flux along the  $z$ -direction is

$$q_{z,12}^{\text{net,prop}} = \frac{1}{4\pi^2} \int_0^\infty d\omega [\Theta(\omega, T_1) - \Theta(\omega, T_2)] \sum_{\gamma=\text{TE, TM}} \int_0^{k_0} k_\rho dk_\rho \frac{(1 - |r_{01}^\gamma|^2)(1 - |r_{02}^\gamma|^2)}{|1 - r_{01}^\gamma r_{02}^\gamma e^{2ik_{z0}^\gamma d}|^2} \quad (4.26a)$$

$$q_{z,12}^{\text{net,evan}} = \frac{1}{\pi^2} \int_0^\infty d\omega [\Theta(\omega, T_1) - \Theta(\omega, T_2)] \sum_{\gamma=\text{TE, TM}} \int_{k_0}^\infty k_\rho dk_\rho e^{-2k_{z0}^\gamma d} \frac{\text{Im}(r_{01}^\gamma) \text{Im}(r_{02}^\gamma)}{|1 - r_{01}^\gamma r_{02}^\gamma e^{-2k_{z0}^\gamma d}|^2} \quad (4.26b)$$

where  $\text{Im}$  denotes imaginary part,  $\gamma$  indicates the state of polarization of the wave (TE: transverse electric and TM: transverse magnetic),  $k_{zj}$  is the  $z$ -component of the wavevector in medium  $j$  ( $k_{zj} = k_{zj}' + ik_{zj}''$ ),  $k_\rho$  is the parallel component of the wavevector which is purely real while the superscripts prop and evan refer to propagating and evanescent components of the radiative heat flux, respectively. Note that for the case shown in Figure 4.3,  $\Theta(\omega, T_2) = 0$  for all frequencies as medium 2 is a heat sink at 0 K. Eqs. (4.26a) and (4.26b) involve integration over the parallel component of the wavevector. Physically, this integration represents a summation over all possible modes contributing to heat exchange.

For the propagating component of the flux (Eq. (4.26a)), the  $k_\rho$ -integration is performed from 0 up to  $k_0$ . The  $z$ -component of the wavevector in vacuum is calculated as  $k_{z0} = (k_0^2 - k_\rho^2)^{1/2}$ . For  $k_\rho$  values between 0 and  $k_0$ ,  $k_{z0}$  is always a real number and can thus be written as  $k_{z0}'$ . This propagating mode can be represented by  $\exp[i(k_{z0}' z - \omega t)]$ , where the wave has both a periodicity in space and in time. The parallel wavevector  $k_\rho$  can also be written as  $k_0 \sin \theta_0$ , where  $\theta_0$  is the polar

angle as shown in Figure 4.4a. The integration from 0 to  $k_0$  is therefore equivalent to an integration over  $\theta_0$  from 0 to  $\pi/2$  (the integration over the azimuthal angle  $\phi$  is already included in Eq. (4.26a)).

For the evanescent flux (Eq. (4.26b)), the  $k_\rho$ -integration is performed from  $k_0$  to infinity. For these modes, the perpendicular wavevector in vacuum is a pure imaginary number ( $k_{z0} = ik''_{z0}$ ). A solution to this mode can be written as  $\exp[(-k''_{z0}z - i\omega t)]$ , which implies that the wave is evanescently decaying along the  $z$ -direction at a rate of  $\exp(-k''_{z0}z)$ . The integration from  $k_0$  to infinity includes both evanescent waves from total internal reflection (Figure 4.4b) and surface polaritons (Figure 4.4c). Although not necessary, it is possible to split the  $k_\rho$ -integration in Eq. (4.26b) into two parts in order to make the distinction between the two aforementioned evanescent modes [49]. An approximate cutoff for the  $k_\rho$ -integration can be determined from the physics of the problem. The penetration depth of evanescent waves in medium  $j$  is given by  $\delta_j \approx |k_{zj}|^{-1}$  [50]. For large wavevector with  $k_\rho \gg k_0$ , the  $z$ -component of the wavevector can be approximated by  $k_{zj} \approx ik_\rho$ , such that  $k_\rho \approx \delta_j^{-1}$ . Physically, it is possible to argue that the smallest evanescent wave contributing to heat transfer has a penetration depth of the size of the gap separating the SiC layers, such that  $k_\rho \approx d^{-1}$ . This result shows explicitly that the number of modes contributing to heat transfer, and thus the evanescent heat flux, increase as the vacuum gap thickness decreases.

In both Eqs. (4.26a) and (4.26b),  $r_{0j}^\gamma$  ( $j = 1, 2$ ) represents the Fresnel reflection coefficient at the interface 0- $j$  in polarization state  $\gamma$  [24]. The terms  $1 - |r_{0j}^\gamma|^2$  in the numerator of Eq. (4.26a) represents the spectral absorptance of medium  $j$  ( $1 - \text{reflectivity of the surface}$ ), and therefore also represents the spectral emittance of layer  $j$ . A similar interpretation can be given to  $\text{Im}(r_{01}^\gamma)$  that represents the spectral emittance/absorptance for evanescent waves. The denominators in Eqs. (4.26a) and (4.26b) account for multiple reflection within the vacuum gap of thickness  $d$ . The exponential factor  $e^{-2k''_{z0}d}$  multiplying the integrand in Eq. (4.26b) shows explicitly the evanescent nature of the radiative heat flux; for a large gap  $d \gg \lambda_w$  (i.e., far-field regime),  $e^{-2k''_{z0}d} \rightarrow 0$  such that the flux due to evanescent waves is nil. In addition, in the limit  $d \gg \lambda_w$ , it can be shown that Eq. (4.26a) reduces to the flux derived from the view factor theory [4]. This demonstrates that the classical theory of thermal radiation based on Planck's blackbody distribution is a special case of the fluctuational electrodynamics formalism.

The spectral near-field radiative heat flux is shown in Figure 4.5 for gap thicknesses of 10, 100 nm, and 1  $\mu\text{m}$ . These results are compared against the blackbody predictions and the flux obtained in the far-field regime. Note that the spectral variable here is in electron-volt (eV), which is calculated from the angular frequency as  $E = \hbar\omega/e$ , where  $e = 1.602 \times 10^{-19}$  J eV $^{-1}$ .

The results of Figure 4.5 show an enhancement of the flux beyond the blackbody predictions due to tunneling of evanescent waves. In the extreme near field (gaps of 10 and 100 nm), the flux increases substantially at a frequency of approximately 0.12 eV. This quasi-monochromatic enhancement is due to surface phonon-polaritons supported by SiC [23]. For a 10-nm-thick vacuum gap, more

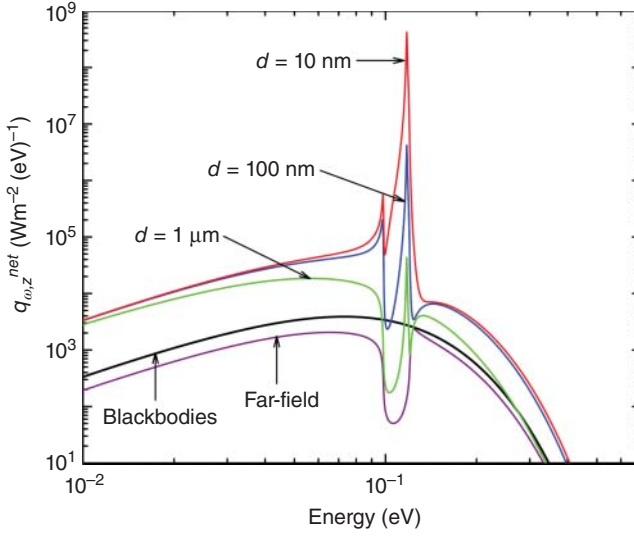


**Figure 4.5** Net monochromatic radiative heat flux as a function of the vacuum gap thickness  $d$ . The layers of SiC are maintained at constant and uniform temperatures of 300 and 0 K.

than 97% of the flux is transferred around 0.12 eV due to a large number of modes concentrated in a narrow spectral band [48].

The dependence of the radiative heat transfer as a function of the gap thickness is analyzed in Figure 4.6. Specifically, the total radiative heat transfer coefficient  $h_r$  is reported for gaps from 1 to 100 nm. The near-field profile is compared against blackbody and far-field predictions. Note that the radiative transfer coefficient is derived by assuming that medium one is at temperature  $T$  (300 K) while medium two is at  $T + \delta T$ , such that  $h_r$  is calculated as the net radiative heat flux between the two layers divided by  $\delta T$  as  $\delta T \rightarrow 0$  [51]:

$$h_r = \frac{1}{\pi^2} \int_0^\infty d\omega \frac{\partial \Theta(\omega, T)}{\partial T} \sum_{\gamma=\text{TE, TM}} \left[ \int_0^{k_0} k_\rho dk_\rho \frac{(1 - |r_{01}^\gamma|^2)(1 - |r_{02}^\gamma|^2)}{4|1 - r_{01}^\gamma r_{02}^\gamma e^{2ik_{z0}^\gamma d}|^2} \right] + \int_{k_0}^\infty k_\rho dk_\rho e^{-2k_{z0}^\gamma d} \frac{\text{Im}(r_{01}^\gamma) \text{Im}(r_{02}^\gamma)}{|1 - r_{01}^\gamma r_{02}^\gamma e^{-2k_{z0}^\gamma d}|^2} \quad (4.27)$$

Both the blackbody and far-field curves do not vary as a function of the vacuum gap thickness as the view factor between two half-spaces is unity [8, 9]. It can be seen in Figure 4.6 that the radiative transfer coefficient varies as  $d^{-2}$  in the extreme near field [23]. For structures with micro/nanosize dimensions, the  $d^{-2}$  power law reported here is not always true owing to surface phonon–polariton coupling within the emitters/absorbers. Francoeur *et al.* [51] reported the coexistence of  $d^{-2}$ ,  $d^{-3}$ , and  $d^{-4}$  regimes for thin films supporting surface polaritons in

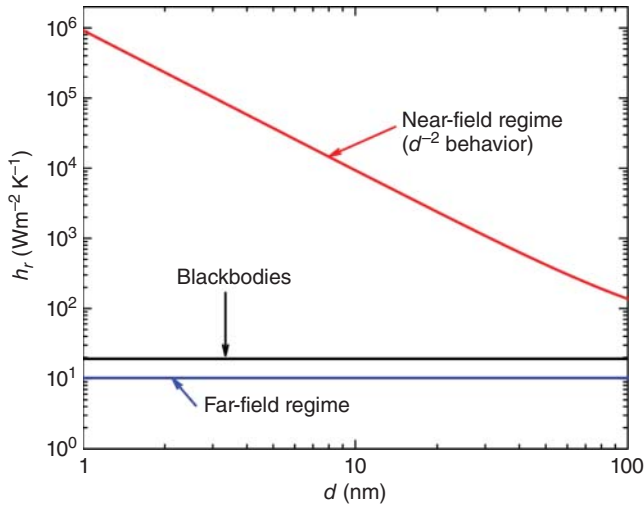


**Figure 4.6** Radiative heat transfer coefficient as a function of the vacuum gap thickness  $d$  (SiC,  $T = 300$  K). The near-field curve shows that the radiative heat transfer

coefficient follows a  $d^{-2}$  power law, while both the far-field and blackbody curves do not vary as a function of the gap thickness.

the infrared such as SiC. A combined  $d^{-2}$  and  $d^{-3}$  regime for thin films was also reported by Ben-Abdallah *et al.* [52].

The next section discusses in greater detail nano-TPV power generation capitalizing on the near-field effects of thermal radiation where both propagating and evanescent modes are directly converted into electricity.

#### 4.3.4

##### Nanoscale-Gap Thermophotovoltaic Power Generation

While conceptually simple, the nano-TPV power generators discussed in the beginning of Section 4.3.3 are challenging to fabricate. Indeed, a gap up to about a micrometer must be maintained between two surfaces having dimensions of a few hundreds of micrometers to a few millimeters in order to obtain significant heat transfer by evanescent modes. In addition, the surfaces must be smooth enough such that the radiator and the cell do not touch each other. Finally, the structure maintaining the gap must have a low thermal conductivity in order to minimize heat transfer by conduction between the radiator and the cell. Owing to these technological challenges, experimental demonstration of enhanced performance in nano-TPV power generators has been essentially qualitative. DiMatteo *et al.* [53–55] experimented on a system comprised of a silicon radiator and indium arsenide (InAs) cells. The gap was maintained via 1- $\mu\text{m}$ -tall silicon dioxide ( $\text{SiO}_2$ ) posts. A short-circuit current enhancement by a factor of 5 [53, 54] and a power output enhancement of uncertain magnitude [55] were reported. Hanamura *et al.* [56–58] performed experiments on a nano-TPV system made of a tungsten

radiator and gallium antimonide (GaSb) cells. A short-circuit current increase by factors of 3 [57] and 3.7 [58] was observed. It is worth noting that experimental demonstration of radiation heat transfer exceeding the blackbody limit in the extreme near field has not been reported between two parallel surfaces. Hu *et al.* [59] showed a flux exceeding by 35% the blackbody predictions by maintaining a 1.6  $\mu\text{m}$ -thick-gap between glass plates via polystyrene spheres. Ottens *et al.* [60] implemented a system that used three stepper motors allowing precise variations of the gap from 100 down to 2  $\mu\text{m}$ . Results between two sapphire surfaces demonstrated an enhancement of the flux by 27% over the blackbody predictions.

Another technological bottleneck of TPV systems is associated with the cell converting radiation into electricity. Silicon-based solar cells have an absorption bandgap of about 1.1 eV such that approximately 75% of the solar spectrum is above this threshold (the solar spectrum can be approximated by a blackbody at a temperature of 5800 K) [8, 9]. TPV power generators operate at temperatures between 1000 and 2000 K, such that lower energy waves (longer wavelengths) need to be converted into electricity. This implies that the absorption bandgap of TPV cells must be lower than 1.1 eV, typically between 0.50 and 0.75 eV. Lower absorption bandgap cells are not readily available, and research has mainly focused on III–V binary compounds, such as gallium arsenide (GaAs) and GaSb, and their ternary and quaternary III–V alloys [61, 62].

Theoretical investigations of nano-TPV power generation are relatively scarce [40, 42, 43, 63–70]. The literature suggests that power generation can be enhanced by a factor of 20–30 when the gap between the radiator and the cell is a few tens

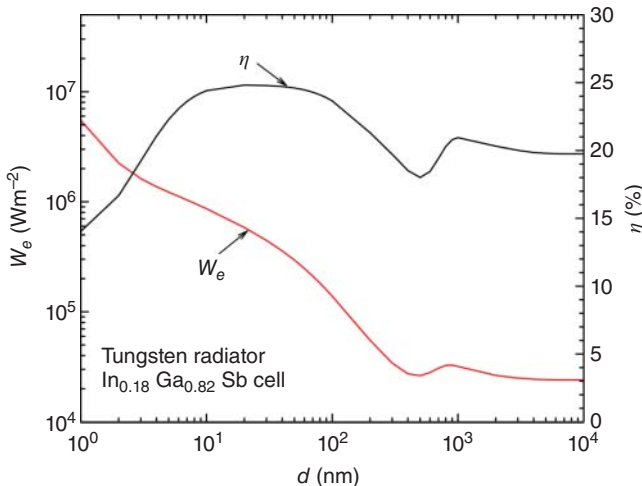


**Figure 4.7** Electrical power output  $W_e$  and conversion efficiency  $\eta$  of a nano-TPV power generator made of a tungsten radiator ( $T_r = 2000$  K) and indium gallium antimonide  $\text{In}_{0.18}\text{Ga}_{0.82}\text{Sb}$  cell ( $T_c = 300$  K).

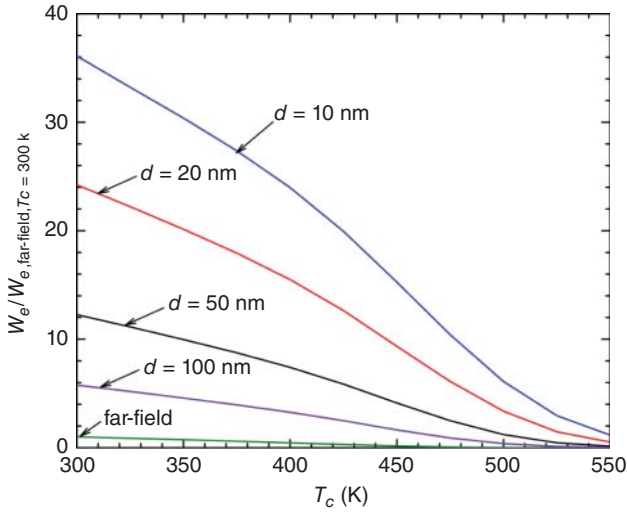


**Figure 4.8** Power output enhancement of a nano-TPV power generator made of a tungsten radiator ( $T_r = 2000$  K) and indium gallium antimonide  $\text{In}_{0.18}\text{Ga}_{0.82}\text{Sb}$  cell as a function of the vacuum gap thickness  $d$  and

the cell temperature  $T_c$ . The power output enhancement is calculated by normalizing the actual power output by the power output obtained in the far-field regime ( $d \gg \lambda_w$ ) when  $T_c$  is fixed at 300 K.

of nanometers [65, 66], provided that the cell is maintained around room temperature [40]. The gain in conversion efficiency is marginal however when a broadband radiator is used. Figure 4.7 shows the electrical power output  $W_e$  and the conversion efficiency  $\eta$  as a function of the separation gap  $d$  for a nano-TPV device made of a tungsten radiator at 2000 K and a 10.4- $\mu\text{m}$ -thick indium gallium antimonide ( $\text{In}_{0.18}\text{Ga}_{0.82}\text{Sb}$ ) cell maintained at 300 K. The details of the multiphysics model combining near-field thermal radiation, charge and heat transport used to generate these results are provided in Ref. [40].

The power output increases substantially as the vacuum gap decreases from 10  $\mu\text{m}$  down to 10 nm. Tungsten is a broadband emitter, which implies that the thermal spectrum increases above the blackbody limit at all frequencies in the near field. For this reason, the gain in conversion efficiency, defined as the electrical power output divided by the radiation absorbed by the cell, is marginal. Figure 4.8 shows the power output of the aforementioned nano-TPV power generator normalized by the power output obtained by the same device when  $d \gg \lambda_w$  and when the cell is maintained at 300 K. This power output enhancement is reported as a function of the cell temperature for vacuum gaps of 10, 20, 50, and 100 nm.

The power output enhancement at 300 K reaches a maximum value of 36 for a 10-nm-thick gap and a minimum value of approximately 6 when the gap is 100-nm-thick. Figure 4.8 also shows that the enhancement decreases as the cell temperature increases, regardless of the gap thickness. This behavior can be

explained by the fact that the dark current of the cell increases as its temperature increases [40]. Francoeur *et al.* [40] showed that it is quite challenging to maintain the temperature gradient of 2000 to 300 K usually discussed in the literature. Modeling the thermal management system as a convective boundary, simulation results suggested that a high heat transfer coefficient of the order of  $10^5 - 10^6 \text{ W m}^{-2} \text{ K}^{-1}$  is needed to maintain the cell at room temperature. Thermal dissipation in the cell is due to three mechanisms. Radiation with energy lower than the bandgap is absorbed by the lattice and the free carriers and is thus converted into heat. Radiation with energy higher than the bandgap dissipates its excess of energy into heat, a phenomenon called *thermalization*. Finally, electron–hole pairs generated by radiation absorption may recombine without generating electricity, and this recombination leads to heat dissipation in the cell.

Better performing nano-TPV power generators can be achieved by tuning radiation heat transfer between the radiator and the cell in order to minimize radiative, electrical, and thermal losses. Laroche *et al.* [65] showed that enhanced power generation can be increased by an additional factor of 15 when using a radiator supporting surface polaritons in the near infrared. Narayanaswamy and Chen [64] suggested using polar crystals such as SiC and cubic boron nitride as nano-TPV radiators. While conceptually correct, this solution is difficult to implement in practice as surface phonon–polaritons supported by polar crystals exist at wavelengths of approximately  $10 \mu\text{m}$  corresponding to energy of 0.12 eV. Metals such as gold and silver support surface plasmon–polaritons in the ultraviolet and visible spectral bands [45]. Therefore, these resonant modes cannot be thermally excited. Surface plasmon–polaritons can be excited in the infrared band via doped silicon [47, 71, 72]. However, the resonant frequency of these modes is similar to those of polar crystals. In fact, materials supporting surface polaritons matching the typical bandgap of TPV cells (near infrared spectral band) are quite challenging to find in nature. A recent survey of plasmonics materials beyond the typical gold and silver has been provided by West *et al.* [73]. For instance, indium-tin-oxide could be an interesting material to be exploited for nano-TPV power generation, as its plasma frequency can be tuned between 0.44 and 6.99 eV by varying the tin doping level [67, 73]. One must keep in mind however that using a bulk radiator supporting surface polaritons still results in an enhancement of the radiative flux beyond the blackbody predictions at all frequencies (e.g., see Figure 4.5). Except for surface polaritons, propagating and evanescent waves in the vacuum are the result of waves propagating within the emitter. Therefore, decreasing the volume of the emitter below the skin depth reduces propagating waves and evanescent waves due to total internal reflection, and thus the radiative flux except at surface polariton resonance [74]. This effect could be exploited for nano-TPV power generation capitalizing on surface polaritons. Graphene has also been considered by Ilic *et al.* [67] and by Messina and Ben-Abdallah [69]. Another potential solution is to use man-made structures, such as photonic crystals or metamaterials, for controlling near-field radiation heat transfer between the radiator and the cell. Regardless of the method employed for tuning radiative heat transfer in nano-TPV systems, it is imperative that the design accounts for the combined effects of

radiative, electrical and thermal losses in the cell. For instance, surface polariton mediated heat transfer seems *a priori* the optimal way of maximizing nano-TPV performance. However, the low penetration depth of surface polaritons into the cell causes significant electrical and thermal losses [75]. As such, thin cells with low surface recombination velocity might be needed when heat transfer between the radiator and the cell occurs mostly via surface polaritons. Finally, nano-TPV power generators could potentially be applied for recycling low-temperature waste heat produced for instance by electronic devices such as computers and photovoltaic cells. Thermal management of low-temperature TPV systems would be easier than for high-temperature applications. On the other hand, such nano-TPV power generators would require a radiator converting long wavelength radiation ( $\sim 10\ \mu\text{m}$ ) to short wavelengths ( $\sim 2\ \mu\text{m}$ ) or a cell with an extremely low absorption bandgap ( $\sim 0.1\ \text{eV}$ ).

#### 4.4

#### Conclusions

In summary, this chapter discussed the fundamentals of TE power generation by demonstrating the Seebeck effect starting from the BTE. It was also pointed out that the efficiency of TE devices can be maximized by using materials having large electrical conductivity and Seebeck coefficient while having a small thermal conductivity due to phonons. The basics covered here will be useful for more detailed discussions on TE power generation given in Chapters 6, 12, and 21.

A large portion of the chapter was devoted to the fundamentals of near-field thermal radiation and its potential application to TPV power generation. Nano-TPV power generation is a promising technology for recycling waste heat and/or solar energy conversion. From an experimental viewpoint, it is clear that demonstrating enhanced power generation is still an open research area. Both precision systems and micro/nanoscale engineering devices showing power output enhancement will have a significant impact on the development of these energy harvesting devices. From a design point of view, modeling and optimization must be made on a system level that accounts not only for radiative transfer but the combined effects of radiative, electrical, and thermal losses. The interplay between these three mechanisms is quite complex and a thorough understanding is needed in order to design and fabricate viable and efficient nano-TPV power generators.

#### Acknowledgments

The author acknowledges the financial support of the National Science Foundation (Grant No. CBET 1253577).



## References

1. Baxter, J. *et al.* (2009) Nanoscale design to enable the revolution in renewable energy. *Energy Environ. Sci.*, **2**, 559–588.
2. Bergman, T.L., Lavine, A.S., Incropera, F.P., and DeWitt, D.P. (2011) *Fundamentals of Heat and Mass Transfer*, 7th edn, John Wiley & Sons, Inc, Hoboken, NJ.
3. Chen, G. (2005) *Nanoscale Energy Transport and Conversion*, Oxford University Press, New York.
4. Zhang, Z.M. (2007) *Micro/Nanoscale Heat Transfer*, McGraw-Hill, New York.
5. Kaviani, M. (2008) *Heat Transfer Physics*, Cambridge University Press, Cambridge.
6. Hodes, M. (2005) One one-dimensional analysis of thermoelectric modules (TEMs). *IEEE Trans. Compon. Packag. Technol.*, **28**, 218–229.
7. Planck, M. (1991) *The Theory of Heat Radiation*, Dover Publications, New York.
8. Howell, J.R., Siegel, R., and Mengüç, M.P. (2010) *Thermal Radiation Heat Transfer*, 5th edn, CRC Press.
9. Modest, M.F. (2013) *Radiative Heat Transfer*, 3rd edn, Elsevier.
10. Polder, D. and Van Hove, M. (1971) Theory of radiative heat transfer between closely spaced bodies. *Phys. Rev. B*, **4** (10), 3303–3314.
11. Rytov, S.M., Kravtsov, Y.A., and Tatarskii, V.I. (1989) *Principles of Statistical Radiophysics 3: Elements of Random Fields*, Springer, New York.
12. Shen, S., Narayanaswamy, A., and Chen, G. (2009) Surface phonon polaritons mediated energy transfer between nanoscale gaps. *Nano Lett.*, **9** (8), 2909–2913.
13. Rousseau, E., Siria, A., Jourdan, G., Volz, S., Comin, F., Chevrier, J., and Greffet, J.-J. (2009) Radiative heat transfer at the nanoscale. *Nat. Photonics*, **3** (9), 514–517.
14. Joulain, K., Drevillon, J., and Ben-Abdallah, P. (2010) Noncontact heat transfer between metamaterials. *Phys. Rev. B*, **81**, 165119.
15. Francoeur, M., Basu, S., and Petersen, S.J. (2011) Electric and magnetic surface polariton mediated near-field radiative heat transfer between metamaterials made of silicon carbide particles. *Opt. Express*, **19**, 18774–18788.
16. Biehs, S.-A., Tschikin, M., and Ben-Abdallah, P. (2012) Hyperbolic metamaterials as an analog of a blackbody in the near field. *Phys. Rev. Lett.*, **109**, 104301.
17. Biehs, S.-A., Tschikin, M., Messina, R., and Ben-Abdallah, P. (2013) Super-Planckian near-field thermal emission with phonon-polaritonic hyperbolic metamaterials. *Appl. Phys. Lett.*, **102**, 131106.
18. Zheng, Z. and Xuan, Y. (2011) Theory of near-field radiative heat transfer for stratified magnetic media. *Int. J. Heat Mass Transfer*, **54**, 1101–1110.
19. Petersen, S.J., Basu, S., and Francoeur, M. (2013) Near-field thermal emission from metamaterials. *Photonics Nanostruct. Fundam. Appl.*, **11**, 167–181.
20. Petersen, S.J., Basu, S., Raeymaekers, B., and Francoeur, M. (2013) Tuning near-field thermal radiative properties by quantifying sensitivity of Mie resonance-based metamaterials design parameters. *J. Quant. Spectrosc. Radiat. Transfer*, **129**, 277–286.
21. Liu, B. and Shen, S. (2013) Broad-band near-field radiative thermal emitter/absorber based on hyperbolic metamaterials: Direct numerical simulation by the Wiener chaos expansion method. *Phys. Rev. B*, **87**, 115403.
22. Basu, S. and Francoeur, M. (2014) Near-field radiative heat transfer between thin films made of metamaterials. *Opt. Lett.*, **39** (5), 1266–1269.
23. Mulet, J.-P., Joulain, K., Carminati, R., and Greffet, J.-J. (2002) Enhanced radiative heat transfer at nanometric distances. *Nanoscale Microscale Thermophys. Eng.*, **6**, 209–222.
24. Novotny, L. and Hecht, B. (2006) *Principles of Nano-Optics*, Cambridge University Press, New York.
25. Joulain, K., Carminati, R., Mulet, J.-P., and Greffet, J.-J. (2003) Definition and measurement of the local density

- of electromagnetic states close to an interface. *Phys. Rev. B*, **68**, 245405.
26. Mandel, L. and Wolf, E. (1995) *Optical Coherence and Quantum Optics*, Cambridge University Press, Cambridge.
  27. Tai, C.-T. (1994) *Dyadic Green's Functions in Electromagnetic Theory*, IEEE Press, Piscataway.
  28. Sipe, J.E. (1987) New Green-function formalism for surface optics. *J. Opt. Soc. Am. B*, **4** (4), 481–489.
  29. Francoeur, M., Mengüç, M.P., and Vaillon, R. (2009) Solution of near-field thermal radiation in one-dimensional layered media using dyadic Green's functions and the scattering matrix method. *J. Quant. Spectrosc. Radiat. Transfer*, **110**, 2002–2018.
  30. Narayanaswamy, A. and Chen, G. (2008) Thermal near-field radiative transfer between two spheres. *Phys. Rev. B*, **77**, 075125.
  31. Rodriguez, A.J., Ilic, O., Bermel, P., Celanovic, I., Joannopoulos, J.D., Soljacic, M., and Johnson, S.G. (2011) Frequency-selective near-field radiative heat transfer between photonic crystal slabs: a computational approach for arbitrary geometries and materials. *Phys. Rev. Lett.*, **107**, 114302.
  32. Wen, S.-B. (2010) Direct numerical simulation of near field thermal radiation based on Wiener chaos expansion of thermal fluctuating current. *ASME J. Heat Transfer*, **132**, 072704.
  33. Rodriguez, A.W., Reid, M.T.H., and Johnson, S.G. (2012) Fluctuating surface-current formulation of radiative heat transfer for arbitrary geometries. *Phys. Rev. B*, **86**, 220302(R).
  34. Edalatpour, S. and Francoeur, M. (2014) The Thermal Discrete Dipole Approximation (T-DDA) for near-field radiative heat transfer simulations in three-dimensional arbitrary geometries. *J. Quant. Spectrosc. Radiat. Transfer*, **133**, 364–373.
  35. Babuty, A., Joulain, K., Chapuis, P.-O., Greffet, J.-J., and De Wilde, Y. (2013) Blackbody spectrum revisited in the near field. *Phys. Rev. Lett.*, **110**, 146103.
  36. Joulain, K., Ben-Abdallah, P., Chapuis, P.-O., De Wilde, Y., Babuty, A., and Henkel, K. (2014) Strong tip-sample coupling in thermal radiation scanning tunneling microscope. *J. Quant. Spectrosc. Radiat. Transfer*, **136**, 1–15.
  37. McCauley, A.P., Reid, M.T.H., Krüger, M., and Johnson, S.G. (2012) Modeling near-field radiative heat transfer from sharp objects using a general three-dimensional numerical scattering technique. *Phys. Rev. B*, **85**, 165104.
  38. Edalatpour, S. and Francoeur, M. (2014) The thermal discrete dipole approximation with surface interaction. 2nd International Workshop and Nano-Micro Thermal Radiation: Energy, Manufacturing, Materials, and Sensing (NanoRad2014), Shanghai, China, June, 6–9, 2014.
  39. Bauer, T. (2011) *Thermophotovoltaics: Basic Principles and Critical Aspects of System Design*, Springer.
  40. Francoeur, M., Vaillon, R., and Mengüç, M.P. (2011) Thermal impacts on the performance of nanoscale-gap thermophotovoltaic power generators. *IEEE Trans. Energy Convers.*, **26**, 686–698.
  41. Lenert, A., Bierman, D.M., Nam, Y., Chan, W.R., Celanovic, I., Soljacic, M., and Wang, E.N. (2014) A nanophotonic solar thermophotovoltaic device. *Nat. Nanotechnol.*, **9**, 126–130.
  42. Whale, M.D. (1997) A Fluctuational electrodynamics analysis of microscale radiative heat transfer and the design of microscale thermophotovoltaic devices. PhD thesis, MIT, Cambridge.
  43. Whale, M.D. and Cravalho, E.G. (2002) Modeling and performance of microscale thermophotovoltaic energy conversion devices. *IEEE Trans. Energy Convers.*, **17** (1), 130–142.
  44. Edalatpour, S. and Francoeur, M. (2013) Size effect on the emissivity of thin films. *J. Quant. Spectrosc. Radiat. Transfer*, **118**, 75–85.
  45. Maier, S.A. (2007) *Plasmonics*, Springer, New York.
  46. Joulain, K., Mulet, J.-P., Marquier, F., Carminati, R., and Greffet, J.-J. (2005) Surface electromagnetic waves thermally excited: radiative heat transfer, coherence properties and Casimir forces revisited in the near field. *Surf. Sci. Rep.*, **57**, 59–112.

47. Fu, C.J. and Zhang, Z.M. (2006) Nanoscale radiation heat transfer for silicon at different doping levels. *Int. J. Heat Mass Transfer*, **49**, 1703–1718.
48. Francoeur, M., Mengüç, M.P., and Vaillon, R. (2010) Local density of electromagnetic states within a nanometric gap formed between two thin films supporting surface phonon polaritons. *J. Appl. Phys.*, **107**, 034313.
49. Rousseau, E., Laroche, M., and Greffet, J.-J. (2010) Radiative heat transfer at nanoscale: closed-form expression for silicon at different doping levels. *J. Quant. Spectrosc. Radiat. Transfer*, **111**, 1005–1014.
50. Francoeur, M., Mengüç, M.P., and Vaillon, R. (2010) Spectral tuning of near-field radiative heat flux between two thin silicon carbide films. *J. Phys. D: Appl. Phys.*, **43**, 075501.
51. Francoeur, M., Mengüç, M.P., and Vaillon, R. (2011) Coexistence of multiple regimes for near-field thermal radiation between two layers supporting surface phonon polaritons in the infrared. *Phys. Rev. B*, **84**, 075436.
52. Ben-Abdallah, P., Joulain, K., Drevillon, J., and Domingues, G. (2009) Near-field heat transfer mediated by surface wave hybridization between two films. *J. Appl. Phys.*, **106**, 044306.
53. DiMatteo, R.S., Greiff, P., Finberg, S.L., Young-Waithé, K.A., Choy, H.K.H., Masaki, M.M., and Fonstad, C.G. (2001) Enhanced photogeneration of carriers in a semiconductor via coupling across a nonisothermal nanoscale vacuum gap. *Appl. Phys. Lett.*, **79** (12), 1894–1896.
54. DiMatteo, R., Greiff, P., Finberg, S., Young-Waithé, K.A., Choy, H.K.H., Masaki, M.M., and Fonstad, C.G. (2003) Micron-gap thermophotovoltaics (MTPV). Proceedings of the 5th Conference on Thermophotovoltaic Generation of Electricity, 2003, pp. 232–240.
55. DiMatteo, R., Greiff, P., Seltzer, D., Meulenbergh, D., Brown, E., Carlen, E., Kaiser, K., Finberg, S., Nguyen, H., Azarkevich, J., Baldasaro, P., Beausang, J., Danielson, L., Dashiell, M., DePoy, D., Ehsani, H., Topper, W., and Rahner, K. (2004) Micron-gap thermophotovoltaics (MTPV), Proceedings of the 6th Conference on Thermophotovoltaic Generation of Electricity, 2004, pp. 42–51.
56. Hanamura, K. and Mori, K. (2007) Nano-gap TPV generation of electricity through evanescent wave in near-field above emitter surface, Proceedings of the 7th Conference on Thermophotovoltaic Generation of Electricity, 2007, pp. 291–296.
57. Hanamura, K., Fukai, H., Srinivasan, E., Asano, M. and Masuhara, T. (2011) Photovoltaic generation of electricity using near-field radiation. Proceedings of the ASME/JSME 2011 8th Thermal Engineering Joint Conference, 2011, pp. 457–461.
58. Yoshida, J., Ashida, Y., and Hanamura, K. (2012) Thermophotovoltaic generation of electricity by GaSb schottokky cell using evanescent effect. International Workshop on Nano-Micro Thermal Radiation, pp. 68–69.
59. Hu, L., Narayanaswamy, A., Chen, X.Y., and Chen, G. (2008) Near-field thermal radiation between two closely spaced glass plates exceeding Planck's black-body radiation law. *Appl. Phys. Lett.*, **92**, 133106.
60. Ottens, R.S., Quetschke, V., Wise, S., Alemi, A.A., Lundock, R., Mueller, G., Reitze, D.H., Tanner, D.B., and Whiting, B.F. (2011) Near-field radiative heat transfer between macroscopic planar surfaces. *Phys. Rev. Lett.*, **107**, 014301.
61. Mauk, M.G. (2006) Survey of thermophotovoltaic (TPV) devices, in *Mid-Infrared Semiconductor Optoelectronics*, Vol. 118, Springer.
62. Gonzalez-Cuevas, J.A., Refaat, T.F., Abedin, M.N., and Elsayed-Ali, H.E. (2007) Calculation of temperature and alloy composition effects on the optical properties of  $\text{Al}_x\text{Ga}_{1-x}\text{As}_y\text{Sb}_{1-y}$  and  $\text{Ga}_x\text{In}_{1-x}\text{As}_y\text{Sb}_{1-y}$  in the spectral range 0.5-6 eV. *J. Appl. Phys.*, **102**, 014504.
63. Whale, M.D. (2001) The influence of interference and heterojunctions on the performance of microscale thermophotovoltaic devices. *Microscale Thermophys. Eng.*, **5**, 89–106.

64. Narayanaswamy, A. and Chen, G. (2003) Surface modes for near field thermophotovoltaics. *Appl. Phys. Lett.*, **82** (20), 3544–3546.
65. Laroche, M., Carminati, R., and Greffet, J.-J. (2006) Near-field thermophotovoltaic energy conversion. *J. Appl. Phys.*, **100**, 063704.
66. Park, K., Basu, S., King, W.P., and Zhang, Z.M. (2008) Performance analysis of near-field thermophotovoltaic devices considering absorption distribution. *J. Quant. Spectrosc. Radiat. Transfer*, **109**, 305–316.
67. Ilic, O., Jablan, M., Joannopoulos, J.D., Celanovic, I., and Soljačić, M. (2012) Overcoming the black body limit in plasmonic and graphene near-field thermophotovoltaic systems. *Opt. Express*, **20**, A366–A384.
68. Simovski, C., Stanislav, M., Nefedov, I., and Tretyakov, S. (2013) Optimization of radiative heat transfer in hyperbolic metamaterials for thermophotovoltaic applications. *Opt. Express*, **21**, 14988–15013.
69. Messina, R. and Ben-Abdallah, P. (2013) Graphene-based photovoltaic cells for near-field thermal energy conversion. *Sci. Rep.*, **3**, 1383.
70. Bright, T.J., Wang, L.P., and Zhang, Z.M. (2014) Performance of near-field thermophotovoltaic cells enhanced with a backside reflector. *ASME J. Heat Transfer*, **136**, 062701.
71. Basu, S., Lee, B.J., and Zhang, Z.M. (2010) Infrared properties of heavily doped silicon at room temperature. *ASME J. Heat Transfer*, **132**, 023301.
72. Basu, S., Lee, B.J., and Zhang, Z.M. (2010) Near-field radiation calculated with an improved dielectric function model for doped silicon. *ASME J. Heat Transfer*, **132**, 023302.
73. West, P.R., Ishii, S., Naik, G.V., Emani, N.K., Shalae, V.M., and Boltasseva, A. (2010) Searching for better plasmonic materials. *Laser Photonics Rev.*, **4**, 795–808.
74. Francoeur, M., Mengüç, M.P., and Vaillon, R. (2008) Near-field radiative heat transfer enhancement via surface phonon polaritons coupling in thin films. *Appl. Phys. Lett.*, **93**, 043109.
75. Bernardi, M.P., Dupre, O., Vaillon, R., and Francoeur, M. (2013) Surface Polariton Mediated Thermophotovoltaic Power Generation, arXiv: 1309.5969.

## 5 Power Conditioning for Energy Harvesting – Theory and Architecture

*Stephen G. Burrow and Paul D. Mitcheson*

### 5.1

#### Introduction

This chapter presents the fundamental principles of power conditioning circuits connected to harvesting transducers. While the focus is on motion-driven harvesters, much of the discussion is relevant to other harvester types. In most cases, the basic requirements of a power processor that connects a harvesting transducer to an electronic load are rectification, voltage regulation, and interface to an energy storage element. However, more sophisticated tasks may also be performed, such as power factor correction, frequency tuning (to increase the harvested power), and maximum power point tracking (MPPT) to ensure maximum system power density is achieved as the prime mover (e.g., mechanical vibration) characteristics change. Examples of circuits which perform these fundamental tasks are explained and the reasoning behind their use with different transduction mechanisms is given. This chapter is closely linked to Chapter 18, where implementations of these concepts are demonstrated as part of prototype energy harvesting systems.

### 5.2

#### The Function of Power Conditioning

The power conditioning circuitry within an energy harvesting systems plays a pivotal role, exerting control over the harvester through its input impedance while at the same time performing power processing functions such as regulation, filtering, and rectification, and finally delivering energy to the load. Circuits which can provide the key power conditioning functions for energy harvesters over a range of power levels have been described in the literature [1]. More recently, circuits providing advanced functionality, particularly related to actively influencing the behavior of the harvesting device such as electrical tuning [2], piezo pre-biasing [3, 4], or improved utilization through schemes such as maximum power tracking, have been described [5]. All the while, the lower limit of power at which

practicable harvesting systems can be implemented has been reduced by developing power conditioning circuits which will operate at lower power levels, with many circuits demonstrated at an integrated level [6, 7], further reducing power levels by lessening losses due to parasitic capacitances.

Although the subcomponents of energy-harvesting power-conditioning systems are not yet themselves “off-the-shelf” items, perhaps the key challenge facing an engineer architecting a power harvesting system today is matching the dynamic power/time profiles of the components and source to produce a system that is in some sense optimized. Published works addressing the topic of complete system design are few, a problem exacerbated by the huge variety of loads and the uniqueness of sources which make system-wide generalizations difficult.

Real-world sources are often intermittent and excitation parameters can vary over time. In Ref. [8] the authors give measured results of several vibration sources and it is possible to see how they differ from idealized sources: typically, the mean value of frequency and amplitude change slowly, but real-world noise will cause both frequency and amplitude to experience a degree of smaller rapid fluctuations. Electronic loads also have a particular characteristic power draw, and in particular it is worth noting that “low-power” loads often achieve the low average power by duty cycling a higher power demand with quiescent periods. If the harvesting system was to be designed such that the peak power demand of the load could be supplied by the harvester in its state of lowest excitation, then the harvester and power electronics would be greatly oversized. To avoid oversizing the harvester, the power conditioning system must store energy and provide a match between the temporal power profiles of the source to the load. As an example, in Ref. [5] the authors realize a harvesting system where a harvester producing  $135\ \mu\text{W}$  continuous power is matched to a wireless sensor node (WSN) drawing short bursts of  $40\ \text{mW}$ , a peak level some 300 times the average harvested.

In this chapter, the fundamental behavior of power conditioning circuits reported in the literature for energy harvesters is considered. The focus is on vibration energy harvesters although many of the circuits and concepts can be exploited for other harvesting technologies. Some specific case studies of the use of power conditioning circuits with harvesters in specific application contexts are described in Chapter 18.

### 5.2.1

#### **Interface to the Harvester**

Along with the source excitation, the impedance presented to a harvester by the power conditioning system (defined as the ratio of input voltage to current), determines the operating condition for any particular harvester. While the source, being some form of ambient excitation, is not normally considered controllable the input impedance of the power electronics is, and this forms the primary mechanism

whereby control can be achieved over the power system. The input impedance of the power conditioning system is synthesized by the action of the passive and active components of the converter, usually by controlling the duty cycle of the active elements in switch mode, and associated control loops. The impedance can have real and imaginary components (in AC systems) as well as nonlinear response.

Where the harvester can be modeled by combinations of linear elements, it is well known that maximum power is produced when the load (in this case, the input impedance of the power processor) is the complex conjugate of the harvester output impedance. However, it is not always possible to operate at this theoretical maximum as physical constraints, such as voltage or excursion limitations, may preclude it. In addition, the quiescent power consumption associated with synthesizing resistive and reactive load impedances may become significant, especially at low harvested power levels, resulting in a situation where a load other than the theoretical optimum produces most usable harvested energy.

When attempting to understand the behavior of a harvester and power conditioning circuit, it is often useful to consider the current and voltage waveforms at the terminals of harvesters in the frequency domain. In-phase current and voltage components appear as a resistive load to the harvester and represent dissipated or harvested power; out-of-phase components at the fundamental frequency appear as “reactive” input impedances, which are described by the displacement power factor, and represent circulating energy between the source and load, which can modify the harvester’s frequency response; and nonlinearities in the input impedance produce harmonic components and are described by the distortion power factor. These higher harmonics modulate energy flow between the source and load at their particular frequency, the effect of which may or may not be significant in terms of average power, depending on the Q-factor of the mechanical system.

### 5.2.2

#### Circuits with Resistive Input Impedance

Confining the discussion to efficient switched-mode topologies, resistive input impedance can be approximated by several topologies in a discontinuous conduction mode or by configuring a feedback loop around a converter to force voltage to follow current or vice versa.

Figure 5.1a shows a circuit schematic of a power conditioning system, consisting of a rectifier followed by a boost converter that approximates as resistive input impedance. Variations on this approach have been published for energy harvesting systems as it is inherently simple and requires few additional components to make a working converter [9]. The operation is as follows: the input rectifier is not followed by a reservoir capacitor; hence the converter is presented with full wave rectified voltage waveform. “Sw1” is turned “on” and “off” at frequencies and duty cycles that keep the inductor in discontinuous conduction, that is, the inductor current falls to zero in each switching cycle. During switch “on” periods, the input

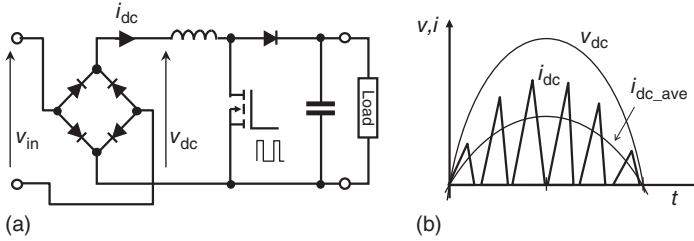


**Figure 5.1** Resistance emulator implemented with a discontinuous mode converter. (a) Schematic and (b) waveforms.

current ramps up to a level determined by the input voltage, hence the average current appears to follow the input voltage. Waveforms illustrating this are shown in Figure 5.1b. In discontinuous conduction mode, the input resistance can be approximated by Eq. (5.1), where  $D$  and  $T$  are the duty cycle and period of the switching waveform, respectively, and  $L$  is the value of the inductor.

$$R_{in} = \frac{2L}{DT} \tag{5.1}$$

Another approach to achieve resistive input impedance is to employ feedback to force in-phase current and voltage waveforms; this technique is used extensively for power factor correction in small power supplies, for example, those used in consumer goods, and hence are well described in the literature. An example system block diagram is shown in Figure 5.2. The circuit is configured in current control mode, using a negative feedback loop around the PWM controller to set the input current to the reference level. The current reference is derived from the input voltage waveform: the instantaneous voltage is divided by the desired input resistance,  $R_{in}$ . The disadvantage of this technique for energy harvesting is the additional circuitry and requirement for micropower current sensing is harder to implement at the lowest power levels. However, a key

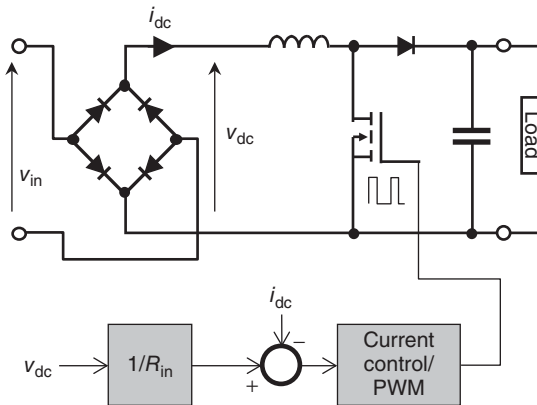


**Figure 5.2** Resistance emulator implemented using feedback.



advantage is that the converter can be operated with discontinuous or continuous inductor current (continuous inductor current results in a lower peak to mean ratio and hence lower conduction losses).

### 5.2.3

#### Circuits with Reactive Input Impedance

Power conditioning circuits with some element of reactive input impedance result in energy circulating between the harvester and power electronics at the fundamental frequency. This can have utility if the harvester itself has reactive output impedance and the conditioning circuit can then partially or completely cancel this out, that is, perform a conjugate impedance match. Resonant-type harvesters display reactive output impedances on being excited away from their mechanical resonance and, in this situation, applying a reactive load to increase output power is sometimes described as “frequency tuning.” In other situations, the harvesting transducer itself introduces reactance, as is common with piezoelectric devices. Analysis of frequency tuning for an electromagnetic vibration harvester is described in [2].

Linear circuits known as *gyrators* can synthesize reactive input impedance and have found application in the related topic of vibration suppression [10]; however, they are not “energy efficient,” consuming significant power to synthesize the reactive components. For energy harvesting, it is therefore necessary to base the circuitry around switched mode electronics, and an example is shown in Figure 5.3. Since a reactive load implies energy flow from load to source and vice versa, it is necessary to employ a converter that can operate in four quadrants. The circuit in Figure 5.3 is a four-quadrant boost rectifier based around a half-bridge. Single-rail versions can be designed around full bridges (see Chapter 18). Similar to the resistance emulator of Figure 5.3, the converter is operated in average

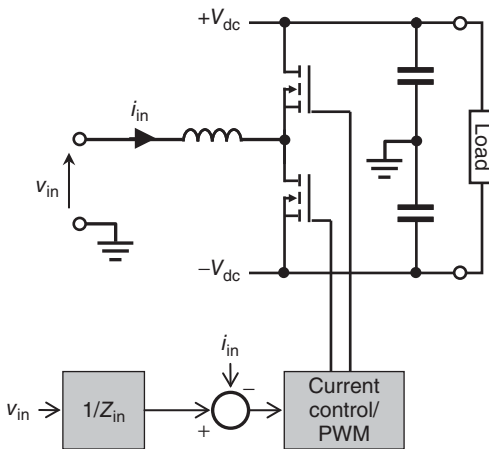


Figure 5.3 Reactive impedance emulator.

current control mode with the current reference derived from the input voltage multiplied by, in this case, the admittance to be synthesized,  $Z_{in}$ .

#### 5.2.4

##### Circuits with Nonlinear Input Impedance

Nonlinearity in the input impedance is generally a consequence of circuit design rather than the goal, and almost always as a result of trying to reduce quiescent power consumption in the circuit. The distortion components of the input waveform produced by nonlinearity are harmonically related to the fundamental input frequency, hence are distinct from switching effects of switch-mode converters.

#### 5.2.5

##### Peak Rectifiers

The well-known peak rectifier (diodes followed by a reservoir capacitor) is widely used as the first power conditioning stage in AC energy harvesting applications; however analysis of such systems is more involved than their simple schematic suggests. The naturally commuted diodes of the rectifier produce discontinuities in the response at conduction and extinction and the timing of these is determined by both input and output voltages.

Considering the basic circuit of Figure 5.2a, the case most commonly found in text books (e.g., Sen [11]) is where  $R_s$  is small, resulting in the waveforms of Figure 5.2b. However an energy harvester will generally have source impedance that is significant compared to the load hence waveforms closer to those of Figure 5.2b will apply. This condition is not often encountered in text books however it is similar to the case presented by Waidelich [12] when considering vacuum tube rectifiers. Figure 5.4b,c illustrate the significant harmonic distortion introduced by the peak rectifying action.

From an inspection of the waveforms, it can be seen that energy flow is unidirectional in the peak rectifier. Even though the current waveform is harmonic rich, the summation of these harmonics results in unidirectional energy flow. This result could also be reasoned from considering the action of the diodes; however, irrespective of the reasoning, the important conclusion is that the peak rectifier behaves as a nonlinear resistive load.

By averaging the waveforms over a cycle, it is possible to describe the input resistance as a function of output voltage (although this is somewhat difficult to do analytically, it can be easily achieved numerically) with the extremes of  $V_l = 0$  where the input resistance of the rectifier appears as a short circuit and at  $V_l = v_{s(\text{peak})}$  appearing as an open circuit. This highlights the key disadvantages of this simple circuit: the input and output conditions are coupled and at cold start-up, a short circuit is placed across the harvester resulting in zero harvested power. Some authors, for example, Ottman *et al.* [13], have exploited the relationship between input resistance and output voltage using a second converter to control the DC output voltage and thus synthesized input resistance.

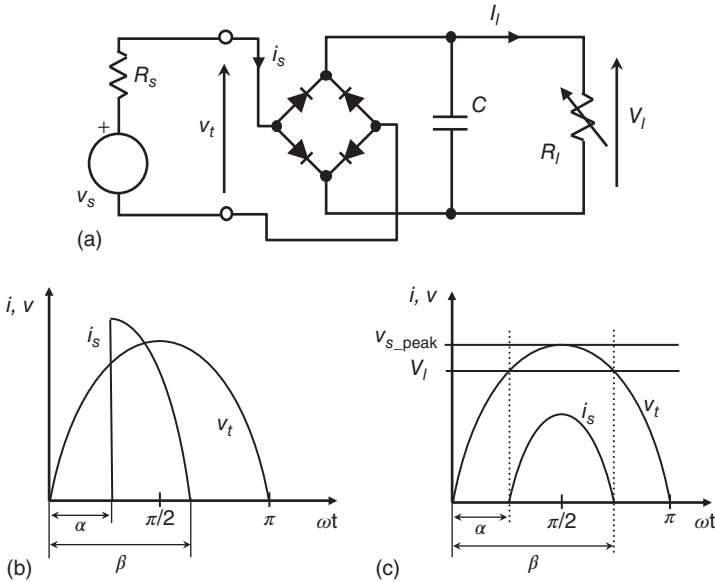


**Figure 5.4** Peak rectifier and associated waveforms for differing source impedances.  $\alpha$  indicates conduction angle;  $\beta$  indicates extinction. (a) Voltage source feeding a peak rectifier, (b) source impedance  $\ll$  load impedance, and (c) source impedance  $\approx$  load impedance [12].

The peak rectifier is a simple way to synthesize resistive input impedance, providing the important rectification function, which can be scaled to a wide range of power levels; yet the current harmonics it introduces have resulted in it falling out of use in many power systems. However, in some harvesting applications, the characteristics of the harvester minimize the impact of the current harmonics. Consider the equivalent circuit of a simplified resonant vibration harvester with electromagnetic transduction and peak rectifier of Figure 5.5. The harvester appears as a filter, hence the differing harmonic components of the rectifier input current “see” different output impedances and, importantly, different resistive components. This is perhaps easiest to show by calculating the output impedance of the harvester: at mechanical resonance, the

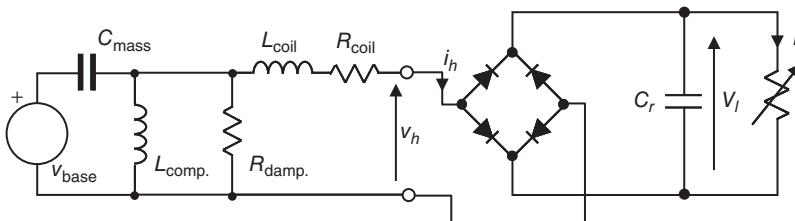


**Figure 5.5** Simplified model of peak rectifier and vibration energy harvester with electromagnetic coupling using mobility analogy (for further reading on electromechanical analogies see Ref. [14]).

impedance due to mass and compliance terms sum to infinity and the output impedance is the sum of the coil terms plus the mechanical damping term. The fundamental current component is presented with a source-resistive component of  $R_{\text{coil}} + R_{\text{damp}}$ ; However, at the frequencies of higher harmonics, the mass term becomes significant, shunting the mechanical damping, leading to an output impedance with restive component that tends to that of just  $R_{\text{coil}}$  as frequency increases.

Since a well-designed harvester will have coil resistance, which is some small fraction of the mechanical damping (when both are reflected into the same domain through the transducer coupling), losses due to harmonic components are much lower than might be expected if the filtering characteristic of the harvester are not considered.

Although a property of the harvester rather than the power conditioning, the fact that resonant vibration harvesters can be tolerant of loads introducing a distortion power factor enables simpler power conditioning circuits to systems to operate in an efficient manner, resulting in counterintuitive situations where for some harvester characteristics at low powers, a half-wave peak rectifier produces most usable power [15].

## 5.2.6

### Piezoelectric Pre-biasing

Energy harvesters utilizing piezoelectric transduction have output impedance that is highly reactive owing to the capacitance of the piezoelectric material and thus the ideal complex conjugate load has a very low power factor. Because a typical piezo harvester produces just a few milliwatts, attempting to synthesize the optimum load with a circuit similar to that of Figure 5.3 is likely to result in a system with greater quiescent demand than power generation capability; hence researchers have turned to a range of nonlinear approaches to improve power output without incurring large quiescent overheads.

Some of the first published work in this area was produced by Guyomar *et al.* [3]. The technique, termed *synchronous switched harvesting on inductor (SSHI)*, involves flipping the polarity of the charge on the piezoelectric material twice per cycle when the mechanical cantilever reaches its maximum displacement by using a physical inductance switched across the harvester. The circuit is shown in Figure 5.6.

Another approach to “pre-biasing” has been reported by Mitcheson *et al.* [4]. The single-supply pre-biasing circuit is shown in Figure 5.7, operation is as follows: Switches  $S_1$  and  $S_4$  always operate as a pair, and  $S_2$  and  $S_3$  also operate as a pair. When the piezoelectric material reaches its maximum deflection, one of the pairs of switches is activated, discharging the energy on the piezoelectric capacitance into the DC link capacitor through the series inductor. This corresponds to the discharge phase shown in Figure 5.8. This resonant discharge pulse happens very quickly compared to the mechanical excitation frequency of the system. As soon as this discharge phase is complete and the voltage on the piezoelectric capacitor has

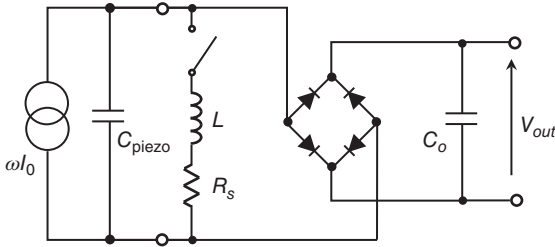


Figure 5.6 SSHI circuit with rectifier [3].

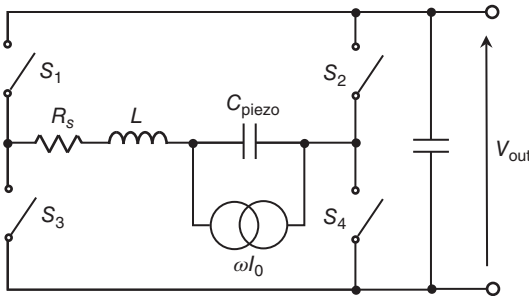


Figure 5.7 Single-supply pre-biasing circuit for a piezoelectric harvester [4].

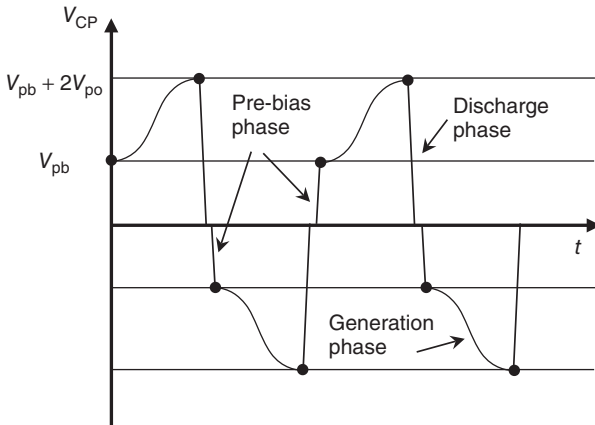


Figure 5.8 Piezoelectric pre-biasing voltage waveforms [4].

reached zero, the opposite switch pair activates and injects some charge onto the piezoelectric capacitor, of opposite polarity to what had just been generated (the pre-biasing phase in Figure 5.8). This increases the force with which the transducer is able to oppose the relative motion between the mass and base, thus increasing the electrical damping. The piezoelectric material then moves to its opposite extreme of position, increasing the voltage (see the generation phase in Figure 5.8) and the process repeats. The waveform produced in this circuit is very similar

to that produced by SSHI, although in pre-biasing, the piezoelectric capacitor remains open circuit during the entire motion of the beam, while in SSHI, the piezoelectric element is shorted by the commutation of the diode rectifier at some point during the motion. This means that the single-supply pre-biasing circuit implements a Coulomb-damped system and thus the analysis of the mechanical system is relatively simple [16]. The usable power extracted by the single supply pre-biasing (SSPB) circuit tends to twice that in the SSHI case assuming a high Q-current path and the need to apply high electrical damping to the harvester [17].

As already discussed, the aim of these charge modification techniques applied to piezoelectric harvesters is intended to improve the power factor of the piezoelectric transducer without the overhead of using a full impedance emulator solution and the necessary control loop overhead. In order to extract energy from a transducer, the force produced by the transducer that opposes the motion should be in phase with transducer's velocity. Owing to the capacitive output impedance, an open circuit piezoelectric transducer has force and velocity  $90^\circ$  out of phase and thus has a power factor of zero (which increases when a resistive load is applied, but in the absence of either a real or emulated inductor, can never approach 1). The discontinuity introduced into the piezoelectric voltage waveform shown in Figure 5.8 effectively corrects the phase of the fundamental of the voltage waveform by the required  $90^\circ$  to produce a system that operates with nearly unity power factor.

## 5.2.7

### Control

#### 5.2.7.1 Voltage Regulation

Regulation is the process whereby the output voltage of a converter is kept constant against varying load power demand. Switched mode converters are true power converters, that is, neglecting losses, output power is equal to input power and thus to regulate the output, switched mode converters typically modify the input power by altering their input impedance, normally via an automatic feedback loop.

Regulation achieved by modifying the input impedance requires a monotonic relationship between power and input impedance over the operating range, but this is often not the case with energy harvesters. Figure 5.9 illustrates the classic power characteristic of a harvester, where peak power is generated into an optimum load between the extremes of short circuit and open circuit. The trend curves for a true voltage and current source are also shown on the diagram and illustrate the problem: to increase power with voltage source, the load resistance should be reduced; to increase power with a current source, the load resistance should be increased. The harvester power response has regions where increasing load resistance will increase power, but also regions where the opposite is true, thus simple feedback regulation is not possible when operating near to the peak power region. A similar issue is encountered with photovoltaic panels.

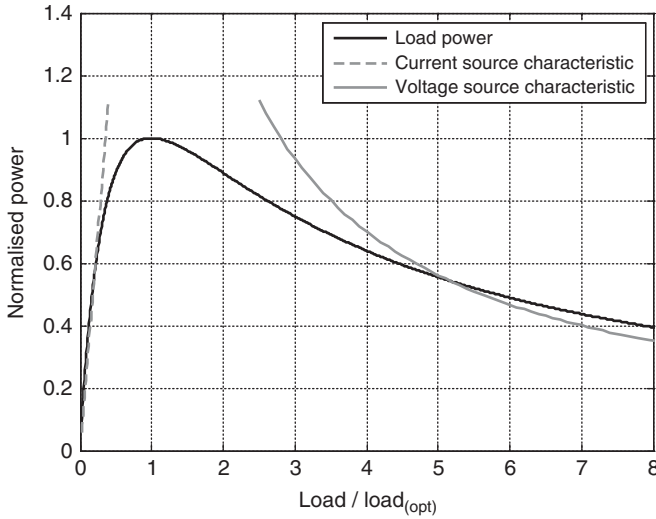


**Figure 5.9** General peak-power curve with characteristics of current and voltage sources superimposed.

This situation is not constrained to harvesters and was encountered when input filters were added to switch mode converters to suppress input harmonics. Analysis undertaken by Middlebrook [18] suggested as a rule of thumb that the input impedance of a converter should be four times greater than the source impedance to ensure stability. In the case of energy harvesters, this implies operation some way from the peak power point.

For resonant vibration harvesters, variations in excitation amplitude cause a translation of the curve described in Figure 5.9 in the vertical axis, however variations in frequency away from mechanical resonance also cause the curve to be translated in the horizontal axis: the peak power point occurring at a lower load resistance for all frequencies other than resonance. Thus it is possible for variations in input excitation to cause a change in operating region from the current to the voltage source approximation.

Because of the difficulty in using the power converter to perform feedback voltage regulation by controlling the input impedance of the converter, energy harvesting applications may benefit from alternative voltage regulation strategies. One possible example is to divorce voltage regulation from setting input impedance, for instance by using a converter operating with fixed input impedance and then using a secondary shunt voltage regulator; an example of this is shown in Figure 5.10. This approach was taken in [9] where an open-loop flyback converter operating in discontinuous mode is followed by a shunt regulator resulting in a low loss, low power conditioning system.

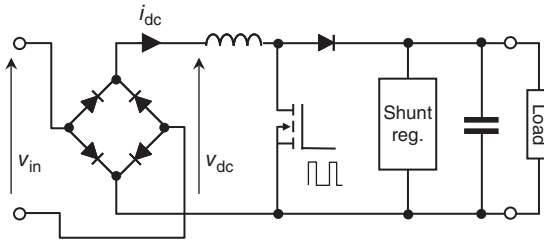


**Figure 5.10** The addition of a shunt regulator to the circuit of Figure 5.1 provides voltage regulation.

### 5.2.7.2 Peak Power Controllers

Power sources, such as photovoltaic cells, are commonly operated at or near the peak power point using a nonlinear feedback scheme to ensure peak power operation is maintained. This type of scheme, often described as MPPT, can be used with energy harvesters.

Peak power converters make repeated small adjustments to their operating point (input impedance) and attempt to find the point with the highest power output or the point where the derivative of power with respect to operating point is zero. Power can be calculated from measured currents and voltages or can be inferred from other variables such as current alone where voltages are slowly changing or the rate of change of voltage on a storage capacitor. In further variations on the technique, power can be measured at the output of the converter (rather than input) and is termed *maximum power transfer tracking (MPTT)*. MPTT takes into account losses in the converter which may result in the peak converter output power point not coinciding with the peak harvester output power.

One of the first published works applying peak power tracking to energy harvesters was produced by the aforementioned Ottman *et al.* [13] where a DC to DC converter was used to control the DC link voltage of a peak rectifier (by extracting energy from the DC link) and maintain the harvester at its peak power point.

When peak power tracking schemes are to be used with vibration energy harvesters, it is important to take note of the stored energy in the mechanical oscillator. When dynamic load is considered, it can be shown that output power is a function of load impedance and the rate of change of load impedance. If the system is not allowed to settle into a steady state before power estimates are made by the controller, then it is possible to “stall” the harvester. This is graphically illustrated in Figure 5.11, showing the load power developed as load resistance is swept between two values at various rates. Results are from numerical simulation of a mass-spring-damper harvester with electromagnetic coupling. It can be seen how reducing the load resistance causes a transient increase in output power, while increasing loads result in reduced output, compared to steady state. Even at the slowest sweep of 4 s, significantly more power than at steady state is produced on the down sweep and conversely less on the up sweep.



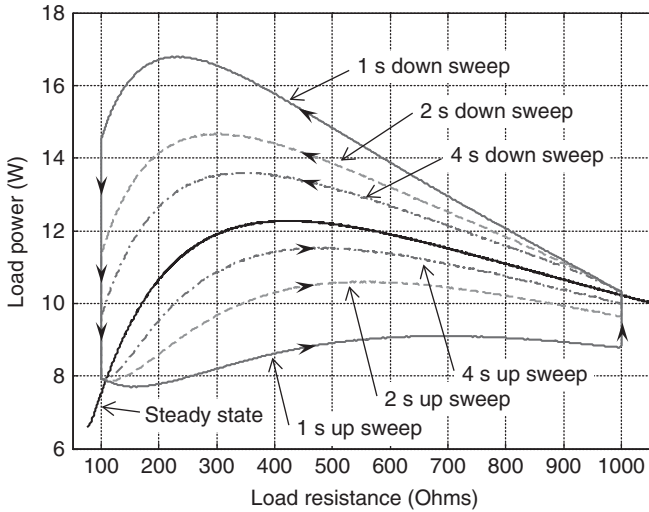


**Figure 5.11** Simulated trajectories of output power as harvester load resistance is swept up and down between 100 and 1000  $\Omega$  at various rates. Simulation parameters: Mass = 3.4g, Comp. =  $260\text{N m}^{-1}$ , Loss =  $0.02\text{N s m}^{-1}$ , Coil res. =  $80\ \Omega$ , and Coupling coeff. =  $2.4\text{V s m}^{-1}$ .

The transient effect on output power is related to the settling time of the mass spring oscillator system and thus the quality factor of the oscillator. It is not unusual to operate resonant harvesters with very high quality factors and resulting settling times of several seconds or more, hence power tracking schemes are not able to adapt to rapidly changing excitation or transient events.

In the work of Ottman *et al.* [13] the stored energy of the large reservoir capacitor limits the rate of change of the MPPT system. A minimum time step is defined for a discrete MPPT algorithm in Ref. [19].

## 5.2.8

### System Architectures

#### 5.2.8.1 Start-Up

Starting up from a completely unpowered state, sometimes called *cold start*, can be challenging for many harvesting systems. With passive power conditioning systems, such as the peak rectifier, the problems are centered on the input impedance: with zero voltage across the reservoir capacitor, the harvester is presented with a near short circuit. The problem is worsened if the capacitor has a large value relative to the nominal harvested power and it can take many minutes to charge. Further to this, it is necessary to ensure the load does not draw significant energy during start-up (electronic loads often draw large currents as they start-up) or the system may find a power equilibrium in a nonfunctioning state. To alleviate this, it may be necessary to incorporate active connection and disconnection of the load,

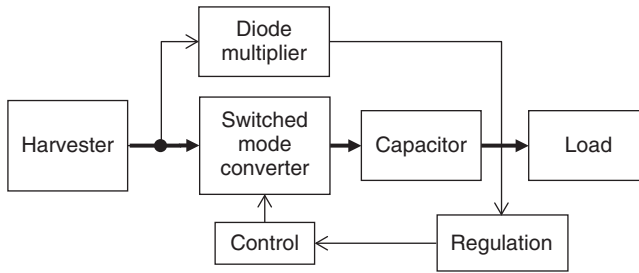


**Figure 5.12** Block diagram of power conditioning circuit with parallel diode multiplier to start up the main converter.

only connecting the load when sufficient energy has been collected to perform a task.

Adding active elements in the power conditioning to control converters, switch devices, or connect the load presents a further challenge as it is necessary to power these up before the main circuits. Where the harvester output is AC, a passive diode multiplier network can be used to provide power to start the main active converter. A simplified block diagram illustrating this, adapted from [5], is shown in Figure 5.12.

Incorporating a diode multiplier arrangement has the additional advantage that it is possible to start up when the harvester has a peak output voltage lower than that required to supply the active circuitry. Several variations on Figure 5.12 are possible, where the control circuitry can be always supplied from the start-up circuit or alternatively this can be switched out once the main circuit is functioning.

### 5.2.9

#### Highly Dynamic Load Power

It has already been observed that many “low-power” loads achieve a low average power by duty cycling a brief high-power active period with longer periods of inactivity. In contrast, most energy harvesters are operated in a continuous manner, with maximum power generated all the time, to keep the size of the harvesting device to a minimum for a given average power output.

This results in a situation where the power conditioning system is required to make a temporal match between the power–time profiles of harvester and load, and it is this consideration which tends to determine the size of energy storage capacitor which places limits on start-up as previously described.

A further complication arises with capacitor energy storage as minimizing the capacitance value to promote quick start-up will result in greater voltage swings for a given load profile which may require additional voltage regulation circuitry. This is illustrated with reference to Figure 5.13, which shows the simplified schematic of a power conditioning system interfacing a vibration energy

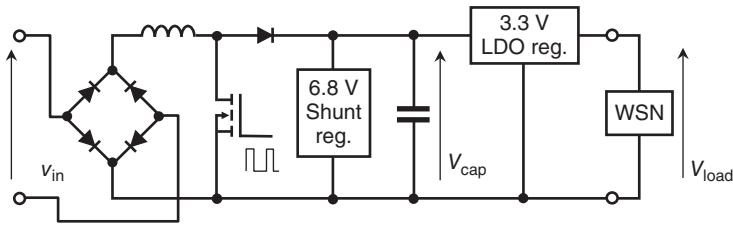


**Figure 5.13** Simplified schematic of a power conditioning circuit supplying a load with duty-cycled power demand.

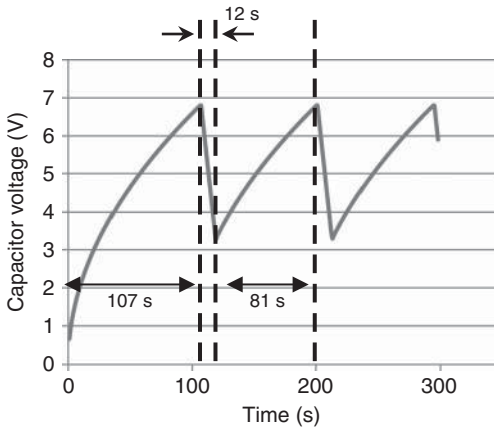


**Figure 5.14** Main capacitor voltage of Figure 5.13 showing start-up and two load cycles.

harvester to a WSN. The harvester is optimally loaded with a resistance-emulating discontinuous converter. The harvested energy is stored in a capacitor with shunt regulation to prevent the maximum voltage being exceeded. This is followed by a low-dropout regulator (LDO) providing the WSN with a constant 3.3 V. The capacitor voltage measured during testing is shown in Figure 5.14. From cold start, the system takes just over 100 s to fully charge the capacitor (6.8 V). The WSN can then perform a transmit operation lasting 12 s. The capacitance has been chosen such that its voltage falls to the minimum (3.3 V) at the end of the transmitting period. The WSN then enters a low-power mode and the capacitor voltage recovers enough to enter a second transmission period after 81 s.

The duty cycle of the WSN must always remain below 15% for the average input and output powers to match, however the choice of capacitance value is a significant design decision, as it trades off start up time against voltage variation (and thus regulation requirements). A switched mode converter may be used in place of the linear regulator; however, it is not always the case that the additional complexity justifies the efficiency gains.

## 5.3

## Summary

Energy harvesting sources rarely present simple demands on the power conditioning system, typically requiring some optimum loading, rectification, voltage-level shifting, and energy storage to perform a temporal match between the source and load.

Technical solutions exist for all these requirements; However, at the very low power levels of some reported harvesting devices, it is important to consider if the system can support the quiescent demand of complex power conditioning circuits. Harvesters producing the lowest power outputs therefore often suffer the compounding problem of lower efficiency power conditioning, which is often further exaggerated because harvesters with the lowest power outputs also require very low parasitics in the semiconductors used to form the power processing circuitry.

## References

1. Szarka, G., Stark, B., and Burrow, S. (2012) Review of power management for energy harvesting systems. *IEEE Trans. Power Electron.*, **27** (2), 803–815, ISSN: 0885-8993.
2. Cammarano, A., Burrow, S.G., Barton, D.A.W., Carrella, A., and Clare, L.R. (2010) Tuning a resonant energy harvester using a generalized electrical load. *J. Smart Mater. Struct.*, **19**, 055003. doi: 10.1088/0964-1726/19/5/055003
3. Guyomar, D., Badel, A., Lefeuvre, E., and Richard, C. (2005) Toward energy harvesting using active materials and conversion improvement by nonlinear processing. *IEEE Trans. Ultrason. Ferroelectr. Freq. Control*, **52**, 584–595.
4. Mitcheson, P.D., Stoianov, I., and Yeatman, E.M. (2012) Power-extraction circuits for piezoelectric energy harvesters in miniature and low-power applications. *IEEE Trans. Power Electron.*, **27**, 4514–4529.
5. Szarka, G.D., Burrow, S.G., and Stark, B.H. (2012) Ultra-low power, fully-autonomous boost rectifier for electromagnetic energy harvesters. *IEEE Trans. Power Electron.*, **28** (7), 3353–3362. doi: 10.1109/TPEL.2012.2219594
6. Maurath, D., Becker, P.F., Spreeman, D., and Manoli, Y. (2012) Efficient energy harvesting with electromagnetic energy transducers using active low-voltage rectification and maximum power point tracking. *IEEE J. Solid-State Circuits*, **47** (6), 1–12.
7. Gao, Y., Made, D.I., Cheng, S.-J., Je, M., and Heng, C.-H. (2013) An energy-autonomous piezoelectric energy harvester interface circuit with 0.3V startup voltage. Solid-State Circuits Conference (A-SSCC), 2013 IEEE Asian, November 11–13, 2013, pp. 445, 448.
8. Beeby, S.P., Wang, L., Zhu, D., Weddell, A.S., Merrett, G.V., Stark, B., and Szarka, G. (2013) A comparison of power output from linear and nonlinear kinetic energy harvesters using real vibration data. *Smart Mater. Struct.*, **22** (7), 075022.
9. Burrow, S.G. and Clare, L.R. (2009) Open-loop power conditioning for vibration energy harvesting. *Electron. Lett.*, **45** (19), 999–1000.
10. Fleming, A., Behrens, S., and Moheimani, S. (2000) Synthetic impedance for implementation of piezoelectric shunt-damping circuits. *Electron. Lett.*, **36** (18), 1525–1526.
11. Sen, P.C. (2008) *Power Electronics*, Tata McGraw-Hill, ISBN-13:978-0-07-462400-5.
12. Waidelich, D.L. (1941) Diode rectifying circuits with capacitance filters. *Trans. AIEE*, **61**, 1161.

13. Ottman, G.K., Hofmann, H.F., Bhatt, A.C., and Lesieutre, G.A. (2002) Adaptive piezoelectric energy harvesting circuit for wireless remote power supply. *IEEE Trans. Power Electron.*, **17** (5), 669–676.
14. Gardino, P. and Brennan, M.J. (2002) On the origins and development of mobility and impedance methods in structural dynamics. *J. Sound Vib.*, **249** (3), 557–573.
15. Clare, L.R. and Burrow, S.G. (2010) Half-wave rectifiers offer advantages for vibration energy harvesters. *Electron. Lett.*, **46** (24), 1623–1624. doi: 10.1049/el.2010.8932, ISSN: 00135194.
16. Miller, L.M., Mitcheson, P.D., Halvorsen, E., and Wright, P.K. (2012) Coulomb-damped resonant generators using piezoelectric transduction. *Appl. Phys. Lett.*, **100**, 233901, ISSN: 0003-695.
17. Dicken, J., Mitcheson, P.D., Stoianov, I., and Yeatman, E.M. (2012) Power-extraction circuits for piezoelectric energy harvesters in miniature and low-power applications. *IEEE Trans. Power Electron.*, **27**, 4514–4529, ISSN 0885-8993.
18. Middlebrook, R.D. (1978) Design techniques for preventing input-filter oscillations in switched-mode regulators. Proceedings of the Powercon, 1978, pp. A3.1–A3.16.
19. Szarka, G.D., Burrow, S.G., Proynov, P., and Stark, B.H. (2013) Maximum power transfer tracking for ultra-low-power electromagnetic energy harvesters. *IEEE Trans. Power Electron.*, **99**. doi: 10.1109/TPEL.2013.2251427.



## 6

# Thermoelectric Materials for Energy Harvesting

*Andrew C. Miner*

### 6.1

#### Introduction

Thermoelectric effects can provide an effective means for harvesting energy in a variety of applications. This chapter outlines several key issues to consider when selecting materials for use in a thermoelectric energy harvester:

- 1) Performance considerations
- 2) Points of caution as the size of the device decreases
- 3) Thermal expansion as it relates to reliability
- 4) Cost of raw materials

Finally, in order to realize these materials in micro energy harvesting systems, several relevant synthesis methods are discussed.

### 6.2

#### Performance Considerations in Materials Selection: $zT$

The principal factor that dictates the ultimate performance of a thermoelectric generator is the material's thermoelectric figure of merit,  $zT$ . By common convention, the thermoelectric figure of merit of a single material is denoted as  $zT$  (lower case  $z$ ), whereas the effective thermoelectric figure of merit of a thermoelectric couple, module, or generator system is denoted as  $ZT$  (upper case  $Z$ ). The figure of merit,  $zT$ , is defined as

$$zT = \frac{\alpha^2}{\lambda\rho} T \quad (6.1)$$

where  $\alpha$  is the Seebeck coefficient,  $\lambda$  is the thermal conductivity,  $\rho$  is the electrical resistivity, and  $T$  is the temperature measured in kelvin.  $zT$  is a ratio of the square of the desirable voltage that is generated within the material when a

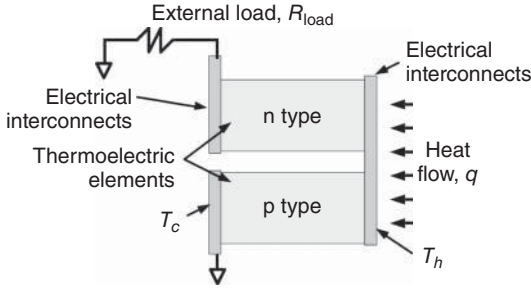


**Figure 6.1** A schematic diagram of a thermoelectric generator couple.

temperature difference occurs across the material ( $\alpha$ ) to the undesirable effects of heat flow through the material ( $\lambda$ ) and the ohmic heating due to electrical current flow through the material ( $\rho$ ). The higher the  $zT$  of the materials utilized in a thermoelectric generator, the higher potential electrical power and conversion efficiency that may be achieved in an energy harvester.

As shown schematically in Figure 6.1, useful electrical power is generated in an external load by a thermoelectric device when heat,  $q$ , flows through the device from a source of heat to a heat sink, generating a temperature difference across the thermoelectric elements. Typically, an  $n$ -type and a  $p$ -type thermoelectric material are arranged thermally in parallel and electrically in series as shown in the figure. An effective thermoelectric figure of merit for two materials used in a module can be defined as follows:

$$ZT = \frac{(\alpha_p - \alpha_n)^2}{\left(\sqrt{\lambda_p \rho_p} + \sqrt{\lambda_n \rho_n}\right)^2} T. \quad (6.2)$$

In eq. 6.2, the subscripts  $n$  and  $p$  denote the properties of the  $n$ - and  $p$ -type materials, respectively. For the two-element couple shown in Figure 6.1, it may be shown that the maximum power is generated when the external load resistance  $R_{\text{load}}$  matches the internal electrical resistance of the couple,  $R$ . At this operating point, the power produced is given by the following expression:

$$W = ((\alpha_p - \alpha_n)(T_h - T_c))^2 / 4R. \quad (6.3)$$

At this maximum power point, the efficiency at which the power is produced can be approximated as follows:

$$\eta = \frac{Z\Delta T}{4 + ZT_h + ZT_m} = \frac{\Delta T}{T_h} \cdot \frac{1}{2 + 4/ZT_h - \Delta T/2T_h} \quad (6.4)$$

where the subscripts denote  $ZT$  evaluated at the hot side or mean temperatures. Equation 6.4 shows the efficiency at the maximum power point in both a compact form and a form which is the product of the Carnot efficiency for a heat engine ( $\Delta T/T_h$ ) and the thermoelectric efficiency with respect to the Carnot efficiency. Note that the maximum power point is not exactly the same as maximum efficiency. Refer to Chapter 10 for a derivation of maximum efficiency and Chapter



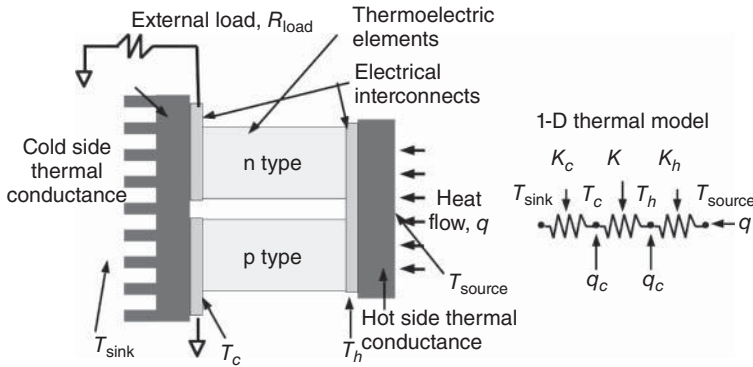


**Figure 6.2** A schematic diagram of a thermoelectric generator couple.

21 for a further discussion of the distinction between the maximum efficiency and maximum power points.

The above equations can be used to estimate the thermoelectric generator performance and aid in the selection of thermoelectric materials; however, in most situations, the temperatures of the hot and cold junctions of the n-type and p-type thermoelectric materials,  $T_h$  and  $T_c$  are not known a priori. As illustrated schematically in Figure 6.2, useful heat is drawn from a heat source at temperature  $T_{source}$  and sunk to a heat sink at  $T_{sink}$ .  $T_{source} - T_{sink}$  represents the maximum temperature difference available across which the device could operate. However, the actual temperature difference across the thermoelectric elements that drives energy conversion is  $T_h - T_c$ . This temperature difference is determined by conducting thermal and electrical analysis of the system that considering the effects of  $K_h$ ,  $K_c$ ,  $R_{load}$ ,  $\eta$ , and so on. A more detailed model for heat flow and electrical flow is shown in a 1-D model in Figure 6.2, which can provide first-order performance predictions helpful for informed selection of thermoelectric materials. Detailed results from such a model, however, is beyond the current scope. Additional levels of accuracy in predicting ultimate performance of a thermoelectric generation system that can aid in materials selection may be obtained by considering effects of the electrical and thermal impedance of interfaces and interconnects, 3-D simulation of electrical and thermal effects, and performance analysis utilizing temperature-dependent electrical and thermo-physical properties as well.

Whatever level of modeling sophistication employed in the design process, knowledge of a material's  $zT$  and its constitutive properties have a key role in the design process. The following sections examine several classes of materials and their thermoelectric properties. References presented are not intended to be comprehensive but are intended to represent early and more recently published work and include the more typical material families used in energy harvesting. Only references where  $\rho$ ,  $\lambda$ , and  $S$  were each measured are included here.

## 6.2.1

**Properties of Chalcogenides (Group 16)**

Chalcogenides are compounds that include group 16 atoms such as selenides and tellurides. This class of materials are the most widely used and studied class of thermoelectric materials with a relatively long history. For applications near room temperature, solid solutions of bismuth telluride, antimony telluride, and bismuth selenide offer good performance. For applications at higher temperatures, lead telluride and related alloys are widely used.

The thermophysical properties of bismuth telluride had been investigated as early as 1910, with early thermoelectric work on this as well as selenides beginning in the 1940s and 1950s. Early efforts to further improve the thermoelectric properties lead to the formation of alloys or solid solutions of  $\text{Bi}_2\text{Te}_3$ ,  $\text{Sb}_2\text{Te}_3$ , and  $\text{Bi}_2\text{Se}_3$ . Most common p-type samples are achieved in solid solutions of  $\text{Bi}_2\text{Te}_3$  and  $\text{Sb}_2\text{Te}_3$  and n-type with solid solutions of  $\text{Bi}_2\text{Te}_3$  and  $\text{Bi}_2\text{Se}_3$  [1–3].

$\text{PbTe}$  was also studied as a potential thermoelectric material as early as the 1940s. In contrast to bismuth-based chalcogenides,  $\text{PbTe}$  has a Na–Cl rock salt crystal structure with a melting point of  $924^\circ\text{C}$ . The material can exhibit n-type conductivity with the introduction of excess lead and p-type conductivity with excess tellurium. More common dopants include sodium (p-type) and iodine (n-type) [4]. As a high-temperature thermoelectric material, early military and space applications drove a considerable development of lead telluride within NASA and firms such as Westinghouse, TRW, 3M, and RCA. This early work established somewhat standard formulations known as 2N ( $\text{PbTe} + 0.3 \text{ mol\% PbI}_2$ ), 3N ( $\text{PbTe} + 0.055 \text{ mol\% PbI}_2$ ), 2P ( $\text{PbTe} + \text{Na}$ ), and 3P (Pb 19.697%, Te 49.491%, Sn 26.880%, Mn 3.458% and Na 0.475%) [5–9].

Figure 6.3 shows a selection of thermoelectric materials based on chalcogenides. Both n- and p-type materials are shown, with bismuth-based materials showing a characteristic maximum  $zT$  near room temperature. Lead telluride-based materials show a maximum performance near  $400^\circ\text{C}$  and higher.

## 6.2.2

**Properties of Crystallogens (Group 14)**

Crystallogen thermoelectric materials include variants of  $\text{Mg}_2\text{Si}$ ,  $\text{Mg}_2\text{Sn}$ ,  $\text{SiGe}$ , and  $\text{MnSi}_2$ .

For mid-range temperatures, Mg–Si–Sn alloys are of particular interest given their good thermoelectric properties, low mass, and the relative low cost of their raw materials.  $\text{Mg}_2\text{Si}$  has a density of  $2 \text{ g cm}^{-3}$  and a melting point of  $1102^\circ\text{C}$ .  $\text{Mg}_2\text{Sn}$  is often alloyed with  $\text{Mg}_2\text{Si}$  to lower thermal conductivity, thereby to improve the performance. It has a density of 3.59 and a melting point of  $778^\circ\text{C}$  [14].  $\text{Mg}_2\text{Si}$  is an inherent n-type semiconductor, and most successful thermoelectric materials based on it are n-type with additives including Bi and Sb. p-type conduction has been observed with dopant elements including Ag and Li [15, 16].

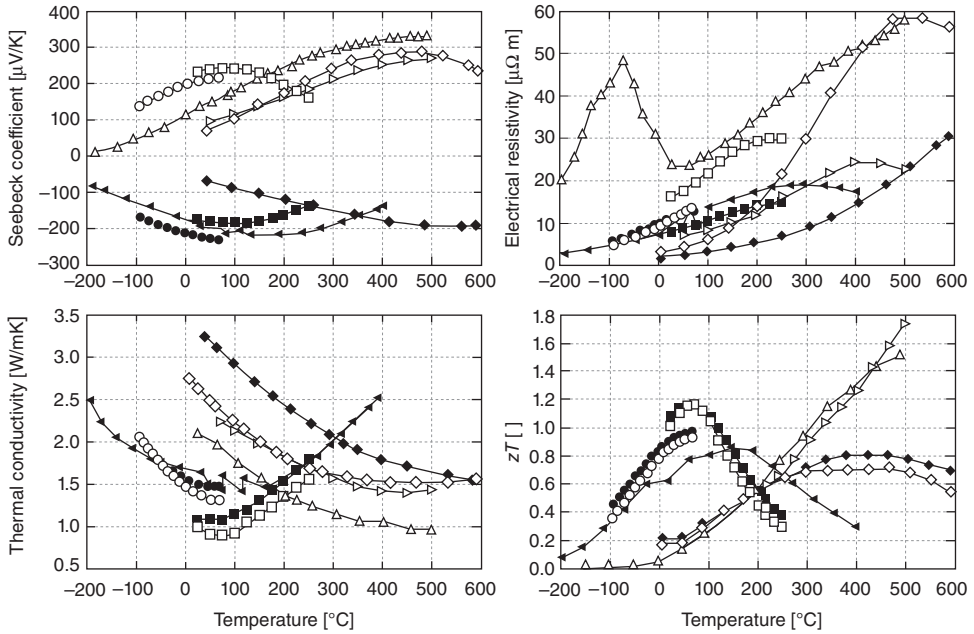


**Figure 6.3** Thermoelectric properties of representative materials based on chalcogenides. n-type materials are shown by filled symbols, p-type by open symbols. ●  $\text{Bi}_2\text{Te}_3\text{-Bi}_2\text{Se}_3$  [10], ◆  $\text{PbTe} + 0.1 \text{ Mol\% PbI}_2$

[4], □  $\text{Bi}_2\text{Te}_3\text{-Bi}_2\text{Se}_3$  [11], ▷  $\text{Pb}_{0.13}\text{Ge}_{0.87}\text{Te} + 3 \text{ mol\% Bi}_2\text{Te}_3$ , [12], ■  $\text{Bi}_2\text{Te}_3\text{-Bi}_2\text{Se}_3$  [11], ○  $\text{Bi}_2\text{Te}_3\text{-Sb}_2\text{Te}_3$  [10], △  $\text{Pb}_{0.02}\text{Pb}_{0.98}\text{Te}$  [13], ◇  $\text{PbTe} + 1.0 \text{ At\% Na}$  [4], ◀  $\text{Bi}_2\text{Te}_{2.4}\text{Se}_{0.6}$  [1]

$\text{MnSi}_2$  has a density of  $5.24 \text{ g cm}^{-2}$  and a melting point of approximately  $1150^\circ\text{C}$  [17]. Typically, this material exhibits p-type conduction with good thermoelectric properties when formulated with excess manganese, commonly referred to as High Manganese Silicide (HMS).

Figure 6.4 presents several representative Mg- and Mn-based silicide thermoelectric materials. The thermal conductivity of  $\text{Mg}_2\text{Si-Mg}_2\text{Sn}$  materials is distinctly lower than that of  $\text{Mg}_2\text{Si}$  materials, translating to a higher  $zT$  for these materials.

Alloys of SiGe are also categorized as crystallogens. They typically exhibit a maximum performance at temperatures above  $800^\circ\text{C}$  with n-type materials having  $zT$  of approximately 1.0 and p-type material about 0.6. As such, they can be useful thermoelectric materials in very high-temperature applications.

### 6.2.3

#### Properties of Pnictides (Group 15)

The most common pnictide thermoelectric materials are compositions of zinc and antimony. As early as the 1950s ZnSb was known and well studied as a p-type thermoelectric material. It is inherently p-type with moderate to high thermal

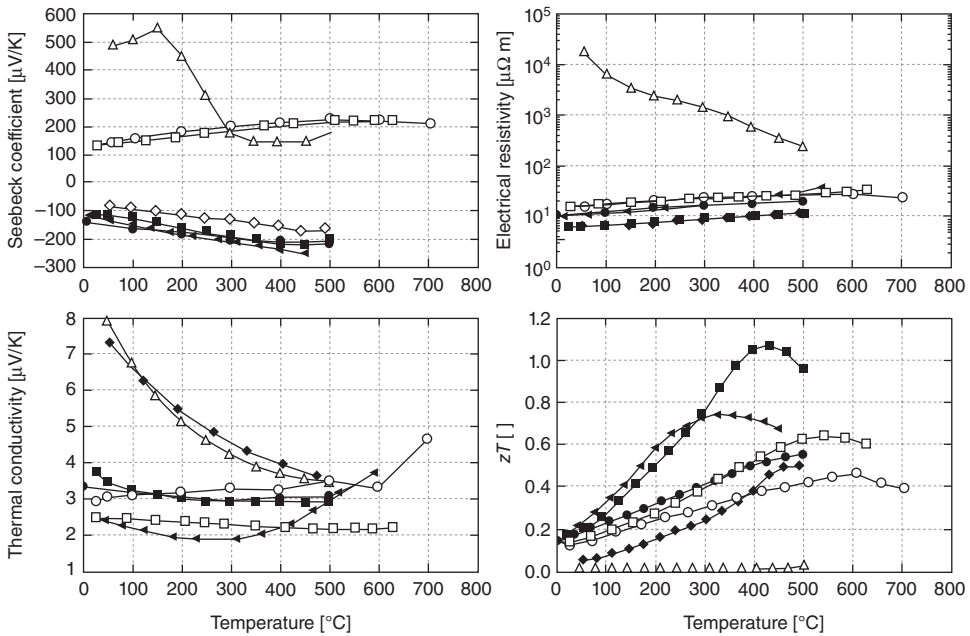


**Figure 6.4** Thermoelectric properties of representative materials based on group 14 elements. n-type materials are shown in filled symbols, p-type in open symbols.

●  $\text{Mg}_2\text{Si-Mg}_2\text{Sn}$  [18], ▲  $\text{Mg}_2\text{Si-Mg}_2\text{Sn}$  [19], △  $\text{Mg}_2\text{Si+Ag}$  [15], ■  $\text{Mg}_2\text{Si-Mg}_2\text{Sn}$  [11], ◇  $\text{Mg}_2\text{Si+Bi}$  [15], ○  $\text{MnSi}_{1.73}$  [20] □  $\text{MnAl}_{0.0015}\text{Si}_{0.9985}$  [21]

conductivity. Additives to and variations of the alloy have been studied, including the addition of excess antimony, tin, and silver yielding a p-type material. Additions of indium have been observed to result in n-type materials [1]. More recent understanding of the zinc-antimony phase diagram led to the discovery of more complex phases that include  $\text{Zn}_4\text{Sb}_3$ . Its beta phase has been shown to have excellent p-type thermoelectric properties, with notably low thermal conductivity attributed to its large and complex unit cell [22, 23].

Several sets of thermoelectric properties for pnictides are shown in Figure 6.5. The lower thermal conductivity of  $\text{Zn}_4\text{Sb}_3$  materials is striking with respect to  $\text{ZnSb}$  materials; however, the higher Seebeck coefficient in the  $\text{ZnSb}$  system allows it to maintain a similar  $zT$  up to approximately 200 °C.

#### 6.2.4

##### Properties of Skutterudites

The term “skutterudite” refers to a class of minerals with naturally occurring deposits found in abundance near the Norwegian town of Skutterud. Skutterudites have a base formula of  $\text{X}_4\text{Y}_{12}$ . In naturally occurring skutterudites, X is typically nickel, cobalt, or iron and Y is arsenic. For thermoelectric applications, synthesized alloys typically based on  $\text{Co}_4\text{Sb}_{12}$  for n-type materials and  $\text{Fe}_4\text{Sb}_{12}$

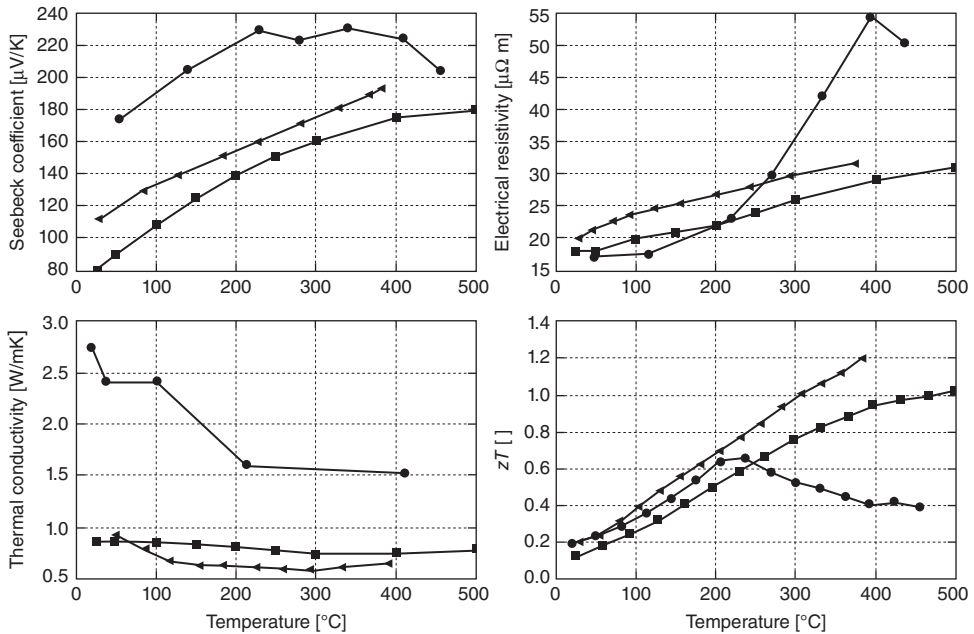


**Figure 6.5** Thermoelectric properties of representative materials based on pnictides. n-type materials are shown by filled symbols, p-type by open symbols. ● ZnSb + Sn, Ag [1], ■  $\text{Zn}_4\text{Sb}_3$  [11], ◄  $\text{Zn}_4\text{Sb}_3$  [22]

for p-type have shown promise. Filled skutterudites contain additional elements in the unit cell with a typical structure of  $\text{W}_1\text{X}_4\text{Y}_{12}$  [24, 25].

Figure 6.6 shows a representation of n-type and p-type skutterudites. A wide range of thermal conductivities is shown for these selected works, with values from 1.5 to 4  $\text{W/mK}$ . Peak  $zT$  typically occurs for the maximum operating temperature, at which point stability due to sublimation can become an issue.

Figure 6.7 shows a compilation of all the reference materials  $zT$  shown in the previous sections. This figure illustrates the dominance of bismuth-based chalcogenides for cooling and power generation near room temperature. Also apparent in the figure is the significant temperature dependence of  $zT$ , making it very difficult to use a single set of n-type and p-type materials to span a large temperature difference and maintain high efficiency, being a strong function of  $zT$ . As such, for applications in which a large temperature difference is available for power generation, techniques such as multistaging and continuously grading material compositions have been developed [29, 30].

It is apparent in Figure 6.7 that for many high-temperature thermoelectric materials the data available in literature ends at a temperature where  $zT$  is still increasing. This may be due to the temperature limitations of the experimental apparatus used; however, it is the case with many high-temperature thermoelectric materials that the peak  $zT$  is reached at elevated temperatures where the material is degrading to the point that makes reliable, repeatable measurements difficult. This can be

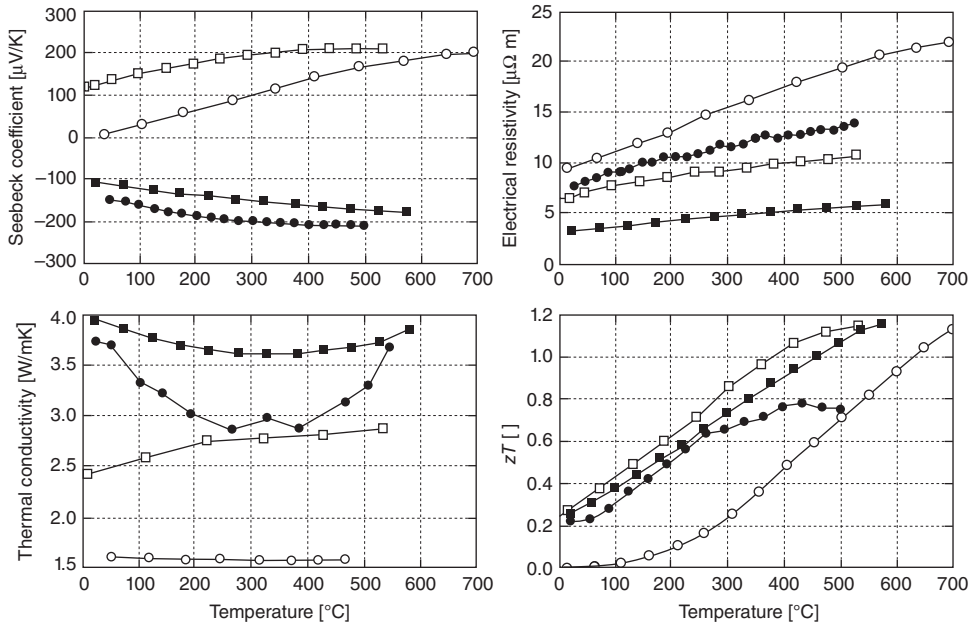


**Figure 6.6** Thermoelectric properties of representative materials based on skutterudites. n-type materials are shown by filled symbols, p-type by open symbols.  $\bullet$   $\text{In}_{0.18}\text{Co}_4\text{Sb}_{12}$  [26],  $\blacksquare$   $\text{Ba}_{0.18}\text{Ce}_{0.05}\text{Co}_4\text{Sb}_{12}$  [27],  $\circ$   $\text{LaFe}_3\text{CoSb}_{12}$  [25],  $\square$   $(\text{didymium})_{0.76}\text{Fe}_{0.34}\text{Ni}_{0.6}\text{Sb}_{12}$  [28]

due to significant sublimation of components, oxidation, irreversible phase transition, separation or segregation of dopants or other constituents, softening, or simply melting. As such, despite the high  $zT$  shown for many of these materials at elevated temperatures, forming these into a module capable of reliable performance at temperatures where their peak  $zT$  is exhibited can be challenging.

### 6.3

#### Influence of Scale on Material Selection and Synthesis

The physical scale of an energy harvester and the thermoelectric elements require by its design often can limit the options for thermoelectric material synthesis. As shown in Figure 6.8, as the characteristic length of the thermoelectric element used decreases, the type of element that is typically appropriate changes from bulk, mini bulk, thick films, nanowires, and thin films.

For the specific length scale of elements required by a design, certain material synthesis methods are more appropriate, and others are incompatible. As shown in the figure, from large to small length scales, common synthesis methods include bulk synthesis (zone melting, mechanical alloying, melt/quench, hot pressing, spark plasma sintering, etc.), flame spraying, electroplating/electrophoresis/dielectrophoresis, sputtering, and evaporation/CVD.

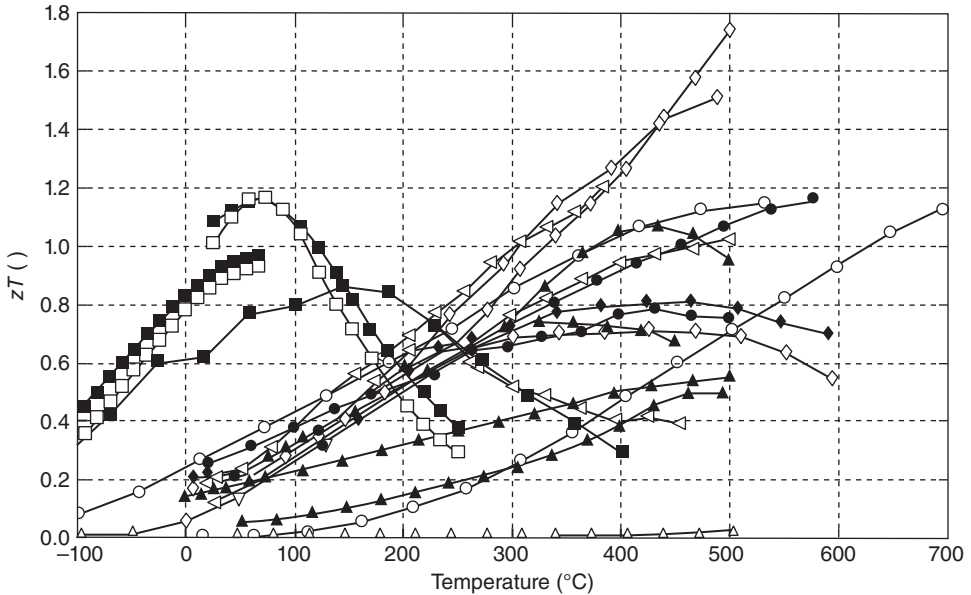


**Figure 6.7** Summary of the thermoelectric figure of merit of materials presented in Figures 6.3–6.6. ● n-type skutterudites, ○ p-type skutterudites, ■ n-type bismuth-based chalcogenides, □ p-type bismuth-based chalcogenides, ◆ n-type lead-based chalcogenides, ◇ p-type lead-based chalcogenides, ◁ pnictides (p-type), ▲ n-type crystallogens, △ p-type crystallogens

As the characteristic dimension of the thermoelectric element is reduced, such as with thin films and nanowires, there are several challenges faced related to performance. Recent decades have seen significant efforts developing thermoelectric materials and devices based on thin films and nanowires [31–34]. Efforts are primarily motivated by the potential to increase the materials' performance; however, other stated motivations include the desire to reduce material or manufacturing costs through alternative synthesis processes. Despite reports of performance increase in low-dimensional materials found in the literature, work demonstrating a thermoelectric module based on low-dimensional materials that offers a higher performance than a similar module based on traditional bulk materials remains elusive. The subsequent section outlines several potential reasons that this is the case, highlighting areas of caution for the micro energy harvester designer.

### 6.3.1

#### Thermal Conductance Mismatch

Thermal conductance mismatch between a low-dimensional thermoelectric element and its external thermal conductances significantly degrades module performance as the thickness of the thermoelectric elements in the direction of current

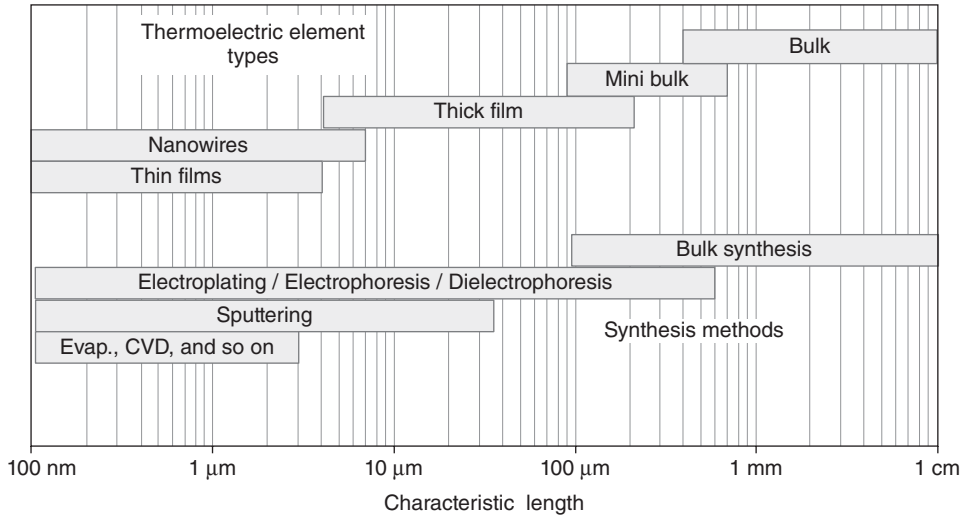


**Figure 6.8** Typical thermoelectric material types and several general material synthesis options are shown for the length scale of the thermoelectric element utilized in an energy harvester.

and heat flow decreases. As noted in Section 6.2 and Figure 6.2, optimal performance occurs when the internal thermal conductance of the module  $K$  balances the external thermal conductance caused by heat sinking and the path from the heat source,  $K_c$  and  $K_h$ . By definition, thin films are thin and have a high thermal conductance  $K$ . Similarly, in the case of nanowires, individual nanowires may have a high aspect ratio; however, the absolute thickness of the arrays is typically small, creating a high internal thermal conductance  $K$  compared to the external conductances  $K_c$  and  $K_h$ . As a result, performance can often suffer from  $K$  of low-dimensional thermoelectric materials being far from optimal. Mitigation efforts include reducing the element's cross section to decrease  $K$ ; however, this introduces challenges such as thermal bypass, which is described later in the chapter [35, 36].

### 6.3.2

#### Domination of Electrical Contact Resistances

As the dimensionality of a thermoelectric element decreases, the undesirable Joule heating at electrical interfaces due to electrical contact resistances can begin to dominate, degrading the performance. The electrical impedance in the bulk of a thermoelectric element is an undesirable but unavoidable factor in module design and can be expressed as  $R = \rho * L/A$ , where  $\rho$  is the material's electrical resistivity,  $L$  is the element's length, and  $A$  is the element's cross-sectional area. The electrical resistance of the interface between thermoelectric material and an electrical interconnect is a wholly undesirable effect and should be minimized. This resistance at the interface can be expressed as  $R_i = \rho_i/A$ , where  $\rho_i$  is the electrical



contact resistivity and  $A$  is the cross-sectional area. The ratio of these resistances should remain high to avoid performance degradation and can be expressed as  $\phi = \rho * L / \rho_i$ . Retaining a high ratio of  $\phi$  and, thereby avoiding having the resistance of the interfaces degrade the performance, is a tremendous challenge when the magnitude of  $L$  drops as thin films or nano wires are introduced into the thermoelectric module design [35, 36].

### 6.3.3

#### Domination of Bypass Heat Flow

In a thermoelectric energy harvester, only the heat that passes through the thermoelectric elements has the chance of being converted into useful electrical power. Any other paths of heat flow that bypass the elements are parasitic and undesirable. Domination of the desirable heat flow through the bulk thermoelectric materials by bypass heat flow can be difficult to manage in modules composed of low-dimensional elements, particularly nanowires. This is often due to the practical requirements of packaging a module to reduce thermal contact resistances and improve reliability. In order to achieve good thermal contact between the heat source and heat sink, significant pressure is typically applied to a module. Additionally, in operation, modules undergo temperature changes that result in thermally induced stress. As such, a thermoelectric module must be designed to take these extreme forces. The high aspect ratio and delicate nature of thermoelectric nanowire arrays can run counter to the need for strong, robust thermoelectric elements to resist these mechanical forces that a module is subjected to. In order to increase robustness of nanowire arrays, efforts have focused on filling the area around the wires with a mechanically robust material. However, given the small cross section of wires, heat flow through the fill material can easily surpass the desired heat flow through the wires themselves, degrading performance. Efforts to reduce the aspect ratio and thereby increase the mechanical stability of the nanowire array by increasing the cross-sectional area of the nanowire can result in the loss of any potential  $zT$  gains obtained due to the nanowire nature of the materials. Efforts to reduce the aspect ratio and thereby increase the mechanical stability of the nanowire array by reducing the length of the nanowire array are then faced with the potential for the domination of electrical contact resistance mentioned in Section 6.3.2.

### 6.3.4

#### Challenges in Thermoelectric Property Measurement

The accurate and reproducible measurements of thermoelectric properties at all length scales is a challenge, particularly due to the lack of generally accepted measurement standards and techniques [37]. As the physical size of samples decreases, it becomes increasingly difficult to perform the high-quality measurements that are needed to make good design decisions about whether or not to integrate low-dimensional materials into an energy harvester.

For example, a method known as the Harman method, or  $ZT$  meter, relies on operating a couple or module and estimating the difference in voltage across the sample during the instant that electrical power is removed [38]. The lower the system time constant, the more difficult high-quality measurements become. The thermal time constant governing the equalization of a temperature difference sustained across a thermoelectric module can be expressed as  $\tau = L^2/\alpha$ , where  $L$  is the element length and  $\alpha$  is the thermal diffusivity of the thermoelectric materials. As  $L$  decreases for thin film and nanowire devices, the ability to accurately resolve this short time scale voltage transient is reduced. For example, on the basis of the time constant, the time resolution for a measurement of a 1  $\mu\text{m}$  film would need to be  $10^6$  times the time resolution for a measurement of a 1 mm thick material in order to resolve the Harman method's transient signal with similar accuracy.

In the case of nanowires, often independent measurements of thermal conductivity, electrical resistivity, and Seebeck coefficient are performed, and used to calculate  $zT$ . Much of the support for nanowires as thermoelectric materials relies on theory that the thermal conductivity may be reduced for small-diameter wires while Seebeck coefficient and electrical resistivity are less negatively affected, thereby increasing  $zT$ . Increases in  $zT$  to as high as 0.6 [34] and 1.0 [39] in silicon nanowires have been reported (improvement of as much as 100-fold over bulk material). Increases in Seebeck coefficient of 60% and reductions in thermal conductivity of 57% over bulk values in Bi–Te nanowire systems have also been reported [40]. This notable enhancement of properties due to nanostructuring makes accurate measurement of these parameters, particularly thermal conductivity, critically important. The extraction of electrical resistivity and thermal conductivity from experimental data requires the measurement of a nanowire's diameter using SEM or TEM, a measurement with error dependent on the operator's skill, wire diameter, system calibration, and system capabilities. Despite these issues, many reports of thermoelectric enhancement in nanowires over bulk materials are light on error analysis, particularly for thermal conductivity.

#### 6.4

##### Low Dimensionality: Internal Micro/Nanostructure and Related Approaches

An area of thermoelectric materials development that has shown promise in improving performance while avoiding the aforementioned pitfalls of low dimensionality are macroscopic material systems with internal micro- or nanostructure. Thermoelectric elements formed from these materials can more easily be designed to provide optimal thermal conductance matching, avoid domination by electrical contact resistance or thermal bypass, and have their properties more accurately characterized. Research in this area includes forming small domains of dissimilar stoichiometry [41], creating small grains [42], and taking advantage of naturally occurring or artificial layered structures [43, 44], all in an effort to increase the material's  $zT$  [45].

A somewhat related approach that may enhance  $zT$  is referred to as distortion or tuning of the density of states. This approach seeks to enhance the Seebeck coefficient without detrimental effects on thermal conductivity or electrical resistivity. One example of this approach in  $Tl_{0.02}Pb_{0.98}Te$  is included in Figure 6.3 [13].

**6.5 Thermal Expansion and Its Role in Materials Selection**

It is important to select materials with high thermoelectric figure of merit in a module design, but to minimize issues from stress that can affect reliability, thermal expansion should be considered carefully as well. Thermoelectric materials are subjected to significant temperature changes, as well as large temperature differences across them during operation, and expand significantly as a result. For a simple structure as shown in Figure 6.1 thermal expansion of both elements can cause shear stresses to develop at the interface between thermoelectric materials and interfaces, which can lead to electrical and thermal contact degradation. Additionally, if n and p have notably different thermal expansion, additional stresses can result at these interfaces, including undesirable stress conditions where the interfaces for the element with a lower thermal expansion are in tension.

Figure 6.9 shows a selection of thermoelectric materials and approximate coefficient of thermal expansion at their typical operating temperature. n-type materials are shown at the left and p-type are shown at the right. For example, n-type and p-type lead telluride materials exhibit similar thermal expansion coefficients, allowing these to be integrated into a module with minimal relative expansion at temperature. However, the expansion of these materials is relatively high and may result in stress dissimilar expansion of interconnects or other components of the module. Similarly, n-type and p-type silicon germanium exhibit relatively low absolute thermal expansion and similar relative thermal expansion. The figure

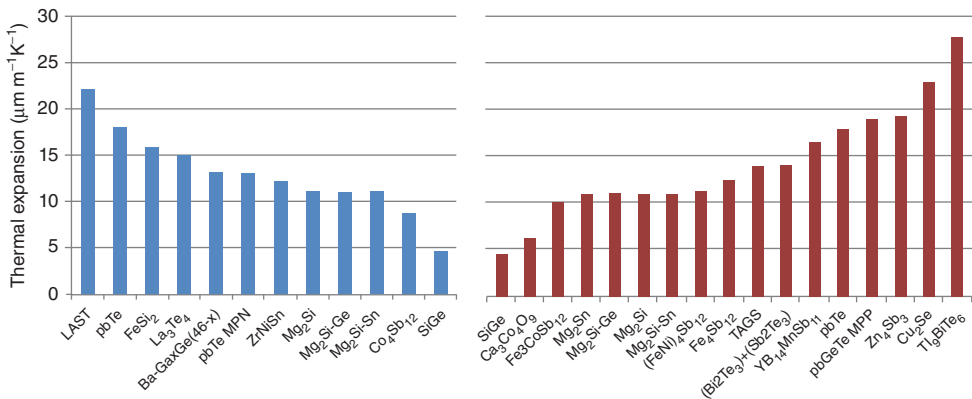


**Figure 6.9** Coefficient of thermal expansion data for several n and p-type thermoelectric materials [46].

illustrates how the selection of, for example, an n-type  $\text{Co}_4\text{Sb}_{12}$  and a p-type  $\text{Cu}_2\text{Se}$  may be attractive for certain design considerations, but they may result in integration and reliability challenges due to their large difference in thermal expansion [46].

## 6.6

### Raw Material Cost Considerations

The breakdown of production costs for an energy harvesting system is highly dependent on production volume, influencing the relative proportion of raw material, assembly, and other costs. The cost of the thermoelectric raw material can be a significant portion of an energy harvester, particularly when the impact of end-of-life disposal issues are included (e.g., for lead bearing materials). The cost of raw materials used as inputs to thermoelectric materials varies widely due to the inherent scarcity of the element in the earth's crust, the lack of production due to few nonthermoelectric uses, and/or the expense in refining and isolating the element [47–49].

When evaluating the cost/benefit of thermoelectric materials, one useful metric is to evaluate the performance a material can offer, quantified by  $zT$ , divided by the raw material cost on an equivalent volume or mass basis. Figure 6.10 shows the material  $zT$  per USD per volume for several thermoelectric materials. This analysis looked at these materials' performance near  $150^\circ\text{C}$  and considered the pricing in 2011 and 2012 for consumption to support an industrial scale thermoelectric product [50].

The figure illustrates how the performance offered per cost can vary by several orders of magnitude for a given temperature. Even at  $150^\circ\text{C}$ , below the optimal temperatures for  $\text{Mg}_2\text{Si}/\text{Mg}_2\text{Sn}$  and  $\text{Zn}_3\text{Sb}_4$ , they offer an order of magnitude higher performance than telluride bearing materials, for example. Similarly, germanium bearing materials exhibit poor performance per cost due to the cost of germanium.

## 6.7

### Material Synthesis with Particular Relevance to Micro Energy Harvesting

Thermoelectric materials for energy harvesting may be synthesized by various methods including melting, melt/quench methods, melt spinning and gas atomization, zone melting, and various crystal growth methods. For manually or semi-manually assembled macroscale devices, the process of material synthesis, element formation, and module assembly generally can take place in a linear manner, allowing the material's synthesis method employed to largely be independent of the module geometry. For microenergy harvesters, the material's synthesis process and the module fabrication process can become more interdependent.

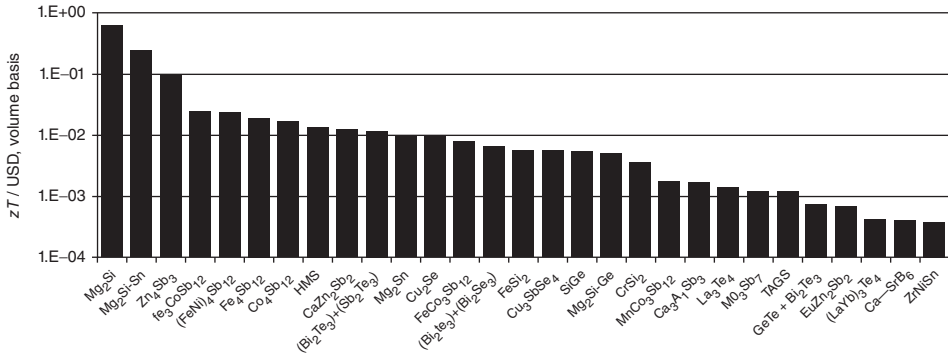


Figure 6.10 The  $zT$  at 150°C per cost on a volumetric basis.

For example, should one utilize micro-electro-mechanical-systems/silicon micro-fabrication for the module, it may necessitate using sputtering or electroplating of thermoelectric materials. As a result, when developing micro energy harvesting devices, a more limited set of practical materials' synthesis techniques may be available to the designer, resulting in a reduced set of thermoelectric material families that are available, or the  $zT$  of materials available by compatible processing techniques may be less than what is available at the macro scale. For example, for creating elements measured in several millimeters for power generation near room temperature, the process of zone melting high-quality ingots from bismuth-based chalcogenides that can be mechanically cut into elements is well established. To construct a micro device with elements measuring in several microns in linear dimension, one may rely on sputtering deposition of bismuth chalcogenides and photolithographic patterning, which may yield elements of the desired dimension, but typically with inferior thermoelectric properties to bulk.

Several methods with particular relevance to micro energy harvesting are outlined below.

### 6.7.1

#### Electroplating, Electrophoresis, Dielectrophoresis

Electroplating is well established in microelectronics and has also been applied to the formation of thermoelectric materials for micro energy harvesters. Challenges to this technique include the difficulty of producing thermoelectric elements of both n-type and p-type on the same device, but various techniques of selectively masking N and P regions have shown promise. Additionally, it can be difficult to form high-quality, uniform elements thick enough to provide optimal thermal resistance as described in Section 6.3.1 (typically on the order of 10's to 100's of microns) [51–53].

Electrophoresis and dielectrophoresis have been investigated as methods to form micro energy harvesters and coolers. Bulk thermoelectric materials may be formed by any number of methods, and then particleized. The particles are

then made to flow along electric field lines and build up deposits that are then subjected to high temperature and pressure operations in order to form finished thermoelectric elements. This, as well as the related effect known as dielectrophoresis, seeks to achieve high-quality thermoelectric material properties from the bulk material precursors but formed in micro scale arrays [54–56].

### 6.7.2

#### **Thin and Thick Film Deposition**

As with electroplating, sputtering and evaporation are well-established methods for the deposition of materials in the semiconductor industry. These methods have also been applied to the synthesis of thermoelectric materials for micro energy harvesters and cooling devices. A single sputtering target may be formed with the desired stoichiometry and doping level and deposited on a target substrate, or multiple targets may be used sequentially or at the same time to achieve the desired material on the substrate. For example, a p-type bismuth antimony telluride thermoelectric layer may be formed by sputtering from three independent targets of bismuth, antimony, and tellurium. Typically, this is followed by high-temperature annealing steps to allow the species to diffuse and form the desired crystal structure [32, 33].

Layers of a thermoelectric material may be similarly formed by evaporation, in which a thermoelectric precursor is heated in a low-pressure system to the point where they evaporate. Due to the long mean free path of the evaporated atoms at low pressure, they are deposited uniformly as a film on a substrate.

Relevant methods such as Atomic Layer Deposition (ALD), Chemical Vapor Deposition (CVD), and Metal Organic Vapor Deposition (MOCVD) similarly can be applied to thermoelectric element formation.

These methods simply deposit thin or thick films, but the challenge to form individual thermoelectric elements of both n-type and p-type conduction remains. Masking and selective etching methods have been used to realize individual elements. As with electrodeposition, forming elements thick enough to provide optimal thermal resistance as described in Section 6.3.1 (typically on the order of 10's to 100's of microns) with uniform stoichiometry and low stress is challenging.

Thermal spray, also known as flame spraying, has also been utilized to form thermoelectric materials in thin films, thick films, and bulk-like deposits as thick as 3 mm [57].

## 6.8

### **Summary**

Thermoelectric materials have been studied since early in the twentieth century, and a huge amount of data on a number of material types are available. However, the selection of thermoelectric materials that are appropriate for a micro energy harvester design is no simple task. With careful thermal and electrical design that considers thermal resistances from the source of heat to the harvester and from

the harvester to the ambient environment, the right choice of element scale and material can become apparent. By considering thermal expansion and its role in the design as well as material and production costs, a high-reliability, volume scalable energy harvester can be realized.

## References

1. Heikes, R.R., Miller, R.C., and Ure, R.W. (1961) Survey of known thermoelectric materials, in *Thermoelectricity: Science and Engineering* (eds R.R. Heikes and R.W. Ure), Interscience Publishers, pp. 405–434.
2. Goldsmid, H.J. and Douglas, R.W. (1957) The use of semiconductors in thermoelectric refrigeration. *Br. J. Appl. Phys.*, **5**, 386.
3. Ioffe, A.F. (1957) *Semiconductor Thermoelements and Thermoelectric Cooling*, Infosearch Limited, London.
4. Fritts, R.W. (1960) Lead telluride alloys and junctions, in *Thermoelectric Materials and Devices* (eds I.B. Cadoff and E. Miller), Reinhold Publishing Corporation, pp. 143–160.
5. Evans, D.B. and Kobren, L. (1969) An electron microprobe study of inclusions in lead telluride thermoelectric elements, NASA Technical Note, NASA TN D-5415.
6. Rowe, D.M. and Cleve, M. (1990) Preparation of high-density small grain size compacts of lead tin telluride. *J. Mater. Sci. - Mater. Electron.*, **1** (3), 129–132.
7. Rowe, D.M. (1991) Applications of nuclear-powered thermoelectric generators in space. *Appl. Energy*, **40** (4), 241–271.
8. orgname AEC Research And Development Report. Compact thermoelectric converter (U). Technical Report WANL PR(CC)-03 3, Westinghouse Astronautical Laboratory; 1968.
9. Rouklove, P. and Truscello, V. (1971) Thermoelectric generators for deep space application. Technical Report Technical Report 32-1495, NASA Jet Propulsion Laboratory.
10. Nolas, G.S., Sharp, J., and Goldsmid, H.J. (2001) *Thermoelectrics, Basic Principles and New Materials Developments*, Springer-Verlag.
11. Miner, A.C. (2013) Thermoelectric properties of lead free materials, Internal thermoelectric materials data (unpublished).
12. Gelbstein, Y., Dado, B., Ben-Yehuda, O., Sadia, Y., Dashevsky, Z., and Dariel, M.P. (2010) Highly efficient Ge-rich  $\text{Ge}_x\text{Pb}_{1-x}\text{Te}$  thermoelectric alloys. *J. Electron. Mater.*, **39** (9), 2049–2052.
13. Heremans, J.P., Jovovic, V., Toberer, E.S., Saramat, A., Kurosaki, K., Charoenphakdee, A., Yamanaka, S., and Snyder, G.J. (2008) Enhancement of thermoelectric efficiency in PbTe by distortion of the electronic density of states. *Science*, **321** (5888), 554–557.
14. Madelung, O., Rossler, U., and Schulz, M. (eds). *Magnesium Stannide ( $\text{Mg}_2\text{Sn}$ ) Debye Temperature, Heat Capacity, Density, Melting Point*, Vol. III/17E-17F-41C: 'Semiconductors' of Landolt-Börnstein – Group III Condensed Matter, Vol. C: Non-Tetrahedrally Bonded Elements and Binary Compounds I, SpringerMaterials – The Landolt-Börnstein Database, doi: 10.1007/10681727\_123.
15. Berthebaud, D. and Gascoin, F. (2013) Microwaved assisted fast synthesis of n and p-doped  $\text{Mg}_2\text{Si}$ . *J. Solid State Chem.*, **202**, 61–64.
16. Zhang, Q., Liu, W., Yan, Y., Li, H., and Tang, X. (2013) Enhanced thermoelectric properties of Li-doped p-type  $\text{Mg}_{2(1-x)}\text{Li}_{2x}\text{Si}_{0.3}\text{Sn}_{0.7}$  solid solutions. Proceedings of the 32nd International Conference on Thermoelectrics, 30 July.
17. Gokhale, A.B. and Abbaschian, R. (1990) The Mn-Si (manganese-silicon) system. *Bull. Alloy Phase Diagrams*, **11** (5), 468–480.
18. Nikitin, E.N., Bazanov, V.G., and Tarasov, V.I. (1961) Thermoelectric properties of  $\text{Mg}_2\text{Si}$ -MgSn Solid Solutions. *Fizika Tverdogo Tela*, **3** (36), 5–9.

19. Isoda, Y., Nagai, T., Fujiu, H., Imai, Y., and Shinohara, Y. (2006) Thermoelectric properties of Sb-doped  $\text{Mg}_2\text{Si}_{0.5}\text{Sn}_{0.5}$ . ICT '06. 25th International Conference on Thermoelectrics; 2006. pp. 406–410.
20. Itoh, T. and Yamada, M. (2009) Synthesis of thermoelectric manganese silicide by mechanical alloying and pulse discharge sintering. *J. Electron. Mater.*, **38** (7), 925–929.
21. Luo, W., Li, H., Fu, F., Hao, W., and Tang, X. (2011) Improved thermoelectric properties of Al-doped higher manganese silicide prepared by a rapid solidification method. *J. Electron. Mater.*, **40** (5), 1233–1237.
22. Caillat, T., Fleurial, J.-P., and Borshchevsky, A. (1997) Preparation and thermoelectric properties of semiconducting  $\text{Zn}_4\text{Sb}_3$ . *J. Phys. Chem. Solids*, **58** (7), 1119–1125.
23. Snyder, G.J., Christensen, M., Nishibori, E., Caillat, T., and Iversen, B.B. (2004) Disordered zinc in  $\text{Zn}_4\text{Sb}_3$  with phonon-glass and electron-crystal thermoelectric properties. *Nat. Mater.*, **3** (7), 458–463.
24. Caillat, T., Borshchevsky, A., and Fleurial, J.P. (1993) Thermoelectric properties of a new semiconductor:  $\text{IrSb}_3$ , in *Proceedings of the XIth International Conference on Thermoelectrics* (ed. K.R. Rao), p. 98.
25. Sales, B.C., Mandrus, D., and Williams, R.K. (1996) Filled skutterudite antimonides: a new class of thermoelectric materials. *Science*, **272** (5266), 1325–1328.
26. Da Ros, V., Leszczynski, J., Lenoir, B., Dauscher, A., Candolfi, C., Masschelein, P., Bellouard, C., Stiewe, C., Mueller, E., and Hejtmanek, J. (2007) Thermoelectric properties of  $\text{In}_x\text{Co}_{4-y}\text{Ni}_y\text{Sb}_{12}$  skutterudite compounds. MRS Proceedings, vol. **1044**.
27. Bai, S.Q., Pei, Y.Z., Chen, L.D., Zhang, W.Q., Zhao, X.Y., and Yang, J. (2009) Enhanced thermoelectric performance of dual-element-filled skutterudites  $\text{Ba}_x\text{Ce}_y\text{Co}_4\text{Sb}_{12}$ . *Acta Mater.*, **57** (11), 3135–3139.
28. Rogl, G., Grytsiv, A., Bauer, E., Rogl, P., and Zehetbauer, M. (2010) Thermoelectric properties of novel skutterudites with didymium:  $\text{DD}_y(\text{Fe}_{1-x}\text{Co}_x)_4\text{Sb}_{12}$  and  $\text{DD}_y(\text{Fe}_{1-x}\text{Ni}_x)_4\text{Sb}_{12}$ . *Intermetallics*, **18** (1), 57–64.
29. Caillat, T., Fleurial, J.-P., Snyder, G.J., Zoltan, A., Zoltan, D., and Borshchevsky, A. (1999) A new high efficiency segmented thermoelectric unicouple. 34th Intersociety Energy Conversion Engineering Conference, p. 2567.
30. Snyder, G.J. (2004) Application of the compatibility factor to the design of segmented and cascaded thermoelectric generators. *Appl. Phys. Lett.*, **84** (13), 2436.
31. Abramson, A.R., Kim, W.C., Huxtable, S.T., Yan, H., Wu, Y., Majumdar, A., Tien, C.-L., and Yang, P. (2004) Fabrication and characterization of a nanowire/polymer-based nanocomposite for a prototype thermoelectric device. *J. Microelectromech. Syst.*, **13** (3), 505–513.
32. Ngai, T., Samavedam, B., and Ghoshal, U. (2004) Method for forming a monolithic thin-film thermoelectric device including complementary thermoelectric materials. Patent Appl. US2005/0150536 A1.
33. Bottner, H., Nurnus, J., Gavrikov, A., Kuhner, G., Jagle, M., Kunzel, C., Eberhard, D., Plescher, G., Schubert, A., and Schlereth, K.H. (2004) New thermoelectric components using microsystem technologies. *J. Microelectromech. Syst.*, **13** (3), 414–420.
34. Hochbaum, A.I., Chen, R., Delgado, R.D., Liang, W., Garnett, E.C., Najarian, M., Majumdar, A., and Yang, P. (2008) Enhanced thermoelectric performance of rough silicon nanowires. *Nature*, **451** (7175), 163–167.
35. Miner, A.C. (2006) The compatibility of thin films and nanostructures in thermoelectric cooling systems. *J. Heat Transfer*, **129** (7), 805–812.
36. Bierschen, J.L. (2009) Optimized thermoelectrics for energy harvesting applications, in *Energy Harvesting Technologies* (eds S. Priya and D.J. Inman), Springer, pp. 337–351.
37. Wang, H. and Johnson, R.D. (2011) Standardization of transport properties measurements: internal energy agency (IEA-AMT) annex on thermoelectric.



- DOE 2011 Thermoelectric Application Workshop, 1 April.
38. Harman, T.C., Cahn, J.H., and Logan, M.J. (1959) Measurement of thermal conductivity by utilization of the Peltier effect. *J. Appl. Phys.*, **30** (9), 1351–1359.
  39. Boukai, A.I., Bunimovich, Y., Tahir-Kheli, J., Yu, J.-K., Goddard, W.A. III, and Heath, J.R. (2008) Silicon nanowires as efficient thermoelectric materials. *Nature*, **451** (7175), 168–171.
  40. Zhou, J., Jin, C., Seol, J.H., Li, X., and Shi, L. (2005) Thermoelectric properties of individual electrodeposited bismuth telluride nanowires. *Appl. Phys. Lett.*, **87** (13), 133109.
  41. Bahk, J.-H., Bian, Z., Zebarjadi, M., Zide, J.M.O., Lu, H., Xu, D., Feser, J.P., Zeng, G., Majumdar, A., Gossard, A.C., Shakouri, A., and Bowers, J.E. (2010) Thermoelectric figure of merit of  $(\text{In}_{0.53}\text{Ga}_{0.47}\text{As})_{0.8}(\text{In}_{0.52}\text{Al}_{0.48}\text{As})_{0.2}$  iii-v semiconductor alloys. *Phys. Rev. B*, **81**, 235209.
  42. Poudel, B., Hao, Q., Ma, Y., Lan, Y., Minnich, A., Yu, B., Yan, X., Wang, D., Muto, A., Vashaee, D., Chen, X., Liu, J., Dresselhaus, M.S., Chen, G., and Ren, Z. (2008) High-thermoelectric performance of nanostructured bismuth antimony telluride bulk alloys. *Science*, **320** (5876), 634–638.
  43. Huxtable, S.T., Abramson, A.R., Tien, C.-L., Majumdar, A., LaBounty, C., Fan, X., Zeng, G., Bowers, J.E., Shakouri, A., and Croke, E.T. (2002) Thermal conductivity of Si/SiGe and SiGe/SiGe superlattices. *Appl. Phys. Lett.*, **80** (10), 1737–1739.
  44. Ikeda, T., Collins, L.A., Ravi, V.A., Gascoin, F.S., Haile, S.M., and Snyder, G.J. (2007) Self-assembled nanometer lamellae of thermoelectric PbTe and  $\text{Sb}_2\text{Te}_3$  with epitaxy-like interfaces. *Chem. Mater.*, **19** (4), 763–767.
  45. Shakouri, A. (2011) Recent developments in semiconductor thermoelectric physics and materials. *Annu. Rev. Mater. Res.*, **41** (1), 399–431.
  46. Miner, A.C. and Uvarov, C. (2012) Thermal expansion of thermoelectric materials. Aggregated Thermal Expansion Data, Various Sources (unpublished).
  47. Zweibel, K. (2010) The impact of tellurium supply on cadmium telluride photovoltaics. *Science*, **328** (5979), 699–701.
  48. Yazawa, K. and Shakouri, A. (2011) Cost-efficiency trade-off and the design of thermoelectric power generators. *Environ. Sci. Technol.*, **45** (17), 7548–7553.
  49. Amatya, R. and Ram, R.J. (2012) Trend for thermoelectric materials and their earth abundance. *J. Electron. Mater.*, **41** (6), 1011–1019.
  50. Miner, A.C. and Uvarov, C. (2012) Performance, cost, and global scalability of thermoelectric materials, (unpublished).
  51. Snyder, G.J., Lim, J.R., Huang, C.-K., and Fleurial, J.-P. (2003) Thermoelectric microdevice fabricated by a MEMS-like electrochemical process. *Nat. Mater.*, **2** (8), 528–531.
  52. Schwyter, E., Glatz, W., Durrer, L., and Hierold, C. (2008) Flexible micro thermoelectric generator based on electroplated  $\text{Bi}_2\text{Te}_3$ . MEMS/MOEMS 2008. Symposium on Design, Test, Integration and Packaging of MEMS/MOEMS, 2008, pp. 46–48.
  53. Boulanger, C. (2010) Thermoelectric material electroplating: a historical review. *J. Electron. Mater.*, **39** (9), 1818–1827.
  54. Lu, W., Ding, Y., Chen, Y., Wang, Z.L., and Fang, J. (2005) Bismuth telluride hexagonal nanoplatelets and their two-step epitaxial growth. *J. Am. Chem. Soc.*, **127** (28), 10112–10116.
  55. Okamoto, T., Horii, S., Uchikoshi, T., Suzuki, T.S., Sakka, Y., Funahashi, R., Ando, N., Sakurai, M., Shimoyama, J., and Kishio, K. (2006) Fabrication of multilayered oxide thermoelectric modules by electrophoretic deposition under high magnetic fields. *Appl. Phys. Lett.*, **89** (8), 081912.
  56. Nozariasbmarz, A., Rad, A.T., Zamanipour, Z., Krasinski, J.S., Tayebi, L., and Vashaee, D. (2013) Enhancement of thermoelectric power factor of silicon germanium films grown by electrophoresis deposition. *Scr. Mater.*, **69** (7), 549–552.
  57. Tewolde, M., Liu, D., Hwang, D.J., and Longtin, J.P. (2013) Laser processing of thermal sprayed coatings for thermoelectric generators. ASME 2013 Heat Transfer Summer Conference, 14 July.



## 7

# Piezoelectric Materials for Energy Harvesting

*Emmanuel Defay, Sébastien Boisseau, and Ghislain Despesse*

### 7.1

#### Introduction

This chapter reviews the materials in use for vibrational energy harvesters. We first describe the physics underpinning vibrational energy harvesting, namely piezoelectricity, in order to identify the properties required for a good material. The main materials in use will then be presented, with examples of harvesters for each case. The perovskite family, in which lead zirconate titanate (PZT) lies, is first described. Fabrication processes and main characteristics of ceramics, screen-printed layers, single crystals, and thin films are detailed. A section is dedicated to perovskite lead-free materials. Wurtzite thin films such as aluminum nitride (AlN) and zinc oxide (ZnO) are then described, followed by polymers such as polyvinylidene fluoride (PVDF), which stand for a very exciting area of research for energy harvesting. The last section details the latest developments performed with nanomaterials, especially ZnO nanowires (NWs).

### 7.2

#### What Is Piezoelectricity?

The piezoelectric effect represents a linear relationship between one mechanical variable and one electric variable. The direct piezoelectric effect was revealed by the Curie brothers in 1880: surface charges accumulate on a piezoelectric material when it experiences mechanical stress [1]. In 1881, Lippmann envisioned the converse effect by thermodynamics considerations [2]. The same year, Pierre and Jacques Curie experimentally observed this converse effect by deflecting two thin and long quartz beams with opposite crystallographic orientations when an external voltage was applied. The deflection was the consequence of voltage-induced mechanical strain developing into quartz, resulting from the so-called converse piezoelectric effect.

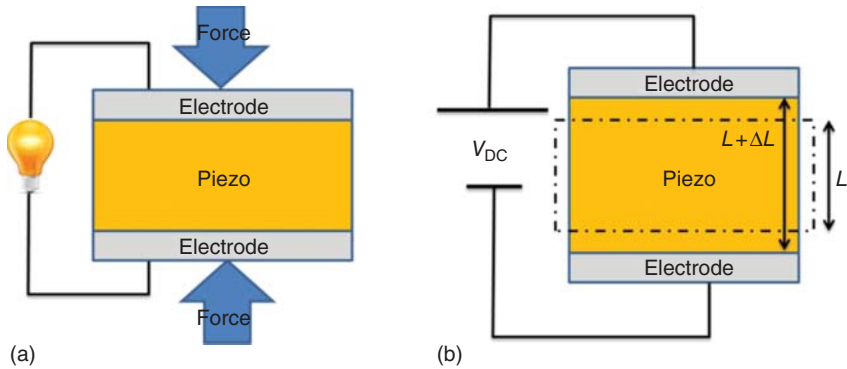


**Figure 7.1** Sketch of direct (a) and converse (b) piezoelectric effects.

Figure 7.1 shows direct and converse piezoelectric effects. In Figure 7.1a, a current flows through the circuit while an external force is applied to the piezoelectric material sandwiched between two electrodes. This stands for the direct piezoelectric effect. Figure 7.1b shows the deformation experienced by the same piezoelectric capacitor while an external voltage is applied to it. In-plane and out-of-plane strains occur simultaneously. Both strains have typically opposite signs, though auxetic materials can experience equivalent signs strains [3].

As far as energy harvesting is concerned, direct piezoelectric effect is the one that matters. Indeed, the standard device for this purpose is a piezoelectric material that accumulates charges as a consequence of external vibrations. However, active frequency control of vibrating beams owing to converse piezoelectric effect can be very useful, as recently shown by Ahmed Seddik *et al.* [4].

There is a more accurate definition of piezoelectricity, based on crystallography. Given that a crystal environment is composed of electrically charged particles, the appearance of polarization charges through mechanical strain is therefore predictable. Thus, the symmetry conditions of crystal structure enable to find out the atom arrangements susceptible to exhibit piezoelectricity. To do so, the crystal should not have a center of symmetry. This is the case of 21 of 32 point groups. Out of these 21 groups, point group 432 displays no piezoelectric effect because the movement of its charges during a mechanical solicitation does not induce the appearance of a dipolar moment. Consequently, 20 groups are actually piezoelectric. Applying a mechanical constraint induces the location of the effective positive charge splits up from that of the effective negative charge for each crystal lattice. Consequently, a dipolar moment appears. A typical example of piezoelectric material is quartz. Note that quartz is not pyroelectric.

Out of these 20 groups, 10 are pyroelectric. They possess a permanent dipolar moment, even without mechanical or thermal stimuli. The preferred direction of dipole is called the polar axis. These groups are called pyroelectric because of the variation of the amplitude of the dipolar moment while temperature changes. Aluminum nitride (AlN) and zinc oxide (ZnO) are pyroelectric.

Among pyroelectric crystals, ferroelectrics exhibit a peculiar property. Their dipoles are strongly mobile in the crystal lattice under the influence of an external electric field. It is even possible to reverse the direction of the dipoles if an external applied electric field is large enough. Although dipoles are mobile, they are stable even when the external field is removed. Most of perovskite materials ( $ABO_3$ ) such as  $Pb(Zr,Ti)O_3$  (PZT),  $BaTiO_3$  (BTO), and  $BiFeO_3$  (BFO) are ferroelectrics.

### 7.3

#### Thermodynamics: the Right Way to Describe Piezoelectricity

Piezoelectricity can be considered a coupling property, as it transforms electric energy into mechanical energy, and vice versa. Consequently, a formal description describing this effect should take into account several physical variables belonging to different forms of energy, namely electric field  $E$  and displacement field  $D$  on the one hand and mechanical stress  $T$  and strain  $S$  on the other hand. The best way to describe their interactions is to utilize thermodynamics and more specifically macroscopic free energies. Indeed, working at the energy level allows understanding the link between all variables involved, according to the boundary conditions such as open or short circuit, no stress or strain at interfaces. Moreover, energy considerations prove that direct and converse piezoelectric effects exhibit the same order of magnitude.

Let us consider the simplest description of piezoelectricity with a 1D-model. Always for the sake of simplicity, we will not consider thermal energy in free energy, though a complete description should take it into account temperature and entropy as conjugated thermal variables [5]. Four electrical–mechanical couples of variables can be chosen to describe piezoelectricity, namely  $(T,E)$ ,  $(S,E)$ ,  $(T,D)$ , and  $(S,D)$ . Note that each choice induces a unique set of equations with one specific piezoelectric coefficient called  $d$ ,  $e$ ,  $g$ , and  $h$ , respectively. Generally speaking, piezoelectricity is described with a third-order matrix and not a simple coefficient, though here we consider a simple 1D-model that only needs one coefficient. Choosing the right couple for a given problem is fundamental in order to simplify as much as possible the formal description. Let us choose here  $(T,E)$  as the proper set of variables. The right free energy to be considered is therefore  $G$ , the so-called Gibbs energy, whose total derivative reads [6]:

$$dG = -SdT - DdE \quad (7.1)$$

Note that  $T$  and  $E$  are both intensive variables, which explains why one has to use two Lagrange transformations from  $U$ , the internal energy, to  $G$ , Gibbs energy. Let us recall that  $dU = TdS + EdD$ , where the variables, namely  $S$  and  $D$ , are the extensive ones.

Next, writing the expression for  $G$  by considering only linear terms including one coupling term between both energy forms yields the following:

$$G - G_0 = -\frac{1}{2}s^E T^2 - \frac{1}{2}\epsilon^T E^2 - dTE \quad (7.2)$$

where  $G_0$  is the Gibbs energy at zero field and zero stress,  $s^E$  is the material compliance at constant  $E$ ,  $\epsilon^T$  is the material dielectric constant at constant  $T$ , and  $d$  is the piezoelectric coefficient.

Equation (7.1) allows writing

$$\left(\frac{\partial G}{\partial T}\right)_E = -S \quad \text{and} \quad \left(\frac{\partial G}{\partial E}\right)_T = -D \quad (7.3)$$

which in turn gives, once combined with Eq. (7.2),

$$\begin{aligned} S &= s^E T + dE \\ D &= \epsilon^T E + dT \end{aligned} \quad (7.4)$$

Here, we have come up with a set of two equations, each containing a linear coupling term involving  $d$ . This is the simplest way of describing piezoelectricity. It is remarkable to observe that the energy description naturally shows that direct and converse piezoelectric effects involve the same piezoelectric coefficient  $d$ . One could think that it would have been simpler to write down these equations at once, skipping the energy level description, only by considering that a linear term with a conjugated variable should be added to the purely mechanical term  $-s^E T$  – and to the purely dielectric term  $-\epsilon^T E$ . However, there are two drawbacks in doing so. (i) There is no clue why direct and converse piezoelectric effects should involve the same coefficient and (ii) there is no clue of what sign should be used with each coupling term. This sign issue is nothing but obvious except if one uses the energy description. Indeed, this latter imposes using the right free energy deduced from  $U$ , internal energy. Lagrange transforms impose the right sign.

Applying this method to three other variable couples gives the respective three other sets of piezoelectric equations:

$$\begin{aligned} T &= c^E S - eE \\ D &= \epsilon^S E + eS \end{aligned} \quad (7.5)$$

$$\begin{aligned} S &= s^D T + gD \\ E &= \beta^T D - gT \end{aligned} \quad (7.6)$$

$$\begin{aligned} T &= c^D S - hD \\ E &= \beta^S D - hS \end{aligned} \quad (7.7)$$

#### 7.4

##### Material Figure of Merit: the Electromechanical Coupling Factor

There are a plenty of figures of merit (FoM) for energy harvesting. They depend on several parameters, and it is difficult to work out one unique FoM as configuration, frequency, and mass can be involved. If one focuses on materials, several FoMs can be defined through what is called electromechanical coupling ( $k$ ).  $k$  depends on material shape, polarization axis, cut, static, or dynamic excitation.

For instance,  $k_{33}$  is the right FoM to define the longitudinal coupling of a long bar vibrating along its length,  $k_{31}$  is the one used when a bar vibrates along its length while the electrodes collect the charges created along its width or thickness,  $k_t$  is the longitudinal coupling of thin plates. Actually, these couplings depend on boundary conditions, which change with material shape and electrode position [7].

In order to exemplify this topic, we describe a quasi-static electromechanical 1D cycle of a piezoelectric material. It allows defining a simple coupling that is useful to compare piezoelectric materials, though it does not take into account all configurations. The cycle applied is displayed in Figure 7.2. The material is applied stress from O to A in open-circuit condition. From A to B, short-circuit conditions are applied at constant stress, resulting in both softening of the material and collection of charges. This step is the one where energy is converted from mechanical into electrical. The last leg (B to O) stands for the stress release in short-circuit conditions to go back to the initial point O.

We define the coupling factor  $k^2$  as the harvested energy  $W_{\text{rec}}$  during leg AB over the maximum applied mechanical energy, namely  $W_{OB}$ . Graphically speaking, the harvested energy is the area of the triangle in Figure 7.2. Therefore, one can write

$$W_{\text{rec}} = W_{OB} - W_{OA} \quad (7.8)$$

and

$$k^2 = \frac{W_{OB} - W_{OA}}{W_{OB}} = 1 - \frac{W_{OA}}{W_{OB}} \quad (7.9)$$

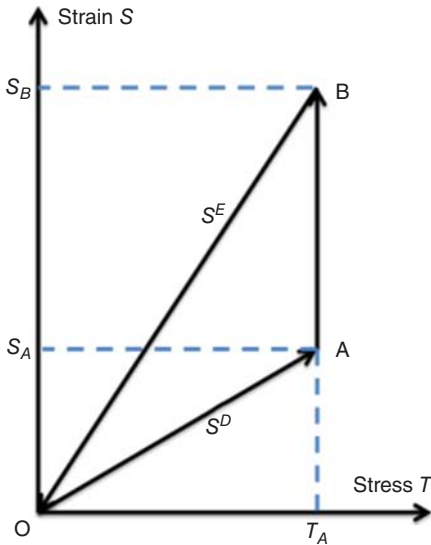


**Figure 7.2** Electromechanical cycle applied to a piezoelectric material. Energy is recovered through discharge at constant stress (leg from A to B).

The elastic works  $W_{OA}$  and  $W_{OB}$  are, respectively, obtained at constant  $D$  (open circuit) and constant  $E$  (short circuit). Consequently, one has

$$W_{OA} = \frac{1}{2}s^D T_O^2 \quad \text{and} \quad W_{OB} = \frac{1}{2}s^E T_O^2 \quad (7.10)$$

$s^D$  and  $s^E$  are, respectively, the material compliances at constant  $D$  and constant  $E$ . Note that  $s^D < s^E$ . Consequently,  $k^2$  reads

$$k^2 = 1 - \frac{s^D}{s^E} \quad (7.11)$$

Equation 7.11 shows that  $k^2$  is hidden into material compliances at constant  $E$  and  $D$ . Therefore, a simple look at those two values gives  $k^2$ . Note that as  $s^D$  is always  $< s^E$ ,  $k^2$  is always  $< 1$ . It makes sense as the transferred energy cannot be larger than the maximum energy given into the system.

One could think it is strange to obtain a coupling factor depending only on compliances, but there are actually several equivalent forms of  $k^2$ . To have a more familiar one, let us transform  $s^D$  in  $s^E$  by using Eqs. (7.4) and (7.6). Eventually, it yields

$$k^2 = \frac{d^2}{s^E \epsilon^T} \quad (7.12)$$

This form gathers a piezoelectric coefficient squared ( $d$ ), a mechanical parameter (compliance  $s^E$ ), and a dielectric parameter (dielectric constant  $\epsilon^T$ ). All electromechanical couplings exhibit such a form, though the very parameters to be used depend on the formalism chosen among the four possibilities and also on the boundary conditions.

#### 7.4.1

##### Special Considerations for Energy Harvesting

The electrode configuration collecting the created charges can play an important role as it changes the coupling factor. Indeed, in-plane electrodes on a piezoelectric sheet or film mechanically elongate work in the so-called  $d_{33}$  mode. On the contrary, the same sheet with top and bottom electrodes works in  $d_{31}$  regime. Therefore,  $k^2$  can be very different, as suggested by Eq. (7.12) as  $d_{31}$  is basically half  $d_{33}$  in most piezoelectric materials. Stiffness also varies with crystallographic directions.

Improving  $k^2$  is not always beneficial for vibrating resonant systems. Indeed, for such systems, at a given amount of acceleration, the optimal  $k^2$  is the one that allows matching the mechanical losses of a vibrating system [8]. It means that increasing  $k^2$  beyond the optimal point would induce a decrease in the quality factor of the resonance, and, therefore, of the vibration amplitude and, in turn, of the harvested energy. Matching  $k^2$  is therefore a key in optimization of vibrating energy harvesters.

The relative dielectric constant  $\epsilon_r$  of piezoelectrics varies a lot from one material to another one, spanning from 10 for AlN to more than 1000 for Pb(Zr,Ti)O<sub>3</sub>



(PZT). It ends up in strong impedance variations when it comes to devices. For a given system, let us suppose that AlN harvests 10 times less energy than PZT as  $k_{\text{PZT}}^2$  is typically 10 times larger than  $k_{\text{AlN}}^2$ . However, as  $\epsilon_{\text{PZT}} \sim 100 \times \epsilon_{\text{AlN}}$ , the output voltage of PZT is 10 times smaller than AlN. Therefore, matching the device impedance depends strongly on the material utilized.

In the case of harvesters using piezoelectric thin films, the mechanical holder is mostly made of silicon. In such a case, one can use a slightly different electromechanical coupling to compare materials as the overall device stiffness is mainly influenced by the holder. Therefore, a figure of merit different from  $k^2$  is used. The idea is to remove the mechanical parameter from  $k^2$ . Normally, this figure of merit (FoM) is defined with  $(S, E)$  formalism by considering a clamped piezoelectric layer on the substrate, which yields [9]

$$\text{FoM} = \frac{e_{31,\text{eff}}^2}{\epsilon^S} \quad (7.13)$$

Note that this FoM applies to materials and not devices.

## 7.5

### Perovskite Materials

Perovskites exhibit the  $\text{ABO}_3$  structure and notably gather barium titanate  $\text{BaTiO}_3$  (BTO) and PZT  $\text{Pb}(\text{Zr}, \text{Ti})\text{O}_3$ . They are the best piezoelectric materials so far, but all of them are ferroelectric, which means that on the one hand they need a poling process to exhibit piezoelectricity and on the other hand there is a temperature called Curie temperature ( $T_C$ ) beyond which piezoelectricity disappears.

#### 7.5.1

##### Structure

Perovskite is the best-known and studied ferroelectric structure. Its name comes from the name of the natural perovskite  $\text{CaTiO}_3$ . Its simplest form is cubic – point group  $m3m$  – as depicted in Figure 7.3. This cubic phase appears above its Curie temperature  $T_C$ . It is, therefore, not ferroelectric above  $T_C$ . The chemical formula of perovskites is  $\text{ABO}_3$ . Figure 7.3 is a representation of the cubic perovskite lattice of lead titanate  $\text{PbTiO}_3$  originating from site A (Pb). A is a bivalent large ionic radius cation with 12 nearest neighbors. B is a cation with smaller radius (Zr or Ti in PZT), is tetravalent, and has six nearest neighbors. In cubic phase, A atoms are at the corners, B at the center, and oxygen occupies the center of the six faces. Consequently, B is at the center of the oxygen octahedron.

##### 7.5.1.1 Ferroelectricity in Perovskites

In ferroelectric materials, polarization can vary depending on the applied external electric field. It can even be reversed if the field is higher than the threshold called the coercive field. Consequently, the macroscopic polarization

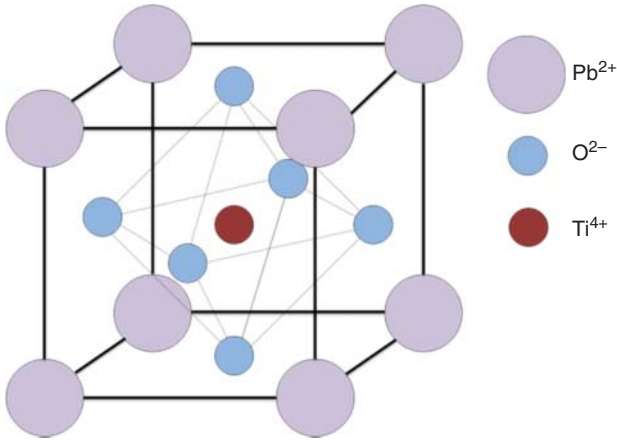


Figure 7.3 Cubic perovskite structure of  $\text{PbTiO}_3$ .

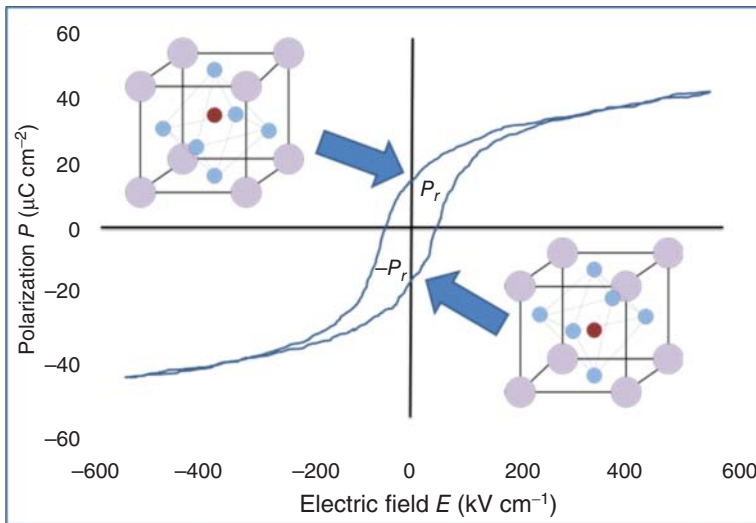


Figure 7.4 Typical polarization versus electric field of a perovskite ferroelectric material. The values correspond to  $0.5\text{ }\mu\text{m}$ -thick PZT.  $P_r$  stands for remnant polarization. It is the remaining polarization once the electric

field is off. This polarization can be positive or negative. The two lattice schemes sketch the positions of the ions in the lattice for  $P_r$  and  $-P_r$ .

of a ferroelectric material versus electric field represents a hysteresis loop as depicted in Figure 7.4.

A ferroelectric material is divided into domains. In each of them, all dipoles are oriented in the same direction. The volume of these domains varies versus the electric field. In the case of PZT, the shape and size of the domains depend on the growth conditions and external mechanical and electrical constraints. When an

electric field is applied, the dipoles tend to follow the electric field. The stronger the field is, the larger the amount of dipoles lining up, which increases their contribution to the macroscopic polarization. The dipole orientation versus the field is sketched in Figure 7.4, through the hysteresis loop exhibited by the macroscopic polarization versus field. The perovskite lattice is represented in Figure 7.4 for the two possible stable states when the electric field is zero. The polarization at zero field is called remnant polarization  $P_r$ . For these two states, the center of positive charges ( $\text{Ti}^{4+}$  or  $\text{Zr}^{4+}$ ) in the cubic lattice is shifted with respect to that of negative charges (oxygen octahedron).

### 7.5.1.2 Piezoelectricity in Perovskites: Poling Required

A preliminary stage of polarization, so-called poling, performed by applying an external electric field larger than the coercive field is mandatory for aligning all the ferroelectric domains in the same direction or at least in a way sufficient to induce a nonzero macroscopic polarization. This is true whether the materials are single crystals, poly crystals, polymers, or ceramics.

## 7.5.2

### PZT Phase Diagram

As an example, we present here PZT phase diagram. PZT has been the most studied piezoelectric material for energy harvesting so far.

The chemical formula of PZT is  $\text{Pb}(\text{Zr}_x\text{Ti}_{1-x})\text{O}_3$ . “ $x$ ” stands for  $[\text{Zr}]/([\text{Zr}] + [\text{Ti}]$ . Basically, the perovskite lattice of PZT can exhibit three main structures depending on temperature and  $x$ :

- Cubic (point group  $m\bar{3}m$ ) when the temperature is above  $T_c$ , which corresponds to the paraelectric phase that does not exhibit a permanent dipole moment;
- Tetragonal (point group  $4mm$ ), when the temperature is below  $T_c$  and  $x < 0.45$  (titanium rich). This phase shows a permanent dipole moment throughout the cubic lattice strain;
- Rhombohedral (point group  $3m$ ) when the temperature is below  $T_c$  and  $x > 0.5$  (zirconium rich). This phase also shows a permanent dipole moment.

The region where  $x$  is included between approximately 0.45 and 0.5 is called morphotropic phase boundary or MPB. It has long been believed that this area is a mixture of tetragonal (T) and rhombohedral (R) phases. However, in 1999, Noheda *et al.* showed the presence of a monoclinic phase in the morphotropic region of the phase diagram [10]. It is coexistence of these three phases that best explains the enhanced ferroelectric and piezoelectric properties of PZT in this zone. Indeed, all these phases facilitate the polarization mobility, which in turn improves the material properties [11]. Figure 7.5 represents PZT’s simplified phase diagram with the MPB area.

In Figure 7.5, the orthotropic Zr-rich phase is antiferroelectric. This property means that locally each perovskite lattice presents a dipole moment, but their directions are systematically opposed between neighbors. This induces a zero

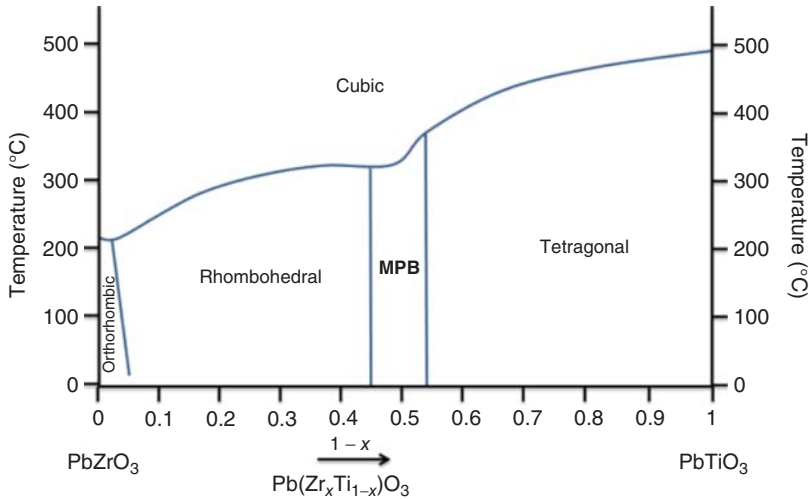


**Figure 7.5** Phase diagram of  $\text{Pb}(\text{Zr}_x\text{Ti}_{1-x})\text{O}_3$  according to  $1-x$  ( $x = \text{Zr}/(\text{Zr} + \text{Ti})$ ) and temperature. In cubic phase, PZT is paraelectric. In rhombohedral, tetragonal, and MPB, PZT is ferroelectric. In Zr-rich orthotropic phase, PZT is antiferroelectric.

macroscopic polarization. There is a permanent dipole moment in each ferroelectric phase. This permanent dipole is a consequence of the phase transition taking place at  $T_C$ , which can be seen as strain imposed to the prototypical cubic lattice. It results in a decrease in the symmetry of the structure. For the tetragonal phase, one side of the cube is stretched out to give the  $c$  [001] axis, whereas the other two sides are compressed to give the  $a$ -axis [100] and [010]. The point group is therefore 4 mm. For the rhombohedral phase, the cube is stretched out along the diagonal that entirely crosses the lattice, for example, in direction [111]. The point group is therefore 3 m. A diagram of how these phases are obtained is given in Figure 7.6. Depending on the phases of the perovskite lattice, the direction of polarization is not the same. Therefore, in the tetragonal phase, the polar axis follows direction [100] of the original cubic lattice, that is, following the tetragonal  $c$ -axis. In the rhombohedral phase, the polar axis follows direction [111] of the original cubic lattice.

### 7.5.3

#### Ceramics

##### 7.5.3.1 Fabrication Process

Ceramics are obtained by powder synthesis. If we use PZT as an example,  $\text{PbO}$ ,  $\text{ZrO}_2$ , and  $\text{TiO}_2$  powders are mixed together and milled in order to obtain a homogeneous powder with grains in the micron range. A solvent can be added during the mixing process. Then the mix is annealed at basically 1000–1100 °C for 10 h with a heating rate around  $1^\circ\text{C min}^{-1}$  in air in order to get rid of solvents and form the perovskite phase. The pellet is grounded again as most of the time the

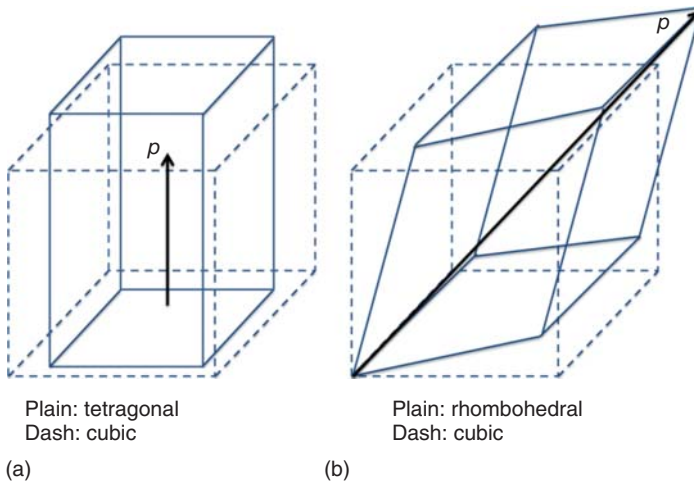


**Figure 7.6** Lattice deformation of the original high-temperature, high-symmetry cubic structure (dashed lines) of PZT resulting in (a) low-temperature, low-symmetry

tetragonal and (b) rhombohedral structures in PZT. The low-temperature phase depends on Zr/(Zr + Ti) ratio. "p" stands for dipole moment along the polar axis.

first annealing process induces porosity into the ceramic. Another annealing process is then performed. Other grinding steps are possible, which in turn improve the density of the final pellet. The final annealing process is performed at a higher temperature (1300–1400 °C) to sinter the ceramic. Ninety five percent of the theoretical density can be achieved. Note that PZT and all lead-based materials need a compensation of lead losses through PbO losses during annealing. It is typically obtained by adding PbO-excess in the mix and by annealing in closed crucibles. Electrodes are typically obtained by screen-printing silver or nickel-based paste subsequently annealed at 600 °C.

As stated in Section 7.4.1, a poling step is mandatory to orientate all dipole moments in the same direction. This is performed by applying an electric field in the  $1\text{--}5\text{ kV mm}^{-1}$  range at 100–150 °C for a couple of minutes. It is normally performed in silicone oil to avoid arching in air.

Perovskite ceramics and PZT in particular are commercially available in all shapes: rods, plates, pellets, wires. The shapes are obtained either by pressing before the first annealing or by machining after sintering. PZTs are often sorted in two categories, namely soft and hard PZTs. Soft PZTs exhibit larger piezoelectric coefficients and dielectric constants and smaller mechanical stiffness. Their softer nature is due to higher mobility of their domain walls, which play a foremost role in all PZTs properties. Doping is the way to change the behavior of domain walls. On the other hand, hard PZTs exhibit weaker piezoelectric properties but are more stable and particularly well suited to power applications. Their mechanical and electrical losses are less compared with soft PZTs.

An alternative to this powder synthesis is tape casting. The technique is mainly used for multilayer ceramic capacitors (MLCCs), one of the most current capacitors in all electronic devices. MLCCs are stacks of dielectrics and electrodes that can reach 200 layers in total. Dielectrics in use are doped-perovskites based on BTO or PZT. Tape casting starts similarly to powder synthesis. The raw oxide powder is mixed by milling. An organic binder is then added to be able to extract foils from the mix. The electrodes are screen printed on cut foils. For MLCCs, several electrode foils are stacked, laminated, and cut. For harvesters, one or two sheets of PZTs are laminated on a holder made of steel or brass. The stack is then annealed first to get rid of the binder and then sintered at temperatures between 1200 and 1400 °C. A final step of electrode deposition can be performed [12]. A closely related technique is screen printing. PZT powder is dispersed in an organic solvent and is subsequently deposited on a substrate through a stencil [13].

### 7.5.3.2 Typical Examples for Energy Harvesting

The most famous example of vibrating energy harvesters is a bimorph cantilever in the centimeter range with two sheets of PZT sandwiching a steel center shim performed by Roundy and Wright [14]. A 1 cm<sup>3</sup>-generator with PZT 5H harvests 190 μW from acceleration of 2.5 m s<sup>-2</sup> at 120 Hz. They also proved that an autonomous radio transmission is possible. Typical characteristics of PZT 5H, defined as soft PZT, are  $\epsilon_r = 3800$ ,  $d_{33} = 650 \text{ pm V}^{-1}$ ,  $d_{31} = -320 \text{ pm V}^{-1}$ ,  $k_{33} = 0.75$ ,  $k_{31} = 0.44$ , density = 7800 kg m<sup>-3</sup>,  $1/s_{33}^E = 50 \text{ GPa}$ ,  $1/s_{11}^E = 62 \text{ GPa}$  [15], and a maximal strain around 0.1%. “s” stands for compliance.

Another interesting concept taking advantage of PZT ceramics high coupling is composite. The idea is to combine PZT fibers encased into Kevlar or/and Kapton. This allows decreasing the overall stiffness of the harvesting device but keeping a high coupling. It has been used, for instance, to harvest energy from a moving magnet by combining a magnetostrictive material, namely Terfenol-D, with a PZT composite. The moving magnet induces strain in Terfenol that in turn generates deformation in the piezoelectric composite and eventually electrical charges [16]. Typical values for PZT composites are strain reaching 0.2%,  $d_{33} = 400 \text{ pm V}^{-1}$ ,  $d_{31} = -170 \text{ pm V}^{-1}$ , density = 5440 kg m<sup>-3</sup>, Young’s modulus in PZT rod direction = 30 GPa, and Young’s modulus perpendicular to PZT rod direction = 15 GPa [17].

Besides, PZT ceramics can be also associated with silicon technology, as shown by Aktakka *et al.* in 2011 [18]. In this work, they took advantage of the excellent piezoelectric properties of PZT ceramics bonded to Si substrate by AuIn liquid phase bonding. PZT is subsequently thinned up to 20 μm. The authors reported that their packaged cantilever harvests 205 μW at 1.5 g and 154 Hz for an active volume of 7 mm<sup>3</sup> × 7 mm<sup>3</sup> × 0.55 mm<sup>3</sup>. Janphuang *et al.* in 2012 proposed a similar approach with 130 μm-thick PZT glued on silicon-on-insulator (SOI) structures, yielding similar results [19].

## 7.5.4

**Bulk Single Crystals**7.5.4.1 **Perovskites**

Although single-crystal PZTs are very difficult to grow, some perovskites can be grown as single crystals. The best examples are  $\text{Pb}(\text{Mg},\text{Nb})\text{O}_3\text{-PbTiO}_3$  (PMN-PT) and  $\text{Pb}(\text{Zn},\text{Nb})\text{O}_3\text{-PbTiO}_3$  (PZN-PT). The technique used to grow such crystals is called *high-temperature flux technique*. It is slightly similar to powder synthesis, though an alumina sealing is used during annealing. For instance, for PMN-PT, the initial powders are  $\text{Pb}_3\text{O}_4$ ,  $\text{MgCO}_3$ ,  $\text{Nb}_2\text{O}_5$ , and  $\text{TiO}_2$ . Excess- $\text{Pb}_3\text{O}_4$  is necessary to compensate lead losses. Here,  $\text{Pb}_3\text{O}_4$  is considered flux. After mixing the powders, they are loaded into a platinum crucible. This latter is sealed into an alumina crucible during annealing performed at  $1200^\circ\text{C}$ . Crystals are extracted from the final product by using  $\text{HNO}_3$  acid [20].

The typical values obtained for  $\text{Pb}(\text{Zn}_{1/3}\text{Nb}_{2/3})\text{O}_3\text{-8\% PbTiO}_3$  are  $\epsilon_r = 5000$ ,  $d_{33} = 2500 \text{ pm V}^{-1}$ ,  $k_{33} = 0.94$ ,  $1/s_{33}^E = 7.7 \text{ GPa}$ , and maximum strain = 1.7%, 1 order of magnitude higher than ceramic PZT [20]. Park *et al.* observed a strong influence of crystalline orientation as [001] direction gives  $d_{33}$  30 times larger than [111] direction does. Note that these extremely high values are also linked to the presence of an MPB between rhombohedral and tetragonal phases, though the best values are obtained close to the MPB but clearly in the rhombohedral phase.

PMN-32% PT is now currently commercially available [21] with values very similar to PZN-PT (cf. Figure 7.8).

7.5.4.2 **Energy Harvesting with Perovskites Bulk Single Crystals**

Badel *et al.* showed in 2006 that bulk single crystals of PMN-PT exhibit a much stronger potential than ceramics exhibit for energy harvesting [22]. Their experiment is based on a steel cantilever ( $40 \times 7 \times 1.5 \text{ mm}^3$ ) on which a piezoelectric element ( $10 \times 7 \times 1 \text{ mm}^3$ ) is sealed, which can be ceramic or single-crystal 0.75PMN-0.25PT. Cantilevers exhibit basically the same resonance frequency. The harvested power for equivalent excitation is 1900 and  $95 \mu\text{W}$  for single crystals and ceramic cantilevers, respectively, which means a 20-fold net improvement in using single crystals.

The unique coupling of single crystals can be utilized to tune frequencies of harvesters, as shown by Ahmed Seddik *et al.* [4] in 2012. The idea is to take advantage of the strong coupling of PZN-PT in mode 33 –  $k_{33} = 0.95$  – to harvest but also tune the resonance frequency owing to the large variation of PZN-PT stiffness according to the electrical boundary conditions applied. Indeed, as  $c_{33}^D = c_{33}^E(1 + k_{33}^2)$ ,  $c_{33}^D/c_{33}^E$  can reach 1.9. The frequency of a 3 cm-long cantilever made of steel and PZN-PT can be tuned between 208 and 294 Hz, which is more than 40%. Besides, the harvester collects  $320 \mu\text{W}$  at 250 Hz and  $1 \text{ m s}^{-2}$ -acceleration.

## 7.5.5

**Polycrystalline Perovskites Thin Films****7.5.5.1 Fabrication Processes**

Here, this is again nearly all about PZT films as their piezoelectric properties in thin films overtake other perovskites properties. The two main methods to produce poly-PZT thin films are sol-gel and sputtering. In the 1990s, both methods were equally appreciated [23]. But in the 2000s, sol-gel became the prominent method owing to the following advantages: the better properties of thin films obtained, a simpler process, and the commercial availability of good quality precursors [24, 25]. Figure 7.7 shows the four processing steps utilized for sol-gel. Deposition is performed by spinning the sol-gel. Note that the precursors are made of organic species containing the mineral of interest, namely Ti, Zr, and Pb for PZT. There is normally one precursor per element. Viscosity lies in a couple of centipoises. After spinning, a soft baking takes place at around 100 °C to get rid of the solvents in the solution. Some studies skip this step. Afterward, another hot plate step evacuates all carbon-based molecules at 350 °C. The three steps are performed three or four times before crystallization in rapid thermal annealing (RTA) furnace at 700 °C for 30 s in air. In the end, each monolayer deposited is around 50–80 nm thick. Therefore, thicknesses in the micrometer range need 13–20 monolayers. Therefore, several whole sequences should be performed to reach such thicknesses. The typical maximum thickness for dense PZT is around 5 μm, though some studies published films as thick as 40 μm [26].

**7.5.5.2 Energy Harvesting with Poly-PZT Films**

PZT thin-film harvesters can be used in  $d_{31}$  or  $d_{33}$  configuration. In  $d_{31}$  configuration, a bottom electrode is required. It is typically made of platinum, one of

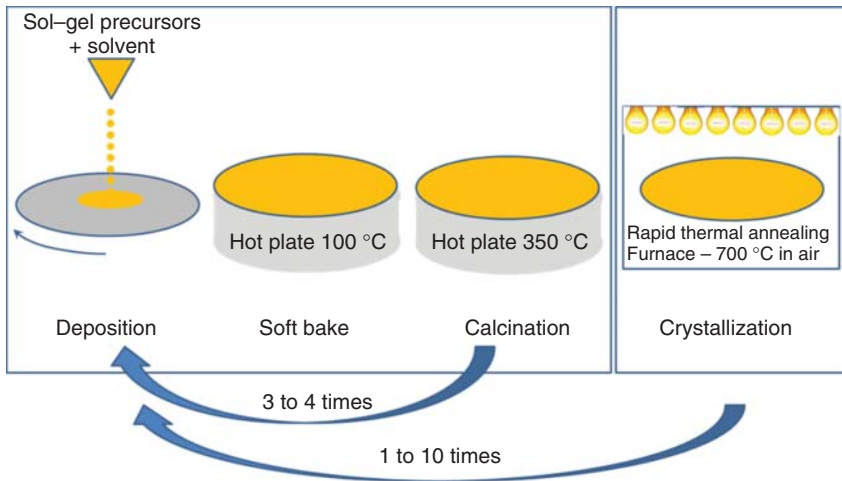


**Figure 7.7** Typical sol-gel process to perform PZT polycrystalline thin films.



the very rare metals that can withstand 700 °C annealing in air without oxidation. Shen *et al.* published in 2008 a PZT film harvester on silicon in  $d_{31}$  configuration [27]. Silicon was used as a proof mass to decrease the resonant frequency. A 5 mm-long device harvests 2.15  $\mu\text{W}$  from 2 g acceleration at 460 Hz. In  $d_{33}$  configuration, electrodes are atop the PZT layer and exhibit the so-called interdigitated configuration, in order to induce an in-plane electric field into PZT. No bottom electrode should be present. As PZT cannot be deposited directly on Si or  $\text{SiO}_2$ , a buffer layer of  $\text{ZrO}_2$  is one of the best options [28].  $d_{33}$  configuration helps in increasing the collected voltage compared with  $d_{31}$ . Indeed, the parallel capacitance decreases in  $d_{33}$ -mode, which in turn increases the voltage for a given harvested energy. It can be beneficial in case a diode bridge is used as the 0.7 V-threshold voltage can be an issue for PZT films in  $d_{31}$ -mode. The most cited paper concerning PZT thin film harvester in  $d_{33}$  configuration was published in 2005 by Jeon *et al.* [29]. A  $170\ \mu\text{m} \times 260\ \mu\text{m}$  beam generates 1  $\mu\text{W}$  at 13.9 kHz. Note that such a frequency is too high for the surrounding vibrating energy that lies in the range 10–500 Hz. But the material characterization remains valuable, though a much larger device would be required to harvest the application-needed 10  $\mu\text{W}$  range from the available 100 Hz vibration range.

#### 7.5.6

##### Single-Crystal Thin Films

As single crystals are believed to have a larger coupling than ceramics, it could be beneficial to grow single crystal (SC) thin films as well.

##### 7.5.6.1 Fabrication Process

Perovskites epitaxy has been known for a long time on special substrates as  $\text{SrTiO}_3$ . However, for energy harvesting, silicon substrate is generally desired to potentially address the mass market. The right way to grow epitaxially SC PZT films is to use a special buffer layer of 10 nm thick made of  $\text{SrTiO}_3$  (STO) between Si and PZT. STO must be SC, which is obtained by molecular beam epitaxy (MBE) [30]. PZT can be subsequently deposited by sputtering, sol-gel, or pulsed laser deposition. A bottom electrode can be deposited before PZT.

##### 7.5.6.2 Energy Harvesting with SC Perovskite Films

Many studies have been interested in SC PZT. In 2011, Isarakorn *et al.* showed that the previously described technique can be used to perform harvesters from silicon technology [31]. Their 1 mm-long harvester collected 13  $\mu\text{W}$  at 1 g acceleration and 2.3 kHz. Using SC PZT films, a very interesting approach had been proposed by Morimoto *et al.* in 2010 [32]. They grew SC PZT on STO substrates. Then, they transferred PZT on a steel substrate by sticking STO/PZT on steel and then etched away STO. Their final device was working at 126 Hz, which is very much desired, and collected 5.3  $\mu\text{W}$  at 0.5 g acceleration. They also reported that this device could withstand 5 g acceleration and was then able to provide 244  $\mu\text{W}$ . In 2011, Baek *et al.* showed that SC PMN-PT films grown by off-axis sputtering on the MBE

STO/Si substrate exhibit the highest ever-reported  $e_{31,\text{eff}}$  ( $-27 \text{ C m}^{-2}$ ) together with the highest FoM  $e_{31,\text{eff}}/\epsilon$  (cf. Eq. (7.13)), namely  $49 \text{ GPa}$ , which is of interest for thin film-based harvesters [9].

### 7.5.7

#### Lead-Free

Lead-free generally means perovskite without lead, though materials such as AlN or ZnO could practically belong to this lead-free family. This topic develops because of the growing concern about lead-based materials. As there is no lead-free material able to compete with PZT, Europe and Japan, the most precautionous communities in the world, still allow industry to sell lead-based piezoelectrics. But this should be discussed again in 2018 in Europe. This is why lead-free stands for a hot topic for the field of piezoelectrics. Historically speaking, the three most interesting lead-free families are alkali niobate ceramics, sodium bismuth titanate-based ceramics, and barium titanate ceramics [33]. In 2009, Liu and Ren [34] showed that one of the most serious PZT's competitors is  $\text{Ba}(\text{Ti}_{0.8}\text{Zr}_{0.2})\text{O}_3 - (\text{Ba}_{0.7}\text{Ca}_{0.3})\text{TiO}_3$  (BCTZ) as depicted in

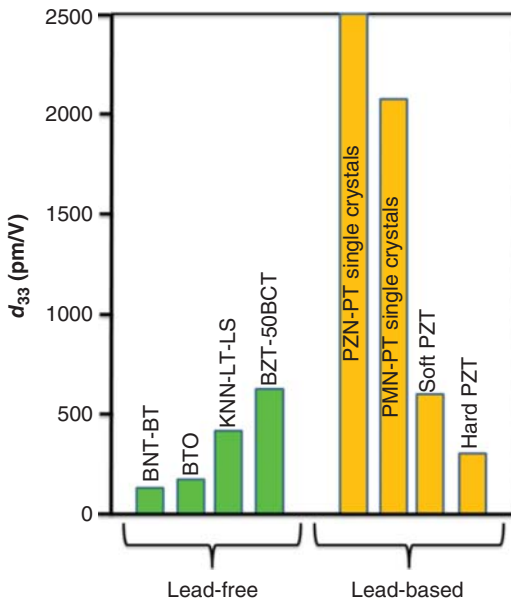


**Figure 7.8**  $d_{33}$  coefficient measured on lead-free and lead-based families (cf. Ref. [34] for lead-free). Here, BCTZ is the only one able to compete with PZT, reaching  $d_{33}$  as high as  $600 \text{ pC N}^{-1}$ . KNN-LT-LS ( $\text{K,Na,Li}(\text{Nb,Ta,Sb})\text{O}_3$ ) is also interesting with  $d_{33} = 416 \text{ pm V}^{-1}$  [37]. Lead-based

PMN-PT and PZN-PT single crystals exhibit much higher  $d_{33}$ , as large as  $2500 \text{ pC N}^{-1}$  [20]. BNT-BT ( $\text{Bi}_{0.5}\text{Na}_{0.5}\text{TiO}_3 - \text{BaTiO}_3$ ), BT ( $\text{BaTiO}_3$ -based ceramics), and ceramics are the other competitors, with much lower  $d_{33}$ .

Figure 7.8. In this figure are shown  $d_{33}$  for lead-free and lead-based piezoelectric materials. While bismuth titanates and alkali niobates lie in the range of 200–300 pC N<sup>-1</sup>, BCTZ and PZT reach values as high as 600 pC N<sup>-1</sup>. However, lead-based PMN-PT and PZN-PT can exhibit a much higher value of  $d_{33}$ , as large as 2500 pC N<sup>-1</sup> [20]. BCTZ thin films have not reached such high values, though Piorra *et al.* showed that BCTZ films of 600 nm thick prepared using pulsed laser deposition exhibit  $d_{33} = 80 \text{ pC N}^{-1}$  [35]. It is also interesting to observe that optimization of lead-free materials stems from seeking morphotropic phase boundaries, as it is performed in lead-based materials [36].

#### 7.5.7.1 Energy Harvesting with Lead-Free Materials

The best example of lead-free-based energy harvesters has been performed with (K,Na)NbO<sub>3</sub> (KNN) thin films deposited by radio frequency (RF) sputtering [38] on SOI wafers. Le Van *et al.* showed that KNN can be compatible with Si technology and exhibit interesting characteristics. Their harvester produced 8 μW at 6 m s<sup>-2</sup> for a typical surface of 5 × 5 mm<sup>2</sup>, taking advantage of an original quatrefoil-shaped silicon proof mass.

## 7.6

### Wurtzites

#### 7.6.1

##### Structure

AlN and zinc oxide (ZnO) are the main piezoelectric materials of wurtzite family. They exhibit a permanent polarization, which means they are pyroelectric materials, and therefore piezoelectric. They exhibit piezoelectric coefficients basically 10 times smaller than perovskites but can potentially work at much higher temperatures as no depolarization occurs.

AlN and ZnO were studied in thin films in the 1980s then put to one side during the advent of perovskites. Interest in wurtzites was renewed at the beginning of the 2000s, however. This was first because of bulk acoustic wave (BAW) acoustic filters that almost exclusively use AlN as piezoelectric material, mainly for its very high acoustic quality factor (low acoustic losses). Second, interest increased because of the propensity of ZnO to grow in the form of NWs under certain conditions. This structure has a hexagonal lattice and is part of the 6 mm point group. It can be seen as a juxtaposition of two compact hexagonal structures for the two sorts of ions composing the structure (see Figure 7.9 for AlN). The two structures are shifted following the *c* axis by a distance of 3/8*c*. This explains the spontaneous polarization for this structure, even in the absence of the electric field. Lattice parameters, by choosing a hexagonal lattice, for AlN are  $a = 3.112 \text{ \AA}$  and  $c = 4.982 \text{ \AA}$ .

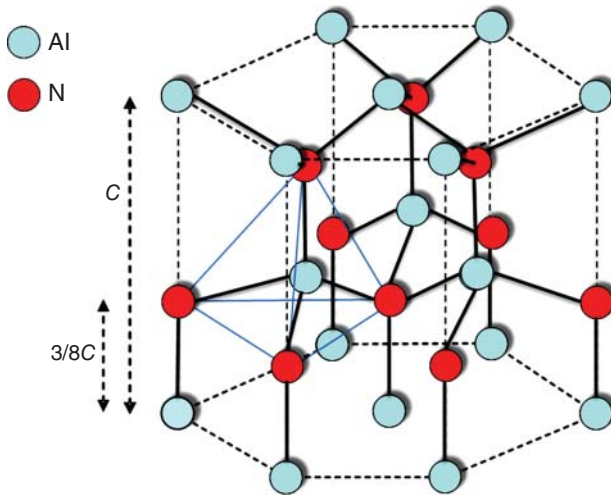


Figure 7.9 Atomic positions of AlN in the wurtzite phase, belonging to 6 mm point group.

### 7.6.2

#### Thin Films and Energy Harvesting

AlN is nowadays mainly deposited by dc-pulsed sputtering. The plasma gas is made of argon and nitrogen in order to perform reactive sputtering. The target is made of pure aluminum. During sputtering, the upper part of the target becomes insulating, because of incorporated positive nitrogen ions. This is why a positive discharge is made regularly on the target to get rid of the nitride upper layer. Although many techniques have been used in the past, the BAW industrial success allows identifying this technique as the most reliable and the one exhibiting the highest throughput. The deposition is typically performed between 350 and 400 °C. The maximum thickness is typically in the 5  $\mu\text{m}$  range.

Regarding energy harvesting, AlN has been extensively used as it allows a decent harvested energy at higher impedance than PZT does. As already mentioned in Section 7.3, it means output voltage is higher, which can be very practical when the harvested signal goes through a simple diode bridge. Also, its simpler process at lower temperatures is obviously of interest for device making.

In 2010, Elfrink *et al.* published the first autonomous wireless sensor node powered by a vacuum-packaged piezoelectric micro-electro-mechanical-system (MEMS) energy harvester, which was based on AlN thin films [39]. This device harvested 100  $\mu\text{W}$  at 572 Hz and 10  $\text{m s}^{-2}$  acceleration. In 2011, Ricart *et al.* showed that a simple AlN layer on the top of Si cantilever was able to harvest 100  $\mu\text{W}$  at 100 Hz and 2  $\text{m s}^{-2}$  [40]. These two examples are among the best results ever published on piezoelectric thin films in the case of vibrating harvesters.

ZnO is not as common as AlN in microsystems, though its coupling coefficient is similar. Since the 2000s, AlN has largely benefited from the huge development of acoustic resonators for RF filters. Indeed, AlN proves to be easier to process

than ZnO. Its stability versus time is also larger. ZnO can exhibit higher current leakage than AlN. Note that ZnO is mainly studied as NWs, which is detailed later in this chapter.

### 7.6.3

#### Doping

A recent discovery could push AlN films even further. Indeed, Akiyama *et al.* observed in 2009 that heavily Sc-doped AlN exhibits an enhancement of its piezoelectric properties. While  $d_{33}$  AlN is around  $5 \text{ pm V}^{-1}$ ,  $d_{33} \text{ Sc}_{0.43}\text{Al}_{0.57} \text{ N}$  reaches  $24.6 \text{ pm V}^{-1}$  [41]. This effect is related to a strong material softening [42]. However, the material stiffness is not taken into account in the thin films' figure of merit  $e_{31,\text{eff}}^2/\epsilon$ . Therefore, as  $\epsilon_{\text{ScAlN}}$  is only slightly larger than  $\epsilon_{\text{AlN}}$ , a significant improvement is foreseen in  $e_{31,\text{eff}}^2/\epsilon$  because of this material in the special case of energy harvesting (cf. Section 7.9) [43].

## 7.7

### PVDFs

PVDF is a polymer. Although piezoelectricity in PVDF was discovered in 1969, this material experiences a revival as several applications require softer materials than stiff solids as perovskites or wurtzites. PVDF is ferroelectric but its piezoelectric properties are very interesting – higher than wurtzites – and it can be potentially synthesized with low-cost processes.

#### 7.7.1

##### Structure

PVDF is a polymer made of  $\text{CH}_2\text{CF}_2$  units that are repeated to form a chain (cf. Figure 7.10a). Each unit bears a dipole moment  $\delta$  equal to  $7 \cdot 10^{-30} \text{ cm}$ , as a consequence of positive hydrogen and negative fluorine atoms. PVDF is semicrystalline, which means crystalline regions surrounded by an amorphous matrix. It can exhibit different phases, called polymorphs, and labeled  $\alpha$ ,  $\beta$ ,  $\gamma$ , and  $\delta$  for the best-known structures. All phases except  $\alpha$  exhibit macroscopic polarization and, therefore, piezoelectric properties, as observed first by Kawai in 1969 [44]. The strongest piezoelectric phase is  $\beta$  where all  $\text{CH}_2\text{CF}_2$  units are linked in the so-called all-trans or TT conformation (cf. Figure 7.10b) and all chains are packed in parallel. In this phase, all dipole moments are pointing upward, summing up to induce the highest possible polarization, which reaches typically  $6\text{--}10 \mu\text{C}/\text{cm}^2$ . In  $\alpha$  phase, monomers follow the so-called  $TGT\bar{G}$  conformation that results in zero macroscopic polarization, though there is a small dipole moment with parallel and perpendicular contributions. However, the antiparallel-like dipole moments (cf. Figure 7.10c) together with the overall

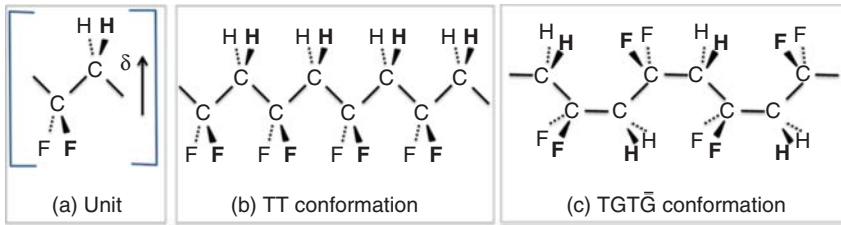


**Figure 7.10** (a) Monomer unit of  $\text{CF}_2\text{CH}_2$  in PVDF. The different electronegativity of F and H atoms induces a permanent dipole moment  $\delta$ . (b) All-trans or TT conformation of 4 units, as observed in  $\beta$  phase, exhibiting the highest possible polarization in PVDF. (c) TGTG conformation as observed in nonpolar  $\alpha$  phase.

contribution of the successive chains cancel out the net polarization in  $\alpha$  phase.

Pure PVDF needs to be mechanically stretched and electrically poled for the chains to be aligned and obtain  $\beta$  phase instead of the more stable but not piezoelectric  $\alpha$  phase. In spite of this mandatory stretching step, the amount of crystalline regions is limited to typically 50% of the whole volume, which in turn limits the piezoelectric properties as only crystalline parts are piezoelectric.

The preferred solution to increase the crystalline proportion into PVDF, and therefore piezoelectricity, is to add copolymers, as suggested by Lando and Doll in 1968 [45]. Indeed, adding copolymer stabilizes  $\beta$  phase. Among them, the most used is trifluoroethylene (TrFE) composed of  $\text{CF}_2\text{CFH}$ . The structure of the monomer is identical to that of PVDF, except one H atom is replaced with one F atom. Its intrinsic polarization is lower than that of pure PVDF, but its presence allows reaching more than 90% crystallites, increasing the overall piezoelectric properties of P(VDF-TrFE).

Another interesting feature of P(VDF-TrFE) is its propensity to experience phase transition between paraelectric and ferroelectric phases, controlled by temperature, copolymer amount, and also electric field (cf. for instance Figure 22 in Ref. [46]). This phase transition induces large strains. Indeed, Zhang *et al.* showed in 1998 that modified P(VDF-TrFE) exhibits a very large strain variation, namely 4%, when the electric field is applied. Zhang added defects in P(VDF-TrFE) by irradiation, which resulted in a well-controlled phase transition avoiding hysteresis effect [47]. However, one should note that such materials are electrostrictive and not piezoelectric. It means that it can be useful for actuation but not for sensing or energy harvesting.

Contrary to ceramics, PVDF, and P(VDF-TrFE) has negative  $d_{33}$  and positive  $d_{31}$  coefficients. Consequently, applying a voltage to a planar PVDF capacitor with full sheet electrodes induces a thickness reduction together with an area increase. Typical values for PVDF and P(VDF-TrFE) are  $d_{33} = -20 \text{ pC N}^{-1}$ ,  $d_{31} = -6 \text{ pC N}^{-1}$ ,  $\epsilon = 10$ , Young's modulus = 2 GPa (cf. Ref. [48]).

### 7.7.2

#### Synthesis

PVDF is obtained by polymerization of VDF monomer and exists in many forms, that is to say sheets, bulky pieces, reels of wires, or powder. The most versatile form is probably powder as it can be melted at 170–180 °C, pressed, and then cooled down at ambient temperature to obtain the desired layer. Typical thicknesses of self-standing sheets are between 10 and 100 μm [48]. PVDF can also be spun onto substrates. To do so, PVDF is typically dissolved in a solvent made of acetone and dimethylformamide (cf. for instance [49] for details). PVDF can also be screen printed.

### 7.7.3

#### Energy Harvesters with PVDF

There are actually few examples of harvesters using PVDF. However, one of the most well-known mechanical harvesters uses PVDF as the active piezoelectric material. It is called the “Parasitic Power Harvester in Shoes” and was published in 1998 by Kymissis *et al.* from MIT [50]. The authors showed that each step was yielding 1 mJ with PVDF and 2 mJ with PZT. In 2010, Chang *et al.* showed that near-field electrospinning of PVDF nanofibers was able to combine mechanical stretching and electrical poling at once [51]. This technique seemed to improve by an order of magnitude the piezoelectric properties of PVDF owing to the nanostructure of PVDF, which is the purpose of the next section. One of the most mature devices presented so far is the pedometer inserted in a shoe, fully supplied by PVDF rolls [52]. PVDF is used as harvester but also as sensor in order to count the steps. They developed a dedicated electronic able to work at 2 V. Finally, it is worth mentioning a recent extensive review on piezoelectric polymers as functional materials for electromechanical transducers [53].

## 7.8

### Nanomaterials

Nanogenerators made of nanomaterials are not intrinsically interesting for applications as the harvested energy lies in the nanowatt range. However, combining billions of them could be worth, especially when it turns out that some of them are easier to produce than ceramics or thin films. This is the case of ZnO NWs, which can be also aligned during the growing process [54]. There are two main techniques to produce aligned ZnO NWs, namely, physical vapor phase growth and hydrothermal approach. The first technique relies on the so-called vapor–liquid–solid process, with gold acting as catalyst. The growth takes place at temperature around 900 °C with very well-controlled oxygen partial pressure [55]. The second technique – hydrothermal – is based on chemical reaction at temperature as low as 70 °C. It utilizes a solution made of zinc nitrate salt together





Material	Type	$d_{33}$ (pm V <sup>-1</sup> )	$d_{31}$ (pm V <sup>-1</sup> )	$-e_{31,eff}$ (C m <sup>-2</sup> )	$k_{33}$	$k_{31}$	$\epsilon$	$1/\epsilon_{33}^E$ (GPa)	References
Ba(Ti <sub>0.8</sub> Zr <sub>0.2</sub> )O <sub>3</sub> - (Ba <sub>0.7</sub> Ca <sub>0.3</sub> )TiO <sub>3</sub> (BCTZ)	Ceramic	600	—	—	—	—	—	—	[34]
PZT	Poly-film	—	—	18.7	—	—	1620	80	[24]
PMNPT	Single crystal film	—	—	27	—	—	1600	—	[9]
AlN	Poly-film	5	-2.5	-1.0	0.07	—	10	300	[5]
ScAlN	Poly-film	25	-2.5	-1.0	0.07	—	10	300	[43]

## 7.10

### Summary

In this chapter, we first stressed the importance of thermodynamics to explain how piezoelectricity macroscopically works. We then listed the different materials that one can come across in the field of vibrating energy harvesting, namely, perovskites, wurtzites, and polymers, but also the different forms they can exhibit, that is to say ceramics, single crystals, thin films, or NWs. As a conclusion, it has to be pointed out that the right material for a given application is not always the most coupled. Indeed, it strongly depends on how much energy is available from the vibration source. Besides, most of the vibration sources are rather weak in terms of acceleration – typically  $1 \text{ m s}^{-2}$  – and proceed at frequencies in the 100 Hz range. Therefore, it means that whatever device envisioned for a given application has to be big enough to harvest enough energy to make a real and useful device. Nowadays as  $10\text{--}100 \mu\text{W}$  are considered the minimum energy to be harvested to be useful for an autonomous sensor, the direct consequence is that harvesters cannot be smaller than a couple of square centimeters. The future of these harvesters is therefore fully linked to cheap and large area technology, contrary to what has been thought initially with microsystems. The combination of polymers and highly efficient piezoelectrics is likely to be a key in this quest.

### References

1. Curie, P. and Curie, J. (1880) *Bull. Soc. Minéral. Fr.*, **3**, 90.
2. Lippmann, G. (1881) *Ann. Chim. Phys., Se Sér.*, **t. XXIV**, 145.
3. Kursumovic, A., Defay, E., Lee, O.J., Tsai, C.F., Bi, Z.X., Wang, H.Y., and MacManus-Driscoll, J.L. (2013) A new material for high-temperature lead-free actuators. *Adv. Funct. Mater.*, **23**, 5881–5886.
4. Seddik, B.A., Despesse, G., and Defay, E. (2012) Autonomous wide-band mechanical energy harvester. 2012 IEEE International Symposium on Industrial Electronics, pp. 1122–1127

5. Defay, E. (2011) *Integration of Ferroelectric and Piezoelectric Thin Films*, Wiley-ISTE, London.
6. Damjanovic, D. (1998) Ferroelectric, dielectric and piezoelectric properties of ferroelectric thin films and ceramics. *Rep. Prog. Phys.*, **61**, 1267–1324.
7. IEEE ANSI/IEEE Std, 176 (1987) IEEE Standard on Piezoelectricity, IEEE.
8. Williams, C.B. and Yates, R.B. (1995) The 8th International Conference on Solid-State Sensors and Actuators, and Eurosensors IX, Stockholm, Sweden, June 25–29, pp. 369–372
9. Baek, S.H., Park, J., Kim, D.M., Aksyuk, V.A., Das, R.R., Bu, S.D., Felker, D.A., Lettieri, J., Vaithyanathan, V., Bharadwaja, S.S.N., Bassiri-Gharb, N., Chen, Y.B., Sun, H.P., Folkman, C.M., Jang, H.W., Kreft, D.J., Streiffer, S.K., Ramesh, R., Pan, X.Q., Trolier-McKinstry, S., Schlom, D.G., Rzchowski, M.S., Blick, R.H., and Eom, C.B. (2011) Giant piezoelectricity on Si for hyperactive MEMS. *Science*, **334**, 958–961.
10. Noheda, B., Cox, D.E., Shirane, G., Guo, R., Jones, B., and Cross, L.E. (1999) A monoclinic ferroelectric phase in the  $\text{Pb}(\text{Zr}_{1-x}\text{Tix})\text{O}_3$  solid solution. *Appl. Phys. Lett.*, **74**, 2059–2061.
11. Mitsui, T. (1969) *Ferro and Antiferroelectric Substances, Landolt-Bornstein: Numerical Data and Functional Relationships in Science and Technology*, vol. 3, Springer-Verlag, Berlin, p. 308.
12. Mistler, R.E. and Twiname, E.R. (2006) *Tape Casting: Theory and Practice*, John Wiley & Sons, Ltd, Chichester.
13. Almusallam, A., Torah, R.N., Zhu, D., Tudor, M.J., and Beeby, S.P. (2013) Screen-printed piezoelectric shoe-insole energy harvester using an improved flexible PZT-polymer composites. *J. Phys. Conf. Ser.*, **476**, 012108.
14. Roundy, S. and Wright, P.K. (2004) A piezoelectric vibration based generator for wireless electronics. *Smart Mater. Struct.*, **13**, 1131–1142.
15. PIEZO <http://www.piezo.com/prodsheet2sq5H.html> (accessed 5 April 2014).
16. Thomas Lafont, Gimeno, L., Delamare, J., Lebedev, G.A., Zakharov, D.I., Viala, B., Cugat, O., Galopin, N., Garbuio, L., and Geoffroy, O. (2012) Magnetostrictive–piezoelectric composite structures for energy harvesting. *J. Micromech. Microeng.*, **22**, 094009.
17. Smart-Material <http://www.smart-material.com/MFC-product-main.html> (accessed 5 April 2014)
18. Aktakka, E.E., Peterson, R.L., and Najafi, K. (2011) Thinned-Pzt On Soi process and design optimization for piezoelectric inertial energy harvesting. Transducers'11, Beijing, China, June 5–9, pp. 1649–1652
19. Janphuang, P., Lockhart, R., Briand, D., and de Rooij, N.F. (2012) Wafer level fabrication of vibrational energy harvesters using bulk PZT sheets. *Procedia Eng.*, **47**, 1041–1044.
20. Park, S.-E. and Shrout, T.R. (1997) Ultra-high strain and piezoelectric behavior in relaxor based ferroelectric single crystals. *J. Appl. Phys.*, **82**, 1804–1811.
21. APC <https://www.americanpiezo.com/product-service/pmn-pt.html> (accessed 5 April 2014).
22. Badel, A., Benayad, A., Lefeuvre, E., Lebrun, L., Richard, C., and Guyomar, D. (2006) Single crystals and nonlinear process for outstanding vibration-powered electrical generators. *IEEE Trans. Ultrason. Ferroelectr. Freq. Control*, **53** (4), 673–684.
23. Murali, P., Kohli, M., Maeder, T., Kholkin, A., Brooks, K., Setter, N., and Luthier, R. (1995) Fabrication and characterization of PZT thin-film vibrators for micromotors. *Sens. Actuators, A*, **48** (2), 157–165.
24. Calame, F. and Murali, P. (2007) Growth and properties of gradient free sol-gel lead zirconate titanate thin films. *Appl. Phys. Lett.*, **90** (6), 062907.
25. Bouyssou, E., Jérisian, R., Cézac, N., Leduc, P., Guégan, G., and Anceau, C. (2005) Wafer level reliability and leakage current modeling of PZT capacitors. *Mater. Sci. Eng., B*, **118** (1-3), 25–29.
26. Bardaine, A., Boy, P., Belleville, P., Acher, O., and Levassort, F. (2008) Improvement of composite sol–gel process for manufacturing 40  $\mu\text{m}$  piezoelectric thick films. *J. Eur. Ceram. Soc.*, **28**, 1649–1655.

27. Shen, D., Park, J.-H., Ajitsaria, J., Choe, S.-Y., Wikle, H.C., and Kim, D.-J. (2008) The design, fabrication and evaluation of a MEMS PZT cantilever with an integrated Si proof mass for vibration energy harvesting. *J. Micromech. Microeng.*, **18**, 055017.
28. Zhang, Q.Q., Gross, S.J., Tadigadapa, S., Yu, H.G., Zou, L., Deng, K., Wolf, R., Tadigadapa, S., and Trolrier-McKinstry, S. (2003) Lead zirconate titanate MEMS accelerometer using interdigitated electrodes. *Sens. Actuators, A*, **105** (1), 91–95.
29. Jeon, Y.B., Sood, R., Jeong, J.-H., and Kim, S.-G. (2005) MEMS power generator with transverse mode thin film PZT. *Sens. Actuators, A*, **122**, 16–20.
30. Wang, Y., Ganpule, C., Liu, B.T., Li, H., Mori, K., Hill, B., Wuttig, M., Ramesh, R., FINDER, J., Yu, Z., Droopad, R., and Eisenbeiser, K. (2002) Epitaxial ferroelectric PZT thin films on Si using SrTiO<sub>3</sub> template layers. *Appl. Phys. Lett.*, **80** (1), 97–99.
31. Isarakorn, D., Briand, D., Janphuang, P., Sambri, A., Gariglio, S., Triscone, J.-M., Guy, F., Reiner, J.W., Ann, C.H., and de Rooij, N.F. (2011) The realization and performance of vibration energy harvesting MEMS devices based on an epitaxial piezoelectric thin film. *Smart Mater. Struct.*, **20**, 025015.
32. Morimoto, K., Kanno, I., Wasa, K., and Kotera, H. (2010) High-efficiency piezoelectric energy harvesters of c-axis-oriented epitaxial PZT films transferred onto stainless steel cantilevers. *Sens. Actuators, A*, **163**, 428–432.
33. Priya, S. and Nahm, S. (2012) *Lead Free Piezoelectrics*, New York, Springer.
34. Liu, W. and Ren, X. (2009) Large Piezoelectric Effect in Pb-Free Ceramics. *Phys. Rev. Lett.*, **103**, 257602.
35. Piorra, A., Petraru, A., Kohlstedt, H., Wuttig, M., and Quandt, E. (2011) Piezoelectric properties of 0.5(Ba<sub>0.7</sub>Ca<sub>0.3</sub>TiO<sub>3</sub>) – 0.5[Ba(Zr<sub>0.2</sub>Ti<sub>0.8</sub>)O<sub>3</sub>] ferroelectric lead-free laser deposited thin films. *J. Appl. Phys.*, **109**, 104101.
36. Xue, D., Zhou, Y., Bao, H., Zhou, C., Gao, J., and Ren, X. (2011) Elastic, piezoelectric, and dielectric properties of Ba(Zr<sub>0.2</sub>Ti<sub>0.8</sub>)O<sub>3</sub>- 50(Ba<sub>0.7</sub>Ca<sub>0.3</sub>)TiO<sub>3</sub> Pb-free ceramic at the morphotropic phase boundary. *J. Appl. Phys.*, **109**, 054110.
37. Saito, Y., Takao, H., Tani, T., Nonoyama, T., Takatori, K., Homma, T., Nagaya, T., and Nakamura, M. (2004) Lead-free piezoceramics. *Nature*, **432** (7013), 84.
38. Van Minh, L., Hara, M., Kuwano, H. (2014) High Performance Nonlinear Micro Energy Harvester Integrated with KNN /Si Composite Quad-cantilever. MEMS 2014, San Francisco, CA, pp. 397–400.
39. Elfrink, R., Renaud, M., Kamel, T.M., de Nooijer, C., Jambunathan, M., Goedbloed, M., Hohlfeld, D., Matova, S., Pop, V., Caballero, L., and van Schaijk, R. (2010) Vacuum-packaged piezoelectric vibration energy harvesters: damping contributions and autonomy for a wireless sensor system. *J. Micromech. Microeng.*, **20** (10), 104001.
40. Ricart, T., Lassagne, P.P., Boisseau, S., Despesse, G., Lefevre, A., Billard, C., Fanget, S., Defay, E. (2012) IEEE, Macro energy harvester based on aluminium nitride thin films. 2011 IEEE International Ultrasonics Symposium, pp. 1928–1931.
41. Akiyama, M., Kamohara, T., Kano, K., Teshigahara, A., Takeuchi, Y., and Kawahara, N. (2009) Enhancement of piezoelectric response in scandium aluminum nitride alloy thin films prepared by dual reactive co-sputtering. *Adv. Mater.*, **21**, 593–596.
42. Tasnadi, F., Alling, B., Hoglund, C., Wingqvist, G., Birch, J., Hultman, L., and Abrikosov, I.A. (2010) Origin of the anomalous piezoelectric response in Wurtzite ScAlN alloys. *Phys. Rev. Lett.*, **104**, 137601.
43. Matloub, R., Hadad, M., Mazzalai, A., Chidambaram, N., Moulard, G., Sandu, C.S., Metzger, T., and Murali, P. (2013) Piezoelectric Al<sub>1-x</sub>Sc<sub>x</sub>N thin films: a semiconductor compatible solution for mechanical energy harvesting and sensors. *Appl. Phys. Lett.*, **102**, 152903.
44. Kawai, H. (1969) The piezoelectricity of poly(vinylidene fluoride). *Jpn. J. Appl. Phys.*, **8**, 975–976.

45. Lando, J.B. and Doll, W.W. (1968) The polymorphism of poly(vinylidene fluoride). 1. the effect of head to-head structure. *J. Macromol. Sci.-Phys.*, **B2**, 205–218.
46. Tashiro, K., Takano, K., Kobayashi, M., Chatani, Y., and Tadokoro, H. (1984) Structural study on ferroelectric phase transition of vinylidene fluoride-trifluoroethylene copolymers (III) dependence of transitional behavior on VDF molar content. *Ferroelectrics*, **57**, 297–326.
47. Zhang, Q.M., Vivek, B., and Zhao, X. (1998) Giant electrostriction and relaxor ferroelectric behavior in electron-irradiated poly(vinylidene fluoride-trifluoroethylene) copolymer. *Science*, **280**, 2101–2104.
48. PIEZOTECH [www.piezotech.fr](http://www.piezotech.fr) (accessed 5 April 2014)
49. Benz, M. and Euler, W.B. (2003) Determination of the crystalline phases of Poly(vinylidene fluoride) under different preparation conditions using differential scanning calorimetry and infrared spectroscopy. *J. Appl. Polym. Sci.*, **89**, 1093–1100.
50. Kymissis, J., Kendall, C., Paradiso, J., and Gershenfeld, N. (1998) Parasitic power harvesting in shoes. Proceeding of the 2nd IEEE International Symposium Wearable Computers, Pittsburgh, pp. 132–139.
51. Chang, C., Tran, V.H., Wang, J., Fuh, Y.-K., and Lin, L. (2010) Direct-write piezoelectric polymeric nanogenerator with high energy conversion efficiency. *Nano Lett.*, **10**, 726–731.
52. Ishida, K., Huang, T.-C., Honda, K., Shinozuka, Y., Fuketa, H., Yokota, T., Zschieschang, U., Klauk, H., Tortissier, G., Sekitani, T., Toshiyoshi, H., Takamiya, M., Someya, T., and Sakurai, T. (2013) Insole pedometer with piezoelectric energy harvester and 2 V organic circuits. *IEEE J. Solid-State Circuits*, **48** (1), 255–264.
53. Ramadan, K.S., Sameoto, D., and Evoy, S. (2014) A review of piezoelectric polymers as functional materials for electromechanical transducers. *Smart Mater. Struct.*, **23**, 033001.
54. Wang, Z.L. (2009) ZnO nanowire and nanobelt platform for nanotechnology. *Mater. Sci. Eng., R*, **64**, 33–71.
55. Song, J., Zhou, J., and Wang, Z.L. (2006) Piezoelectric and semiconducting dual-property coupled power generating process of a single ZnO belt/wire—a technology for harvesting electricity from the environment. *Nano Lett.*, **6**, 1656–1662.
56. Zhao, M.H., Wang, Z.L., and Mao, S.X. (2004) Piezoelectric characterization of individual zinc oxide nanobelt probed by piezoresponse force microscope. *Nano Lett.*, **4** (4), 587–590.
57. Zhu, G., Wang, A.C., Liu, Y., Zhou, Y., and Wang, Z.L. (2012) Functional electrical stimulation by nanogenerator with 58 V output voltage. *Nano Lett.*, **12**, 3086–3090.
58. Wang, Z., Hu, J., Suryavanshi, A.P., Yum, K., and Yu, M.-F. (2007) Voltage generation from individual BaTiO<sub>3</sub> nanowires under periodic tensile mechanical load. *Nano Lett.*, **7**, 2966–2969.
59. Su, W.S., Chen, Y.F., Hsiao, C.L., and Tu, L.W. (2007) Generation of electricity in GaN nanorods induced by piezoelectric effect. *Appl. Phys. Lett.*, **90**, 063110.
60. Qi, Y. and McAlpine, M.C. (2010) Nanotechnology-enabled flexible and biocompatible energy harvesting. *Energy Environ. Sci.*, **3**, 1275–1285.
61. Smart-Material <http://www.smart-material.com/MFC-product-main.html> (accessed 23 May 2014).

## 8

### Electrostatic/Electret-Based Harvesters

*Yuji Suzuki*

#### 8.1

##### Introduction

In an electrostatic/electret generator, capacitance change in response to mechanical vibration is used to convert mechanical energy into electricity. Its energy density per unit volume is estimated to be  $\epsilon\epsilon_0 E^2/2$ , where  $\epsilon$ ,  $\epsilon_0$ , and  $E$  are respectively the relative permittivity of the gap medium, the permittivity of vacuum, and the magnitude of the electrical field [1]. Compared with a piezoelectric generator, the energy conversion element of an electrostatic/electret generator is independent of mechanical springs supporting the oscillating mass. Therefore, instead of using fragile piezoelectric materials as the flexure member, proven spring materials with high fatigue limit can be used. This is particularly advantageous for a small-scale vibration generator with low resonant frequencies [2].

In this chapter, electrostatic/electret generator models, different configurations of electrodes, electret materials/charging methods, generator design, and prototyped micro-electro-mechanical-system (MEMS) devices are discussed.

#### 8.2

##### Electrostatic/Electret Conversion Cycle

Figure 8.1 shows a  $Q$ - $V$  diagram for electrostatic conversion cycle with an external voltage source (e.g., [3]). Cycle 1–2–3–1 represents a conversion cycle with voltage constraint. The cycle starts with priming a variable capacitor with an external voltage source at its maximum capacitance  $C_{\max}$  (Path 1–2). Then the capacitance is decreased from  $C_{\max}$  to  $C_{\min}$ , while the capacitor is kept connected to the voltage source (Path 2–3). In this step, mechanical energy is converted to electrical energy, and charges are stored back to the voltage source or sent to the external load. In Path 3–1, the charge remaining on the capacitor is recovered at  $C_{\min}$ . The net energy gained per cycle is

$$E_{1231} = \frac{1}{2}(C_{\max} - C_{\min})V_{\max}^2 \quad (8.1)$$

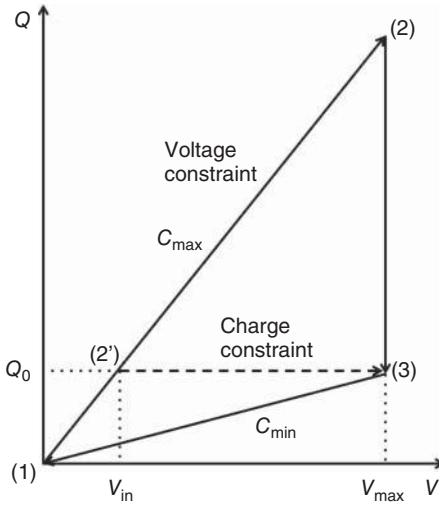


**Figure 8.1** Electrostatic conversion cycle with external voltage source.

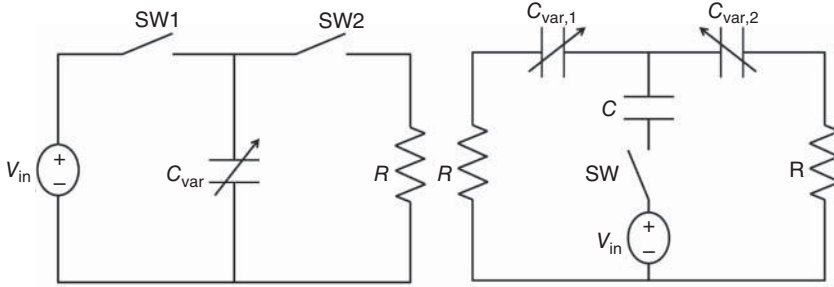
On the other hand, in a charge–constraint cycle (Cycle 1–2′–3–1), the priming voltage  $V_{in}$  is much lower than  $V_{max}$  such that  $Q_0 = C_{max} V_{in} = C_{min} V_{max}$ . After priming, the variable capacitor is disconnected from the external circuits, and the capacitance is decreased from  $C_{max}$  to  $C_{min}$ . Then, the capacitor is connected to the voltage source and charge is stored back at the voltage source or sent to the load. In this case, the net energy gained per cycle is given by

$$E_{12'31} = \frac{1}{2}(C_{max} - C_{min})V_{max}V_{in} = \frac{1}{2}\left(\frac{1}{C_{min}} - \frac{1}{C_{max}}\right)Q_0^2 \quad (8.2)$$

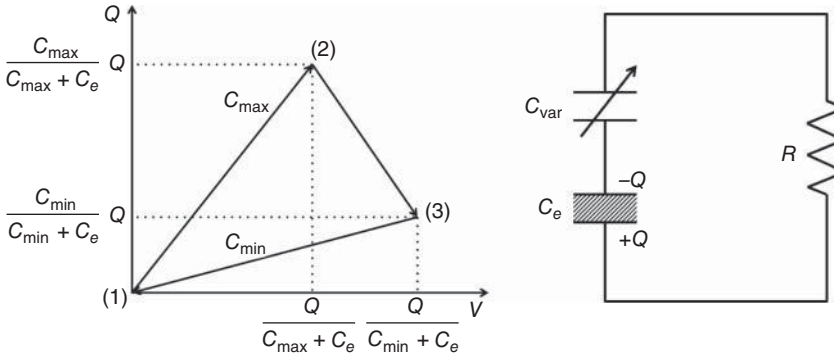
Although  $E_{1231}$  is larger than  $E_{12'31}$ , the charge–constraint cycle is usually used for its simpler configuration.

Figure 8.2 shows circuit examples of the charge–constraint electrostatic generator. The example in Figure 8.2a has two synchronous switches with a single variable capacitor. SW1 is closed during the priming period (Path 1–2′) and SW2 during the discharge period (Path 3–1). The disadvantage of this approach is that a low-power-consumption switch synchronized to the mechanical vibration is required [4]. Figure 8.2b shows a differential circuit with a single switch for priming, where the sum of  $C_{var,1}$  and  $C_{var,2}$  is constant, while  $dC_{var,1}/dt = -dC_{var,2}/dt$  during operation. In this configuration, charge stored in the capacitor  $C$  is used to obtain induced charges in  $C_{var,1}$  and  $C_{var,2}$ , and no electrical current goes in/out of this capacitor (e.g., [5]).

Figure 8.3a shows the conversion cycle of the electret generator in analogy of the electrostatic one. As described below, electret could be modeled with a pre-charged capacitor (amount of charge  $Q$ ). When a series variable capacitor is connected at its maximum capacitance as shown in Figure 8.3b, the voltage and the charge stored in the capacitor are  $Q/(C_{max} + C_e)$  and  $Q_0 = QC_{max}/(C_{max} + C_e)$ , respectively (Path 1–2). Then, the capacitance is decreased from  $C_{max}$  to  $C_{min}$ ,



**Figure 8.2** Circuit examples for the charge-constraint electrostatic generator. (a) Circuit with synchronous switch and (b) differential capacitor circuit.



**Figure 8.3** Electret generator. (a) Electret conversion cycle in analogy of electrostatic generator and (b) circuit model of electret generator.

which leads to the external current (Path 2–3). The net energy gained per cycle is given by

$$E_{1231} = \frac{1}{2} \frac{C_{\min}}{(C_{\min} + C_e)^2} Q^2 - \frac{1}{2} \frac{C_{\max}}{(C_{\max} + C_e)^2} Q^2 = \frac{1}{2} \frac{Q_0^2}{C_{\max}} \left\{ \frac{C_{\min}}{C_{\max}} \frac{(C_{\max} + C_e)^2}{(C_{\min} + C_e)^2} - 1 \right\} \quad (8.3)$$

In electret generators, there is no need for an external voltage source or synchronous switches. More detailed discussion will be given in Section 8.4.

### 8.3 Electrostatic/Electret Generator Models

#### 8.3.1 Configuration of Electrostatic/Electret Generator

Although the discussion in Section 8.1 is based on rather simplified models, it is shown in Eqs. (8.1)–(8.3) that the capacitance change is the key parameter for the net energy gained and the output power of electrostatic/electret generators. In

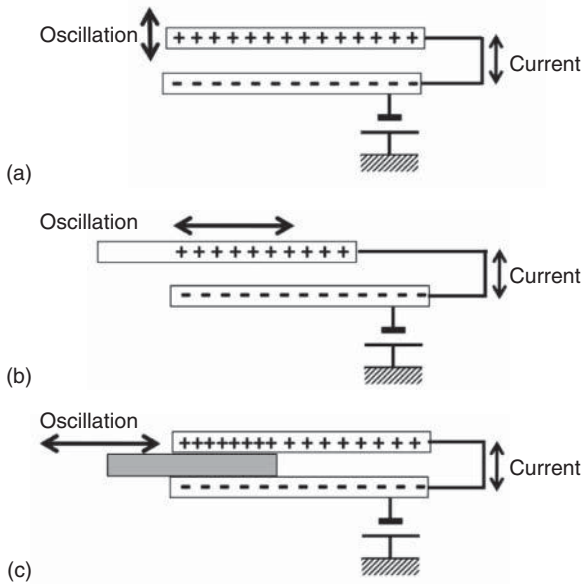


**Figure 8.4** Different types of electrostatic/electret generators. (a) Gap-closing, (b) overlapping-area-change, and (c) permittivity change.

this section, different configurations of the variable capacitor are discussed. The configuration of the generator should be carefully chosen on the basis of the rate of change of the capacitance.

Electrostatic/electret generators can be grouped into three basic types, namely, gap-closing, overlapping-area change, and permittivity change as shown in Figure 8.4. Here, a pair of parallel plate electrodes with a gap  $g$  is assumed. Its capacitance  $C$  is given by

$$C = \epsilon\epsilon_0 \frac{LH}{g} \quad (8.4)$$

where  $L$  and  $H$  are the electrode length and the electrode depth, respectively. One of the plates is connected to a voltage source for the priming voltage. In an electret generator model described later, the voltage source is replaced with an electret layer with stored charges formed on one of the electrodes. The equivalent circuit of an electret is an electrode connected with the voltage source through a capacitor, the capacitance of which is the same as that of the electret layer. Thus, with electret, the capacitance given by Eq. (8.4) should be modified to

$$C = \epsilon\epsilon_0 \frac{LH}{g + d/\epsilon_e} \quad (8.4')$$

where  $d$  and  $\epsilon_e$  are thickness of the electret layer and the relative permittivity of electret, respectively.

In the gap-closing type (Figure 8.4a), one of the electrodes moves toward/away from the other electrode. Since the gap  $g$  is a function of time  $g(t)$ , the rate of



change of the capacitance becomes

$$\frac{dC}{dt} = -\varepsilon\varepsilon_0 \frac{LH}{g(t)^2} \frac{dg}{dt} \quad (8.5)$$

Therefore, the gap-closing type has an inherent nonlinear response, and the magnitude of  $dC/dt$  is rapidly increased when the amplitude becomes closer to the initial gap (i.e.,  $g(t) \rightarrow 0$ ). On the other hand, when the amplitude is much smaller than the initial gap,  $dC/dt$  diminishes.

In the overlapping-area change type (Figure 8.4b), one of the electrodes slides while keeping the gap constant. Since the overlapping area (length) between the top and bottom electrodes is a function of time  $L(t)$ , the rate of change of the capacitance is

$$\frac{dC}{dt} = \varepsilon\varepsilon_0 \frac{H}{g} \cdot \frac{dL}{dt} \quad (8.6)$$

where  $dC/dt$  is proportional to the electrode sliding velocity  $dL/dt$ .

In the permittivity change type (Figure 8.4c), both electrodes are fixed in space, and a dielectric plate with high relative permittivity oscillates in between the electrodes. When the inserted length of the dielectric plate (relative permittivity  $\varepsilon_d$ ) is  $L(t)$ , the rate of change of the capacitance is

$$\frac{dC}{dt} = (\varepsilon_d - \varepsilon)\varepsilon_0 \frac{H}{g} \frac{dL}{dt} \quad (8.7)$$

Therefore, again,  $dC/dt$  is proportional to the sliding velocity of the dielectric  $dL/dt$ .

### 8.3.2

#### Electrode Design for Electrostatic/Electret Generator

Figure 8.5 shows two types of in-plane electrode configurations with comb drives, which are typical design of MEMS electrostatic generators. The gap-closing type (Figure 8.5a) has characteristics similar to those of the single-sided out-of-plane generator model shown in Figure 8.4a, but each finger pair forms two capacitors; when the movable finger is displaced in the lateral ( $y$ -) direction normal to the electrodes, one side of the capacitance is increased, while the other side is decreased. Thus, its combined capacitance is given by

$$C(y) = n\varepsilon\varepsilon_0 \frac{HL}{g_0 - y} + n\varepsilon\varepsilon_0 \frac{HL}{g_0 + y} = 2n\varepsilon\varepsilon_0 \frac{HLg_0}{g_0^2 - y^2} \quad (8.8)$$

where  $n$ ,  $H$ ,  $L$ ,  $g_0$ , and  $y=y(t)$  are the number of comb finger pairs, the height of the finger, the overlapping length, the initial gap between the electrodes, and the displacement of the movable finger, respectively. Obviously, the capacitance change should have nonlinear relationship with the displacement.

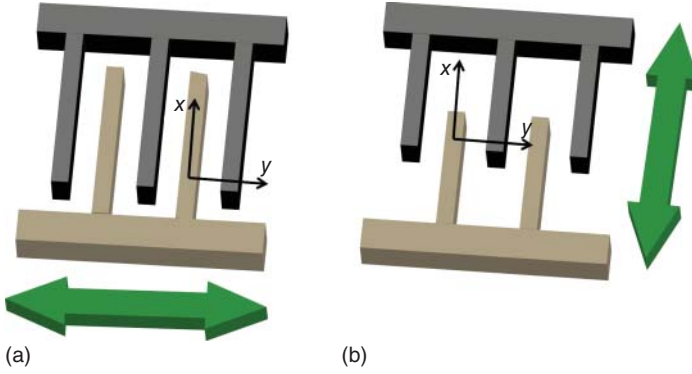


**Figure 8.5** In-plane generator with comb drive. (a) Gap-closing and (b) overlapping-area-change.

Stiction is a well-known issue for the gap-closing type. The electrostatic force  $F_{y,e}$  with the applied voltage  $V$  is given by

$$F_{y,e} = \frac{d}{dy} \left( \frac{1}{2} CV^2 \right) = 2n\epsilon\epsilon_0 \frac{HLg_0 V^2 y}{(g_0 - y^2)^2} \quad (8.9)$$

which acts toward either side of the electrodes. When  $F_{y,e}$  becomes larger than the restoration spring force  $F_s = k_y y$  ( $k_y$  is the spring constant in the  $y$ -direction), stiction happens. The critical displacement for onset of the stiction  $y_{\text{crit}}$  is then given by Eq. (8.10),

$$y_{\text{crit}} = \sqrt{g_0^2 - \sqrt{\frac{2n\epsilon\epsilon_0 HLg_0}{k_y}} V} \quad (8.10)$$

In actual operation of vibration energy harvesters, the maximum amplitude cannot be defined. Therefore, the gap-closing generator should have a mechanical stopper in such a way that the amplitude is within the stable amplitude range of  $0 < y < (g_0 - y_{\text{crit}})$ .

For the overlapping-area-change type (Figure 8.5b), each finger pair forms two capacitors with the same capacitance, and the vibration direction is in the longitudinal ( $x$ -) direction along the finger. Thus, the combined capacitance is

$$C(x) = 2n\epsilon\epsilon_0 \frac{H(L_0 + x)}{g} \quad (8.11)$$

where  $L_0$ ,  $x = x(t)$ , and  $g$  are the initial overlapping length, the displacement of the movable finger, and the gap between electrodes, respectively. The electrostatic force in the longitudinal direction  $F_{x,e}$  given by

$$F_{x,e} = \frac{d}{dx} \left( \frac{1}{2} C(x) V^2 \right) = n\epsilon\epsilon_0 \frac{H}{g} V^2 \quad (8.12)$$

is independent of the displacement  $x$ . Therefore, unlike the gap-closing type, the overlapping-area-change type has no stiction problem in the vibration ( $x$ -) direction.

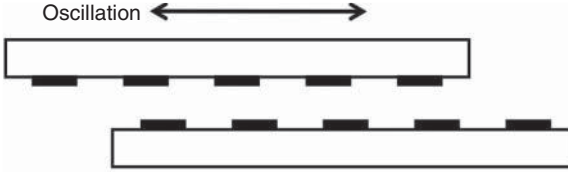


**Figure 8.6** In-plane overlapping-area-change generator with patterned electrodes.

However, for the overlapping-area-change type, so-called lateral instability limits the maximum displacement [6]. When the movable finger is displaced in the lateral ( $y$ -) direction as well as in the longitudinal ( $x$ -) direction, the electrostatic force in the  $y$ -direction is given by

$$F_{y,e} = \frac{\partial}{\partial y} \left( \frac{1}{2} CV^2 \right) = n\epsilon\epsilon_0 \frac{H(L_0 + x)}{2(g - y)^2} V^2 - n\epsilon\epsilon_0 \frac{H(L_0 + x)}{2(g + y)^2} V^2 \quad (8.13)$$

Thus, the electrostatic “negative” spring constant  $k_{y,e}$  becomes

$$k_{y,e} = \left. \frac{\partial F_{y,e}}{\partial y} \right|_{y=0} = \frac{2n\epsilon\epsilon_0 H(L_0 + x)}{g^3} V^2 \quad (8.14)$$

The lateral stability condition is then given by  $k_y > k_{y,e}$ , where  $k_y$  is the mechanical spring constant in the  $y$ -direction. Therefore, the critical displacement in the  $x$ -direction is given by

$$x_{\text{crit}} = \frac{k_y g^3}{2n\epsilon\epsilon_0 H V^2} - L_0 \quad (8.15)$$

Another typical configuration of the in-plane overlapping-area-change type is with two parallel substrates as shown in Figure 8.6. Instead of using comb drives, stripe-shaped electrodes are patterned on the top and bottom substrates. The advantage of using this configuration is that the rate of capacitance change becomes much larger. In the basic model shown in Figure 8.4b, the capacitance changes from  $C_{\text{max}}$  to  $C_{\text{min}}$  (or vice versa) with the in-plane displacement of the whole plate length  $L$ . On the other hand, with the patterned electrode of width  $w$ , the same capacitance change can be made with a smaller displacement of  $w$  ( $\ll L$ ).

Figure 8.7 shows typical capacitance change for different generator configurations when the mass motion is sinusoidal. The vertical axis is the capacitance normalized with its maximum value. The out-of-plane gap-closing type and the in-plane overlapping-area-change type with comb drive gives the capacitance change once per cycle, while the in-plane gap-closing type with comb drive gives the capacitance change twice per cycle. On the other hand, in the two-plate overlapping-area-change type with patterned electrodes (Figure 8.6), the number of capacitance changes per cycle is equal to twice the amplitude/(electrode width). Thus, the number of the capacitance changes is increased with the amplitude of the mass. This is beneficial for vibration energy harvesters, because

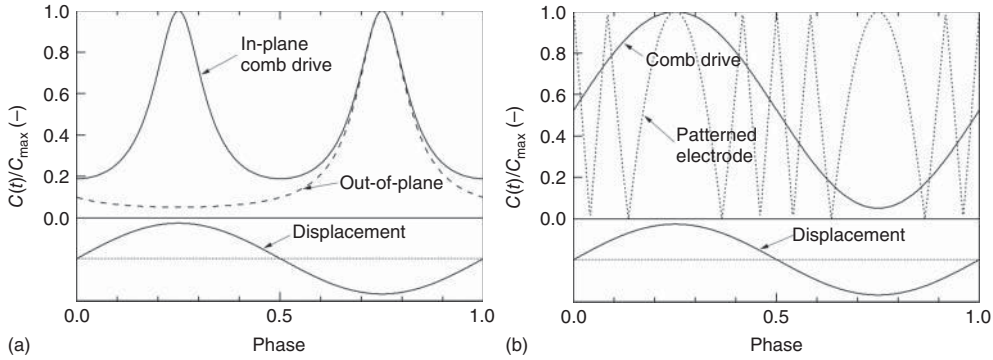


**Figure 8.7** Capacitance change of electrostatic generator during one cycle of the sinusoidal mass motion. (a) Gap-closing type and (b) overlapping-area-change type. The vertical axis is normalized with its maximum value.

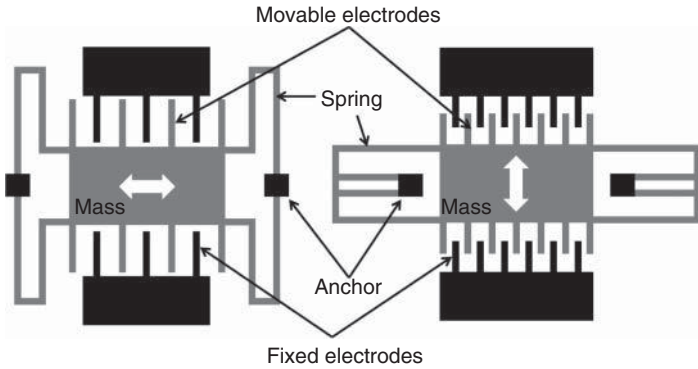
the mechanical energy conversion limit called the *VDRG* (*velocity-damped resonance generator*) limit is also proportional to the amplitude of the mass [7].

## 8.4 Electrostatic Generators

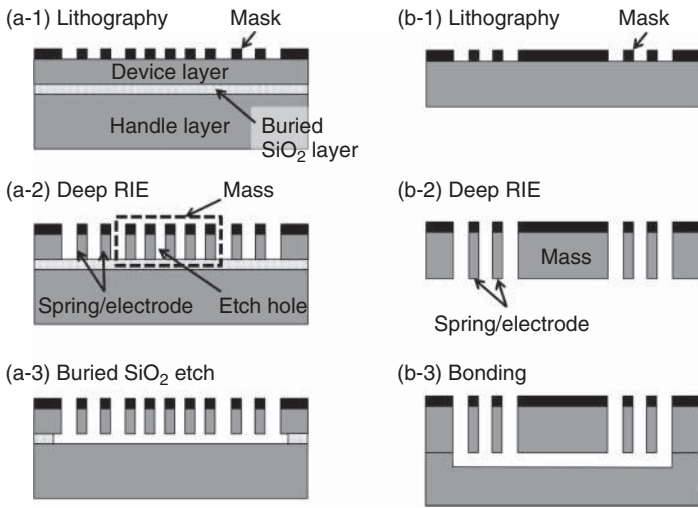
### 8.4.1 Design and Fabrication Methods

Figure 8.8 shows typical designs of electrostatic generator with comb drives, that is, the gap-closing and the overlapping-area-change types. As described in previous sections, the characteristics of the capacitance change are different for these two electrode configurations. However, the choice of the electrode configuration is also dependent on the MEMS process to be used.

Figure 8.9 shows commonly used MEMS process for electrostatic generator with comb drives. In the SOI (silicon-on-insulator) process shown in Figure 8.9a, first, the etch mask is patterned using lithography on the device layer. Then, the top Si device layer (thickness  $< 100 \mu\text{m}$ ) is etched with deep-RIE (DRIE) to pattern fixed/movable electrodes and mass. Etching holes are also made on the mass. Finally, the buried  $\text{SiO}_2$  layer is removed with sacrificial etching such as vapor HF to release the structure. The advantage of this process is that the minimum feature, that is, the gap between comb fingers could be as small as a few micrometers, which is suitable for the overlapping-area-change type as well as the gap-closing type. In addition, this process needs only one mask without any assembling step, which makes the process potentially low cost. Bartsch *et al.* [8] and Tvedt *et al.* [9] employed this process. One drawback is that the weight of the oscillation mass is reduced owing to distributed etch holes on the mass, and thus the VDRG limit becomes relatively low.



**Figure 8.8** Typical design of MEMS electrostatic generator with comb drives. (a) Gap-closing and (b) overlapping-area-change.



**Figure 8.9** MEMS process for electrostatic generator with comb drive. (a) SOI process with buried SiO<sub>2</sub> etch and (b) process with substrate bonding.

Figure 8.9b shows alternative process with wafer bonding. First, the etch mask is patterned using lithography on a Si wafer. Then, fixed/movable electrodes and mass are patterned by etching through the wafer using DRIE. Finally, another wafer with a recess is prepared and bonded with the structural wafer. The advantage of using this approach is that a thick wafer can be used as the structural layer. Therefore, the capacitor area of the comb drives could be large and the weight of the oscillation mass could be large. Nguyen *et al.* [10] and Basset *et al.* [11] employed this process. However, for thick Si wafers (~400 μm), the minimum feature is limited to around 20 μm owing to the maximum allowable aspect ratio

of DRIE, which is too large for the overlapping-area-change type. Therefore, this process is suitable for the gap-closing type, in which the initial gap could be large.

#### 8.4.2

##### Generator Examples

Miao *et al.* [12] developed an out-of-plane gap-closing electrostatic generator using a three-wafer process. The device can be categorized into a Coulomb force parametric generator [7] having no resonant frequency. The dimensions of the mass are  $11\text{ mm} \times 11\text{ mm} \times 0.4\text{ mm}$ , and  $C_{\max}$  and  $C_{\min}$  are 50 and 5.5 pF, respectively. They obtained the output power up to 120 nJ per cycle.

Basset *et al.* [11] developed a gap-closing comb-drive electrostatic generator based on the process in Figure 8.9b. The device layer is  $380\text{ }\mu\text{m}$  in thickness. The mass is 66 mg, and, a total of 142 electrode pairs are integrated (Figure 8.10). The initial gap and the minimum gap defined by the mechanical stopper are  $43.5\text{ }\mu\text{m}$  and  $7.5\text{ }\mu\text{m}$ .  $C_{\max}$  and  $C_{\min}$  are 88 and 40 pF, respectively. At large amplitude, the mechanical spring behaves as a hardening nonlinear spring. On the other hand, the electrostatic force between the gap-closing electrodes works as a softening nonlinear spring, so that the overall behavior significantly depends on the priming voltage; on increasing the priming voltage, the frequency for the maximum output power is decreased owing to the electrical softening effect. At the resonant frequency of 150 Hz, they obtained up to  $2.2\text{ }\mu\text{W}$  at  $1g$  acceleration.

Nguyen *et al.* [13] developed an overlapping-area-change comb-drive electrostatic generator based on Figure 8.9b. The device layer is  $300\text{ }\mu\text{m}$  in thickness. The mass is 30.4 mg and supported with an initially curved softening spring. In total, 125 electrode pairs with  $15\text{-}\mu\text{m}$  gap are integrated. With a bias voltage of 150 V, an output power of  $7\text{ }\mu\text{W}$  is obtained at around 400 Hz and  $0.36g$  acceleration.

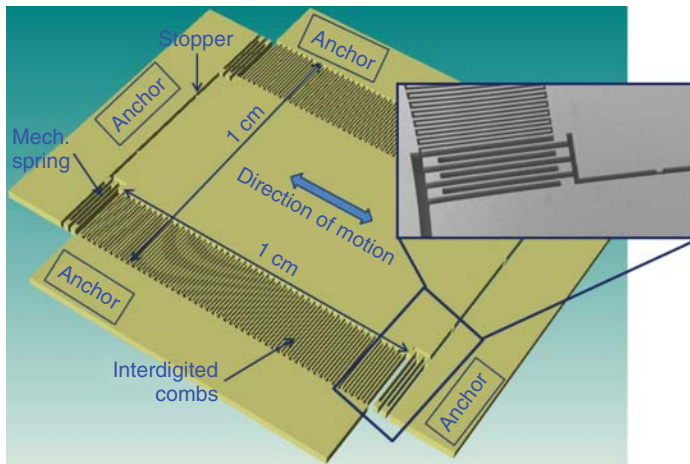
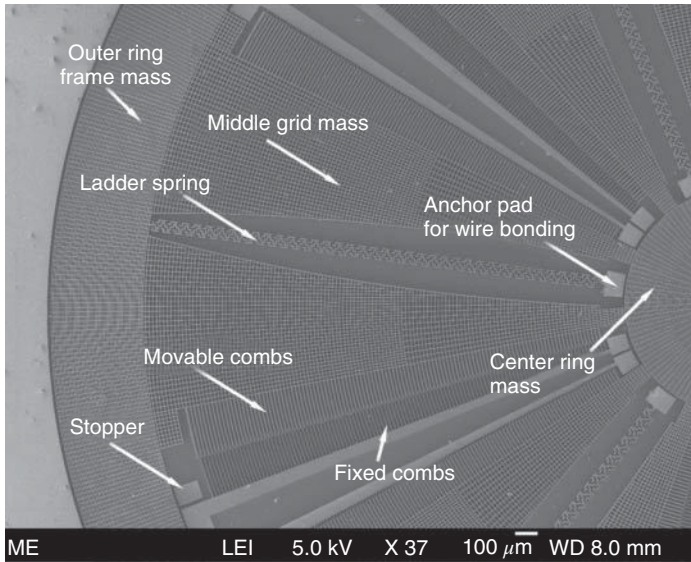


Figure 8.10 MEMS gap-closing electrostatic generator [11]. Courtesy of Dr. P. Basset.



**Figure 8.11** SEM image of a rotary-comb capacitive generator with ladder spring [15]. Courtesy of Dr. C.-K. Lee.

Hoffman *et al.* [5] developed an overlapping-area-change comb-drive electrostatic generator with the configuration shown in Figure 8.2b, by which no switching mechanism is needed. They employed a modified bonding-based process; they first made a 50- $\mu\text{m}$  deep cavity into a Si wafer and grew a thermal  $\text{SiO}_2$  layer for electrical isolation. Then, they bonded a highly doped Si wafer to the substrate and used a chemical mechanical polishing to get a 50- $\mu\text{m}$ -thick Si layer suspended on the cavity. Finally, they patterned mass, electrodes, and springs with DRIE. The mass is 0.6 mg, and, a total of 936 electrode pairs with 2.9- $\mu\text{m}$  wide gap are integrated. The resonant frequency is 1.33–1.48 kHz, and the capacitance change is 13.3 pF. With the priming voltage of 50 V, 1.75  $\mu\text{W}$  is obtained at the external acceleration of 13g. They also reported that when the bias capacitor is disconnected from the voltage source, the capacitor voltage drops by 30% after 2 h operation. However, about 20 times more electricity is generated in the external load if compared with the energy loss in the capacitor. The effectiveness  $E_H$ , which is defined as the electrical output power divided by the VDRG limit [14], is as high as 45%.

Yang *et al.* [15] developed an overlapping-area-change generator with in-plane rotary combs. They employed an SOI process shown in Figure 8.9a. The generator diameter is 6 mm, and the thickness of the device layer is 30  $\mu\text{m}$ . By using a 6mm wide ladder spring as shown in Figure 8.11, a low resonant frequency of 63 Hz is achieved. They obtained 0.39  $\mu\text{W}$  at 0.25g acceleration in vacuum environment.

## 8.5

## Electrets and Electret Generator Model

## 8.5.1

## Electrets

An electret is a dielectric with quasi-permanent charges, which was coined by Heaviside in the analogy of magnet. Eguchi [16] first developed the electret using carnauba wax, which was poled under a high static electric field at its melting temperature. The lifetime of charges is much longer than the RC time constant and the charges can be stabilized for tens of years. For instance, Takamatsu [17] examined long-term stability of carnauba wax electrets, and found that the surface charge density is unchanged after 35 years. Electrets have been commercialized for use in microphones and air dust filtering systems [18]. The electret generator was also proposed by Jefimenko and Walker [19] and Tada [20]. For microphones or air filters, surface potential on the order of 10 V is sufficient, so that the main research focus was on development of low-cost electret material using hydrocarbon polymer. However, as described below, high surface potential is necessary for an electret energy harvester, which triggered recent developments of high-performance electret materials.

The performance of an electret is often characterized with the surface charge density  $\sigma$ . However, the charge is not located on the surface but distributed in the depth direction as shown in Figure 8.12a. Assume an electret layer ( $d$ : thickness;  $\epsilon$ : relative permittivity) formed on an electrode, which is facing to another electrode with an air gap of  $g$ . The volume charge density  $\rho$  is a function of the distance to the bottom electrode  $x$ . Assuming that the amount of charge located at  $x$  is  $\rho(x)\Delta x$ , the Gauss's law and the Kirchhoff's law are given by

$$\begin{cases} \epsilon\epsilon_0 E_a - \epsilon\epsilon_0 E_b = \rho(x) \Delta x, \\ \epsilon\epsilon_0 E_b = \epsilon_0 E_2, \\ xE_a + (d-x)E_b + gE_2 = 0. \end{cases} \quad (8.16)$$

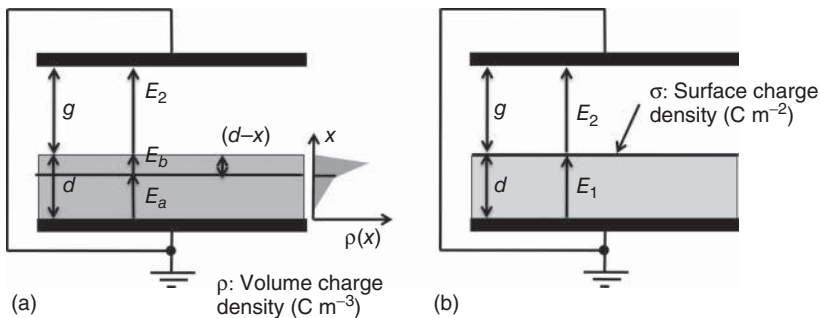


**Figure 8.12** Surface charge density of electret.(a) electrical field due to the volume charge, (b) electrical field due to the surface charge.



By solving these equations, the surface potential increase with the volume charge  $\rho(x)\Delta x$  is given by

$$\Delta V_s = E_a x + E_b(d - x) = \frac{\rho(x)\Delta x}{\epsilon\epsilon_0} \frac{x}{1 + \frac{d}{\epsilon g}} \approx \frac{x\rho(x)\Delta x}{\epsilon\epsilon_0}. \quad (8.17)$$

The last equality is usually valid because  $d \ll g$ . The surface potential  $V_s$  is obtained by integrating Eq. (8.17) from  $x = 0$  to  $d$ , and given by

$$V_s = \frac{\sigma d}{\epsilon\epsilon_0}, \quad \sigma = \frac{1}{d} \int_0^d x\rho(x)dx. \quad (8.18)$$

Therefore, the surface charge density  $\sigma$  is the mean charge density weighted with the distance from the bottom electrode; charge near the surface has large contribution to  $\sigma$ , and vice versa. Since accurate measurement of  $\rho(x)$  is extremely difficult especially for thin electret films on the order of  $10\ \mu\text{m}$ , “virtual” surface charge density  $\sigma$  is usually used to represent the charge stored in the film as shown in Figure 8.12b [21, 18]. The quantity  $\sigma$  is estimated with Eq. (8.18) by measuring the surface potential  $V_s$  with an electrostatic probe.

### 8.5.2

#### Electret Materials

Electret materials can be divided into two groups, namely,  $\text{SiO}_2$ -based inorganic electrets and polymer-based organic electrets [18].  $\text{SiO}_2$  provides an extremely-high surface charge density, but the long-term stability of charges is of concern. In order to solve this problem, multilayer structures using  $\text{SiO}_2$  and  $\text{Si}_3\text{N}_4$  are often used [22, 23]. On the other hand, fluorinated polymer materials such as PTFE (Figure 8.13a) and FEP provide better long-term stability. However, PTFE and FEP are not compatible with MEMS processes, because they are insoluble in solvents.

Hsieh *et al.* [24] and Boland *et al.* [25] used Teflon AF (DuPont Inc., Figure 8.13b), which is perfluorinated amorphous polymer, as their electret film. Lo and Tai [26] found that fluorinated parylene (parylene HT, SCS) provides a very high surface charge density of  $3.7\ \text{mC m}^{-2}$  for a  $7.3\text{-}\mu\text{m}$ -thick film. Sakane *et al.* [27] reported that amorphous perfluorinated polymer CYTOP (Asahi Glass Co., Ltd.) can provide a surface charge density of up to four times greater than that of Teflon AF. As shown in Figure 8.13c, the molecular structure of CYTOP is characterized by its perfluorinated cyclic structure. Kashiwagi *et al.* [28] also examined

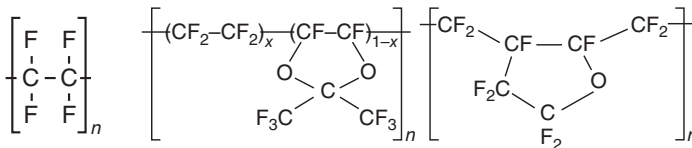


**Figure 8.13** Molecular structures of fluorinated polymer electret. (a) PTFE, (b) Teflon AF, and (c) CYTOP.

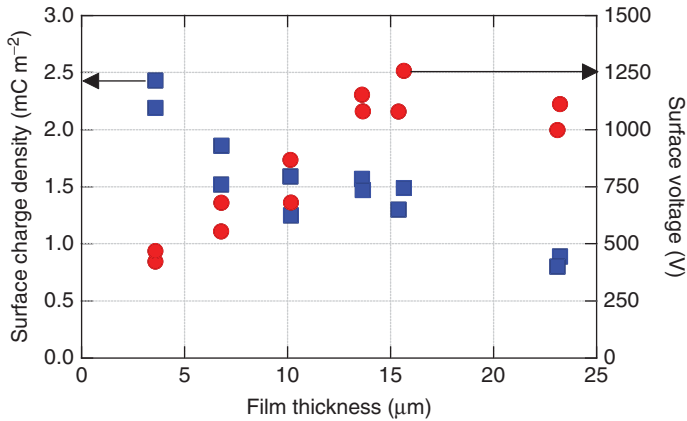


**Figure 8.14** Surface charge density and surface voltage for CYTOP CTL-M films of different film thicknesses [27].

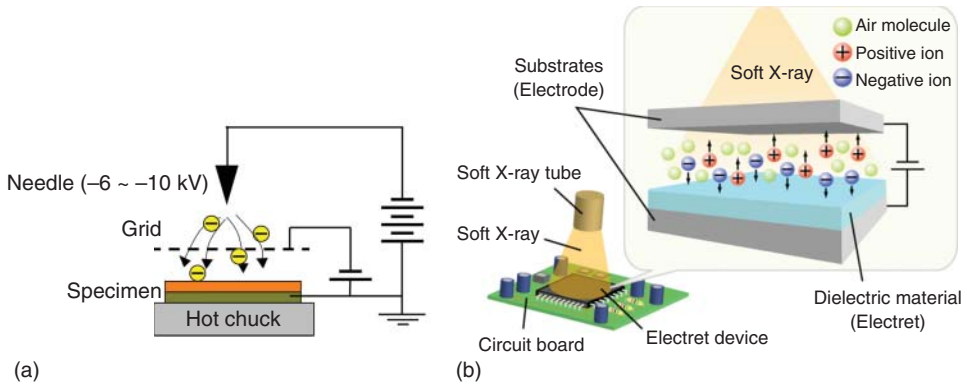
CYTOP-based electret (CYTOP EGG), in which additive-based nanoclusters are formed. Using a 15- $\mu\text{m}$ -thick film, they obtained extremely high surface charge density of more than  $2 \text{ mC m}^{-2}$ . They also reported that the surface potential of the nanocluster-enhanced electret is decreased only by a small percentage at  $100^\circ\text{C}$  for 2000 h, which is much better than PTFE or Teflon AF electrets.

Figure 8.14 shows the surface charge density and the surface potential for CYTOP (CTL-M) films of different thicknesses. While the surface potential is proportional to the film thickness (Eq. (8.18)), the surface charge density is decreased on increasing the film thickness. Thus, the surface potential levels off for thick films at around the film thickness of  $15 \mu\text{m}$ . This type of phenomena is common for most electret materials. Therefore, measurement of the surface charge density with the same film thickness is necessary for fair comparison among different materials. As will be shown later, the surface potential  $V_s$  should be the measure of electret performance, as the theoretical output power of electret generators is proportional to  $V_s^2$ .

### 8.5.3

#### Charging Technologies

Corona charging, thermal poling, contact charging, and electron-beam irradiation are often used for poling electrets [18]. Among them, corona charging (Figure 8.15a) is the most commonly used method. By attracting corona ions with the electrostatic field between the grid electrode and the substrate, charges are transferred from the ions to the electret surface. The surface potential of electrets after charging is usually the same as the grid voltage. It is noted that optimization of various parameters in corona charging such as the needle voltage, and the needle–grid and grid–sample distances is not a straightforward process



**Figure 8.15** Schematic of electret-charging methods. (a) A typical coronacharging system and (b) through-substrate soft-X-ray charging (Hagiwara *et al.*). Courtesy of Mr. K. Hagiwara.

and can be tricky. A backlighted thyratron (BLT) [24] and ion implantation using phosphorous/boron [29] are also used for charging tests.

Hagiwara *et al.* [30] developed a new charging method using photoionization, in which soft X-rays ionize gas molecules and the ions are attracted to the electret surface by an imposed electric field (Figure 8.15b). Since soft X-rays can penetrate substrates, electrets can be charged even in a narrow space or after packaging process. Hagiwara *et al.* [31] also examined soft-X-ray-charged CYTOP electrets, and found that the stability of these electrets is almost the same as that of corona-charged electrets. Honzumi *et al.* [32] also propose a high-speed charging method using vacuum UV-based photoionization.

#### 8.5.4

#### Electret Generator Model

Figure 8.16a and b shows a simplified model of the in-plane electret generator and its equivalent circuit, in which two capacitors (one for the electret and the other for the air gap) are connected in series. Charges with the opposite sign are induced on the counter electrode by the electrostatic field of the electrets, and the amount of the induced charges changes with the overlapping area between the electret and the counter electrode, generating an alternative current in the external circuit.

For simplicity, a rotational generator with  $n$  poles and total area  $A_0$  running at a rotational frequency of  $f$  is assumed, in which the rate of change in the overlapping area  $dA/dt$  is constant. By neglecting the parasitic capacitance  $C_p$ , Boland *et al.* [25] derived the following theoretical formula for the output power:

$$P = \frac{\sigma^2 d^2 R}{\left\{ \varepsilon_2 \varepsilon_0 R + \frac{1}{n A_0 f} (\varepsilon_2 g + \varepsilon_1 d) \right\}^2} \quad (8.19)$$

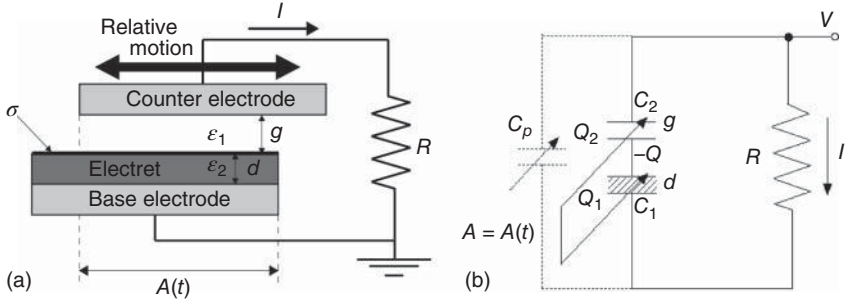


**Figure 8.16** Electret generator model. (a) Simplified model of the in-plane electret generator and (b) equivalent circuit.

where  $\sigma$ ,  $\epsilon_1$ ,  $\epsilon_2$ ,  $d$ , and  $g$  are the surface charge density of the electret, the relative permittivities of the air gap and the electret, the thickness of the electret, and the gap distance between the electret and the counter electrode, respectively. The optimum load  $R_i$  is

$$R_i = \frac{1}{\epsilon_0 n A_0 f} \left( \frac{g}{\epsilon_1} + \frac{d}{\epsilon_2} \right) \quad (8.20)$$

and the maximum power and the output voltage at the matched impedance are

$$P_{\max} = \frac{\sigma^2 \cdot n A_0 f}{4 \frac{\epsilon_2 \epsilon_0}{d} \left( \frac{\epsilon_2 g}{\epsilon_1 d} + 1 \right)} = \frac{\epsilon_0 V_s^2 \cdot n A_0 f}{4 \left( \frac{g}{\epsilon_1} + \frac{d}{\epsilon_2} \right)} \quad (8.21a)$$

$$V_{\max} = \frac{\sigma d}{2 \epsilon \epsilon_0} = \frac{V_s}{2} \quad (8.21b)$$

where Eq. (8.18) is used to replace  $\sigma$  with  $V_s$ . It can be seen in Eq. (8.21a) that the output power is proportional to the frequency  $f$  and the area  $A_0$ . On the other hand, in electromagnetic generators, the output power is proportional to  $(A_0 f)^2$ . Therefore, electret/electrostatic generators are superior to electromagnetic counterparts for small area and low operation frequency, which is usually true for vibration energy harvesters. In addition, the output voltage is independent of  $f$  or  $A_0$ , showing high output voltage of electret/electrostatic generators.

In Eq. (8.21a), as the output power is proportional to  $V_s^2$ , development of electret materials with high surface potential is crucial for larger output power. Note that Eq. (8.21a) overestimates the output power  $P_{\max}$  when the parasitic capacitance  $C_p$  has a finite value. In addition,  $R_i$  given by Eq. (8.20) overestimates the matched impedance.

Bartsch *et al.* [33] incorporated the effect of the parasitic capacitance for rotational generators and derived an analytical formula for output power:

$$P = \frac{d^2 \sigma^2 R}{\epsilon_2^2 \epsilon_0^2 (R + R_i)^3} \left\{ R + R_i - 4 C_p n f R R_i \tanh \left( \frac{R + R_i}{4 C_p n f R R_i} \right) \right\} \quad (8.22)$$

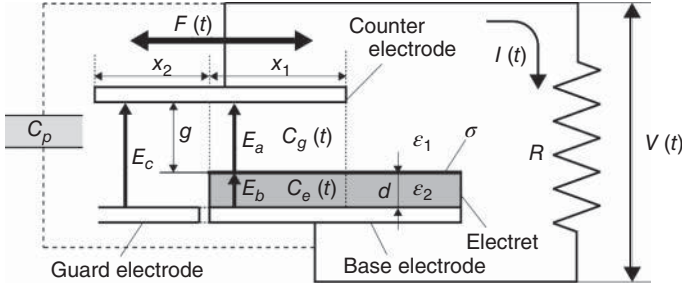


Figure 8.17 One-dimensional model of an in-plane electret generator.

They demonstrated that Eq. (8.22) can mimic the response of generators for different values of  $C_p$ . Equation (8.21a) is recovered by setting  $C_p = 0$  in Eq. (8.22). Note that both Eqs. (8.21ab) and (8.22) can only be applied to rotational generators, in which the rate of change in the overlapping area is constant. Therefore, for vibration generators, numerical simulation is required for quantitative prediction.

Figure 8.17 shows a generator model assuming the one-dimensional electrostatic field, in which a guard electrode is employed to reduce the parasitic capacitance  $C_p$ . The external load is assumed to be a pure resistance  $R$ . The length  $x_1$  represents the length of the overlapping area between the electret film and the counter electrode. The parasitic capacitance is assumed to be constant with time. Applying the Gauss's law at the electret surface, we get

$$-\epsilon_2 \epsilon_0 E_b + \epsilon_1 \epsilon_0 E_a = \sigma \quad (8.23)$$

where  $E_b$  and  $E_a$  are the electrostatic fields in the electret film and the air gap, respectively. Using the Kirchhoff's law, we obtain

$$V + dE_b + gE_a = 0 \quad (8.24)$$

and

$$V + (d + g)E_c = 0 \quad (8.25)$$

where  $V$  and  $E_c$  are respectively the output voltage and the electrostatic field between the counter electrode and the guard electrode.

The induction current  $I(t)$  is given by the conservation of charges:

$$\frac{d}{dt}(\sigma_{i1}bx_1 + \sigma_{i2}bx_2) + I(t) = 0 \quad (8.26)$$

where  $\sigma_{i1}$  and  $\sigma_{i2}$  are the induced charges on the counter electrode, which are given by

$$\sigma_{i1} = -\epsilon_1 \epsilon_0 E_a, \text{ and } \sigma_{i2} = -\epsilon_1 \epsilon_0 E_c \quad (8.27)$$

The quantity  $b$  represents the depth of the electrodes. Substituting Eqs. (8.23)–(8.25) and (8.27) into Eq. (8.26), a differential equation with respect to the output voltage  $V(t)$  is obtained, which can be solved numerically. For the

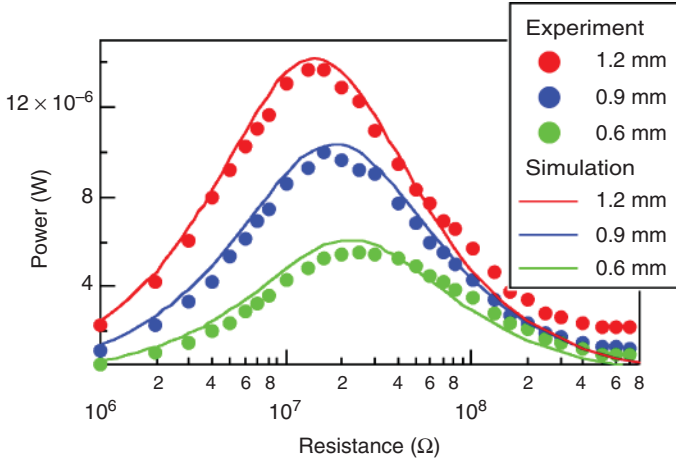


**Figure 8.18** Output power versus external load for vibration-driven electret generators [34].

length of the overlapping area  $x_1$ , a sinusoidal function with given amplitude and frequency is assumed.

Figure 8.18 shows the experimental data for the output power versus external load in comparison with the simulation results obtained using Eqs. (8.24)–(8.27) [34]. The electret and the counter electrode plates have dimensions of 20 mm × 20 mm, and the counter electrode plate is moved sinusoidally at 20 Hz in the in-plane direction. The oscillation amplitude is changed from 0.6 to 1.2 mm. The width of electret/electrode and the gap between the electret surface and the counter electrode are 300 and 70 μm, respectively. The surface potential of the electret film and the parasitic capacitance are −545 V and 30 pF, respectively. The peak value of the output power increases with the amplitude. The experimental data for different oscillation amplitudes are in good agreement with the numerical results, indicating the validity of the present generator model assuming a one-dimensional electrical field.

The electrostatic damping force in the in-plane direction can be examined as follows. Considering the conservation of energy, the work done by the external force  $F_e dx/dt$ , the power consumption at the load resistance  $V^2/R$  and the electrostatic potential energy  $E_s$  should satisfy

$$\frac{dE_s}{dt} + \left\{ \frac{V^2}{R} + C_p V \frac{dV}{dt} \right\} + F_e \frac{dx}{dt} = 0 \quad (8.28)$$

where  $F_e(t)$  is the force in the in-plane direction needed for the prescribed oscillation amplitude. The electrostatic potential energy  $E_s$  can be computed with  $E_a$ ,  $E_b$ , and  $E_c$ . Note that by integrating Eq. (8.28) with respect to time, the work done by the external force  $F_e dx/dt$  is equal to the electrical output power  $V^2/R$ .

With the conventional single-phase arrangement, in which all the electret/electrode strips overlap at the same time, the horizontal electrostatic

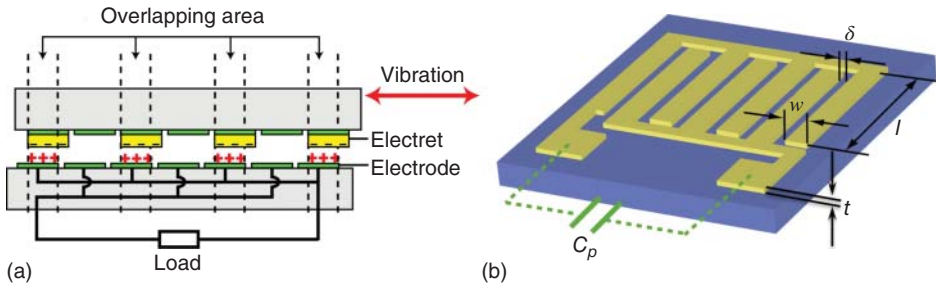


**Figure 8.19** Schematic of (a) in-plane two-plate electret generator and (b) fixed plate with interdigital electrodes.

damping force,  $F_e$ , exhibits a square waveform. This is typical for electrostatic generators classified as Coulomb-damped resonant generators (CDRGs) [7], in which the unidirectional Coulomb force is dominant. Suzuki *et al.* [35] proposed a dual-phase arrangement, in which half of the strips overlap 100% and the other half overlap 0%. With this approach, the unidirectional Coulomb force is almost canceled out, and  $F_e$  becomes mostly proportional to the mass velocity, which is similar to VDRG.

Figure 8.19a shows a typical configuration of in-plane two-plate electret generators, where guard electrodes are formed between the patterned electrets on the oscillating plate. On the fixed plate, two sets of interdigital electrodes are formed, and the induced current flows from one side to the other when the electret plate slides. With this approach, no electrical connection is required to the electret plate. Ideally, the electrical current in Figure 8.19a is doubled if compared with that in Figure 8.17. However, in practice, one side of the load in Figure 8.19a is grounded, and thus the two configurations are actually equivalent. As shown in Figure 8.19b, the interdigital electrodes inevitably introduce the build-in capacitance between two sets of electrodes, which has the main contribution to the parasitic capacitance  $C_p$ .

Chen and Suzuki [36] employ a parasitic capacitance model based on the analytical equation between two parallel conductive wires [37] as shown below:

$$\frac{C_p}{l} = \frac{\pi \epsilon_0 \kappa_{\text{eff}}}{\ln(\alpha + \sqrt{\alpha^2 - 1})} \quad (8.29a)$$

$$\alpha = \frac{\pi}{2} \cdot \frac{1 + \delta/w}{1 + t/w} \approx \frac{\pi}{2} \left(1 + \frac{\delta}{w}\right) \quad (8.29b)$$

where  $w$ ,  $\delta$ , and  $t$  denote the width, the gap, and the thickness of the electrode, respectively. The length  $l$  is the electrode length perpendicular to the sheet, while  $\epsilon_0$  and  $\kappa_{\text{eff}}$  are the vacuum permittivity and the effective relative permittivity. Since  $t/w \ll 1$ ,  $\alpha$  is a function of  $\delta/w$  only. However,  $\delta/w$  should be minimized to maximize the electrode area, so that  $C_p$  given by Eq. (8.29a) cannot be reduced by changing the electrode configurations. The only possible approach for reducing  $C_p$  is to reduce the effective permittivity  $\kappa_{\text{eff}}$ , which can be estimated as the mean

permittivity between the substrate and the gap (air), that is,

$$\kappa_{\text{eff}} = \frac{(1 + \kappa_s)}{2} \quad (8.30)$$

It is found in an electrical field analysis that the low permittivity layer underneath the electrode should have similar thickness as the electrode width (usually much larger than 100  $\mu\text{m}$ ). Thus, the conventional low- $k$  materials for semiconductor processes cannot be used for this purpose. Chen and Suzuki [36] propose suspended electrodes on a honeycomb polymer structure with a large void fraction of 76%. They obtained  $\kappa_{\text{eff}}$  as low as 1.8, which leads to 35% increase in the output power of the electret generator.

## 8.6

### Electret Generators

Chiu and Lee [38] and Takahashi *et al.* [39] separately developed an out-of-plane electret generator having a structure similar to that in Figure 8.4a. Boisseau *et al.* [40] prototyped a cantilever-shaped out-of-plane generator with a mass and an electrode on the cantilever tip. The advantage of this type of generators is that a plain electret layer can be used, by which charging issues for patterned electrets could be avoided. However, to suppress permanent stiction and to obtain higher output power with larger oscillation amplitude, device thickness is usually much larger than in-plane generators.

For in-plane electret generators with two-substrate approach as shown in Figure 8.6, a large electrostatic attractive force acts between the substrates owing to the high surface potential of the electret. Thus, gap control is crucial, as stiction should be avoided while keeping the gap on the order of 10  $\mu\text{m}$ .

Lo and Tai [26] developed an electret generator without tethers. The rotor can slide freely relative to the stator, and then induced charges on the electrodes vary with the position of the rotor. With a rotor coated with parylene HT electrets (5 mm  $\times$  6 mm  $\times$  9 mm), a maximum output power of 18  $\mu\text{W}$  was obtained at 50 Hz and acceleration.

Masaki *et al.* [41] developed an in-plane electret generator (20 mm  $\times$  20 mm  $\times$  4 mm) using a CYTOP EGG electret [42] as shown in Figure 8.20ab. They employ a low-friction mechanical support to keep the gap. They also devised a trench between the stripe-shaped electrodes to reduce the parasitic capacitance, and obtained output power as large as 100  $\mu\text{W}$  at 30 Hz and 0.15 g acceleration, which corresponds to effectiveness of about 20%.

Suzuki *et al.* [35] and Matsumoto *et al.* [43] developed a MEMS electret generator as shown in Figure 8.21. The top substrate consists of a Si proof mass (8.6 mm  $\times$  10.2 mm) supported by the 20- $\mu\text{m}$ -wide parylene high-aspect-ratio springs [44] for low resonant frequency. A nonlinear hardening spring enables large amplitude in the wide frequency range. Patterned electrets and electrodes in a dual-phase arrangement are formed on both the Si mass and the bottom



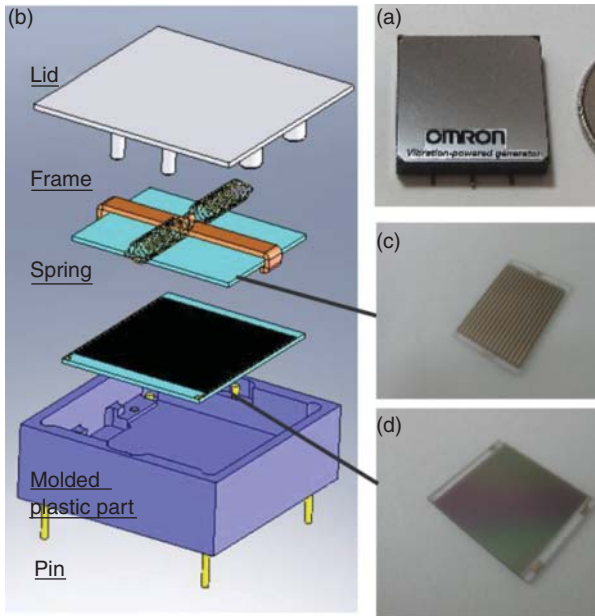


**Figure 8.20** In-plane electret generator fabricated with precision machining [41]. Courtesy of Dr. T. Seki.

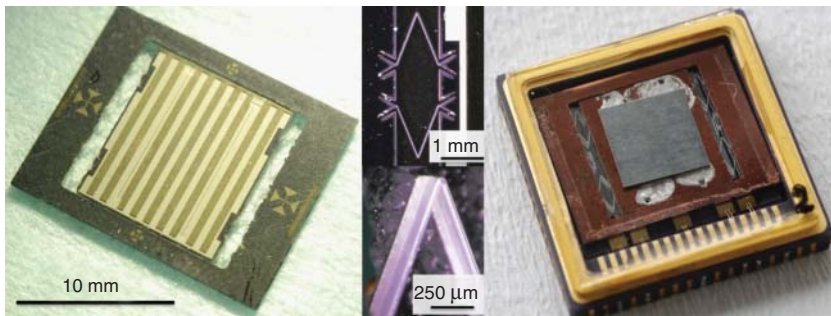


**Figure 8.21** In-plane electret generator with parylene high-aspect-ratio spring [35].

substrate. Electrostatic repulsive force using the patterned electret is used to keep the gap at around  $35\ \mu\text{m}$ . The width of the patterned electret and electrode is  $480\ \mu\text{m}$ . Up to output power of  $6\ \mu\text{W}$  is obtained at 40 Hz and  $1.4g$  acceleration, which corresponds to effectiveness of 1%. They also demonstrated intermittent radio frequency (RF) transmission using the output power of this generator.

Naruse *et al.* [45] used a micro-ball bearing to realize large amplitude oscillation in their electret generator. They employ  $\text{SiO}_2$ -based electrets with an air gap of  $38\text{--}57\ \mu\text{m}$ . By using an in-plane amplitude as large as 15 mm, they obtained an

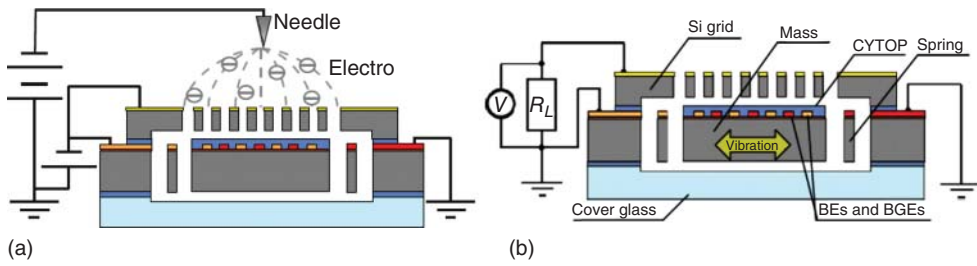


**Figure 8.22** In-plane electret generator with shared electrodes [47]. Connection for (a) corona charging and (b) power generation. Courtesy of Dr. T. Fujita.

output power of  $40 \mu\text{W}$  at a very low frequency vibration of 2 Hz at  $0.4g$  acceleration, which corresponds to effectiveness of 4%.

Charge density/stability of an electret is often deteriorated by patterning the electret layer. This is partially explained by the surface conduction along the electret [46]. Therefore, stripe-shaped charged electret without patterning the electret layer itself is also pursued.

Fujii *et al.* [47] developed an electret generator with a Si spring. They employ a plain CYTOP film on interdigital electrodes as the electret; during the corona charging, by applying the grid voltage to one side of the electrode, only the CYTOP film above the other side of the electrodes is charged (Figure 8.22). They also made slits in between the fixed electrodes, and used the slits as the grid. A maximum output power is  $0.23 \mu\text{W}$  at 10 Hz and  $0.1g$  acceleration.

Renaud *et al.* [48] developed a high-frequency electret generator with a Si spring. They first etch a Si substrate to form  $250 \mu\text{m}$ -wide striped-shaped recesses with a depth of  $100 \mu\text{m}$  and oxidized the substrate to form a corrugated surface with a  $\text{SiO}_2\text{-Si}_3\text{N}_4$  electret layer. The air gap and the maximum amplitude are  $10 \mu\text{m}$  and  $100 \mu\text{m}$ , respectively. They obtained output power up to  $160 \mu\text{W}$  at 728 Hz and  $2.9g$  acceleration, which corresponds to effectiveness of 14%.

Although comb drives are often used for electrostatic generators, corona charging cannot be applied, as the possible charge accumulation near the gap opening suppresses penetration of corona ions into the gap. Sterken *et al.* [49] employed electret for priming charge to the comb-drive capacitors, but the possible stiction due to electrostatic attractive force impedes this approach.

Suzuki *et al.* [50] used a bias-temperature method for drifting potassium ions in potassium-rich  $\text{SiO}_2$  electret at 700 K. They obtained up to 90 V surface potential on the comb finger. They also made the prototype of an in-plane overlapping-area-charge electret generator using this charging technology.

Fu *et al.* [51] used the soft-X-ray charging method [31] for in-plane comb-drive electret generator with a  $7\text{-}\mu\text{m}$ -wide gap. They confirmed that up to  $\pm 60$  V surface potential is obtained with the bias voltage of 130 V through the surface potential measurement using Kelvin force microscopy. Figure 8.23 shows their prototype using the SOI process (Figure 8.9a). They obtained up to  $1.6 \mu\text{W}$  at 266 Hz and  $2g$  acceleration. The effectiveness is as high as 57%.

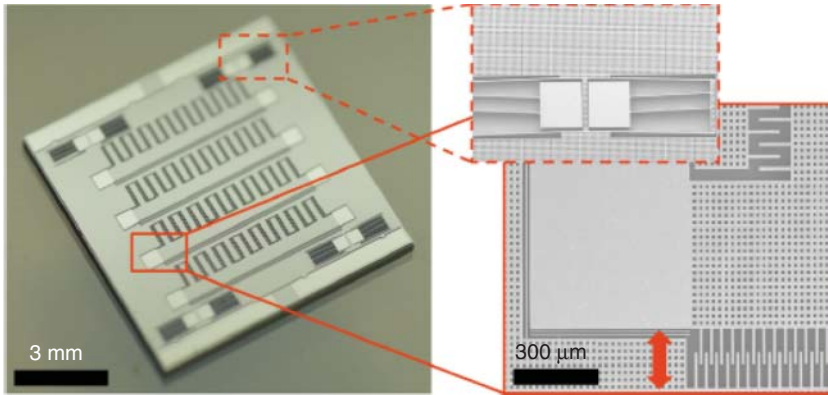


Figure 8.23 Soft-X-ray-charged in-plane electret generator [51].

## 8.7

### Summary

This chapter covers the principle, electrode design, modeling, fabrication, and device examples of electrostatic/electret generators. Although the power generation principle of electrostatic induction is straightforward, its application to energy harvesting requires a number of considerations in order to be practical, as described above.

The advantages of electrostatic/electret generators include freedom of spring material choice, high output voltage, and applicability to low-profile devices. In addition, as shown by recent prototypes, electrostatic/electret generators give high effectiveness more than 50% even in small volume or at low resonant frequency.

For most applications, electret generators are preferred as an external voltage source is not necessary, which makes “cold” start of the device possible. Recent development of new electret materials and charging methods is encouraging to adopt electret as the energy conversion principle for vibration energy harvesters.

### References

1. Roundy, S., Wright, P.K., and Rabaey, J. (2004) *Energy Scavenging for Wireless Sensor Networks*, Springer.
2. Suzuki, Y. (2011) Recent progress in MEMS electret generator for energy harvesting. *IEEE J. Trans. Electr. Electr. Eng.*, **6**, 101–111.
3. Meninger, S., Mur-Miranda, J.O., Amirtharajah, R., Chandrakasan, A.P., and Lang, J.H. (2001) Vibration-to-electric energy conversion. *IEEE Trans. Very Large Scale Integr. VLSI Syst.*, **9**, 64–76.
4. Basset, P., Galayko, D., Paracha, A.M., Marty, F., Dudka, A., and Bourouina, T. (2009) A batch-fabricated and electret-free silicon electrostatic vibration energy

- harvester. *J. Micromech. Microeng.*, **19**, 115025.
5. Hoffmann, D., Folkmer, B., and Manoli, Y. (2009) Fabrication, characterization and modeling of electrostatic micro-generators. *J. Micromech. Microeng.*, **19**, 094001.
  6. Hirano, T., Furuhashi, T., Gabriel, K.J., and Fujita, H. (1992) Design, fabrication, and operation of submicron gap comb-drive microactuators. *J. Microelectromech. Syst.*, **1**, 52–59.
  7. Mitcheson, P.D., Green, T.C., Yeatman, E.M., and Holmes, A.S. (2004) Architectures for vibration-driven micropower generators. *J. Microelectromech. Syst.*, **13**, 429–440.
  8. Bartsch, U., Trautmann, A., Ruther, P., Gaspar, J., and Paul, O. (2007) Electrostatic transducers for micro energy harvesting based on SOI technology. 14th International Conference on Solid-state Sensors, Actuators, and Microsystems (Transducers' 07), Lyon, France, pp. 141–144.
  9. Tvedt, L.G.W., Nguyen, D.S., and Halvorsen, E. (2010) Nonlinear behavior of an electrostatic energy harvester under wide- and narrowband excitation. *J. Microelectromech. Syst.*, **19**, 305–316.
  10. Nguyen, D.S., Halvorsen, E., Jensen, G.U., and Vogl, A. (2010) Fabrication and characterization of a wideband MEMS energy harvester utilizing nonlinear springs. *J. Micromech. Microeng.*, **20**, 125009.
  11. Basset, P., Galayko, D., Cottone, F., Guillemet, R., Blokhina, E., Marty, F., and Bourouina, T. (2014) Electrostatic vibration energy harvester with combined effect of electrical nonlinearities and mechanical impact. *J. Micromech. Microeng.*, **24**, 035001.
  12. Miao, P., Mitcheson, P.D., Holmes, A.S., Yeatman, E.M., Green, T.C., and Stark, B.H. (2006) MEMS inertial power generator for biomedical applications. *Microsyst. Technol.*, **12**, 1079–1083.
  13. Nguyen, S. D., Halvorsen, E., and Jensen, G. U. (2013) Wideband MEMS energy harvester driven by colored noise, *J. Microelectromech. Syst.*, Vol. **22**, pp. 892-900.
  14. Mitcheson, P.D., Yeatman, E.M., Rao, G.K., Holmes, A.S., and Green, T.C. (2008) Energy harvesting from human and machine motion for wireless electronic devices. *Proc. IEEE*, **96**, 1457–1486.
  15. Yang, B., Lee, C., Kotlanka, R.K., Xie, J., and Lim, S.P. (2010) A MEMS rotary comb mechanism for harvesting the kinetic energy of planar vibrations. *J. Micromech. Microeng.*, **20**, 065017.
  16. Eguchi, M. (1925) On the permanent electret. *Philos. Mag.*, **49**, 178.
  17. Takamatsu, T. (1991) Life time of thermal electrets of carnauba wax, esters, fatty acids and alcohols. 7th International Symposium on Electrets, Berlin, Germany, pp 106–110.
  18. Sessler, G.M. (1998) *Electrets*, 3rd edn, Laplacian Press.
  19. Jefimenko, O.D. and Walker, D.K. (1978) Electrostatic current generator having a disk electret as an active element. *IEEE Trans. Ind. Appl.*, **14**, 537–540.
  20. Tada, Y. (1992) Experimental characteristics of electret generator using polymer film electrets. *Jpn. J. Appl. Phys.*, **31**, 846–851.
  21. Sessler, G.M. (1997) Charge distribution and transport in polymers. *IEEE Trans. Dielectr. Electr. Insul.*, **4**, 614–628.
  22. Minami, T., Utsubo, T., Yamatani, T., Miyata, T., and Ohbayashi, Y. (2003) SiO<sub>2</sub> electret films prepared by various deposition methods. *Thin Solid Films*, **426**, 47–52.
  23. Chen, Z., Lv, Z., and Zhang, J. (2008) PECVD SiO<sub>2</sub>/Si<sub>3</sub>N<sub>4</sub> double layers electrets on glass substrate. *IEEE Trans. Dielectr. Electr. Insul.*, **15**, 915–919.
  24. Hsieh, W.H., Yao, T.J., and Tai, Y.-C. (1999) A High performance MEMS thin-film teflon electret microphone. 10th International Conference on Solid State Sensors Actuators (Transducers '99), Sendai, Japan, pp. 1064–1067.
  25. Boland, J., Chao, C., Suzuki, Y., and Tai, Y.-C. (2003) Micro electret power generator. 16th IEEE International Conference Micro Electro Mechanical Systems (MEMS'03), Kyoto, Japan, pp. 538–541.
  26. Lo, H.-W. and Tai, Y.-C. (2008) Parylene-based electret power generators. *J. Micromech. Microeng.*, **18**, 104006.

27. Sakane, Y., Suzuki, Y., and Kasagi, N. (2008) Development of high-performance perfluorinated polymer electret film and its application to micro power generation. *J. Micromech. Microeng.*, **18**, 104011.
28. Kashiwagi, K., Okano, K., Miyajima, T., Sera, Y., Tanabe, N., Morizawa, Y., and Suzuki, Y. (2011) Nano-cluster-enhanced high-performance perfluoro-polymer electrets for micro power generation. *J. Micromech. Microeng.*, **21**, 125016.
29. Mescheder, U., Müller, B., Baborie, S., and Urbanovic, P. (2009) Properties of SiO<sub>2</sub> electret films charged by ion implantation for MEMS-based energy harvesting systems. *J. Micromech. Microeng.*, **19**, 094003.
30. Hagiwara, K., Goto, M., Iguchi, Y., Yasuno, Y., Kodama, H., Kidokoro, K., and Tajima, T. (2010) Soft X-ray charging method for a silicon electret condenser microphone. *Appl. Phys. Express*, **3**, 091502.
31. Hagiwara, K., Goto, M., Iguchi, Y., Tajima, T., Yasuno, Y., Kodama, H., Kidokoro, K., and Suzuki, Y. (2012) electret charging method based on soft x-ray photoionization for MEMS applications. *IEEE Trans. Dielectr. Electr. Insul.*, **19**, 1291–1298.
32. Honzumi, M., Hagiwara, K., Iguchi, Y., and Suzuki, Y. (2011) High-speed electret charging method using vacuum UV irradiation. *Appl. Phys. Lett.*, **98**, 052901.
33. Bartsch, U., Sander, C., Blattmann, M., Gaspar, J., and Paul, O. (2009) Influence of parasitic capacitances on the power output of electret-based energy harvesting generators. 9th International Workshop Micro and Nanotechnology for Power Generation and Energy Conversion Applications (PowerMEMS 2009), Washington, DC, pp. 332–335.
34. Miki, D., Suzuki, Y., and Kasagi, N. (2009) Effect of nonlinear external circuit on electrostatic damping force of micro electret generator. 15th International Conference on Solid-state Sensors, Actuators, and Microsystems (Transducers' 09), Denver, CO, pp. 636–639.
35. Suzuki, Y., Miki, D., Edamoto, M., and Honzumi, M. (2010) A MEMS electret generator with electrostatic levitation for vibration-driven energy harvesting applications. *J. Micromech. Microeng.*, **20**, 104002.
36. Chen, R. and Suzuki, Y. (2013) Suspended electrodes for reducing parasitic capacitance in electret energy harvesting devices. *J. Micromech. Microeng.*, **23**, 125015.
37. Baxter, L.K. (1996) *Capacitive Sensors: Design and Applications*, John Wiley & Sons, Inc., New York, p. 15.
38. Chiu, Y. and Lee, Y.-C. (2013) Flat and robust out-of-plane vibrational electret energy harvester. *J. Micromech. Microeng.*, **23**, 015012.
39. Takahashi, T., Suzuki, M., Nishida, T., Yoshikawa, Y., and Aoyagi, S. (2013) A miniature harvester of vertical vibratory capacitive type achieving several tens microwatt for broad frequency of 20-40 Hz. 17th International Conference on Solid-state Sensors, Actuators, and Microsystems (Transducers' 13), Barcelona, Spain, pp. 1340–1343.
40. Boisseau, S., Despesse, G., Ricart, T., Defay, E., and Sylvestre, A. (2011) Cantilever-based electret energy harvester. *Smart Mater. Struct.*, **20**, 105013.
41. Masaki, T., Sakurai, K., Yokoyama, T., Ikuta, M., Sameshima, H., Doi, M., Seki, T., and Oba, M. (2011) Power output enhancement of a vibration-driven electret generator for wireless sensor applications. *J. Micromech. Microeng.*, **21**, 104004.
42. Kashiwagi, K., Okano, K., Miyajima, T., Sera, Y., Tanabe, N., Morizawa, Y., and Suzuki, Y. (2011) Nano-cluster-enhanced high-performance perfluoro-polymer electrets for micro power generation, *J. Micromech. Microeng.*, Vol. **21**, No. 125016.
43. Matsumoto, K., Saruwatari, K., and Suzuki, Y. (2011) Vibration-powered battery-less sensor node using electret generator. 11th International Workshop on Micro and Nanotechnology for Power Generation and Energy Conversion Applications (PowerMEMS 2011), Seoul, South Korea, pp. 134–137.
44. Suzuki, Y. and Tai, Y.-C. (2006) Micromachined high-aspect-ratio parylene spring and its application

- to low-frequency accelerometers. *J. Microelectromech. Syst.*, **15**, 1364–1370.
45. Naruse, Y., Matsubara, N., Mabuchi, K., Izumi, M., and Honma, K. (2009) Electrostatic micro power generator from low frequency vibration such as human motion. *J. Micromech. Microeng.*, **19**, 094002.
  46. Genda, T., Tanaka, S., and Esashi, M. (2005) Charging method of micropatterned electrets by contact electrification using mercury. *Jpn. J. Appl. Phys.*, **44**, 5062–5067.
  47. Fujii, K., Toyonaga, T., Fujita, T., Jiang, Y.G., Higuchi, K., and Maenaka, K. (2011) Electret based energy harvester using a shared Si electrode. 16th International Conference on Solid-state Sensors, Actuators, and Microsystems (Transducers' 11), Beijing, People's Republic of China, pp. 2634-2637.
  48. Renaud, M., Altena, G., Goedbloed, M., de Nooijer, C., Matova, S., Naito, Y., Tamakawa, T., Takeuchi, H., Onishi, K., and van Schaijk, R. (2013) High performance electrostatic MEMS vibration energy harvester with corrugated inorganic SiO<sub>2</sub>-Si<sub>3</sub>N<sub>4</sub> electret. 17th International Conference on Solid-state Sensors, Actuators, and Microsystems (Transducers' 13), Barcelona, Spain, pp. 693–696.
  49. Sterken, T., Fiorini, P., Baert, K., Puers, R., and Borghs, G. (2003) An electret-based electrostatic  $\mu$ -generator. 12nd International Conference on Solid-State Sensors, Actuators and Microsystems (Transducers '03), Boston, MA, pp. 1291–1294.
  50. Suzuki, M., Hayashi, H., Mori, A., Sugiyama, T., and Hashiguchi, G. (2012) Electrostatic micro power generator using potassium ion electret forming on a comb-drive actuator. 12nd International Workshop Micro and Nanotechnology for Power Generation and Energy Conversion Applications (PowerMEMS 2012), Atlanta, GA, pp. 247–250.
  51. Fu, Q. and Suzuki, Y. (2014) MEMS vibration electret energy harvester with combined electrodes. 27th IEEE International Conference Micro Electro Mechanical Systems (MEMS'14), San Francisco, CA, pp. 409–412.

## 9

# Electrodynamic Vibrational Energy Harvesting

*Shuo Cheng, Clemens Cepnik, and David P. Arnold*

This chapter provides an overview of the theory, design, and fabrication of energy harvesters that scavenge vibrational/motional energy using electrodynamic transduction. Electrodynamic transduction is a classic electromechanical energy conversion mechanism that relies on relative motion between magnets and electrical conductors. The basic operating principles of electrodynamic vibrational energy harvesting and a brief historical context are first introduced. A more detailed description of the electrodynamic transduction mechanism is then presented, followed by a classification scheme for categorizing different harvester architectures. Modeling and optimization techniques are also explained for device performance prediction and optimization. Practical design and fabrication tips for realizing high-performing electrodynamic energy harvesters are included, along with a summary and outlook of the field.

### 9.1

#### Introduction

Electrodynamic vibrational energy harvesters employ mechanisms that translate external environmental vibrations into relative motions between magnets and electrical conductors. Energy is converted on the basis of the change of the magnetic flux in a coil. Specifically, the internal motions “induce” an electric potential (voltage), called an *electromotive force* or *emf*, across the coil conductors. This phenomenon is known as Faraday’s law of induction. When the conductors are connected to an external load, an electric current flows, and energy is supplied from the harvester. This flow of current incites a mechanical reaction force, described by the Lorentz force acting on a current-carrying wire. Further mathematical description of these physics is reserved for Section 9.2.

Figure 9.1 shows a schematic diagram of a typical electrodynamic vibrational energy harvester. It comprises a one degree-of-freedom mass-spring resonator in a frame that is attached to the vibrating surface (the base). A permanent magnet serves as an inertial proof mass, and a coil-shaped conductor is attached to

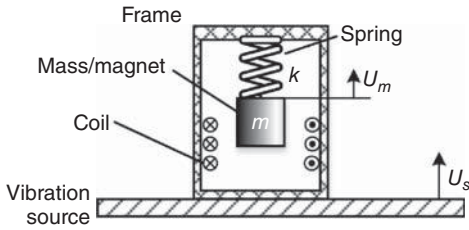


**Figure 9.1** Schematic drawing of a canonical resonant-type electrodynamic energy harvester.

the frame. During operation, when the base is externally excited, the resonator works in the base excitation mode. The base vibration creates a relative motion between the magnet and the coil. As the magnet moves, the magnetic flux in the coil changes over time. According to Faraday's law, a voltage is generated across the coil, which is proportional to the time rate change of the magnetic flux. When a load is connected to the coil, current will flow from the harvester to the load, and electric power is delivered.

In practice, there are numerous variations to the canonical configuration as shown in Figure 9.1. For example, the spring may be absent, leaving the magnets sliding freely in the frame, as found in “shake-powered” consumer flashlights, similar the one shown in Figure 9.2. Another variation is that the coil may be used as the moving mass, and the magnet may be affixed to the frame. Other designs and a more systematic classification of harvester architectures are discussed in Section 9.3.

Compared to piezoelectric or electrostatic harvesters, electrodynamic vibrational energy harvesters have the advantage of lower electrical output impedance, yielding maximum power delivery with loads typically in the ohm to kilohm range. Another advantage is that they are purely passive, requiring no external voltage supply to operate. The electrodynamic architecture is also known to be highly robust and scalable across different size/power regimes. Furthermore, because the operating principles are similar to rotating permanent magnet machines, one can leverage the vast knowledge, materials, manufacturing processes, and machine design guidelines that have accrued over the last century.

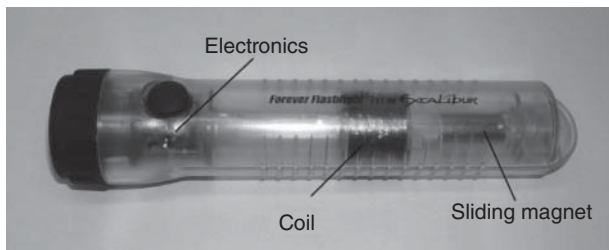


**Figure 9.2** A picture of shake-powered flashlight [1].



The fundamentals of electrodynamic energy conversion were discovered nearly two centuries ago. It all began with the breakthrough discovery of electromagnetism in 1820 by Hans Christian Ørsted, a Danish physicist. Ørsted noted the deflection of a compass needle when in proximity to current-carrying wires, and further systematic investigation confirmed the link between electricity and magnetism. One year later, British inventor Michael Faraday demonstrated the continuous circular motion of a current-carrying wire around a magnet, often accredited as the first electric motor. This experiment showcased the first important principle of electrodynamic transduction, namely, the electromagnetic force acting on a current-carrying wire. However, an accurate mathematical description was not formalized until nearly 70 years later in 1889 by English mathematician Oliver Heaviside. Three years later in 1892, the Dutch physicist Hendrik Lorentz provided a unifying vector formula combining the magnetic and electric forces acting on a charged particle, known today as the *Lorentz force*.

The second important principle for electrodynamic transduction is the phenomenon of electromagnetic induction, which is generally credited to Faraday in 1831. Records suggest that American scientist Joseph Henry may have independently demonstrated induction earlier in 1830, but did not immediately publish his findings. There is also evidence that Italian physicist Francesco Zantedeschi may have discovered induction even earlier in 1821. Nevertheless, the mathematical formula describing this phenomenon is today known as *Faraday's Law*. This law, together with the Lorentz force, describes the electrodynamic conversion from mechanical to electrical energy and vice versa.

Since the nineteenth century, many types of motors and generators have been built using these principles. The vast majority have been rotational-type machines, spanning from tiny motors in toys to gigantic generators found in hydroelectric power plants. Linear motors and generators received far less attention until the mid 1990s. Then, motivated by the higher efficiency of power electronic circuits and emerging application areas such as energy harvesting, research was accelerated on linear generators and other new types of architectures.

The use of electrodynamic transduction for energy harvesting can be traced back to the self-powered SEIKO AGS Kinetic Quartz Watch introduced in 1988 [2, 3]. In addition, the first resonant-type vibrational energy harvester device, published by Williams and Yates in 1995 [4], also used electrodynamic transduction. Since then, research groups all over the world have published hundreds of papers on electrodynamic energy harvesting prototypes intended for many different applications, such as machine vibrations and human motion. Stand-alone electrodynamic energy harvesters are even now commercially available [5–8], as shown in Figure 9.3.

While a sampling of different devices and architectures will be discussed in Section 9.3, the reader is directed to review papers by Mitcheson *et al.* [9–11], Arnold [12], Beeby *et al.* [13], Khaligh *et al.* [14], Paulo and Gaspar [15], Zhu *et al.* [16], and Cepnik *et al.* [17] for a broader of the field of energy harvesting.

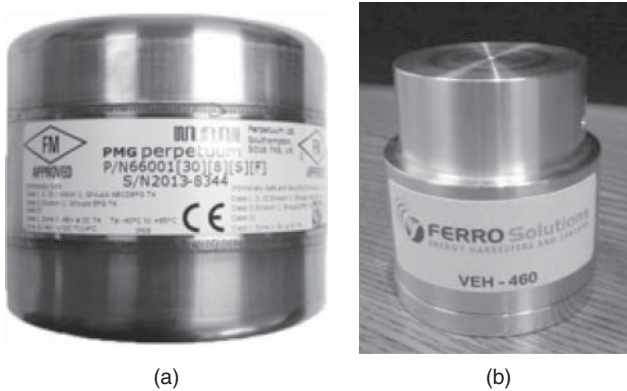


**Figure 9.3** Commercial electrodynamic vibrational energy harvesting devices: (a) Perpetuum, Ltd. and (b) Ferro Solutions, Inc.

## 9.2

### Theoretical Background

In this section, the core working principle of electrodynamic vibrational energy harvesters is explained along with a mathematical description of the physics of electrodynamic transduction.

#### 9.2.1

##### Energy Storage, Dissipation, and Conversion

From an energy perspective, an electrodynamic harvester can be described as a system of energy storage elements, energy dissipation elements, and an electromechanical energy conversion element (converting energy between the electrical and mechanical domains). The energy storage and dissipation mechanisms can occur in both the mechanical and electrical domains.

In operation, the harvester absorbs mechanical energy from the environment, converts or “transduces” this energy into electrical energy, which is delivered to the electrical load. The absorbed energy must pass through the harvester with a positive net flow toward the load. In practice, this energy conversion chain is not perfect. A portion of the mechanical energy absorbed by the harvester is not immediately converted; it remains as mechanical energy in the form of kinetic energy associated with the moving mass or potential energy stored in the spring. Some mechanical energy is also lost owing to friction or other mechanical loss mechanisms. A portion of the absorbed mechanical energy, however, is converted into electrical energy whenever there is a change in magnetic flux in the coil. Some of this converted electrical energy is stored in the magnetic field of the coil and some is lost as ohmic dissipation in the coil. The remaining energy is ultimately delivered to the electrical load and represents the net “generated” electrical energy. A more detailed model of these processes is described in Section 9.4.

## 9.2.2

## Electrodynamic Physics

There are two fundamental physical interactions that describe the electromechanical energy transfer of electrodynamic transduction. In modern physics, these two interactions are generally known as *Faraday's law of induction* and the *Lorentz force*. Each is described more fully below.

## 9.2.2.1 Faraday's Law

Faraday's law of induction describes the induced voltage (emf)  $V_{\text{emf}}$  that arises with the time-varying magnetic flux through a coil. For a single-turn coil,

$$V_{\text{emf}} = -\frac{d\Phi}{dt} = -\frac{d}{dt} \left( \int_S \vec{\mathbf{B}} \cdot d\vec{\mathbf{s}} \right) \quad (9.1)$$

where  $\Phi$  is the flux through the coil, defined by the integration of the magnetic flux density  $\vec{\mathbf{B}}$  passing through the surface  $S$ . By applying the chain rule to the derivative, this voltage can be further expanded into a sum of two terms [18]

$$V_{\text{emf}} = \underbrace{-\int_S \frac{\partial \vec{\mathbf{B}}}{\partial t} \cdot d\vec{\mathbf{s}}}_{\text{transformer}} + \underbrace{\oint_C (\vec{\mathbf{U}} \times \vec{\mathbf{B}}) \cdot d\vec{\ell}}_{\text{motional}} = V_{\text{emf}}^{\text{tr}} + V_{\text{emf}}^m \quad (9.2)$$

where  $\vec{\mathbf{U}}$  is the velocity of the coil defined by the contour  $C$ . The “transformer emf” describes the voltage induced by a time-varying magnetic field acting on a stationary coil, whereas the “motional emf” describes the voltage induced by the coil moving in a static magnetic field. The voltage induced in a multi-turn coil would be computed as the linear sum of the voltages induced in each turn.

In a vibrational energy harvester, the determination of whether the field is changing or the conductor is moving is all based on perspective. Consider the canonical harvester shown schematically in Figure 9.4, with a duck standing on the magnet, and a rabbit standing on the coil. In operation (base excitation), both the magnet (duck) and the coil (rabbit) are moving relative to the laboratory reference frame. However, from the perspective of the duck, the coil is moving

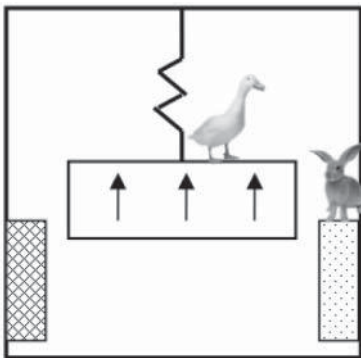


**Figure 9.4** Cartoon illustrating the different perspectives for calculating the induced voltage from Faraday's law. The duck perceives a coil moving in a static magnetic field, whereas the rabbit perceives a time-varying magnetic field acting up a stationary coil.

in a static magnetic field; hence the voltage should be calculated using the motional emf. Conversely, from the perspective of the rabbit, the magnetic field acting on the coil is changing; hence the voltage should be calculated using the transformer emf.

Which perspective is right? Indeed, either is correct. The problem could be solved with either equation, and the numeric answer would be the same in both cases. This leads to an interesting, yet fairly generalizable conclusion: most electrodynamic interactions can be solved using either the transformer emf equation or the motional emf equation. Typically, solving the motional emf equation is much easier, as it involves a 1-D line integral, as opposed to a 2-D surface integral in the case of the transformer equation.

From here onward, the motional emf will be defined as

$$V_{\text{emf}} = \oint_{\ell_{\text{coil}}} (\vec{U} \times \vec{B}) \cdot d\vec{\ell}, \quad (9.3)$$

where  $\ell_{\text{coil}}$  is the contour of the coil.

### 9.2.2.2 Lorentz Force

The Lorentz force describes the electromagnetic forces acting on charged particles. For a discrete charged particle with charge  $q$  and velocity  $\vec{U}$ , the total force is the superposition of forces arising from the electric field  $\vec{E}$  and magnetic field  $\vec{B}$ ,

$$\vec{F}_{\text{particle}} = \vec{F}_{\text{elec}} + \vec{F}_{\text{mag}} = q\vec{E} + q(\vec{U} \times \vec{B}) \quad (9.4)$$

Electrodynamic transduction is only concerned with the magnetic term. A current-carrying conductor represents a flow of negatively charged electrons. Hence, the net magnetic force on the conductor is expressed by the integration of the forces from all the electrons within the wire. Assuming a filamentary conductor carrying electrical current  $I$ , the equation is given as

$$\vec{F}_{\text{mag}} = I \oint_{\ell_{\text{coil}}} d\vec{\ell} \times \vec{B} \quad (9.5)$$

### 9.2.3

#### Simplified Electrodynamic Equations

The Faradaic induction (linking voltage and velocity) and Lorentz force (linking current and force) interactions are graphically illustrated in Figure 9.5. When functioning as a generator as in the case of an energy harvester, the force and velocity are in opposite directions (mechanical energy absorbed), and electric current flows out of the positive terminal (electrical energy supplied), as depicted.

In the case of Faradays law, consider a coil segment moving in a transverse direction (perpendicular to the conductive path) with velocity magnitude  $U$ . In this case, the voltage is given by the simple expression

$$V_{\text{emf}} = B_{\text{avg}} \ell_{\text{coil}} U \quad (9.6)$$

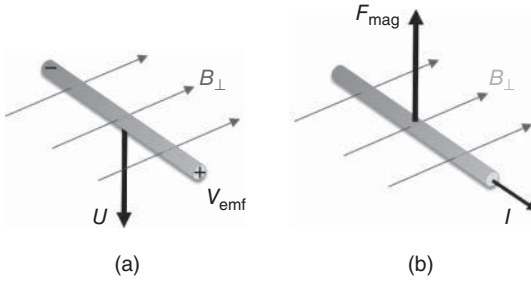


**Figure 9.5** Schematics showing (a) voltage/velocity and (b) current/force relationships for electrodynamic transduction.

where  $B_{avg}$  is the magnitude of the average orthogonal magnetic flux density, defined as

$$B_{avg} = \frac{1}{\ell_{coil}} \int_{\ell_{coil}} B_{\perp} d\ell \quad (9.7)$$

and  $B_{\perp}$  is the magnitude of the B-field in the direction orthogonal to both the conductive path and the velocity. Simultaneously, there is an electromagnetic force in direct opposition to the velocity given by

$$F_{mag} = B_{avg} \ell_{coil} I \quad (9.8)$$

Equations (9.6), (9.7), and (9.8) define the electrodynamic link between the mechanical and electrical domains. The proportionality term

$$K = B_{avg} \ell_{coil} \quad (9.9)$$

is common to both equations, where  $K$  is known as the *electrodynamic transduction coefficient*.

In a linear time-invariant model, it is assumed that  $K$  is constant in time, that is, the magnetic field or coil length does not change with any motion of the coil. In an energy harvester, this assumption holds true for small relative motions. But in cases of large motion, a time-dependent  $K$  must be considered.

### 9.3

#### Electrodynamic Harvester Architectures

A wide variety of electrodynamic harvester designs and architectures are possible. In this section, different types of harvesters are introduced, and a framework is presented for categorizing them on the basis of external excitation conditions and internal device constructions.

First, electrodynamic energy harvesters can be distinguished on the basis of the excitation for which they are designed. As shown in Figure 9.6, there are two main aspects, the type of excitation and its temporal characteristics. Most energy harvesting research efforts have focused on simple, one-dimensional vibrations. Such vibrations can be found in many places, for example, in buildings, on machines, or

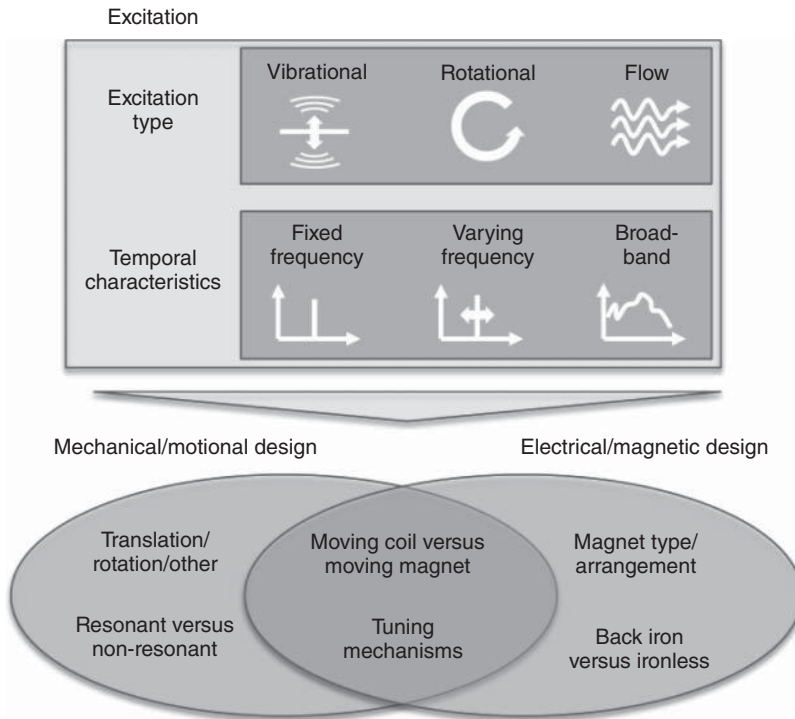


**Figure 9.6** Framework for categorizing electrodynamic harvesters.

on moving objects [19, 20]. Rotating motions are also widely available, but far less explored [21]. Another excitation type that has inspired significant creativity is air flow, for example, in air ducts or even around buildings [8, 22, 23]. Harvesting from natural human movements has also been explored [24, 25] and such movements often comprise linear and rotational accelerations in all three dimensions.

In addition to their excitation types, vibrations or other motional sources can be distinguished by their temporal characteristics. The simplest type is single-frequency harmonic oscillation, that is, purely sinusoidal vibrations [26]. Much more complicated are excitations with time-varying, multitone, or broadband frequency contents [16]. In order to harvest from a time-varying harmonic vibration, tuning mechanisms can be used to alter the resonant behavior of the harvester, for example, see Ref. [27]. Harvesting from predefined multiple tonal frequencies can be realized by cascading multiple harvesters with different resonance frequencies. Harvesting from broadband excitations can be possible by utilizing inherent nonlinearities in the mechanical design. Research in the field of broadband harvesting is still in its infancy and investigations are ongoing.

Harvesters can be further categorized according to their internal electromechanical design. The goal of any electrodynamic architecture is to transform an external motion into an internal relative motion that changes the magnetic flux in a coil. The simplest approach is to use a sliding or rolling mass that moves because

of its inertia within an excited housing [24]. However, to realize an amplified internal motion, resonant-type designs are commonly used. These designs employ a moving mass and a restoring force, which function as mass-spring (-damper) system. Here, different types of restoring forces have been explored. Most harvesters use spring-like mechanical flexures, such as beams or membranes, for example, see Ref. [28, 29]. An alternative is the use of repulsive forces between opposing magnets to create “magnetic springs” [30]. A third type of restoring force is the use of gravity for pendulum-type motion [31, 32], but this type of behavior cannot be described by a simple mass-spring(-damper) system.

Special attention should also be given to the mechanisms used to convert flow into a defined relative motion. One approach is to employ small windmill-like harvesters and a rotating machine for energy conversion [22]. Additionally, clever mechano-fluidic designs can be used to excite oscillating or flapping-type responses [8, 23].

Criterion to distinguish harvesters is whether the coil, the magnet, or both components are movable. Architectures that employ moving magnets must consider potential unwanted eddy current generation (and damping) in nearby metal structures. Furthermore, harvesters can be differentiated by the design of the magnetic circuit, that is, the permanent magnet(s) and soft magnetic back iron(s) used to shape the magnetic flux path. Most commonly, a single permanent magnet is used with no back iron, having the key advantage of simplicity. In this case, the magnetic flux is not guided and the flux densities realized within the coil are usually comparatively lower. In addition, a significant magnetic field penetrates other parts of the harvester and the surroundings such that eddy currents can be significant, and the corresponding magnetic forces can change the dynamic behavior. At the other extreme is a complex magnetic circuit with multiple magnets and back irons to shape and concentrate the magnetic field. The design and manufacture of such structures is obviously more complicated, and requires more components, and hence cost. This complication and expense may be warranted in exchange for higher performance.

Some common magnetic circuit designs are shown in Figure 9.7. Design (a) is known as the *voice-coil architecture* and is commonly used in loudspeakers, or, for example, see Ref. [33]. Design (b) follows the design of the head actuator in hard drives [34, 35] and was first used in energy harvesting by the group of Beeby [36]. Design (c) uses opposing magnets to create a strong radial flux and was used in [37] (without the back iron spacer). Design (d) shows a one-sided flux array, known as the *Halbach array* [38], which has been utilized in [23].

## 9.4

### Modeling and Optimization

This section describes different approaches to model electrodynamic harvesters. Attention is then given to describing key objectives for maximizing the output power, and hence performance, of an electrodynamic energy harvesting device.

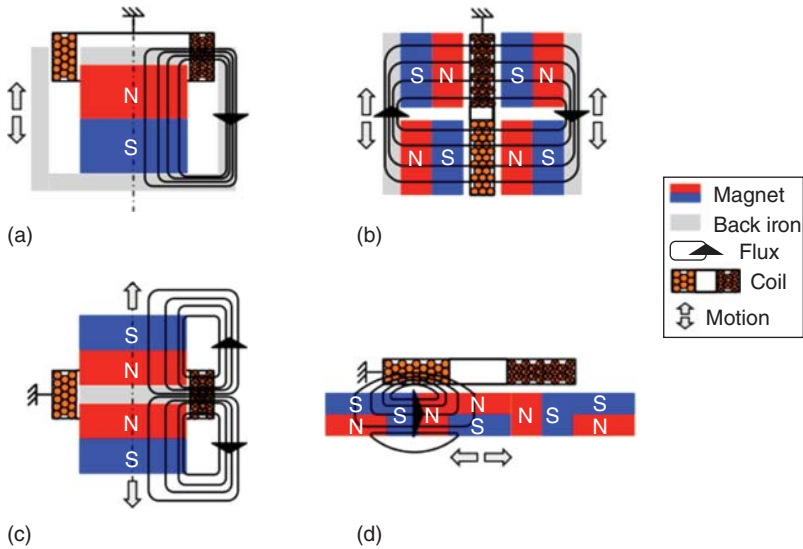


**Figure 9.7** Different configurations of electrodynamic transduction, a) voice-coil, b) head actuator, c) opposing magnet and d) Halbach array architecture.

#### 9.4.1

##### Modeling

Modeling provides the tools necessary for predicting the harvester performance and hence enabling systematic design and optimization. Two complementary modeling techniques are commonly used for electrodynamic harvesters: the lumped element method and the finite element method. The lumped element method is a simple and effective approach, which provides an analytic description of the physics of the system. The system behavior is defined by equations that are calculated from engineering design variables such as geometries and material properties. The lumped element method hence provides physical insight of the system and provides an ideal framework for design and optimization. Conversely, the finite element method is a numerical modeling approach that provides more accuracy for more specific problems. Table 9.1 summarizes the advantages and recommended usage of lumped element method and finite element method. Both methods will be introduced for the purpose of modeling electrodynamic energy harvesters. In addition, a hybrid approach will be presented that combines the two methods.

##### 9.4.1.1 Lumped Element Method

The lumped element method divides a multi-energy-domain physical system into discrete elements based on the energy interactions in the system. Each element has one or more “ports,” through which it exchanges energy with other elements. The energy transfer rate (power) into or out of a port is described by the product of an effort variable and a flow variable acting on that port. For example, in the



**Table 9.1** An overview of the lumped element method and finite element method.

	Lumped element model	Finite element model
Advantages	<ul style="list-style-type: none"> <li>• Simple and fast</li> <li>• Provides analytic expressions based on design variables</li> <li>• Enables physical insight</li> <li>• Easy interfacing with complex electronic loads</li> </ul>	<ul style="list-style-type: none"> <li>• Accurate and versatile</li> <li>• Provides spatially distributed field solutions</li> <li>• Accommodates material nonlinearities</li> </ul>
Suggested uses	<ul style="list-style-type: none"> <li>• System-level model</li> <li>• Design-oriented modeling</li> </ul>	<ul style="list-style-type: none"> <li>• Estimation of physical parameters</li> <li>• Detailed design evaluation</li> </ul>

electrical domain, voltage is an effort variable, and current is a flow variable. In the mechanical domain, force is the effort variable, and velocity is the flow variable. Effort and flow variables are called *conjugate power variables* of the system.

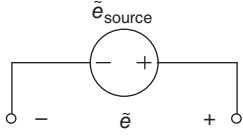
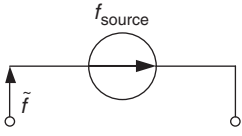
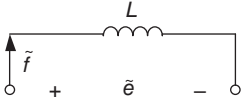
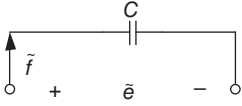
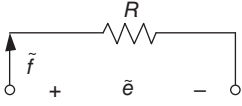
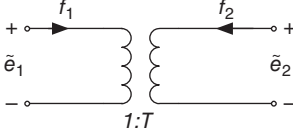
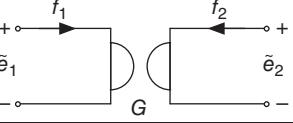
There are five common one-port elements: effort source, flow source, dissipater (resistor), compliance (capacitor), and inertance (inductor). Their behaviors are summarized in Table 9.2. Two common energy-conserving two-port elements – the transformer and gyrator – are also summarized. The reader is directed to [39–41] for more detail on the lumped element modeling approach.

In this chapter, electrical circuits are used to represent the lumped element model, and an impedance analogy is assumed. “Effort” in any energy domain is represented by a voltage, and “flow” is represented by current. Elements that share the same effort are connected in parallel, while those that share the same flow are connected in series. In this way, a multi-energy-domain system can be expressed using a single-domain, circuit representation. This equivalent circuit can be analyzed using basic circuit analysis techniques or simulated with standard circuit simulation tools (e.g., PSPICE) for convenient analysis and design.

To illustrate the modeling process, the canonical electrodynamic harvester shown previously in Figure 9.1 is used for reference. Conceptualization of the model follows the energy transfer behavior described in Section 9.2.1. The equivalent circuit for the harvester is shown in Figure 9.8, which is briefly described below. For more detailed descriptions and experimental validations of the lumped element model for electrodynamic energy harvesters, readers are directed to [42].

The model involves electrical and mechanical domains, which are coupled by electrodynamic transduction. The mechanical domain models the mechanical components of the harvester (e.g., mass, spring, and damper) and provides a mechanical input port to which is connected a vibration source. The electrical domain models the electrical components (e.g., resistance, inductance of the coil) and provides an electrical output port to which is connected power electronic circuits and/or energy storage devices. The two domains are coupled by a gyrator, which represents the electrodynamic transduction.

**Table 9.2** List of general representations of elements in a lumped element model.

Element	Symbol	Characteristic equation
Effort source		$\tilde{e} = \tilde{e}_{source}$
Flow source		$\tilde{f} = \tilde{f}_{source}$
Inertance		$\tilde{e} = L \frac{d\tilde{f}}{dt}$
Compliance		$\tilde{f} = C \frac{d\tilde{e}}{dt}$
Dissipator		$\tilde{e} = R\tilde{f}$
Transformer		$\tilde{e}_2 = T\tilde{e}_1$ $\tilde{f}_2 = -\frac{1}{T}\tilde{f}_1$
Gyrator		$\tilde{e}_2 = G\tilde{f}_1$ $\tilde{f}_2 = -\frac{1}{G}\tilde{e}_1$

In vibrational energy harvesting, it is customary to assume that the mass of the vibration source is much greater than that of the harvester, and that the mechanical connection between the vibration source and the harvester is perfectly rigid. Under these conditions, an ideal flow source of velocity  $U_s$  can be used to model the vibration source. This velocity represents the motion of the frame (and coil) in the laboratory reference frame. The velocity  $U_m$  represents the velocity of the magnet, again in the laboratory reference frame. The term  $U_r = U_s - U_{mss}$  represents the *relative* velocity between the magnet and the frame, and is the key parameter of the spring and also the damping velocity. Therefore, as shown in Figure 9.8, the model consists of current source that represents the vibration base velocity, an inductor that represents the mass of the magnet  $m$ , a capacitor that represents the compliance of the spring  $1/k$  ( $k$  is the spring constant), and a resistor that

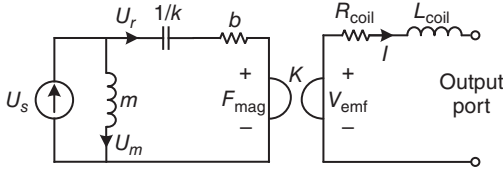


**Figure 9.8** A circuit representation of the electrodynamic vibrational energy harvester lumped element model.

represents the mechanical damping  $b$  (with a unit of N·s/m, not to be confused with the dimensionless damping ratio).

According to the electrodynamic transduction principle explained in Section 9.2.3, relative motion between the magnet and the coil induces a voltage  $V_{\text{emf}}$  on the coil, which is proportional to the relative velocity by the electrodynamic transduction coefficient  $K$ . Meanwhile, the electric current in the coil  $I$  creates a mechanical force  $F_{\text{mag}}$  that attempts to resist the relative motion, and this force is proportional to the current by the same factor  $K$ . These two equations, which phenomenologically describe electrodynamic transduction, are represented by a gyrator with gyration resistance  $K$ .

The electrical part of the model represents the electrical energy storage/dissipation of the coil. The coil can be simply represented by a resistor  $R_{\text{coil}}$  and an inductor  $L_{\text{coil}}$  connected in series. For the low operating frequencies of a vibrational energy harvester, the impedance associated with the capacitance of the coil is typically so small that it can be ignored. The voltage across the electrical output port of the lumped model represents the open-circuit voltage across the terminals of the coil. Various electric loads can be connected to this port.

As an example of the utility of the lumped model, consider the vibration source to be a sinusoidal source with velocity amplitude  $U_s$  and angular frequency  $\omega_s$  (equivalently, an acceleration amplitude  $A_s = U_s \omega_s$  and displacement amplitude of  $X_s = U_s / \omega_s$ ). Furthermore, consider a simple resistive load that is connected to the output port of the harvester, and assume that the coil inductance can be ignored (true for most applications). Basic circuit analysis techniques can be used to derive the conditions and the expression for maximum time-average load power. It can be shown that the maximum load power is obtained when the source excitation frequency  $\omega_s$  matches the natural frequency  $\omega_n$  of the mass-spring resonator,

$$\omega_s = \omega_n = \sqrt{\frac{k}{m}} \quad (9.10)$$

and the load resistance matches the output resistance of the energy harvester,

$$R_{\text{load}} = R_{\text{coil}} + \frac{K^2}{b} \quad (9.11)$$

When both conditions apply, the time-average load power is given by [42, 43]

$$P_{\text{avg}} = \frac{m^2 A_s^2}{8b \left(1 + \frac{R_{\text{coil}} b}{K^2}\right)} \quad (9.12)$$

This equation shows how the power scales with the input vibration and harvester system parameters.

There are some other possible extensions to the simple linear model described above. First, in the case that the vibration source and/or the interface between the source and the harvester is more complicated (e.g., the source mass is comparable to that of the harvester, the interface having finite compliance), the source of the model can be changed to reflect reality. For example, in order to model the vibration source with finite mass, the flow source can be replaced with an effort source in series with a generalized inertance. The second possible extension is that nonlinear components can be incorporated in the model to represent nonlinear spring, damping, or position-dependent transduction coefficient [44].

#### 9.4.1.2 Finite Element Method

The lumped element method provides a good system-level description of a device. However, it is often necessary to obtain more detailed spatially distributed field information, for example, stress/strain distribution of the spring or magnetic flux density around the magnets and the coils. The finite element method can be used to generate and analyze such information. The finite element method is a numerical technique used to find approximate solutions for partial differential equations with known boundary conditions. It can be used to solve physical problems that involve complicated shapes, nonlinear material properties, or other conditions where analytical approaches are impractical.

In finite element models, the system is divided into subdomains. Each subdomain is governed by a set of differential equations that describe its physical behavior. The subdomains are then spatially “meshed” into a large number of discrete, interconnected elements. These elements are similar to those in the lumped element model, in that the physical properties within each element are assumed to have simple spatial variations, for example, linear variation across the element. Equations that describe the behavior and connectivities of the elements are then combined to form a global set of equations for the system. An approximate solution of the equation set can be found by using various algorithms. The reader is directed to [45, 46] for more detail on the finite-element modeling approach.

There are several key advantages of using the finite element method for design. First, finite element models can accurately solve problems with complex geometries and material compositions. This is very useful in simulating the performance of a real-world energy harvester where complex components are involved. Figure 9.9 shows the simulated magnetic flux density of the magnetic structure in Figure 9.7c. It clearly demonstrates that the radial component of the magnetic flux density is concentrated around the air gap between the two opposing magnets, where the coil is placed. Estimation of the transduction coefficient is much easier and more accurate using the finite element method than using analytical methods. Second, it is relatively convenient to estimate parasitic effects in the system. For example, the finite element model can be used to estimate the parasitic magnetic force between the magnet and the environmental

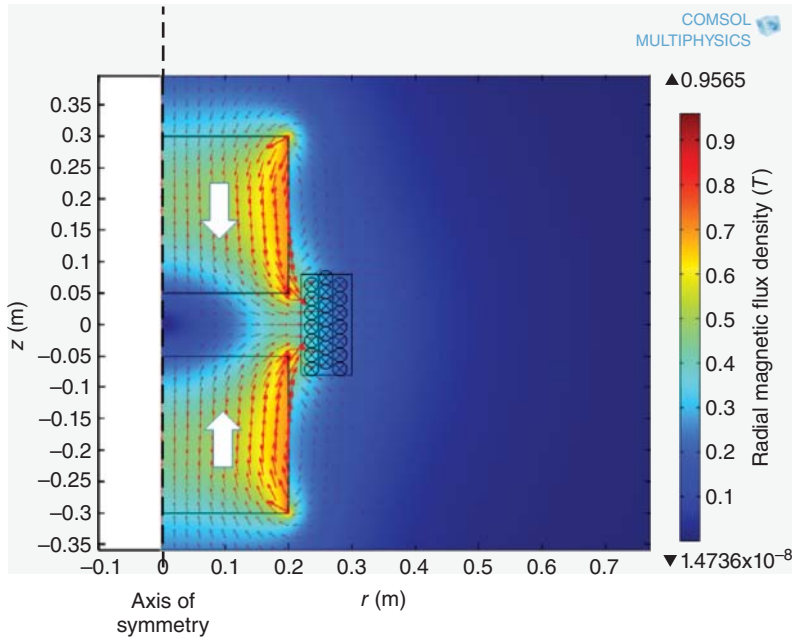


**Figure 9.9** Finite element simulation result of the magnetic flux density in the magnetic structure shown in Figure 9.7c.

ferromagnetic materials. Third, it can easily simulate nonlinear properties, such as nonlinear mechanical properties or complex magnetic material behavior.

Although a finite element model can ideally give much more accurate results comparing to the lumped element model, it is generally not recommended to model the system completely using the finite element model. The main concern is the computation cost that is required to simulate any reasonably complex system. Computation time and resource increase dramatically with the complexity of the system and the required accuracy. It is advisable to use the finite element model to solve localized or domain-specific subproblems, for example, to find out the stress/strain distribution of the spring or to calculate the magnetic field distribution of the magnet.

#### 9.4.1.3 Combination of Lumped Element Model and Finite Element Model

The lumped element model provides a simple and effective system-level representation of an energy harvester. The model gives physical insight of the system as well as easy interface with the environment and peripherals. On the other hand, the finite element model is versatile with complexities in geometry and material composition, and provides precise estimates of local effects and parasitic effects. The power of the two modeling approaches can be combined to achieve a powerful tool set for energy harvesting system analysis and design. This section provides a general guideline for using the combined modeling approach at different stages in the energy harvester design.

At the device conceptualization stage, the lumped element model can be used to evaluate different device architectures. Rough estimation of performance can be rapidly generated for initial evaluation of concepts. To evaluate each generation of the design, the lumped element model can still be used to model the device structure, while a number of finite element models are used to extract model parameters with reasonable accuracy. For example, a static mechanical model can be used to extract the spring constant, a magnetostatic model can be used to extract the transduction coefficient, and an electromagnetic model can be used to extract the coil inductance. The extracted model parameters can then be substituted into the lumped element model for more accurate system performance evaluation and optimization.

After a design with satisfactory performance is achieved, finite element models can be used to evaluate the practical aspects of the design. For example, a static mechanical model can be used to evaluate the stress/strain distribution of the spring. Other appropriate finite element tools can be used to evaluate the parasitic interactions between the device and the environment (magnetic, aerodynamic, etc.).

After a final design is achieved with all the model parameters extracted. The interaction between the harvester and the power electronic circuits, as well as the vibration source can be evaluated using the final lumped element model.

#### 9.4.2

##### **Optimization**

Optimization of an energy harvester may have different meanings, depending on the application. In many cases, the goal is to maximize the power delivered to the load or total energy delivered for storage within certain duration. It is also possible that the loading effect of the energy harvester is significant to the vibration source (e.g., human or other small moving objects), and so a different goal may be to maximize the efficiency given that certain amount of power output is achieved.

The design of an energy harvester is typically subject to certain constraints. The size/weight of the device is limited by the available space and the loading capability of the vibration source. A significant portion of the space/weight budget may be occupied by the frame. For example, the frame may need to be thick enough to minimize the effects of stray magnetic fields to the outside world. The available functional space inside the frame determines the maximum value of the proof mass, total volume of the coils, the range of motion, and so on. The operating temperature of the harvester may restrict the available materials for permanent magnets.

In general, a top-down approach is used to optimize the performance of an electrodynamic energy harvester. In the first step, the relationship between the overall performance and system-level parameters is determined through model analysis. For example, using a lumped element model, simulation of the equivalent circuit model can reveal the importance of each system parameters (mass, spring constant, transduction coefficient, etc.). Coupling this relationship with the design

constraint, an optimized space/weight budget allocation can be achieved, so that the design constraints and objects for each harvester components can be set. In the next step, optimization of each component can be performed using either analytical or numerical tools. For example, a magnetostatic finite element model can be used to optimize the shapes of the magnets and the coils so that the transduction coefficient is optimized.

Consider again the canonical energy harvester shown in Figure 9.1 and the corresponding lumped model in Figure 9.8. Equation (9.12) provides the system-level formula defining the power generation capabilities for the energy harvester. For a given vibration excitation, the power is maximized by maximizing the mass  $m$  and minimizing the mechanical damping  $b$ . The upper bound of the mass is limited to the available materials and space. Strategies for the damping will be presented in the next section. However, the ratio in parentheses in the denominator requires additional attention. The inverse of this unitless ratio has recently been coined as the *coupling strength* [47].

$$\gamma = \frac{K^2}{R_{\text{coil}}b}. \quad (9.13)$$

The coupling strength plays an important role in the effectiveness of a vibrational harvester and should be maximized in order to maximize the average load power. It can be reexpressed by substituting more explicit definitions of the coil resistance and the transduction coefficient (Eq. (9.9))

$$\gamma = \frac{K^2}{R_{\text{coil}}b} = \frac{(B_{\text{avg}}l_{\text{coil}})^2}{\left(\frac{\rho_{\text{coil}}l_{\text{coil}}}{A_{\text{coil}}}\right)b} = \frac{(A_{\text{coil}}l_{\text{coil}})B_{\text{avg}}^2}{\rho_{\text{coil}}b} = \frac{\kappa\mathcal{V}_{\text{coil}}B_{\text{avg}}^2}{\rho_{\text{coil}}b} \quad (9.14)$$

where  $\rho_{\text{coil}}$ ,  $l_{\text{coil}}$ , and  $A_{\text{coil}}$  are the resistivity, length, and cross-section area of the coil conductor, respectively; and  $\mathcal{V}_{\text{coil}}$  and  $\kappa$  are the total volumetric space occupied by the coil (including insulating layer and air gaps between windings) and the fill factor of the coil (percentage of the coil volume occupied by the conductor), respectively [26]. Therefore, a low-resistivity coil conductor is needed with the maximum possible fill factor and the coil architecture should be designed to maximize the product  $\mathcal{V}_{\text{coil}}B_{\text{avg}}^2$ . Besides using a stronger magnetic material for the permanent magnet, geometrical optimization should be performed to optimize the shape and dimensions of the magnet and the coil, as well as their relative positions. This task can best be handled using the finite element model of the magnet and the coil, and numerical optimization methods [48]. Additional methodologies for optimizing an electrodynamic harvester can be found in [49].

## 9.5

### Design and Fabrication

After considering common architectures in Section 9.3 and the procedures to mathematically model a harvester in Section 9.4, some practical aspects should be addressed: How to go from a conceptual design to a physical implementation?

What fundamental limitations (physics, material properties) need consideration?  
 What are practical constraints for fabrication/manufacturing?

### 9.5.1

#### Design of Electrodynamic Harvesters

Design aspects with significant impact on the harvester behavior and performance are highlighted here. Owing to the complexity of the harvester design, some of these aspects can be easily overlooked, but all are important factors for maximizing harvester performance.

---

#### *System damping*

Damping is the main limiting factor for the output power of a harvester (see Eq. (9.12)). Although damping is rarely discussed in energy harvesting literature, its consideration in the harvester design is critical to increase the power generation performance. For harvesters at millimeter size and above, anchor loss, acoustic damping, and magnetic hysteresis loss usually are negligible. Depending on the harvester design and dimensions, some of the following damping types have to be considered [50]. Unfortunately, most of these phenomena are nonlinear and depend on multiple design parameters, so their direct consideration in the design and optimization is often quite challenging.

- a) *Eddy current damping*: While the primary role of the harvester is to induce a current in the coil, unwanted eddy currents can also be induced in metal components in and around the harvester. Because metal components may represent a “short-circuited” electrical path, a very weak magnetic field can induce losses with a value comparable to the energy conversion in the coil. A key to avoid eddy current damping is to avoid the use or proximity of conductive metal structures, and to be especially cautious in the design of “moving-magnet” type structures.
  - b) *Viscid damping*: The smaller the air gaps between the magnetic circuit and the coil and the larger the footprint of the magnetic circuit, the stronger the magnetic field can be. However, reducing these air gaps increases viscid damping. Especially for miniaturized harvesters (with an unfavorable surface to volume ratio), viscid damping can become the dominating loss. Vacuum packaging technology can potentially decrease the viscid damping dramatically by removing most of the air molecules in the air gaps.
-



- c) *Thermoelastic damping*: Thermoelastic damping is due to thermal fluctuations in the mechanical flexures when subjected to alternating stresses during vibration. With improper spring design, the fluctuation can resonate and therefore significantly damp the harvester. The challenge is to adapt the spring geometry (e.g., the thickness of the beam/membrane for beam/membrane springs) to minimize the thermoelastic damping but without changing the resonance frequency. However, a trade-off can result, as maximum stress and material hysteresis damping can both increase.
- d) *Material hysteresis damping*: In polycrystalline materials, micro-defects can cause high losses that can dominate the losses of a harvester. One solution is to use single-crystalline materials for the springs/flexures.
- e) *Friction damping*: Friction can be caused by an imperfect mounting of the oscillator. To minimize this effect, the spring/flexures should be rigidly anchored and must not allow any unwanted slippage at the mounting points.

#### *Material based limitations*

Two major material limitations are often encountered in electrodynamic harvesters.

- a) *Maximum operating temperature of the magnets*: A magnet must be kept below the maximum operating temperature to avoid irreversible magnetization losses. This limiting temperature is much lower than the Curie temperature (the temperature where a ferromagnet loses all of its magnetization). The strongest permanent magnets made of NdFeB have maximum operating temperatures ranging from 80 to 150 °C, depending on the specific alloy.
- b) *Fatigue limit of the spring/flexure material*: Fatigue is the weakening of a material after cyclic loading and is an important consideration in the spring design. For certain materials, a fatigue limit can be defined as the stress that causes failure after a large number of cycles, and so influences the choice of spring dimensions and material. This limit is typically no more than half of the ultimate tensile strength of a material. Also, there is generally a trade-off between fatigue and hysteresis damping. Single-crystalline materials such as silicon have low material hysteresis damping but generally lower fatigue limits, whereas polycrystalline materials such as spring steel offer a higher fatigue limit but higher material damping.

---

<i>Nonlinear behaviors</i>	In practice, most harvester mechanics show some degree of nonlinearity. For example, mechanical flexures typically exhibit a stiffening behavior at large excitations caused by higher-order bending terms [16]. Also, the electrodynamic coupling coefficient may change with relative motion between the magnet and coil. These subtle nonlinearities can impact the harvester behavior, even when nonlinear behavior is not specifically intended. Consequences may include a changing resonant frequency and/or varying optimal load conditions for different excitation amplitudes.
<i>Harvester housing</i>	The housing of a harvester is important to prevent particles or liquids from entering the mechanical system or even to provide a vacuum environment. In addition, the housing can play an important role to shield the magnetic field of the harvester from affecting the external environment or to shield external magnetic fields from affecting the harvester operation. Without this shielding, magnetic forces can significantly disturb the harvester behavior [50].
<i>Harvester output</i>	The harvester output, that is, voltage and impedance, needs to meet the requirements of the connected load circuit. By adjusting the wire thickness and correspondingly the number of windings of the harvester coil, the voltage can in principle be adapted without affecting the harvester power. One challenge is that achieving modest voltage levels ( $\sim 1$ V or higher) in a miniaturized energy harvester may require wires with thicknesses below $40\ \mu\text{m}$ , which makes manufacturing and handling difficult. It is often undesired to change the coil resistance and therefore the required optimum load resistance. Therefore, the coil volume must be adjusted to achieve the desired voltage level.

---

### 9.5.2

#### Fabrication of Electrodynamic Harvesters

Electrodynamic harvesters offer enormous flexibility in their architecture. Hence many different materials and manufacturing approaches can be considered for their construction. At the macroscale, most electrodynamic harvesters are built using an assembly of components including the following:

- *Magnet* – typically one or more high-energy-density permanent magnets, made from Nd–Fe–B or Sm–Co alloys
- *Conductor* – typically one or more coils formed from a lacquer-coated copper wire, known as *magnet wire*
- *Spring/Flexure* – many options such as coil springs, cantilever beams, “magnetic springs,” ball bearing sliders, or even springless designs

- *Core (optional)* – iron structures to shape the magnetic fields and/or close the magnetic path and thereby increase the magnetic fields (typically, a high-magnetic-saturation ferromagnetic metal such as Fe, Ni–Fe, or Fe–Co alloys)
- *Housing* – an external frame or structure to which all other components are assembled, such as plastic, metal (in the case of moving-magnet designs, electrically nonconductive frames are preferred to avoid eddy-current damping in the housing).

From a commercialization standpoint, one advantage of an electrodynamic harvester is that all of these materials are readily available, well characterized, reliable/stable, and of fairly low cost. It is worth noting that a fully functioning system would require additional power electronics and possibly power storage (e.g., capacitors or batteries), which are not described here.

Besides conventionally manufactured macroscale devices, many emerging applications demand energy harvesters with significantly miniaturized size. Keeping in mind that the power output of a harvester scales with size, a “miniature” (few cm<sup>3</sup>) energy harvester may only generate microwatts of power. For harvesters at these size scales, a host of manufacturing technologies are available. Bulk magnets can be readily obtained with dimensions down to 0.5 mm. Windings can be fabricated using fine-scale magnet wire, printed circuit board (PCB) traces, low-temperature co-fired ceramics (LTCCs), or even 3-D printed electronics.

For even smaller “micro” size scales (few mm<sup>3</sup>), microsystem (MEMS, microelectromechanical systems) fabrication technologies can provide a viable manufacturing platform, but it is worth noting that devices at this size scale may only generate nanowatts or picowatts of power. The microfabrication of coils with microscale dimensions is fairly routine and makes use of photolithographically patterned thick-film metals such as electroplated copper or gold. Dense, complex winding patterns can be achieved using multiple metal layers, each with thickness ranging from micrometers up to tens of micrometers in thickness. Complex mechanical flexures can also be created by creative micromachining of various materials including silicon, polymers, ceramics, and metals. The microfabrication of high-quality permanent magnet materials at micrometer scale dimensions, however, is more challenging [51]. Common approaches include electroplating, sputtering, or methods for microforming bonded powders all with various manufacturing and performance trade-offs.

Figure 9.10a shows an example of a fully microfabricated electrodynamic harvester using a bonded-NdFeB-powder magnet and an out-of-plane vibration architecture [52]. Figure 9.10b shows another recent example making use of sputtered Nd–Fe–B magnets and a multipole, in-plane vibration architecture [53]. A few other devices have also been reported demonstrating the feasibility of full microfabrication [54–56], but there is plenty of room for improvement in both performance and manufacturability.

Owing to challenges in permanent magnet microfabrication and integration, many small-scale electrodynamic harvester prototypes investigated to date have

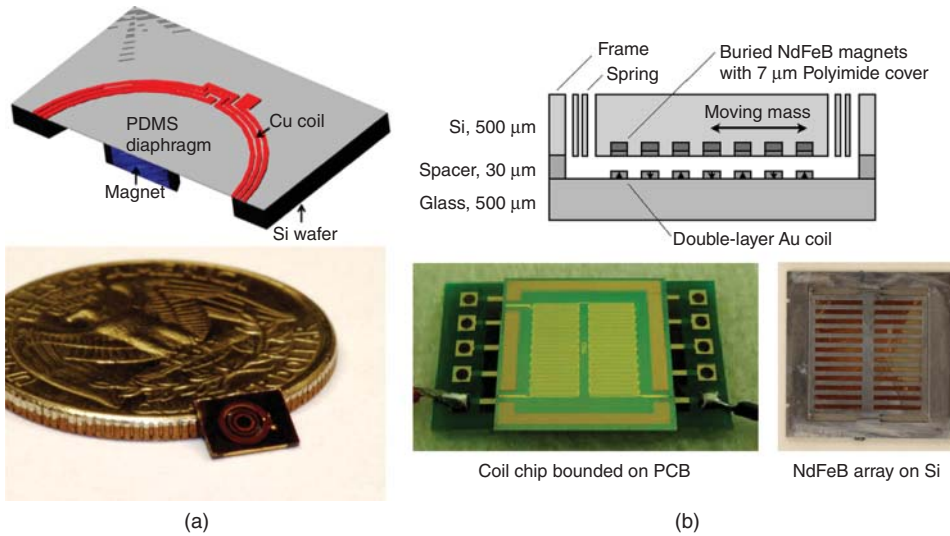


**Figure 9.10** Microfabricated electrodynamic energy harvesters showing (a) out-of-plane, single-magnetic architecture (Image courtesy of D. P. Arnold, University of Florida) and (b) in-plane multipole architecture (Image courtesy of T. Fujita, University of Hyogo).

merged millimeter-scale, bulk magnets with other microfabricated subcomponents. Examples include the original resonant-type harvester by Williams *et al.* [4, 57], a harvester using a silicon flexure [58], and a frequency up-conversion structure by Kulah and Najafi [59]. While fine for laboratory prototypes, serial assembly of magnets is undesirable for commercial-scale manufacturing. In addition, because the performance of a system can be highly sensitive to magnet misalignment, alignment tolerances become increasingly more challenging at smaller size scales.

## 9.6

### Summary

Electrodynamic transduction affords great flexibility for vibrational energy harvester design. Many different architectures are possible to enact time-varying changes in magnetic flux within a coil, using resonant or nonresonant approaches. This enables the design of structures with very different sizes, shapes, and form factors. Furthermore, unlike piezoelectric transducers, the decoupling of the vibration flexure from the electrodynamic transduction mechanism enables one to target a wide range of frequencies in the dynamic response, even at different system size scales.

One ongoing area for investigation is the advancement of fully microfabricated electrodynamic vibrational energy harvesters. Advances in ultralow power

electronics are creating more application platforms for microscale electrodynamic energy harvesters that may generate only nanowatts or microwatts of power. The major challenge for achieving fully microfabricated electrodynamic energy harvesters is the precise batch fabrication and integration of microscale magnets on electromechanical structures.

There are also several design opportunities to improve electrodynamic vibrational energy harvesters. One key is maximizing the electrodynamic coupling strength of the design. In addition, there are opportunities for new materials, mechanical structures, and packaging technologies to minimize mechanical damping, which is critical for maximizing output power. Another promising area is hybrid energy harvesters, which combine electrodynamic transduction with other transduction mechanisms, such as piezoelectric transduction, and take advantage of both [60].

A final area for investigation is the development of high-performance power electronics to maximize the power delivery to an electrical load. Electrodynamic energy harvesters typically have relatively low output impedance and low voltage levels, ranging from single-digit volts, down to even microvolts for microscale devices. Hence, they demand specialized interface electronics to address these low voltages and also to provide adaptive impedance matching to maximize the load power even when the operation condition is varying. Szarka *et al.* [61] provide a good starting point for investigation of this important topic.

## References

1. Motomu Hayakawa, Seiko Epson Corporation Wikipedia [http://en.wikipedia.org/wiki/Mechanically\\_powered\\_flashlight](http://en.wikipedia.org/wiki/Mechanically_powered_flashlight) (accessed 10 November 2014).
2. Hayakawa, M. (1991) Electronic wrist-watch with generator. US Patent US5001685, Seiko Epson Corporation, p. 3.
3. SEIKO Watch Corporation (1988) SEIKO AGS Kinetic Quartz Watch, <http://www.seikowatches.com/story/landmarks/index.html/Kinetic> (accessed 10 November 2014).
4. Williams, C.B. and Yates, R.B. (1995) Analysis of a micro-electrical generator for microsystems. Proceedings of Transducers'95, Stockholm, Sweden, IEEE, pp. 369–372.
5. PMG17 (2009) PMG17 Technical Data Sheet Rev 3.0. Document No. 26999, Perpetuum Ltd.
6. VEH-460 (2009) VEH-460 Electromechanical Vibration Energy Harvester, Document No. 20090516. FerroSolutions Inc.
7. TREMONT Electric. nPower(R) PEG (2012) <http://www.npowerpeg.com> (accessed 10 November 2014).
8. Frayne, S. (2007) Humdinger Wind Energy, LLC, <http://www.humdingerwind.com/> (accessed 21 October 2010).
9. Mitcheson, P.D., Green, T.C., Yeatman, E.M., and Holmes, A.S. (2004) Architectures for vibration-driven micropower generators. *J. Microelectromech. Syst.*, **13**, 429.
10. Mitcheson, P.D., Reilly, E.K., Toh, T.T., Wright, P.K., and Yeatman, E.M. (2007) Performance limits of the three mems inertial energy generator transduction types. *J. Micromech. Microeng.*, **17** (9), 211–216.
11. Mitcheson, P.D., Yeatman, E.M., Rao, G.K., Holmes, A.S., and Green, T.C. (2008) Energy harvesting from human and machine motion for wireless electronic devices. *Proc. IEEE*, **96** (9), 1457–1486.

12. Arnold, D.P. (2007) Review of microscale magnetic power generation. *IEEE Trans. Magn.*, **43**, 3940–3951.
13. Beeby, S.P., Tudor, M.J., and White, N.M. (2006) Energy harvesting vibration sources for microsystems applications. *Meas. Sci. Technol.*, **17**, R175–R195.
14. Khaligh, A., Zeng, P., and Zheng, C. (2010) Kinetic energy harvesting using piezoelectric and electromagnetic technologies—state of the art. *IEEE Trans. Ind. Electron.*, **57** (3), 850–860.
15. Paulo, J. and Gaspar, P.D. (2010) Review and future trend of energy harvesting methods for portable medical devices. Proceedings of the World Congress on Engineering, Vol. 2.
16. Zhu, D., Tudor, M.J., and Beeby, S.P. (2010) Strategies for increasing the operating frequency range of vibration energy harvesters: a review. *Meas. Sci. Technol.*, **21**, 022001-1–022001-29.
17. Cepnik, C., Lausecker, R., and Wallrabe, U. (2013) Review on electrodynamic energy harvesters – a classification approach. *Micromachines*, **4** (2), 168–196, <http://www.mdpi.com/2072-666X/4/2/168> (accessed 20 January 2015).
18. Ulaby, F.T., Michielssen, E., and Ravaoli, U. (2010) *Fundamentals of Applied Electromagnetics*, 6th edn, Prentice Hall.
19. Roundy, S., Wright, P.K., and Rabaey, J.M. (2003) A study of low level vibrations as a power source for wireless sensor nodes. *Comput. Commun.*, **26** (11), 1131–1144.
20. Sazonov, E., Li, H., Curry, D., and Pillay, P. (2009) Self-powered sensors for monitoring of highway bridges. *IEEE Sens. J.*, **9**, 1422–1429.
21. Toh, T.T., Mitcheson, P.D., Holmes, A.S., and Yeatman, E.M. (2008) A continuously rotating energy harvester with maximum power point tracking. *J. Micromech. Microeng.*, **18**, 104008-1-7.
22. Howey, D.A., Bansal, A., and Holmes, A.S. (2011) Design and performance of a centimetre-scale shrouded wind turbine for energy harvesting. *Smart Mater. Struct.*, **20**, 085021.
23. Zhu, D., Beeby, S., Tudor, J., Harris, N., and White, N. (2011) Airflow energy harvester for wireless sensing in air duct. Proceedings of PowerMEMS 2011, Seoul, Korea.
24. Bowers, B.J. and Arnold, D.P. (2009) Spherical, rolling magnet generators for passive energy harvesting from human motion. *J. Micromech. Microeng.*, **19**, 094008.
25. Riemer, R. and Shapiro, A. (2011) Biomechanical energy harvesting from human motion: theory, state of the art, design guidelines, and future directions. *J. NeuroEng. Rehabil.*, **8**, 22.
26. Cepnik, C., Radler, O., Rosenbaum, S., Ströhla, T., and Wallrabe, U. (2011) Effective optimization of electromagnetic energy harvesters through direct computation of the electromagnetic coupling. *Sens. Actuators, A*, **167**, 416–421.
27. Ayala-Garcia, I.N., Zhu, D., Tudor, J., and Beeby, S.P. (2010) A tunable kinetic energy harvester with dynamic over range protection. *Smart Mater. Struct.*, **19** (11), 1–10.
28. Beeby, S.P., Torah, R.N., Tudor, M.J., Glynne-Jones, P., O'Donnell, T., Saha, C.R., and Roy, S. (2007) A micro electromagnetic generator for vibration energy harvesting. *J. Micromech. Microeng.*, **17**, 1257–1265.
29. Yuen, S.C.L., Lee, J.M.H., Li, W.J., and Leong, P.H.W. (2007) An AA-sized vibration-based microgenerator for wireless sensors. *IEEE Pervasive Comput.*, **6** (1), 64–72 [http://ieeexplore.ieee.org/xpls/abs\\_all.jsp?arnumber=4101144&tag=1](http://ieeexplore.ieee.org/xpls/abs_all.jsp?arnumber=4101144&tag=1) (accessed 20 January 2015).
30. Mann, B.P. and Owens, B.A. (2010) Investigations of a nonlinear energy harvester with a bistable potential well. *J. Sound Vib.*, **329** (9), 1215–1226.
31. Sasaki, K., Osaki, Y., Okazaki, J., Hosaka, H., and Itao, K. (2005) Vibration-based automatic power-generation system. *Microsyst. Technol.*, **11**, 965–969.
32. Spreemann, D., Manoli, Y., Folkmer, B., and Mintenbeck, D. (2006) Non-resonant vibration conversation. *J. Micromech. Microeng.*, **16**, 169–173.
33. Sneller, A.J. and Mann, B.P. (2010) On the nonlinear electromagnetic coupling between a coil and an oscillating magnet. *J. Phys. D Appl. Phys.*, **43**, 295005.

34. Dijkstra, D. (1979) Electrically controllable carrying-arm arrangement. US Patent US4150407, U.S. Philips Corporation, Apr. 1979.
35. Bauck, R.C. and Kleczkowsky, P.S. (1986) Symmetrical coil actuator for a magnetic disk drive. US Patent US4620252, Iomega Corporation, Oct. 1986.
36. El-Hami, M., Glynne-Jones, P., White, N.M., Hill, M., Beeby, S.P., James, E., Brown, A.D., and Ross, J.N. (2001) Design and fabrication of a new vibration-based electromechanical power generator. *Sens. Actuators, A: Phys.*, **92**, 335–342.
37. Duffy, M. and Carroll, D. (2004) Electromagnetic generators for power harvesting. PESC' 04: 2004 IEEE 35th Annual IEEE Power Electronics Specialists Conference, 2004, Vol. 3, pp. 2075–2081.
38. Mallinson, J. (1973) One-sided fluxes—a magnetic curiosity? *IEEE Trans. Magn.*, **9** (4), 678–682.
39. Senturia, S.D. (2001) *Microsystems Design*, Springer.
40. Tilmans, H.C. (1996) Equivalent circuit representation of electromechanical transducers: I. Lumped-parameter systems. *J. Micromech. Microeng.*, **6**, 157–176.
41. Bush-Vishniac, I.J. (1999) *Electromechanical Sensors and Actuators*, Springer.
42. Cheng, S., Wang, N., and Arnold, D.P. (2007) Modeling of magnetic vibrational energy harvesters using equivalent circuit representations. *J. Micromech. Microeng.*, **17**, 2328–2335.
43. Stephen, N.G. (2006) On energy harvesting from ambient vibration. *J. Sound Vib.*, **293**, 409–425.
44. Cheng, S., Wang, N., and Arnold, D.P. (2007) Optimization of magnetic vibrational energy harvesting systems using equivalent circuit representations. *PowerMEMS 2007*, pp. 89–92.
45. Reddy, J. (2005) *An Introduction to the Finite Element Method*, Engineering Series, 3rd edn, McGraw-Hill Science/Engineering/Math.
46. Zienkiewicz, O.C., Taylor, R.L., and Zhu, J.Z. (2013) *The Finite Element Method: Its Basis and Fundamentals*, 7th edn, Butterworth-Heinemann.
47. Challa, V.R., Cheng, S., and Arnold, D.P. (2013) The role of coupling strength in the performance of electrodynamic vibrational energy harvesters. *Smart Mater. Struct.*, **22**, 025005.
48. Vanderplaats, G.N. (2001) *Numerical Optimization Techniques for Engineering Design*, 3rd edn, Vanderplaats Research and Development, Inc.
49. Spreeman, D. and Manoli, Y. (2012) *Electromagnetic Vibration Energy Harvesting Devices*, Springer, New York.
50. Cepnik, C. (2013) Towards high performing resonant electrodynamic vibration energy harvesters. PhD thesis. University of Freiburg, IMTEK.
51. Arnold, D.P. and Wang, N. (2009) Permanent magnets for MEMS. *J. Microelectromech. Syst.*, **18**, 1255–1266.
52. Wang, N. and Arnold, D.P. (2009) Fully batch-fabrication MEMS magnetic vibrational energy harvesters. *PowerMEMS 2009*, pp. 348–351.
53. Miki, S., Fujita, T., Kotoge, T., Jiang, Y.G., Uehara, M., Kanda, K., Higuchi, K., and Maenaka, K. (2012) Electromagnetic energy harvester by using buried NdFeB magnets. *IEEE MEMS 2012*, Paris, France, pp. 1221–1224.
54. Pan, C.T., Hwang, Y.M., Hu, H.L., and Liu, H.C. (2006) Fabrication and analysis of a magnetic self-power microgenerator. *J. Magn. Magn. Mater.*, **304** (1), e394–e396.
55. Yuan, Q., Sun, X., Fang, D., and Zhang, H. (2011) Design and microfabrication of integrated magnetic MEMS energy harvester for low frequency application. *Transducers 2011*, pp. 1855–1858.
56. Jiang, Y., Masaoko, S., Fujita, T., Uehara, M., Toyonaga, T., Fujii, K., Higuchi, K., and Maenaka, K. (2011) Fabrication of a vibration-driven electromagnetic energy harvester with integrated NdFeB/Ta multilayered micro-magnets. *J. Micromech. Microeng.*, **21** (9), 095014.
57. Williams, C.B., Shearwood, C., Harradine, M.A., Mellor, P.H., Birch, T.S., and Yates, R.B. (2001) Development of an electromagnetic micro-generator. *IEE Proc. Circuits Devices Syst.*, **148** (6), 337–342.
58. Koukharenko, E., Beeby, S.P., Tudor, M.J., White, N.M., O'Donnell, T.,

- Saha, C., Kulkarni, S., and Roy, S. (2006) Microelectromechanical systems vibration powered electromagnetic generator for wireless sensor applications. *Microsyst. Technol.*, **12** (10-11), 1071–1077.
59. Kulah, H. and Najafi, K. (2004) An electromagnetic micro power generator for low-frequency environmental vibrations. Proceedings of the 17th International Conference on MEMS (MEMS 2004), Maastricht, The Netherlands, January, 2004, pp. 237–240.
60. Yang, B., Kee, W.L., Lim, S.P., and Lee, C. (2010) Hybrid energy harvester based on piezoelectric and electromagnetic mechanisms. *J. MOEMS*, **9**, 023002.
61. Szarka, G.D., Stark, B.H., and Burrow, S.G. (2012) Review of power conditioning for kinetic energy harvesting systems. *IEEE Trans. Power Electron.*, **27**, 803–815.



## 10

### Piezoelectric MEMS Energy Harvesters

*Jae Yeong Park*

The energy harvesting technology that converts ambient waste energy into usable electrical power has been considered as a viable solution for clean and sustainable energy source. Solar energy is the most promising power source because solar cells have the highest output power density under direct sunlight. However, solar cells cannot be used indoors or in areas with no light. Electrical power can also be scavenged from electromagnetic fields, vibrations, thermal gradients, and so on. Among these resources, vibration energy has considerable potential for micropower energy harvesting because it provides a high power density, has an infinite lifetime, and is reliable in harsh environments owing to no physical connection to the outside of the system [1–3]. In this chapter, the miniaturized vibration energy harvesters using micro-electro-mechanical-systems (MEMS) technology and piezoelectric thin film are discussed for ambient vibration energy harvesting applications.

#### 10.1

##### Introduction

There are three types of transduction methods that can be used for MEMS vibration energy harvesters: electrostatic, electromagnetic, and piezoelectric. Among these methods, piezoelectric transducers have received much attention for milli- and microscaled energy harvesters, because of their simple configuration and higher conversion efficiency than the others [2, 4–6]. The general principle for piezoelectric vibration energy harvesting is a conversion of mechanical stress into electrical energy using piezoelectric transducers coupled with a resonant structure. Figure 10.1 presents the typical piezoelectric MEMS energy harvester to scavenge ambient vibrations. It consists of a cantilever structure, which is composed of a supporting membrane, piezoelectric layer, and electrodes. The proof mass is built at the free end of the cantilever to adjust the resonance frequency and reduce the spring constant. The piezoelectric layer with electrodes is attached on the supporting membrane to convert the strain induced by kinetic energy of the oscillated proof mass to electricity via the piezoelectric effect. The

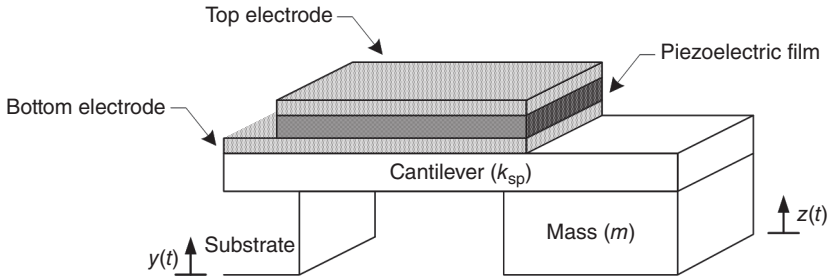


**Figure 10.1** Schematic drawing of a cantilever-based piezoelectric vibration energy harvester.

resonance of the cantilever beam structure amplifies the small ambient vibration into an in-plane strain governed by the Euler–Bernoulli beam equation [7–9].

### 10.1.1

#### The General Governing Equation

The general model for the vibration energy harvester which converts kinetic energy of an inertial mass to electrical power is based on a mass-spring damper system without a specific conversion mechanism [9, 10]. As shown in Figure 10.2, this simple model consists of inertial mass ( $m$ ) to vibrate, elastic spring ( $k_{sp}$ ), mechanical damping ( $b_m$ ), and electrical damping ( $b_e$ ) derived from Figure 10.1 and is described as

$$m\ddot{z} + (b_m + b_e)\dot{z} + k_{sp}z = -m\ddot{y} \quad (10.1)$$

where  $z$  is the displacement of the inertial mass relative to the input vibrations and  $y$  is the input vibration.

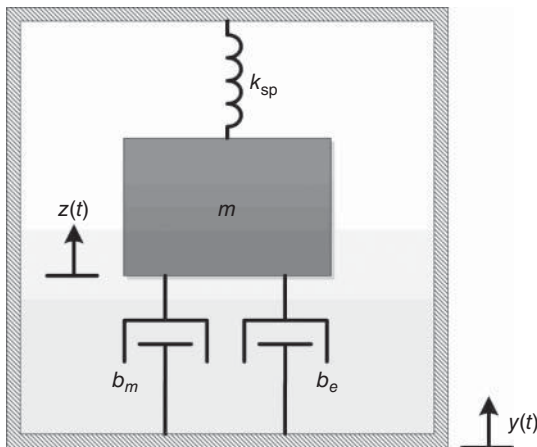


**Figure 10.2** Schematic drawing of a mass-spring damper system for vibration energy harvester.

In this model, the conversion from kinetic energy of the oscillating mass to electricity is represented as an electrically induced damping coefficient which is a linear damper in the mass spring system because the energy conversion always contributes as a loss of kinetic energy. The conversion mechanism in the electromechanical system for the energy harvester is not always linear to the induced velocity of the inertial mass. Even though it is not an accurate model, important conclusions can be extrapolated from the analysis of the proposed system. The converted electrical power which reduces the oscillation of inertial mass is derived by using the electrical damping as

$$P = \frac{1}{2} b_e \dot{z}^2 \quad (10.2)$$

It is assumed that the applied vibration is sinusoidal,  $y = Y \cos \omega t$ . The analytical expression of converted power derived from Eq. (10.2) is expressed as

$$|P| = \frac{m \zeta_e \omega_n Y^2 \left( \frac{\omega}{\omega_n} \right)^4 \omega^2}{\left\{ 1 - \left( \frac{\omega}{\omega_n} \right)^2 \right\}^2 + \left\{ 2 (\zeta_e + \zeta_m) \left( \frac{\omega}{\omega_n} \right) \right\}^2} \quad (10.3)$$

where  $\zeta_e$  and  $\zeta_m$  are the electrical and mechanical damping ratios given by  $\zeta_e = b_e/2m\omega_n$  and  $\zeta_m = b_m/2m\omega_n$ , respectively,  $\omega$  is the input vibration frequency and  $\omega_n$  is the resonance frequency of the mass-spring damper system. When the excited vibration is matched with the resonance frequency of the mass-spring system, Eq. (12.4) can be rewritten as

$$|P| = \frac{\zeta_e}{4\omega_n(\zeta_e + \zeta_m)^2} mA^2 \quad (10.4)$$

where  $A$  is the acceleration of the input vibration given by  $A = \omega^2 Y$ .

The electrical damping for a piezoelectric energy harvester is derived by the electrical coupling term based on piezoelectric effect for power conversion. The equivalent electrically induced damping ratio is given as [3]

$$\zeta_e = \frac{\omega_n k_p^2}{2\sqrt{\omega_n^2 + \left( \frac{1}{RC_p} \right)^2}} \quad (10.5)$$

where  $k_p$  represents the electromechanical coupling coefficient defined by the elastic modulus ( $Y$ ), piezoelectric constant ( $d$ ), and permittivity of piezoelectric material,  $k_p^2 = Yd^2/\epsilon$ ,  $R$  is the load resistor, and  $C_p$  is the total capacitance of the piezoelectric transducer.

### 10.1.2

#### Design Consideration

As shown in Eq. (10.3), the power is maximized when the excited vibration is matched to the resonance frequency of the energy harvester because the strain on the piezoelectric layer is amplified. The magnitude of the output power at

resonance is affected by the total damping. It is assumed that the mechanical damping ratio ( $\zeta_m$ ) and electrical damping ratio ( $\zeta_e$ ) are same,  $\zeta_e = \zeta_m$ . An increase of total damping ( $\zeta_T = \zeta_e + \zeta_m$ ) results in a decrease of output power, however, the frequency bandwidth of the energy harvester is increased. It is assumed that the energy harvester is driven sinusoidally, the  $Q$ -factor of device is inversely proportional to the damping ratio,  $Q = 1/2\zeta_T$ , and the frequency bandwidth ( $\Delta\omega$ ) is given as  $\Delta\omega = \omega_n/Q$ . Therefore, the energy harvester with small damping (high  $Q$ -factor) has high output power at the resonance frequency ( $\omega_n$ ) and high sensitivity to the frequency of the exciting vibrations. On the other hand, the large damping (low  $Q$ -factor) results in small output power with a wideband frequency response. There is a trade-off in damping coefficient.

The output power of the energy harvester significantly drops off as the increase of the mechanical ( $\zeta_m$ ) or electrical damping ratio ( $\zeta_e$ ) increases, and it is more sensitive to mechanical damping than electrical damping as shown in Eq. (10.4). The vibration energy harvester with a larger mechanical damping ratio than electrical damping ratio,  $\zeta_m > \zeta_m$ , may be handicapped in output power. The output power in the general model is maximized when the electrical damping is equal to the mechanical damping,  $\zeta_e = \zeta_m$ . Therefore, the mechanical damping should be minimized and electrical damping must be designed to the appropriate value which is equal to or greater than the value of the mechanical damping because electrical damping is a function of circuit parameters or material properties as shown in Eq. (10.5).

The output power is linearly proportional to mass. Therefore, the energy harvester should have the largest proof mass as possible as while staying within the device's area. When the exciting vibration is matched with the resonance frequency of the energy harvester, the output power is inversely proportional to vibration frequency at fixed acceleration. Therefore, if the acceleration of the vibrations is constant, the energy harvester should be designed to have a low resonance frequency by increasing and decreasing the mass and spring constant of device, respectively.

## 10.2

### Development of Piezoelectric MEMS Energy Harvesters

#### 10.2.1

##### Overview

Much research has been performed to develop micromachined piezoelectric vibration energy harvesters. Since a lead zirconate titanate (PZT) thin film has a larger piezoelectric constant than aluminum nitride (AlN) or zinc oxide (ZnO) thin films do, several PZT-based energy harvesters have been reported. Zurn *et al.* presented the fabrication and structural characterization of a resonator-based PZT micro-cantilever without a proof mass [11]. In 2006, Fang *et al.* reported the fabrication and performance of a MEMS PZT cantilever energy harvester

with a Ni proof mass [12]. It could generate an output power of  $2.1 \mu\text{W}$  at its resonance frequency of 608 Hz. Shen *et al.* and Lee *et al.* also presented a PZT cantilever-based vibration energy harvester [13–15]. Most micromachined energy harvesters were designed to operate in {3-1} piezoelectric mode [12, 13, 15]. The {3-3} piezoelectric mode, which was configured by an interdigital shaped electrode, was effective in generating a larger output voltage than the {3-1} mode. In addition, its piezoelectric constant was also much higher than that of the harvester operating in the {3-1} mode. For this reason, Jeon *et al.* and Park *et al.* reported the fabrication and performance of a PZT cantilever vibration energy harvester using {3-3} mode [7, 13, 16].

While PZT cantilever-based energy harvesters were actively reported, there were some obstacles to be addressed in the fabrication of PZT thin films. Renaud *et al.* and Marzencki *et al.* reported an AlN thin-film cantilever-based energy harvester that can generate 40 and  $0.038 \mu\text{W}$  at the resonance frequency of 1.8 kHz and 204 Hz, respectively [6, 17]. Elfrink *et al.* reported an AlN-based energy harvester for improving the output power to generate up to  $60 \mu\text{W}$  from the resonant frequency of 572 Hz in 2009 [18]. Furthermore, vacuum-packaged devices with  $85 \mu\text{W}$  of output from the resonant frequency of 325 Hz were presented in 2010 [19].

The properties of PZT thin films for MEMS energy harvesters are different in comparison with those of bulk ceramics because of the influence of the substrate [20]. Thus, Aktakka *et al.* presented a thinned-PZT/Si process for unimorph and multimorph cantilever-based vibration energy harvesters by using a bulk PZT piece bonded onto a silicon-on-insulator (SOI) wafer [21, 22]. Table 10.1 presents the state of the art for piezoelectric MEMS energy harvesters.

## 10.2.2

### Fabrication Technologies

A typical piezoelectric MEMS cantilever for an energy harvesting device is a multilayer structure which consists of a supporting membrane, piezoelectric layer, and electrodes. Silicon is usually utilized for the supporting membrane in cantilever structures and for the proof mass. Since most of piezoelectric MEMS energy harvesting devices are fabricated by using SOI wafers and bulk-micromachining technology [7, 19, 21], the device layers are utilized for the cantilever membrane and the proof mass is formed by using the bulk silicon. In order to reduce the resonance frequency of an energy harvester, the proof mass is attached at the free end of cantilever structure. Tungsten, nickel, and iron–nickel alloy are also preferred by assembling at the free end of the silicon cantilever for a heavier proof mass [12, 21].

The selection of piezoelectric material is also important because it performs the conversion of electromechanical energy from applied vibration. The piezoelectric layer comprising of the MEMS energy harvester is usually made of PZT, AlN, or ZnO. Table 10.2 presents a comparison of the electromechanical properties

Table 10.1 Comparison of current state of the art of piezoelectric MEMS energy harvesters.

References	Material	Area (cm <sup>2</sup> )	Volume (cm <sup>3</sup> )	Acceleration (g)	Frequency (Hz)	Power (μW)	Power density (mW cm <sup>-3</sup> )	Normalized power density (mW cm <sup>-3</sup> g <sup>2</sup> )
[23]	PZT, d33	4.4 × 10 <sup>-4</sup>	2.4 × 10 <sup>-5</sup>	13.2	13.9	1	41.14	0.24
[12]	PZT, d31	1.2 × 10 <sup>-2</sup>	1.3 × 10 <sup>-3</sup>	1	608	2.16	1.71	1.71
[17]	AlN	9.6 × 10 <sup>-3</sup>	5.0 × 10 <sup>-4</sup>	4	1368	2	3.97	0.25
[14]	PZT, d31	3.2 × 10 <sup>-2</sup>	6.5 × 10 <sup>-4</sup>	2	461.15	2.15	3.30	0.82
[5]	PZT, d33	9.6 × 10 <sup>-3</sup>	4.8 × 10 <sup>-4</sup>	2	870	1.4	2.92	0.73
[13]	Aerosol PZT d31	5.3 × 10 <sup>-2</sup>	2.6 × 10 <sup>-3</sup>	2.5	255.9	2.77	1.05	0.17
	Aerosol PZT d33	5.6 × 10 <sup>-2</sup>	2.8 × 10 <sup>-3</sup>	2	214	1.29	0.46	0.11
[7]	PZT, d33	1.8 × 10 <sup>-2</sup>	9.9 × 10 <sup>-4</sup>	0.39	528	1.1	1.11	7.31
[19]	AlN	5.7 × 10 <sup>-1</sup>	3.2 × 10 <sup>-2</sup>	1.75	325	85	2.69	0.88
[24]	Thick PZT, d31	3.6 × 10 <sup>-1</sup>	2.1 × 10 <sup>-2</sup>	1.45	243	33.2	1.57	0.75
[21]	Bulk PZT, d31	4.9 × 10 <sup>-1</sup>	2.7 × 10 <sup>-2</sup>	1.5	154	205	7.61	3.38
[25]	Sputtered KNN	8.1 × 10 <sup>-3</sup>	3.1 × 10 <sup>-4</sup>	1.0	1509	0.731	2.39	2.30

**Table 10.2** Electromechanical properties of piezoelectric thin film.

Coefficients	PZT [26]	AlN [27]	ZnO [28]
Piezoelectric coefficient (pC N <sup>-1</sup> )	60–130	3.9–5.5	5.9
Permittivity	300–1300	10.5	10.9
Elastic modulus (GPa)	98	395	208
Electromechanical coupling coefficient	0.07–0.15	0.065	0.074

of these piezoelectric thin films. Typically, the electromechanical coupling coefficient indicates the energy conversion ability of piezoelectric materials for piezoelectric transducers. Therefore, owing to its outstanding piezoelectric properties as shown in Table 10.2, PZT is one of the most preferred materials for energy harvesting. In order to compare with different piezoelectric materials for the energy harvester, the energy stored in dielectric materials is considered with the open circuit load situation. The electrical energy density in dielectric materials,  $\epsilon E^2/2$ , can be expressed by the relationship between the dielectric displacement and mechanical deformations (or strains) of piezoelectric materials with open circuit load condition,  $dY\delta = -\epsilon E$ . The figure of merit (FOM) for energy harvesting is derived by dividing the electrical energy density by the mechanical deformations in dielectric materials,  $\epsilon E^2/\delta^2$ , [18, 3]. Therefore, the FOM can be defined as

$$\text{FOM} = \frac{d^2 Y^2}{\epsilon} = \frac{e^2}{\epsilon} \quad (10.6)$$

where  $E$  is electric field,  $d$  is the piezoelectric strain coefficient,  $Y$  is the elastic modulus,  $\delta$  is the mechanical deformation (strain),  $\epsilon$  is the permittivity, and  $e$  is piezoelectric stress coefficient,  $e = dY$ .

Although the PZT has large piezoelectric coefficient and electromechanical coupling as shown in Table 10.2, the calculated FOM shows that AlN is comparable or even higher than that of PZT material because of its low dielectric constant. Thus the AlN can also be a good choice for piezoelectric energy harvesters [18]. The fabrication sequence of AlN and ZnO films is also compatible with the semiconductor fabrication process. However, these thin films exhibit relatively low piezoelectric constant.

The ferroelectric and piezoelectric properties of PZT films depend on many condition parameters, including the composition, crystallographic structure, grain, and film orientation [20]. In particular, a high piezoelectric constant is generally observed at the morphotropic phase boundaries (MPB) in PZT thin films with Zr/Ti ratios of 52:48 because the phase diagram of PZT is dominated by a concentrations of zirconate (Zr) and titanate (Ti) crystallized in a two-phase system of rhombohedral and tetragonal perovskite phase, respectively. The fabrication of PZT thin films has been actively researched for ferroelectric random access memories (FeRAM) and piezoelectric MEMS sensors and actuators. At present, high-quality PZT thin films can be deposited by several techniques such as sol-gel [29–31], sputtering [32–34], pulse laser deposition (PLD) [31, 35],

metal organic chemical vapor deposition (MOCVD) [36, 37], plasma-enhanced chemical vapor deposition (PECVD) [38, 39], and atomic layer deposition (ALD) [40]. These deposition methods have pros and cons in deposition rate, processing temperature, film uniformity, compositional control, productivity, and cost. The sol-gel method is one of the most preferred deposition techniques for PZT thin films for MEMSs-related microelectronics due to its cost effectiveness. However, the textured growth of PZT thin film for optimizing piezoelectric and ferroelectric properties is complicated and requires a precise control.

Micromachining is used for MEMS energy harvesters because the mechanical structure must be released to oscillate. This process results in a cantilever structure with a membrane, proof mass, and cavity underneath the membrane. Both front and back side of surface and bulk micromachining are optionally utilized for the release process. Bulk micromachining is widely implemented to form a proof mass and cavity in bulk silicon by using a wet or dry etching technique. Wet etching of silicon in potassium hydroxide (KOH) or tetramethylammonium hydroxide (TMAH) is presented in [18, 19]. Dry etching is also used to define a cantilever shape or proof mass and remove bulk silicon to form a cavity by using reactive-ion etching (RIE) or deep reactive-ion etching (DRIE) [7, 14, 22]. Figure 10.3 illustrates the fabrication process using KOH wet etching of silicon. The fabrication process starts with the deposition of  $\text{SiO}_2$  and  $\text{Si}_3\text{N}_4$  to form an isolation layer. Next, the deposition and patterning of a Pt bottom electrode with

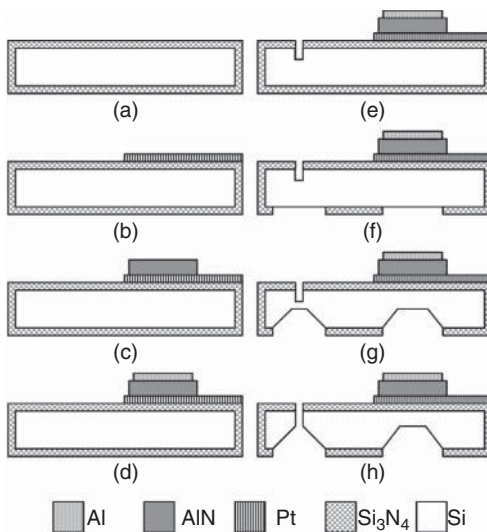


**Figure 10.3** Fabrication sequences by using wet etching of silicon: (a)  $\text{Si}_3\text{N}_4$  and  $\text{SiO}_2$  deposition, (b) Pt bottom electrode deposition and patterned, (c) AlN film deposited by reactive sputtering and patterned, (d) Al top electrode deposition, (e) define the cantilever by DRIE, (f) backside  $\text{Si}_3\text{N}_4/\text{SiO}_2$  patterning as hardmask for KOH wet etching, (g) formation of the mass by KOH etching and stopping before complete release, and (h) complete release by TMAH etching [18].



the Ta adhesion layer follows. Then, an AlN piezoelectric layer is deposited and patterned with a thickness of 400 nm by reactive sputtering from an Al target. The aluminum (Al) top electrode is deposited and patterned to form the piezoelectric transducer. In order to define the silicon cantilever, DRIE is performed with depth of designated thickness of the cantilever. The back of  $\text{SiO}_2/\text{Si}_3\text{N}_4$  is patterned as a hardmask for the KOH etching process and the mass is formed by KOH etching. The etching process must be stopped before it completely releases the cantilever because KOH has bad etch selectivity toward Al and AlN. The release is done either with dry etching or wet etching with TMAH solution. Figure 10.4 illustrates the fabrication process using DRIE of silicon. The fabrication process is based on the front- and backside DRIE of a SOI substrate. Firstly, thermal oxidation is performed to obtain a silicon oxide layer for the electric diffusion barrier. Then, a  $\text{ZrO}_2$  buffer layer is deposited for the PZT deposition process and a  $\text{PbTiO}_3$  seed layer is applied as an interlayer between the  $\text{ZrO}_2$  and PZT thin film. Next, a PZT thin film is deposited with a Zr/Ti ratio of 52/48. These thin films are processed using the sol-gel deposition method and a Pt layer is sputtered for electrodes. The Pt and PZT layers are patterned by the inductively coupled plasma (ICP) dry etching technique to form interdigital shaped electrodes and piezoelectric transducers on cantilevers. A silicon cantilever beam and inertial mass were defined by front- and backside silicon DRIE etching, respectively. The buried silicon oxide

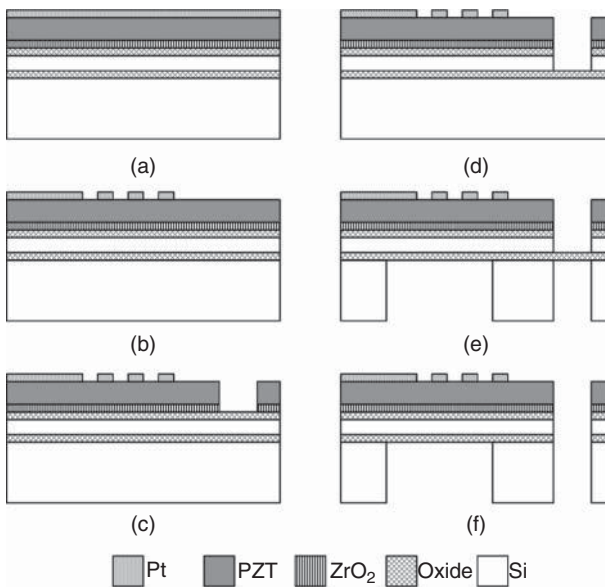


**Figure 10.4** Fabrication sequences by using SOI wafer: (a) thermal oxidation and buffer-layer/seed-layer/PZT/electrode deposition, (b) PZT etching by ICP dry etching, (c) PZT etching by ICP dry etching, (d) Si beam patterning by DRIE, (e) proof mass patterning by DRIE, and (f) release via buried oxide etching by RIE [7].

especially was utilized as an etch-stop for DRIE to control the thickness of the cantilever beam accurately. Finally, the cantilever device is released by RIE etching the buried oxide.

The packaging technology for the MEMS energy harvester is also very important for the energy harvesting module and for improving the performance. Elfrink *et al.* investigated the vacuum- and atmospheric pressure-level packaging for the AlN-based MEMS energy harvester [18, 19]. They presented a wafer-level vacuum packaging process for maximum output because parasitic damping contributes to performance deterioration of the energy harvester, and demonstrated a low-power-consuming wireless sensor system powered by the fabricated piezoelectric energy harvester [19]. Aktakka *et al.* also reported a die-level hermetic packaging process for a thinned-PZT-based MEMS energy harvester [21]. The die-level hermetic packaging consists of the top and bottom cap pieces and is performed in a single bonding step using mechanical registration for alignment. The top cap of packaging is fabricated by using a glass–silicon substrate with electrical vias and aluminum interconnects can be used as a platform for the integration of surface-mounted power management integrated circuits (ICs) and components. They presented the energy harvesting module by the integration of a power management IC and additional surface-mounted components by using die-level hermetic packaging [41] (Figure 10.5).

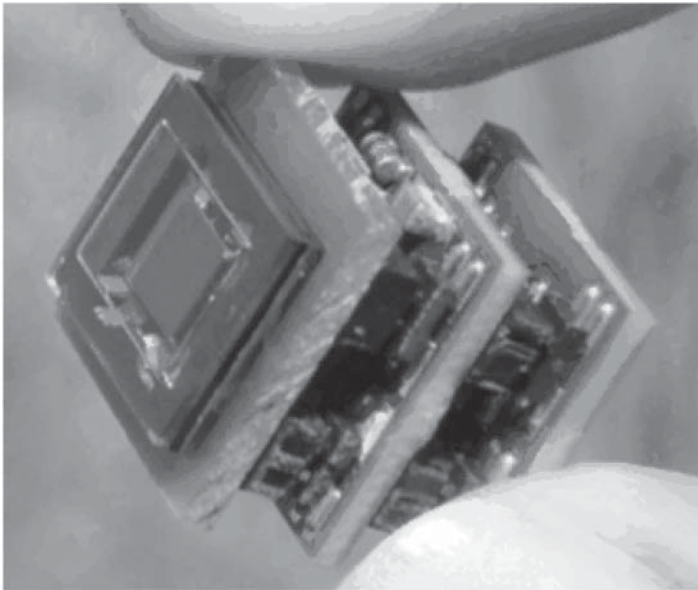


**Figure 10.5** The cube-shaped wireless autonomous sensor system using the AlN-based MEMS energy harvester placed on top to generate  $17\mu\text{W}$  from an induced vibration frequency of 353 Hz and acceleration of 0.64g [19].

## 10.2.3

**Characterization**

The characterization of piezoelectric MEMS energy harvesters is performed using a vibration exciter, function generator to control induced vibration, accelerometer, and voltmeter. However, as the output impedance of a piezoelectric MEMS device is larger than input impedances of these meters, miniaturized or micro-sized energy harvesters may not be characterized accurately. For measuring and characterizing these devices accurately, ultra-high-impedance meters should be used. The fabricated device is connected to an impedance voltmeter and an input acceleration is then applied and monitored by the attached accelerometer. To measure the output of a MEMS energy harvester, the device must be attached on a vibration exciter. When a continuous vibration with specified acceleration is applied to the device, an output voltage or current across an external load is measured. The following test procedure is performed:

- 1) A specified vibration is induced to the MEMS energy harvester.
- 2) The voltage or current across the external load which is connected to the terminals of energy harvester is measured using a voltage or current meter.
- 3) The resonance frequency is defined by measuring the voltage or current with various induced frequencies controlled by a function generator connected to an amplifier.
- 4) The voltage and current are measured with various accelerations by adjusting the amplifying ratio of the amplifier connected to the vibration exciter.
- 5) The maximum voltage and current are derived from various external loads to find the optimal load by adjusting a potentiometer.

**10.2.3.1 Frequency Response**

The resonance frequency is a measured frequency, normally expressed in hertz, at which the piezoelectric MEMS energy harvester generates the largest output power to be used in a subsystem and system applications. As shown in Figure 10.6, the piezoelectric MEMS energy harvester generated a maximum output power at its resonance frequency. The  $Q$ -factor is calculated from the peak output voltage and power at the resonance frequency. While a high  $Q$ -factor is effective for energy conversion, the output power will be sharply reduced if there is a slight deviation of the vibration frequency from the resonance frequency. The bandwidth is the working frequency range of the energy harvester having designated output power to be used in subsystem and system applications. It is the measured range, normally expressed in hertz, of the separation between the lower and upper frequencies relative to the specified value of the frequency response curve.

**10.2.3.2 Output Power of Piezoelectric MEMS Energy Harvesters**

The output voltage is the voltage measured across the terminals of the piezoelectric MEMS energy harvester with a specified external load and induced vibration. It is generally measured at the resonance frequency. The optimal load impedance ( $R_{\text{opt}}$ ) for maximum power transfer is found by varying the external load at the

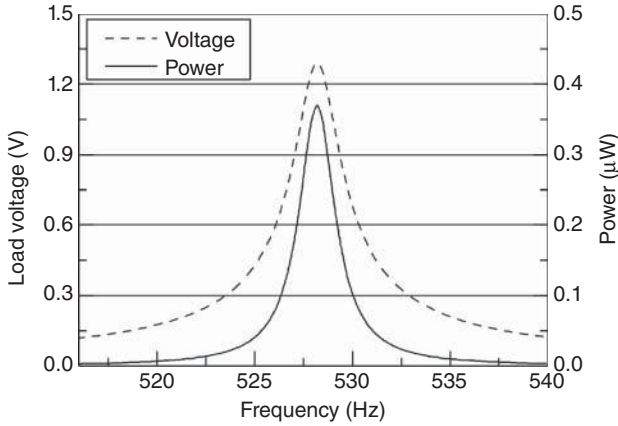


**Figure 10.6** Output voltage and power of piezoelectric MEMS energy harvester using {3-3} mode from various frequencies at a load of 2.2 MΩ and an fixed acceleration of 0.2g [7].

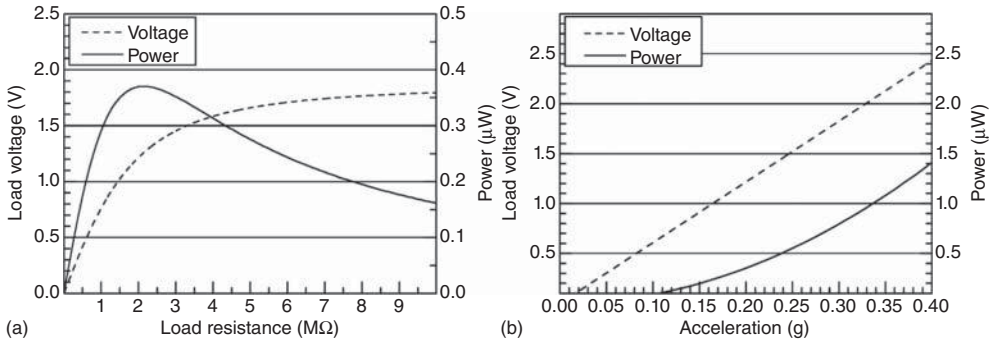


**Figure 10.7** Output voltage and power of piezoelectric MEMS energy harvester using {3-3} mode from various loads at a fixed acceleration of 0.2g (a) and various accelerations with an optimal load of 2.2 MΩ and resonance frequency of 528 Hz (b) [7].

resonance frequency. The maximum output power is obtained at the optimal load of the device as shown in Figure 10.7a. The optimal load also can be predicted by the measured capacitance ( $C_p$ ) of the piezoelectric MEMS harvester by using the following equations.

$$R_{\text{opt}} = \frac{1}{\omega_n C_p} \frac{2\zeta}{\sqrt{4\zeta^2 + k_p^4}} \quad (10.7)$$

Figure 10.7b shows the performance characteristics of a MEMS energy harvester at various accelerations. The output power of MEMS energy harvesters is proportional to the square of the induced acceleration as presented Eq. (10.4). The FOM factors for all different MEMS energy harvesters can be defined as the ratio of generated power over the device volume (volume power density, microwatts per square centimeter) or over the device area (area power density, microwatts

per square centimeter). Since the resonance frequency for all MEMS energy harvesters is different, the normalized output power also takes into account both volume and acceleration as shown in Table 10.1.

### 10.3

#### Challenging Issues in Piezoelectric MEMS Energy Harvesters

Many piezoelectric MEMS energy harvesters have been reported as listed in Table 10.1. Most of the reported devices show several microwatts of output power from their resonance frequencies. This is not sufficient for practical applications such as wireless sensor nodes because low-power ICs have a power consumption of tens to hundreds of microwatts and the ambient vibration is nonperiodic and omnidirectional. Several studies have been actively conducted to address the challenges of large output power, improved frequency response, and good piezoelectric materials.

#### 10.3.1

##### Output Power

The most simple and direct approach to improve the output power or voltage of MEMS energy harvester with fixed size or volume is the increment of the piezoelectric coefficient. Aktakka *et al.*, presented the thinned-PZT/Si process for unimorph and multimorph cantilever-based vibration energy harvesting [21, 22, 42]. Figure 10.8 illustrates the fabrication of the thinned-PZT/Si process. This process employed a bulk PZT piece bonded onto a SOI wafer which has higher electromechanical coupling and efficiency than the thin film AlN or PZT do. This process included the bonding process of PZT pieces to Si using AuIn transient liquid phase (TLP) and a thinning process. Typical bulk-micromachining was utilized to release the cantilever. The proof mass could be formed by using either a silicon or tungsten piece. Die-level hermetic packaging of the cantilever was also presented by using a glass substrate and low resistivity silicon with a bonding process. An unpackaged harvester with a tungsten proof mass produced  $205 \mu\text{W}$  at 1.5 g (154 Hz) at resonance. The active device volume was  $27 \text{ mm}^3$  ( $7 \text{ mm} \times 7 \text{ mm} \times 0.55 \text{ mm}$ ) [21, 41].

Further, Stewart *et al.* reported efficient coverage of electrodes for PZT film on a cantilever-based vibration energy harvester [43]. The strain-stress of the piezoelectric layer due to the bending of the cantilever has an inhomogeneous distribution with distance from the fixed area. The inhomogeneous distribution of strain causes internal loss because the charge flows from the highly strained fixed area of the cantilever to the unstrained tip. This charge redistribution process uses electrical energy and reduces the effectiveness of the harvester. The analytic model and experimental results indicated that the output power can be increased up to 18% with electrode coverage of two-thirds of the cantilever.

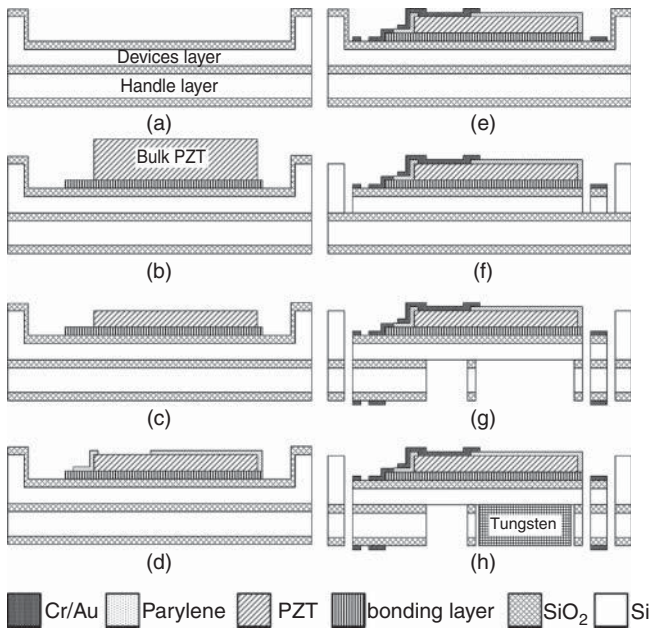


**Figure 10.8** Fabrication sequences using the thinned-PZT/Si harvester: (a) DRIE recess on SOI and oxidation, (b) evaporation of bonding layer and bonding of bulk PZT piece, (c) mechanical thinning of bulk PZT, (d) deposition and patterning of parylene, (e) Cr/Au sputtering and patterned by wet etching, (f) etching of front-side oxide and silicon, (g) etching of backside oxide and silicon, and (h) evaporation of bonding layer and bonding of tungsten mass [21].

In order to improve the output voltage and conversion efficiency, the piezoelectric mode of cantilever also has been considered. In the piezoelectric cantilever using PZT thin film, the two main modes of operation can be defined by the configuration of electrodes. The {3-1} mode is typically utilized for the PZT cantilever because of its simple structure and fabrication issues of PZT thin film. In order to improve the output voltage of MEMS energy harvesters, the electrodes for the {3-3} mode were arranged in the transverse direction as shown in Figure 10.9. The {3-3} mode is more effective for the energy harvesting of low-level vibrations because this mode prevents charge redistribution and generates a larger voltage than the {3-1} mode, with less displacement of the cantilever due to its larger piezoelectric constant and lower capacitance [7, 13, 16, 23]. Jeon *et al.* developed a {3-3} mode thin-film PZT cantilever device with interdigitated electrodes that can generate  $1.0 \mu\text{W}$  from  $10.8g$  vibration at a resonance frequency of  $13.9 \text{ kHz}$  [23]. Park *et al.* reported a bulk-micromachined MEMS energy harvester using the {3-3} mode. It generated an electrical power of  $1.1 \mu\text{W}$  from an extremely low acceleration of  $0.39g$ . The corresponding power density was  $7.3 \text{ mW cm}^{-3} \text{ g}^{-2}$  [7].

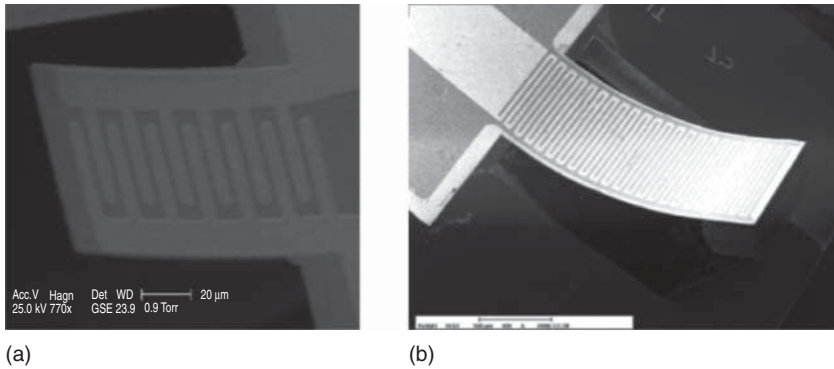


**Figure 10.9** Piezoelectric MEMS energy harvester using {3-3} mode: (a) thin-film PZT cantilever device with interdigitated electrodes [23] and (b) bulk-micromachined MEMS energy harvester using {3-3} mode [13].

### 10.3.2

#### Frequency Response

Typical piezoelectric MEMS energy harvesters consist of a cantilever with unimorph or multimorph piezoelectric layers and a proof mass attached at the end. Single degree of freedom (SDOF) cantilever-based energy harvesters have a single resonance frequency peak with a narrow frequency bandwidth from one-dimensional vibration and they may not generate sufficient power from a nonperiodic or omnidirectional vibration which has time-variant frequency or direction, respectively. Energy harvesters with improved frequency response have been actively investigated by many researchers.

The frequency bandwidth can be simply improved by a parallel arrangement of SDOF cantilever structures. Ferrari *et al.* reported multifrequency vibration energy harvesters by using multiple bimorph cantilevers with different natural frequencies [44]. These piezoelectric cantilevers individually fed rectifying circuits and were connected to a single storage capacitor. The experimental results presented the feasibility of the energy harvester with a wide frequency bandwidth. Xue *et al.* reported a similar method for wideband energy harvesting by integrating multiple piezoelectric bimorphs with different resonance frequencies [45]. Experimental results presented wideband output power for 10 piezoelectric bimorphs in series with various thicknesses of piezoelectric layers. Kim *et al.* reported a different method for wideband energy harvesting by using a two degree of freedom (DOF) piezoelectric energy harvesting device [46]. The proposed structure was comprised of two piezoelectric cantilevers for translational and rotational degrees of freedom. The experimental results presented double frequency peaks and an increased frequency bandwidth. Soliman *et al.* also reported a different method for wideband energy harvesting [47, 48]. The analytic model and experimental results reported that the operation bandwidth was increased up to 240% by using a mechanical stopper to change the stiffness of the resonator. Recently,

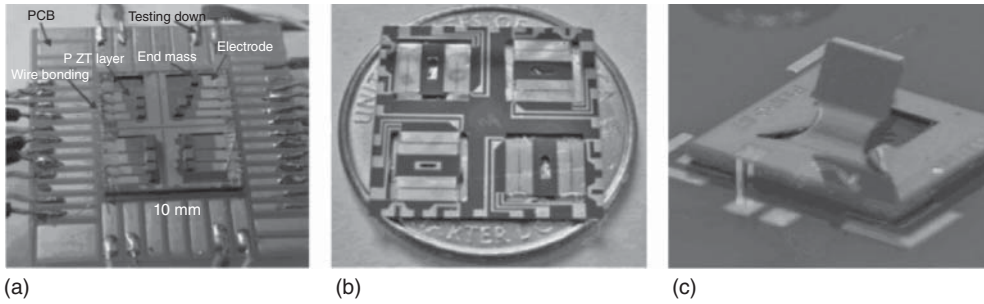


**Figure 10.10** Various structures to improve frequency response for piezoelectric MEMS energy harvesters: (a) wideband vibration energy harvester using arrayed PZT cantilevers [50], (b) nonlinear resonant piezoelectric energy harvester [52], and (c) mimetic structure of multi-DOF by using a curled cantilever for a two-dimensional vibration energy harvester [53].

bistable oscillators have been introduced for nonlinear vibration energy harvesting by using a buckled configuration. Cottone *et al.* reported a theoretical model and experimental results under wideband random vibrations by using a thin piezoelectric axially loaded beam [49]. However, they only demonstrated a prototype of a bulk-sized device and a few devices were demonstrated in MEMS.

Figure 10.10 presents various structures for MEMS energy harvesters to improve the frequency response. Liu *et al.* demonstrated a wideband vibration energy harvester using arrayed PZT cantilevers [50]. The vibration energy harvesters were comprised of PZT cantilever with Ni proof mass and array-based PZT cantilevers were connected in series. The fabricated devices exhibited an output of  $3.98 \mu\text{W}$  from an excitation frequency of 229 Hz and bandwidth of 8 Hz. This was a promising result for expanded bandwidth for energy harvesting. Liu *et al.* also reported a piezoelectric MEMS energy harvester for low frequency and wide frequency bandwidth by using a parallel arrangement of 10 PZT cantilever elements [51]. These PZT cantilever elements were electrically isolated and integrated with the proof masses at the end of the cantilever elements. The measured output power was varied from 19.4 to  $51.3 \text{ nW}$  within the operation frequency bandwidth ranging from 30 to 47 Hz at  $1.0g$ . Hajati *et al.* also demonstrated a MEMS-based nonlinear resonant piezoelectric energy harvester for achieving the wide bandwidth [52]. The nonlinear resonance-based energy harvester exhibited an ultrawide bandwidth of  $>20\%$  of the center frequency and output power of more than  $22 \mu\text{W}$ . The consideration for omnidirectional vibration energy harvesting applications led to the introduction of a three-dimensional structure for the vibration energy harvester. Park *et al.* reported a curled cantilever which is the mimetic structure of multi-DOF for two-dimensional vibration energy harvesting [53]. While the conventional SDOF cantilever energy harvester maintains almost its maximum output power when it is installed within 20 degrees of the operating direction, the curled cantilever device exhibited significantly improved results in that the output power is independent of the installation angle.



## 10.3.3

**Piezoelectric Material**

Epitaxially grown PZT thin films are ideal for MEMS energy harvesters owing to their larger piezoelectric constant and lower dielectric constant than polycrystalline PZT films. The MPB of PZT is considered to have a superior ferroelectric and piezoelectric properties due to its large number of possible polarization directions (eight [1 1 1] for the rhombohedral phase and six [1 0 0] for the tetragonal phase) and the consequent extrinsic contributions of this boundary. However, the properties of PZT thin films show a different results compared with bulk ceramics due to their polycrystalline structure, because PZT thin films are typically deposited on Pt-coated silicon substrates directly. Thus, several studies have been performed to improve the piezoelectric properties of epitaxial PZT films. To improve the piezoelectric properties of PZT thin films, the interfacial between the PZT thin film and substrate was controlled by applying a buffer-layer such as SrTiO<sub>3</sub> (STO), yttria-stabilized zirconia (YSZ), and MgO [54–56]. Han *et al.* reported improved piezoelectric and ferroelectric properties of PZT films by adjusting the residual stress by depositing on various substrates with different thermal expansion coefficients [54]. The ferroelectric and piezoelectric properties of a PZT thin film are also dependent on the thickness of the film [57]. For improving energy conversion efficiency, Morimoto *et al.* demonstrated a piezoelectric energy harvester using a *c*-axis-oriented PZT thin film. The epitaxially grown PZT thin film on a Pt/MgO substrate was transferred onto a stainless steel cantilever. Although the transferred PZT film had a lower piezoelectric constant ( $d_{31}$ ) of  $-49 \text{ pm V}^{-1}$  than bulk PZT ( $d_{31} = -93.5 \text{ pm V}^{-1}$ ), the transferred film showed a higher electromechanical coupling coefficient of 0.39, which is larger than that of bulk PZT (0.313) owing to the low dielectric constant ( $\epsilon_r = 166$ ) [58].

For the application for wireless sensor nodes distributed in the environment, a lead-free piezoelectric material is desirable owing to the toxicity of Pb. Potassium sodium niobate ( $\text{K}_x\text{Na}_{1-x}\text{NbO}_3$ , (KNN) is a promising alternative to PZT as lead-free piezoelectric material because KNN has a high electromechanical coupling coefficient and can be deposited on the substrate using RF magnetron sputtering [59]. Hara *et al.* and Kanno *et al.* reported a KNN-based piezoelectric MEMS energy harvester as shown in Figure 10.11a [60, 61]. According to Kanno *et al.*, KNN has similar piezoelectric and ferroelectric properties resulting in 1.1 and  $1.0 \mu\text{W}$  for KNN/Si and PZT/Si cantilever devices, respectively [61].

AlN film also has been considered as a promising alternative to PZT for MEMS energy harvesters. AlN has a large electromechanical coupling coefficient and can be deposited through Complementary metal-oxide-semiconductor (CMOS)-compatible sputtering processes. Since, Elfrink *et al.* reported an AlN-based MEMS energy harvester which resulted in a maximum output power of  $85 \mu\text{W}$  from a resonance frequency of 325 Hz and an acceleration of  $1.75g$  [63]. Yen *et al.* also reported an AlN-based energy harvester to improve the energy conversion effectiveness by applying a corrugated structure as shown in Figure 10.11b [62].

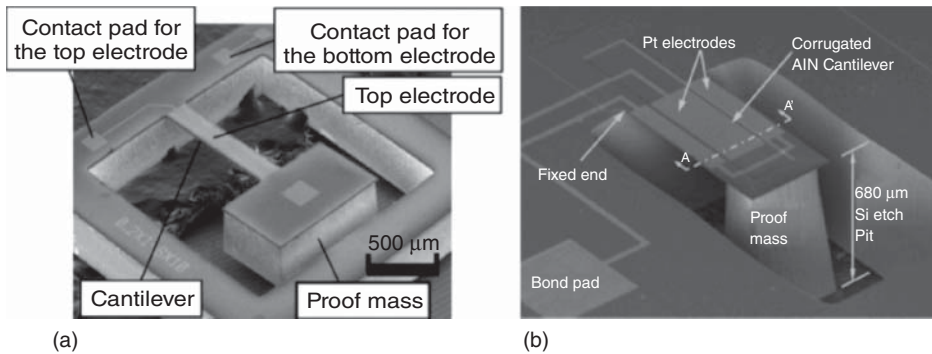


**Figure 10.11** Lead-free piezoelectric material-based MEMS energy harvesters: (a) KNN-based piezoelectric MEMS energy harvester [60] and (b) AlN-based energy harvester using corrugated structure to improve the energy conversion effectiveness [62].

#### 10.4 Summary

Energy harvesting technology is an ideal power source for wireless sensor networks because it can provide low maintenance cost and infinite lifetime for wireless autonomous systems. Piezoelectric MEMS energy harvesters with a volume less than  $1 \text{ cm}^3$  will replace or support the battery of autonomous microsystems by generating several hundred microwatts of power from the ambient vibration with continuous operation and low maintenance cost.

Piezoelectric MEMS energy harvesters have been developed to achieve large output power and improved frequency response. The current state of the art is still generating several tens of microwatts, which is smaller than the needs of practical applications and has narrow frequency bandwidth. Therefore, the advances for MEMS energy harvesters focus on the piezoelectric materials and structure, individually or in combination. Many of the studies on the fabrication of epitaxial piezoelectric thin films or lead-free materials with a large piezoelectric constant will lead to an increase in the electromechanical energy conversion efficiency of piezoelectric harvesters. Furthermore, nonlinear resonators or three-dimensional mimetic structures are promising to generate electrical energy from a much wider bandwidth or omnidirectional vibration, respectively. In the near future, a MEMS energy harvesting module will appear for autonomous wireless sensor nodes or microsystems by harvesting about  $100 \mu\text{W}$  of sustainable power from ambient vibration with low frequency below 200 Hz and acceleration less than  $1g$ .

#### References

1. Anton, S.R. and Sodano, H.A. (2007) A review of power harvesting using piezoelectric materials (2003–2006). *Smart Mater. Struct.*, **16**, R1.
2. Beeby, S.P., Tudor, M.J., and White, N. (2006) Energy harvesting vibration sources for microsystems applications. *Meas. Sci. Technol.*, **17**, R175.

3. Roundy, S., Wright, P.K., and Rabaey, J. (2003) A study of low level vibrations as a power source for wireless sensor nodes. *Comput. Commun.*, **26**, 1131–1144.
4. Gilbert, J.M. and Balouchi, F. (2008) Comparison of energy harvesting systems for wireless sensor networks. *Int. J. Autom. Comput.*, **5**, 334–347.
5. Muralt, P., Marzencki, M., Belgacem, B., Calame, F., and Basrou, S. (2009) Vibration energy harvesting with PZT micro device. *Procedia Chem.*, **1**, 1191–1194.
6. Renaud, M., Karakaya, K., Sterken, T., Fiorini, P., Van Hoof, C., and Puers, R. (2008) Fabrication, modelling and characterization of MEMS piezoelectric vibration harvesters. *Sens. Actuators, A*, **145**, 380–386.
7. Park, J.C., Park, J.Y., and Lee, Y.-P. (2010) Modeling and characterization of piezoelectric d33-mode MEMS energy harvester. *J. Microelectromech. Syst.*, **19**, 1215–1222.
8. Roundy, S. and Wright, P.K. (2004) A piezoelectric vibration based generator for wireless electronics. *Smart Mater. Struct.*, **13**, 1131.
9. Roundy, S., Wright, P.K., and Rabaey, J.M. (2004) *Energy Scavenging for Wireless Sensor Networks: with Special Focus on Vibrations*, Springer.
10. Williams, C. and Yates, R.B. (1996) Analysis of a micro-electric generator for microsystems. *Sens. Actuators, A*, **52**, 8–11.
11. Zurn, S., Hsieh, M., Smith, G., Markus, D., Zang, M., Hughes, G., Nam, Y., Arik, M., and Polla, D. (2001) Fabrication and structural characterization of a resonant frequency PZT microcantilever. *Smart Mater. Struct.*, **10**, 252.
12. Fang, H.-B., Liu, J.-Q., Xu, Z.-Y., Dong, L., Wang, L., Chen, D., Cai, B.-C., and Liu, Y. (2006) Fabrication and performance of MEMS-based piezoelectric power generator for vibration energy harvesting. *Microelectron. J.*, **37**, 1280–1284.
13. Lee, B., Lin, S., Wu, W., Wang, X., Chang, P., and Lee, C. (2009) Piezoelectric MEMS generators fabricated with an aerosol deposition PZT thin film. *J. Micromech. Microeng.*, **19**, 065014.
14. Shen, D., Park, J.-H., Ajitsaria, J., Choe, S.-Y., Wikle, H.C. III, and Kim, D.-J. (2008) The design, fabrication and evaluation of a MEMS PZT cantilever with an integrated Si proof mass for vibration energy harvesting. *J. Micromech. Microeng.*, **18**, 055017.
15. Shen, D., Park, J.-H., Noh, J.H., Choe, S.-Y., Kim, S.-H., Wikle, H.C. III, and Kim, D.-J. (2009) Micromachined PZT cantilever based on SOI structure for low frequency vibration energy harvesting. *Sens. Actuators, A*, **154**, 103–108.
16. Choi, W., Jeon, Y., Jeong, J.-H., Sood, R., and Kim, S.-G. (2006) Energy harvesting MEMS device based on thin film piezoelectric cantilevers. *J. Electroceram.*, **17**, 543–548.
17. Marzencki, M., Ammar, Y., and Basrou, S. (2008) Integrated power harvesting system including a MEMS generator and a power management circuit. *Sens. Actuators, A*, **145**, 363–370.
18. Elfrink, R., Kamel, T., Goedbloed, M., Matova, S., Hohlfeld, D., Van Andel, Y., and Van Schaijk, R. (2009) Vibration energy harvesting with aluminum nitride-based piezoelectric devices. *J. Micromech. Microeng.*, **19**, 094005.
19. Elfrink, R., Renaud, M., Kamel, T., De Nooijer, C., Jambunathan, M., Goedbloed, M., Hohlfeld, D., Matova, S., Pop, V., and Caballero, L. (2010) Vacuum-packaged piezoelectric vibration energy harvesters: damping contributions and autonomy for a wireless sensor system. *J. Micromech. Microeng.*, **20**, 104001.
20. Trolier-McKinstry, S. and Muralt, P. (2004) Thin film piezoelectrics for MEMS. *J. Electroceram.*, **12**, 7–17.
21. Aktakka, E., Peterson, R., and Najafi, K. (2011a) Thinned-PZT on SOI process and design optimization for piezoelectric inertial energy harvesting. Paper presented at 2011 16th International (IEEE) Solid-State Sensors, Actuators and Microsystems Conference (TRANSDUCERS).
22. Aktakka, E.E., Peterson, R.L., and Najafi, K. (2010). A CMOS-compatible piezoelectric vibration energy scavenger based on the integration of bulk PZT films on silicon. Paper Presented at 2010 IEEE

- International (IEEE) Electron Devices Meeting (IEDM).
23. Jeon, Y., Sood, R., Jeong, J.-h., and Kim, S.-G. (2005) MEMS power generator with transverse mode thin film PZT. *Sens. Actuators, A*, **122**, 16–22.
  24. Xu, R., Lei, A., Dahl-Petersen, C., Hansen, K., Guizzetti, M., Birkelund, K., Thomsen, E.V., and Hansen, O. (2012) Screen printed PZT/PZT thick film bimorph MEMS cantilever device for vibration energy harvesting. *Sens. Actuators, A*, **188**, 383–388.
  25. I. Kanno, T. Ichida, K. Adachi, H. Kotera, K. Shibata, and T. Mishima (2012) Power-generation performance of lead-free (K,Na)NbO<sub>3</sub> piezoelectric thin-film energy harvesters. *Sens. Actuators, A: Phys.*, **179**, 132–136.
  26. Ledermann, N., Mural, P., Babrowski, J., Gentil, S., Mukati, K., Cantoni, M., Seifert, A., and Setter, N. (2003) {1 0 0}-Textured, piezoelectric Pb(Zrx, Tl1-x)O<sub>3</sub> thin films for MEMS: integration, deposition and properties. *Sens. Actuators, A*, **105**, 162–170.
  27. Dubois, M.-A. and Mural, P. (1999) Properties of aluminum nitride thin films for piezoelectric transducers and microwave filter applications. *Appl. Phys. Lett.*, **74**, 3032–3034.
  28. Carlotti, G., Socino, G., Petri, A., and Verona, E. (1987) Acoustic investigation of the elastic properties of ZnO films. *Appl. Phys. Lett.*, **51**, 1889–1891.
  29. Budd, K.D., Key, S., and Payne, D. (1985) Sol-gel processing of PbTiO<sub>3</sub>, PbZrO<sub>3</sub>, PZT and PLZT thin films. Paper presented at Proceedings of the British Ceramic Society.
  30. Dey, S., Budd, K.D., and Payne, D.A. (1988) Thin-film ferroelectrics of PZT of sol-gel processing. *IEEE Trans. Ultrason. Ferroelectr. Freq. Control*, **35**, 80–81.
  31. Pandey, S., James, A., Prakash, C., Goel, T., and Zimik, K. (2004) Electrical properties of PZT thin films grown by sol-gel and PLD using a seed layer. *Mater. Sci. Eng., B*, **112**, 96–100.
  32. Bouregba, R., Sama, N., Soyer, C., and Remiens, D. (2009) Analysis of size effects in Pb (ZrTi) O thin film capacitors with platinum and LaNiO conducting oxide electrodes. *J. Appl. Phys.*, **106**, 044101.
  33. Hata, T., Kawagoe, S., Zhang, W., Sasaki, K., and Yoshioka, Y. (1998) Proposal of new mixture target for PZT thin films by reactive sputtering. *Vacuum*, **51**, 665–671.
  34. Wang, C. and Kryder, M.H. (2009) Low Fatigue in Epitaxial Pb (Zr<sub>0.2</sub>Ti<sub>0.8</sub>) O<sub>3</sub> on Si Substrates with LaNiO<sub>3</sub> Electrodes by RF Sputtering. *J. Electron. Mater.*, **38**, 1921–1925.
  35. Walker, D., Thomas, P.A., and Collins, S.P. (2009) A comprehensive investigation of the structural properties of ferroelectric PbZr<sub>0.2</sub>Ti<sub>0.8</sub>O<sub>3</sub> thin films grown by PLD. *Phys. Status Solidi A*, **206**, 1799–1803.
  36. Otani, Y., Okamura, S., and Shiosaki, T. (2004) Recent developments on MOCVD of ferroelectric thin films. *J. Electroceram.*, **13**, 15–22.
  37. Sakashita, Y., Ono, T., Segawa, H., Tominaga, K., and Okada, M. (1991) Preparation and electrical properties of MOCVD-deposited PZT thin films. *J. Appl. Phys.*, **69**, 8352–8357.
  38. Chung, S.O., Kim, J.W., Kim, S.T., Kim, G.H., and Lee, W.J. (1998) Microstructure and electric properties of the PZT thin films fabricated by ECR PECVD: the effects of an interfacial layer and rapid thermal annealing. *Mater. Chem. Phys.*, **53**, 60–66.
  39. Lee, H.-C. and Lee, W.-J. (2002) Characterization of Pb (Zr, Ti) O<sub>3</sub> thin films fabricated by plasma enhanced chemical vapor deposition on Ir-based electrodes. *J. Vac. Sci. Technol., A: Vac. Surf. Films*, **20**, 1939–1947.
  40. Watanabe, T., Hoffmann-Eifert, S., Waser, R., and Hwang, C.S. (2006) Atomic layer deposition of Pb (Zr, Ti) O<sub>x</sub> thin films by a combination of binary atomic layer deposition processes. Paper Presented at Applications of Ferroelectrics, 2006 ISAF'06 15th IEEE International Symposium on the (IEEE).
  41. Najafi, K., Galchev, T., Aktakka, E., Peterson, R., and McCullagh, J. (2011) Microsystems for energy harvesting. Paper presented at 2011 16th International (IEEE) Solid-State Sensors,

- Actuators and Microsystems Conference (TRANSDUCERS).
42. Aktakka, E.E., Peterson, R.L., and Najafi, K. (2011b) Multi-layer PZT stacking process for piezoelectric bimorph energy harvesters. *Diamond*, **10**, 8000.
  43. Stewart, M., Weaver, P.M., and Cain, M. (2012) Charge redistribution in piezoelectric energy harvesters. *Appl. Phys. Lett.*, **100**, 073901.
  44. Ferrari, M., Ferrari, V., Guizzetti, M., Marioli, D., and Taroni, A. (2008) Piezoelectric multifrequency energy converter for power harvesting in autonomous microsystems. *Sens. Actuators, A*, **142**, 329–335.
  45. Xue, H., Hu, Y., and Wang, Q.-M. (2008) Broadband piezoelectric energy harvesting devices using multiple bimorphs with different operating frequencies. *IEEE Trans. Ultrason. Ferroelectr. Freq. Control*, **55**, 2104–2108.
  46. Kim, I.-H., Jung, H.-J., Lee, B.M., and Jang, S.-J. (2011) Broadband energy-harvesting using a two degree-of-freedom vibrating body. *Appl. Phys. Lett.*, **98**, 214102.
  47. Soliman, M., Abdel-Rahman, E., El-Saadany, E., and Mansour, R. (2008) A wideband vibration-based energy harvester. *J. Micromech. Microeng.*, **18**, 115021.
  48. Soliman, M., Abdel-Rahman, E.M., El-Saadany, E.F., and Mansour, R.R. (2009) A design procedure for wideband micropower generators. *J. Microelectromech. Syst.*, **18**, 1288–1299.
  49. Cottone, F., Gammaitoni, L., Vocca, H., Ferrari, M., and Ferrari, V. (2012) Piezoelectric buckled beams for random vibration energy harvesting. *Smart Mater. Struct.*, **21**, 035021.
  50. Liu, J.-Q., Fang, H.-B., Xu, Z.-Y., Mao, X.-H., Shen, X.-C., Chen, D., Liao, H., and Cai, B.-C. (2008) A MEMS-based piezoelectric power generator array for vibration energy harvesting. *Microelectron. J.*, **39**, 802–806.
  51. Liu, H., Tay, C.J., Quan, C., Kobayashi, T., and Lee, C. (2011) Piezoelectric MEMS energy harvester for low-frequency vibrations with wideband operation range and steadily increased output power. *J. Microelectromech. Syst.*, **20**, 1131–1142.
  52. Hajati, A. and Kim, S.-G. (2011) Ultra-wide bandwidth piezoelectric energy harvesting. *Appl. Phys. Lett.*, **99**, 083105.
  53. Park, J., Khym, S., and Park, J. (2013) Micro-fabricated lead zirconate titanate bent cantilever energy harvester with multi-dimensional operation. *Appl. Phys. Lett.*, **102**, 043901–043904.
  54. Han, G., Ryu, J., Yoon, W.-H., Choi, J.-J., Hahn, B.-D., Kim, J.-W., Park, D.-S., Ahn, C.-W., Priya, S., and Jeong, D.-Y. (2011) Stress-controlled Pb (Zr<sub>0.52</sub>Ti<sub>0.48</sub>) O<sub>3</sub> thick films by thermal expansion mismatch between substrate and Pb (Zr<sub>0.52</sub>Ti<sub>0.48</sub>) O<sub>3</sub> film. *J. Appl. Phys.*, **110**, 124101–124105.
  55. Kanno, I., Fujii, S., Kamada, T., and Takayama, R. (1997) Piezoelectric properties of c-axis oriented Pb (Zr, Ti) O<sub>3</sub> thin films. *Appl. Phys. Lett.*, **70**, 1378–1380.
  56. Kanno, I., Kotera, H., and Wasa, K. (2003) Measurement of transverse piezoelectric properties of PZT thin films. *Sens. Actuators, A*, **107**, 68–74.
  57. Nguyen, M.D., Dekkers, M., Vu, H.N., and Rijnders, G. (2013) Film-thickness and composition dependence of epitaxial thin-film PZT-based mass-sensors. *Sens. Actuators, A*, **199**, 98–105.
  58. Morimoto, K., Kanno, I., Wasa, K., and Kotera, H. (2010) High-efficiency piezoelectric energy harvesters of c-axis-oriented epitaxial PZT films transferred onto stainless steel cantilevers. *Sens. Actuators, A*, **163**, 428–432.
  59. Li, J.F., Wang, K., Zhu, F.Y., Cheng, L.Q., and Yao, F.Z. (2013) (K, Na) NbO<sub>3</sub>-based lead-free piezoceramics: fundamental aspects, processing technologies, and remaining challenges. *J. Am. Ceram. Soc.*, **96**, 3677–3696.
  60. Hara, M., Horikiri, F., Shibata, K., Mishima, T., and Kuwano, H. (2013) Bulk micromachined energy harvesters employing (K, Na) NbO<sub>3</sub> thin film. *J. Micromech. Microeng.*, **23**, 035029.
  61. Kanno, I., Ichida, T., Adachi, K., Kotera, H., Shibata, K., and Mishima, T. (2012) Power-generation performance of lead-free (K, Na) NbO<sub>3</sub> piezoelectric thin-film

- energy harvesters. *Sens. Actuators, A*, **179**, 132–136.
62. Yen, T.-T., Hirasawa, T., Wright, P.K., Pisano, A.P., and Lin, L. (2011) Corrugated aluminum nitride energy harvesters for high energy conversion effectiveness. *J. Micromech. Microeng.*, **21**, 085037.
63. Renaud, M., Elfrink, R., Jambunathan, M., de Nooijer, C., Wang, Z., Rovers, M., Vullers, R., and van Schaijk, R. (2012) Optimum power and efficiency of piezoelectric vibration energy harvesters with sinusoidal and random vibrations. *J. Micromech. Microeng.*, **22**, 105030.

## 11

# Vibration Energy Harvesting from Wideband and Time-Varying Frequencies

*Lindsay M. Miller*

### 11.1

#### Introduction

##### 11.1.1

#### Motivation

Most of the theoretical and experimental work on vibration energy harvesting over the past decade has assumed a single-frequency sinusoidal input excitation to drive an energy harvesting device. The harvester is typically designed to display a linear frequency response at the same fixed single frequency as the input vibration. However, in real applications of harvesting energy from vibrations, the input excitation is most often composed of multiple frequencies that vary over time or may even resemble white noise more closely than a single-frequency sinusoid [1–3]. Therefore, a vibration harvester with a single fixed resonant frequency is very ineffective for generating energy from these real-world vibration sources. For that reason, many researchers are now studying devices for harvesting energy from wideband and time-varying frequencies, building on the large body of work around linear fixed-frequency harvesters.

The goal of this chapter is to give an overview of the strategies for tunable and wideband energy harvesting devices that have been proposed, as well as an example from the literature for each strategy. This chapter also touches on areas for improvement in future research, including which strategies are most promising for implementation in microscale devices. For those readers interested in a thorough literature review, which this chapter does not aim to provide [4], and [5] are excellent starting points.

##### 11.1.2

#### Classification of Devices

There are several important categorizations of the design strategies for harvesters that utilize wideband and time-varying frequency inputs. First, the harvesters themselves are either “tunable resonant devices” or “wideband devices.” The

distinction is that tunable resonant systems have a frequency response with a sharp peak at a single frequency, while wideband systems have a plateau-shaped frequency response. In tunable resonant systems, the design challenge is how to shift the sharp peak to different frequencies to achieve a tuned state without requiring more power than the system can harvest, while in the wideband systems the challenge is how to incorporate nonlinearities to get the desired width of frequency response plateau without sacrificing too much of the output magnitude.

The “tunable resonant devices” class can be further divided into “active” or “passive” strategies (the wideband class of devices are typically all categorized as passive). “Active” is defined here to mean that the system requires an input of either power or human intervention to achieve the tuned state. For example, the input could be a microcontroller, an actuator, and/or a stepper motor, and the power could be supplied by the harvester itself or an external power source. Human intervention for tuning could be in the form of turning a screw, for example.

The “active” classification is subdivided into “continuous,” “intermittent,” and “manual” categories. Continuous systems require electrical power for both achieving and maintaining the tuned state. Intermittent systems require electrical power only for achieving the tuned state, after which the system requires no power to hold the tuned configuration. Manual systems are similar to intermittent systems in that they do not require power input to maintain a tuned state, but the power input used to achieve tuning is manual instead of electrical. In this definition, a system is not considered manual unless a human hand actually doing the tuning. An input typed into a computer sending a signal to actuate the tuning mechanism is not considered manual.

A “passive” system is defined in this chapter to mean that no power, no microcontroller, and no human intervention at all is required to achieve or maintain a tuned state. Passive systems are constantly tuning themselves within the bounds of their operating regime since they rely only on the driving vibration source to achieve the tuned state. This definition of “passive” is different than what has often been used in the literature, in which intermittent systems are considered passive because they do not need power to maintain the tuned state. However, new tunable resonant devices have been recently presented that operate without requiring any power input at all, thus necessitating the strict definition of “passive” that is used in this chapter.

Another important classification is whether or not a system is “self-tuning.” A self-tuning device must be able to sense the driving frequency and tune its resonance to match without requiring any manual intervention. An active system may be capable of self-tuning but still have negative net power generation because it requires more power for frequency sensing, control circuitry, or tuning actuation than it is able to generate. While only some active systems are self-tuning, all passive tunable resonant systems are self-tuning. The term “self-tuning” does not apply to wideband energy harvesters, as they rely on wideband design rather than frequency tuning to take advantage of wideband or time-varying vibration frequencies.



**Table 11.1** Summary of wideband and tunable harvester classifications.

Strategy	Type	Tuning input required	In situ tunable?	Self-tuning?
Tunable resonant	Active	Continuous electrical	Typically yes	Possibly
		Intermittent electrical	Typically yes	Possibly
	Passive	Manual	Typically no	No
Wideband	Passive	None	Yes	Yes

One last notable classification for tuning strategies is whether or not tuning can take place *in situ*, without interrupting the operation of the device. All passive devices (both tunable resonant and wideband) achieve tuning *in situ*, as do self-tuning systems, while only some active devices can. These classifications and characteristics of wideband and tunable harvesters are summarized in Table 11.1

### 11.1.3

#### General Comments

To avoid confusion about the operation of each tunable or wideband device, it is useful to keep in mind that there are three different purposes for which transducers are used. First, all of the devices cited in this chapter have a transducer or other method for tuning or creating a wideband response. Second, many devices incorporate transducers to convert them from simple resonators to vibration energy harvesters. Third, some systems encompass frequency-sensing capability to automate their tuning. Finally, many of the strategies for tuning and increasing bandwidth are presented without an energy harvesting transducer but could be modified easily to include such a component. Similarly, devices that are presented using one type of energy harvesting may possibly be modified to incorporate electrostatic, electromagnetic, or piezoelectric transduction instead. Also, although most systems presented in the literature consist of cantilever, double-clamped, or folded flexure beam geometries, the tuning and wideband concepts may be applied to structures of different geometry.

## 11.2

### Active Schemes for Tunable Resonant Devices

Frequency is given by  $\omega = \sqrt{(k_{\text{eff}}/m_{\text{eff}})}$ , thus schemes for active tuning of resonance frequency focus on modifying either  $k_{\text{eff}}$ , effective stiffness, or  $m_{\text{eff}}$ , effective mass. In the case of a beam in bending,  $k_{\text{eff}} = k_m$ , the mechanical stiffness, and is proportional to  $EI/L^3$ , where  $E$  is elastic modulus,  $I$  is second moment of inertia, and  $L$  is beam length. The moment of inertia is  $wt^3/12$  for a beam in bending, where  $w$  and  $t$  are width and thickness of the beam, respectively. These

relationships show which variables may be adjusted in the energy harvester system in order to modify resonance frequency.

It is not typically possible to adjust  $w$  or  $t$  of an energy harvesting beam without completely rebuilding it, so  $I$  is not a parameter used to tune frequency. However, there have been several methods proposed for varying  $L$  or  $E$ , as well as numerous techniques for adjusting  $k_{\text{eff}}$  or  $m_{\text{eff}}$  for frequency tuning purposes. This section gives an overview of the methods that have been proposed for active modification of effective stiffness and mass for frequency tuning.

### 11.2.1

#### Stiffness Modification for Frequency Tuning

##### 11.2.1.1 Modify $L$

One technique to modify stiffness of a beam is to adjust the clamp location to change length, since  $k_m \propto 1/L^3$ . This could be achieved by manual adjustment of a mechanical clamp, but that is not ideal because operation must be halted while changes are made. A more realistic and *in situ* method that has been demonstrated uses MEMS electrostatic actuators to anchor the beams of a four-spring MEMS comb resonator in order to shorten their original length [6], as illustrated in Figure 11.1. The anchors can be actuated or left off, so the resonator can operate with zero, two, or four of its springs shortened by an electrostatic anchor, thus achieving three discrete resonance frequencies. This device was a resonator, not a harvester, but electrostatic harvesting would be compatible with this design as well as possibly piezoelectric. The authors suggest that the frequency adjustment can be made more continuous instead of only three discrete frequencies by increasing the number of spring beams used or by incorporating optimized comb finger shapes that result in nonlinear electrostatic force, as described in [7] and shown in Figure 11.2.

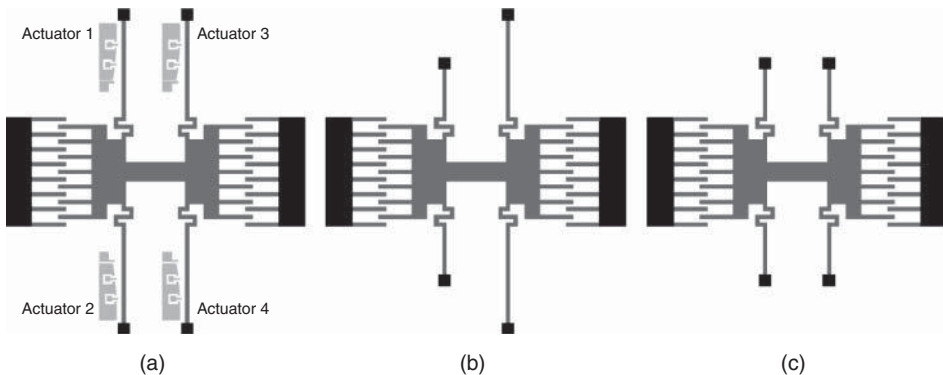


**Figure 11.1** A schematic showing electrostatic actuation as an *in situ* method to change the length of a MEMS resonator when (a) zero, (b) two, or (c) all four of the actuators are under bias [6]. © IOP publishing. Reproduced with permission. All rights reserved.

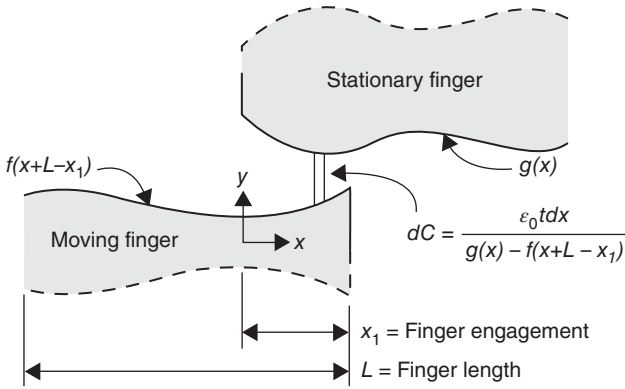


**Figure 11.2** Illustration of nonlinear electrostatic force produced by arbitrarily shaped comb fingers [7]. © IEEE. Reproduced with permission. All rights reserved.

### 11.2.1.2 Modify $E$

Tuning can be achieved through modification of elastic modulus because  $k_m \propto E$ . The elastic modulus can be adjusted using Joule heating, which takes advantage of temperature dependence of elastic modulus of certain materials and utilizes thermally generated residual stress to induce tensile or compressive stress. This technique has been demonstrated on a MEMS resonator using filament-like heating to reduce Young's modulus of a polysilicon layer while simultaneously introducing compressive stresses as the structure expands [8]. Both mechanisms serve to reduce the system's elastic modulus and stiffness, thereby decreasing the resonance frequency. This thermal approach has been demonstrated on mechanical resonators but not on energy harvesters, likely due to the high power demands (tens of megawatts) of a resistive heater.

### 11.2.1.3 Modify $k_{\text{eff}}$ Using Axial Force

A different technique to modify the resonance frequency is to apply an axial force to the beam structure to modify  $k_{\text{eff}}$ . An equation for the change in frequency resulting from an axial load,  $F$ , on a cantilever in the first bending mode is

$$\omega_2 = \omega_1 \sqrt{1 + \frac{F}{F_B}} = \sqrt{\frac{k_m}{m} \left(1 + \frac{F}{F_B}\right)}, \quad (11.1)$$

where  $F_B$  is the buckling force,  $\omega_2$  is the resonance frequency after tuning, and  $\omega_1$  is the original resonance frequency, which is equal to  $\sqrt{k_m/m}$  (where  $k_m$  is the beam's mechanical spring stiffness) [9, 10]. Thus, applying axial force to a beam to strain it modifies the effective stiffness according to

$$k_{\text{eff}} = k_m + k_m \frac{F}{F_B}. \quad (11.2)$$

$F$  can be applied through mechanical, piezoelectric, electrostatic, or magnetic means.

Mechanical application of axial force to a double-clamped resonating harvester structure has been demonstrated using manual adjustment of a clamping screw that is set prior to installation [11], but this cannot be done *in situ*. Another mechanical axial force approach has been modeled, but not built, that can feasibly be adjusted *in situ* through manual adjustment of a pin connected through a linkage mechanism to diagonal springs [12]. The springs are then fixed to the tips of two parallel beams so strain can be applied. Both devices used piezoelectric transduction for harvesting.

Using piezoelectric actuator arms instead of a mechanical screw avoids the need for manual input and has a more compact size. A device has been presented in which the piezoelectric arms are attached at the base and the top of the beam to apply the axial preload [13]. As shown in Figure 11.3, the primary piezoelectric harvester and the actuator arms are the same piece of bimorph material, but the arms are polarized as a linear actuator, while the harvester beam is polarized as a bending actuator. The arms can be actuated during the harvester's operation in order to change the axial force on the beam, thus achieving a tuned state. It is worth noting that a mechanical clamping screw has a larger range of motion, and therefore larger tuning range, than a piezoelectric actuator, but the two approaches could be combined to achieve both coarse and fine control over frequency.

Two concepts for using electrostatic force to apply axial load have been demonstrated. One used a MEMS resonator beam that was fixed to a stationary support on one side and to a movable support on the other side [14]. The movable support was actuated by applying a voltage to parallel plate electrodes which caused it to rotate around a torsion bar, straining the beam in either tension or compression depending on the rotation direction. The device is a resonator, but it is feasible that piezoelectric or electrostatic transducer elements could be incorporated for harvesting. It is also feasible that other electrostatic geometries could be applied to this technique.

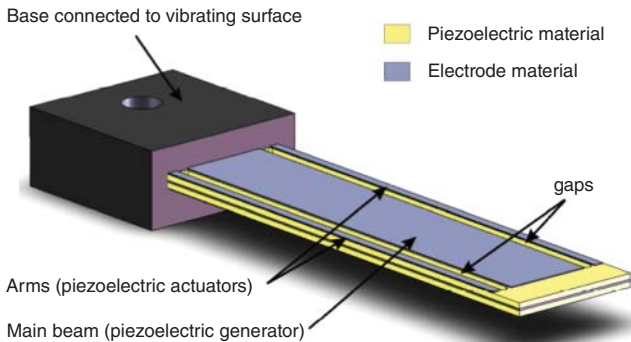


**Figure 11.3** Tunable piezoelectric generator constructed from one piece of dual-layer piezoelectric ceramic where the main beam and the arms are polarized differently [13].

A method for frequency modification with magnetically applied axial force has been reported where tuning is achieved by actuating a magnet on a stepper motor, which applies tension to a cantilever beam with a magnetic proof mass [9]. The magnet moves in line with the length of the beam so that the applied force is only axial, and the magnets are curved such that the force remains constant as the beam vibrates. This system uses electromagnetic transduction for energy harvesting and is fully automated, or self-tuning. It generates positive net power, although it experiences an energy debt after a tuning event takes place. The time required to recover to positive energy generation depends on the frequency change that was needed for tuning and on the acceleration of the driving frequency. Therefore, the duty cycle of the tuning events varies from several minutes to several hours depending on the operating environment. The system senses frequency using the output from the electromagnetic energy harvesting component. It then determines approximately where the motor should move the tuning magnet by using a look-up table of magnet positions correlated to resonance frequency. Finally, phase data is used to fine-tune the magnet position.

#### 11.2.1.4 Modify $k_{\text{eff}}$ Using an External Spring

Instead of using axial force to modify the effective stiffness of the harvester, it is possible to use an external potential to add an extra spring in parallel with the beam, thus changing the system's effective stiffness. A spring softening effect can be achieved by incorporating a “negative” external spring in parallel with the main spring of the harvester, resulting in

$$k_{\text{eff}} = k_m + k_{\text{ext}}, \quad (11.3)$$

where  $k_{\text{ext}}$  is the extra spring added to the mechanical spring of the beam. The negative spring effect is most often achieved through electrostatic or magnetic means, but piezoelectric methods have also been demonstrated.

The stiffness magnitude of an external spring that uses electrostatic principles is proportional to a tuning control voltage applied to the tuning electrodes. One design used a double-clamped MEMS beam with comb fingers extending perpendicular to the beam length but in the same areal plane as the beam [15]. The structure oscillates in the direction of the comb fingers which, as shown in Figure 11.4, taper from the longest in the center of the beam to the shortest at the

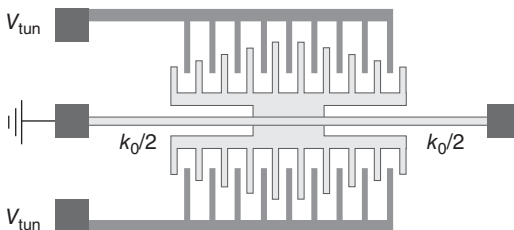


**Figure 11.4** Electrostatic spring design for stiffness modulation (negative springs) [15].  
© Elsevier. Reproduced with permission. All rights reserved.

edges of the beam. The tuning electrode fingers were stationary and interdigitated with the moving fingers on the beam resonator. As a voltage was applied to the tuning electrodes, electrostatic softening resulted, thereby tuning the resonance frequency. Another geometry used parallel plate electrodes below or on both sides of a cantilever beam to tune frequency [16]. Electrostatic tuning has not been demonstrated as part of an energy harvesting system.

One device that uses a magnetic external spring to tune resonance frequency consists of a piezoelectric energy harvesting cantilever beam with a magnetic tip mass and movable magnets positioned above and below the beam, setting up a magnetic field in which the beam oscillates (schematic shown in Figure 11.5) [17]. The system is nearly self-tuning, as it is able to sense the driving frequency through the piezoelectric voltage signal and automatically adjust the magnet positions to tune the system using a microcontroller and look-up table. However, adjustments to the load resistor are made manually to ensure that the mechanical and electrical impedance match as the frequency changes. Although the system requires some manual input and consumes more power than it can generate, self-tuning can be achieved with further optimization of this method.

Piezoelectric external springs have been demonstrated in two configurations. In one approach, shown in Figure 11.6, a first piezoelectric beam is clamped in the center and a second piezoelectric beam is connected to the first with hinges at the free ends of both beams, leaving the second beam free in the center [18]. A tuning voltage is then applied to the piezoelectric beams to change the stiffness as the system resonates. In the second approach, one layer of a piezoelectric bimorph is used for energy harvesting while the other layer is used as an actuator by applying a voltage for stiffness control [19]. As can be seen in Figure 11.7 schematic, a piezoelectric disk is used for sensing beam deflection, while an accelerometer gives the base acceleration, and the phase angle between the two is used to control the voltage applied to the piezoelectric tuning actuator, making the system

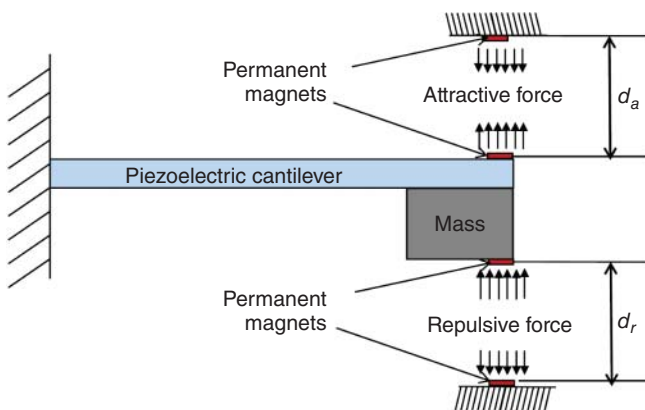


**Figure 11.5** A schematic of system using magnetic external springs to tune resonance frequency [17]. © IOP publishing. Reproduced with permission. All rights reserved.

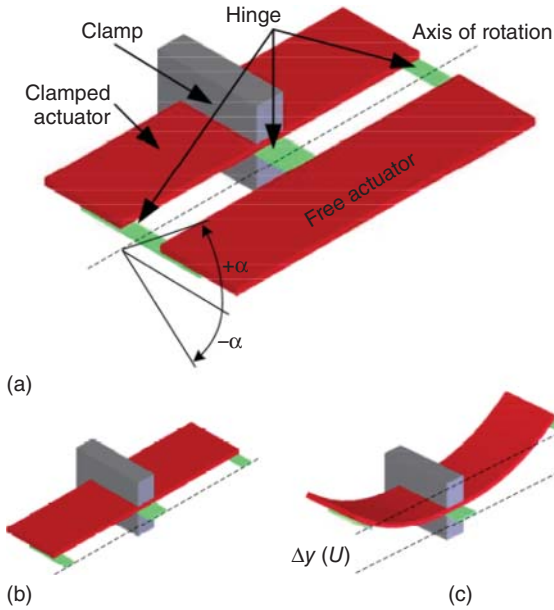


**Figure 11.6** (a) Device schematic (b) without applied voltage (c) with applied voltage [18].

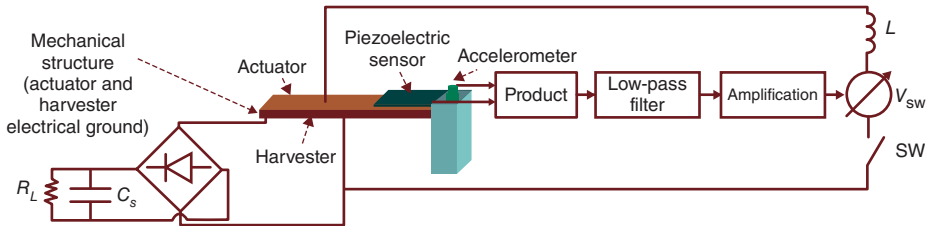


**Figure 11.7** Schematic of self-tuning harvester using piezoelectric tuning actuator [19]. © SAGE publishing. Reproduced with permission. All rights reserved.

self-tuning. The system was able to power itself as long as the frequency change needed was small.

#### 11.2.1.5 Modify $k_{\text{eff}}$ Using an Electrical External Spring

The effective stiffness of an energy harvester or resonator can be modified by adjusting the electrical circuit it is connected to, thus changing the damping through the electrical side rather than the mechanical side of the system. One option is to modify the load resistance, but this causes a reduction in power output since optimal operation is only possible when the mechanical and electrical impedance match. Another option is to vary the inductance but that is difficult in practice, so adjusting the load capacitance has been the preferred method for electrical tuning.

An expression for frequency tuning by varying the load capacitor,  $C_L$ , is given by

$$\omega_2 = \omega_1 \sqrt{1 + \frac{C_m}{C_p}}, \quad (11.4)$$

where  $C_p = C_o + C_L$ ,  $C_o$  is the capacitance of the piezoelectric layer with electrodes on both sides, and  $C_m$  is the electrical representation of the mechanical spring [20]. Because the mechanical analog for capacitance is  $1/k$ , substitutions can be made for  $C_m = 1/k_m$  and  $C_p = 1/k_p$ . Using  $\omega_1 = \sqrt{k_m/m}$ , the expressions for tuned frequency and effective stiffness can then be written as

$$\omega_2 = \sqrt{\frac{k_m + k_p}{m}}, \quad k_{\text{eff}} = k_m + k_p. \quad (11.5)$$

Thus, changing load capacitance modifies the effective stiffness.

In a practical implementation of this electrical tuning concept, one of the piezoelectric layers in a bimorph beam can be connected to a shunt capacitor to serve as a tuning layer while the other is used as an harvesting layer [20]. The beam's effective stiffness can then be adjusted by connecting various load capacitances in parallel with the piezoelectric layer. The highest resonance frequency occurs when the load capacitor is in open circuit, and the lowest resonance frequency occurs when there is a short circuit across the load capacitor or when  $C_p$  is much larger than  $C_m$  [20, 21]. Derivations for the frequency response as a function of capacitance are given in [22].

### 11.2.2

#### Mass Modification for Frequency Tuning

Just as it is usually impractical to change  $w$  or  $t$ , it is also hard to modify the proof mass. The two options for frequency tuning through modifying mass are adjusting the size of mass or the location of the center of mass. One system presented consisted of a mass with a screw threaded in the length direction of the beam such that it could be manually adjusted to change the center of mass, thus tuning the frequency [23]. The drawback of this design is that the changes must be made manually and cannot be conducted *in situ*.

### 11.3

#### Passive Schemes for Tunable Resonant Devices

Section 11.2 outlined ways to achieve a tuned state in a resonant device using active methods and this section describes passive methods. While the active methods have the advantage that there can be a high degree of control to ensure that tuning is achieved, the glaring disadvantage is that power has to be sacrificed to attain the tuned state (or human intervention is required instead), and the tuning process cannot always be achieved *in situ*. It is very challenging to automate



tuning without consuming more power than generated, forcing manual input, or limiting the range or duty cycle at which frequency tuning can be conducted. Conversely, the passive methods require no input power or human intervention and are always *in situ*. They also have the advantage of requiring less overall system volume because they eliminate the need for linear motors, complicated actuators, extra sensors, or bulky feedback control systems. In addition, the duty cycle of these passive self-tuning systems depends only on the time for the system to self-adapt, which is on the order of minutes, rather than the duty cycle depending on storing enough energy to tune, which is often on the order of hours. However, a threshold cut-in acceleration is more often required to enable the tuning process in a passive self-tuning system than an active one.

### 11.3.1

#### Modify $m_{\text{eff}}$ by Coupling Mass Position with Beam Excitation

A double-clamped beam with a proof mass that is free to slide along the length of the beam has richly complex nonlinear coupling behavior between the beam and the mass. The resonance frequency of the beam–mass system is at a maximum when the mass slides to either end of the beam and is at a minimum when the mass is at the center of the beam. The system should be able to passively self-tune its frequency within those bounds. The mass slides because of coupling between the vibrating beam and the mass as the motion of the beam creates an effective potential. The mass's motion then impacts the beam's vibration.

The relationship between the resonance frequency of the system and the sliding mass's position along the beam is given in nondimensional form in Ref. [24] and is rearranged here in dimensional form as

$$\omega_{2,1} = \sqrt{\frac{k_m}{\rho AL + m\phi_{y1}^2}}, \quad k_m = \frac{EI\lambda_1^4}{L^3}, \quad (11.6)$$

where the subscript 1 indicates the fundamental resonance mode,  $m$  is the sliding proof mass,  $\rho$  and  $A$  are the density and cross-sectional area of the beam, and  $\phi_{y1}$  is the beam mode shape normalized by the beam length, evaluated at the position of the mass.  $\lambda_1$  is the first mode solution to the beam's characteristic equation, which depends on boundary conditions and is derived in Ref. [25] or any vibrations textbook. For a beam with double-clamped boundary conditions, the characteristic equation is  $\cos \lambda \cosh \lambda - 1 = 0$  and the first mode solution is  $\lambda_1 \approx 4.73$ . The effective mass in this scenario is

$$m_{\text{eff}} = \rho AL + m\phi_{y1}^2. \quad (11.7)$$

As the mass changes position along the beam, the beam shape changes and so does the value of the beam shape evaluated at the location of the mass,  $\phi_{y1}$ , thus causing the resonance frequency to change.

Self-tuning using this approach was first demonstrated using a taut piano wire with a bead for a proof mass and was excited by external magnetic field [26]. The same self-tuning mechanism was demonstrated using mechanical vibrations

exciting a metallic beam with a sliding rectangular proof mass [27]. The mass motion is slow compared to the beam vibration and the self-tuning process can often take several minutes, depending on how far the mass starting position is from the resonant position. The passive self-tuning system was demonstrated with beam resonators of 30 and 6 cm in length but can be converted to an energy harvester once a transducer is incorporated, such as a piezoelectric patch.

### 11.3.2

#### Modify $k_{\text{eff}}$ by Coupling Axial Force with Centrifugal Force from Rotation

An energy harvesting beam mounted radially on a rotating device experiences a centrifugal force,  $F_c = mv^2/r$ , where  $m$  is mass,  $v$  is velocity, and  $r$  is radius. A proof mass that is large relative to the beam mass at the tip of the beam will increase this force felt by the beam, which effectively applies a tensile force to the beam, tuning its frequency according to

$$\omega_2 = \omega_1 \sqrt{1 + \frac{F_c}{F_B}} \quad (11.8)$$

This can be rearranged to show that

$$k_{\text{eff}} = k_m + k_m \frac{F_c}{F_B} \quad (11.9)$$

The higher the rotation velocity, the greater the tensile force on the beam. This coupling of rotational speed with applied tensile force on the beam can be designed such that the beam's resonance frequency increases with the rotational frequency, thus tuning the system within the design limits. This was illustrated with a device mounted on a rotating fan that consisted of a beam made of ABS plastic with a mass at the tip and a patch of PZT piezoelectric at the root of the cantilever [28].

### 11.3.3

#### Modify $L$ by Using Centrifugal Force to Toggle Beam Clamp Position

A passively self-tuning energy harvester has been presented that uses centrifugal force for tuning even though it operates in a non-rotating environment [29]. The device, shown in Figure 11.8, consists of a polyvinylidene fluoride (PVDF) piezoelectric beam that has an off-center slot and a proof mass on each end. This beam is packaged such that a bump structure protrudes up through the slot in the beam, creating two beams of different lengths that oscillate freely off both sides of the package and are able to slide back and forth between the limits of the slot, similar to a switch. As the flexible polymer beam oscillates, the masses each experience a centrifugal force in the direction away from the package. Since the two beams are of different lengths, the radius of rotation is different and the centrifugal forces are not equal, causing the beam to slide from one position to another depending on the forces. The system used a pair of such beams and therefore has four discrete

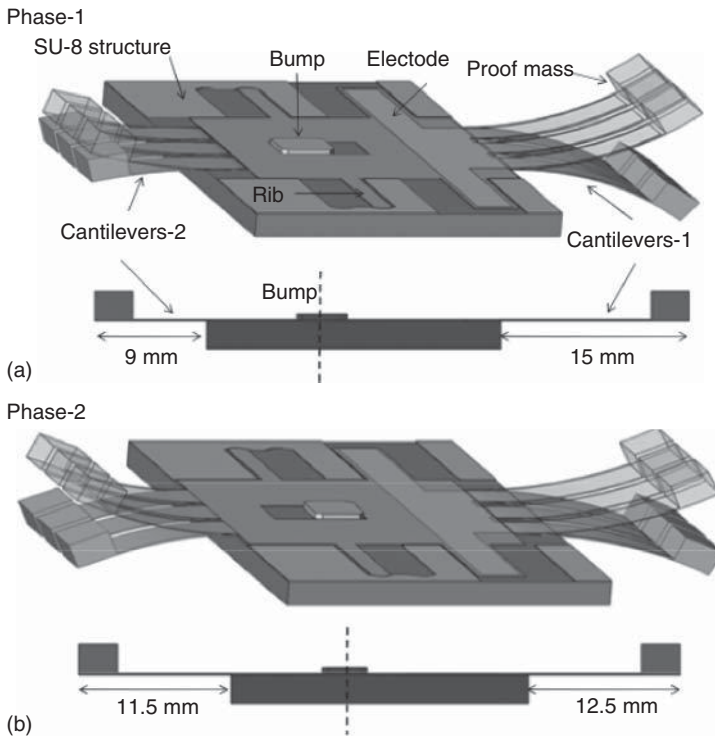


**Figure 11.8** "Illustration of the first (a) and second (b) resonant modes of the device, which can switch between modes passively under the right input vibration conditions [29].

possible frequencies, as both beams can have two different lengths depending on the slot position. The centrifugal forces change as the driving frequency changes, and the system has been shown to be capable of switching between slot positions completely passively.

## 11.4

### Wideband Devices

The frequency response of the tunable resonant devices that have been discussed so far is sharp, with a narrow bandwidth and a relatively large magnitude. These resonant devices generate orders of magnitude less power when operated off-resonance. In contrast, the frequency response of wideband devices is shaped like a plateau such that many frequencies may be utilized. The challenge is in maintaining a high enough magnitude to generate the desired power output.

Wideband systems tend to be passive rather than active, using multimodal or nonlinear device designs rather than power input or human intervention to achieve a widened frequency response. It has been demonstrated that wideband

harvesters do not necessarily perform better than resonant harvesters when subjected to input vibrations that resemble white or colored noise, but do offer an advantage when the harvester must operate off-resonance, such as when vibration frequency is rapidly changing or unknown [30]. Because wideband devices do not tune in a resonant sense, they do not focus on adjusting  $m$  and  $k$ , but rather on using designs that allow for multiple vibration modes or incorporate spring nonlinearities.

#### 11.4.1

##### Multimodal Designs

In multiple vibration mode (multimodal) designs, the possible resonant frequencies are fixed at discrete values rather than being continuous within a range. The discrete frequencies may be close enough that the peaks nearly overlap, forming a plateau-shaped frequency response. Alternatively, they may be an order of magnitude apart due to a large frequency difference in adjacent modes, making it possible that the driving frequencies do not excite the resonance of the system. Multimodal designs include those utilizing arrays of harvesters or incorporating geometries that lend themselves to multiple bending modes, sometimes by using multiple fixed masses.

Harvester arrays consist of beams of slightly different dimensions, and therefore different frequencies. Usually  $L$  and  $m$  are the differing dimensions, but  $w$  or  $t$  could be used as well. The harvester arrays can be connected electrically with each other in series or parallel, and likewise with the power conditioning electronics [31, 32]. Harvester arrays can be an effective way to increase the bandwidth of the overall system without sacrificing the output magnitude. However, the disadvantage is that they are not an efficient use of device area, causing an increase in cost and size.

Multiple bending modes may be utilized in device design to broaden the frequency response since different driving frequencies excite different vibration modes. For example, nesting a secondary beam into a cutout inside a primary beam such that the tip of the primary beam is also the base of the secondary beam increases the possible number of vibration modes within a given frequency range [33]. A hybrid method shown in Figure 11.9 uses a cantilever beam's first bending mode for electromagnetic harvesting, with a magnet as the proof mass and a coil on the package, and adheres piezoelectric elements at the nodes of the second mode vibration [34].

A harvester with multiple fixed masses can resonate in various modes, each with different frequencies. For example, a double-clamped beam with three discrete proof masses fixed along its length has more possible resonance modes with significant magnitude than a beam with only one mass [35]. In general, there are many possible ways to use asymmetric or complex beam geometries, such as L-shapes, and mass placement to invoke extra vibration modes. While using piezoelectric transduction, care must be taken to design electrodes such that charge cancellation does not take place.

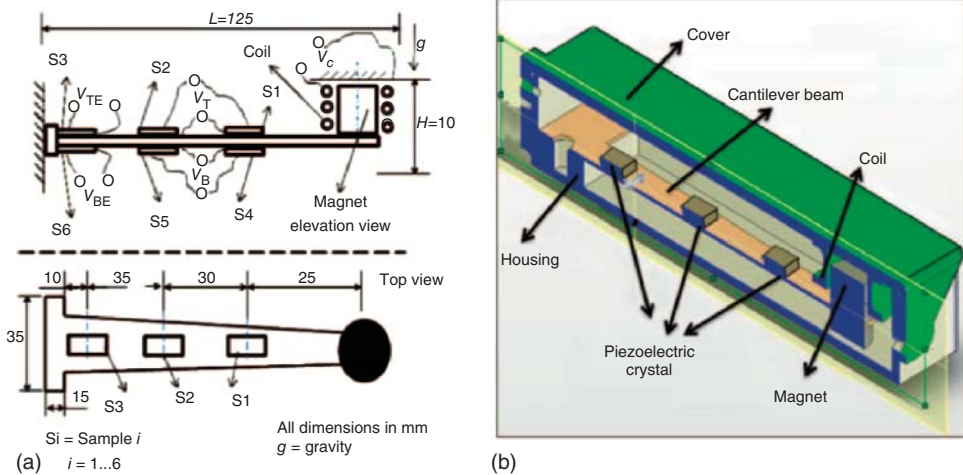


**Figure 11.9** Schematic showing operation of the hybrid multi-modal harvester, including cross section and top views (a) and isometric device view (b) [34].

#### 11.4.2

##### Nonlinear Designs

Nonlinear systems do not have the drawback of discrete frequencies, but their disadvantage compared to multi-modal designs is that they require a threshold acceleration input below which the nonlinear physics are not observed. Thus, “nonlinear” systems may display a linear, narrow-band response unless the input vibrations have high enough acceleration. Techniques for incorporating nonlinearities to create a wideband response include using mechanical end stops, spring hardening or softening, and bistable configurations.

Mechanical end stops refer to a range-of-motion limiter that the harvesting beam strikes as it vibrates. At their most simple, mechanical end stops can be the rigid frame of the harvester package and can be used to prevent mechanical failure by limiting the harvester’s range of motion. However, those types of rigid end stops are rarely beneficial to system operation other than preventing catastrophic failure. A much more clever design is pictured in Figure 11.10 and it uses mechanical end stops that are secondary spring transducers instead of rigid structures [36]. In this configuration, especially at accelerations above several  $g$ ’s, the transducer end stops serve to limit the motion of the device while generating significant additional power and broadening the bandwidth of the system due to the nonlinearity of the impact mechanism. One disadvantage to using end stops is the potential for mechanical wear and fatigue.

A different approach is to design beams to display nonlinear spring behavior such that a plot of spring force versus displacement,  $x$ , is no longer linear

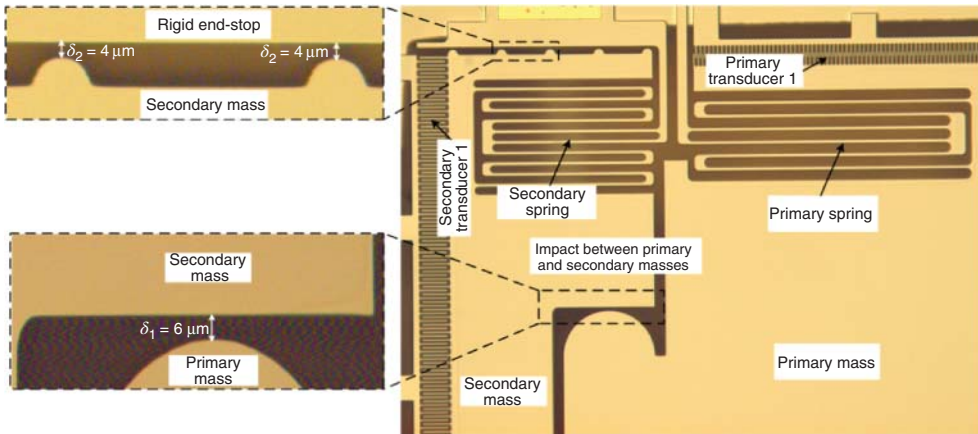


**Figure 11.10** Micrograph of a MEMS electrostatic energy harvester design with end stops that also serve as secondary springs [36]. © IOP Publishing. Reproduced with permission. All rights reserved.

and the equation  $F_{\text{spring}} = kx$  no longer applies. Instead, the spring force may be modeled as a polynomial such that  $F_{\text{spring}} = k_1x + k_3x^3 + k_5x^5 + k_7x^7$  [37]. Thus, for very small displacements, the third-order and higher terms are insignificant and the system displays linear behavior, while for large displacements the nonlinearities are pronounced. The frequency response of such a nonlinear spring system often displays hysteresis in which there are a high-energy branch and a low-energy branch. While the low-energy path may closely resemble a linear frequency response, the high-energy path looks like a peak that has been smeared severely to the left or right (for spring softening or hardening, respectively), effectively forming a plateau response and increasing the bandwidth as shown in Figure 11.11. This approach has been demonstrated with both electrostatic [37] and piezoelectric [38] harvesting systems.

A significant disadvantage of these nonlinear spring approaches is that it is very difficult to ensure that the system will follow the desired high-energy branch during operation. The harvester only continues to follow this path if the acceleration is high enough and the frequency is swept continuously in one direction. The harvester can suddenly jump from the high-energy branch to the linear low-energy branch due to unstable regimes if the driving frequency or sweep direction changes suddenly, or if the acceleration decreases or experiences an impulse. It is then difficult to get back onto the high-energy branch.

Finally, bistable nonlinear systems can provide a wideband response using either mechanical or magnetic “snap-through” designs. In the magnetic system, shown schematically in Figure 11.12, a cantilever beam with piezoelectric elements and a magnetic proof mass are configured with permanent magnets fixed symmetrically off-axis below the free end [39]. A MEMS implementation of a mechanical bistable

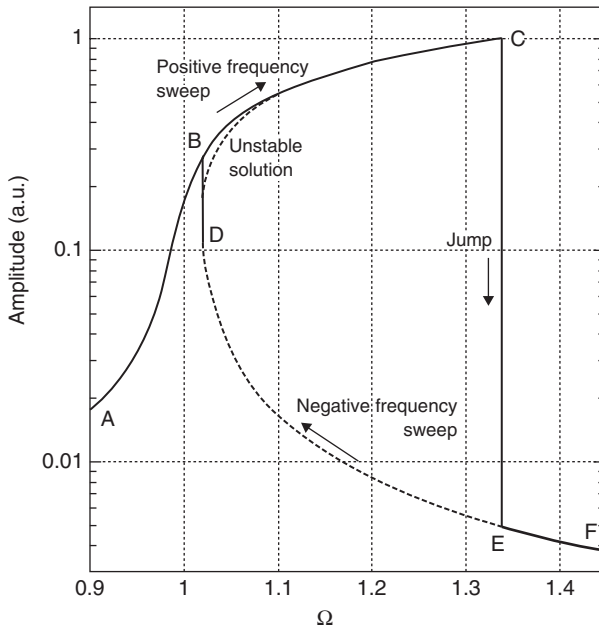


**Figure 11.11** Example of a generic nonlinear frequency response highlighting the hysteresis between positive and negative frequency sweep directions and the “smearing” of the resonance peak [38]. © IEEE. Reproduced with permission. All rights reserved.

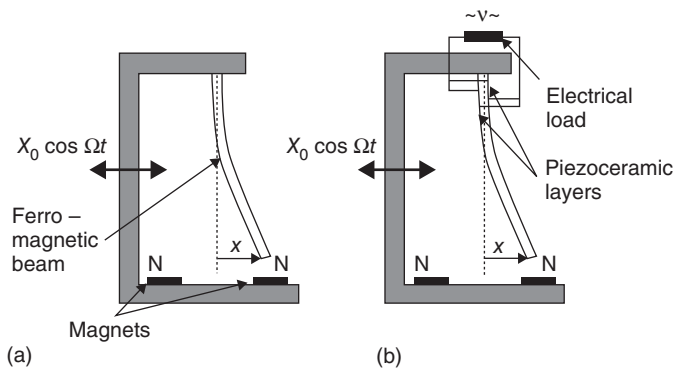


**Figure 11.12** Schematics of (a) magnetoelastic and (b) piezomagnetoelastic nonlinear systems [39]. © AIP. Reproduced with permission. All rights reserved.

device has also been demonstrated [40]. Bistable systems have the advantage of being able to operate under periodic or stochastic input vibrations. However, the disadvantage is that a threshold level of input acceleration magnitude is required to get the system to snap through or oscillate back and forth between its stable points.

## 11.5

## Summary and Future Research Directions

## 11.5.1

## Summary of Tunable and Wideband Strategies

A summary of the important attributes of each tunable resonant device mentioned in this chapter is given in Table 11.2, with wideband devices in Table 11.3. Note that only experimentally demonstrated devices are listed, not theoretically modeled concepts. The ideal device would have an energy conversion method incorporated, would be self-tuning and passive without requiring a cut-in acceleration, would have a continuum of possible resonance frequencies, and would be MEMS scalable. The attributes listed in these tables come from the example devices demonstrated and cited in this chapter. It should be understood that these are device-specific rather than strategy-specific and future design improvements on these strategies will surely change and improve these metrics.

The headings of each column are explained for clarity. “Tuning variable” shows which variable is modified to adjust the resonance frequency. “Tuning method” specifies the strategy used to conduct the tuning. “Energy conv method” states what type of energy conversion is used to convert between mechanical and

**Table 11.2** Table summarizing tunable resonant strategies. Detailed description of abbreviations and headings is given in text.

Tuning variable	Tuning method	Energy conv method	Freq sensing method	Self-tuning	Tuning input req'd	Cut-in accel	Discrete freq	MEMS feasible
	ES, anchor [6]	—	—	N	Cont	N	Y, 3	Y
$L$	$F_c \leftrightarrow L$ [29]	P	—	Y	None <sup>a)</sup>	Y	Y, 4	M
$E$	Thermal [8]	—	—	N	Cont	N	N	Y
	Screw [11]	P	—	N	Man <sup>b)</sup>	N	N	N
$k_{\text{eff}}$ , axial force	P, arms [13]	P	—	N	Cont	N	N	M
	ES, plates [14]	—	—	N	Cont	N	N	Y
	Magnetic [9]	EM	EM	Y	Int	N	N	N
	$F_c \leftrightarrow$ tension [28]	P	—	Y	None <sup>a)</sup>	Y	N	N
	ES, combs [15]	—	C	Y <sup>c)</sup>	Cont	N	N	Y
$k_{\text{eff}}$ , extra spring	ES, plates [16]	—	—	N	Cont	N	N	Y
	Magnetic [17]	P	P	Y <sup>c)</sup>	Int	N	N	N
	P, hinges [18]	P	P	Y <sup>c)</sup>	Cont	N	N	M
	P, bimorph [19]	P	P	Y	Cont	N	N	N
$k_{\text{eff}}, C_L$	$C_L$ [20]	P	P	Y <sup>c)</sup>	Cont	N	N	M
$m_{\text{eff}}$	COM screw [23]	P	—	N	Man <sup>b)</sup>	N	N	N
	mass $\leftrightarrow$ beam [27]	—	—	Y	None <sup>a)</sup>	Y	N	M

a) System is passive, not active.

b) System is not *in situ* tunable.

c) System is not self-powered.



**Table 11.3** Table summarizing wideband strategies. Detailed description of abbreviations and headings is given in text.

Tuning variable	Tuning method	Energy conv method	Cut-in accel	Discrete freq	MEMS feasible
Multi-mode	Array with 3 beams [31]	P	N	Y, 3	Y
	Bending, 2 nested beams [33]	P	N	Y, 2	M
	Bending, hybrid [34]	P, EM	N	Y, 2	N
	Bending, 3 masses [35]	P	N	Y, 3	M
Nonlinear	End stops [36]	ES	Y	N	Y
	Spring, double-clamped [38]	P	Y	N	Y
	Spring, four-beam [37]	ES	Y	N	Y
	Bistable, magnet [39]	P	Y	N	N
	Bistable, mechanical [40]	ES	Y	N	Y

electrical energy, where P is piezoelectric, ES is electrostatic, EM is electromagnetic, and a dash indicates that the device is a resonator, not a harvester. “Freq sensing method” lists the type of sensor used to determine the driving frequency in an active self-tuning system, where C is capacitive. “Self-tuning” states whether the device is able to tune itself autonomously without human intervention, and a footnote is given to indicate when the system is self-tuning but not self-powered. *Tuning input req’d* refers to whether the system requires continuous, intermittent, or manual power input (or none, in the case of passive systems) in order to achieve the tuning. “Cut-in accel” states whether a threshold driving acceleration is needed in order for the tuning method to function properly. “Discrete freq” lists the number of possible discrete fixed resonance frequencies or indicates that the frequency possibilities are a continuum. “MEMS feasible” is labeled “yes” if the example system is a MEMS device, “maybe” if the example system is not MEMS but the system lends itself to microfabrication, and “no” if MEMS implementation is probably not feasible.

Several important metrics of the tuning and wideband strategies have been excluded from these tables, namely, frequency operating range, frequency resolution, type of input vibrations that can be accommodated, and tuning duty cycle. These factors vary greatly from device to device depending on all design decisions and are discussed briefly in the following section.

## 11.5.2

### Areas for Future Improvement in Tunable and Wideband Strategies

#### 11.5.2.1 Tuning range and resolution

Each system has a specific range of frequencies in which tuning can occur. This may be limited by the physics of the tuning method, the design of the system, the degree of coupling possible with the tuning mechanism, or the change in frequency that can be made without going power-negative. Each

tuning method has also a frequency resolution which depends on the type of control system and the actuation method. Future research is needed to tackle the challenge of achieving a large tuning range and a fine resolution at the same time.

#### 11.5.2.2 Tuning sensitivity to driving vibrations

Some systems are able to tune their resonance when driven by a multiple-frequency vibration input, yet others can only tune properly when the input is a single-frequency sine wave. In addition, while some systems do not depend on any particular acceleration level for tuning, others require a threshold acceleration in order to execute tuning operations. All systems have the potential to produce more power as acceleration increases, so self-powered self-tuning devices will be able to afford a higher tuning duty cycle with greater acceleration inputs. Another factor related to input vibrations is that if the driving frequency changes over time more quickly than the system's tuning duty cycle, it may not be able to operate. The challenges posed by long duty cycles make it clear why passive self-tuning systems are attractive. Continued research is needed to reduce the sensitivity of tunable and wideband energy harvesters to the driving vibration characteristics.

#### 11.5.2.3 System Size considerations

Some of the demonstrated tunable and wideband systems are compact and simple. However, others are comprised of numerous components, including the energy harvester, tuning actuator mechanism, sensors, and control electronics. These parts often need to be precisely aligned and calibrated in order to tune properly and require a large volume. Device volume may or may not be a concern in some applications, but installation complexity and system robustness are always of concern. Future research should improve the overall system design and possibly use MEMS for at least part of the system. Some components scale to MEMS more easily than others. For example, systems that rely on 3-dimensional configurations pose a challenge in MEMS, such as electromagnetic coils or movable tuning magnets that are required above and below a beam structure. MEMS structures can also have difficulty overcoming friction and stiction in moving or sliding parts. Finally, power output is typically lower in a micro scale harvester than in a bulk device, partly due to the smaller proof mass, but the power required for actuation may also be lower. Novel fabrication techniques will be needed to make compact designs possible.

These are only a few of the many possible areas for future research on tunable and wideband energy harvesters. The eventual ubiquitous adoption of energy harvesters requires that they are easily adaptable to their operating environment, require no customization or maintenance, and provide reliable power even if the operating environment changes. Therefore, there is a great opportunity for research in addressing these issues so that energy harvesters can be made compatible with wideband and time-varying driving frequencies.

## References

1. Miller, L.M., Halvorsen, E., Dong, T., and Wright, P.K. (2011) Modeling and experimental verification of low-frequency MEMS energy harvesting from ambient vibrations. *J. Micromech. Microeng.*, **21**, 045 029.
2. duToit, N.E., Wardle, B.L., and Kim, S.G. (2005) Design consideration for MEMS-scale piezoelectric mechanical vibration energy harvesting. *Integr. Ferroelectr.*, **71**, 121–160.
3. Miller, L.M. (2012) Micro-scale piezoelectric vibration energy harvesting: from fixed-frequency to adaptable-frequency devices. PhD thesis. University of California, Berkeley.
4. Zhu, D., Tudor, M.J., and Beeby, S.P. (2010) Strategies for increasing the operating frequency range of vibration energy harvesters: a review. *Meas. Sci. Technol.*, **21**, 022 001.
5. Tang, L., Yang, Y., and Soh, C.K. (2010) Toward broadband vibration-based energy harvesting. *J. Intell. Mater. Syst. Struct.*, **21**, 1867–1897.
6. Zine-El-Abidine, I. and Yang, P. (2009) A tunable mechanical resonator. *J. Micromech. Microeng.*, **19**, 125 004.
7. Jensen, B.D., Mutlu, S., Miller, S., Kurabayashi, K., and Allen, J.J. (2003) Shaped comb fingers for tailored electromechanical restoring force. *J. Microelectromech. Syst.*, **12**, 373–383.
8. Remtma, T. and Lin, L. (2001) Active frequency tuning for micro resonators by localized thermal stressing effects. *Sens. Actuators, A*, **91**, 326–32.
9. Ayala-Garcia, I.N., Zhu, D., Tudor, M.J., and Beeby, S.P. (2010) A tunable kinetic energy harvester with dynamic over range protection. *Smart Mater. Struct.*, **19**, 115 005.
10. Blevins, R.D. (2001) *Formulas for Natural Frequency and Mode Shape*, Krieger Publishing Company.
11. Leland, E. and Wright, P.K. (2006) Resonance tuning of piezoelectric vibration energy scavenging generators using compressive axial preload. *Smart Mater. Struct.*, **15**, 1413–1420.
12. Niri, E.D. and Salamone, S. (2012) A passively tunable mechanism for a dual bimorph energy harvester with variable tip stiffness and axial load. *Smart Mater. Struct.*, **21**, 125 025.
13. Eichhorn, C., Goldschmidtboeing, F., Porro, Y., and Woias, P. (2009) A piezoelectric harvester with an integrated frequency tuning mechanism. *Technical Digest PowerMEMS 2009*, pp. 45–48.
14. Cabuz, C., Fukatsu, K., Hashimoto, H., Shoji, S., Kurabayashi, T., Minami, K., and Esashi, M. (1994) Fine frequency tuning in resonant sensors. *Proceedings IEEE Workshop on Micro Electro Mechanical Systems*, Oisa, Japan, pp. 245–250.
15. Scheibner, D., Mehner, J., Reuter, D., Kotarsky, U., Gessner, T., and Doetzel, W. (2004) Characterization and self-test of electrostatically tunable resonators for frequency selective vibration measurements. *Sens. Actuators, A*, **111**, 93–9.
16. Yao, J.J. and MacDonald, N.C. (1995) A micromachined, single crystal silicon, tunable resonator. *J. Micromech. Microeng.*, **5**, 257–264.
17. Challa, V.R., Prasad, M.G., and Fisher, F.T. (2011) Towards an autonomous self-tuning vibration energy harvesting device for wireless sensor network applications. *Smart Mater. Struct.*, **20**, 025 004.
18. Peters, C., Maurath, D., Schock, W., and Manoli, Y. (2008) Novel electrically tunable mechanical resonator for energy harvesting. *Proceedings PowerMEMS 2008+ microEMS2008*, Sendai, Japan, pp. 253–256.
19. Lallart, M., Anton, S.R., and Inman, D.J. (2010) Frequency self-tuning scheme for broadband vibration energy harvesting. *J. Intell. Mater. Syst. Struct.*, **21**, 897–906.
20. Wu, W.J., Chen, Y.Y., Lee, B.S., He, J.J., and Peng, Y.T. (2006) Tunable resonant frequency power harvesting devices. *Proc. SPIE*, **6169**, 55–62.
21. Charnegie, D. (2007) Frequency tuning concepts for piezoelectric cantilever beams and plates for energy harvesting. Master's thesis, School of Engineering, University of Pittsburgh.

22. Roundy, S. (2003) Energy scavenging for wireless sensor nodes with a focus on vibration to electricity conversion. PhD thesis, University of California Berkeley.
23. Wu, X., Lin, J., Kato, S., Zhang, K., Ren, T., and Liu, L. (2008) A frequency adjustable vibration energy harvester. *Proceedings PowerMEMS 2008 + microEMS2008*.
24. Miranda, E.C. and Thomsen, J.J. (1998) Vibration induced sliding: theory and experiment for a beam with a spring-loaded mass. *Nonlinear Dyn.*, **16**, 167–186.
25. Rao, S.S. (2007) *Vibrations of Continuous Systems*, John Wiley & Sons, Inc.
26. Boudaoud, A., Couder, Y., and Amar, M.B. (1999) A self-adaptive oscillator. *Eur. Phys. J. B*, **9**, 159–165.
27. Miller, L.M., Pillatsch, P., Halvorsen, E., Wright, P.K., Yeatman, E.M., and Holmes, A.S. (2013) Experimental passive self tuning behavior of a beam resonator with sliding proof mass. *J. Sound Vibr.*, **332**, 7142–7152.
28. Gu, L. and Livermore, C. (2010) Passive self-tuning energy harvester for extracting energy from rotational motion. *Appl. Phys. Lett.*, **97**, 081 904.
29. Jo, S.E., Kim, M.S., and Kim, Y.J. (2011) Passive-self-tunable vibration energy harvester. *Proceedings of the 16th International Solid-State Sensors, Actuators, and Microsystems Conference (TRANSDUCERS)*, pp. 691–694.
30. Halvorsen, E. (2013) Fundamental issues in nonlinear wideband-vibration energy harvesting. *Phys. Rev. E*, **87**, 042 129.
31. Liu, J.Q., Fang, H.B., Xu, Z.Y., Mao, X.H., Shen, X.C., Chen, D., Liao, H., and Cai, B.C. (2008) A MEMS-based piezoelectric power generator array for vibration energy harvesting. *Microelectron. J.*, **39**, 802–806.
32. Lin, H.C., Wu, P.H., Lien, I.C., and Shu, Y.C. (2013) Analysis of an array of piezoelectric energy harvesters connected in series. *Smart Mater. Struct.*, **22**, 094 026.
33. Wu, H., Tang, L., Yang, Y., and Soh, C.K. (2011) A novel 2dof piezoelectric energy harvester. *International Conference on Adaptive Structures and Technologies*, Corfu, Greece.
34. Tadesse, Y., Zhang, S., and Priya, S. (2009) Multimodal energy harvesting: piezoelectric and electromagnetic. *J. Intell. Mater. Syst. Struct.*, **20**, 625–632.
35. Roundy, S., Leland, E., Baker, J., Carleton, E., Reilly, E.K., Lai, E., Otis, B., Rabaey, J., Wright, P.K., and Sundararajan, V. (2005) Improving power output for vibration based energy scavengers. *IEEE Pervasive Computing*, Jan-March 2005, pp. 28–36.
36. Le, C.P., Halvorsen, E., Sorasen, O., and Yeatman, E.M. (2013) Wideband excitation of an electrostatic vibration energy harvester with power-extracting end-stops. *Smart Mater. Struct.*, **22**, 075 020.
37. Tvedt, L.G.W., Nguyen, D.S., and Halvorsen, E. (2010) Nonlinear behavior of an electrostatic energy harvester under wide- and narrowband excitation. *J. Microelectromech. Syst.*, **19** (2), 305–316.
38. Marzencki, M., Defosseux, M., and Basrour, S. (2009) MEMS vibration energy harvesting devices with passive resonance frequency adaptation capability. *J. Microelectromech. Syst.*, **18** (6), 1444–1453.
39. Erturk, A., Hoffmann, J., and Inman, D.J. (2009) A piezomagnetoelastic structure for broadband vibration energy harvesting. *Appl. Phys. Lett.*, **94**, 254 102.
40. Ando, B., Baglio, S., L'Episcopo, G., and Trigona, C. (2012) Investigation on mechanically bistable MEMS devices for energy harvesting from vibrations. *J. Microelectromech. Syst.*, **21**, 779–790.

## 12

# Micro Thermoelectric Generators

Ingo Stark

### 12.1

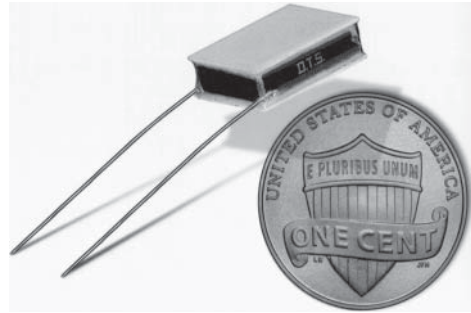
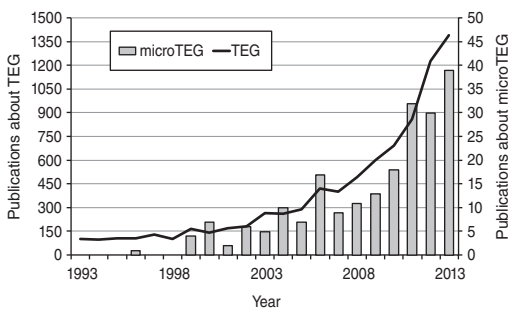
#### Introduction

In recent years, thermoelectric (TE) energy conversion has experienced a legendary renaissance after several decades of attracting little attention. A search [1] for the number of published articles about thermoelectric generators (TEGs) and in particular micro thermoelectric generators (microTEGs) over the last two decades reflects this exciting trend with a fast rising number of recent publications in this field as shown in Figure 12.1a. This promising technology has a high potential of significantly contributing to the need of energy sustainability and managing the resources of our planet more efficiently. For example, in the United States alone, 2 billion used batteries are disposed of in landfills annually [2]. Beyond lifetime extension or replacement of batteries, the deployment of microTEGs opens up new application fields with energy sustainability mainly in the industrial (e.g., microsensor networks) and wearable electronics (e.g., health and fitness) arena, in which batteries and their replacement are not feasible or are cost prohibitive.

As shown by market trends, microTEGs will help to address the power demand of a tremendously growing number of ubiquitous electronic devices in our daily life. In 2012, the market for wearable electronics was worth \$2.7 billion in terms of revenue and this is expected to reach \$8.3 billion in 2018, growing at an estimated compound annual growth rate (CAGR) of 17.71% from 2013 to 2018 [3]. A rapidly growing market for TE energy harvesters is predicted to reach \$875 million by 2023 [4].

The interest in micro TE energy harvesting is mainly based on the vast abundance of low-heat sources (e.g., warm pipes, living body, solar heat, waste heat, process heat) providing sufficient temperature differences  $\Delta T$  resulting in heat flows, that can be converted into useful electrical power. There are multiple significant advantages of TE conversion, such as silent operation without moving parts as well as a compact and small construction of a solid device having a virtually unlimited lifetime.

Early efforts to miniaturize TEGs applying thin film deposition techniques were made in the 1960s [5]. Further miniaturization was reported in 1989, utilizing SOS



(a)

(b)

**Figure 12.1** (a) Published articles about TEGs and in particular microTEGs over the last two decades using scholar.google search [1] and (b) low-power thermoelectric generator (LPTG) made by D.T.S. in comparison with a US 1 cent coin.

(silicon on sapphire)-integrated circuit technology [6]. Then, in 1997, the company D.T.S. presented the first commercially developed thin film microTEG based on highly efficient  $\text{Bi}_2\text{Te}_3$ -type compounds (V–VI materials, data in Table 12.3) displayed in Figure 12.1b. The miniaturization and commercialization efforts continued at Thermo Life Energy Corp. after D.T.S. was acquired by them in 2003. Besides the thin film approach, bulk TEGs in the micropower range ( $<1\text{ mW}$ ) developed in the early 1970s featured a monolithic construction primarily used for radioisotope-powered pacemakers (nuclear battery) [7]. The development of miniaturized bulk TE devices resulted in the first TE-powered wristwatch made by Bulova [8], which was introduced into the market in 1982, followed by Citizen and Seiko in 1998 [9].

Although well-established macroTEGs based on bulk material technology can be utilized for a number of industrial micropower applications with generated and conditioned power levels in the same range as achieved with microTEGs and demonstrated in Section 12.5.1, the miniaturization from macro to microTEGs may offer a variety of benefits, including the following:

- capability of high-volume production as a result of small device size and/or utilization of standard volume process equipment for micro-electro-mechanical-system (MEMS) technologies,
- lightweight devices with a low amount of consumed TE material due to thin film deposition and size restrictions. This is important in case of  $\text{Bi}_2\text{Te}_3$ -type materials showing a sharp increase in cost of tellurium over time, especially in the last decade [10],
- variable size and shape adjustable to specific applications for maximizing power generation due to a variety of different configurations, materials, and high freedom of design,
- low cost and small form factor of devices, opening up new and high-volume application fields.

In Section 12.2, an approach of categorizing various types of microTEGs as well as distinguishing them from state-of-the-art bulk TEGs is discussed. Section 12.3 addresses important thermal and material design aspects for maximum power output of TEGs, including the principle of thermal match and material anisotropy of  $\text{Bi}_2\text{Te}_3$ -type materials. On a component level, the first part of Section 12.4 introduces some of the current technological approaches of harvesting energy from a temperature difference using various material systems and fabricating techniques. Many of these technologies are still being researched, reflecting numerous and diverse activities in recent years. In the second part of Section 12.4, more advanced and commercialized micro technologies, based on physical vapor deposition (PVD) and metallorganic chemical vapor deposition (MOCVD) for the application of  $\text{V}_2\text{VI}_3$ -compounds, are presented. Section 12.5 provides selected industrial and wearable applications on a full system level.

## 12.2

### Classification of Micro Thermoelectric Generators

The prefix in microTEG stands for a micro geometry of the TE converter associated with a micro manufacturing technology, which may include thin film deposition, patterning by photolithography and/or etching, and pick-and-place tooling for assembly as modified semiconductor device fabrication technologies for MEMS (see Table 12.1). Geometries of TE legs, such as the length and cross section, can be used to differentiate from state-of-the-art (macro) bulk TEGs as shown in Figure 12.2. MicroTEGs from Table 12.3, which are sorted into four technology groups based on Table 12.1, can be identified by cross sections smaller than about  $0.2 \text{ mm}^2$ .

The overall size of microTEGs is not a suitable measure for its classification owing to the fact that, for proper functioning of a TEG, a temperature gradient across the device has to be maintained. This requires in most cases a heat exchanger at the cold side for heat dissipation to surrounding air and often also a heat collector at the warm side of a microTEG, significantly inflating the occupied volume of the device.

MicroTEGs exist in two principal configurations, cross-plane and in-plane, depending on the direction of the heat flow through the thermocouples (TCs) and the orientation to the substrate surface, as depicted in Figure 12.3.

In the cross-plane configuration (CPC), heat flows perpendicularly to the substrate. This configuration is found in all macro bulk TEGs as well as in several microTEG designs with pillar-type TCs sandwiched between highly thermally conductive heat couple plates acting as substrate forming the typical  $\pi$ -shape pattern illustrated in Figure 12.4. A number of TCs are connected electrically in series and are thermally parallel.

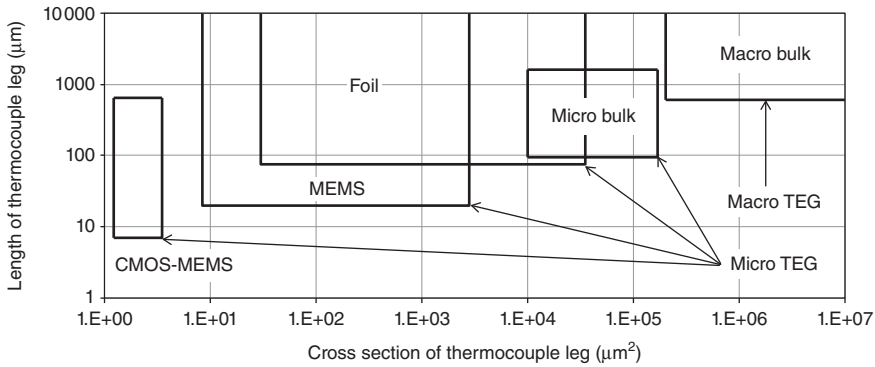
On the other hand, in the in-plane configuration (IPC), heat flows parallel to the substrate, which preferably has a low thermal conductance in order to minimize

Table 12.1 MicroTEG technologies and materials applied for fabrication of TEGs.

	Foil	MEMS	Micro bulk
<b>Cross-plane</b>	ECD Bi <sub>2</sub> Te <sub>3</sub> -type [11]	Sputtering Bi <sub>2</sub> Te <sub>3</sub> -type [12, 13]	Hot pressing Bi <sub>2</sub> Te <sub>3</sub> -type [9]
	ECD Cu-Ni [11]	ECD Bi <sub>2</sub> Te <sub>3</sub> -type [14]	Thinning bulk Bi <sub>2</sub> Te <sub>3</sub> -type [15]
	Spray printing Bi <sub>2</sub> Te <sub>3</sub> -type [16]	MOCVD Bi <sub>2</sub> Te <sub>3</sub> -type [17, 18] ECD Bi <sub>2</sub> Te <sub>3</sub> nanowire array [20]	MBE PbTe-type quantum-dot superlattice (QDSL) [19]
	Foil	MEMS	CMOS-MEMS
<b>In-plane</b>	Sputtering Bi <sub>2</sub> Te <sub>3</sub> -type [21 – 23]	Spin coating organic P3HT [24]	LPCVD poly-Si [25, 26]
	Sputtering Bi, Sb [27]	Therm. evaporation Ni-Ag [28]	CVD poly-Si and poly-SiGe [29 – 31]
	Co-sputtering Bi, Sb, Te [32]	Flash evaporation Bi <sub>2</sub> Te <sub>3</sub> -type [33, 34]	<i>BiCMOS SiGe quantum well-like TC</i> [35]
	EB evaporation Cu, Ni [36, 37]	ECD CuNi-Cu [38]	
	Co-evaporation Bi/Te and Sb/Te [39]	LPCVD poly-Si-Al [40, 41]	
	Screen printing Bi, Sb [27]	LPCVD poly-Si [42 – 45], poly-SiGe [46, 47]	
	Dispenser printing [48]	CVD poly-Si [6], poly-SiGe [45]	

Approaches with nanostructures are marked in italic font.





**Figure 12.2** Typical length and cross section of thermocouple legs of microTEGs and commercially available bulk TEGs.

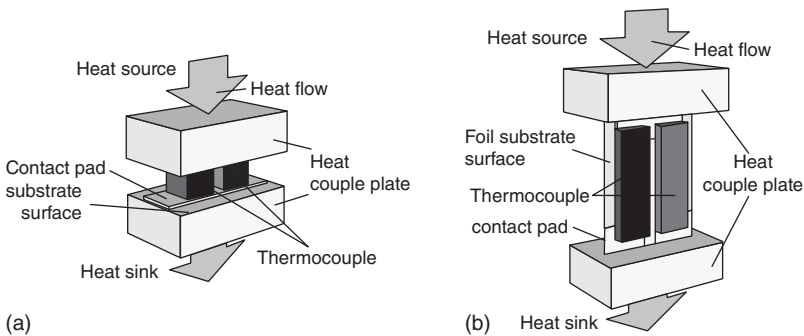


**Figure 12.3** Comparison cross-plane (a) versus in-plane (b) configuration.

parasitic heat flow. An advantage of this configuration is the ability to generate relatively high voltages even at small temperature differences, owing to a longer length of TCs.

Figure 12.5 demonstrates the two basic types of packaging of a microTEG with IPC. In the lateral arrangement (a), a vertical heat flow is diverted via thermally conductive elements in a horizontal direction, while passing through laterally placed and thermally insulated TCs.

In a vertical arrangement (b), heat flows always vertical through the entire device. This arrangement allows a very compact construction with a high density of TCs either by stacking multiple short segments of a thin film-substrate system as, for example, demonstrated in [49] and shown in Figure 12.1b, or by coiling up a long strip of a thin film-substrate system resulting in a circular device as, for example, introduced in [22]. This microTEG incorporates over 5000 TCs in a volume less than  $0.1 \text{ cm}^3$  (Table 12.3).

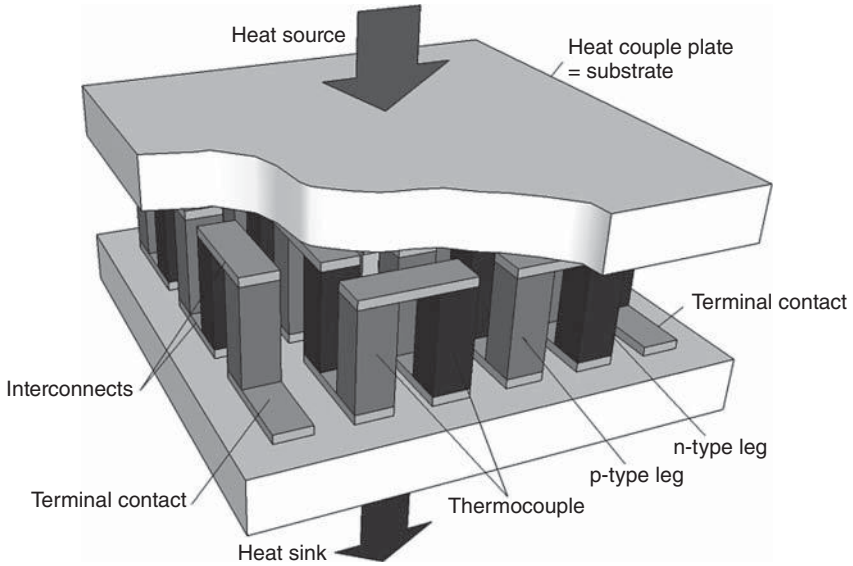


Figure 12.4 Packaging of TEG having a CPC. Substrate can be rigid or flexible.

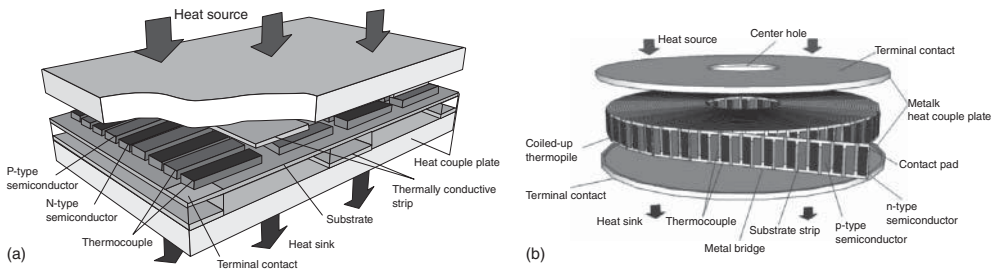


Figure 12.5 Packaging of a microTEG having an IPC as lateral arrangement with a plane or curved substrate (a) or vertical arrangement with a stacked (not shown) or coiled-up substrate (b).

### 12.3 General Considerations for MicroTEGs

A temperature difference across a thermopile  $\Delta T_{TP}$  at a series of TCs, also called *thermopile* (TP), inside a TEG results in an open voltage  $V_{oc}$  at the terminal contact pads (see Figures 12.4 and 12.5) due to the Seebeck effect:

$$V_{oc} = n \cdot (\alpha_p - \alpha_n) \cdot \Delta T_{TP} \tag{12.1}$$

where  $n$  is the total number of TCs and  $\alpha_p$  and  $\alpha_n$  are the Seebeck coefficients for p- and n-type materials, respectively. The optimal output power  $P$ , without consideration of contact resistance, is obtained under matched load condition  $R_{LOAD} = R_{TEG}$  with the electrical resistance of the load and TEG,  $R_{LOAD}$  and  $R_{TEG}$ ,

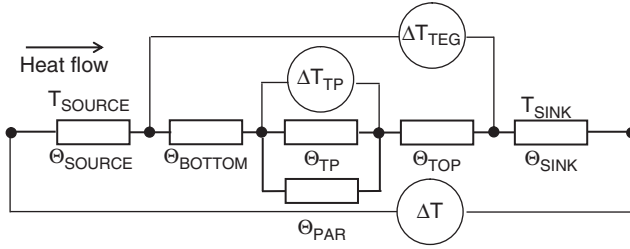


**Figure 12.6** Equivalent thermal circuit of a TE energy harvester with temperature drops across several thermal resistances  $\Theta$  in series and parallel.  $\Theta_{\text{BOTTOM, TOP, TP, PAR}}$  describe a TEG,  $\Theta_{\text{SOURCE, SINK}}$  represent ambience.

respectively:

$$P = \frac{V_{\text{oc}}^2}{4R_{\text{TEG}}} \quad (12.2)$$

Given a thermal environment, maximum power generation is achieved, if the TEG operates under thermal match condition. Shown in detail in Ref. [50], the optimum temperature difference across the thermopile  $\Delta T_{\text{TP, max}}$ , corresponding to the maximal generated power, is

$$\Delta T_{\text{TP, max}} = \frac{\Delta T}{2} \cdot \frac{G_{\text{PS}}}{G_{\text{PS}} + G_{\text{PAR}}} \quad (12.3)$$

where  $G_{\text{PS}}$  is the thermal conductance of all parasitic thermal resistances in series to the TP and  $G_{\text{PAR}}$  represents the parasitic, parallel, thermal conductance of the same TEG, but lacking TCs (“empty TEG”). Equation 12.3 also indicates that for negligible  $G_{\text{PAR}}$  the maximum  $\Delta T_{\text{TP}}$  is half of  $\Delta T$ . The equivalent thermal circuit of a TE energy harvester illustrates all relevant thermal resistances  $\Theta$  and corresponding temperature drops in Figure 12.6. Please refer to Chapter 17 for further derivations of maximum power operating conditions and thermal match conditions for TEGs.

The thermal resistance of a heat source  $\Theta_{\text{SOURCE}}$  is an important parameter in differentiating between application fields for microTEGs. In most industrial applications,  $\Theta_{\text{SOURCE}}$  is low, often due to available metal surfaces providing  $\Delta T$ s of several 10 K. On the other hand, body heat applications are heat-flow limited owing to the low thermal conductivity of human skin, resulting in a thermal resistance per unit area from 200 to over 1000 cm<sup>2</sup> KW<sup>-1</sup>, depending on the location and the level of activity. More information about TEGs in wearable applications can be found in [51] and in an analysis of TE energy harvesting for biomedical applications with wearable and implantable devices [52].

$\Theta_{\text{BOTTOM, TOP}}$  describe the thermal coupling of the thermopile with the ambience including heat couple plates and thermal interfaces and materials. The parasitic, parallel, thermal resistance  $\Theta_{\text{PAR}}$  takes into account all contributions from surrounding gases, supporting structures, and substrate.

$\Theta_{\text{SINK}}$  is usually high owing to heat dissipation into ambient air and can be decreased by attaching fin or pin heat exchangers to the cold side of the microTEG.

Significantly higher heat transfer efficiency is achievable with fluids, for example, using a microfluidic heat exchanger. Wojtas *et al.* [53] reported a heat transfer resistance of  $0.74 \text{ cm}^2 \text{ KW}^{-1}$  at a very low pumping power of  $0.073 \text{ mW cm}^{-2}$ .

Independent of the thermal match condition, the smaller the thermal resistance in series to the thermal resistance of the thermopile, the higher is the power output. This means that the more efficient the heat exchanger, the more heat can flow through the converter system and be converted into power. On the same note, considering the thermal match condition, a TEG design always needs to be matched with a given thermal environment and heat coupling, and not vice versa.

## 12.4

### Micro Device Technologies

Table 12.1 organizes micro device technologies in four categories (Foil, MEMS, CMOS-MEMS, Micro Bulk), similar to Figure 12.2, although some technologies may overlap adjacent categories. The most widely used TE material for the fabrication of microTEGs is based on  $\text{Bi}_2\text{Te}_3$ -type compounds owing to their highest TE performance with a  $ZT$  up to  $\sim 1$  in the room temperature range ( $Z$ : TE figure of merit,  $T$ : absolute temperature) and even higher for nanostructured thin film materials [54]. Furthermore Si-based microTEGs utilize only IPC. A comprehensive overview is given about fabricated TEGs found in literature in Table 12.3.

$\text{Bi}_2\text{Te}_3$ -type single crystals or polycrystalline material having a preferred distribution of crystallographic orientations (texture) possess a distinct anisotropy in their transport properties as shown in Table 12.2. For micro bulk TEGs, the semiconductor material can be diced in the preferred direction having the highest  $ZT$  with the leg axis along the cleavage planes, that is, perpendicular to the trigonal  $c$ -axis. In case of thin film deposition, the orientation, crystalline structure, and transport properties depend on substrate and start materials as well as deposition technique and parameters, including postdeposition processes such as annealing. Thin films with high  $ZT$  value in a direction parallel to the substrate as desired for IPC can be achieved, for example, with physical vapor deposition by sputtering in combination with a post-annealing process. On the other hand, electrochemical deposition (ECD) is currently the only technique obtaining high  $ZT$  values in a

**Table 12.2** Anisotropy of  $\text{V}_2\text{V}_3$ -material – ratio of properties in a direction perpendicular to parallel regarding trigonal  $c$ -axis of single crystals from [56].

Material	$\alpha \perp / \alpha \parallel$	$\sigma \perp / \sigma \parallel$	$\kappa \perp / \kappa \parallel$	PF $\perp /$ PF $\parallel$	Z $\perp /$ Z $\parallel$
p-type $(\text{Bi}_{1-x}\text{Sb}_x)_2\text{Te}_3$ , $x = 0.75$	$\sim 1$	3.2–3.3	1.9–2.3	3.2–3.4	1.5–1.7
n-type $\text{Bi}_2(\text{Te}_{1-x}\text{Se}_x)_3$ , $x = 0.025$	$\sim 1$	4.4–6.7	2.2–2.4	4.6–7.7	2.2–3.2

$\alpha$ : Seebeck coefficients;  $\sigma$ : electrical conductivity;  $\kappa$ : thermal conductivity; PF: power factor; PF =  $S^2\sigma$ ; Z: figure of merit,  $Z = S^2\sigma\kappa^{-1}$ .

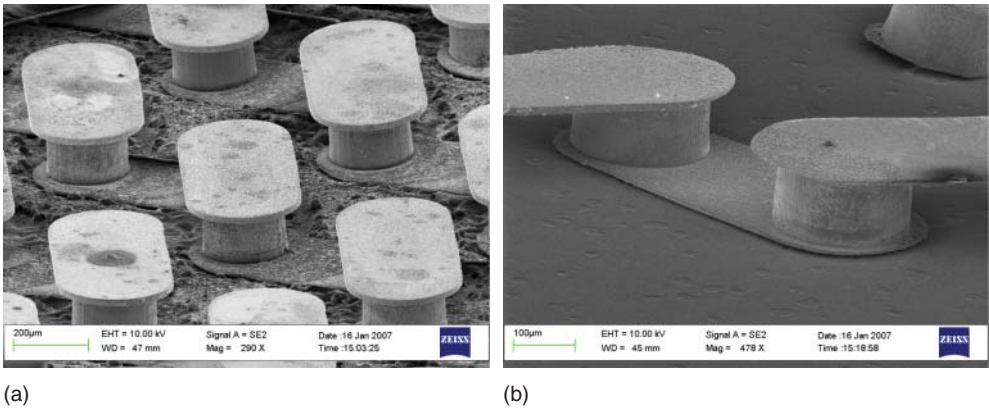


**Figure 12.7** SEM of TCs consisting of round Cu and Ni legs (dia =  $210\mu\text{m}$ , height =  $153\mu\text{m}$ ) with top and bottom interconnects as part of a microTEG made by ECD. The photoresist SU-8 mold has been removed to reveal the TCs (a). Enlargement (b). (Photographs and permission from gTEG, Switzerland.)

direction perpendicular to the substrate, which is the preferable CPC orientation [55].

#### 12.4.1

##### Research and Development

###### 12.4.1.1 Electrodeposition

Electrodeposition, also called *electrochemical deposition*, is a promising and cost-effective, wet method with high deposition rate of  $\sim 50\mu\text{h}^{-1}$  [11] for fabrication of  $\text{Bi}_2\text{Te}_3$ -type TCs and metal interconnects. Up to now, the achieved TE performance of ECD material is still lower in comparison to material resulting from dry deposition processes. Early efforts fabricating an ECD-based MEMS-like TE device were reported by Lim *et al.* [57]. Boulanger [55] provided a detailed chronological overview about TE material deposition with the focus on  $\text{V}_2\text{VI}_3$ -type compounds including nanostructures, which were investigated, for example, by Wang *et al.* [20]. A flexible microTEG with curvatures down to  $7.5\text{mm}$  was demonstrated by Glatz *et al.* [11, 58] (see also [59]) applying a novel mixed method of electrodeposition, combining voltage-controlled deposition pulses with current-controlled resting pulses. Cu–Ni type TCs as seen in Figure 12.7 and later on also p- and n- $\text{Bi}_2\text{Te}_3$ -type TCs were deposited into a photoresist SU-8 mold.

###### 12.4.1.2 Silicon-MEMS Technology

In order to decrease TEG production cost, TCs can be significantly miniaturized using well-established microelectronics Si technologies in conjunction with surface and/or bulk micromachining well known in MEMS fabrication. Main TC materials are polycrystalline Si (poly-Si) and SiGe (poly-SiGe), despite at least a  $10\times$  lower  $ZT$  than  $\text{V}_2\text{VI}_3$  compounds.

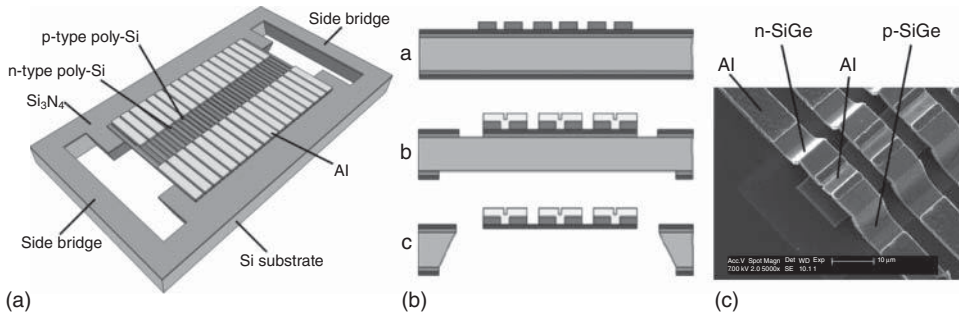


**Figure 12.8** Two fabrication approaches in Si-technology: Thermopile die with IPC (a) with main fabrication steps (b) [42]. (With permission from IFSA Publishing, S.L.). SEM picture of surface micromachined arcade TCs made with sacrificial  $\text{SiO}_2$  bump process (c). Figure 12.8c is a reprint of Figure 4a in

Su, J. et al. "Batch process micromachined TE energy harvester: fabrication and characterization," *J. Micromech. Microeng.* 20 (2010) 104005 (6 pp), reprinted with the permission of the author and the Transducer Research Foundation [47].

A microTEG specifically engineered for human body applications and based on a surface micromachined poly-SiGe thermopile was developed by Wang *et al.* [46]. Leonov *et al.* [42] demonstrated a microTEG with IPC and self-supported TCs made by bulk micromachining and shown in Figure 12.8a,b. The microTEG was integrated in a T-shirt producing  $1 \mu\text{W}$  in an office environment. Fabrication steps of the die include: (i) growth of  $\text{SiO}_2$  and  $\text{Si}_3\text{N}_4$ , deposition, patterning, and selective doping of poly-Si legs; (ii) deposition and patterning of aluminum thermal shunts and interconnects, and opening etch windows; and (iii) removal of  $\text{SiO}_2$  layer and side bridges, replaced by plastic supports. The SEM micrograph features freestanding  $6\text{-}\mu\text{m}$  tall SiGe/Al TCs of a microTEG, consisting of up to 2500 TCs and producing a power of  $0.4 \mu\text{W}$  at  $V_{\text{oc}} = 1.49 \text{ V}$  at  $\Delta T = 3.5 \text{ K}$ .

More realizations of microTEGs using Si technology and bulk micromachining processes are described in [41], in combination with an integrated heater for evaluation purposes in [43], and with an integrated catalytic combustion in [45]. The microTEG developed by Glosch *et al.* [41] consists of 1000 TCs made of poly-Si and aluminum on a  $10\text{-}\mu\text{m}$  thick membrane of size  $11 \text{ mm} \times 1.5 \text{ mm}$  providing  $1.5 \mu\text{W}$  power with a  $\Delta T = 10 \text{ K}$ . Aluminum docking elements were used to stabilize and thermally connect the Si chip. On the basis of this technology, the application report [60] offers a packaged device featuring an output of  $400 \text{ mV K}^{-1}$  and  $40 \mu\text{W}$  at  $\Delta T = 40 \text{ K}$ .

Huesgen *et al.* [40] demonstrated a technology to fabricate a microTEG with n-poly Si/Al TCs and combined silicon surface and bulk micromachining as well as ECD processes.

#### 12.4.1.3 CMOS-MEMS Technology

CMOS-MEMS technology describes the fabrication of MEMS devices using a commercial CMOS process usually followed by a post-micromachining process to release suspended structures. This enables a thermal insulation pattern in order

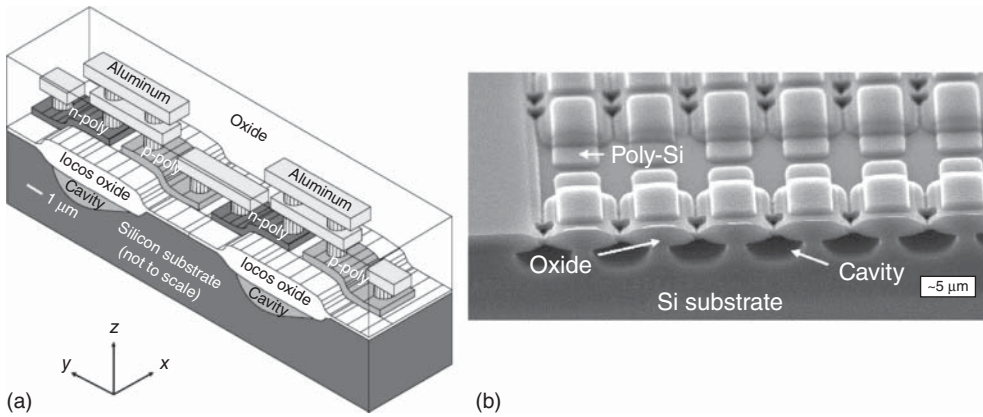


**Figure 12.9** Schematic view of two TCs made by BiCMOS technology. In addition, cavities can be etched into the substrate to increase thermal insulation (a).

SEM micrograph (b) showing cavities etched into the Si-substrate using  $\text{CF}_4$  dry etchant. View prior to metallization along the  $y$ -direction [30]. (With permission from Elsevier.)

to form temperature differences in thin film TCs deposited on a high thermally conductive Si wafer [25, 26, 31].

Strasser *et al.* [29, 30] developed microTEGs consisting of up to 59 400 poly-Si (poly-SiGe used as well) TCs on an area of about  $6 \text{ mm}^2$  based on a standard BiCMOS process as shown in a schematic view and SEM micrograph in Figure 12.9. Micromachined cavities underneath a  $1.6\text{-}\mu\text{m}$  thick oxide layer, called *LOCOS* oxide, improve the thermal efficiency of the TP, resulting in a  $V_{oc}$  of up to  $200 \text{ mV K}^{-1}$ .

Utilizing the same standard BiCMOS process, Yang *et al.* [35] reported the development of a microTEG with quantum well-like TCs. They followed the idea to improve the TE material quality by using a low-dimensional material for the TCs as originally proposed by Hicks and Dresselhaus [61] and covered in more detail in Chapter 19 of this book. First results show improved performance (see Table 12.3).

#### 12.4.1.4 Other

A broad variety of diverse microTEG technologies is listed in Table 12.1. Printing techniques, such as screen printing [27], dispenser printing [48], or spray printing [16], could become an alternative low-cost technology with easily scalable thermopile geometries in the future, provided a significant improvement of TE properties of deposited TCs.

On the other hand, micro bulk technology based on cutting techniques as presented in Ref. [15] or Ref. [9] utilizes highly efficient TE material. However, it is not a large-volume scalable technology.

The development of a novel transparent microTEG for solar energy conversion applications reported by Chen [44] is based on suspending bridge-type poly-Si TCs and transparent conductive indium tin oxide (ITO) thin films as the hot side

Table 12.3 Overview of design, material, and performance of various fabricated TEGs.

Group based on	Citation		TC/Device Design				TC Material		Device performance								
	Author (et al.)	Year	In-/cross-plane lateral/vertical	Substrate	Leg-length (µm)	Leg-cross section (µm <sup>2</sup> )	Area of device (mm <sup>2</sup> )	Number of TC	TC material	Seebeck coeff. of TC (µV/K)	Electrical resistance (Ω)	ΔT across device (K)	V <sub>OC</sub> of device (V) at ΔT	Matched power @ ΔT (µW)	TE eff. factor (µW/K <sup>2</sup> cm <sup>-2</sup> )		
CMOS-MEMS	Strasser	02	30	in/lat	Si	~3.4×0.4	6	59400	p-poly Si	n-poly Si	160	12MΩ	5	0.73	0.01	0.007	
	Xie	10	25	in/lat	Si	5×0.7	100	125,144	p-poly Si	n-poly Si	279	52.8MΩ	5	16.7	1.3	0.052	
	Strasser	03	29	in/lat	Si	6×0.4	7	15,872	p-poly Si	n-poly Si	160	2.1MΩ	5	0.93	0.103	0.059	
	Kao	10	31	in/lat	Si	640	5×0.3	24	245kΩ	p-poly Si	n-poly Si	4	2.45kΩ	20	671	0.5pW	6.4E-05
	Yang	11	35	in/lat	Si	60	4×~0.3	2.25	2,250	poly-Si	poly-Ge	160	2.3MΩ	1	0.251	2.26	0.251
	Böttner	04	62	cross	Si	20	—	1.12	12	P-(Bi <sub>2</sub> Sb) <sub>2</sub> Te <sub>3</sub>	n-Bi <sub>2</sub> Te <sub>2</sub>	340	~7	5	0.0043	0.67	2.4
	Micropelt	13	12,13	cross	Si	36	35×35	14.2	~578	(Bi <sub>2</sub> Sb) <sub>2</sub> (Te <sub>2</sub> Se <sub>3</sub> )	—	—	300	5	0.55	252	71
	Lim	02	57	cross	Glass	Si	20	dia 60	2.89	p-Bi <sub>2</sub> Sb <sub>2</sub> Te <sub>3</sub>	n-Bi <sub>2</sub> Te <sub>3</sub>	—	4	1.25	0.004	1	22.1
	Nextreme	13	17,18	cross	Si	—	—	10.23	—	Bi <sub>2</sub> Te <sub>3</sub> -type superlattice	—	—	11.3	10	0.26	1500	147
	Rowe	89	6	in/lat	Sapphire	4,500	100×0.4	9	5	p-poly Si	n-poly Si	530	69kΩ	11	0.024	0.002	2.0E-04
MEMS	Giosch	99	41	in/lat	Si	500	7×1.2	16.5	1,000	Al	n-poly Si	240	900kΩ	10	2.4	1.5	0.091
	Suzuki	10	24	in/lat	Glass	—	—	—	4	P3HT;FeCl <sub>3</sub>	P3HT	—	744kΩ	52	0.0069	16pW	—
	Huesgen	08	40	in/lat	Si	120	40×0.7/5×0.25	1.7	125	poly-Si	Al	106	84kΩ	5	0.048	0.007	0.016
	Takahashi	07	34	in/lat	Glass	15,000	1,000×1	300	7	p-Bi <sub>0.4</sub> Te <sub>3</sub> 0.6Sb <sub>1.6</sub>	n-Bi <sub>2</sub> Te <sub>2.7</sub> Se <sub>0.3</sub>	434	8.2kΩ	30	0.083	0.21	7.8E-05
	Wang	09	46	in/lat	Si	—	3×3	16	4,700	poly-Si	poly-Ge	225	20MΩ	0.15	0.15	0.3nW	0.026
	Su	10	47	in/lat	Si	—	10×0.7	2.5	1,766	poly-Si	poly-Ge	—	6MΩ	29	3.2	0.45	0.021
	Kim	96	33	in/vert	Glass	20,000	670×4	120	300	p-Bi <sub>0.5</sub> Sb <sub>1.5</sub> Te <sub>3</sub>	n-Bi <sub>2</sub> Te <sub>2.4</sub> Se <sub>0.6</sub>	320	89kΩ	40	4	45	0.023
	Leonov	11	42	in/vert	Si	100	19×—	225	2,300	p-poly Si	n-poly Si	—	3.8MΩ	~9	2	1	0.0055
	Glatz	09	11	cross	Polyimide	126	dia 210	52	90	p-n-Bi <sub>2-x</sub> Te <sub>3-x</sub>	—	340	7.11	51.2	0.106	393	0.288
	Stark	06	22	in/lat	Polyimide	142	dia 210	52	69	Cu	Ni	21.3	0.202	40	0.0013	2.16	0.0026
Foil	Perpetua	13	23	in/lat	Polyimide	—	—	640	5,074	p-Bi <sub>2</sub> Te <sub>3</sub> -type	n-Bi <sub>2</sub> Te <sub>3</sub> -type	—	236kΩ	5	5.2	29	1.69
	Chen	11	48	in/lat	Polyimide	5,000	640×90	500	50	p-Bi <sub>2</sub> Te <sub>3</sub> -type	n-Bi <sub>2</sub> Te <sub>3</sub> -type	—	6.5kΩ	5	3.6	500	3.13
	Francoso	13	32	in/lat	Polyimide	3,000	50/145×1	2,500	2,778	p-Sb <sub>2</sub> Te <sub>3</sub>	n-Bi <sub>2</sub> Te <sub>3</sub>	317	2.55kΩ	20	0.343	10.5	0.0053
	Stordeur	97	21,49	in/vert	Polyimide	1,000	50×2.5	63.7	2,250	p-Bi <sub>0.5</sub> Sb <sub>1.5</sub> Te <sub>3</sub>	n-Bi <sub>2</sub> Te <sub>2.7</sub> Se <sub>0.3</sub>	370	1MΩ	5	2	0.43	7.0E-04
	Itoigawa	05	36,37	in/vert	Polyimide	~2,200	300×~0.15	2,700	380	Cu	Ni	16	6kΩ	1	0.006	1.6nW	5.7E-05
	Kishi	99	9	cross	Si	600	80×80	10×4	10×52	p-Bi <sub>2</sub> Te	n-Bi <sub>2</sub> Te	400	1kΩ	1	0.3	22.5	56.25
	Harman	06	19	cross	none	95	2,000 <sup>2</sup>	4	1	PbS <sub>2</sub> Te/PbTe QD/SL, Cu	—	~219	0.01	220	0.05	89mW	46

Data from references including graphs and figures if not explicitly given.



and cold side electrodes on glass or quartz wafer. The microTEG, fabricated by surface micromachining MEMS technologies, could be applied in windows of buildings for energy harvesting and thermal insulation in the future.

On the basis of micro technologies described in this subchapter, the comprehensive and representative overview in Table 12.3 provides the design, material, and performance of fabricated microTEGs on a component level. TEGs perform best if they are designed to thermally match with a specific environment for maximum power generation. Two principle scenarios may occur:  $\Delta T$  limitation due to low thermal resistance of environment (e.g., industrial applications) or heat flow limitation due to high thermal resistance of environment (e.g., body heat). Therefore, it is difficult to compare microTEGs designed for different applications. Furthermore, significant power losses may occur in the process of boosting low voltages to achieve a usable voltage input level (see Chapters 16 and 3).

#### 12.4.2

### Commercialized Micro Technologies

#### 12.4.2.1 Micropelt Technology

The German company Micropelt [13] was founded in 2006 and established a scalable two-wafer-concept-based production platform for TE thin film devices, developed at Fraunhofer IPM [62] and originally focused on miniaturized cooling devices. Using MEMS-based technologies,  $(\text{Bi,Sb})_2(\text{Te,Se})_3$ -based compound semiconductors are sputtered on 4" and 6"  $\text{SiO}_2$ -passivated wafers in a pilot production line. The main technology steps comprise the following:

- 1) depositing and patterning of metal structures as electrical interconnects;
- 2) overgrowth with up to 36- $\mu\text{m}$  thick TE materials and solder metals;
- 3) patterning of TE materials using an etch mask and reactive dry etching;
- 4) steps 1–3 are separate for p- and n-type wafers and including also an annealing process;
- 5) cutting of wafers, flip chip bonding of the p- and n-type dies with solder and packaging.

A challenging aspect of this technology is the realization of sufficiently thick films corresponding to the leg heights, due to significant differences in expansion coefficients between the TE material and Si substrate by a factor between 5 and 8, in combination with very low contact resistances of  $<10^{-11} \Omega\text{m}^2$ .

Because of CPC (see Figure 12.4), Micropelt's TEG chips possess a high TC density with up to 100 TCs per  $\text{mm}^2$  and a high output voltage of up to  $1.75 \text{ V W}^{-1}$  of thermal heat flow through the device. Internal leg geometries may range from 30 to 600  $\mu\text{m}$  in size and overall geometries from 0.5 to 25  $\text{mm}^2$  are available. Figure 12.10 demonstrates TE legs on a wafer substrate with etching angles steeper than  $80^\circ$ .

A half- and full-packaged Micropelt TEG is also presented in Figure 12.10, together with a performance chart based on data from [13]. The package TGP751 with 10 mm  $\times$  15 mm  $\times$  9.3 mm ( $l \times w \times h$ ) consists of a rectangular metal-base

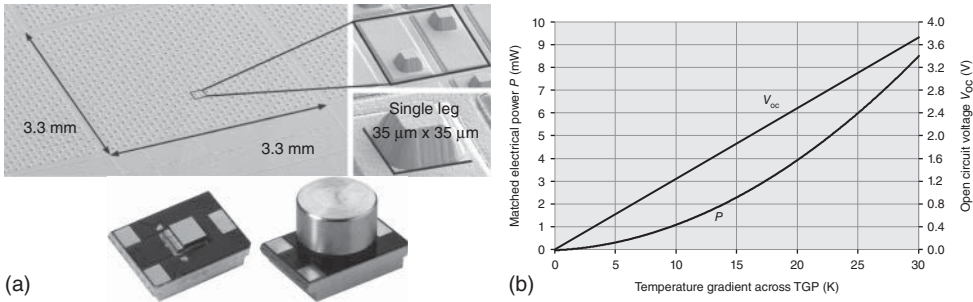


**Figure 12.10** (a) TE legs on wafer substrate (top), TEG on circuit board (half packaged device, left) and TGP (full-packaged device, right). (b) Performance of a packaged device TPG751 [13]. (With permission from Micropelt GmbH, Germany, chart reproduced.)

laminate with ring isolator around the TEG and a metal top. More details can be found in Ref. [12, 63].

#### 12.4.2.2 Nextreme/Laird Technology

In 2013, Laird Technologies [18] acquired the US-based company Nextreme Thermal Solutions Technology, founded in 2005, which manufactures miniaturized, thin film TE devices in CPC (see Figure 12.4), primarily addressing spot-cooling applications. The technology features a thin film nanoscale approach with TE (phonon-blocking/electron-transmitting) superlattice (SL) structures grown by MOCVD developed at Research Triangle Institute (RTI, United States). Maximum  $ZT$  at 300 K are reported of  $\sim 2.4$  for p-type  $\text{Bi}_2\text{Te}_3/\text{Sb}_2\text{Te}_3$  and of  $\sim 1.4$  for n-type  $\text{Bi}_2\text{Te}_3/\text{Bi}_2\text{Te}_{2.83}\text{Se}_{0.17}$  SL devices showing a significant enhancement in comparison to state-of-the-art bulk  $\text{Bi}_2\text{Te}_3$ -type materials with  $ZT \sim 1$  [54].

The TEG device HV56, shown in Figure 12.11 with its performance characteristics, has a size of 3.1 mm  $\times$  3.3 mm  $\times$  0.6 mm and is capable of producing 1.5 mW of output power, with an open circuit voltage of 0.25 V at a temperature gradient of 10 K across the device.

The Nextreme/Laird-technology consists of the following steps summarized from Ref. [17, 64]:

- 1) epitaxial growth of p-type  $\text{Bi}_2\text{Te}_3/\text{Sb}_2\text{Te}_3$  (1/5 nm) and n-type  $\text{Bi}_2\text{Te}_3/\text{Bi}_2\text{Te}_{2.85}\text{Se}_{0.15}$  (1/5 nm) SLs with a 5–20 μm thickness on separate  $\langle 100 \rangle$  GaAs wafers;
- 2) metallized and diced/scribed p- and n-type strips alternatingly placed and separated side by side, with the epitaxial film side down and solder bonded on an AlN heat couple plate having a metal structure as interconnects;
- 3) removal of GaAs substrate by selective etching;
- 4) ECD of metal posts on the exposed SL and dicing of the SL into individual TC legs;
- 5) bonding the other side to a ceramic heat couple plate with a complementary metal interconnect structure.

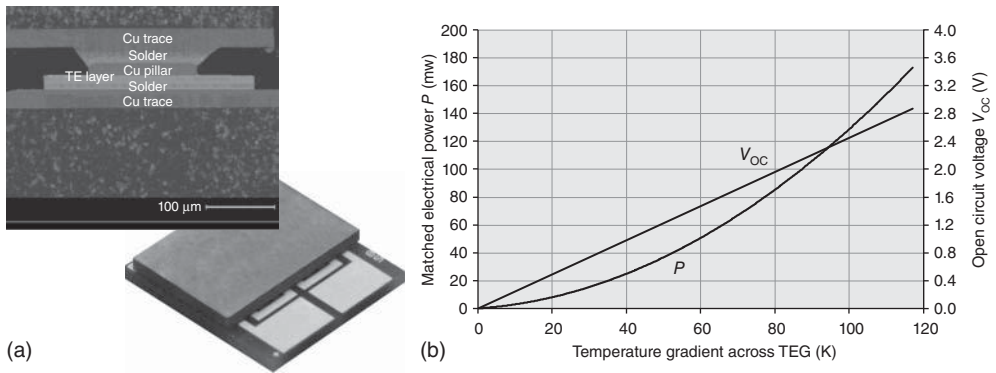


**Figure 12.11** (a) Cross-sectional view of thermal CPB [65] (top), Nextreme's eTEG HV56 device (bottom). (b) Device performance [18]. (With permission from Laird Durham, Inc., US, chart reproduced.)

The thermal copper pillar bump (CPB) solution represents the integration of a thin film TE material into solder bumps for flip chip packaging. This provides a thermal path from one side of the bump to the other with low thermal contact resistances at the chip's surface. An SEM cross section of a TC leg is displayed in Figure 12.11 [65].

#### 12.4.2.3 Thermogen Technology

Thermogen Technologies, Inc., a Perpetua Power Source Technologies, Inc. spin-off company, [23] was established in late 2015 to develop and market commercial applications for an innovative TE thin film technology based on highly efficient  $\text{Bi}_2\text{Te}_3$ -type materials on flexible thin foils. This technology was developed at the Battelle Memorial Institute – operator of Pacific Northwest National Laboratory (PNNL) for the US Department of Energy. With the acquisition of Thermo Life Energy Corporation in 2010, Perpetua Power Source Technologies, founded in 2005, accelerated the development of its TEGwear™ technology, specifically designed for body heat energy harvesting. This technology utilizes the advantages of an inexpensive and highly temperature stable polyimide foil substrate, having a similar thermal expansion coefficient as the TE material in the room temperature range, in combination with an optimized high-rate sputtering process resulting in TE films with a preferable crystallographic orientation due to the lateral IPC of the device, illustrated in Figure 12.5a. This enables the highest TE efficiency of the applied anisotropic TE material, as described in Section 12.3. Furthermore, the foil substrate, in conjunction with the IPC, allows a high freedom of the design for optimal fit of TE structures as well as the overall shape of the device in a specific application.

Figure 12.12 illustrates a typical TC structure and shows an example of a planar TEG and electrical characteristics.

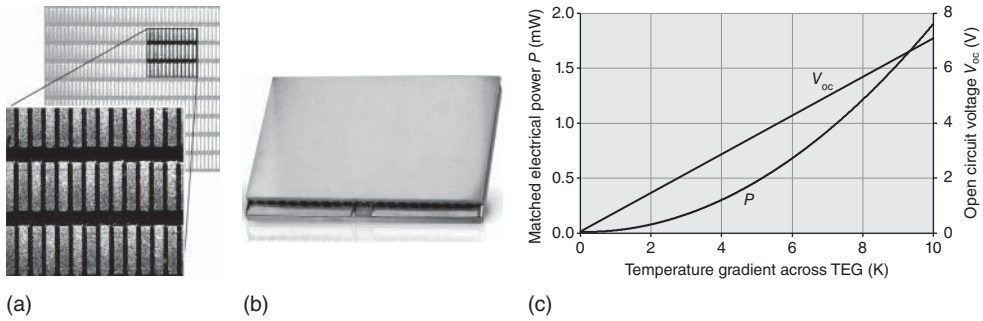


**Figure 12.12** Thermogen TC structure on polyimide foil substrate with enlargement (a), an example of a planar TEG device with dimensions  $32\text{ mm} \times 20\text{ mm} \times 3.4\text{ mm}^3$  ( $l \times w \times h$ ) (b), and device performance chart (c) (With permission from Perpetua Power Source Technologies, Inc., US).

The wafer-like handling of foil substrate allows the utilization of standard processes well known in microelectronic and MEMS technology. The major Thermogen technology steps are as follows:

- 1) photolithographic lift-off mask generation followed by metal deposition and lifting to generate metal interconnects;
- 2) p-semiconductor deposition on foil followed by photolithographic pattern generation for p-legs and wet etching;
- 3) n-semiconductor deposition on foil and p-semiconductor structure followed by photolithographic pattern generation for n-legs and selective wet etching;
- 4) annealing and foil dicing;
- 5) assembly of foil sandwiched between two heat couple plates and sealing of device.

## 12.5

### Applications of Complete Systems

Changing temperature gradients in real applications may result in a discontinuous and nonsteady energy flow due to the nature of the TE energy conversion requiring the integration of a power-efficient, electronic low power management in a complete energy harvesting system. The conditioning electronics needs to provide usable power with a stabilized voltage output and may consist of a DC/DC boost converter, energy storage (capacitors, rechargeable batteries, thin film rechargeable batteries), and electronic switch as described in more detail in Chapters 16 and 3 of this book.

The following five examples of micro TE energy harvesting solutions cover industrial and wearable applications. The first two examples utilize small bulk TEGs in order to demonstrate the general feasibility in the micropower harvesting range.

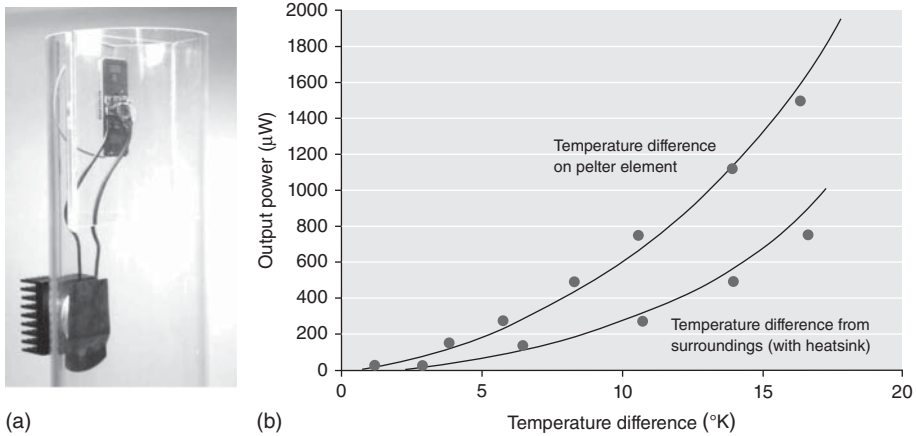


**Figure 12.13** Energy-autonomous sensor for air flow temperature (a) and ECT 310 output power versus temperature difference (b) [68]. (With permission from Enocean GmbH, Germany.)

### 12.5.1

#### Energy-Autonomous Sensor for Air Flow Temperature

Figure 12.13a shows a prototype of an energy-autonomous sensor for air flow temperature made by Enocean. A small bulk Peltier module (TEC2L-15-15-5.6 distributed by Eureka [66] with the size 15 mm × 15 mm × 4.4 mm), which can also be utilized as a TE generator [67], is placed in the wall of the tube and sandwiched between a thin copper film, which adjusts to the air flow temperature and a finned heat sink on the outside creating a temperature gradient across the TEG. The conditioned output power of the bulk TEG as a function of the temperature is given in Figure 12.13b.

The generated power is boosted by Enocean's ECT 310 DC/DC converter, an optimized oscillator that starts to resonate at an input voltage over 10 mV. At 20 mV or higher ( $\geq 2^\circ\text{C}$ ) the output voltage is more than 3 V with a converter efficiency of 30%. Eventually, the generated power drives a temperature sensor and Enocean's wireless sensor module STM 312.

For example, about 100  $\mu\text{W}$  is produced at a total temperature difference of 7 K. With a typical EnOcean wireless module and a 2-min wake-up cycle to send a telegram, only about 5  $\mu\text{W}$  are needed. The remaining 95  $\mu\text{W}$  can be used to power actuators, water valves, or air flaps [68].

### 12.5.2

#### Wireless Pulse Oximeter SpO<sub>2</sub> Sensor

IMEC has designed, fabricated, and tested a body-powered medical device demonstration, a wireless pulse oximeter SpO<sub>2</sub> sensor noninvasively measuring

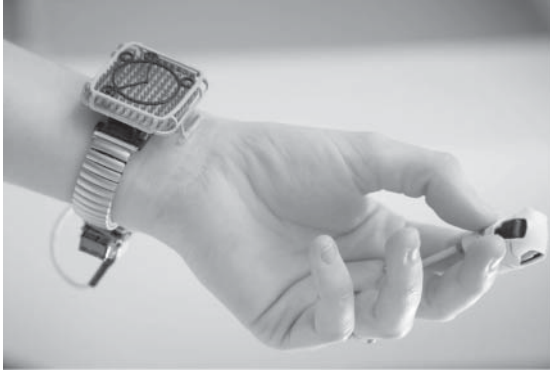


**Figure 12.14** Body-powered wireless pulse oximeter SpO<sub>2</sub> sensor. (Photograph and permission from IMEC, Belgium.)

the oxygen content in arterial blood [69]. A watch-size bulk TEG powered by the human body provides a minimal power of about  $100\ \mu\text{W}$  at night and between 100 and  $600\ \mu\text{W}$  during the day. The power consumption of battery-powered pulse oximeters existing in the market was significantly reduced by 2 orders of magnitude down to  $62\ \mu\text{W}$ , as a result of, for example, application of a low-power radio and duty cycling. The device, as demonstrated in Figure 12.14, can automatically switch into sleeping mode in case the power generation is less than the power consumed.

### 12.5.3

#### Intelligent Thermostatic Radiator Valve (iTRV)

The intelligent thermostatic radiator valves (iTRVs) from Micropelt communicate with thermostats via standard radio protocols enabling intelligent temperature control of a room. These devices use a Micropelt TEG as power supply, exploiting the temperature difference between the hot radiator and the ambient room temperature, and therefore eliminating the need for cabling and replacement of batteries.

According to [70], the TEG starts to generate usable power from temperature differences  $\geq 4\text{K}$ , enabling operation throughout the year. The device has a rechargeable storage element to store surplus energy to be used in times of lower input power, as, for example, in spring and fall. During summer time, the iTRV goes into sleep mode.

An efficient electronic power management and actuator design, including gear-box control and motor and wireless communication, allows multiple adjustments each day and communicates regularly with the room thermostat.

Figure 12.15 illustrates a block diagram and the design of the iTRV device with dimensions  $60\text{ mm} \times 70\text{ mm} \times 50\text{ mm}$  ( $l \times w \times h$ ).

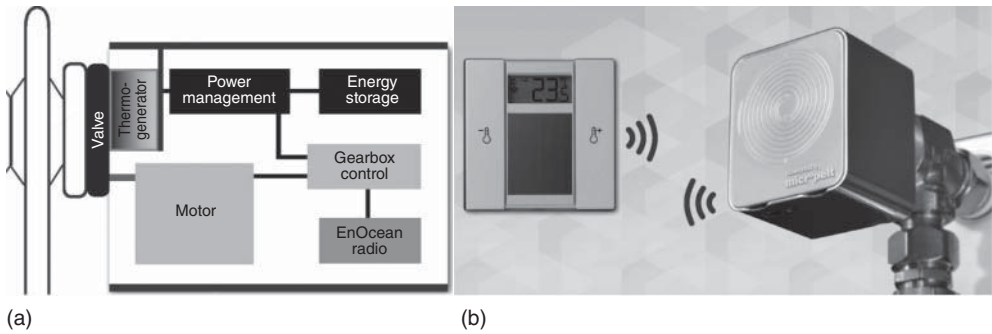


**Figure 12.15** Block diagram of the intelligent thermostatic radiator valves (iTRVs) (a) and mounted iTRV with thermostat (b) [70]. (With permission from Micropelt GmbH, Germany.)

#### 12.5.4

##### Wireless Power Generator Evaluation Kit

Laird offers a wireless TEG kit, called Thermobility™ WPG-1 as power source for self-contained, autonomous systems shown with performance data in Figure 12.16. This device provides a constant DC voltage output of 3.3, 4.1, or 5.0 V to electrical loads of 15 k $\Omega$  or higher. The WPG-1, with a size of 35 mm  $\times$  39 mm  $\times$  27 mm ( $l \times w \times h$ ), consists of a pin-finned heat sink, a custom circuit board, Laird eTEG™ HV56 TEG, and a metal attachment plate as heat collector that needs to be applied to a heat source. The device uses Linear Technology's LTC 3108, an ultralow voltage step-up converter and power management IC to provide up to 1 mW of electrical power, and operates at temperature differences down to 15–20 K. The WPG-1 is designed for any flat surface heat source, such as a laboratory-grade hotplate with temperature control for simple bench-top testing. A 6-pin connector mates to the eZ430 wireless target board from Texas Instruments, offering the WPG-1 as power source for the eZ430 development platform [71].

#### 12.5.5

##### Jacket-Integrated Wireless Temperature Sensor

The integration of TE energy harvesters and wireless sensor electronics into first responder jackets was an objective of Perpetua Power's development for the Department of Homeland Security Science and Technology. The exciting vision driving this development was the common goal of helping first responders do their work more safely and effectively. In the near future, emergency response personnel is expected to be equipped with a number of electronic devices, such as personal location devices, physiological sensors, displays, and personal alert systems. Perpetua Power's unique TEGwear™ technology can help to address the corresponding energy needs. The jacket integrated demonstration system measures temperatures and transmits user data to an eZ430 Chronos wristwatch

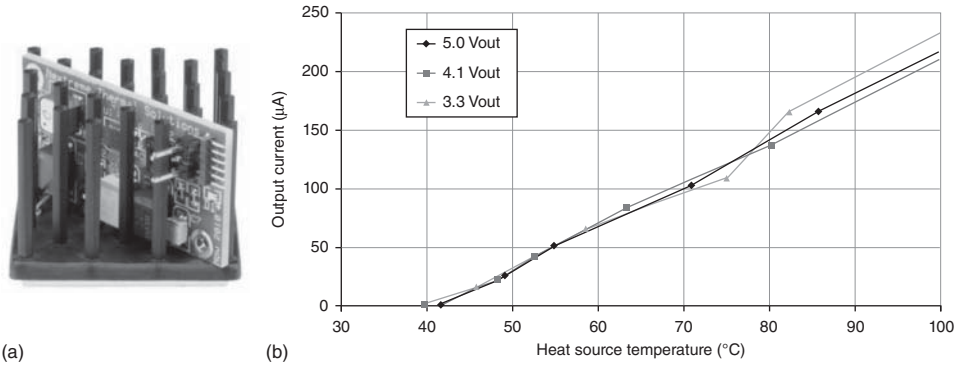


**Figure 12.16** Thermobility™ WPG-1 wireless power generator evaluation kit (a) and its performance at natural convection and  $T_{\text{ambient}} = 24\text{ }^{\circ}\text{C}$  (b) [71]. (With permission from Laird Durham, Inc., US, chart reproduced.)

for data collection. It incorporates the following main components: Perpetua Power's TEGwear™ TEGs, a Texas Instruments (TIs) BQ25504 boost converter, a TI MSP430 microcontroller, a thin film battery, and the TI eZ430 Chronos temperature sensor and transceiver system. Figure 12.17 illustrates a TEGwear jacket with robust and hermetically sealed TEGs integrated into sleeves as well as the eZ430 Chronos wristwatch providing user data, including the Node ID, temperature measurement, a TEGwear performance factor, and a wireless data upload for further data analysis. TEGwear system performance metric depends on activity and environment and can be approximately expressed as transmit events per hour (in parentheses) for the following tested scenarios: office work (125), subterranean search and rescue (130), manufacturing work (150), cliffside search and rescue (250), and horseback search and rescue (320).

## 12.6

### Summary

The increasing trend of micro TE energy harvesting in recent years is based on growing market demand for autonomous micropower supplies mainly for industrial and consumer applications, including wearable electronics. Broad academic research continues to investigate and optimize a wide range of TE materials including nanostructures and corresponding thin film technologies. Besides intensive efforts to develop Si-based microTEGs, mainly driven by the availability of semiconductor and MEMS process technologies, the focus of R&D activities is on TE  $\text{V}_2\text{VI}_3$ -type material systems providing the highest TE figure of merit in the room temperature range as a key factor for maximum device performance. Up to now, only a few approaches to commercialize microTEGs can be observed.  $\text{V}_2\text{VI}_3$ -type materials are preferably applied by utilization of standard dry processes, such as vacuum thin film deposition. With further optimization,





(a)



(b)

**Figure 12.17** TEGwear jacket in an external field trail with the Corvallis Mountain Rescue Unit (CMRU) at Crater Lake National Park in southern Oregon/United States (a)

and EZ430 Chronos wristwatch from Texas Instruments for data reception, display, and storage (b) (With permission from Perpetua Power Source Technologies, Inc., US).

wet processes, such as electrodeposition of efficient TE materials, have the potential to become another attractive alternative in the future. MicroTEGs have been developed with different design configurations and TC arrangements for industrial and consumer applications and are capable of converting heat energy from moderate and even very small temperature differences of a few Kelvin directly into useful electrical power. This makes microTEGs an attractive TE energy harvester solution.

## References

1. Google <http://scholar.google.com> (accessed 10 January 2014).
2. U.S. Environmental Protection Agency, [http://www.epa.gov/superfund/students/clas\\_act/haz-ed/ff06.pdf](http://www.epa.gov/superfund/students/clas_act/haz-ed/ff06.pdf) (accessed 15 January 2014).
3. Research and Markets Wearable Electronics Market and Technology Analysis (2013 – 2018) by Components, Applications, Products, e-Materials & Geography, [http://www.researchandmarkets.com/publication/acd4s1/wearable\\_electronics\\_market\\_and\\_technology\\_an](http://www.researchandmarkets.com/publication/acd4s1/wearable_electronics_market_and_technology_an) (accessed 15 January 2014).
4. Zervos, H. (2013) *Thermoelectric Energy Harvesting 2013–2023: Devices, Applications, Opportunities*, IDTechEx, Cambridge, MA.
5. Abowitz, G., Klints, V., Lancaster, E., Levy, M., and Mountvala, A. (1965) Thin film thermoelectrics (Thin films of thermoelectric alloys formed with vacuum evaporation technique). *Semicond. Prod. Solid State Technol.*, **8** 18–22.
6. Rowe, D.M., Morgan, D.V., and Kiely, J.H. (1989) Miniature low-power/high-voltage thermoelectric generator. *Electron. Lett.*, **25** (2), 166–168.
7. Rowe, D.M. (ed) (1995) Miniature semiconductor thermoelectric devices, in

- CRC Handbook of Thermoelectrics*, vol. 35, CRC Press, London.
8. Bulova Thermatron [http://www.hknebel.org/Uhren/Hersteller/Bulova/Thermatron/Bulova\\_Thermatron/bulova\\_thermatron.html](http://www.hknebel.org/Uhren/Hersteller/Bulova/Thermatron/Bulova_Thermatron/bulova_thermatron.html) (accessed 15 January 2014).
  9. Kishi, M., Nemoto, H., Hamao, T., Yamamoto, M., Sudou, S., Mandai, M., and Yamamoto, S. (1999) Micro-thermoelectric modules and their application to wrist-watches as an energy source. Proceeding of the 18th International Conference on Thermoelectrics, Baltimore, MD, 1999.
  10. USGS <http://minerals.usgs.gov/ds/2005/140/tellurium.xls> (accessed 15 January 2014).
  11. Glatz, W., Schwyter, E., Durrer, L., and Hierold, C. (2009) Bi<sub>2</sub>Te<sub>3</sub>-based flexible micro thermoelectric generator with optimized design. *J. Micromech. Systems*, **18** (3), 763–772.
  12. Böttner, H. and Nurnus, J. (2012) Miniaturized thermoelectric converters, technologies, and applications, in *Modules, Systems, and Applications in Thermoelectrics*, vol. 17 (ed D.M. Rowe), CRC Press, Boca Raton, FL.
  13. Micropelt [http://www.micropelt.com/downloads/thermo\\_generator\\_package.pdf](http://www.micropelt.com/downloads/thermo_generator_package.pdf) (accessed 15 January 2014).
  14. Snyder, G.J., Lim, J.R., Huang, C.-K., and Fleurial, J.-P. (2003) Thermoelectric microdevice fabricated by a MEMS-like electrochemical process. *Nat. Mater.*, **2**, 528–533.
  15. Semenyuk, V. (2001) Thermoelectric micro modules for spot cooling of high density heat sources. Proceeding of the 20th International Conference Thermoelectrics, Beijing, P. R. China.
  16. Navone, C., Soulier, M., Testard, J., Simon, J., and Caroff, T. (2011) Optimization and fabrication of a thick printed thermoelectric device. *J. Electron. Mater.*, **40** (5), 789–793.
  17. Venkatasubramanian, R. *et al.* (2012) Thin-film superlattice thermoelectric devices for energy harvesting and thermal management, in *Modules, Systems, and Applications in Thermoelectrics*, vol. 21 (ed D.M. Rowe), Boca Raton, FL, CRC Press.
  18. Laird <http://www.lairdtech.com/brandworld/library/THR-DS-eTEC-HV56%200512.pdf>.
  19. Harman, T.C., Reeder, R.E., Walsh, M.P., LaForge, B.E., Hoyt, C.D., and Turner, G.W. (2006) High electrical power density from PbTe-based quantum-dot superlattice uncouple thermoelectric devices. *Appl. Phys. Lett.*, **88** (24), 243504.
  20. Wang, W., Jia, F., Huang, Q., and Zhang, J. (2005) A new type of low power thermoelectric micro-generator fabricated by nanowire array thermoelectric material. *Microelectron. Eng.*, **77** (3), 223–229.
  21. Stark, I. & Stordeur, M. (1999) New micro thermoelectric devices based on bismuth telluride-type thin solids films. Proceeding of the 18th International Conference Thermoelectrics, Baltimore, MD.
  22. Stark, I. (2006) Thermal energy harvesting with Thermo Life. Proceeding of the International Workshop on Wearable and Implantable Body Sensor Networks, BSN 2006, Cambridge, MA.
  23. Thermogen <http://www.thermogentech.com> (accessed 25 December 2014).
  24. Suzuki, T., Yoshikawa, K., and Momose, S. (2010) Integration of organic photovoltaic and thermoelectric hybrid module. IEEE International Electron Devices Meeting, San Francisco, CA, December 6–8, 2010.
  25. Xie, J., Lee, C., and Feng, H. (2010) Design, fabrication, and characterization of CMOS MEMS-based thermoelectric power generators. *J. Micromech. Systems*, **19** (2), 317–324.
  26. Yang, M.-Z., Chyan-Chyi, W., Dai, C.-L., and Tsai, W.-J. (2013) Energy harvesting thermoelectric generators manufactured using the complementary metal oxide semiconductor process. *Sensors*, **13**, 2359–2367.
  27. Weber, J., Potje-Kamloth, K., Haase, F., Detemple, P., Völklein, F., and Doll, T. (2006) Coin-size coiled-up polymer foil thermoelectric power generator for wearable electronics. *Sens. Actuators, A*, **132**, 325–330.

28. Yadav, A., Pipe, K.P., and Shtein, M. (2008) Fiber-based flexible thermoelectric power generator. *J. Power Sources*, **175** (2), 909–913.
29. Strasser, M., Aigner, R., Lauterbach, C., Sturm, T.F., Franosch, M., and Wachutka, G. (2004) Micromachined CMOS thermoelectric generators as on-chip power supply. *Sens. Actuators, A*, **114** (2), 362–370.
30. Strasser, M., Aigner, R., Franosch, M., and Wachutka, G. (2002) Miniaturized thermoelectric generators based on poly-Si and poly-SiGe surface micro-machining. *Sens. Actuators, A*, **97-98**, 535–542.
31. Kao, P.H., Shih, P.J., Dai, C.L., and Liu, M.C. (2010) Fabrication and characterization of CMOS-MEMS thermoelectric micro generators. *Sensors*, **10** (2), 1315–1325.
32. Francioso, L., De Pascali, C., Siciliano, P., De Risi, A., D'Amico, S., Veri, C., and Pasca, M. (2013) Thin film technology flexible thermoelectric generator and dedicated ASIC for energy harvesting applications. 5th IEEE International Workshop on Advances in Sensors and Interfaces (IWASI), 2013.
33. Kim, I.H. and Lee, D.H. (1996) Thin film thermoelectric generator cell of Bi-Sb-Te-Se system. 15th International Conference on Thermoelectrics.
34. Takashiri, M., Shirakawa, T., Miyazaki, K., and Tsukamoto, H. (2007) Fabrication and characterization of bismuth-telluride-based alloy thin film thermoelectric generators by flash evaporation method. *Sens. Actuators, A*, **138** (2), 329–334.
35. Yang, S.M., Cong, M., and Lee, T. (2011) Application of quantum well-like thermocouple to thermoelectric energy harvester by BiCMOS process. *Sens. Actuators, A*, **166** (1), 117–124.
36. Itoigawa, K., Ueno, H., Shiozaki, M., Toriyama, T., and Sugiyama, S. (2005) Fabrication of flexible thermopile generator. *J. Micromech. Microeng.*, **15** (9), 233–238.
37. Hasebe, S., Ogawa, J., Shiozaki, M., Toriyama, T., Sugiyama, S., Ueno, H., and Itoigawa, K. (2004) Polymer based smart flexible thermopile for power generation. 17th IEEE International Conference on MEMS, 2004.
38. Pelegrini, S., Adami, A., Collini, C., Conci, P., Lorenzelli, L., and Pasa, A.A. (2003) Simulation, design and fabrication of a planar micro thermoelectric generator. SPIE Microtechnologies, International Society for Optics and Photonics, May, 2013, p. 876322.
39. Carmo, J.P., Gonçalves, L.M., and Correia, J.H. (2010) Thermoelectric microconverter for energy harvesting systems. *IEEE Trans. Ind. Electron.*, **57** (3), 861–867.
40. Huesgen, T., Woias, P., and Kockmann, N. (2008) Design and fabrication of MEMS thermoelectric generators with high temperature efficiency. *Sens. Actuators, A*, **145**, 423–429.
41. Glosch, H., Ashauer, M., Pfeiffer, U., and Lang, W. (1999) A thermoelectric converter for energy supply. *Sens. Actuators, A*, **74** (1), 246–250.
42. Leonov, V., van Andel, Y., Wang, Z., Vullers, R.J.M., and Van Hoof, C. (2011) Micromachined polycrystalline Si thermopiles in a T-shirt. *Sens. Trans. J.*, **127** (4), 15–26.
43. Jacquot, A., Liu, W.L., Chen, G., Fleuriel, J.P., Dauscher, A., and Lenoir, B. (2002) Fabrication and modeling of an in-plane thermoelectric micro-generator. Proceeding 21st International Conference on Thermoelectrics, 2002.
44. Chen, G.M., Huang, I.Y., Ma, L.Y., & Wu, T.E. (2011) Development of a novel transparent micro-thermoelectric generator for solar energy conversion. IEEE International Conference on Nano/Micro Engineered and Molecular Systems (NEMS), 2011.
45. Schaevitz, S.B., Franz, A.J., Jensen, K.F., and Schmidt, M. A. (2001) A combustion-based MEMS thermoelectric power generator. Proceeding of the 11th International Conference Solid-State Sensors and Actuators, Munich, Germany, 2001.
46. Wang, Z., Leonov, V., Fiorini, P., and Van Hoof, C. (2009) Realization of a wearable miniaturized thermoelectric generator for human body applications. *Sens. Actuators, A*, **156** (1), 95–102.

47. Su, J., Leonov, V., Goedbloed, M., van Andel, Y., de Nooijer, M.C., Elfrink, R., Wang, Z., and Vullers, R.J.M. (2010) Batch process micromachined thermoelectric energy harvester: fabrication and characterization. *J. Micromech. Microeng.*, **20**, 104005 (6pp).
48. Chen, A., Madan, D., Wright, P.K., and Evans, J.W. (2011) Dispenser-printed planar thick-film thermoelectric energy generators. *J. Micromech. Microeng.*, **21**, 104006 (8pp).
49. Stordeur, M. and Stark, I. (1997) Low power thermoelectric generator-self-sufficient energy supply for micro systems. Proceeding of the 16th International Conference on Thermoelectrics, Dresden, Germany, 1997.
50. Leonov, V. and Fiorini, P. (2007) Thermal matching of a thermoelectric energy scavenger with the ambience. Proceeding of the 5th European Conference Thermoelectrics (ECT 07), 2007.
51. Leonov, V. (2011) Energy harvesting for self-powered wearable devices, in *Wearable Monitoring Systems* (eds A. Bonfiglio and D. De Rossi), Springer Science, Business Media, LLC, pp. 27–49.
52. Chen, A. and Wright, P.K. (2012) Medical applications of thermoelectrics, in *Modules, Systems, and Applications in Thermoelectrics*, vol. **26** (ed D.M. Rowe), CRC Press, Boca Raton, FL.
53. Wojtas, N., Schwyter, E., Glatz, W., Kühne, S., Escher, W., and Hierold, C. (2012) Power enhancement of micro thermoelectric generators by microfluidic heat transfer packaging. *Sens. Actuators, A*, **188**, 389–395.
54. Venkatasubramanian, R., Siivola, E., Colpitts, T., and O'Quinn, B. (2001) Thin-film thermoelectric devices with high room-temperature figures of merit. *Nature*, **413**, 597–602.
55. Boulanger, C. (2010) Thermoelectric material electroplating: a historical review. *J. Electron. Mater.*, **39** (9), 1818–1827.
56. Scherrer, H. and Scherrer, S. (1995) Bismuth telluride, antimony telluride and their solutions, in *CRC Handbook of Thermoelectrics*, vol. **19** (ed D.M. Rowe), CRC Press, Boca Raton, FL.
57. Lim, J.R., Snyder, G.J., Huang, C.K., Herman, J.A., Ryan, M.A., and Fleurial, J.P. (2002) Thermoelectric microdevice fabrication process and evaluation at the Jet Propulsion Laboratory (JPL). Proceeding of the 21st International Conference Thermoelectrics, Long Beach, CA, 2002.
58. Glatz, W., Durrer, L., Schwyter, E., and Hierold, C. (2008) Novel mixed method for the electrochemical deposition of thick layers of  $\text{Bi}_{2+x}\text{Te}_{3-x}$  with controlled stoichiometry. *Electrochim. Acta*, **54** (2), 755–762.
59. gTEG [http://www.greenteg.com/wp-content/uploads/gTEG\\_Technical-overview.pdf](http://www.greenteg.com/wp-content/uploads/gTEG_Technical-overview.pdf) (accessed 15 January 2014).
60. HSG-IMIT [http://www.hsg-imit.de/fileadmin/gfx/Unser\\_Angebot/F\\_E\\_Dienstleistungen/Sensoren\\_Systeme/Thermische\\_Sensoren/0801\\_AB\\_34\\_Mikro-Energietechnik\\_Thermoelektrischer\\_Generator\\_d\\_e.pdf](http://www.hsg-imit.de/fileadmin/gfx/Unser_Angebot/F_E_Dienstleistungen/Sensoren_Systeme/Thermische_Sensoren/0801_AB_34_Mikro-Energietechnik_Thermoelektrischer_Generator_d_e.pdf) (accessed 15 January 2014).
61. Hicks, L.D. and Dresselhaus, M.S. (1993) Effect of quantum-well structures on the thermoelectric figure of merit. *Phys. Rev. B*, **47** (19), 12727–12731.
62. Böttner, H., Schubert, A., Schlereth, K.H., Eberhard, D., Gawrikov, A., Jägle, M., Kühner, G., Künzel, C., Nurnus, J., and Plescher, G. (2004) New thermoelectric components using micro-system-technologies. *J. Micromech. Systems*, **13** (3), 414–420.
63. Böttner, H., Nurnus, J., and Schubert, A. (2006) Miniaturized thermoelectric converters, in *Thermoelectric Handbook: Macro to Nano*, vol. **46** (ed D.M. Rowe), Taylor & Francis Group, Boca Raton, FL.
64. Venkatasubramanian, R. (2001) Thin-film thermoelectric device and fabrication method of same. US Patent 6,300,150.B1, Oct. 9 2001.
65. Magill, P.A. (2008) The Thermal CPB An Approach to Thermal and Power Management, Solid State Technology, <http://electroiq.com/blog/2008/01/the-thermal-cpb-an-approach-to-thermal-and-power-management> (accessed 15 January 2014).
66. Eureka <http://www.eureka.de/datasheets/03.xx.xxxx/03.05.xxxx/>

- 03.05.0001/TEC2L-15-15-5.6\_73.pdf (accessed 15 January 2014).
67. Min, G. and Rowe, D.M. (1995) Peltier devices as generators, in *CRC Handbook of Thermoelectrics*, vol. 38 (ed D.M. Rowe), CRC Press, Boca Raton, FL.
68. Enocean <http://www.enocean.com/en/white-papers/> (accessed 15 January 2014).
69. Leonov, V. and Vullers, R.J.M. (2009) Wearable electronics self-powered by using human body heat: the state of the art and the perspective. *J. Renewable Sustainable Energy*, 1, 062701.
70. Micropelt <http://www.micropelt.com/itriv.php> (accessed 15 January 2014).
71. Laird <http://www.lairdtech.com/brandworld/library/Laird-THR-DS-Thermobility-WPG-1-040013.pdf> (accessed 25 December 2014).



## 13

# Micromachined Acoustic Energy Harvesters

*Stephen Horowitz and Mark Sheplak*

### 13.1

#### Introduction

Acoustic energy harvesting is defined here as the conversion of acoustic fields and waves (fluidic or structural) into usable electrical energy. All fluidic acoustics and some (mainly ultrasonic) structural acoustics (vibrations) fall under this definition; however, harvesting from lower frequency (and thus longer wavelength) vibrations (i.e., traditional vibration energy harvesting) are treated elsewhere in this book. The acoustic energy available for harvesting may originate from other vibrating structures, airflow, or thermal sources before propagated acoustically and ultimately converted to electrical energy.

The focus of this chapter is on micromachined implementations of acoustic energy harvesters (AEHs); however, mesoscale devices will also be discussed in depth to provide a historical and technical background to the field. The chapter begins with a historical introduction to the field, providing an overview of devices, applications, and approaches. Following this, an in-depth theoretical background on acoustic fundamentals is provided, including basic concepts, physical derivations, characteristics of acoustical energy sources, and challenges of acoustic energy harvesting. A significant part of the chapter is devoted to electroacoustic transduction, including detailed surveys and comparisons of transduction methods and the modeling and optimization techniques that enable efficient transducer design. Next, energy harvesting design and fabrication strategies will be discussed, followed by testing and characterization methods and results, including a survey of reported performance metrics. The chapter concludes with a discussion of practical constraints and fundamental limitations and potential paths forward in the field of acoustic energy harvesting.

## 13.2

## Historical Overview

## 13.2.1

## A Brief History

Harvesting energy from acoustic fields has a relatively short history, dating back to only 1998. It was in that year and the subsequent that Amirtharajah and Chandrakasan [1, 2] published their work on using vibration-based power generation as a source for self-powered signal processing. While primarily focused on the harvesting of energy from structural vibrations, they did briefly explore the possibility of using acoustic fields as a power source, demonstrating sufficient harvested energy to power their digital signal processing (DSP) system from a 114-dB incident sound field. In 2003, Sood [3] attempted acoustic energy harvesting using a micromachined cantilever structure but found difficulty directly coupling to the open cantilever designed primarily for structural excitation.

The first successful in-road into acoustic energy harvesting was presented in 2001 by Mandurino *et al.* [4], who published a paper on a self-powered noise reduction system, employing acoustic energy as the power source. Their system utilized a piezoelectric buzzer for energy capture and a second buzzer to generate an out-of-phase wave for destructive interference and noise cancelation. They directly wired the output from the “energy drier” buzzer, as they called it, to the input of the control buzzer. No power conversion or storage circuitry was used or needed in their arrangement.

Shortly thereafter, in 2002, the first device specifically designed to combine the harvesting of acoustic energy with power conversion and storage circuitry was presented in a paper by Horowitz *et al.* [5]. In this and follow-on work by Taylor *et al.* [6], Liu *et al.* [7, 8], and Phipps *et al.* [9], researchers at the University of Florida developed mesoscale Helmholtz resonator-based AEHs targeted for self-powered sensing in aircraft engine nacelles (Figure 13.1). These harvesters combined Helmholtz resonators with commercially available

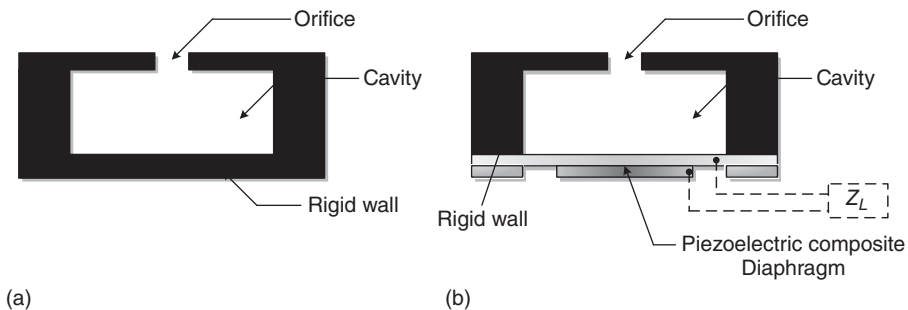


**Figure 13.1** Cross-sectional drawings of an (a) Helmholtz resonator as a single cell of an aircraft engine liner. (b) Helmholtz resonator-based AEH via incorporation of a piezoelectric composite diaphragm.



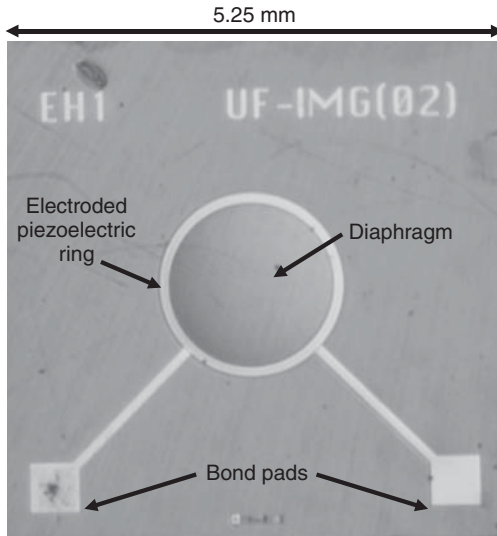


**Figure 13.2** Optical micrograph of a released, micromachined AEH die.

mesoscale piezoelectric diaphragms to harvest sufficient energy to power sensors and active flow-control systems. In 2005 and 2006, the piezoelectric diaphragms of these AEHs were miniaturized using micromachining to create a microelectromechanical system (MEMS)-based AEH [10–12] (Figure 13.2).

Also in 2005, Kim *et al.* [13, 14] investigated the use of regrouped electrodes on piezoelectric diaphragms for the purpose of acoustic energy harvesting. In these papers, they explored the theoretical and experimental effects of different electrode configurations to improve overall harvesting performance.

More recently, other researchers have increased the performance of AEHs using piezoelectric diaphragms [15–18]. In 2010, Shinoda *et al.* [15] improved upon the micromachined piezoelectric diaphragm-based AEH by using a thicker piezoelectric film (1- $\mu\text{m}$  thick PZT) with improved material properties and employing a fully electroded diaphragm to better capture energy at the third resonance of the diaphragm, rather than the fundamental. Kimura *et al.* [16] further improved the performance by eliminating a wet etching step for the top electrode which was suspected of damaging the piezoelectric diaphragm in a manner that increased the internal resistance. Replacing the etch step with a dry etching process reduced the internal resistance from 550 to 75  $\Omega$ . As a result, the output energy density increased from 4.9 to 98  $\mu\text{W m}^{-2}$ . Tsujimoto *et al.* [17] and Iizumi *et al.* [18] then replaced the single-electrode design with a dual electrode to capture both polarizations and thereby increased the total captured energy.

In 2010, Lallart *et al.* [19] demonstrated a nonlinear switching technique for acoustic energy harvesting that improved the harvested power density by a factor of 10–1000 $\times$  greater than that of Horowitz *et al.* [12] and Liu *et al.* [7]. The technique is referred to as *synchronized switch harvesting on inductor (SSHI)* and

works by switching the polarity of the piezoelectric voltage generated by a piezoelectric diaphragm synchronously with the motion.

Rather than focusing on improved piezoelectric diaphragms, in 2013, Peng *et al.* [20, 21] instead concentrated on improving the acoustic coupling to the diaphragms by using dual Helmholtz resonators to create a 3 degree of freedom (DOF) AEH. They utilized commercially available PZT bonded to a custom annular brass plate that serves to separate the two HR chambers. Their approach demonstrated improvements in output power by up to 1600% along with increased harvesting bandwidth due to multiple closely spaced resonances.

Wu *et al.* [22] and Wang *et al.* [23] took a drastically different approach than diaphragms or HRs, using piezoelectric beams nested within a lattice defect of a sonic crystal. The defect served as a resonant cavity within the crystal, amplifying the acoustic field prior to conversion.

Several groups have demonstrated harvesting of acoustic energy originating from various types of airflow. In 2008, Kim *et al.* [24] published work on two types of electromagnetic-based airflow energy harvesters. One type works on a windbelt-based approach, whereby a mechanical structure protrudes into the airflow and is vibrationally excited. The second type is based on a Helmholtz resonator strategy similar to many of the AEHs listed previously. Rather than use a piezoelectric diaphragm, they employ an electromagnetic generator based on a diaphragm-mounted magnet moving inside a coil winding. In this approach, they leverage flow-induced vibrations to create acoustic pressure fluctuations and drive the Helmholtz resonator/diaphragm structure. In a similar vein, in 2010, Wang *et al.* [25] utilized flow-induced vibrations in a cavity to drive a piezoelectric film and harvest energy. Jing *et al.* [26] took a different approach to capture flow energy, utilizing a piezoelectric diaphragm with an attached standing beam protruding into the flow. In 2012, Sun *et al.* [27] developed a “mean flow acoustic engine(MFAE)” as the first stage in an airflow-driven energy harvester. The MFAE converts mean flow into an oscillating acoustic field via a cross-junction resonator tube configuration. The system was demonstrated to achieve an acoustic amplitude of 6.2 kPa for a mean flow of  $50 \text{ m s}^{-1}$ .

Harvesting of acoustic energy within fluidic hydraulic systems is also an active area of research. Cunefare *et al.* [28, 29] have been developing AEHs for capturing acoustic pressure fluctuations in pumped hydraulic systems, demonstrating collection of up to 1.2 mW from a 400-kPa pressure fluctuation. The higher available acoustic energy densities in such systems make this a promising approach for further research.

### 13.2.2

#### Survey of Reported Performance

For a convenient comparison, a summary of reported performance metrics from the literature is provided in Table 13.1 The table is grouped by type, and then sorted by year. Areas were calculated from the smallest rectangular region that

Table 13.1 Reported acoustic energy harvester performance.

Type	Year	Authors	Transduction method	Structure	Frequency (kHz)	Pressure (dB SPL)	Power out (mW)	Area (cm <sup>2</sup> )	Power density (mW cm <sup>-2</sup> )
Airborne	1998	Amirtharajah and Chandrakasan [1]	Electromagnetic	Mass spring	0.002	114	1.80E-02	—	—
Airborne	2002	Horowitz <i>et al.</i> [5]	Piezoelectric	Diaphragm/HR	2.18	149	7.40E+00	6.450	1.50E+00
Airborne	2004	Taylor <i>et al.</i> [6]	Piezoelectric	Diaphragm/HR	2.5	151	2.50E+01	6.310	3.96E+00
Airborne	2005	Horowitz [10]	Piezoelectric	Diaphragm	13.6	149	2.00E-05	0.590	3.40E-04
Airborne	2008	Liu <i>et al.</i> [7]	Piezoelectric	Diaphragm/HR	2.6	161	3.00E+01	6.150	4.88E+00
Airborne	2009	Wu <i>et al.</i> [22]	Piezoelectric	Curved beams	4.02	—	4.00E-05	—	—
Airborne	2009	Phipps <i>et al.</i> [9]	Piezoelectric	Diaphragm/HR	2.5	—	1.20E+00	11.900	1.00E-01
Airborne	2010	Kimura <i>et al.</i> [16]	Piezoelectric	Diaphragm	6-16	100	1.40E-07	0.014	9.80E-06
Airborne	2010	Lallart <i>et al.</i> [19]	Piezoelectric	Diaphragm	0.245	100	5.50E-02	100.000	7.00E-04
Airborne	2010	Shinoda <i>et al.</i> [15]	Piezoelectric	Diaphragm	24	100	1.10E-08	0.023	4.80E-07
Airborne	2011	Tsujimoto <i>et al.</i> [17]	Piezoelectric	Diaphragm	4.92	100	9.50E-08	0.040	2.37E-06
Airborne	2011	Iizumi <i>et al.</i> [18]	Piezoelectric	Diaphragm	4.9	100	8.30E-08	0.040	2.07E-06
Airborne	2013	Peng <i>et al.</i> [20]	Piezoelectric	Diaphragm/HR	1.1-1.4	100	3.00E-03	39.690	7.56E-05
Airborne	2013	Peng <i>et al.</i> [21]	Piezoelectric	Diaphragm/HR	0.96	100	1.25E-03	39.690	3.15E-05
Flow induced	2008	Kim <i>et al.</i> [24]	Electromagnetic	HR	1.4	80	—	0.212	—
Flow induced	2010	Wang <i>et al.</i> [25]	Piezoelectric	Diaphragm	0.026	155	2.00E-04	0.063	3.20E-03
Hydraulic	2013	Cunefare <i>et al.</i> [28, 29]	Piezoelectric	Stack	0.45	194	1.20E+00	0.462	2.60E+00

encloses the active element (generally the diaphragm), to reflect realistic packing densities for arrays.

### 13.3

#### Acoustics Background

##### 13.3.1

##### Principles and Concepts

The field of physical acoustics concerns itself with generation and propagation of sound. If a perturbation is introduced into a gas, liquid, or solid with a time-dependent external source that transfers momentum and energy to the medium, the response of the medium will be composed of three mechanisms: diffusion of momentum away from the source driven by a velocity gradient, diffusion of heat (energy) away from the source driven by a temperature gradient, and the propagation of an acoustic wave away from the source at a finite speed (that is a function of the elastic properties and density of the medium) governed by the wave equation.

##### 13.3.2

##### Fundamentals of Acoustics

The wave equation governing linear, lossless acoustic motion is derived for a linearized version of conservation of mass and momentum while assuming an isentropic equation of state [30]

$$\frac{1}{c_0^2} \frac{\partial^2 p'}{\partial t^2} - \nabla^2 p' = 0 \quad (13.1)$$

where  $c_0$  is the isentropic speed of sound and  $p'$  is the pressure fluctuation with respect to the mean pressure. To address the wide range in amplitudes of acoustic waves present in nature, the sound pressure level SPL is defined as a logarithmic measure of the effective sound pressure of a sound relative to a reference value,  $p_{\text{ref}}$ ,  $\text{SPL} = 20 \log(p_{\text{rms}}/p_{\text{ref}})$  [dB], where  $p_{\text{rms}}$  is the root mean square value of the pressure fluctuation and  $p_{\text{ref}} = 20 \mu\text{Pa}$  which is the nominal threshold of hearing for humans. For a plane, progressive acoustic wave propagating along the  $x$ -axis,  $p'(x, t)$ , the relationship between the pressure fluctuation and the acoustic particle velocity,  $u'(x, t)$ , is

$$p'(x, t) = \rho_0 c_0 u'(x, t) \quad (13.2)$$

where  $Z_0 = \rho_0 c_0$  is the specific acoustic impedance of the medium. Physically, the specific acoustic impedance is related to the sound radiated away from a vibrating body. For a constant acoustic velocity, the pressure fluctuation will linearly increase with  $Z_0$ . The instantaneous acoustic intensity is the acoustic power per unit area and is defined as

$$\vec{i}(x, y, z, t) = p'(x, y, z, t) \vec{V}'(x, y, z, t) \quad (13.3)$$

**Table 13.2** The SPL and available power per unit area (intensity) for some representative sound source levels.

SPL (dB)	Intensity	Example source
20	$0.01 \text{ pW cm}^{-2}$	Whisper
60	$100 \text{ pW cm}^{-2}$	Conversation
80	$10 \text{ nW cm}^{-2}$	Vacuum cleaner
120	$100 \mu\text{W cm}^{-2}$	Threshold of pain
160	$1 \text{ W cm}^{-2}$	Jet engine nacelle
194	$2.5 \text{ kW cm}^{-2}$	Rocket engine

where  $\vec{V}'(x, y, z, t)$  is the acoustic particle velocity vector. The corresponding acoustic power  $W$  of a sound source is determined by integrating the intensity over the area enclosing the source. Similar to the SPL, a power level (PWL) is defined as a logarithmic measure of sound power with respect to a reference value,  $p_{\text{ref}}$ ,  $\text{PWL} = 10 \log(W/W_{\text{ref}})$  [dB], where is typically  $W_{\text{ref}} = 10^{-12} \text{ W}$ .

### 13.3.3

#### Challenges of Acoustic Energy Harvesting

Because airborne acoustic waves are a small (linear) perturbation about atmospheric pressure, a major challenge of AEH is to identify appropriately large acoustic sources to scavenge energy from. Physical insight is provided by examining a plane progressive wave, where  $I_x = p_{\text{rms}}'^2(x)/\rho_0 c_0$ . For example, a plane wave in air at the threshold of human pain (SPL = 120 dB) only contains  $I_x = (20 \text{ Pa})^2 / (1.2 \text{ kg m}^{-3})(344 \text{ m s}^{-1}) \approx 100 \mu\text{W cm}^{-2}$ . This result indicates that AEH requires either very large SPL acoustic sources and/or large area harvesters are required to provide meaningful power levels, especially when only a small fraction of this power is actually available owing to typically poor coupling efficiencies of AEHs. Acoustic energy reclamation becomes feasible in very loud acoustic environments, such as near rocket engines (SPL = 194 dB) that possess  $I_x \approx 2.5 \text{ kW cm}^{-2}$  or even in aircraft jet engine nacelles (SPL = 160 dB) that possess  $I_x \approx 1 \text{ W cm}^{-2}$ . Table 13.2 provides typical values of intensity for a range of sound source levels.

## 13.4

### Electroacoustic Transduction

Acoustic energy harvesting requires one or more stages of transduction, whereby energy is converted from one energy domain to another, ultimately from acoustical to electrical energy, but may involve intermediary energy domains along the way. Furthermore, within a single energy domain (e.g., acoustical), structures may

be implemented to improve efficiency, typically by focusing energy or matching impedance.

#### 13.4.1

##### Modeling

Design, optimization, and analysis of AEHs require some form of modeling (analytical or numerical) to predict behavior. Either analytical or numerical modeling or a combination both may be appropriate for a given harvester, depending on the structures, transduction techniques, and accuracy required. For some harvesting systems, prediction of behavior can be accurately and efficiently achieved using exact analytical methods. Typically however, the systems are not readily represented by an exact form, which often involve partial differential equations. Furthermore, exact approaches are not readily conducive to complete harvesting system-level design including the source, transducer, and electronics. Even when an exact mathematical description is available and allows for precise prediction of performance, it is often too complex to yield much physical insight in the design, limiting optimization potential.

Alternatively, finite element modeling (FEM) methods can be used to predict acoustical and mechanical system behavior via a numerical approach. Precision is generally high with this method; however, physical insight is less readily available without combining this method with other forms of modeling.

##### 13.4.1.1 Lumped Element Modeling (LEM)

In order to facilitate a more physics-based approach for design, analysis, and optimization, a simplified, reduced-order model can be used that accurately captures critical geometric and material dependencies. The reduced-order modeling approach typically employs lumped elements [31, 32] (also sometimes known as *lumped parameters* [33]) to represent key components of the system based on the manner in which they interact with energy. The total energy in any system may be divided into three distinct categories: potential energy, kinetic energy, and dissipated energy.

When all the physical dimensions of the system are on the order of or larger than the wavelength, a distributed parameter approach [34] can then be utilized. Conversely, when this condition is not met and the dimensions are much smaller than the relevant wavelength of interest, the system can be accurately modeled using a lumped element approach. In this regime, there is little variation of the energy distribution across the system. Mathematically, this implies the spatial and temporal variations are decoupled and allows for the use of ordinary differential equations instead of partial differential equations. Physically, this means that energy storage and dissipation mechanisms can be represented by equivalent elements that are lumped to a chosen spatial location (a point). The energy stored or dissipated in each of those elements is intentionally equivalent to the integrated value of the corresponding energy distributed across the actual system.

Lumped element modeling has a long history of use in electrical engineering, where most circuit design takes place in the electroquasistatic (EQS) regime. In this regime, the wavelengths of interest are typically many orders of magnitude larger than the physical dimensions of the circuit components (resistors, capacitors, inductors, etc.). Physically, for example, the resistance of a resistor occurs as a result of dissipation mechanisms occurring over a finite space (along the length and width of the resistor); however, a simple lumped element model representing the total resistance is typically used. Similarly, lumped inductors are used to represent the storage of kinetic energy in a magnetic field and lumped capacitors are used to represent the storage of potential energy in an electric field.

In mechanical systems, kinetic energy is stored via motion of a mass, potential energy is stored via the compression, stretching, or bending of a spring, or other elastic structure and dissipation occurs via frictional or other mechanical loss mechanisms (e.g., radiation away from the system). In acoustical systems, kinetic energy is stored via motion of an acoustic mass ( $\text{kg m}^{-4}$ ) and is represented by an inductor in an equivalent electrical circuit. Similarly, potential energy is stored via compression of an acoustic compliance ( $\text{m}^3 \text{Pa}^{-1}$ ) and is represented by a capacitor in the equivalent circuit. Dissipation in acoustic systems, which can also occur from frictional and radiative losses is modeled as an acoustic resistance ( $\text{m}^4 \text{s}$ ) and is represented by a resistor in the equivalent circuit. Table 13.3 summarizes these equivalent lumped elements.

#### 13.4.1.2 Equivalent Circuits

Using an LEM approach, the overall behavior of the system can be predicted after decomposing the system into discrete lumped elements and applying a system-wide equivalent circuit analysis. Other techniques, such as bond-graphs [35, 36], can yield the same results; however, by using an equivalent circuit approach, the extensive circuit analysis techniques available to electrical systems can be applied to equivalent mechanical or acoustical systems.

Power in any system can be expressed as the product of an effort variable and a flow variable, together known as *conjugate power variables*. In the electrical energy domain, the effort variable is voltage,  $V$ , and the flow variable is current,  $I$ . Similarly, in the mechanical and acoustical energy domains, the effort variables are force,  $F$ , and pressure,  $P$ , respectively and the flow variables are velocity,  $v$ , and

**Table 13.3** Equivalent lumped elements in mechanical, acoustical, and electrical energy domains.

	Kinetic energy storage	Potential energy storage	Energy dissipation
Electrical	Inductance (H)	Capacitance (F)	Resistance ( $\Omega$ )
Mechanical	Mass (kg) (point mass)	Compliance ( $\text{m N}^{-1}$ ) (spring)	Mechanical resistance (damper) ( $\text{m} \cdot \text{s}$ )
Acoustical	Acoustic mass ( $\text{kg m}^{-4}$ )	Acoustic compliance ( $\text{m}^3 \text{Pa}^{-1}$ ) or ( $\text{m}^5 \text{N}^{-1}$ )	Acoustic resistance ( $\text{m}^4 \text{s}$ )

**Table 13.4** Equivalent circuit parameters.

	Electrical	Mechanical	Acoustical
Effort	Voltage $V$	Force $F$	Pressure $P$
Flow	Current $I = dQ/dt$	Velocity $v = dx/dt$	Volume velocity $Q = \Delta\text{Vol}/dt$
Power	Electrical power $\text{Pow}_e = VI$	Mechanical power $\text{Pow}_m = Fv$	Acoustic power $\text{Pow}_a = PQ$
Impedance	Electrical impedance $Z_e = V/I$	Mechanical impedance $Z_m = F/v$	Acoustic impedance $Z_a = P/Q$
Compliance	Capacitance $C_e = \int Idt/V = q/V$	Mechanical compliance $C_m = \int vdt/F = x/F = 1/k$	Acoustic compliance $C_a = \int Qdt/P = \Delta\text{Vol}/P$
Inertance	Inductance $L = V/(dI/dt)$	Mass $M = F/(dv/dt)$	Acoustic mass $M_a = P/(dQ/dt)$
Resistance	Resistance $R = \text{Re}(V/I)$	Damping coefficient $b = \text{Re}(F/v)$	Acoustic resistance $R_a = \text{Re}(P/Q)$

volume velocity,  $Q$ , respectively. Using these variables, other important terms can be defined, as listed in Table 13.4. For instance, in the electrical energy domain, power is the product of voltage (effort) and current (flow), while impedance is the ratio of voltage to current. Analogously, in the other energy domains, power is defined as the product of the local effort and flow, while impedance is defined as the ratio of the local effort to flow. Using this technique, equivalent lumped elements can be defined for compliance, inertance, and resistance. With the exception of power, these parameters all have unique units associated with their respective energy domains, yet they are functionally equivalent.

To create an equivalent circuit model for a system, the elements must be connected according to some rules. Whenever an effort variable is shared between two or more elements, they are connected in parallel in the equivalent circuit. Conversely, whenever a flow variable is shared between elements, they are connected in series.

### 13.4.1.3 Transduction

Using conjugate power variables to represent the lumped elements in the system facilitates the construction of a single circuit to represent the entire multi-energy domain system. Transduction stages are used in such a circuit to represent the coupling of energy from one domain to another. There are many ways to represent transduction in an equivalent circuit, including the use of transformers or gyrators. In keeping with common electrical elements, we will employ a transformer-based approach to represent transduction.

There are two types of transduction, direct and indirect, distinguished by the manner in which they interact with energy. Direct transduction (e.g., electromagnetic) implies a direct and total transduction of energy between the



energy domains. On the other hand, indirect transduction (e.g., piezoelectric) implies that some of the energy is stored internally instead of converted, resulting in lower transduction efficiencies. For direct transduction, only the transformer is needed in the equivalent circuit representation. For indirect transduction however, additional energy storage elements (e.g., capacitors) that are inherent to the transduction process must be included as well. The magnitude of the energy conversion is represented by a transformer “turns-ratio.” For actual electrical transformers, this ratio is dimensionless and represents the ratio of wire turns on each side of the transformer and thus the voltage gain when reflecting across the transformer. In the equivalent circuit representation of multi-energy domain systems, this concept is generalized to represent the magnitude and unit conversion that occurs when transducing from one energy domain to another. In these multi-energy situations the turns-ratio is not a dimensionless number.

#### 13.4.1.4 Numerical Approaches

In addition to using analytical approaches to compute lumped element values, numerical methods are also used, particularly when the complexity or required accuracy exceeds analytical capabilities. When used properly, numerical approaches (such as FEM) can provide useful physical insight. This is particularly true when the resulting response is converted to equivalent lumped elements and incorporated into the rest of the equivalent circuit [37].

### 13.4.2

#### Impedance Matching and Energy Focusing

Impedance matching and energy focusing may initially sound like distinctly different phenomenon but in the context of energy harvesting, they may be thought of as having highly similar effects. Impedance matching describes the concept of converting the input impedance of a transduction stage to match the output impedance of a previous stage. As a result of the increased matching, less energy is reflected and greater energy is captured.

### 13.4.3

#### Transduction Methods

While there is a large array of possible transduction methods to ultimately get from acoustical to electrical energy, in practice only a few are commonly used and relevant owing to practicality and efficiency. Most acoustical energy harvesters employ piezoelectric, electromagnetic, or electrostatic transduction methods.

#### 13.4.3.1 Piezoelectric Transduction

Piezoelectric transduction relies upon the behavior of certain materials (i.e., piezoelectric materials) to exhibit a coupling between the stress and strain in the material and the charge polarization and electric field. More specifically, a mechanical stress leads to a physical rotation of electric dipoles throughout the material,

leading to an alteration of the surface charge density as a result of the applied stress. The reverse is also true, whereby an applied electric field causes a physical rotation in the electrical dipoles, leading to a mechanical strain in the material. For acoustic energy harvesting applications, the stress and strain are usually generated in the piezoelectric material by physically attaching it to an acoustically driven structure (e.g., a diaphragm or cantilever). Note that piezoelectric transduction is an indirect type of transduction, due to inherent electrical capacitance and acoustic (actually mechanical) compliance.

#### 13.4.3.2 Electromagnetic Transduction

Electromagnetic transduction generally utilizes a moving magnet to alter the magnetic flux through a coil, thus generating an electromotive force (EMF) according to Faraday's law. Typically, the magnet is configured to move through an air gap in a ferromagnetic circuit containing a coil, thus altering the magnetic flux through that circuit and the coil. Formally, the EMF generated in the coil is defined by  $EMF = -Nd\Phi_B/dt$ , where  $N$  is the number of turns in the coil and  $\Phi_B$  is the magnetic flux through a single loop of wire. Any configuration of magnet and coil that leads to a changing magnetic flux as a function of an applied mechanical and acoustical input can be utilized for transduction, although certain configurations will be more optimal for particular applications. For acoustic energy harvesting, the magnetic material can be directly mounted to an acoustically sensitive structure or otherwise mechanically linked to the structure. Electromagnetic transducers can be modeled using lumped element modeling. For an extensive introduction to electromagnetic transducer equivalent circuits, see [33]. In contrast to piezoelectric transduction, electromagnetic is a direct type of transduction.

#### 13.4.3.3 Electrostatic Transduction

Electrostatic (or capacitive) transduction relies upon using a mechanical force to change the capacitance of an element within a circuit. The changing capacitance leads to a change in voltage for a constant charge or change in charge for a constant voltage. The capacitor is typically biased either via embedding of a static charge in certain electret-type materials or via connection to a voltage source. For an energy harvester, only an electret approach generates net power, as no external bias is needed. In the electret approach, the fixed charge on the variable capacitor leads to change in output voltage as the capacitance is altered by the mechanical force. The oscillating voltage and related current can then be captured via typical harvesting circuit approaches.

Various structural configurations can lead to a capacitance that is a function of the applied pressure, including parallel plate and interdigitated (comb-finger) approaches. Parallel plate configurations are most amenable to diaphragm-type structures with large surface areas. Care should be taken with parallel plate approaches to avoid a situation known as *electrostatic pull-in*, whereby below a minimum gap distance the electrostatic attraction force exceeds the restorative spring force of the structure, resulting in catastrophic collapse (pull-in) of the

movable electrode. Again, the reader is referred to [33] for an in-depth treatment of the equivalent circuit of an electrostatic transducer.

#### 13.4.3.4 Comparative Analysis

All of the above transduction methods can be successfully used for acoustic energy harvesting with various trade-offs. Piezoelectric approaches are the most commonly implemented for microscale acoustic energy harvesting, for the following reasons:

- Thin-film piezoelectric materials are possible.
- Fabrication processes are well defined.
- Piezoelectric materials are intended to deform and are thus well suited to direct attachment to deformable structures such as diaphragms and cantilevers.

The following points are on the negative side for piezoelectric transduction:

- Thin films exhibit some degradation in performance compared to thick films or bulk materials.
- Indirect transduction limits the efficiency.
- High temperatures (approaching the Curie temperature) lead to depolarization of the material resulting in a loss of piezoelectric activity.

In contrast, electromagnetic and electrostatic approaches have rarely been attempted for microscale acoustic energy harvesting. There have been many implementations of these transduction methods for vibrational energy harvesting and these could readily be adapted for acoustic energy, but little has been attempted to date.

Some positive attributes of electromagnetic transduction include

- direct transduction of energy leading to improved efficiency;
- ability to easily scale the voltage/current relationship through adjustment of the number of coil turns.

The following points are on the negative side for electromagnetic transduction:

- Size and mass of the magnetic materials limit miniaturization.
- It is difficult to maintain magnetic performance at smaller sizes or for thin films.
- Stiff and brittle magnetic materials limit use in attachment to deformable structures such as diaphragms and cantilevers.

For electrostatic transduction, some positive attributes include the following:

- IC-compatible fabrication technologies that enable integration of the power electronics with the harvesting transducer.

The following point is on the negative side for electrostatic transduction:

- Indirect transduction limits the efficiency.

## 13.4.4

**Transduction Structures**

Structures play a significant role in the performance of an acoustic energy harvester. The physical structures of the energy harvester affect acoustic impedance matching, enable the conversion of acoustical to mechanical energy, and ultimately guide the final conversion to electrical energy.

13.4.4.1 **Structures for Impedance Matching**

**Helmholtz Resonators** A Helmholtz resonator is a commonly used device for various acoustical applications including the unit cell of a locally reacting aircraft engine liner [38–41], photoacoustic spectroscopy [42], and numerous musical instruments. Recently it has been used as an impedance transformer for an acoustic energy harvester [8]. A Helmholtz resonator is comprised of an enclosed cavity with a small opening, referred to as a *neck*. The neck is effectively a short open tube. As the pressure oscillates from an incoming acoustic wave, an oscillatory flow is established in the neck. On the cavity side of the neck, this oscillatory flow leads to compression and rarefaction in the cavity, as the volume is contained. As discussed earlier, in acoustic systems, compression indicates storage of potential energy and can be modeled as a lumped acoustic compliance. Similarly, the oscillatory fluid motion in the neck indicates storage of kinetic energy and can be modeled as an acoustic mass. In addition, viscous and radiation losses in the neck are modeled as a combined acoustic resistance. These three elements are then connected in series as the same flow is common to all. The result is the simplified acoustic circuit shown in Figure 13.3.

The impedance of this structure can be calculated from the equivalent circuit and is frequency dependent. At resonance, the impedance drops to just the value of the resistance, as the reactances cancel. A typical impedance spectrum of a Helmholtz resonator with a volume of  $1 \text{ cm}^3$ , a neck length and radius of  $1 \text{ mm}$  is shown in Figure 13.4. These values were normalized by the characteristic impedance of air. As can be seen in the figure, the magnitude of the impedance drops to a minimum at resonance. In addition, at resonance, the reactance is seen to pass through zero. Near resonance, the impedance matches the characteristic impedance and so the normalized value reaches 1. Under this condition, maximum energy can be transferred into the system, for example, there is no reflected energy.

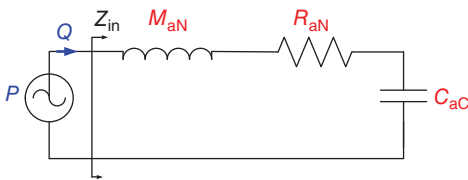


**Figure 13.3** Equivalent circuit of a Helmholtz resonator.

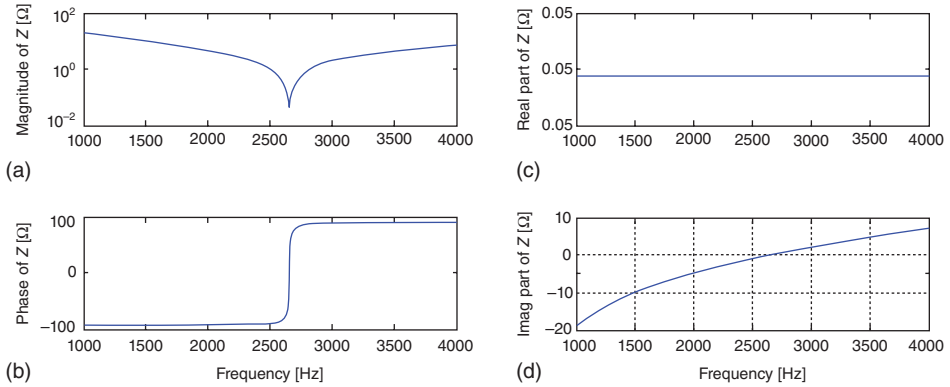


**Figure 13.4** Normalized impedance spectrum of a Helmholtz resonator. (a) Magnitude, (b) phase, (c) real part, and (d) imaginary part.

The situation gets more complicated when a diaphragm or other flexible element is added to provide the conversion to mechanical and electrical energy. The frequency-dependent impedance of that structure gets added into the equivalent circuit, generally adding at least one degree of freedom and a second resonance. Further details of the combined circuit and resulting performance are provided in several papers by Liu *et al.* [7, 8, 43].

**Resonator Tubes** A resonator tube can be either an open-ended or closed-ended tube that can provide impedance transformation for matching purposes. An open end on a tube approximates a pressure release termination ( $Z = 0$ ), while a closed end approximates a rigid termination ( $Z = \infty$ ). As a result of the impedance mismatch at the end, a standing wave is set up within the tube. For an open-ended tube, the impedance at any point in the tube can be calculated [30] as  $Z(d) = jZ_0 \tan kd$ , where  $Z_0$  is the characteristic impedance,  $k = \omega/c$  is the wavenumber, and  $d$  is the distance from the open end. For a closed end tube a similar relation gives  $Z(d) = -jZ_0 \cot kd$ . Through proper placement of an acoustical-to-mechanical transducer (e.g., diaphragm), the impedance of each of the elements can be better matched for improved conversion efficiency at a targeted wavelength.

**Horns** A change in cross-sectional area,  $A$ , can be used to transform an acoustic impedance, as the impedance of a propagating wave is given by  $Z_{ac} = \rho c/A$ . An abrupt step in cross-sectional area, however, would lead to significant reflections at the interface, negating any improvements due to matching to the transducer. Instead, a horn can be used as a means to gradually transition the area and transform the impedance. The horn itself, however, has a frequency-dependent impedance [30] which is a function of the horn shape (e.g., conical or exponential) and must be considered for efficient design.

### 13.4.4.2 Structures for Acoustical to Mechanical Transduction

Various types of structures can be used for acoustical to mechanical conversion including flexible structures (e.g., diaphragms and beams) and rigid structures (e.g., pistons).

**Diaphragms** A diaphragm, defined here as a thin, flexible disk that bends in response to acoustic pressure fluctuations, can be classified as either a plate or a membrane, depending upon the state of in-plane tension. The level of tension can be defined by a nondimensional tension parameter [44],

$$k = \frac{a}{h} \sqrt{\frac{12(1-\nu^2)N_o}{Eh}} \quad (13.4)$$

where  $a$  and  $h$  are the diaphragm radius and thickness,  $\nu$  and  $E$  are Poisson's ratio and Young's modulus of the diaphragm material, and  $N_o$  is the in-plane tension load.

At low levels of tension ( $k < 1$ ), the diaphragm approximately behaves and is modeled as a pure plate ( $k = 0$ ) and has a deflection shape [44] defined as a function of radial position,  $r$ , by

$$w(r) = 0.174P \left( 1 - \left( \frac{r}{a} \right)^2 \right)^2 \quad (13.5)$$

where the loading parameter,  $P = pa^4/Eh^4$  and  $p$  is the applied acoustic pressure.

For higher levels of tension ( $k > 20$ ), the diaphragm approximately behaves like a pure membrane ( $k \rightarrow \infty$ ) and has a deflection shape [44] that includes the tension parameter and is given by

$$w(r) = \frac{2.78P}{k^2} \left( 1 - \left( \frac{r}{a} \right)^2 \right) \quad (13.6)$$

Notice the lack of a second squared exponent on the outer parentheses for the membrane case as compared to the plate case. Thus the membrane deflection has a decidedly different shape than the plate deflection, with most of the curvature moving very close to the clamped outer edge.

In either case, the diaphragm can be modeled using a lumped element approach, equating the stored potential energy to an equivalent lumped mechanical compliance (capacitor) and the stored kinetic energy to an equivalent lumped mechanical mass (inductor). These lumped elements can be then be combined (Figure 13.5)

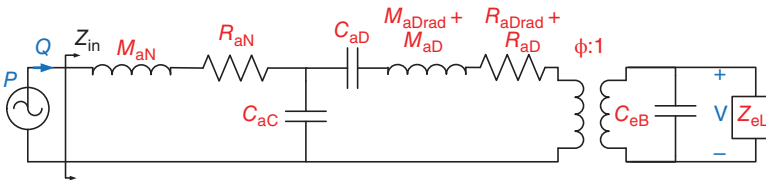


**Figure 13.5** Equivalent circuit for an electromechanical Helmholtz resonator comprised of an acoustic neck and cavity, a flexible piezoelectric diaphragm, and an electrical load.

with the equivalent circuits for the acoustic and piezoelectric components of an acoustic energy harvester to model total system behavior [10, 39, 45].

For composite structures containing multiple layers of differing materials, as is commonly the case for piezoelectric diaphragms, the deflection curves take on more complex behavior. In some instances, analytical modeling is still possible [46, 47], and in many cases, the isotropic plate and membrane equations are sufficiently accurate (using appropriate effective material and geometric parameters); however, FEM is sometimes needed to predict the deflection with greater accuracy, particularly when trying to tease out the effects of various combinations of material and geometric parameters [37].

As the diaphragm deflects upward, much of the central region has a negative curvature, leading to a stretching of a top-mounted piezoelectric material and a particular polarity voltage (depending on the signs of the piezoelectric coefficients). Near the edges of the diaphragm, however, to accommodate the clamped boundary condition, the curvature generally becomes positive, leading to a compression of a top-mounted piezoelectric material and the opposite polarity voltage. Thus an electrode cannot cover the entire diaphragm or else surface charges would cancel out.

To maximize the capture of energy, different electrode configurations (Figure 13.6) have been explored over the years by various researchers. Most designs have used either a central electrode, ring electrode, or a combination of the two with reversed connections to account for the opposite polarity. The central electrode typically offers a larger capture area resulting in larger capacitance, but generally has a lower energy density.

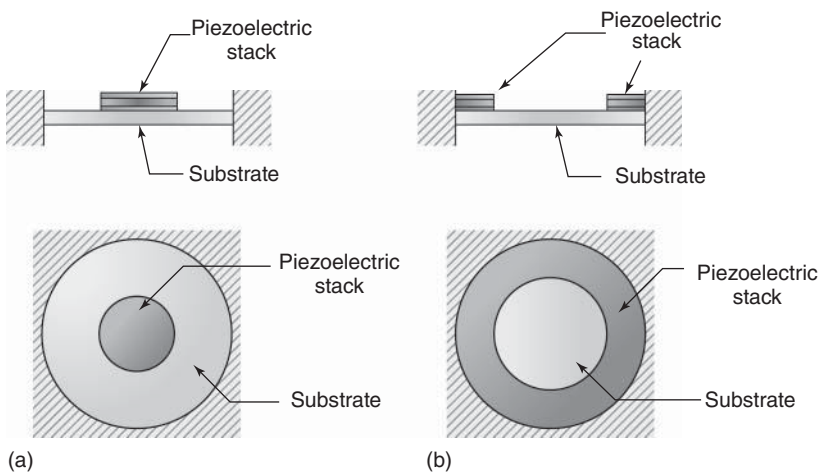


**Figure 13.6** Different electrode configurations including (a) central piezoelectric stack and electrodes and (b) ring-shaped piezoelectric stack and electrodes.

**Beams** Although more frequently used in vibrational energy harvesting, flexible beams are sometimes used to convert acoustic to mechanical energy [22, 23]. In general, beam structures may be of cantilever (single clamped end) or clamped–clamped types. Narrow gaps or highly flexible sealed coverings are generally required when using flexible beams in order to maintain a large pressure gradient across the beam, as it is the pressure gradient that drives the deflection.

Modeling of beams can be accomplished analytically [48–50] or numerically [51, 52], as with diaphragm structures and converted to equivalent lumped elements.

**Piston/Spring Arrangements** Occasionally, a piston/spring-type arrangement is employed for converting acoustic into mechanical energy [1, 2]. The piston is treated as a rigid structure, thus piezoelectric integration in the piston is not useful. Instead, either electromagnetic transduction is employed [1, 2] or piezoelectric transduction within the spring could be used (not tried to date).

## 13.5

### Fabrication Methods

Micromachined AEHs can be comprised wholly of microfabricated components or constructed in a hybrid fashion from mesoscale and microscale components. The latter approach is more common, utilizing mesoscale acoustic components (e.g., Helmholtz resonators) combined with microscale mechanical components (e.g., MEMS-based piezoelectric diaphragms).

#### 13.5.1

##### Materials

A number of thin-film piezoelectric materials can be employed for transduction, including lead zirconate titanate (PZT), aluminum nitride (AlN), polyvinylidene fluoride (PVDF), and zinc oxide (ZnO) [53]. In addition, recent progress in developing nanostructured composite piezoelectric materials [54, 55] has led to materials with customizable mechanical and piezoelectric properties. Each material offers various trade-offs between piezoelectric coupling coefficient, piezoelectric constants (e.g.,  $d_{31}$ ), dielectric constant, elastic modulus, density, fabrication complexity, and CMOS compatibility. Applications will dictate which parameters are most critical.

Most approaches to acoustic energy harvesting leverage the use of a thin, flexible diaphragm. Creation of a high-quality, controlled-stress, precise-geometry diaphragm often presents one of the greatest challenges during fabrication. The choice of materials will dictate the controllability of stress and the fabrication methods used to produce the desired geometry. Common diaphragm materials include bulk silicon [56, 57], top silicon from a silicon-on-insulator (SOI) wafer [45] and silicon nitride [58, 59].



## 13.5.2

**Processes**

Piezoelectric materials can be deposited in a number of different ways including sol–gel methods [60–63], sputtering [64–73], e-beam evaporation, chemical vapor deposition (CVD) [74], or directly grown through a hydrothermal process [75–77]. Nanostructured ZnO can be grown using hydrothermal [78–81] or VLS (vapor–liquid–solid) techniques [82–84]. For nanostructured AlN, use of anodic aluminum oxide (AAO) templates [85] and direct nitridation [86] are two techniques among many that can produce one-dimensional piezoelectric nanostructures. Patterning of piezoelectric materials can be achieved through standard wet- and dry-etching techniques [87, 88], lift-off methods, and microcontact printing [89].

For diaphragm formation, most commonly a backside release process is used, such as through deep reactive ion etching (DRIE) [54, 90] or potassium hydroxide (KOH) etching [91]. In both methods, a hard etch stop such as a buried oxide (BOX) layer or deposited silicon dioxide ( $\text{SiO}_2$ ) can be used to precisely define the diaphragm thickness. One challenge of diaphragm formation is precisely defining the diameter. Etching from the backside generally produces a moderate amount of error in the final geometry. One way to overcome this is through a stepped release process via wafer bonding (after stepped cavity formation) [92] or through a sacrificial oxide release [93].

## 13.6

**Testing and Characterization**

Determination of acoustic energy harvester performance is generally made through combinations of acoustic, mechanical, and electrical measurements. The ultimate measurement of performance is the conversion of acoustic to electrical energy, quantified either via efficiency, power, or power density. These quantities all require accurate measurement of both the input acoustic power and the output electrical power. Electric power output measurement is a fairly easy process, for example, taking the voltage measurement across a known resistance or measuring the accumulated charge on a storage capacitor. Acoustic input power measurement, however, requires a more elaborate test setup. The acoustic input power is the product of the incoming acoustic pressure and volume velocity.

A standard process for measuring the acoustic input power is via an acoustic plane wave tube and a pair of microphones implementing the two-microphone method [7, 94–96]. Other related techniques such as the standing wave method and multipoint method [97] can achieve similar results. The direct objective of any of these methods is to obtain the reflection coefficient of a sample placed at the end of the plane wave tube. Traditionally used for determination of acoustic impedance of acoustic liners, the method works well for determination of input acoustic power when the sample is an acoustic energy harvester. The acoustic input power can be calculated [10] from the measured reflection coefficient,  $R$ ,

and the acoustic pressure,  $p_+$ , of the incoming waves via  $\text{Pow}_{\text{in}} = (1 - R^2)p_+^2/Z_{\text{tube}}$ , where  $Z_{\text{tube}} = \rho c/A_{\text{tube}}$  is the acoustic impedance of the plane wave tube. In addition, the acoustic impedance can easily be calculated from the measured reflection coefficient as  $Z_{\text{in}} = Z_{\text{tube}}[(1 + R)/(1 - R)]$ .

While the true measure of performance is the conversion of acoustic to electrical energy, it is generally useful to understand the behavior of the deformable mechanical components, such as diaphragms. Laser vibrometry is one method to obtain such information, allowing for measurement of the deformation mode shape and mechanical resonance frequency. Measurement of the true mode shape and frequency response allows for verification of the mechanical lumped elements and diagnosis of the source of possible deviations from theory.

Finally, on the electrical side, besides measurement of output power, it is often useful to measure output impedance. This can be achieved through a number of means including manual voltage application with current monitoring and automated electrical impedance analyzers [98, 99].

### 13.7

#### Summary

Acoustic energy harvesting is a relatively new offshoot of energy scavenging technologies, with only 16 years of development as of the time of this writing. However, interest and efforts in acoustic energy harvesting R&D has accelerated over that period. In the first 8 years since acoustic energy harvesting was first attempted, roughly only 10 papers were published, compared to 18 during the last 8 years. Still, the number of groups and researchers reporting developments in acoustic energy harvesting are much lower than for vibrational energy harvesting during that same period. Much of that difference is probably a result of the more limited applications and environments where acoustic energy harvesting makes practical sense. The generally lower energy densities present in airborne sound limit utility to only intense sound environments. Aside from high-intensity airborne applications, the harvesting of acoustic energy in hydraulic systems also shows promise, where high dynamic pressure “ripples” lead to correspondingly high energy densities.

#### Acknowledgments

The authors are grateful to Dr. Tai-An Chen for preparation of many of the figures presented in this chapter.

#### References

1. Amirtharajah, R. and Chandrakasan, A.P. (1998) Self-powered signal processing using vibration-based power generation. *IEEE J. Solid-State Circuits*, 33 (5), 687–695.
2. Amirtharajah, R. (1999) *Design of Low Power VLSI Systems Powered*

- by *Ambient Mechanical Vibration*, Massachusetts Institute of Technology.
3. Sood, R. (2003) *Piezoelectric Micro Power Generators (PMPG): A MEMS-Based Energy Scavenger*, Massachusetts Institute of Technology.
  4. Mandurino, P. *et al.* (2001) Energy recovering PZT-panel for noise reduction: numerical analysis for fully coupled fluid-PZT structure-electric interaction experimental verification. *Smart Struct. Mater.*, **4331**, 408–419.
  5. Horowitz, S., Kasyap, A., Liu, F., Johnson, D., Nishida, T., Ngo, K., Sheplak, M., and Cattafesta, L. (2002) Technology development for self-powered sensors. 1st Flow Control Conference, AIAA 2002-2702, pp. 1–10.
  6. Taylor, R., Liu, F., Horowitz, S., Ngo, K., Nishida, T., Cattafesta, L., and Sheplak, M. (2004) Technology development for electromechanical acoustic liners, Paper #A04-093. Active 04, pp. 1–10.
  7. Liu, F., Phipps, A., Horowitz, S., Ngo, K., Cattafesta, L., Nishida, T., and Sheplak, M. (2008) Acoustic energy harvesting using an electromechanical Helmholtz resonator. *J. Acoust. Soc. Am.*, **123** (4), 1983–1990.
  8. Liu, F., Phipps, A., Horowitz, S., Cattafesta, L., Nishida, T., and Sheplak, M. (2009) Acoustic energy harvesting using an electromechanical Helmholtz resonator. *J. Acoust. Soc. Am.*, **125** (4), 2596.
  9. Phipps, A., Liu, F., Cattafesta, L., Sheplak, M., and Nishida, T. (2009) Demonstration of a wireless, self-powered, electroacoustic liner system. *J. Acoust. Soc. Am.*, **125** (2), 873–881.
  10. Horowitz, S.B. (2005) *Development of a MEMS-Based Acoustic Energy Harvester*, University of Florida.
  11. Horowitz, S., Sheplak, M., Cattafesta, L.N., and Nishida, T. (2005) MEMS acoustic energy harvester. Proceedings of PowerMEMS, 2005, pp. 13–16.
  12. Horowitz, S.B., Sheplak, M., Cattafesta, L.N., and Nishida, T. (2006) A MEMS acoustic energy harvester. *J. Micromech. Microeng.*, **16** (9), S174–S181.
  13. Kim, S. (2005) Piezoelectric energy harvesting with a clamped circular plate: analysis. *J. Intell. Mater. Syst. Struct.*, **16** (10), 847–854.
  14. Kim, S. (2005) Piezoelectric energy harvesting with a clamped circular plate: experimental study. *J. Intell. Mater. Syst. Struct.*, **16** (10), 855–863.
  15. Shinoda, S., Tai, T., Itoh, H., Sugou, T., Ichioka, H., Kimura, S., and Nishioka, Y. (2010) Lead zirconate titanate acoustic energy harvester proposed for microelectromechanical system/IC integrated systems. *Jpn. J. Appl. Phys.*, **49** (4), 04DL21.
  16. Kimura, S., Sugou, T., Tomioka, S., and Iizumi, S. (2010) Acoustic energy harvester fabricated using sol/gel lead zirconate titanate thin film. Proceedings of PowerMEMS, 2010, pp. 13–16.
  17. Tsujimoto, K., Tomioka, S., Kimura, S., and Iizumi, S. (2011) Utilization of different charge polarizations on pzt diaphragm of acoustic energy harvesters. Proceedings of PowerMEMS, 2011, pp. 209–212.
  18. Iizumi, S., Kimura, S., Tomioka, S., Tsujimoto, K., Uchida, Y., Tomii, K., Matsuda, T., and Nishioka, Y. (2011) Lead zirconate titanate acoustic energy harvesters utilizing different polarizations on diaphragm. *Procedia Eng.*, **25**, 187–190.
  19. Lallart, M., Guyomar, D., Richard, C., and Petit, L. (2010) Nonlinear optimization of acoustic energy harvesting using piezoelectric devices. *J. Acoust. Soc. Am.*, **128** (5), 2739–2748.
  20. Peng, X., Wen, Y., Li, P., Yang, A., and Bai, X. (2013) A wideband acoustic energy harvester using a three degree-of-freedom architecture. *Appl. Phys. Lett.*, **103** (16), 164106.
  21. Peng, X., Wen, Y., Li, P., Yang, A., and Bai, X. (2013) Enhanced acoustoelectric coupling in acoustic energy harvester using dual. *IEEE Trans. Ultrason. Ferroelectr. Freq. Control*, **60** (10), 2121–2128.
  22. Wu, L.-Y., Chen, L.-W., and Liu, C.-M. (2009) Acoustic energy harvesting using resonant cavity of a sonic crystal. *Appl. Phys. Lett.*, **95** (1), 013506.

23. Wang, W.-C., Wu, L.-Y., Chen, L.-W., and Liu, C.-M. (2010) Acoustic energy harvesting by piezoelectric curved beams in the cavity of a sonic crystal. *Smart Mater. Struct.*, **19** (4), 045016.
24. Kim, S., Ji, C., Galle, P., and Herrault, F. (2008) An electromagnetic energy scavenger from direct airflow. Proceedings of PowerMEMS, 2008, pp. 133–136.
25. Wang, D. and Ko, H.-H. (2010) Piezoelectric energy harvesting from flow-induced vibration. *J. Micromech. Microeng.*, **20** (2), 025019.
26. Jing, X.M., Miao, J.M., Xu, T., Olfatnia, M., and Norford, L. (2010) Vibration characteristics of micromachined piezoelectric diaphragms with a standing beam subjected to airflow. *Sens. Actuators, A: Phys.*, **164** (1-2), 22–27.
27. Sun, D., Xu, Y., Chen, H., Wu, K., Liu, K., and Yu, Y. (2012) A mean flow acoustic engine capable of wind energy harvesting. *Energy Convers.*, **63**, 101–105.
28. Cunefare, K.A., Skow, E.A., Erturk, A., Savor, J., Verma, N., and Cacan, M.R. (2013) Energy harvesting from hydraulic pressure fluctuations. *Smart Mater. Struct.*, **22** (2), 025036.
29. Cunefare, K.A., Skow, E.A., and Erturk, A. (2013) Transduction as energy conversion; harvesting of acoustic energy in hydraulic systems. *Proc. Meet. Acoust.*, **19**, 030070.
30. Blackstock, D.T. (2000) *Fundamentals of Physical Acoustics*, John Wiley & Sons, Inc., New York, pp. 153–156.
31. Rossi, M. (1988) *Acoustics and Electroacoustics*, Artech House, Norwood, MA, pp. 309–371.
32. Fischer, F.A. (1955) *Fundamentals of Electroacoustics*, Interscience Publishers, Inc, New York, pp. 96–101.
33. Tilmans, H.A.C. (1996) Equivalent circuit representation of electromechanical transducers: I. Lumped-parameter systems. *J. Micromech. Microeng.*, **6**, 157–176.
34. Tilmans, H. (1997) Equivalent circuit representation of electromechanical transducers: II. Distributed-parameter systems. *J. Micromech. Microeng.*, **7**, pp. 285–309.
35. Margolis, D.L. (1985) A survey of bond graph modelling for interacting lumped and distributed systems. *J. Franklin Inst.*, **319** (1), 125–135.
36. Gawthrop, P.J. and Bevan, G.P. (2007) Bond-graph modeling. *IEEE Control Syst. Mag.*, **27** (2), 24–45.
37. Horowitz, S.B., Mathias, A.D., Fox, J.R., Cortes, J.P., Sanghadasa, M., and Ashley, P. (2012) Effects of scaling and geometry on the performance of piezoelectric microphones. *Sens. Actuators, A: Phys.*, **A185**, 24–32.
38. Horowitz, S.B., Nishida, T., Cattafesta, L.N., and Sheplak, M. (2001) Impedance tuning of an electromechanical acoustic liner. *J. Acoust. Soc. Am.*, **110** (5), 2773.
39. Horowitz, S.B., Nishida, T., Cattafesta, L.N., and Sheplak, M. (2002) Characterization of a compliant-backplate Helmholtz resonator for an electromechanical acoustic liner. *Int. J. Aeroacoustics*, **1** (2), 183–205.
40. Jones, M.G. (1997) An improved model for parallel-element liner impedance prediction. 3rd AIAA/CEAS Aeroacoustics Conference, pp. 519–526.
41. Hersh, A.S., Celano, J.W., and Walker, B.E. (2003) Helmholtz resonator impedance model, part 1: nonlinear behavior. *AIAA J.*, **41** (5), 795–808.
42. Kästle, R. and Sigrist, M.W. (1996) Temperature-dependent photoacoustic spectroscopy with a Helmholtz resonator. *Applied Physics B*, **63** (4), pp. 389–397.
43. Liu, F., Horowitz, S., Nishida, T., Cattafesta, L., and Sheplak, M. (2007) A multiple degree of freedom electromechanical Helmholtz resonator. *J. Acoust. Soc. Am.*, **122** (1), 291–301.
44. Sheplak, M. and Dugundji, J. (1998) Large deflections of clamped circular plates under initial tension and transitions to membrane behavior. *J. Appl. Mech.*, **65**, 1–28.
45. Horowitz, S., Nishida, T., Cattafesta, L., and Sheplak, M. (2007) Development of a micromachined piezoelectric microphone for aeroacoustics applications. *J. Acoust. Soc. Am.*, **122** (6), 3428–3436.
46. Wang, G., Sankar, B.V., Cattafesta, L.N., and Sheplak, M. (2002) Analysis

- of a composite piezoelectric circular plate with initial stresses for MEMS. International Mechanical Engineering Congress & Exposition, ASME Paper IMECE2002-39337, Nov. 2002, pp. 339-346.
47. Chen, C.-F. and Chen, J.-H. (2011) Nonlinear study of large deflection of simply supported piezoelectric layered-plate under initial tension. *Int. J. Mech. Sci.*, **53** (7), 485–493.
  48. Kasyap, A., Phipps, A., Sheplak, M., Ngo, K., Nishida, T., and Cattafesta, L.N. (2006) Lumped Element Modeling of Piezoelectric Cantilever Beams for Vibrational Energy Reclamation, 2006.
  49. Kasyap, A., Lim, J., Johnson, D., Horowitz, S., Nishida, T., Ngo, K., Sheplak, M., and Cattafesta, L. (2002) Energy reclamation from a vibrating piezoceramic composite beam. Proceedings of 9th International Congress on Sound and Vibration, 2002, Vol. 9, no. 271, pp. 36–43.
  50. Erturk, A. and Inman, D.J. (2008) On mechanical modeling of cantilevered piezoelectric vibration energy harvesters. *J. Intell. Mater. Syst. Struct.*, **19** (11), 1311–1325.
  51. Hwang, W.-S. and Park, H.C. (1993) Finite element modeling of piezoelectric sensors and actuators. *AIAA J.*, **31** (5), 930–937.
  52. Ajitsaria, J., Choe, S.-Y., Shen, D., and Kim, D.J. (2007) Modeling and analysis of a bimorph piezoelectric cantilever beam for voltage generation. *Smart Mater. Struct.*, **16** (2), 447.
  53. Trolrier-McKinstry, S. and Muralt, P. (2004) Thin film piezoelectrics for MEMS. *J. Electroceram.*, **12** (1-2), 7–17.
  54. Horowitz, S.B., Mathias, D., Hernandez, C.D., Sanghadasa, M., and Ashley, P. (2010) Miniaturization of piezoelectric microphones. AIAA Infotech@Aerospace.
  55. Horowitz, S., Mathias, D., Cortes, J., Fox, J., Sanghadasa, M., and Ashley, P. (2010) Nanostructured piezoelectric acoustic sensors. Hilton Head 2010 (Open Poster), 2010, Vol. 27, no. 4.
  56. Ried, R.P., Member, S., Kim, E.S., Hong, D.M., and Muller, R.S. (1993) Piezoelectric microphone with on-chip CMOS circuits. *J. Microelectromech. Syst.*, **2** (3), 111–119.
  57. Royer, M., Holmen, J.O., Wurm, M.A., Aadland, O.S., and Glenn, M. (1983) ZnO on Si integrated acoustic sensor. *Sens. Actuators*, **4**, 357–362.
  58. Baumgartel, L., Vafanejad, A., Chen, S., and Kim, E.S. (2012) Resonance-enhanced piezoelectric microphone array for broadband or prefiltered acoustic sensing. *J. Microelectromechanical Syst.*, **22** (1), 1–8.
  59. Zhao, H.-J., Ren, T.-L., Liu, L.-S., Liu, L.-T., and Li, Z.-J. (2003) A Novel Structure for PZT-Based Piezoelectric Microphone. Technical Proceedings of the 2003 Nanotechnology Conference and Trade Show, Nanotech 2003, Vol. 1, pp. 356–359.
  60. Pu, X., Luo, W., Ding, A., Tian, H., and Qiu, P. (2000) One-step firing process in synthesis of sol-gel derived PZT thick films. *Phys. Status Solidi*, **182** (2), R10–R12.
  61. Lian, L. (2004) Stress effects in sol-gel derived ferroelectric thin films. *J. Appl. Phys.*, **95** (2), 629.
  62. Bahr, D.F., Merlino, J.C., Banerjee, P., Yip, C.M., and Bandyopadhyay, A. (1998) Reliability and properties of Pzt thin films for mems applications. *MRS Proc.*, **546**, 153.
  63. Bernstein, J., Houston, K., Niles, L., Finberg, S., Chen, H., Cross, L.E., Li, K., and Udayakumar, K. (1997) Micro-machined ferroelectric transducers for acoustic imaging. Proceedings of International Solid State Sensors and Actuators Conference (Transducers '97), Vol. 1, pp. 421–424.
  64. Castellano, R.N. and Feinstein, L.G. (1979) Ion-beam deposition of thin films of ferroelectric lead zirconate titanate (PZT). *J. Appl. Phys.*, **50** (6), 4406.
  65. Sreenivas, K., Sayer, M., and Garrett, P. (1989) Properties of D.C. magnetron-sputtered lead zirconate titanate thin films. *Thin Solid Films*, **172** (2), 251–267.
  66. Blossfeld, L., Larson, W., Kammerdiner, L., Banko, B., and Wickersham, C. (1990) Ferroelectric Pb(Zr, Ti)O<sub>3</sub> thin films by reactive sputtering from

- a metallic target. *Vacuum*, **41** (4), 1428–1430.
67. Huffman, M., Goral, J., Al-Jassim, M., Mason, A., and Jones, K. (1990) Compositional and microstructural characterization of thin film lead zirconate titanate ferroelectrics. *Thin Solid Films*, **193**, 1017–1022.
  68. Surowiak, Z., Łoposzko, M., Zakharchenko, I.N., Bakirov, A.A., Marchenko, E.A., Sviridov, E.V., Mukhortov, V.M., and Dudkevich, V.P. (1991) Thin ferroelectric films of the lead zirconate-titanate type obtained by r.f. sputtering. *Thin Solid Films*, **205** (1), 76–84.
  69. Trolier-McKinstry, S., Hu, H., Krupanidhi, S.B., Chindaudom, P., Vedam, K., and Newnham, R.E. (1993) Spectroscopic ellipsometry studies on ion beam sputter deposited Pb(Zr, Ti)O<sub>3</sub> films on sapphire and Pt-coated silicon substrates. *Thin Solid Films*, **230** (1), 15–27.
  70. Tvarozek, V., Novotny, I., Sutta, P., Flicyngerova, S., Schtereva, K., and Vavrinsky, E. (2007) Influence of sputtering parameters on crystalline structure of ZnO thin films. *Thin Solid Films*, **515** (24), 8756–8760.
  71. Subramanyam, T.K., Srinivasulu Naidu, B., and Uthanna, S. (2000) Physical properties of zinc oxide films prepared by dc reactive magnetron sputtering at different sputtering pressures. *Cryst. Res. Technol.*, **35** (10), 1193–1202.
  72. Wacogne, B., Roe, M.P., Pattinson, T.J., and Pannell, C.N. (1995) Effective piezoelectric activity of zinc oxide films grown by radio-frequency planar magnetron sputtering. *Appl. Phys. Lett.*, **67** (12), 1674.
  73. Ondo-Ndong, R. (2003) Properties of RF magnetron sputtered zinc oxide thin films. *J. Cryst. Growth*, **255** (1-2), 130–135.
  74. Yoon, S.-G., Lee, H.-Y., and Kim, H.-G. (1989) Compositional analysis of lead titanate thin films by Auger electron spectroscopy and their electrical properties. *Thin Solid Films*, **171** (2), 251–262.
  75. Morita, T., Wagatsuma, Y., Morioka, H., Funakubo, H., Setter, N., and Cho, Y. (2004) Ferroelectric property of an epitaxial lead zirconate titanate thin film deposited by a hydrothermal method. *J. Mater. Res.*, **19** (6), 1862–1868.
  76. Morita, T. and Cho, Y. (2004) A hydrothermally deposited epitaxial lead titanate thin film on strontium ruthenium oxide bottom electrode. *Appl. Phys. Lett.*, **85** (12), 2331.
  77. Morita, T. (2000) A cylindrical shaped micro ultrasonic motor utilizing PZT thin film (1.4 mm in diameter and 5.0 mm long stator transducer). *Sens. Actuators, A: Phys.*, **83** (1-3), 225–230.
  78. Greene, L.E., Law, M., Goldberger, J., Kim, F., Johnson, J.C., Zhang, Y., Saykally, R.J., and Yang, P. (2003) Low-temperature wafer-scale production of ZnO nanowire arrays. *Angew. Chem. Int. Ed.*, **42** (26), 3031–3034.
  79. Greene, L.E., Law, M., Tan, D.H., Montano, M., Goldberger, J., Somorjai, G., and Yang, P. (2005) General route to vertical ZnO nanowire arrays using textured ZnO seeds. *Nano Lett.*, **5** (7), 1231–1236.
  80. Deng, S.-R., Chen, T., Liu, S.-Y., Chen, Y.-F., Huq, E., Liu, R., and Qu, X.-P. (2010) Highly ordered growth of ZnO nanostructures by combination of nanoimprint lithography and hydrothermal method. Nanoelectronics Conference (INEC), 2010 3rd International, 3–8 January 2010, pp. 941–942.
  81. Hsu, J.W.P. (2008) Development of Nanostructured and Surface Modified Semiconductors for Hybrid Organic-Inorganic Solar Cells.. Sandia Report SAND2008-5999, Sandia National Laboratories, Albuquerque, NM, September, 2008.
  82. Fan, Z. and Lu, J.G. (2005) Zinc oxide nanostructures: synthesis and properties. *J. Nanosci. Nanotechnol.*, **5** (10), 1561–1573.
  83. Cheng, C., Lei, M., Feng, L., Wong, T.L., Ho, K.M., Fung, K.K., Loy, M.M.T., Yu, D., and Wang, N. (2009) High-quality ZnO nanowire arrays directly fabricated from photoresists. *ACS Nano*, **3** (1), 53–58.
  84. Weintraub, B., Deng, Y., and Wang, Z.L. (2007) Position-controlled seedless

- growth of ZnO nanorod arrays on a polymer substrate via wet chemical synthesis. *J. Phys. Chem. C*, **111** (28), 10162–10165.
85. Wu, Q. (2004) A simple route to aligned AlN nanowires. *Diamond Relat. Mater.*, **13** (1), 38–41.
  86. Zhang, P.G., Wang, K.Y., and Guo, S.M. (2010) Large-scale synthesis of AlN nanofibers by direct nitridation of aluminum. *Ceram. Int.*, **36** (7), 2209–2213.
  87. Zheng, K., Lu, J., and Chu, J. (2003) Study on wet-etching of PZT thin film. 2003 International Microprocesses and Nanotechnology Conference. Digest of Papers Microprocesses and Nanotechnology 2003, Vol. 3, pp. 248–249.
  88. Baborowski, J. (2004) Microfabrication of Piezoelectric MEMS. *J. Electroceram.*, **12** (1/2), 33–51.
  89. Hsu, J.W.P. (2005) Spatial organization of ZnO nanorods on surfaces via organic templating. *Proc. SPIE*, **5592**, 158–163.
  90. Horowitz, S.B., Nishida, T., Cattafesta, L.N. III, and Sheplak, M. (2005) Design and characterization of a micromachined piezoelectric microphone. 11 th AIAA/CEAS Aeroacoustics Conference (26 th Aeroacoustics Conference), Monterey, CA, 2005 May, pp. 1–10.
  91. Földner, M., Dehé, A., Aigner, R., Bever, T., and Lerch, R. (2001) Silicon microphones with low stress membranes. Proceedings of Transducers 2001.
  92. Williams, M.D., Griffin, B.A., Reagan, T.N., Underbrink, J.R., and Sheplak, M. (2012) Characterization of aeroacoustic, silicon micromachined microphones for aircraft fuselage arrays. *AIAA J.*, **50** (12), 2744–2752.
  93. Williams, M.D., Griffin, B.A., Reagan, T.N., Underbrink, J.R., and Sheplak, M. (2012) An AlN MEMS piezoelectric microphone for aeroacoustic applications. *J. Microelectromech. Syst.*, **21** (2), 270–283.
  94. Jones, M.G. and Stiede, P.E. (1997) Comparison of methods for determining specific acoustic impedance. *J. Acoust. Soc. Am.*, **101** (5), 2694.
  95. Schultz, T., Cattafesta, L.N., Nishida, T., and Sheplak, M. (2002) Uncertainty Analysis of the Two-Microphone Method for Acoustic Impedance Testing, 8th AIAA / CEAS Aeroacoustics Conference Breckenridge, CO, AIAA 2002–2465, June 2002.
  96. Schultz, T., Cattafesta, L.N., and Sheplak, M. (2006) Modal decomposition method for acoustic impedance testing in square ducts. *J. Acoust. Soc. Am.*, **120** (6), 3750–3758.
  97. Jones, M.G. and Parrott, T.L. (1989) Evaluation of a multi-point method for determining acoustic impedance. *Mech. Syst. Sig. Process.*, **3** (1), 15–35.
  98. Agilent 4294A Precision Impedance Analyzer (2008) Datasheet.
  99. (2009) *Agilent Impedance Measurement Handbook: A Guide to Measurement Technology and Techniques*, Agilent Technologies, Inc.





## 14

# Energy Harvesting from Fluid Flows

*Andrew S. Holmes*

### 14.1

#### Introduction

Energy harvesting from fluid flows is a relatively unexplored area in the context of wireless sensor networks. Large-scale wind turbines for generation of grid-connected power are, of course, long established. In addition, in recent years, smaller-scale wind turbines with rotor diameters up to a few meters have become commonplace [1]. Such systems are typically used to provide local off-grid power in locations where grid power is unavailable or less accessible, for example, in homes and businesses in remote locations, on yachts and caravans, and for roadside signage and telemetry equipment. The last of these applications is a typical energy harvesting scenario where the harvester is used to provide power for a specific piece of instrumentation. However, the smallest turbines available commercially are still relatively large by energy harvesting standards, with rotor diameters of around 1 m and power ratings of the order of 100 W, and for wireless sensing applications more generally it is of interest to consider what might be possible at smaller scale.

This chapter reviews the state of the art in miniature devices for flow-driven energy harvesting, and in particular for airflow harvesting which has been the main focus of research to date. The emphasis is on devices that are able to extract power from either a free stream (i.e., an unbounded flow) or a ducted flow where the duct cross section is substantially larger than the device. Free-stream devices are more widely deployable than those designed to be operated only in-line within a pipeline or duct; however, they are subject to more severe constraints in terms of the power levels that can be generated as a result of the limited pressure differentials that can be achieved. While much of the work to date has been on miniaturized wind turbines, a number of alternative devices based on flow-induced vibrations have also been demonstrated and these are also discussed. Vibration-based harvesters are expected to be less effective than turbines at extracting power from a flow, but they are potentially cheaper to manufacture and more reliable because they do not require bearings.

Miniature airflow energy harvesters could provide wind power for wireless sensors in a range of outdoor applications, including smart agriculture (e.g., automatic control of irrigation and agrochemical delivery) [2], environmental monitoring (e.g., air quality), and security surveillance in the built environment [3]. Inside buildings, where the ambient air is relatively static, it is envisaged that they would be deployed mainly within HVAC (heating, ventilation, and air-conditioning) ducts to provide long-term power for sensors associated with HVAC control and/or air quality monitoring [4]. The HVAC application is particularly attractive because there is a continuous flow of air and a stable environment compared to outdoors.

## 14.2

### Fundamental and Practical Limits

The task of a flow-driven energy harvester in a free stream is to extract kinetic energy from the flow and convert it to another form, usually electrical. The kinetic energy per unit volume in a fluid flowing at speed  $U_0$  is  $\rho U_0^2/2$  where  $\rho$  is the fluid density, corresponding to a power flow of  $\rho U_0^3/2$  per unit cross-sectional area. One might therefore expect a device with cross-sectional area  $A$  to be able to extract a power of up to  $\rho A U_0^3/2$  when placed in the flow. However, the available output power is always lower than this, typically being expressed in the form

$$P_{\text{out}} = \eta C_p \cdot \frac{1}{2} \rho A U_0^3 \quad (14.1)$$

where  $C_p$  is the *power coefficient*, representing the fraction of the fluid power that is extracted as raw mechanical power (e.g., the shaft power in a turbine) and  $\eta$  is the efficiency with which this raw mechanical power is converted to electrical output power.

The power coefficient  $C_p$  has a theoretical maximum value of  $16/27 = 0.593$ , referred to as the *Betz limit* after Alfred Betz who first derived it circa 1920. It is useful to review the derivation of the Betz limit [5] as it illustrates some important general principles relating to energy extraction from a free stream. Figure 14.1 shows the scenario considered, in which power is extracted from the fluid as it passes through an idealized *actuator disc*, the exact nature of which need not be defined. The fluid intercepting the disc is assumed to remain within a stream tube indicated by the dashed lines. The analysis assumes inviscid and incompressible flow, and neglects both radial components of velocity and radial variations in the axial velocity.

The actuator disc obstructs the flow, causing it to decelerate on approach so that the flow speed across the disc is

$$U_1 = U_0(1 - a) \quad (14.2)$$

where  $a$  is referred to as the *axial induction factor* (a solid actuator disc would correspond to  $a = 1$ ). As the flow decelerates, the stream tube expands so as to ensure constant mass flow. According to Bernoulli's equation [5], the deceleration

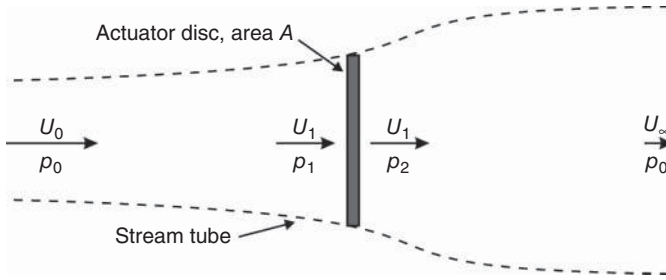


**Figure 14.1** Betz construction for idealized energy extraction device in a free stream. The stream tube indicated by the dashed lines is the boundary enclosing fluid that intercepts the actuator disc.

is also accompanied by an increase in pressure, so that the pressure  $p_1$  on the upstream side of the disc is

$$p_1 = p_0 + \frac{1}{2}\rho(U_0^2 - U_1^2) \quad (14.3a)$$

where  $p_0$  is the pressure far upstream. The flow speed is continuous across the actuator disc, as it must be to satisfy mass conservation, but is assumed to continue decreasing on the downstream side as the flow continues to expand in the wake. Since the pressure must revert to  $p_0$  far downstream, this implies a reduced pressure on the downstream side of the disc. In this case, Bernoulli's equation gives

$$p_2 = p_0 + \frac{1}{2}\rho(U_\infty^2 - U_1^2) \quad (14.3b)$$

The rate of working by the fluid on the actuator disc is given by

$$P = (p_1 - p_2)A \cdot U_1 = \frac{1}{2}\rho A U_1 (U_0^2 - U_\infty^2) \quad (14.4)$$

where the final form has been obtained by substituting for  $p_1$  and  $p_2$  from Eq. (14.3a and b). Equation (14.4) is simply an expression of energy conservation; the mass flow rate is  $\dot{m} = \rho A U_1$ , so the final expression represents the difference between the initial and final kinetic energy fluxes of the fluid, which must equal the rate of working and the power extracted from the flow.

A second relation between the pressure drop ( $p_1 - p_2$ ) and the velocities may be obtained from the law of conservation of momentum. The axial force (or thrust)  $T$  exerted by the fluid on the disc must be equal and opposite to its rate of change of momentum, that is,

$$T = (p_1 - p_2)A = \dot{m}(U_0 - U_\infty) = \rho A U_1 (U_0 - U_\infty) \quad (14.5)$$

Taken together, Eqs. (14.4) and (14.5) imply that  $U_1 = (U_0 + U_\infty)/2$ , from which it follows that the flow speed in the far wake of the device is

$$U_\infty = U_0(1 - 2a) \quad (14.6)$$

Combining Eqs. (14.2), (14.4), and (14.6), the extracted power can be expressed as

$$P = C_p \cdot \frac{1}{2} \rho A U_0^3 \quad \text{where } C_p = 4a(1 - a)^2 \quad (14.7)$$

The Betz limit is obtained by finding the maximum value of the function  $C_p = 4a(1 - a)^2$ . This occurs at  $a = 1/3$ , corresponding to a power coefficient of  $C_p = 16/27$ .

The origin of the Betz limit can be most easily understood with reference to Eq. (14.4). As the induction factor increases from zero, the pressure drop ( $p_1 - p_2$ ) at the actuator disc increases while the velocity  $U_1$  decreases, and the power extracted (which is proportional to the product of these two) passes through a maximum. The Betz analysis ignores important effects that arise in real devices, such as viscous losses and rotation induced in the flow (in the case of turbines). However, such effects reduce the available output power and consequently the Betz limit provides a valid upper bound on the power coefficients of real extraction devices. The actuator disc model also makes incorrect predictions at high induction factors ( $a \geq 0.4$ ) where the wake behind a real extraction device becomes turbulent, but again this does not affect the validity of the final result. Adjustments to the theory are required for situations where the flow near the device is modified, for example, by a duct or diffuser, but these are well understood [6].

While large-scale wind turbines can be highly efficient, routinely achieving  $C_p$  values of around 0.5, miniaturized flow-driven energy harvesters invariably show lower performance, primarily because of increased viscous losses. Nevertheless, because of the relatively high power density in the flow, it is still feasible to generate useful levels of power for wireless sensing applications. For example, as will be shown in the next section, it is quite possible to realize a centimeter-scale device with an overall efficiency of  $\eta C_p \approx 0.1$ . Such a device, when placed in an airstream at room temperature and pressure ( $\rho = 1.2 \text{ kg m}^{-3}$ ), will generate an output power of  $160 \mu\text{W}$  per  $\text{cm}^{-2}$  of cross-sectional area at a flow speed of  $3 \text{ m s}^{-1}$ , increasing to  $6 \text{ mW cm}^{-2}$  at  $10 \text{ m s}^{-1}$ . These flow speeds are the minimum and maximum that might be expected in a typical air-handling duct [7]. They are also representative of flow speeds that might be encountered in an urban outdoor environment. For example, according to [8] the wind speed in the 50 largest US cities is  $4 \text{ m s}^{-1}$  on average with a standard deviation of  $0.6 \text{ m s}^{-1}$ . These figures suggest that it should be possible to realize centimeter-scale (several square centimeter cross section) flow-driven harvesters that can generate a few milliwatts of average power from either wind or duct flow. Such devices could provide long-term power for a range of environmental sensors in applications requiring low-duty-cycle operation and short-range transmission.

## 14.3

## Miniature Wind Turbines

Miniaturization of the classical wind turbine is a natural starting point for air-flow energy harvesting research, and several groups have reported devices based on this principle. The first demonstration was by Federspiel and Chen [9] who combined a 10.2-cm-diameter fan rotor with a brushless DC motor operating as an AC generator (i.e., without a commutator). The generator output was rectified using a three-phase bridge. The device could deliver 8 mW of DC power at  $2.5 \text{ m s}^{-1}$  air speed and 28 mW at  $5.1 \text{ m s}^{-1}$ . A similar device with a smaller rotor diameter of 4.2 cm was subsequently demonstrated by Rancourt *et al.* [10] which delivered raw AC power levels of 2.4 and 130 mW at air speeds of 5.5 and  $11.8 \text{ m s}^{-1}$  respectively. Myers *et al.* [11] developed a novel design of a piezoelectric windmill in which a set of three 12.7-cm-diameter commercial fan rotors was coupled via a crank mechanism to an array of plucked piezoelectric bimorphs. This device could deliver 5 mW after rectification at an air speed of  $4.47 \text{ m s}^{-1}$ . Further designs based on off-the-shelf rotor and generator parts have been demonstrated more recently by Xu *et al.* [12] and Carli *et al.* [13]. The key parameters for these devices, and for those described above, can be found in Table 14.1. The overall efficiency ( $\eta C_p$ ) values were calculated using Eq. (14.1) assuming an air density of  $1.2 \text{ kg m}^{-3}$ .

For many energy harvesting scenarios, including power generation in an air duct, it is desirable to minimize the harvester size. The smallest free-stream turbine harvester reported as of 2014 was a custom device developed by Howey *et al.* [14]. This consisted of a shrouded turbine stage with an axial-flux permanent magnet (AFPM) AC generator integrated into the shroud. The rotor diameter was 2.0 cm, and the overall diameter including the shroud was 3.2 cm, corresponding to an area of  $8 \text{ cm}^2$ . The device could operate at air speeds down to  $3 \text{ m s}^{-1}$ , and could deliver AC output power levels of between  $80 \mu\text{W}$  and 4.3 mW at air speeds in the range  $3\text{--}10 \text{ m s}^{-1}$ . Figure 14.2a shows a cross-sectional view illustrating the device geometry and construction, while Figure 14.2b shows a photograph of the

**Table 14.1** Turbine-based energy harvesters reported in the literature.

References	Rotor diameter (cm)	Area A ( $\text{cm}^2$ )	Flow speed range ( $\text{m s}^{-1}$ )	$\max\{P_{\text{out}}\}$ (mW)	$\max\{\eta C_p\}$ (%)
Federspiel and Chen [9]	10.2	81	2.5–5.1	28	10.5
Rancourt <i>et al.</i> [10]	4.2	13.9	5.5–11.8	130	9.5
Myers <i>et al.</i> [11]	12.7	$\sim 380^{\text{a}}$	2.4–4.5	5.0	0.25
Xu <i>et al.</i> [12]	7.6	45	3.0–4.5	18	8.6
Carli <i>et al.</i> [13]	6.3	31	8.6–16.8	10	7.8
Howey <i>et al.</i> [14]	2.0	$8.0^{\text{b}}$	3.0–10.0	4.3	1.5

a) Device has three partially overlapping rotors; area is estimated from a photograph.

b) Area includes shroud.

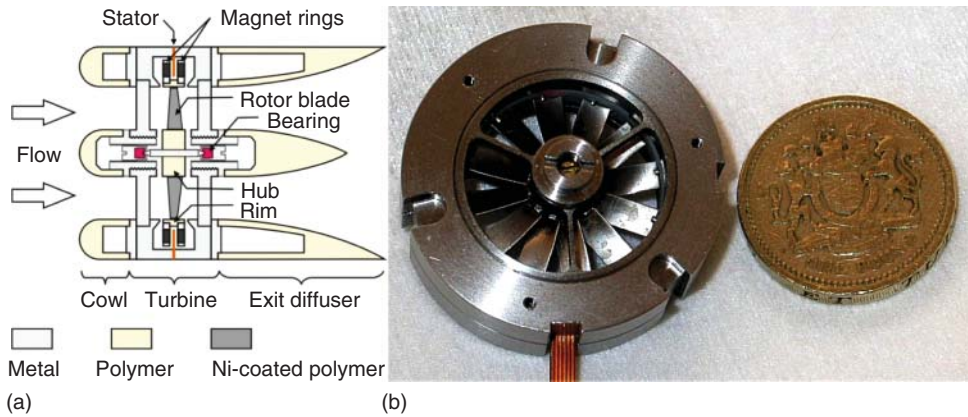


**Figure 14.2** Centimeter-scale shrouded turbine developed by Howey *et al.* [14], showing (a) device cross section, including cowl and exit diffuser, and (b) photograph of turbine stage with British pound coin for scale.

device with its cowl and exit diffuser removed. The AFPM generator comprised a fixed stator coil, fabricated using flexible printed circuit technology, sandwiched between two rotor-mounted rings of neodymium-boron-iron (NdBFe) permanent magnets. The rotor was supported on miniature jewel bearings.

### 14.3.1

#### Scaling Effects in Miniature Wind Turbines

The overall efficiency values in the right-most column of Table 14.1 are significantly lower than would be expected for a large-scale wind turbine, with the best-performing devices achieving efficiencies of around 10%. The relatively poor performance is the combined result of scaling effects arising in the turbine, the generator, and the bearings.

##### 14.3.1.1 Turbine Performance

The scaling of turbine performance is traditionally discussed in terms of nondimensional parameters. The key variables in wind turbine design are the shaft power  $P_{\text{shaft}}$ , the rotational speed  $\Omega$ , the free-stream flow speed  $U_0$ , the rotor diameter  $D$ , the roughness of the machine surfaces  $\varepsilon$ , and the density  $\rho$  and kinematic viscosity  $\nu$  of the working fluid [15]. These seven variables can be combined to form the following nondimensional groups:

$$C_p = \frac{P_{\text{shaft}}}{\pi \rho D^2 U_0^3 / 8}; \quad \lambda = \frac{\Omega D}{2U_0}; \quad \text{Re}_\Omega = \frac{\Omega D^2}{4\nu}; \quad \varepsilon_{\text{rel}} = \frac{\varepsilon}{D} \quad (14.8)$$

The parameter  $C_p$  is the power coefficient as defined earlier in Eq. (14.1);  $\lambda$  is the tip speed ratio, representing the ratio of the peripheral rotor speed to the free-stream flow speed;  $\text{Re}_\Omega$  is the rotational Reynolds number and  $\varepsilon_{\text{rel}}$  is the relative roughness. The Reynolds number is a key parameter for any fluid mechanical

system because it determines the flow regime, and in particular whether the flow is laminar (low  $Re$ ) or turbulent (high  $Re$ ) [5].

The functional relationship between  $C_p$ ,  $\lambda$ ,  $Re_\Omega$ , and  $\epsilon_{rel}$  will be scale invariant for any geometrically similar (homologous) series of turbines. Consequently, if  $\lambda$ ,  $Re_\Omega$ , and  $\epsilon_{rel}$  can be maintained constant as a given turbine design is scaled down, then  $C_p$  should also be invariant. In practice, however, downscaling is normally accompanied by a reduction in both  $\lambda$  and  $Re_\Omega$ , as well as an increase in  $\epsilon_{rel}$ . The most important consideration is that the Reynolds number will fall unless the rotational speed can be scaled according to  $\Omega \propto 1/D^2$ , and this is always impractical beyond a certain point because of bearing limitations.

The effect of Reynolds number on performance can be understood in terms of the lift and drag the turbine blades. A turbine blade is an aerofoil, and it is the aerodynamic lift generated by the blades that is responsible for the shaft torque and output power. Referring to Figure 14.3, which shows a cross section through a blade at an arbitrary radius  $r$ , the flow across the blade gives rise to lift and drag forces per unit length,  $F_L$  and  $F_D$ , which are defined as being normal to and parallel to the relative velocity  $W$  of the incoming flow and given by

$$F_L = \frac{1}{2}\rho W^2 c C_L; \quad F_D = \frac{1}{2}\rho W^2 c C_D \quad (14.9)$$

where  $c$  is the blade chord and  $C_L$ ,  $C_D$  are dimensionless lift and drag coefficients. The contributions of a radial blade element to the torque  $\tau$  and axial thrust  $T$  may be expressed in terms of these forces as

$$\delta\tau = r(F_L \sin \varphi - F_D \cos \varphi)\delta r \quad (14.10)$$

$$\delta T = (F_L \cos \varphi + F_D \sin \varphi)\delta r \quad (14.11)$$

where  $\delta r$  is the element thickness in the radial direction. The angle  $\varphi$  is the sum of the blade pitch angle  $\beta$ , which is set by the rotor design, and the angle of attack  $\alpha$  (the angle between the incoming flow and the blade).

The relative velocity  $W$  is the vector sum of axial and tangential components as indicated by the velocity triangle in Figure 14.3. Deceleration of the flow on approach to the turbine is described by an axial induction factor  $a$ , as in the Betz analysis. In addition, the rotor induces rotation or swirl in the flow which is accounted for by a second, tangential induction factor  $a'$ . A common approach for determining the values of  $a$  and  $a'$  is to equate the torque and thrust contributions given by Eqs. (14.10) and (14.11) with those required by the laws of linear and angular momentum conservation; this is the basis of the blade element momentum (BEM) method which is widely used in turbine design and modeling [16, 17]. In this approach, blade elements at different radii are treated independently, which amounts to dividing the flow through the turbine into a series of annular streamtubes which do not interact with each other. Once the elemental torque contributions are known, the overall torque, and hence the shaft power  $P_{shaft} = \tau\Omega$ , can be evaluated.

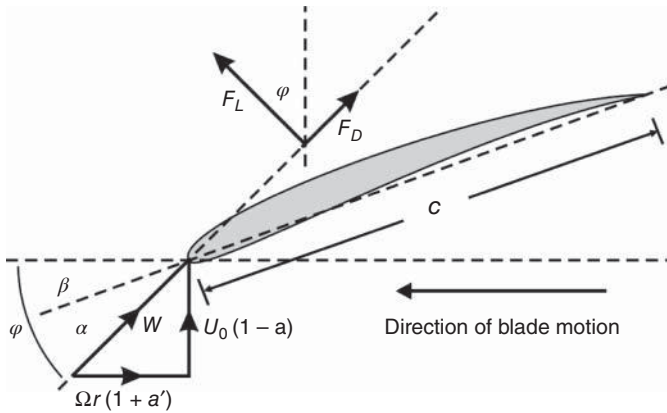


**Figure 14.3** Cross section through a turbine blade (looking radially), showing aerodynamic lift and drag forces and the velocity triangle for calculation of the relative velocity  $W$  of the incoming flow.

The lift and drag coefficients are functions of the aerofoil shape, the angle of attack, and the chord Reynolds number ( $Re_c = Wc/\nu$ ). While the lift coefficient at low angles of attack is only a weak function of  $Re_c$ , the drag coefficient increases strongly at low Reynolds number as a result of viscous forces. Consequently, while a large-scale turbine operating at  $Re_c > 10^6$  might operate at a lift-to-drag ratio  $C_L/C_D$  of around 100 [18], a centimeter-scale turbine with  $Re_c \sim 10^3$  is likely to have  $C_L/C_D < 10$  [19].

Increased drag has a detrimental effect on performance, as might be expected from the negative sign attached to the drag force term in Eq. (14.10). According to classical wind turbine theory [20], in the absence of drag, the power coefficient of an idealized turbine should approach the Betz limit as the tip speed ratio approaches infinity. In contrast, in a real turbine, the power coefficient passes through a maximum at a finite tip speed ratio  $\lambda_{opt}$  and the values of both  $C_{p,max}$  and  $\lambda_{opt}$  decrease as the lift-to-drag ratio diminishes. The reduction in  $\lambda_{opt}$  contributes to loss of performance because it leads to higher torque for a given output power, and through conservation of angular momentum this results in more rotational energy being coupled into the flow and lost in the wake of the turbine.

As a result of these scaling effects, miniaturized wind turbines tend to operate at  $C_p$  and  $\lambda$  values significantly below those of their larger-scale counterparts. As an example, Figure 14.4 shows measured performance data for the 2-cm-diameter turbine reported [14], together with the predictions of a BEM model which made use of published aerofoil lift and drag coefficients [19, 21]. The model predicts a maximum power coefficient of around 0.11 at  $\lambda \approx 1$ , while the experimental data suggests  $\lambda_{opt} \approx 0.6$  and  $C_{p,max} \approx 0.09$ . For comparison, a large-scale turbine might be operated at a tip speed ratio of 6–7 and achieve a power coefficient of 0.45.



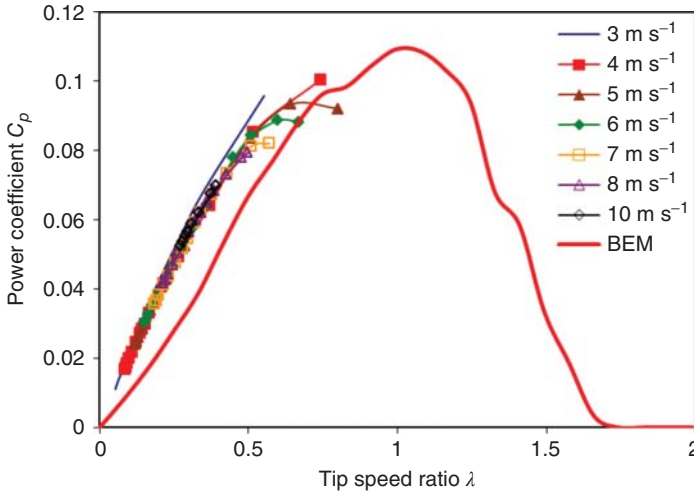


**Figure 14.4** Measured variations of  $C_p$  with  $\lambda$  over a range of flow speeds for the 2 cm-diameter turbine in Figure 14.2, and comparison with BEM model predictions, after [14].

#### 14.3.1.2 Generator and Bearing Losses

Comparing the performances of large-scale and miniaturized turbines, it is evident that  $C_{p\max}$  scales more slowly than the rotor diameter  $D$ , at least down to centimeter-scale, that is, that  $C_{p\max} \propto D^\delta$ , where  $0 \leq \delta < 1$ . On the basis of this observation, and considering the definition of  $C_p$  in Eq. (14.8), it is reasonable to assume that for a fixed free-stream flow speed, the turbine shaft power should satisfy

$$P_{\text{shaft}} \propto D^{(2+\delta)}; \quad 0 \leq \delta < 1 \quad (14.12)$$

It is of interest to compare this with the scaling law for maximum available power from a permanent magnet electromagnetic generator [22], which is of the form  $P_{\text{out}} \propto \Omega^2 D^5$ . If it is also assumed that the optimum tip speed ratio scales more slowly than  $D$ , this implies

$$P_{\text{out}} \propto D^{(3+2\varepsilon)}; \quad 0 \leq \varepsilon < 1 \quad (14.13)$$

Comparing these two relations, it can be seen that the generator output power is always expected to scale at least as rapidly as the turbine power. A consequence of this is that generators in small-scale harvesters are likely to be operated near their maximum power points, where there will be significant losses in the generator source resistance. This suggests that improvements in generator technology that can increase the generator constant (output voltage per unit rotation speed) or reduce the source resistance should have a noticeable effect on the overall harvester efficiency.

Bearing losses can also be an important factor in the overall performance of miniaturized turbine harvesters. The friction torque in miniature bearings tends

to be approximately linear in the rotation speed, resulting in a quadratic variation of the bearing loss with flow speed if the turbine is operated at constant tip speed ratio. Under these conditions, the turbine shaft power will scale down more rapidly with flow speed than the bearing losses, and this can result in a significant loss of efficiency at low flow speeds, while at the same time raising the minimum operating speed.

Both of the above effects were clearly evident in the device shown in Figure 14.2. The bearing efficiency (i.e., the fraction of shaft power remaining after bearing losses are subtracted) was found to increase from 27% to 69% for flow speeds from 3 to 10 m s<sup>-1</sup>, while the generator efficiency at the maximum power point fell from 93% to 76% over the same range. This resulted in an overall mechanical-to-electrical conversion efficiency  $\eta$  which peaked at 51% and fell as low as 25% at the lowest flow speed.

In addition to lowering the overall efficiency of the harvester, the losses in the generator and bearings will tend to shift the maximum power point away from the optimal operating point of the turbine. In order to avoid this, it is necessary to adopt a more holistic approach to design and optimization, taking account of all of the known loss contributions. This has been recognized in a recent publication on turbine harvester design [23].

#### 14.4

#### Energy Harvesters Based on Flow Instability

This section reviews a range of alternative energy harvesting devices that rely on flow-induced vibration of a mechanical structure. Such devices tend to be relatively simple in construction compared to miniature turbines, and they do not require bearings. They therefore offer potential advantages in terms of both manufacturing costs and long-term reliability. However, compared to miniature turbines their capabilities are less well understood; up to now there has been no comprehensive analysis of the performance limits, and only a small number of practical devices have been demonstrated.

Most vibration-based flow harvesters fall into one of two categories: (i) vortex shedding devices, where instabilities in the flow past a bluff body are used to excite a resonant mechanical structure and (ii) galloping- or flutter-based devices, where the fluid forces driving the vibration are strongly influenced by the motion of the resonant structure itself. The following sections briefly introduce the operational principles involved and give examples of practical energy harvesters reported in the literature. For a more detailed discussion of the fundamentals, see, for example, [24, 25]. Other devices relying on self-excited oscillations in an air cavity have been also been investigated [26, 27], but these have displayed only extremely low overall efficiencies and will not be discussed further.

## 14.4.1

**Vortex Shedding Devices**

Except at extremely low Reynolds numbers, the wake behind a bluff body placed in a free stream will be unsteady, with fluctuations in pressure and flow velocity that are more or less ordered, depending on the flow regime. A bluff body may be defined as one where the length parallel to the flow is comparable to at least one of the transverse dimensions, implying rapid tapering of the width toward the downstream side at one or more points. When a fluid flows past such an object, the pressure gradients that develop are unable to force the flow to follow the profile all the way from front to back. Instead the flow separates from the body at some earlier point and trails downstream, forming the boundaries of the wake.

Because it will have been subject to viscous drag while still attached to the body, the separated flow will be sheared (i.e., it will have a velocity gradient normal to the flow direction), with the outer layers flowing faster than the inner layers. This causes the flow to turn in on itself, resulting in the formation of discrete vortices which are carried downstream in the wake. For most flow conditions, this process of *vortex shedding* is periodic in the case of prismatic bodies, with vortices being shed alternately from one side of the body and then the other, as illustrated in Figure 14.5 for the case of a circular cylinder. This characteristic pattern of vortices is known as a *vortex street*. For a circular cylinder, regular vortex shedding is observed for Reynolds numbers above  $\sim 40$ , except in a transitional range at higher Reynolds numbers ( $3 \times 10^5 < \sim \text{Re} < 3 \times 10^6$ ) where the process may become disordered, depending on the surface roughness of the body.

In regimes where vortex shedding is periodic, the vortex-shedding frequency, representing the rate at which pairs of vortices are shed, may be expressed as:

$$f_s = \frac{SU_0}{D} \quad (14.14)$$

where  $U_0$  is the free-stream flow speed,  $D$  is a characteristic dimension (for example, the diameter in the case of a circular cylinder), and  $S$  is a dimensionless parameter known as the *Strouhal number*. The Strouhal number depends on both the body shape and the Reynolds number, the latter being defined in this case as  $\text{Re} = U_0 D / \nu$ . The variations of  $S$  with  $\text{Re}$  for various prismatic bodies can be found in [24]; in all cases shown,  $S$  lies in the range 0.1–0.3.

For a circular cylinder, it is found that  $S \approx 0.2$  is a good approximation over the Reynolds number range  $300 < \sim \text{Re} < 10^5$ . This range encompasses the flow

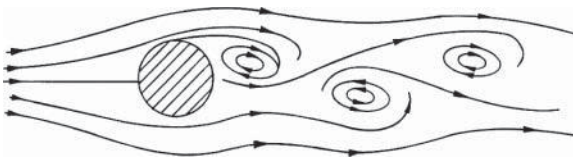


**Figure 14.5** Flow past a circular cylinder in a regime where regular vortex shedding leads to the formation of a vortex street.

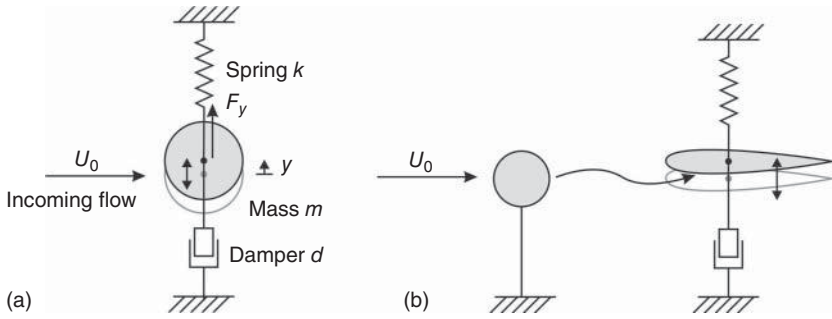


**Figure 14.6** Alternative vortex shedding energy harvester designs in which (a) the bluff body oscillates and (b) the bluff body is fixed and a secondary body oscillates.

regimes likely to be found in a miniaturized energy harvester. For example, a 1-cm-diameter cylinder in an airstream flowing at  $5 \text{ m s}^{-1}$  will have a  $\text{Re} \approx 3300$  (using  $\nu = 1.51 \times 10^{-5} \text{ m}^2 \text{ s}^{-1}$  for air). Such a cylinder will shed vortices at a frequency of  $\sim 100 \text{ Hz}$ , and this frequency will vary in direct proportion to the flow speed.

The shedding of vortices is accompanied by fluctuations in the surface pressure over the bluff body, resulting in an oscillatory lift (i.e., transverse) force at the vortex shedding frequency, and an oscillatory component to the drag force (longitudinal) at twice the vortex shedding frequency. Consequently, if the body is mounted on an elastic suspension, it will undergo forced oscillations with amplitude dependent on the level of damping and the relationship between the vortex shedding frequency and the mechanical resonance frequency.

The simplest vortex shedding energy harvester would comprise a bluff body on a single-axis suspension, with an electrical damper or transducer to extract power. For the configuration in Figure 14.6a, where the compliant axis is transverse to the flow, the displacement  $y$  will satisfy:

$$m\ddot{y} + d\dot{y} + ky = F_y \quad (14.15)$$

where  $m$  is the mass,  $k$  is the spring constant,  $d$  is the damping coefficient (including both structural damping and the electrical damping associated with power extraction), and  $F_y$  is the oscillatory lift force arising from vortex shedding. All quantities are per unit length.

In the simplest analysis, the lift force in Figure 14.6a may be modeled as:

$$F_y = \frac{1}{2} \rho U_0^2 D C_{Lvs} \sin(\omega_s t) = F_{L0} \sin(\omega_s t) \quad (14.16)$$

where  $C_{Lvs}$  is an effective lift coefficient associated with the vortex shedding process, and  $\omega_s = 2\pi f_s$ . If  $C_{Lvs}$  is independent of the motion, then the response will be that of a linear second-order system, and the oscillation amplitude  $A_y$  will reach a maximum value of

$$A_y|_{\omega_s=\omega_n} = \frac{F_{L0}}{d\omega_n} \quad (14.17)$$

when the system is excited at the resonance frequency  $\omega_n = \sqrt{k/m}$ . It is convenient to recast this equation in terms of dimensionless parameters

$$\left. \frac{A_y}{D} \right|_{\omega_s = \omega_n} = \frac{C_{Lvs}}{4\pi S^2 \sigma_r} \quad (14.18)$$

where  $\sigma_r = 4\pi\zeta \cdot m_r$  is the *reduced damping* or *Scruton number* [28], defined in terms of the conventional damping factor  $\zeta = d/2m\omega_n$  and the reduced mass  $m_r = m/\rho D^2$ . The latter is a measure of the structure's susceptibility to excitation by fluidic forces.

Equation (14.18) suggests that the response should be inversely proportional to the damping, and this is indeed the case when the damping is strong and the oscillation amplitude is small. However, for lighter damping and larger oscillation amplitudes, nonlinear effects arise owing to the interaction between the body motion and the fluid. When the oscillation amplitude becomes appreciable compared to  $D$ , the motion of the body tends to reinforce and strengthen the vortex shedding effect. Furthermore, the actual frequency of vortex shedding can become "locked in" to the resonant frequency when the natural vortex shedding frequency, as given by Eq. (14.14), is close to resonance. If the damping is decreased further, the amplitude does not increase indefinitely but rather tends to a limiting value, reflecting the fact that the effective lift coefficient decreases again at large amplitudes. For example, for a circular cylinder it is found that  $A_y/D \approx 1.4$  in the limit of light damping.

Various semiempirical models have been developed that take account of the above effects, for example, through the use of amplitude-dependent lift coefficients [25]. Such models are beyond the scope of this discussion. However, it is of interest to estimate the theoretical maximum output power that might be achieved from a vortex shedding energy harvester. From empirical data, it is known that, for a cylinder, the transition between the lightly damped regime ( $A_y \approx \text{const}$ ) and the heavily damped regime ( $A_y \propto 1/\sigma_r$ ) occurs at around  $\sigma_r = 1$ , at which point the oscillation amplitude  $A_y/D \approx 1$ . This is the point at which maximum power dissipation in the damper is expected to occur.

The total power dissipated in the damper at an oscillation frequency  $\omega$  is given by

$$P_d = \frac{1}{2} L d \omega^2 A_y^2 = \frac{1}{2} \frac{\omega_n \rho L D^2 \sigma_r}{2\pi} \omega^2 A_y^2 \quad (14.19)$$

where  $L$  is the length of the bluff body. Assuming all of this power is extracted as electrical output power (i.e., that there are no parasitic damping or electrical losses), and putting  $\omega = \omega_n = \omega_s = 2\pi S U_0/D$ ,  $A_y \approx D$ ,  $\sigma_r = 1$ , the maximum output power is obtained as

$$P_{\text{out}} \approx \frac{1}{2} \rho L D U_0^3 \cdot (4\pi^2 S^3) \quad (14.20)$$

Comparing this equation with Eq. (14.1), it can be seen that the last term in brackets is effectively the power coefficient of the device. This assumes a device cross section of  $A = L \times D$ ; any additional cross section associated with supports

is neglected, as is the effective increase in cross section due to displacement of the body. With  $S = 0.2$ , Eq. (14.20) predicts a power coefficient of  $C_p \approx 0.3$ , suggesting that devices of the type shown in Figure 14.6a have the potential to be highly effective as flow energy harvesters.

An alternative approach to energy harvesting by vortex shedding is shown in Figure 14.6b. Here the bluff body is fixed, and the oscillating cross flow associated with its vortex street is used to excite a secondary structure in its near wake. The secondary structure is shown as an aerofoil on an elastic suspension, although it need not take this precise form. This system is more complex and less well understood than the one in Figure 14.6a. Nevertheless, it has been the preferred configuration for practical vortex shedding harvesters to date, and a number of devices have been realized. For example, Pobering and Schwesinger [29] demonstrated a device in which the secondary structure was a piezoelectric bimorph cantilever attached directly to the leeward side of the bluff body. This was a development of an earlier device aimed at water flow harvesting [30]. The bluff body on the airflow harvester was rectangular in cross section with chamfered corners on the windward side, and the area presented to the flow was  $L \times D = 11.8 \times 10.53 \text{ mm}^2$ . A maximum output power of  $108 \mu\text{W}$  was obtained at a flow speed of  $45 \text{ m s}^{-1}$ , corresponding to an overall efficiency of only 0.0016%. Li and Lipson subsequently reported a “flapping-leaf generator” [31] comprising a half-cylinder bluff body ( $D = 2 \text{ cm}$ ,  $L = 10 \text{ cm}$ ) and a piezoelectric element (“stalk”) with a polymer flap (“leaf”) attached to its free end via a plastic hinge. Several design variants were investigated, with the best performing device achieving a power output of  $300 \mu\text{W}$  at  $8 \text{ m s}^{-1}$  ( $\eta C_p = 0.049\%$ ). More recently, Weinstein *et al.* [32] reported a device where the secondary structure is separate from and downstream of the bluff body. Figure 14.7 shows a photograph of this device. The bluff body was a 2.5-cm-diameter cylinder, 11 cm in length, and the secondary structure was a piezoelectric cantilever which was fixed to the device frame at the downstream end and had a balsa-wood fin attached at its upstream end. The role of the fin was to increase the lift forces due to the vortex-induced cross flow generated by the cylinder. The authors investigated the effect of varying the spacing between the cylinder and the fin, and were also able to tune the resonant frequency of the secondary structure (by loading the fin) to match the vortex shedding frequencies at different flow rates. The device could be operated down to  $2 \text{ m s}^{-1}$  flow speed and, with retuning, could deliver output powers from  $100 \mu\text{W}$  to  $3 \text{ mW}$  for flow speeds in the range  $2\text{--}5 \text{ m s}^{-1}$ . The overall efficiency at the upper end of the range was 1.7% which set a new benchmark for this kind of device.

#### 14.4.2

##### Devices Based on Galloping and Flutter

Galloping and flutter are related oscillatory phenomena that result from feedback between the motion of an object and the fluidic forces acting upon it. The term *flutter* originated in the field of aerodynamics, and is typically reserved for aerofoils and other streamlined bodies, whereas *galloping* is normally applied to

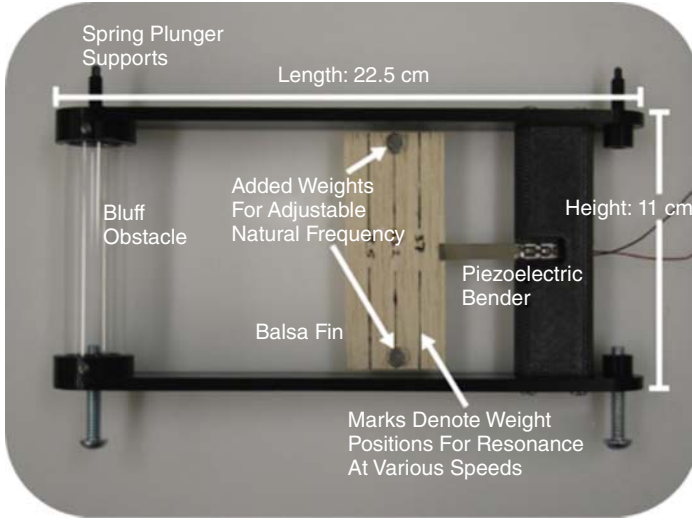


**Figure 14.7** Vortex shedding device developed by Weinstein *et al.* [32], comprising rapid-prototyped ABS frame, acrylic cylinder, balsa wood fin, and piezoelectric cantilever.

bluff bodies, a classical example being the wind-induced oscillation of ice-laden overhead power cables.

The origin of galloping is most easily explained using the model in Figure 14.8, in which a bluff body of non-circular cross-section, mounted on a single-axis elastic suspension, is immersed in a uniform flow. In general the body will be subject to lift and drag forces which will vary in both magnitude and direction when the body moves, and under certain conditions this can result in dynamic instability and spontaneous oscillation.

In basic analysis of galloping it is usual to assume that the fluid forces acting on the body can be calculated using the static lift and drag coefficients, as would be measured in a wind tunnel. Under this so-called *quasistatic* assumption, dynamic effects such as vortex shedding are assumed to occur at substantially higher frequency so that their effects are averaged out.

Under the quasistatic assumption the net downward driving force in Figure 14.8 can be expressed as:

$$F_y = -(C_L \cdot \cos \alpha + C_D \cdot \sin \alpha) \cdot \frac{1}{2} \rho D W^2 \quad (14.21)$$

where  $W = \sqrt{U_0^2 + \dot{y}^2}$  is the relative velocity between the incoming flow and the body,  $\alpha = \tan^{-1}(\dot{y}/U_0)$  is the angle of attack, and  $C_L$  and  $C_D$  are the lift and drag coefficients. Expanding this equation in  $\alpha$ , and assuming  $\dot{y} \ll U_0$  so that  $W \approx U_0$ ,  $\alpha \approx \dot{y}/U_0$  and only linear terms need be retained:

$$F_y \approx F_y|_{\alpha=0} - \left( \frac{\partial C_L}{\partial \alpha} + C_D \right) \cdot \frac{1}{2} \rho D U_0 \dot{y} \quad (14.22)$$

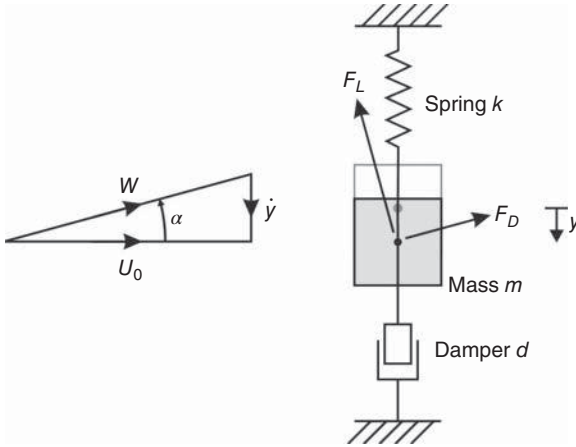


**Figure 14.8** Model for galloping in a system with only transverse oscillation, also showing the velocity triangle for relative velocity  $W$  of the incoming flow. Note that the vertical displacement  $y$  is defined as being positive downward so that  $y$  and  $\alpha$  have the same sign.

Substituting this driving force into the equation of motion (see Eq. (14.15)), it can be seen that the effect of the body motion is to modify the damping term so that the effective damping coefficient becomes:

$$d_{\text{eff}} = d + \left( \frac{\partial C_L}{\partial \alpha} + C_D \right) \cdot \frac{1}{2} \rho D U_0 \quad (14.23)$$

While  $d_{\text{eff}}$  remains positive the system will be stable and any oscillations initiated by instabilities in the flow will tend to be damped out. However, if  $d_{\text{eff}}$  becomes negative then the system will go unstable and galloping oscillations will develop at the resonance frequency. This can happen only if the term in brackets is negative, which in turn requires that  $\partial C_L / \partial \alpha < 0$  (as  $C_D$  is always  $> 0$ ). Furthermore, according to Eq. (14.23) there is expected to be a critical flow speed for the onset of galloping, given by:

$$U_{0,\text{crit}} = \frac{2d}{\rho D \partial C_y / \partial \alpha}; \quad \frac{\partial C_y}{\partial \alpha} = - \left( \frac{\partial C_L}{\partial \alpha} + C_D \right) \quad (14.24)$$

The value of  $\partial C_y / \partial \alpha$  for any particular will bluff body will depend on its shape and orientation relative to the flow (which may be influenced by other effects such as vortex shedding). However, with the exception of a circular cylinder, for which  $C_L = 0$ , all types of bluff body can be made to gallop under the right conditions. Once galloping oscillations are initiated they will grow until non-linearities cause the average damping to go to zero and a limiting amplitude to be reached. The linear analysis above cannot yield any information about the resulting amplitude; however, as in the case of vortex shedding, non-linear models exist that allow the variation of oscillation amplitude with flow speed to be predicted [25].

Up to now there have not been any reports of galloping energy harvesters based on the simple configuration shown in Figure 14.8. However, several harvesters



have been demonstrated in which one body undergoes galloping oscillations in the wake of another. This scenario is ostensibly similar to that shown in Figure 14.6b. However, the behavior is qualitatively different from vortex-induced vibration in that oscillation of the downstream body occurs at its resonance frequency (rather than at the vortex-shedding frequency) and may continue with appreciable amplitude over a relatively wide range of flow speeds. This kind of *wake galloping* can occur even with circular cylinders and it has been studied extensively in the context of power cable bundles [33]. In the area of energy harvesting, Jung and Lee [34] investigated a device based on a pair of 5 cm-diameter, 0.85 m-long cylinders. The upstream cylinder was fixed while the downstream one was mounted on a single-axis spring suspension with an electromagnetic damper for power extraction. The results were interesting in that cut-in flow speeds below  $1 \text{ m s}^{-1}$  could be achieved at the same time as continuous operation up to  $5 \text{ m s}^{-1}$ . The cut-in speed was found to increase with resonance frequency, with the maximum value of  $\sim 1.2 \text{ m s}^{-1}$  corresponding to a resonance frequency of 4.8 Hz, consistent with the galloping oscillations being initiated by vortex shedding. Measurements of output voltage were presented indicating output power levels of up to several hundred mW. Unfortunately, however, there was insufficient information to allow a reliable calculation of the overall efficiency.

An alternative energy harvester based on motion-derived forces was reported by Zhu *et al.* [35]. This device comprises a rectangular bluff body with a wing or aerofoil mounted behind it on a cantilever spring, as shown in Figure 14.9. Electrical damping is provided by a permanent magnet generator comprising wing-mounted magnets and a coil fixed to the base. Oscillations are initiated by the unsteady flow behind the bluff body, but once the aerofoil is in motion it experiences a lift force that is strongly motion-dependent owing to the changing flow conditions. A detailed theoretical analysis of the device operation has not been reported.

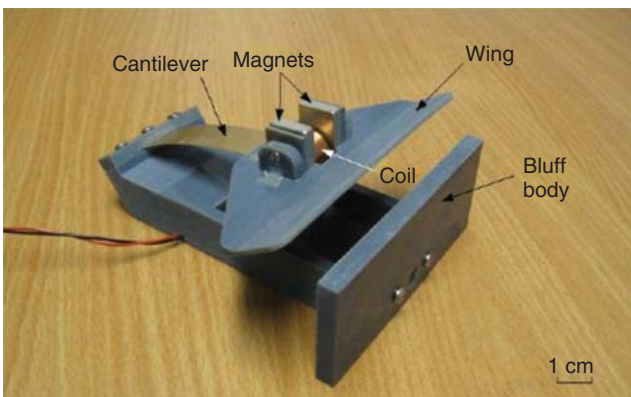


**Figure 14.9** Flapping wing energy harvester developed by Zhu *et al.* (horizontal flow version), as described in [35].

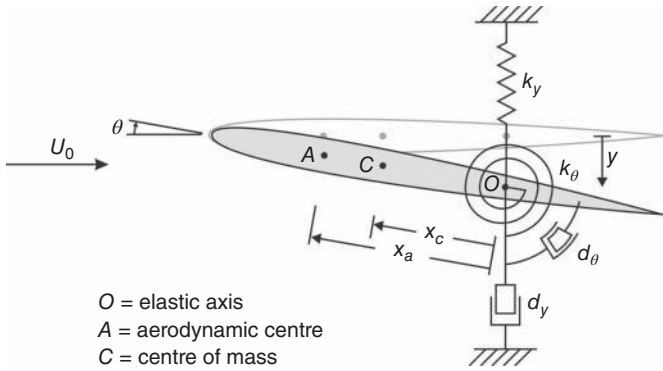


**Figure 14.10** Flutter model comprising an aerofoil supported on an elastic suspension with both linear and torsional degrees of freedom.

However, the authors investigated experimentally the effect on performance of key design parameters, in particular the initial position and orientation of the aerofoil in relation to the bluff body. Two prototype harvesters were produced, optimized for horizontal and vertical flows respectively. The vertical device had a cut-in speed of  $2.5 \text{ m s}^{-1}$ , and the output power varied roughly linearly with flow speed from  $470 \mu\text{W}$  at  $2.5 \text{ m s}^{-1}$  ( $\eta C_p = 0.96\%$ ) to  $2 \text{ mW}$  at  $6 \text{ m s}^{-1}$  ( $0.3\%$ ). The overall efficiency values in brackets are based on the reported device cross-section of  $8 \text{ cm} \times 6.5 \text{ cm}$ . The horizontal device produced comparable, but slightly lower, output power levels, and had an even lower cut-in flow speed of  $1.5 \text{ m s}^{-1}$ .

The key features of flutter can be illustrated by means of the model in Figure 14.10 which shows an aerofoil mounted on an elastic suspension with both linear and rotational degrees of freedom. The equations of motion for this case are:

$$m\ddot{y} - mx_c\ddot{\theta} + d_y\dot{y} + k_y y = F_y \quad (14.25)$$

$$J\ddot{\theta} - mx_c\ddot{y} + d_\theta\dot{\theta} + k_\theta\theta = M \quad (14.26)$$

where  $m$  is the aerofoil mass,  $J$  is the moment of inertial referred to the elastic axis  $O$  (about which the aerofoil rotates),  $k_y$  and  $k_\theta$  are the linear and torsional spring constants respectively,  $d_y$  and  $d_\theta$  are the corresponding damping coefficients (either or both of which might include an electrical damping contribution in an energy harvesting device), and  $x_c$  is the distance from the elastic axis to the center of mass. The aerofoil is subject to a vertical driving force  $F_y$  (+ve downward) and a turning moment  $M$  (+ve clockwise) about the elastic axis.

Equations (14.25) and (14.26) are coupled inertially through the terms in  $x_c$ , except when the elastic axis coincides with the center mass. Furthermore, cross-coupling also occurs through  $F_y$  and  $M$  because these are influenced by the angle of attack, which in turn depends on both the linear and torsional motion. The effect of vertical motion on  $\alpha$  is the same as in the galloping case of Figure 14.8.

However,  $\alpha$  also varies with the aerofoil pitch angle  $\theta$ , and with the angular rate  $\dot{\theta}$ , which leads to a position-dependent velocity component at the aerofoil surface. In the quasistatic approximation we can therefore write

$$F_y = F_y(\theta, \dot{\theta}, \dot{y}); \quad M = M(\theta, \dot{\theta}, \dot{y}) \quad (14.27)$$

By analogy with the galloping case, the dependencies of  $F_y$  and  $M$  on  $\dot{y}$  and  $\dot{\theta}$  respectively, might be expected to result in linear and torsional galloping instabilities. However, this is shape dependent. In particular, aerofoils are stable against torsional galloping and prone to linear galloping or *stall flutter* only at high angles of attack, while bluff bodies tend to be prone to both. Two other important potential modes of instability are divergence and classical flutter. The first results from the variation of  $M$  with  $\theta$ , which under certain conditions can reduce the effective torsional stiffness to zero, resulting in very large angular deflections (this can occur only if the elastic axis is downstream of the aerodynamic center, that is, if  $x_a > 0$ , and so can easily be precluded by design). The second is a combined torsional/linear motion in which the linear and torsional oscillations occur at the same frequency.

The idea of using classical flutter of an aerofoil to extract power from the wind was explored in the early 1980s in the context of larger-scale power generation [36]. More recently, several groups have developed models of flutter-based energy harvesters that are based on more sophisticated aerofoil theory and include power extraction based on piezoelectric damping. For example, Bryant and Garcia [37] modeled a benchtop-scale device with a 15-cm-span aerofoil and investigated the idea of switching the electrical load to expand the operational envelope in terms of flow speed. Erturk *et al.* [38] validated their model by wind-tunnel testing of a slightly larger device (50 cm span), and explored the effect of electrical loading on the flutter speed (i.e., the flow speed at the onset of flutter). The flutter speeds observed were relatively high ( $\sim 16$  and  $\sim 9 \text{ m s}^{-1}$  respectively); however, minimization of the flutter speed was not a stated aim in either case. Models of the kind demonstrated will be essential tools for the development of optimized flutter-based harvesters at smaller scale.

Flutter can also be induced by transverse airflow across a flexible ribbon or belt, and energy harvesting based on this principle has also been explored. The company Humdinger Wind Energy LLC produced a range of devices at different scales, under the name “Windbelt.” As shown in Figure 14.11, these devices were very simple in structure, comprising just a suitably tensioned polymer/fiber composite belt, with attached permanent magnets that interacted with adjacent coils for electrical damping. The most interesting from a wireless sensing standpoint was the “ $\mu$ Windbelt” [39] which was palm sized ( $A = 37 \text{ cm}^2$ ) and could generate 0.2 mW at  $3.5 \text{ m s}^{-1}$  ( $\eta C_p = 0.21\%$ ) and 5 mW at  $7.5 \text{ m s}^{-1}$  (0.53%). Similar devices were subsequently demonstrated by several other groups (see, for example, [40]).

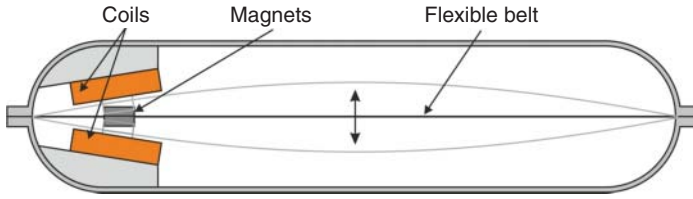


Figure 14.11 “Windbelt” energy harvester concept, as developed by Humdinger LLC [39].

## 14.5 Performance Comparison

Figure 14.12 compares the overall efficiencies achieved at different flow speeds by the various airflow harvesters discussed in the preceding sections. Also shown are lines corresponding to overall efficiencies of 0.593, 0.1, and 0.0025, corresponding to the Betz limit and the best and worst-performing turbine-based harvesters. In all cases, the calculation of overall efficiency is based on the entire device cross section presented to the flow, as this makes for the fairest comparison. So, for example, the calculation for the device of Zhu *et al.* [35] includes the bluff body because it is an integral part of the device.

It can be seen that turbine-based devices generally show better performance than non-turbine designs. With the exception of one outlier, all the turbine harvesters achieve efficiencies in the range 1–10%. There is no strong correlation between performance and device size, except that the shrouded device of Howey *et al.* is at the bottom of the range; this is to be expected because of its small size.

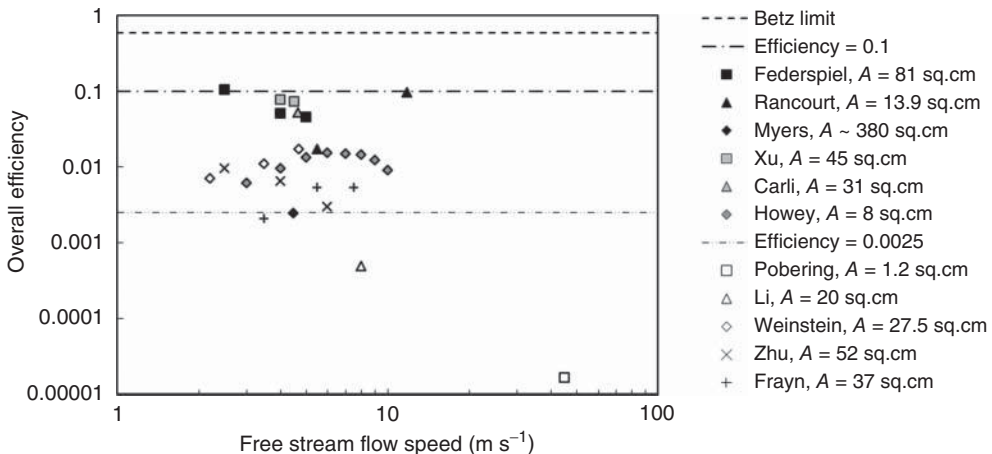


Figure 14.12 Performance comparison for air-flow harvesters reported in the literature, showing variations of overall power coefficient with free stream flow speed. The data

includes miniature turbines (solid symbols), vortex shedding devices (open symbols) and devices based on galloping/flutter (×,+).

This lack of correlation is a reflection of the fact that the various designs have not been fully optimized.

The spread of performance is even wider among the non-turbine designs, which is unsurprising given their relatively undeveloped nature. The best-performing devices are already achieving efficiencies of around 1%, and further improvements can be expected as design methods become more established.

## 14.6

### Summary

Compared to other energy harvesting techniques, energy harvesting from airflow is still relatively undeveloped. Few working harvesters have been demonstrated, and in most cases, these have been proof of principle devices that have not been designed for optimal operation.

On the basis of results to date, miniaturized wind turbines would appear to offer the best performance in terms of overall efficiency, with values in the range 5–10% being accessible for centimeter-scale devices. They can also achieve the low cut-in speeds of 2–3 m s<sup>-1</sup> that are likely to be required for indoor applications such as duct monitoring. On the other hand, they are relatively complex and may remain too expensive to manufacture. They also require bearings, raising questions over long-term reliability.

Among the vibration-based devices, those based on wake oscillation appear to be the most promising as they can achieve low cut-in speeds while at the same time operating over a wide range of flow rates. Vortex shedding devices are more limited because they have a resonant response; however, they may be useful in applications where a relatively constant flow speed can be guaranteed. Overall efficiencies of around 1% have been demonstrated in devices of both types, and improvements on this can be expected over time as understanding of the design criteria (e.g., optimum geometry, operating frequency, and damping strength) improves.

The basic design methods for miniature turbines are well understood, and future work should be focused on the bearing solutions that can guarantee long-term reliability and on holistic design that includes the turbine, generator, and bearings. For vibration-based devices, further experimental and theoretical investigations are required to establish more fully the relative capabilities of the different approaches. It will also be interesting to explore the scaling of vibration-based designs to smaller sizes, particularly as their relatively simple construction makes them highly compatible with microfabrication techniques.

### References

1. Fleck, B. and Huot, M. (2009) Comparative life-cycle assessment of a small wind turbine for residential off-grid use. *Renew. Energy*, **34**, 2688–2696.
2. Morais, R., Matos, S.G., Fernandes, M.A., Valente, A.L.G., Soares, S.F.S.P., Ferreira, P.J.S.G., and Reis, M.J.C.S. (2008) Sun, wind and water flow as

- energy supply for small stationary data acquisition platforms. *Comput. Electron. Agric.*, **64**, 120–132.
3. Glaser, S.D. (2004) Some real-world applications of wireless sensor nodes. *Proc. SPIE*, **5391**, 344–355.
  4. Matiko, J.W., Grabham, N.J., Beeby, S.P., and Tudor, M.J. (2014) Review of the application of energy harvesting in buildings. *Meas. Sci. Technol.*, **25**, 0012002, (25 pp).
  5. White, F.M. (1999) *Fluid Mechanics*, McGraw Hill International Editions Series, Science Engineering & Math.
  6. Jamieson, P. (2008) Generalized limits for energy extraction in a linear constant velocity flow field. *Wind Energy*, **11**, 445–457.
  7. CIBSE (2008) *CIBSE Concise Handbook* (ed J. Armstrong), The Chartered Institution of Building Services Engineers, London.
  8. National Climatic Data Center (2011) Comparative Climate Data for the United States through 2011, National Oceanic and Atmospheric Administration, Asheville, CCD-2011.
  9. Federspiel, C.C. and Chen, J. (2003) Air-powered sensor. *Proc. IEEE Sens.*, **1**, 22–25.
  10. Rancourt, D., Tabesh, A., and Fr chet te, L.G. (2007) Evaluation of centimeter-scale micro wind mills: aerodynamics and electromagnetic power generation. *Proceeding of PowerMEMS 2007*, pp. 93–96.
  11. Myers, R., Vickers, M., Kim, H., and Priya, S. (2007) Small scale windmill. *Appl. Phys. Lett.*, **90**, 054106.
  12. Xu, F.J., Yuan, F.G., Hu, J.Z., and Qiu, Y.P. (2010) Design of a miniature wind turbine for powering wireless sensors. *Proc. SPIE*, **7646**, 764741-1.
  13. Carli, D., Brunelli, D., Bertozzi, D., and Benini L. (2010) A high-efficiency wind-flow energy harvester using micro turbine. *Proceeding of the International Symposium on Power Electronics Electrical Drives, Automation and Motion, SPEEDAM 2010*, pp. 778–783.
  14. Howey, D.A., Bansal, A., and Holmes, A.S. (2011) Design and performance of a centimetre-scale shrouded wind turbine for energy harvesting. *Smart Mater. Struct.*, **20**, 085021(12 pp.).
  15. Douglas, J. et al. (2005) *Fluid Mechanics*, 5th edn, Pearson Prentice Hall, Harlow.
  16. Dixon, S. (2005) *Fluid Mechanics and Thermodynamics of Turbomachinery*, 5th edn, Elsevier, Amsterdam.
  17. Liu, S. and Janajreh, I. (2012) Development and application of an improved blade element momentum method model on horizontal axis wind turbines. *Int. J. Energy Environ. Eng.*, **3**, 30, (30 pp.).
  18. Jamieson, P. (2011) *Innovation in Wind Turbine Design*, John Wiley & Sons, Ltd, Chichester.
  19. Kunz, P. (2003) Aerodynamics and design for ultra-low Reynolds number flight. PhD thesis, Department of Aeronautics and Astronautics, Stanford University.
  20. Gasch, R. and Twele, J. (eds) (2012) *Wind Power Plants: Fundamentals, Design, Construction and Operation*, Springer-Verlag.
  21. Kesel, A.B. (2000) Aerodynamic characteristics of dragonfly wing sections compared with technical aerofoils. *J. Exp. Biol.*, **203** (20), 3125–3135.
  22. Holmes, A.S., Hong, G., and Pullen, K.R. (2005) Axial-flux permanent magnet machines for micropower generation. *J. Microelectromech. Syst.*, **14** (1), 54–62.
  23. Rancourt, D., Landry, C., Fr chet te, L., and Mavris, D.N. (2014) Design space exploration of centimeter-scale wind turbines using a physics-modified optimization formulation. *J. Mech.*, **30**, 537–548. doi: 10.1017/jmech.2014.23
  24. Blevins, R.D. (1990) *Flow-Induced Vibration*, 2nd edn, Van Nostrand-Reinhold.
  25. Dowell, E.H. (ed) (2004) *A Modern Course in Aeroelasticity*, 4th edn, Kluwer Academic Publishers.
  26. Kim, S.-H., Ji, C.-H., Galle, P., Herrault, E., Wu, X., Lee, J.-H., Choi, C.-A., and Allen M.G. (2008) An electromagnetic energy scavenger from direct airflow. *Proceeding of PowerMEMS 2008*, pp. 133–136.
  27. St, C.D., Bibo, A., Sennakesavababu, V.R., Daqaq, M.F., and Li, G. (2010) A

- scalable concept for micropower generation using flow-induced self-excited oscillations. *Appl. Phys. Lett.*, **96**, 144103, (3 pp.).
28. Hansen, S.O. (2013) Vortex-induced vibrations – the Scruton number revisited. *Struct. Build.*, **166** (SB10), 560–571.
  29. Pobering, S. and Schwesinger, N. (2008) Power supply for wireless sensor system. *Proc. IEEE Sens.*, 685–688.
  30. Pobering, S. and Schwesinger, N. (2004) A novel hydropower harvesting device. Proceeding of the ICMENS 2004, pp. 480–485.
  31. Li, S. and Lipson, H. (2009) Vertical-stalk flapping-leaf generator for wind energy harvesting. Proceeding of the ASME Conference on SMASIS 2009, pp. 611–619.
  32. Weinstein, L.A., Cacan, M.R., So, P.M., and Wright, P.K. (2012) Vortex shedding induced energy harvesting from piezoelectric materials in heating, ventilation and air conditioning flows. *Smart Mater. Struct.*, **21**, 045003 (9 pp.).
  33. Brika, D. and Laneville, A. (1999) The flow interaction between a stationary cylinder and a downstream flexible cylinder. *J. Fluids Struct.*, **13**, 579–606.
  34. Jung, H.-J. and Lee, S.-W. (2011) The experimental validation of a new energy harvesting system based on the wake galloping phenomenon. *Smart Mater. Struct.*, **20**, 055022 (10 pp.).
  35. Zhu, D., Beeby, S.P., Tudor, M.J., and White, N.M. (2013) Novel miniature airflow energy harvester for wireless sensing applications in buildings. *IEEE Sens. J.*, **13** (2), 691–700.
  36. McKinney, W. and DeLaurier, J. (1981) The wingmill: an oscillating-wing windmill. *J. Energy*, **5** (2), 109–115.
  37. Bryant, M. and Garcia, E. (2009) Development of an aeroelastic vibration power harvester. *Proc. SPIE*, **7288**, 728812 (10 pp.).
  38. Erturk, A., Vieira, W.G.R., De Marqui, C. Jr., and Inman, D.J. (2010) On the energy harvesting potential of piezoaeroelastic systems. *Appl. Phys. Lett.*, **96**, 184103 (3 pp.).
  39. Humdinger Wind Energy LLC (2008) microWindbelt Data Sheet.
  40. Fei, F. and Li, W.J. (2009) A flutter-to-electrical energy transduction system for consumer electronics applications. Proceeding of the IEEE Conference on Robotics and Biomimetics 2009, pp. 580–585.





## 15

# Far-Field RF Energy Transfer and Harvesting

*Hubregt J. Visser and Ruud Vullers*

This chapter deals with radio frequency (RF) energy transfer over a distance. After explaining the differences between nonradiative and radiative RF energy transfer, definitions for transfer and harvesting are given. The subcomponents of an RF energy transfer system are identified and the receiving rectifying antenna is then discussed in detail. After that, the transmission and propagation of RF signals is treated, followed by the demonstration of some examples and an outline of future perspectives. It is concluded that far-field RF energy transfer is feasible, but requires a careful co-design of the several subsystems that make up the whole far-field RF energy transfer system. Adaptivity, both at the transmit side (in radiation) and at the receiving side (in impedance matching) is seen as a future path in research and development.

### 15.1

#### Introduction

To accommodate an increase in the employment of wireless sensors in areas as diverse as health monitoring, automotive, predictive maintenance, structural integrity monitoring, and smart buildings, alternatives to powering by batteries are required. The need for long lifetime and small form factors of future wireless sensor nodes do not match up well with currently available battery technology [1]. Replacing batteries will often be impossible, nearly always be impractical, and disposing of the old batteries will generate an environmental problem. Alternative ways of powering may be found in energy harvesting (formerly known as energy scavenging) where energy is taken from ambient sources such as vibration, thermal differences, light, and RF signals.

## 15.2

**Nonradiative and Radiative (Far-Field) RF Energy Transfer**

When employing RF signals for the transfer of energy, we make a distinction between nonradiative and radiative RF energy transfer. The former is based on (inductive) coupling, while the latter uses the transmission and reception of radio waves. Furthermore, we make a distinction between RF energy harvesting and RF energy transfer. By energy harvesting, we mean the process wherein we obtain energy from the ambient. So, for RF signals that means obtaining energy from signals that are transmitted for telecommunication services (radio- and television-broadcasting, GSM, Wi-Fi, etc.). By RF energy transfer, we mean the process wherein we employ a dedicated RF source for wirelessly powering a device. Strictly speaking, RF energy harvesting is then a particular form of RF energy transfer. In our definition, the transmitted signals in RF harvesting are unintentional and those in RF transfer systems are intentional.

## 15.2.1

**Nonradiative Transfer**

Nonradiative RF energy transfer is mostly employed in inductive systems, obeying the Qi standard [2]. Two coils are brought in each other's vicinity for transferring RF energy (Figure 15.1). The two coils in close proximity form an electrical transformer. By applying capacitors, a resonant coupling system is created [3], increasing the power transfer efficiency.

In the circuit shown in Figure 15.1, an RF source is connected to a coil  $L_s$ , that is resonated with a capacitor  $C_s$ . A receiving coil  $L_r$ , resonated with a capacitor  $C_r$ , is placed in close proximity and the received signal is rectified, eventually accumulated and used to power a source that is represented by load resistance  $R_L$ . The resistances  $R_s$  and  $R_r$  represent the losses in the transmitting and receiving coils, respectively.

The benefit of this resonant coupling energy transfer, apart from being subject to a standard, lies in the high power transfer efficiency [4].

The drawbacks are in the limited transferring distance – the transfer efficiency falls off very steeply for distances larger than approximately one coil diameter – which also makes harvesting (taking energy from the ambient) impossible,

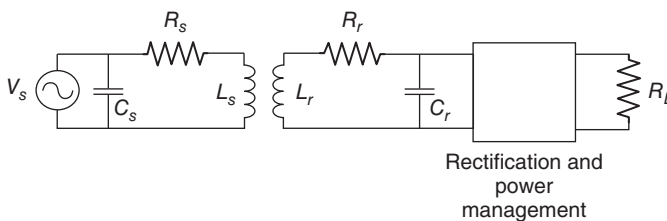


**Figure 15.1** Resonant coupling (non-radiative) RF energy transfer system.

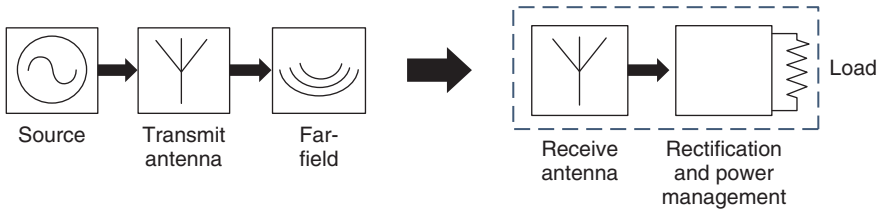


**Figure 15.2** Radiative RF energy transfer system. The dashed box is commonly denoted rectenna.

with the added inconvenience of not being able to move a device around while it is being charged this way.

For RF energy transfer over a distance, we need to employ radiative transfer.

### 15.2.2

#### Radiative Transfer

In a radiative transfer system, an RF source (unintentional or intentional) is connected to an antenna that emits radio waves. At a distance from this radio source, a receiving antenna intercepts a part of the radiated waves and the RF signal captured by the antenna is rectified, eventually to be accumulated and transferred to a load (wireless sensor) (see Figure 15.2). The dashed box in this figure is in fact a *rectifying antenna*, commonly known as *rectenna*.

The power transfer between transmitting antenna and receiving antenna is described by the Friis or transmission equation [5]. The derivation is rather straightforward. If the transmit antenna would radiate equally in all directions, the power density  $S$  (in watts per square meter) of the radio waves at a distance  $r$  from the transmit antenna would be

$$S(r) = \frac{P_T}{4\pi r^2} \quad (15.1)$$

where  $P_T$  is the transmit power delivered to the antenna. This equation simply tells us that the power in the radio waves spreads out spherically. In reality, an antenna will not radiate equally in all directions; it will radiate more in certain directions and less in other directions. The maximum amount of power that it radiates (in the direction of maximum power radiation) relative to radiating the same power delivered to the antenna equally in all directions is called the *gain*  $G_T$ . So the power density at a distance ( $r$ ) in the direction of maximum radiation is

$$S(r) = \frac{P_T G_T}{4\pi r^2} \quad (15.2)$$

The receive antenna, positioned at a distance  $r$  (in the direction of maximum radiation of the transmit antenna), intercepts a part of the radiated power. It intercepts the power density over a so-called effective aperture  $A_{eR}$  (in square meters) so that the received power  $P_R$  is given by

$$P_R(r) = S(r)A_{eR} = \frac{P_T G_T A_{eR}}{4\pi r^2} \quad (15.3)$$

The receiving antenna is not equally sensitive in all directions. It is more sensitive in certain directions and less sensitive in other directions. The distribution of the sensitivity over all directions in receiving mode is equal to the distribution of radiation over all directions in transmitting mode. Antennas are reciprocal. Therefore, we can describe the receive antenna sensitivity also with a gain,  $G_R$ . This gain  $G_R$  is related to the effective aperture  $A_{eR}$  through [5]

$$A_{eR} = \frac{G_R \lambda^2}{4\pi} \quad (15.4)$$

where  $\lambda$  is the wavelength used.

Now substituting Eq. (15.4) in Eq. (15.3) yields the well-know Friis equation:

$$P_R = P_T G_T \frac{G_R \lambda^2}{(4\pi)^2 r^2} \quad (15.5)$$

In using this equation, one has to bear in mind that the equation assumes that both antennas are lined up with respect to gain (having maximum directivity and sensitivity pointing toward each other) and that both antennas are lined up with respect to polarization (transmitting and receiving the electric field in the same direction). Furthermore, the antennas must be operated at a sufficiently large distance from each other so that they do not disturb each other (i.e., they must be positioned in each other's far-field regions [5]). One also has to bear in mind that  $G_T$  and  $G_R$  are only constant for a fixed  $\lambda$ . If  $\lambda$  changes, also  $G_T$  and  $G_R$  change.

### 15.2.3

#### Harvesting versus Transfer

To decide on the feasibility of harvesting RF energy we need to have an idea about our power needs and we have to make an assessment on the power levels that can be harvested. On the basis of state-of-the-art power consumption of commercially available wireless sensors, we aim for a power level of about 100  $\mu\text{W}$  and envisage a wireless sensor node with a few square centimeters (on the casing) available for a receiving antenna.

For RF energy *harvesting*, the most interesting systems to be explored in Europe are GSM900 (downlink: 935–960 MHz), GSM1800 (downlink: 1805.2–1879.8 MHz) and worldwide Wi-Fi (2.4–2.5 GHz). These systems are omnipresent in urban environments and allow antennas of sizes in the order of 10–50  $\text{cm}^2$  [6]. From power density measurements, obtained in a large European survey between 1996 and 2001, it was revealed that the power density integrated over the GSM900 downlink frequency band is expected to be in the range 0.01–0.3  $\mu\text{Wcm}^{-2}$  between 25 and 100 m from a base station, indoors everywhere, and outdoors on an elevated level [7, 6]. Power density levels from GSM1800 are in the same order of magnitude while from Wi-Fi, measured power density levels are 1 order of magnitude lower [8]. This means that using

**Table 15.1** ISM frequency bands of interest for far-field RF energy transfer and E(I)RP restrictions.

Frequency band (MHz)	Power	Dutty cycle/Tx type	Channel spacing/BW	Region
2446–2454	500 mW EIRP 4 W EIRP	Up to 100% $\leq$ 15%	No spacing	Europe
865.0–865.6	100 mW ERP		200 kHz	Europe
865.6–867.6	2 W ERP		200 kHz	Europe
867.6–868.0	500 mW ERP		200 kHz	Europe
902–928	4 W EIRP	FH ( $\geq$ 50 channels) or DSSS		USA Canada
2400–2483.5	4 W EIRP	FH ( $\geq$ 75 channels) or DSSS		USA Canada
2400–2483.5	10 mW EIRP		1 MHz BW	Japan Korea

ambient (GSM900) RF energy, we need to employ antennas occupying at least<sup>1)</sup> 330–1000 cm<sup>2</sup> to power a 100- $\mu$ W application. So, RF energy harvesting is not feasible for the applications we had in mind<sup>2)</sup> and we have to resort to RF energy transfer, that is, bring in our own dedicated RF source.

In doing so, we restrict ourselves to the license-free frequency bands for industry, science, and medicine (ISM) around 868 MHz (Europe), 900 MHz (North America), and 2.4 GHz (worldwide). These frequency bands are limited in the allowed maximum power to transmit [10, 11]. The limitation is on the combination of transmit power  $P_T$  and transmit antenna gain  $G_T$  (see Eq. (15.5)). The product of the two is known as the effective isotropic radiated power (EIRP).

$$P_T G_T = \text{EIRP} \quad (15.6)$$

The EIRP is the power that would be equally radiated in all directions by an isotropic radiator.

The restrictions in transmit power and transmit gain are specified in the EIRP or in the effective radiated power (ERP). ERP is the power that would be radiated by a half-wavelength dipole.

$$\begin{aligned} P_T G_{Td} &= \text{ERP} \\ \text{EIRP} &= 1.64 \text{ERP} \end{aligned} \quad (15.7)$$

The frequency bands of interest and the E(I)RP restrictions are stated in Table 15.1 [6].

- 1) The physical area of an antenna will in general be larger than the effective area. Furthermore, power will be lost in the RF-to-DC conversion and power management manipulations.
- 2) Niche applications requiring very little power and/or using extreme duty cycles, might be operated by RF energy harvesting [9].

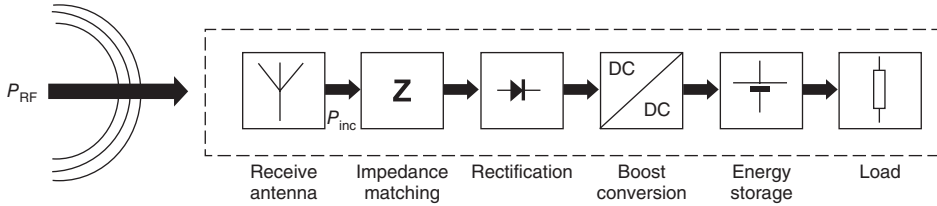


**Figure 15.3** Receiving part of a wireless RF far-field power transfer system.

Now that the RF source part of the far-field RF energy transfer system has been discussed in detail, we can concentrate on the receiving part of the system.

### 15.3

#### Receiving Rectifying Antenna

The receiving part of a wireless RF far-field power transfer system is schematically shown in Figure 15.3. This figure corresponds to the right side of Figure 15.2, but here showing more detail.

The receiver consists of a rectifier, connected at the RF-side to the receiving antenna and on the DC-side to a load. In general, an impedance matching circuit is applied between the antenna and the rectifier. The load – in its most general form – consists of a DC-to-DC boost conversion circuit connected to an energy storage system (battery or capacitor) that is connected to the load (application to be powered). The thus created rectifying antenna is commonly denoted *rectenna*.

#### 15.3.1

##### Antenna – Rectifier Matching

Before going into the details of the rectifier and the antenna, we start with discussing the impedance matching between these subcomponents (Figure 15.4).

In the figure, we have replaced the antenna by an equivalent circuit consisting of a voltage source in series with a resistor. The rectifier and load are combined into a single complex load admittance  $Y_L = G_L + jB_L$ . The matching network is depicted as an “L-network.” This is not a fundamental restriction.

The input power  $P_{in}$  is given by

$$P_{in} = \frac{1}{2} v_{in}^2 \Re\{Y_{in}\} \quad (15.8)$$

where  $Y_{in} = 1/Z_{in}$  is as indicated in Figure 15.4 and  $\Re\{x\}$  denotes the real part of complex variable  $x$ ,  $v_{in}$  is as indicated in Figure 15.4 and follows from applying Kirchhoff's voltage and current laws to the circuit, that is,  $v_s - IR_s = v_{in} = I/Y_{in}$ , where  $I$  is the current flowing through  $R_s$ , so that

$$P_{in} = \frac{1}{2} \left| \frac{1}{1 + Y_{in}R_s} \right|^2 v_s^2 \Re\{Y_{in}\} \quad (15.9)$$

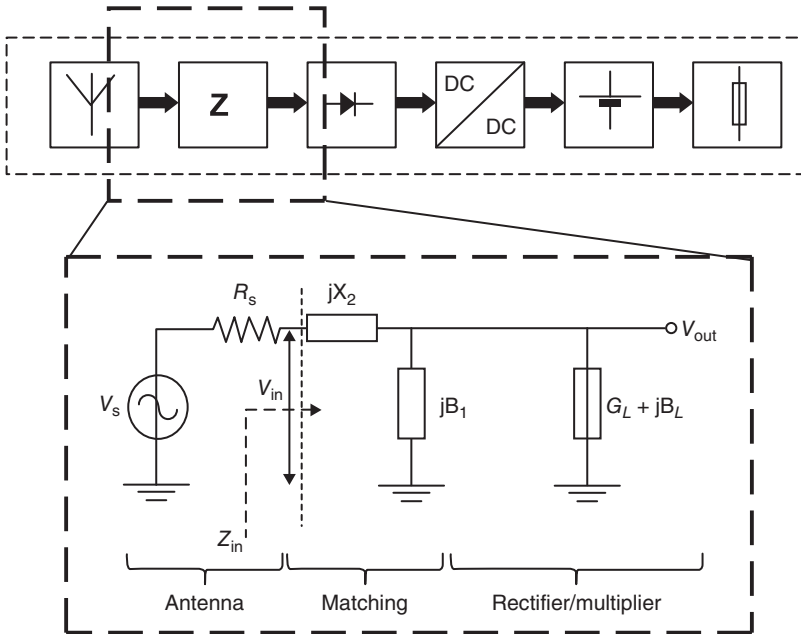


Figure 15.4 Antenna-rectifier matching.

The output power is given by

$$P_{out} = \frac{1}{2} v_{out}^2 \Re\{Y_L\} \tag{15.10}$$

where  $v_{out}$  is as indicated in Figure 15.4 and  $Y_L$  is the admittance as seen at the input of the rectifier/voltage multiplier.

We assume the impedance matching network to be lossless. For a lot of applications this will be a fair assumption and – more importantly – it will simplify the calculations considerably.

### 15.3.1.1 Voltage Boosting Technique

In the last few years, several papers have been published in which a so-called “voltage boosting technique” is proposed to be used for connecting the antenna to the rectifier, see for example, Ref. [8, 12–15]. The technique is based on the voltage gain  $G_v$  of a lossless LC-circuit as shown in Figure 15.5, that is, the ratio of output to input voltage that is given by

$$G_v = \frac{v_{out}}{v_{in}} = \frac{1}{1 - \omega^2 LC} \tag{15.11}$$

where  $\omega = 2\pi f$  is the angular frequency.

At resonance ( $\omega^2 LC = 1$ ), the voltage gain becomes infinite and an infinite voltage (in practice – due to losses – a very high voltage) might be offered to the rectifying circuit. Thus an efficient operation of the diodes or diode-switched FETs in the rectifier will be ensured.

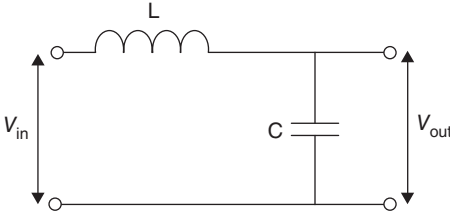


Figure 15.5 Basic RF “voltage boost circuit.”

As has been shown in [16], which will be repeated and expanded here, this is only true for an infinite load impedance of the circuit shown in Figure 15.5.

The reality is that by a proper impedance matching of the antenna to the rectifying circuit, a resonant LC circuit is realized having a fairly high quality factor. So, the high Q-factor is the result of the matching and not the other way around. The output voltage of the matching circuit is dictated by the RF power incident upon the antenna and the input impedance of the rectifying circuit. The value cannot be chosen freely.

To prove this, we will first take a closer look at the situation where the antenna is matched to the rectifier and then we will look at the situation where this matching constraint is waived.

#### 15.3.1.2 Antenna Matched to Rectifier

We will use the L-network shown in Figure 15.4 to complex conjugately impedance-match the antenna to the rectifying circuit. That means that  $Z_{in} = R_s$  or  $Y_{in}R_s = 1$  and – as we are dealing with a lossless network and thus  $P_{out} = P_{in}$  – the voltage gain is given by

$$G_v = \frac{v_{out}}{v_s} = \frac{1}{2} \sqrt{\frac{\Re\{Y_{in}\}}{\Re\{Y_L\}}} \quad (15.12)$$

From Figure 15.4, we can calculate the input impedance as

$$Z_{in} = jX_2 + \frac{1}{G_L + j(B_1 + B_L)} = \frac{G_L}{G_L^2 + (B_1 + B_L)^2} + jX_2 - j\frac{B_1 + B_L}{G_L^2 + (B_1 + B_L)^2} \quad (15.13)$$

For  $Z_{in}$  to be equal  $R_s$ , the following conditions apply

$$R_s = \frac{G_L}{G_L^2 + (B_1 + B_L)^2} \quad (15.14)$$

$$X_2 = \frac{B_1 + B_L}{G_L^2 + (B_1 + B_L)^2} \quad (15.15)$$

With the real part of the input admittance now being equal to

$$\Re\{Y_{in}\} = \frac{G_L^2 + (B_1 + B_L)^2}{G_L} \quad (15.16)$$



the voltage gain becomes

$$G_v = \frac{v_{\text{out}}}{v_s} = \frac{1}{2} \sqrt{1 + \left( \frac{B_1 + B_L}{G_L} \right)^2} = \frac{1}{2} \sqrt{1 + Q^2} \quad (15.17)$$

where  $(B_1 + B_L)/G_L$  is the quality factor at the output of the matching circuit.

Up to this point, we have been following [8].

With  $G_L$  and  $B_L$  being defined by the load, that is, the rectifier/multiplier circuit, Eq. (15.17) leaves the impression that by a proper choice of  $B_1$  that we can choose the output voltage  $v_{\text{out}}$  and then determine  $R_s$  and  $X_2$  using Eqs. (15.14) and (15.15), respectively.

The error made in this reasoning is that it implicitly assumes that  $v_s$  and  $R_s$  can be chosen independently, while in fact they are interrelated through the power available from the antenna,  $P_{\text{inc}}$

$$P_{\text{inc}} = \frac{v_s^2}{8R_s} \quad (15.18)$$

Substituting Eqs. (15.18) and (15.14) in Eq. (15.17) now results in

$$v_{\text{out}} = G_v v_s = \sqrt{\frac{2P_{\text{inc}}}{G_L}} \quad (15.19)$$

The voltage at the input of the rectifier/multiplier is thus dictated by the available power from the antenna and the real part of the input admittance of the rectifier/multiplier.

To maximize  $v_{\text{out}}$  which will be beneficial for the RF-to-DC power conversion efficiency (PCE) as well as for the DC output voltage level, we thus need to design a rectifier/multiplier having a real part of the input admittance that is as low as possible.

Before discussing the rectifier/multiplier, we will first take a look at the situation where we waive the constraint of complex conjugate matching.

### 15.3.1.3 Antenna Not Matched to the Rectifier/Multiplier

When the antenna is not matched to the rectifier/multiplier,  $Y_{\text{in}}R_s \neq 1$  and

$$\left| \frac{1}{1 + Y_{\text{in}}R_s} \right| = \frac{1}{\sqrt{(1 + G_{\text{in}}R_s)^2 + B_{\text{in}}^2 R_s^2}} \quad (15.20)$$

where

$$Y_{\text{in}} = \Re\{Y_{\text{in}}\} + j\Im\{Y_{\text{in}}\} = G_{\text{in}} + jB_{\text{in}} \quad (15.21)$$

The output voltage  $v_{\text{out}}$  is then calculated as

$$v_{\text{out}} = \sqrt{\frac{2P_{\text{inc}}}{G_L}} \cdot 2 \sqrt{\frac{G_{\text{in}}R_s}{(1 + G_{\text{in}}R_s)^2 + B_{\text{in}}^2 R_s^2}} \quad (15.22)$$

The output voltage is identical to the output voltage for the matched situation times a multiplicative factor. This factor will be equal to 1 for the case where

$G_{in} = 1/R_s$  and  $B_{in} = 0$  (matched situation) and will be smaller than 1 for all other cases. So, for voltage maximization, the antenna should be impedance matched.

#### 15.3.1.4 Consequences for the Rectifier and the Antenna Design

We have seen that for a maximum power transfer and for creating a maximum voltage at the input of the rectifier (i.e., for a maximum sensitivity), the voltage at the output of the antenna-to-rectifier matching circuit  $v_{out}$  should satisfy

$$v_{out} = \sqrt{\frac{2P_{inc}}{G_L}}. \quad (15.23)$$

In terms of the rectifier's input impedance  $Z_L = R_L + jX_L$ , where  $Z_L = 1/Y_L$ , this condition becomes

$$v_{out} = \sqrt{2P_{inc} \frac{R_L^2 + X_L^2}{R_L}}. \quad (15.24)$$

This means that for maximizing the voltage at the input of the rectifier (which is the voltage at the output of the antenna-to-rectifier matching circuit), we should either design a rectifier for a maximum input resistance and minimum absolute value of the input reactance or the other way around.

## 15.4 Rectifier

The most basic rectifier consists of a single diode. When lumped elements are used, a Schottky diode is preferred owing to its very fast switching action and low forward bias voltage compared to other diode types. Figure 15.6 shows the diode in a series configuration (the preferred configuration for RF energy harvesting [17]) with a source  $V_g$  and load. In this circuit, the Schottky diode is represented by the equivalent electric circuit of a packaged diode (dashed box). The source has

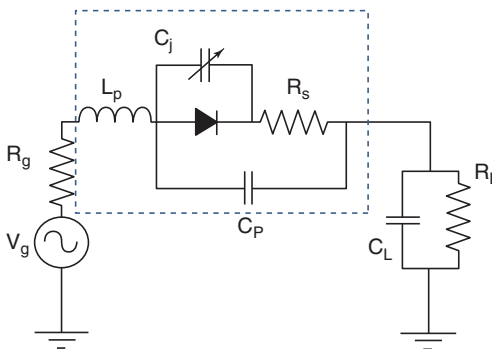


**Figure 15.6** Packaged Schottky diode (dashed box) in series configuration with a source and load.

an internal resistance  $R_g$  and the load consists of a resistor  $R_L$  in parallel with a capacitor  $C_L$ .

The resistance  $R_s$  represents the conduction losses in the diode's substrate. This value may be found in the diode's data sheet.  $C_j$  is the capacitance formed by the two diode contacts and the substrate. The value of  $C_j$  depends on the applied voltage  $v_d$  over the ideal diode [18]

$$C_j(v_d) = \frac{C_{j0}}{\sqrt{1 - v_d/\varphi}} \quad (15.25)$$

where  $C_{j0}$  is the zero-bias differential barrier capacitance and  $\varphi$  is the barrier potential of the diode. Values for these parameters may be found in the diode's data sheet. The relation between the voltage  $v_d$  over and the current  $i_d$  through the ideal diode in Figure 15.6 is given by

$$i_d = I_s \left( e^{\frac{q}{nkT} v_d} - 1 \right) \quad (15.26)$$

where  $I_s$  is the saturation current,  $q$  is the electron charge,  $k$  is Boltzmann's constant,  $T$  is the temperature (kelvin) and  $n$  is the ideality factor of the diode.  $I_s$  and  $n$  may be found in the diode's data sheet.  $C_p$  and  $L_p$  are the parasitic packaging capacitance and inductance, respectively. The values may again be found in the diode's data sheet.

#### 15.4.1

##### RF Input Impedance

The RF input impedance may be obtained by applying a harmonic balance simulation, employing commercially available software. An alternative analysis method is provided by the fourth-order Runge–Kutta (RK4) time-marching algorithm, provided that a sufficiently large capacitor  $C_L$  is applied ( $C_L \geq 0.1 \mu\text{F}$ , for  $0.1 \text{ GHz} < f < 2.5 \text{ GHz}$  [16]). Then the load may be considered as a short circuit. This applies to most commercially available Schottky diodes in the range of frequencies  $f$  stated. The differential equations describing the system shown in Figure 15.6 for a short-circuit load are given by [17]

$$\begin{aligned} \frac{dv_d}{dt} &= \frac{1}{R_s C_j} \left[ V_g - R_g I_g - v_d - L_p I_x - R_s I_s \left( e^{\frac{q}{nkT} v_d} - 1 \right) \right] \\ \frac{dI_x}{dt} &= \frac{1}{C_p L_p} \left[ I_s \left( e^{\frac{q}{nkT} v_d} - 1 \right) + C_j \frac{dv_d}{dt} + C_p \frac{dV_g}{dt} - C_p R_g I_x - I_g \right] \\ \frac{dI_g}{dt} &= I_x \end{aligned} \quad (15.27)$$

The system parameters  $v_d$ ,  $I_g$ , and  $I_x$  are known at time  $t = t_0$ , as is  $dV_g/dt$ , the time derivative of the impressed generator (source) voltage. We choose, at  $t = t_0$ ,  $v_d = I_g = I_x = dV_g/dt = 0$  and solve the system with an RK4 method employing an adaptive step-size algorithm.  $V_g$  follows from the relation between generator

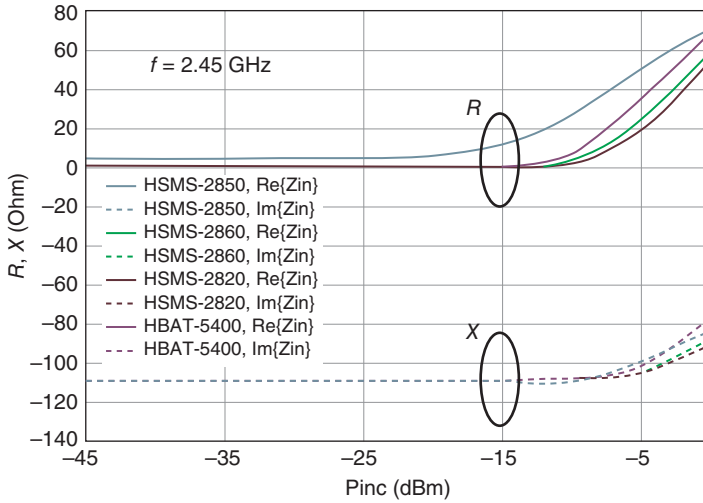


**Figure 15.7** Input impedance versus  $P_{inc}$  at  $f = 2.45$  GHz for a number of commercially available Schottky diodes.

voltage and available incident power  $P_{inc}$

$$P_{inc} = \frac{|V_g|^2}{8R_g} \tag{15.28}$$

The input impedance in the frequency domain is finally obtained after applying a Fourier transform.

As an example, Figure 15.7 shows the calculated real and imaginary parts of the input impedance as a function of available power  $P_{inc}$  at a frequency  $f = 2.45$  GHz for a number of commercially available Schottky diodes. Measurement results may be found in [17].

We do see that at low input power levels ( $P_{inc} < -10$  dBm), the input impedance satisfies the conditions for high sensitivity and RF-to-DC power conversion (Eq. (15.24)): the real part of the input impedance is low and the absolute value of the imaginary part is high.

#### 15.4.2

#### DC Output Voltage

The RK method fails for analyzing the DC behavior of the circuit shown in Figure 15.6. Owing to the RC time of the load being much larger than the period of the source, the equations tend to become stiff [6]. Therefore, an approximate – Ritz–Galerkin averaging – method [19] is being used for calculating the DC output voltage. The output voltage  $V_0$  is implicitly given by [19]

$$B_0 \left( \frac{q}{nkT} \sqrt{8R_g P_{inc}} \right) = \left( 1 + \frac{V_0}{R_L I_s} \right) e^{\left( 1 + \frac{R_g + R_s}{R_L} \right) \frac{q}{nkT} V_0} \tag{15.29}$$

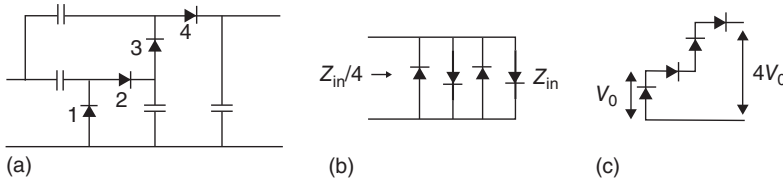


**Figure 15.8** Four-stage voltage multiplier. (a) Circuit topology, (b) RF equivalent circuit, and (c) DC equivalent circuit.

In this equation,  $B_0$  is the zero-order modified Bessel function of the first kind; all other parameters have already been specified.

For increasing the DC output voltage,  $N$  diodes may be connected in cascade to create an  $N$ -times multiplier; see Figure 15.8 for  $N = 4$ .

The topology of the Villard cascaded multiplier is shown in Figure 15.8a. The RF input impedance can be determined using the equivalent circuit shown in Figure 15.8b that is obtained by considering the capacitors as short circuits. The input impedance is that of a single diode divided by the number of cascaded sections. The DC output voltage is determined – in a first order approximation – by considering the capacitors as open circuits, which leads to the equivalent circuit shown in Figure 15.8c, which is regarded as a series circuit of individual diode “DC voltage sources.”

While the RF input impedance determination is correct, the DC voltage source series connection is too crude an approximation. A better approximation is obtained by considering the cascaded circuit as a single diode so that Eq. (15.29) may be applied. For converting the cascaded diode circuit into a single diode, the transformation as described in [20] is partly applied. The generator resistance  $R_g$  is multiplied by  $N$ , the load resistance  $R_L$  is divided by  $N$ , but the voltage  $V_0$  is *not* multiplied by  $N$  [16].

$$B_0 \left( \frac{q}{nkT} \sqrt{8NR_g P_{\text{inc}}} \right) = \left( 1 + \frac{NV_0}{R_L I_s} \right) e^{\left( 1 + \frac{N^2 R_g + NR_s}{R_L} \right) \frac{q}{nkT} V_0} \quad (15.30)$$

This approximation yields fair results up to  $N = 6$  in the available power range  $-15 \text{ dBm} < P_{\text{inc}} < 0 \text{ dBm}$ . Figure 15.9 shows thus simulated results for multipliers based on the Avago HSMS-2850 Schottky diode [21] for  $N = 2$  and  $N = 4$  at a frequency  $f = 2.45 \text{ GHz}$ .

Equations (15.29) and (15.30) do not take the junction capacitance and therefore the frequency dependence into account. As is shown by the measurement results for a voltage doubler ( $N = 2$ ) in Figure 15.10, this is a valid simplification.

Although the DC output voltage is more or less frequency independent, the same is not true for the RF input impedance. Therefore, the design of a rectenna should start with the characterization of the input impedance of the rectifier/multiplier.

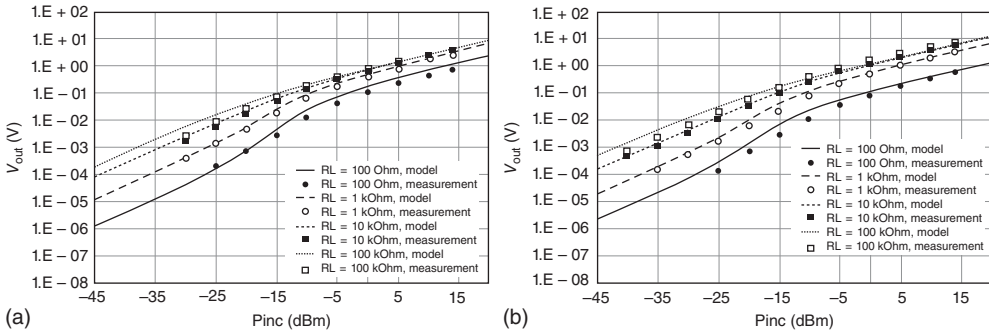


**Figure 15.9** Calculated and measured DC output voltage as a function of available power for cascaded HSMS-2850 Schottky diodes at  $f = 2.45$  GHz. (a)  $N = 2$  and (b)  $N = 4$ .  $R_g = 50 \Omega$ .

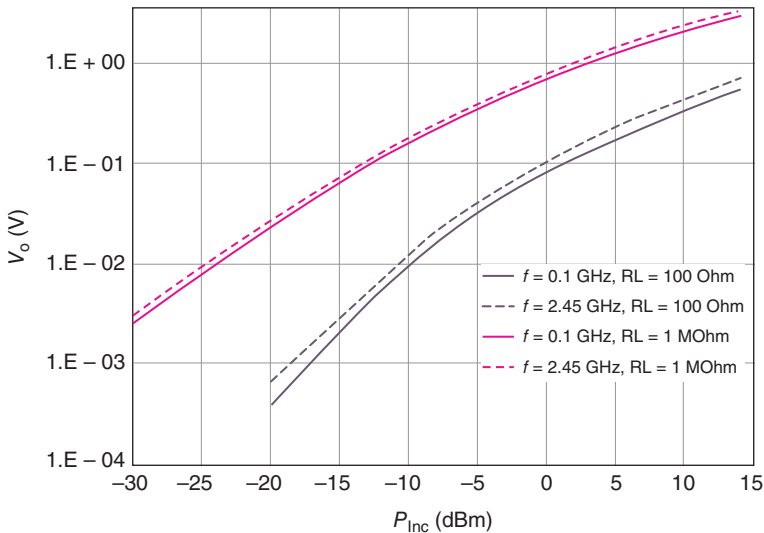


**Figure 15.10** Measured DC output voltage as a function of available power for a HSMS-2850-based voltage doubler at  $f = 0.1$  GHz and  $f = 2.45$  GHz.

15.4.3

**Antenna**

In a rectenna, an antenna needs to be connected to a rectifier/multiplier. Once the frequency or frequency band has been decided upon, we need to start with determining the input impedance of the rectifier/multiplier.

As an example we will make a rectenna to be operated in the 868-MHz European license-free frequency band for ISM for an assessed input power level  $P_{in} = -10$  dBm ( $100 \mu\text{W}$ ), that is, the power at the clamps of the receiving antenna. As a rectifier/multiplier we will use a voltage doubler based on the Avago

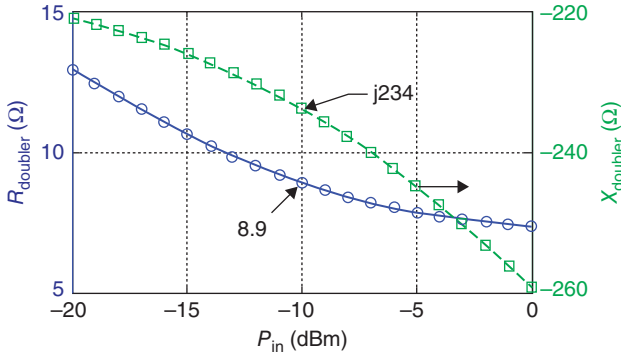


**Figure 15.11** Simulated real and imaginary parts of the input impedance of an Avago HSMS-2850 Schottky diode based voltage doubler versus input power  $P_{in}$  at a frequency  $f = 868$  MHz.

HSMS-2850 Schottky diode [21]. Using ADS harmonic balance simulation, the input impedance  $Z_{doubler} = R_{doubler} + jX_{doubler}$  is determined as a function of input power  $P_{in}$ . The results are shown in Figure 15.11.

We do see that, again, the rectifier/multiplier satisfies the requirements for obtaining a high sensitivity and RF-to-DC PCE.

Now, we may proceed in two ways. We can either use a “standard” 50- $\Omega$  antenna and employ an impedance matching circuit between the antenna and the rectifier/multiplier or we can design an antenna having an input impedance that is the complex conjugate value of the rectifier’s input impedance.

#### 15.4.3.1 50 $\Omega$ Antenna

A printed Yagi–Uda-like antenna that has been introduced in [22] and described in detail in [23] is used as a 50- $\Omega$  antenna. The antenna is printed on a 1.6-mm-thick FR4 board ( $\epsilon_r = 4.3$ ), see Figure 15.12a. The other dimensions are as shown in Figure 15.12b.

The matching circuit consists of a 1-pF lumped element capacitor and a 32-nH lumped element inductor, as shown in Figure 15.13, see also Figure 15.11.

Before discussing the rectenna results, we will first discuss the complex conjugately matched antenna.

#### 15.4.3.2 Complex Conjugately Matched Antenna

If we want to design an antenna that is directly impedance matched to the antenna, that is, without using an impedance matching circuit, we need to design an antenna having input impedance that is the complex conjugate of the rectifier’s input impedance. That means that we must design an antenna with a low resistive part of the input impedance. To realize such an antenna, we must make the antenna electrically small. Furthermore, we must design the antenna such that it has a relatively high inductance, which means that we need a small loop antenna to start with.

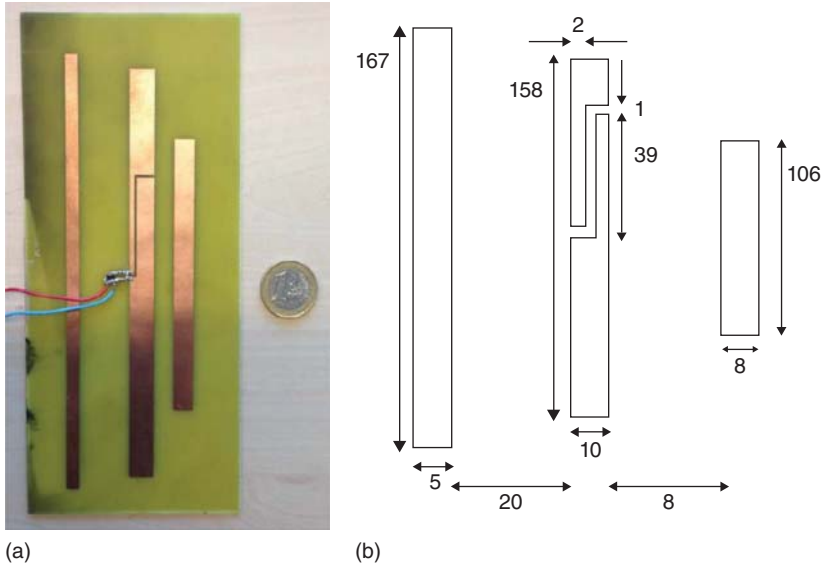


**Figure 15.12** A  $50\text{-}\Omega$ ,  $f = 868\text{MHz}$ , printed Yagi–Uda-like antenna. (a) Antenna printed on FR4 and connected via an impedance matching circuit to the rectifier. (b) Planar antenna dimensions in millimeters.

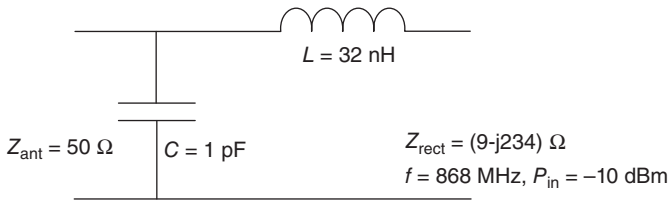


**Figure 15.13** Impedance-matching circuit for  $f = 868\text{MHz}$  and  $P_{in} = -10\text{dBm}$ .

Starting with a small loop, the printed antenna shown in Figure 15.14b has been realized.

We see that with respect to the  $50\text{-}\Omega$  antenna (Figure 15.14a), the antenna has been miniaturized considerably. The additional arms in the loop are used for impedance control. With the shown antenna, input impedance and radiation efficiency can be controlled independently. Enlarging the outer loop will increase the radiation efficiency.

#### 15.4.4 Rectenna Results

Using both antennas (the  $50\text{-}\Omega$  one and the compact one), rectennas have been made for characterization purposes only. Therefore, the rectennas consist of an



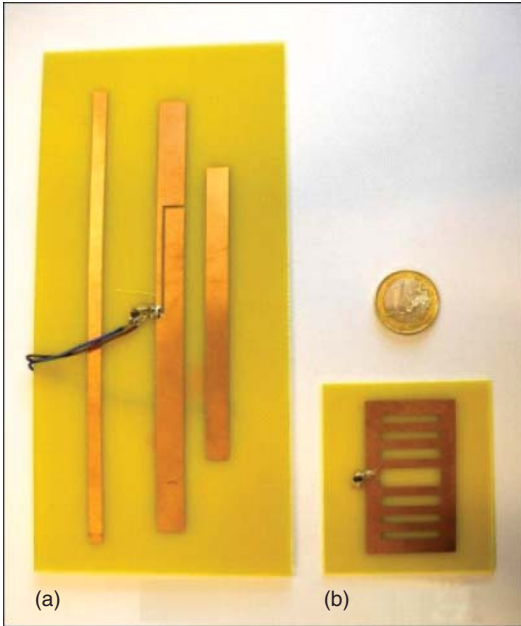


**Figure 15.14** Prototyped rectennas (a) 50- $\Omega$  antenna with impedance-matching circuit. (b) Complex conjugately impedance-matched antenna.

antenna, eventually an impedance matching circuit, and a voltage doubler rectifier/multiplier loaded with a parallel capacitor and resistor.

Figure 15.15 shows the measured DC output voltage as a function of the load resistor  $R_L$  for both rectennas in the situation where a transmitter has been used such that the power at the clamps of the 50- $\Omega$  antenna that is before the matching circuit is  $-10$  dBm.

We do see that the rectenna based on the 50- $\Omega$  antenna with matching circuit yields up to twice the DC output voltage of the rectenna based on the compact antenna. This is mainly due to the difference in gain of both antennas. The gain of the 50- $\Omega$  antenna is 4.2 dBi while the gain of the compact antenna is 1.2 dBi. Therefore, the power at the input of the rectifier/multiplier in combination with the compact antenna is about half that for the rectenna with the 50- $\Omega$  antenna. (The word “about” has been used because the losses of the matching circuit have not been taken into account.)

For a fair comparison of the RF-to-DC PCE, the transmitter power is tuned such that for the rectenna with the compact antenna  $-10$  dBm is present at the clamps of the antenna. The PCE is then obtained from

$$\text{PCE} = \frac{P_{\text{load}}}{P_{\text{in}}} = \frac{V_{\text{DC}}^2}{R_L} \frac{1}{P_{\text{in}}} \quad (15.31)$$

The measurement results for both rectennas (PCE vs  $R_L$  for  $f = 868$  MHz) are shown in Figure 15.16.

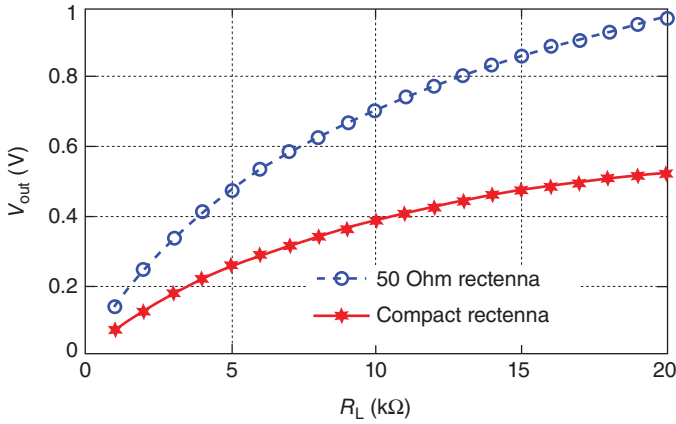


**Figure 15.15** DC output voltage of the rectennas shown in Figure 15.14 as a function of  $R_L$  for the situation where the transmit power of a distant transmitter at  $f = 868$  MHz is tuned such that the power at the clamps of the 50- $\Omega$  antenna is  $P_{in} = -10$  dBm.

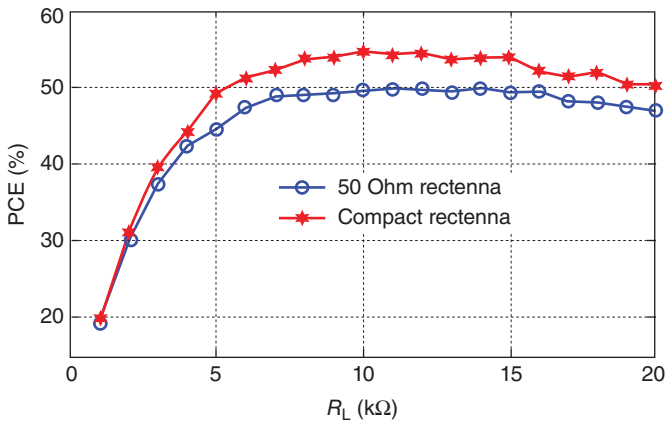


**Figure 15.16** PCE of the rectennas shown in Figure 15.14 as a function of  $R_L$ . For  $P_{in} = -10$  dBm and  $f = 868$  MHz.

We see that in this comparison the rectenna with compact antenna is up to 5% more efficient than the rectenna with 50- $\Omega$  antenna and impedance matching circuit. The difference is due to the losses in this matching circuit.

So, owing to the high input reactance and low input resistance of a Villard type rectifier/multiplier, we can design a high-sensitivity and high-PCE rectenna that is very small in size. Although this is a desirable feature for most wireless sensor applications where size is a tight constraint, the drawback of employing a small receiving antenna is the limited DC output voltage that may be obtained

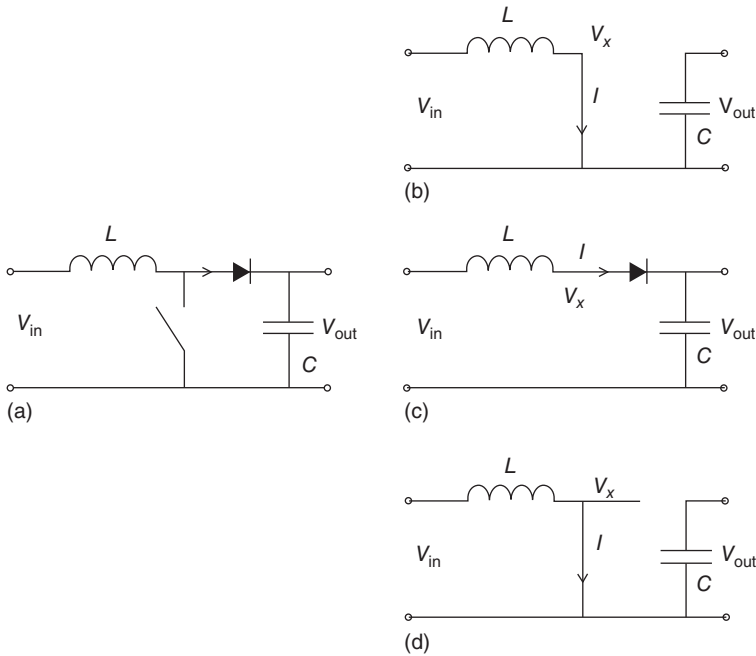


**Figure 15.17** Inductive voltage boost converter. (a) Basic circuit, (b) switch on, (c) switch off, and (d) switch on again.

(see Figure 15.15). If the size of the antenna cannot be increased, we will need to employ voltage-boosting techniques.

#### 15.4.5

#### Voltage Up-Conversion

Voltage-up or boost conversion may be accomplished by switching reactive components. Figure 15.17a shows a basic inductive boost converter. The switch (an FET device) is turned on and off by a periodic (clock) signal.

When the switch is turned “on,” a current  $I$  is flowing through the inductance  $L$  (Figure 15.17b). The voltage  $V_x$  is identical to the input voltage,  $V_x = V_{in}$ . The diode is unbiased and the output voltage  $V_{out}$  is the voltage over the capacitor  $C$ . When the switch is turned “off,” the inductor develops a voltage  $V_L$  to keep the current  $I$  flowing. The diode is now forward biased (Figure 15.17c) and the voltage  $V_x = V_{in} + V_L$  is transferred to the capacitor:  $V_{out} = V_{in} + V_L$ . When the switch is turned “on” again (Figure 15.17d) the diode is unbiased. A resistive load will drain the charge from  $C$ . Again  $V_x = V_{in}$ . Upon opening the switch,  $C$  will be recharged again. An example of an inductive boost converter is described in [6].

Although an inductive boost converter has the advantage that, unlike charging of capacitors, the process of charging inductors is not intrinsically lossy [17], the

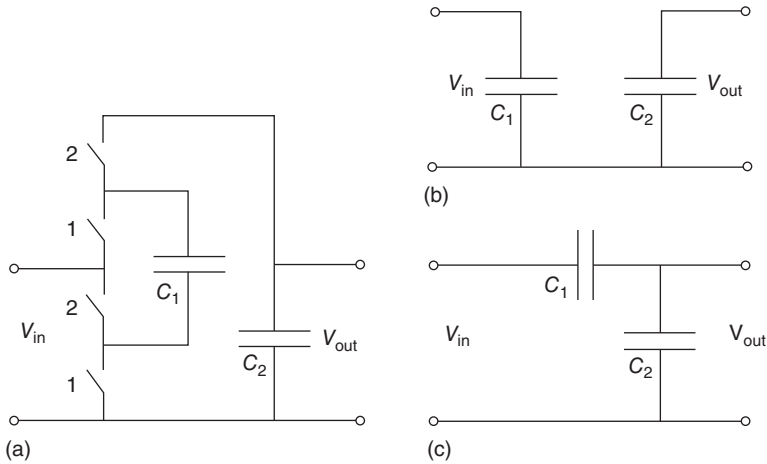


**Figure 15.18** Capacitive voltage boost converter. (a) Basic circuit, (b) switches 1 on, switches 2 off, and (c) switches 1 off, switches 2 on.

implementation is not straightforward and lumped inductors are used often. For an integrated solution, a capacitive boost converter is more convenient.

Figure 15.18a shows a basic capacitive boost converter. The switches (FET devices) are pair-wise turned on and off by periodic, in anti-phase (clock) signals.

When the switches 1 are “on” and the switches 2 are “off,” the equivalent electrical circuit is the one shown in Figure 15.18b. The voltage over capacitor  $C_1$ ,  $V_C$  is equal to  $V_{in}$  and the output voltage  $V_{out}$  is equal to the voltage over capacitor  $C_2$ . When switches 1 are now opened and switches 2 are closed, the circuit is represented by the equivalent electrical circuit of Figure 15.18c. The output voltage is now  $V_{out} = V_{in} + V_C$ .

To maximize the efficiency of the voltage boost converter, its dynamic range should be minimized (see Ref. [6]). Thus the voltage at the input and so the voltage at the input of the rectifier should be maximized using the techniques described earlier. With the voltage boost converter we have finished describing the rectenna. Apart from the receiving side we may also influence the transmitting and propagation part of the system.

## 15.5

### Transmission

While the propagation of radio waves in free space (no obstacles or boundaries) is accurately described by the Friis equation (Eq. (15.5)),

$$P_R = P_T G_T \frac{G_R \lambda^2}{(4\pi)^2 r^2} \quad (15.32)$$

in indoor situations the propagation is more complicated. The spherical spreading of the waves – commonly known as *path loss*  $P_L$ <sup>3)</sup> – may in first order be given by [24–27]

$$P_L(r)|_{\text{dB}} = 20 \log \left( \frac{4\pi r_0}{\lambda} \right) + 10n \log \left( \frac{r}{r_0} \right) \quad (15.33)$$

where  $r$  is the distance and  $r_0$  is a reference distance and  $n$  equals 2 for free space. For line of sight,  $n$  may vary from 0.8 in a highly reflective environment to 1.8 in a common indoor environment [6].

A transmit antenna that can adaptively produce multiple beams that are directed to the rectenna directly and to the reflection points that result in a constructive interference with the direct contributions at the rectenna, may help in optimizing the power transfer. Such a transmit antenna could be a switched-array antenna, forming a cost-effective alternative to the phased-array antenna [20].

## 15.6

### Examples and Future Perspectives

The examples of far-field wireless RF energy transfer shown in this section are mostly demonstrators showing the feasibility of the concept. Because of this demonstration characteristic, most examples are completely (rechargeable) battery-free. For that same reason, most examples do not use a DC-to-DC voltage up-converter. The converter that is being used in one demonstrator needs the rechargeable battery that is being charged for providing start-up power.

The first example shows two wireless RF-powered clocks (see also Ref. [6]). An array of rectennas is used to deliver 1.2 V or more to a standard electric wall clock at a distance of a few meters from a 1-W EIRP source at 2.45 GHz (Figure 15.19).

The elements of the array of rectennas are either a strip-folded dipole antenna connected to a HSMS-2852 Schottky diode-based voltage doubler or a microstrip patch antenna connected to the same type of rectifier. The DC outputs of the individual rectennas are connected in series to create the voltage needed to operate the electric clock positioned at the desired distance from the source. A voltage boost converter is not being used. The elements are optimized for an RF input power of 0 dBm.

Figure 15.20 shows a demonstrator-setup wherein two rectennas – one operating in the 900-MHz GSM frequency band, the other one operating in the 2.4-GHz Wi-Fi frequency band – are combined and used to collect power emitted by a

3) Path loss,  $(4\pi r/\lambda)^2$ , might easily give the impression that there is actually such a thing as loss and that this loss is frequency dependent. What we actually see in the Friis equation is that radio waves spread out spherically. The wavelength in the “path loss term” is compensated for by the gain of the (receive) antenna that is inversely proportional to this wavelength. Often the Friis equation is wrongly interpreted, assuming that the gains in the equation are constants.



**Figure 15.19** Wireless RF-powered wall clocks. Left: clock powered by an array of folded-dipole rectennas. Right: clock powered by an array of microstrip patch rectennas.



**Figure 15.20** Smartphone-operated temperature sensor and display. Through a QR-code the smartphone is connecting to the Internet, thus transmitting power – either in the GSM or Wi-Fi frequency bands – that is partly intercepted by the dual-frequency rectenna.

smartphone. The power is used to operate a temperature sensor and liquid crystal display.

The rectennas are both based on Yagi–Uda strip antennas, where the higher-frequency antenna functions as a director of the lower-frequency antenna. Both antennas are directly impedance matched to a voltage-doubling rectifier and are optimized for 0-dBm RF input power.



**Figure 15.21** Mobile phone, powered by the 2.45-GHz signals leaking through the filter in the door of a microwave oven. The harvesting system consists of two microstrip patch antenna-based rectennas.



**Figure 15.22** Wireless RF battery consisting of a microstrip patch antenna, conjugately matched to a voltage-doubling rectifier that is connected to a discrete, inductive boost converter, charging a 3-V Li-ion battery.

Figure 15.21 shows an array of two microstrip patch antenna-based rectennas [6], directly connected (that is without energy storage or energy management systems) to the DC input of a GSM phone. With the aid of a magnet, the system is connected to the door of a microwave oven, and the 2.45-GHz RF signal leaking through the (frequency-selective surface) filtering, screen in the door is used to charge the phone's battery. The electronics of the phone is used for energy management.

As a final example, we show the microstrip patch antenna-based rectenna, combined with a DC-to-DC voltage boost converter and rechargeable 3-V Li-ion battery (Figure 15.22).

The figure shows the wireless RF battery together with a commercially available wireless temperature sensor. The sensor operates at 3 V and requires an average power of  $55 \mu\text{W}$ . The boost converter requires  $18 \mu\text{W}$  [6] and leaves room for improvement. Obeying international EIRP restrictions, this sensor may be

powered over a distance of several meters. More rectenna examples may be found in [6].

With the feasibility of far-field RF energy transfer shown, it remains to optimize far-field wireless power transfer systems. On the one hand, a need exists for ultralow power applications. On the other hand, the rectenna needs to be carefully designed. The available power level needs to be well assessed, (integrated) rectifiers need to be co-designed with the antenna (see Ref. [28] for example) and if possible, the transmit antenna radiation pattern needs to be adaptable. Adaptive impedance matching at the rectenna side is one of the possibilities to further improve on the power transfer system.

## 15.7

### Conclusions

The anticipated growth in the use of mobile and wearable, wireless devices asks for alternative sources for powering these devices or charging their batteries. Even though the development of ultra-low-power electronics is progressing, using ambient RF energy as a power source is only feasible now for some niche applications requiring a minimum of power and that operate with extremely low duty cycles, due to the low power densities available from the ambient.

RF powering over a distance (radiating or far-field RF energy transfer), within the internationally agreed EIRP limits, is feasible but requires a careful adjustment of all the subsystems in a wireless far-field powering system, namely, the transmit antenna, propagation channel, receive antenna, rectifier design, antenna-to-rectifier impedance matching, boost converter design, and load.

Adaptivity, both at the transmit and the receive sides of a far-field, the wireless power transfer system is seen as one of the possibilities to further improve on the power transfer technology.

### References

1. Vullers, R.J.M., van Schaijk, R., Visser, H.J., Penders, J., and Van Hoof, C. (2010) Energy harvesting for autonomous wireless sensor networks. *IEEE Solid-State Circuits Mag.*, 29–38.
2. Qi Wireless Power Consortium <http://www.wirelesspowerconsortium.com/technology/> (accessed 16 January 2014).
3. Kurs, A., Karalis, A., Moffet, R., Joannopoulos, J.D., Fisher, P., and Soljačić, M. (2007) Wireless power transfer via strongly coupled magnetic resonances. *Science*, **317** (5834), 83–86.
4. Mayordomo, I., Dräger, T., Spies, P., Bernhard, J., and Pflaum, A. (2013) An overview of technical challenges and advances of inductive wireless power transmission. *Proc. IEEE*, **101** (6), 1302–1311.
5. Balanis, C.A. (1997) *Antenna Theory, Analysis and Design*, 2nd edn, John Wiley & Sons, Inc., New York.
6. Visser, H.J. and Vullers, R.J.M. (2013) RF energy harvesting and transport for wireless sensor network applications: principles and requirements. *Proc. IEEE*, **101** (6), 1410–1423.



7. Visser, H.J., Reniers, A.C.F., and Theeuwes, J.A.C. (2008) Ambient RF energy scavenging: GSM and WLAN power density measurements. *European Microwave Conference*, pp. 721–724.
8. Shamel, A., Safarian, A., Rofougaram, A., Rofougaram, M., and de Flaviis, F. (2007) Power harvester design for passive UHF RFID tag using a voltage boosting technique. *IEEE Trans. Microwave Theory Tech.*, **55** (6), 1089–1097.
9. Pinuela, M., Yates, D.C., Lucyszyn, S., and Mitcheson, P.D. (2012) Current State of Research at Imperial College London in RF harvesting and inductive power transfer. *International Workshop on Wireless Energy Transport and Harvesting*, 4 pp.
10. European Radiocommunications Committee (2009) ERC Recommendation 70-03 Relating to the Use of Short Range Devices (SRD), ERC/REC 70-03.
11. Federal Communications Commission (2002) Code of Federal Regulations, Title 47, Part 15, 2002.
12. Le, T., Mayaram, K., and Fiez, T. (2008) Efficient far-field radio frequency energy harvesting for passively powered sensor networks. *IEEE J. Solid-State Circuits*, **43** (5), 1287–1302.
13. Urgan, T., Le Polozec, X., Walker, W., and Reindl, L. (2009) RF energy harvesting design using high Q resonators. *IEEE MTT-S International Microwave Workshop on Wireless Sensing, Local Positioning and RFID, IMWS2009*, 4 pp.
14. Ogawa, K., Ozaki, K., Yamada, M., and Honda, K. (2012) High-efficiency small-sized rectenna using high-Q LC resonator for long distance WPT at 950 MHz. *IEEE MTT-S International Microwave Workshop Series on Innovative Wireless Power Transmission: Technologies, System and Applications, CIMWS2012*, pp. 255–258.
15. Yamashita, T., Honda, K., and Ogawa, K. (2013) High efficiency mw-band rectenna using a coaxial dielectric resonator and distributed capacitors. *International Symposium on Electromagnetic Theory, IEICE2013*, pp. 823–826.
16. Visser, H.J., Pop, V., Op het Veld, B., and Vullers, R.J.M. (2010) Remote RF battery charging. *PowerMEMS*, pp. 37–40.
17. Pinuela, M., Mitcheson, P.D., and Lucyszyn, S. (2010) Analysis of scalable rectenna configurations for harvesting high frequency electromagnetic ambient radiation. *PowerMEMS*, pp. 41–44.
18. Fleri, D.A. and Cohen, L.D. (1973) Non-linear analysis of the Schottky-barrier mixer diode. *IEEE Trans. Microwave Theory Tech.*, **21** (1), 39–43.
19. Harrison, R.G. and Le Polozec, X. (1994) Nonsquarelaw behavior of diode detectors analyzed by the ritz-galerking method. *IEEE Trans. Microwave Theory Tech.*, **42** (5), 840–846.
20. Agilent Technologies (1999) Designing the Virtual Battery, Application Note 1088.
21. Avago Tech (2009) HSMS-285x Series, Datasheet.
22. Keyrouz, S., Perotto, G., Visser, H.J., and Tijhuis, A.G. (2012) Novel broadband Yagi-Uda antenna for ambient energy harvesting. *European Microwave Conference EuMC2012*, pp. 518–521.
23. Keyrouz, S. and Visser, H.J. (2013) Efficient direct-matching rectenna design for RF power transfer applications. *PowerMEMS*, 4 pp.
24. Phaiboon, S., Phokharatkul, P., Somkuarnpanit, S., and Boonpiyathud, S. (2005) Upper- and lower-bound path-loss modeling for indoor line-of-sight environments. *Proceedings Asia-Pacific Microwaves Conference*.
25. Duangsuwan, S., Lenkachorn, T., Chinsawatpand, S., and Prongwang, S. (2009) Experimental study of polarimetric measurement of rfid transfer function within an indoor environment. *Proceedings Malaysia International Conference on Communications*, pp. 686–690.
26. Hwu, S.U., Loh, Y.-C., and Sham, C.C. (2004) Propagation characteristics of international space station wireless area network. *Proceedings Radio and Wireless Conference*, pp. 407–410.

27. Molkar, D. (1991) Review on radio propagation into and within buildings. *IEEE Proc.*, **138** (1), 61–73.
28. Stoopman, M., Keyrouz, S., Visser, H.J., Philips, K., and Serdijn, W.A. (2013) Co-design of a 90 nm CMOS rectifier and small loop antenna for large range RF energy harvesters. Proceedings VLSIC, 2013, pp. C226–C227.

## 16

### Microfabricated Microbial Fuel Cells

*Hao Ren and Junseok Chae*

#### 16.1

##### Introduction

Significant progress has been made in micro-electro-mechanical-system (MEMS) and lab-on-a-chip through successful miniaturization of sensors, actuators, and systems [1]. Microfabrication, the technology adopted in standard semiconductor manufacturing industry such as thin film deposition, photolithography, etching, has driven MEMS and lab-on-a-chip toward batch fabrication, low expense, and precisely controlled geometry. Besides popularly commercialized MEMS sensors and actuators, MEMS-based energy harvest applications have been an active research recently, including piezoelectric energy harvester, thermoelectric energy harvester, MEMS fuel cell [2–4]. MEMS microbial fuel cell (MFC), one of many endeavors of MEMS fuel cells, is a miniaturized energy converter that harvests electrons produced by microorganisms. The MEMS MFC is a carbon-neutral and renewable energy converter, which became attractive in the past several years because of the growing concern over energy crisis and global warming.

According to prior art, production of both oil and gas will peak within next 20 years [5–7], and afterward our society will suffer from postpeak reduction. Global warming, possibly caused by the green house effect of CO<sub>2</sub> accumulation by the massive fossil energy consumption in the past two centuries, has been a worldwide issue because it may change global climate, increase the sea level, and endanger the lives of plants and animals, and so on. Thus, exploring carbon-neutral, renewable energy is increasingly critical for the sustainability of our planet.

There are quite a few candidates for carbon-neutral, renewable, and sustainable energy sources, including hydroenergy, solar energy, geothermal energy, wind energy, and bioenergy. Among them bioenergy is attractive owing to its abundance and ease of access. A recent report presents that biomass in wastewater contain approximately  $1.5 \times 10^{11}$  kWh of potential energy, equivalent to 17 GW, and agricultural practice could produce  $1.34 \times 10^{12}$  kg of biomass, equivalent to a

power of 600 GW, which could provide 120% of annual electricity generation in the United States [8–12].

MFC is a fuel cell that converts biomass directly to electricity via the catalytic activity of some specific bacteria, named exoelectrogen or anode-respiring bacteria (ARB). MFC is an attractive candidate as it directly converts biomass to electricity with high efficiency, unlike conventional conversion techniques, including methanogenic anaerobic digestion, bioethanol production, incineration, and gasification. During the past 10 years, more than 2000 papers have been published in this area [13]. Of them, most are in macro- or mesoscale forms that aim for wastewater treatment and renewable energy production, bioremediation, and/or power supply for remote sensors in harsh environments. MEMS MFCs, via miniaturization of an MFC to be in micrometer scale, are useful for a small-size power supply or lab-on-a-chip devices for scientific research on exoelectrogen. Since the first MEMS MFC was published in 2002 [14], several research groups have reported microscale MFCs, aiming for exploring fundamental phenomena of exoelectrogen as well as for enhancing the power performance of microscale MFCs [9, 15–24].

Remarkable progress has been made in MEMS MFC since the first MFC was reported in 2002; however, many challenges remain to overcome, and one of them is low power density. The areal and volumetric power densities have improved by more than  $10^4$  and  $10^5$  folds in the past decade, and the highest areal power density of  $0.83 \text{ W m}^{-2}$  and volumetric power density of  $3320 \text{ W m}^{-3}$  have been reported [21]. Yet those areal and volumetric power densities are still approximately 2 orders of magnitudes lower than those of conventional lithium ion battery and hydrogen fuel cell. Thus, enhancing the power density of microfabricated MFCs is still important.

Besides applications as an energy converter, MEMS MFC is useful for scientific studies, including the mechanism of extracellular electron transfer (EET) of exoelectrogen, screening the electricity generation capability of individual exoelectrogen. MEMS MFC enables integrating multiple MFCs on one chip for parallel analysis, thus enhancing the efficiency of analysis, owing to batch fabrication features. Miniaturized MFC-on-a-chip devices also find application in biosensors for toxic chemical detection.

## 16.2

### Fundamentals of MEMS MFC

#### 16.2.1

##### Operation Principle

###### 16.2.1.1 Structure

Figure 16.1 is a schematic illustration of a two-chamber configuration MEMS MFC. The MFC includes two chambers, anode and cathode chambers, separated by an ion exchange membrane, such as PEM (proton exchange membrane). Two

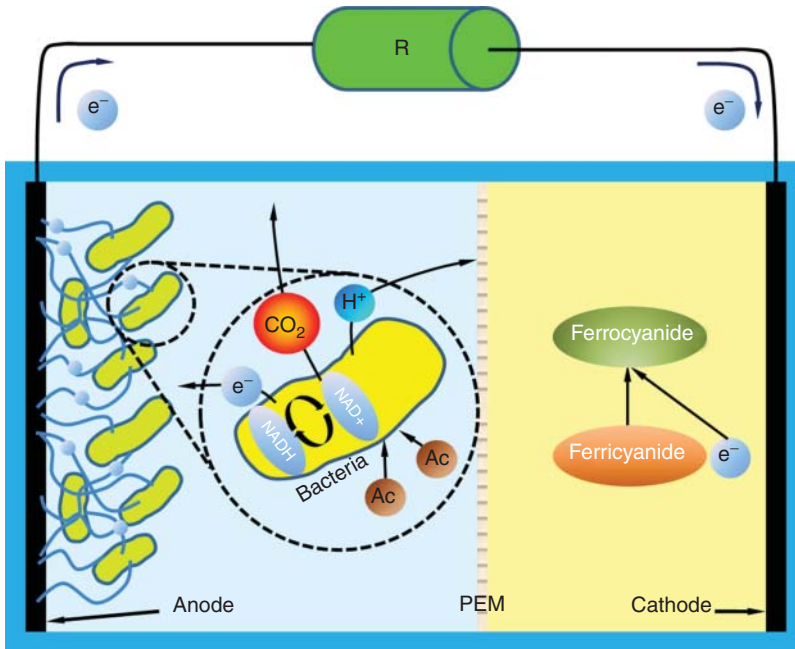


**Figure 16.1** A schematic illustration of a two-chamber MEMS MFC. The MFC includes two chambers, anode and cathode chambers, separated by an ion exchange membrane. Two electrodes, anode and cathode, reside in the anode and cathode chambers, respectively. In operation, specific species of bacteria, named exoelectrogen, which are able to transfer electrons produced by bacterial catabolic reactions outside their outer

membrane, break down organic molecules, such as acetic ions, and generate and transfer electrons to the anode. The electrons can be oxidized by oxidants at the cathode, ferricyanide, after passing through an externally connected load. During this process, electrical current flows through an electrical load, and it can be named a fuel cell that converts chemical energy into electricity.

electrodes, anode and cathode, reside in the anode and cathode chamber, respectively. In operation, specific species of bacteria, named exoelectrogen, which can transfer electrons generated by bacterial catabolic reactions outside their outer membrane, break down organic molecules, such as acetic ion (as shown in the figure), and generate and transfer electrons to the anode. Electrons can be oxidized by oxidants at the cathode, ferricyanide (as shown in the figure), after passing through an externally connected load. During this process, electrical current flows through an electrical load, and it can be named a fuel cell that converts chemical energy into electricity. Besides the conventional two-chamber MEMS MFCs, Mink and Hussain have presented a single-chamber MFC recently, which utilized air cathode [25].

### 16.2.1.2 Materials

**Electrodes** Metal thin film, such as gold, has been used for the electrode material, owing to its excellent conductivity, biocompatibility, and compatibility with microfabrication. Some other electrode materials, such as carbon nanotubes (CNT), carbon cloth, graphene have also been implemented for MEMS MFCs. CNTs and graphene are attractive candidates due to low expense, compatibility with microfabrication, and high conductivity and high surface-area-to-volume ratio.

**Ion Exchange Membrane** An ion exchange membrane allows only specific ions to cross. Two types of ion exchange membranes are typically used in MFCs, cation exchange membrane (CEM) and anion exchange membrane (AEM). CEMs permit only cations to pass and AEMs allow only anions to cross. The majority of MFCs use CEM as membrane, such as Nafion 117, CMI-7000 [22].

**Chamber** Chambers allow the storage of anolyte and catholyte. Conventional MEMS MFCs utilize polydimethylsiloxane (PDMS) as chamber materials or implement PDMS microfluidic channel as chamber. Recently some groups have adopted traditional gaskets into MEMS MFCs, such as silicone gasket [23].

**Exoelectrogen** Diverse microbes have been reported to be capable of oxidizing organic substrates by catabolic reaction and transporting electrons to anode, including the *Geobacter* species (*Geobacter sulfurreducens*, *Geobacter metallireducens*), *Shewanella* species (*Shewanella oneidensis* MR-1, *Shewanella putrefaciens* IR-1, *Shewanella oneidensis* DSP10), *Pseudomonas* species (*Pseudomonas aeruginosa* KRP1), *Rhodopseudomonas palustris* DX-1 [26], *Saccharomyces cerevisiae* [27, 28], *Escherichia coli* [29]. These microbes are often called exoelectrogen or anode-respiring bacteria. In MEMS MFC research, *Geobacter sulfurreducens* and *Shewanella MR-1* are the most widely used exoelectrogen. Of them, *Geobacter sulfurreducens* recorded significantly higher current density than *Shewanella MR-1* did, yet *Geobacter sulfurreducens* are only able to oxidize limited types of organic substrates, mainly acetate, while *Shewanella MR-1* are capable of oxidizing a variety of organic substrates, such as lactate, glucose.

## 16.2.2

### Critical Parameters for Testing

#### 16.2.2.1 Anode and Cathode Potential, the Total Cell Potential

Electrochemical potential at anode and cathode determines the voltage of a fuel cell. Electrochemical potential is calculated by the Nernst equation:

$$E_0' = E_0 - \frac{RT}{nF} \ln \frac{[\text{products}]^p}{[\text{reactants}]^r} \quad (16.1)$$

where  $E^0$  is the standard anode or cathode potentials (V),  $n$  is the number of moles of electrons transferred in the cell reaction,  $[\text{products}]^p/[\text{reactants}]^r$  is the reaction quotient, which is the ratio of the activities of the products divided by the reactants raised to their respective stoichiometric coefficient. The Nernst equation is used to calculate the anode and cathode potentials, and the total cell potential,  $E'_{\text{EMF}}$  (electromotive force), is calculated by

$$E'_{\text{EMF}} = E'_{\text{cathode}} - E'_{\text{anode}} \quad (16.2)$$

#### 16.2.2.2 Open Circuit Voltage ( $E_{\text{OCV}}$ )

Open circuit voltage (OCV), denoted by  $E_{\text{OCV}}$ , is the voltage between anode and cathode when an MFC is at open circuit. OCV is different from the total cell potential; generally OCV is lower than the total cell potential, due to unwanted overpotentials. In experiment, OCV is usually measured under open circuit by multimeters or data acquisition systems.

#### 16.2.2.3 Areal/Volumetric Current Density and Areal/Volumetric Power Density

According to Ohm's law, current flowing through the external load can be written as follows:

$$I = \frac{V}{R_e + R_i} \quad (16.3)$$

Here  $I$ ,  $R_i$ , and  $R_e$  are current [A], internal resistance [ $\Omega$ ], and external load resistance of an MFC [ $\Omega$ ], respectively. Output power of an MFC can be written in the following expression:

$$P = I^2 R_e = \frac{E_{\text{OCV}}^2 R_i}{(R_i + R_e)^2} \quad (16.4)$$

when  $R_i = R_e$ , maximum power can be obtained:

$$P_{\text{max}} = \frac{E_{\text{OCV}}^2}{4R_i} \quad (16.5)$$

In order to evaluate the performance of an MFC, the maximum current and power output are usually normalized to unit of projected electrode area or unit of chamber volume to get the areal or volumetric current/power density.

$$i_{\text{max, areal}} = \frac{I_{\text{max}}}{A, p_{\text{max, areal}}} = \frac{P_{\text{max}}}{A} \quad (16.6)$$

$$i_{\text{max, volumetric}} = \frac{I_{\text{max}}}{V, p_{\text{max, volumetric}}} = \frac{P_{\text{max}}}{V} \quad (16.7)$$

where  $i_{\text{max, areal}}$ ,  $i_{\text{max, volumetric}}$ ,  $p_{\text{max, areal}}$ ,  $p_{\text{max, volumetric}}$  are the areal current density, volumetric current density, areal power density, and volumetric power density, respectively.

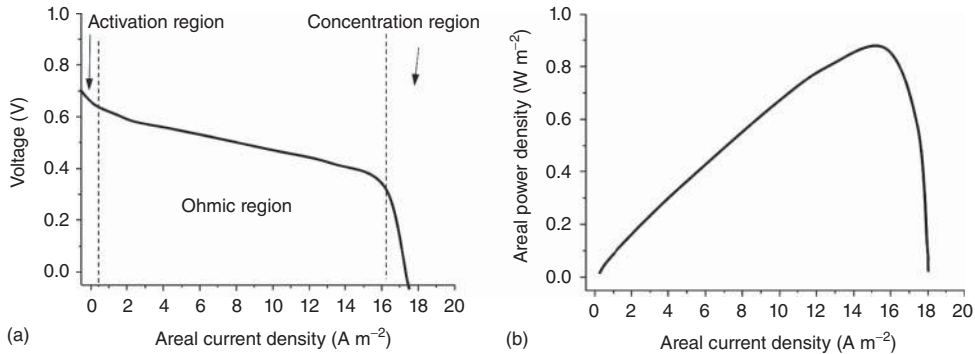


**Figure 16.2** An example of polarization curve of a microscale MFC: (a) Voltage versus current density chart; (b) areal power density versus areal current density chart. In

(a), three distinct zones exist, representing activation resistance, ohmic resistance, and concentration resistance zones, respectively.

#### 16.2.2.4 Internal Resistance and Areal Resistivity

Internal resistance,  $R_i$ , is a critical parameter of an MFC because  $R_i$  determines the maximum power output (Eq. (16.5)). A polarization curve measurement is a popular method to extract  $R_i$ . MFC output voltage is measured by connecting a series of external resistors across anode and cathode. Polarization curve, that is, current density versus voltage and current density versus power density, is plotted (shown in Figure 16.2). In Figure 16.2a, at low current density, activation resistance dominates, and the voltage across the external load drops fast with an increase in current density. When the current density increases to be an intermediate range, the voltage versus current density profile becomes approximately linear, indicating ohmic resistance dominates. As the current density further increases, again the voltage drops quickly; this is because the concentration resistance dominates.

Through linearly fitting the ohmic region in output voltage versus current density plot (Figure 16.2a), the slope is approximately equal to the internal resistance of ohmic region,  $R_i$ . As shown in Eq. (16.5), minimizing internal resistance yields a high-power-density MFC.

However, it is often difficult to compare the internal resistance of different sizes of MFCs side by side. For a macro- or mesoscale MFC, the internal resistance can be as low as several to tens of ohms, while most MEMS MFCs have their internal resistance on the order of kilohms, sometimes tens of kilohms. This is because a larger-size electrode typically results in a smaller internal resistance. The larger-size electrode results in more exoelectrogen population, which in turn results in higher current and power. As a result, it is useful to characterize the internal resistance, independent of the electrode surface area. Electrical resistance can be shown as

$$R = \frac{\rho l}{A} \quad (16.8)$$



where  $R$  [ $\Omega$ ] is the electrical resistance,  $\rho$  is the resistivity [ $\Omega \text{ m}$ ],  $l$  is the length [m], and  $A$  is the effective area where the reaction occurs [ $\text{m}^2$ ].  $R$  is directly proportional to  $1/A$ ; thus it is fair to normalize the resistance at a given reaction area. Areal resistivity,  $r_i$  [ $\Omega \text{ m}^2$ ], denotes the normalized internal resistance at a given active electrode area.

As a result, the areal and volumetric current and power density can be written as follows:

$$i_{\max, \text{areal}} = \frac{I_{\max}}{A} = \frac{E_{\text{OCV}}}{2R_i \cdot A}, \quad p_{\max, \text{real}} = \frac{P_{\max}}{A} = \frac{E_{\text{ocv}}^2}{4R_i \cdot A} \quad (16.9)$$

$$\begin{aligned} i_{\max, \text{volumetric}} &= \frac{I_{\max}}{A} = \frac{E_{\text{OCV}}}{2R_i \cdot V} \cdot \text{SAV} & p_{\max, \text{volumetric}} &= \frac{P_{\max}}{A} = \frac{E_{\text{ocv}}^2}{4R_i \cdot V} \\ &= \frac{E_{\text{OCV}}^2}{4R_i \cdot A} & & \end{aligned} \quad (16.10)$$

Assuming that the areal resistivity ( $R_i \cdot A$ ) and open circuit voltage ( $E_{\text{OCV}}$ ) remain constant, the areal current and power densities remain unchanged, while the volumetric areal and power densities increase linearly with surface area to volume ratio (SAV), as the device dimensions are scaled.

#### 16.2.2.5 Efficiency

There are mainly two efficiency parameters: Coulombic efficiency (CE) and energy conversion efficiency (EE).

**Coulombic Efficiency** Coulombic efficiency is the percentage of charge that is collected by an MFC, and it is the ratio of coulombs harvested by an MFC via oxidizing organic substrates by exoelectrogen to the theoretical maximum coulombs converted from the organic substrates, and it is calculated by

$$\text{CE} = \frac{C_p}{C_T} \times 100\% \quad (16.11)$$

where  $C_p$  is the total coulombs calculated by integrating the current over time for substrate consumption [C] and  $C_T$  is the maximum possible coulombs of the substrate to produce, which is calculated by

$$C_T = V \times b \times N_A \times e \times \text{mol}_{\text{substrate}} \quad (16.12)$$

where  $V$  is the volume of the anode chamber [ $\text{m}^3$ ],  $b$  is the number of moles of electrons produced by oxidation of the substrate ( $b = 8 \text{ mol } e^-/\text{mol acetate}$ ),  $N_A$  is Avogadro's number ( $6.023 \times 10^{23}$  molecules per mol),  $e$  is electron charge ( $1.6 \times 10^{-19} \text{ C}$  per electron), and  $\text{mol}_{\text{substrate}}$  is the number of moles of acetate oxidized. Theoretical CE can reach 100%, and the actual CE can vary largely from 0.1% to more than 90%. MEMS MFCs often show low CE, primarily due to electron loss in the anode compartment, such as oxygen leakage.

**Energy Conversion Efficiency** Energy conversion efficiency represents how much percentage of energy is extracted by an MFC and is calculated by the ratio of total energy harvested by an MFC to the maximum possible energy of biomass:

$$EE = \frac{E_p}{E_T} \times 100\% \quad (16.13)$$

where  $E_p$  is the total energy calculated by integrating the power output over time for substrate consumption and  $E_T$  is the maximum possible energy of the biomass, which is calculated by

$$E_T = V \times c \times \Delta_f H^\circ \quad (16.14)$$

where  $V$  is the volume of anode chamber [ $\text{m}^3$ ],  $c$  is the concentration of biomass in the anode chamber,  $\Delta_f H^\circ$  is standard molar enthalpy of formation.

### 16.3

#### Prior Art MEMS MFCS

It has been more than a decade since MEMS MFC was introduced by M. Chiao *et al.* in 2002, who implemented *Saccharomyces cerevisiae* as exoelectrogen and glucose as organic substrate [14]. Despite the low power density of  $5.72 \text{ nW m}^{-2}$  with an electrode area of  $0.07 \text{ cm}^2$ , this is the pioneer work of the first microfabricated MFC. Later on, they reported largely refined successful MEMS MFCS by introducing microfluidic channels and micropillars to increase the surface-area-to-volume ratio, which resulted in a power density of  $23 \mu\text{W m}^{-2}/0.276 \text{ W m}^{-3}$ , and  $4 \text{ mW m}^{-2}$  and  $40 \text{ W m}^{-3}$ , respectively, which corresponds to 4–6 orders of magnitude improvement. The MEMS MFC marked CE of 14.7% [14, 28]. Their successful development continued to implement CNT forest anodes and *Geobacter sulfurreducens*, reporting a remarkable power density of  $73.8 \text{ mW m}^{-2}$  and  $343 \text{ W m}^{-3}$  [18]. Mink *et al.* also adopted CNT-based materials, vertically aligned CNTs to increase the surface-area-to-volume ratio and Ni silicide to reduce the contact resistance, and reported power density of  $20 \text{ mW m}^{-2}$  and  $392 \text{ W}$  [19].

The first MEMS MFC that utilized *Shewanella* species as exoelectrogen was presented by Qian *et al.* in 2009. The MFC delivered a power density of  $1.5 \text{ mW m}^{-2}$  and  $15 \text{ W m}^{-3}$  [20]. The enhanced performance was reported by implementing microfluidic channels, and  $6.25 \text{ mW m}^{-2}$  and  $62.5 \text{ W m}^{-3}$  were demonstrated. The work reported a CE of 2.8% [30].

The first single-chamber air cathode MEMS MFC was presented by Mink *et al.* in 2013 [25]. They used vertically aligned CNT as anode and implemented an air cathode. The power density was reported to be  $9 \text{ mW m}^{-2}$ .

By mitigating oxygen intrusion through applying *L-cysteine* into the anode chamber, Choi *et al.* reported an MEMS MFC with a power density of  $47 \text{ mW m}^{-2}$  and  $2333 \text{ W m}^{-3}$  [16]. Later on, they presented the first microscale MFC array in a series stack to mark a power output of  $100 \mu\text{W}$  and a power density of

$0.33 \text{ W m}^{-2}$  and  $667 \text{ W m}^{-3}$  [15]. By improving mass transfer in MEMS MFCs, the same group improved the power density to  $0.83$  and  $3320 \text{ W m}^{-2}$  [21]. A CE of 79% was reported by the same group through mitigating oxygen intrusion.

Besides generating power, MEMS MFCs have also been implemented as sensors for toxic chemical detection and exoelectrogen screening. Davila *et al.* developed an MEMS MFC that demonstrated the current profile as a function of toxic chemicals [31]. Hou *et al.* presented two MEMS MFCs in 2009 and 2013, respectively [32], for screening exoelectrogen. Figure 16.3 and Table 16.1 illustrate some of the examples of different MEMS MFCs discussed above.

## 16.4

### Future Work

According to [22], as we scale down MFC dimensions, areal and volumetric power densities increase based on the scaling effect. As a result, the MEMS MFCs still have significant potential. In this section, we discuss the future work for further improving the performance of MEMS MFCs.

#### 16.4.1

##### Reducing Areal Resistivity

In order to further improve the current/power density, the areal resistivity needs to be minimized, as shown in Eqs. (16.9) and (16.10). It is helpful to look at different components of the areal resistivity:

$$r_i = r_a + r_c + r_e + r_m \quad (16.15)$$

where  $r_a$ ,  $r_c$ ,  $r_e$ , and  $r_m$  are the areal resistivity of anode, cathode, electrolyte, and membrane, respectively.  $r_a$  includes the areal resistivity of the anode and resistance of electron generation and transfer from exoelectrogen to the anode. It is a function of material, population of exoelectrogen, and mechanism of electron transfer from exoelectrogen to anode, and so on.  $r_c$  is the areal resistivity of the cathode and of ferricyanide ions transferring from the bulk solution to the vicinity of the cathode and reduce electrons, which is mainly determined by the material properties.  $r_m$  is the areal resistivity of the ion exchange membrane, which is mainly determined by the properties of electrolytes across the membrane, such as pH, concentration, substance.  $r_e$  is determined by the distance between two electrodes. As discussed previously, because the majority of areal resistivity comes from the resistivity of the anode [22], it is important to reduce the anode resistivity.

##### 16.4.1.1 Applying Materials with High Surface-Area-to-Volume Ratio

The first approach to reduce the areal resistivity is to increase the electrode surface-area-to-volume ratio. According to Eq. (16.10), by increasing the surface-area-to-volume ratio, the maximum volumetric current/power density improves.

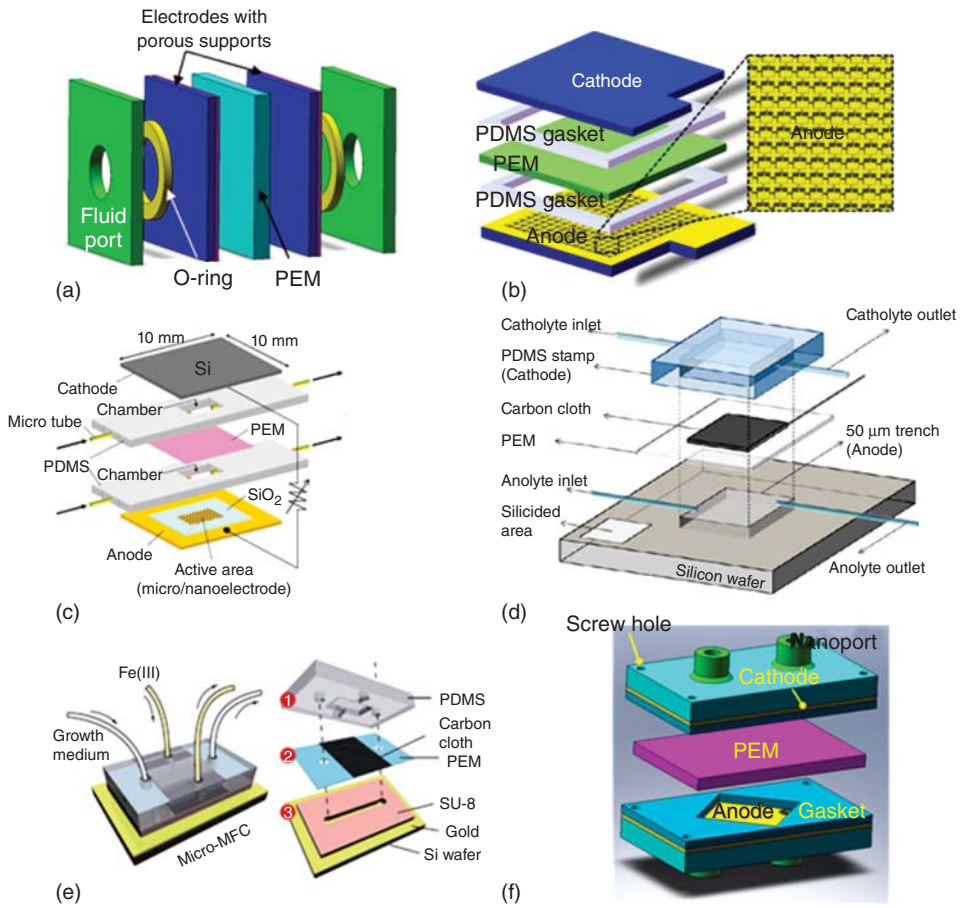


**Figure 16.3** Prior art of MEMS MFCs: (a) the first miniaturized MFC, using *Saccharomyces cerevisiae*, by Chiao *et al.*, in 2002, which produced an areal power density of  $5.72 \text{ nW m}^{-2}$ . (b) Miniaturized MFC presented by [28], using baker's yeast, *Saccharomyces cerevisiae*, by introducing micropillars, enhanced areal/volumetric power density of  $4 \text{ mW m}^{-2}$  and  $40 \text{ W m}^{-3}$ . (c) Miniaturized MFCs presented by Inoue *et al.* 2012, using *Geobacter sulfurreducens*, and CNT-based anodes, which marked a power

density of  $73.8 \text{ mW m}^{-2}$  and  $16.4 \text{ W m}^{-3}$  [33]. (d) MEMS MFC reported by Mink *et al.* [19] adopting CNT electrodes, marked a power density of  $20 \text{ mW m}^{-2}$  and  $343 \text{ W m}^{-3}$ . (e) Miniaturized MFCs presented by Qian *et al.*, which used *Shewanella* as exoelectrogen, and it produced a power density of  $1.5 \text{ mW m}^{-2}$  and  $15 \text{ W m}^{-3}$ . (f) Miniaturized MFCs with a bare gold electrode, using *Geobacter sulfurreducens* mixed culture, presented by Ren *et al.* [23], which achieved a record high areal power density of  $0.83 \text{ W m}^{-2}$ .

Table 16.1 A summary of different MEMS MFCs.

Reporters	Volume (total) ( $\mu\text{l}$ )	Anode size/material	Inoculum	$P_{\text{max, areal}}$ ( $\text{W m}^{-2}$ )	$P_{\text{max, volumetric}}$ ( $\text{W m}^{-3}$ )	CE (%)	$r_i$ ( $\Omega\text{-cm}^2$ )	SAV ( $\text{m}^{-1}$ )
[16]	9	2.25 $\text{cm}^2$ /gold	<i>Geobacter sulfurreducens</i> mixed	0.047	2333	31	22.5 k	50 000
[15]	100 (per cell)	1 $\text{cm}^2$ /gold	<i>Geobacter sulfurreducens</i> mixed	0.33	667	NA	32 k	4 000
[33]	80	0.24 $\text{cm}^2$ /carbon nanotube	<i>Geobacter sulfurreducens</i> mixed	0.0738**	16.4**	NA	NA	589.5
[34]	550	0.01 $\text{cm}^2$ /gold	<i>Geobacter sulfurreducens</i> mixed	0.12*	0.343*	NA	3.3 k	2.9
[30]	8	0.4 $\text{cm}^2$ /gold	<i>Shewanella oneidensis</i> MR-1	0.0625*	62.5	NA	6.4 k	10 000
[20]	3	0.15 $\text{cm}^2$ /gold	<i>Shewanella oneidensis</i> MR-1	0.0015	15.3	2.8	36 k	10 000
[28]	30	1.2 $\text{cm}^2$ /gold	<i>Saccharomyces cerevisiae</i>	0.000424	4.24*	14.7	3 k	10 000
[19]	3	0.25 $\text{cm}^2$ /carbon nanotube	<i>Geobacter sulfurreducens</i> mixed	0.02	392	NA	NA	19 600
[21]	200	4 $\text{cm}^2$ /gold	<i>Geobacter sulfurreducens</i> mixed	0.83	3320	79	5.6 k	4 000
[25]	75	0.25 $\text{cm}^2$ /CNT anode, air cathode	<i>Geobacter sulfurreducens</i> mixed	0.019	339	NA	NA	333

\*calculated based on the reported data.

\*\*calculated based on the enhancement of current outputs by the CNT electrode 205%, with regard to the flat-reference electrode

Furthermore, considering that the areal current/power density is calculated by the total current/power divided by the projected surface area, the higher the surface-area-to-volume ratio is, the higher the ratio of actual area over projected area will be, and consequently the higher the areal current density will be.

There are quite a few reports of utilizing electrode materials with high surface-area-to-volume ratio to increase both areal and volumetric power densities; Inoue *et al.* and Mink *et al.* [19] utilized CNT-based materials to improve the current and power density. Chiao *et al.* [24] and Qian *et al.* [20] adopted microfluidic channels to increase the surface-area-to-volume ratio and thus improved the current and power density, and Siu and Chiao [28] implemented PDMS micropillars to increase the surface-area-to-volume ratio.

#### 16.4.1.2 Mitigating Oxygen Intrusion

*Geobacter sulfurreducens* is the exoelectrogen that marked high current/power density in the literature. *Geobacter sp.*, on the other hand, is important to mitigate oxygen intrusion in the anode chamber because oxygen intrusion will result in the electrons generated by the exoelectrogen be scavenged by oxygen, thus reducing the current/power density and CE. An example to demonstrate the effectiveness is presented by Choi *et al.* [16], who demonstrated that by adding L-cysteine, the OCV increased from 300 to 600 mV (Figure 16.4).

In order to mitigate oxygen intrusion, materials with low oxygen permeability need to be used (see Table 16.2) [22]. In contrast, PDMS, which has an oxygen permeability as high as water, should be avoided in MFCs with *Geobacter sulfurreducens*.

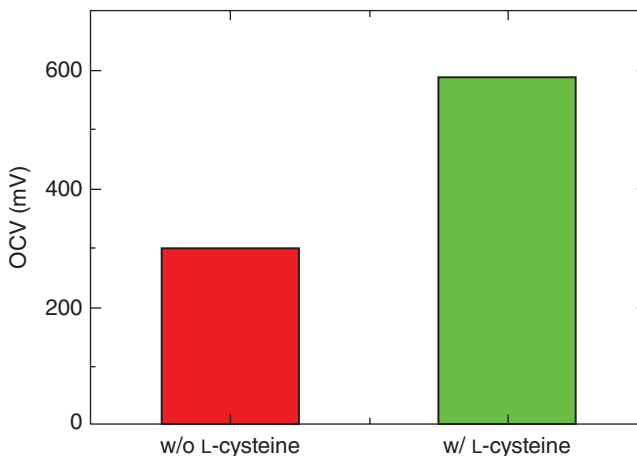


**Figure 16.4** OCV of the MEMS MFC presented by Choi *et al.* [16]: with L-cysteine, the OCV is around 600 mV, much larger than that obtained without L-cysteine, which is around 300 mV.

**Table 16.2** Oxygen permeability of several materials.

Materials	PDMS [35]	Parylene C (SCS Parylene C film)	Silicone rubber	PTFE dupont Teflon	Epoxy-based thermoplastics 0000 series	PET dupont Mylar	Metal, silicon, glass
Oxygen permeability ( $\text{cm}^3 \cdot \text{mm} \cdot \text{m}^{-2} \cdot \text{day} \cdot \text{atm}$ )	$52531 \pm 1313$	2.83	19 685	223	0.8	2.4	Nearly zero

SCS-special coating system; PTFE-polytetrafluoroethylene.

#### 16.4.2

##### Autonomous Running

Another critical challenge with MEMS MFCs is that all reported MEMS MFCs utilize pumps to feed anolyte and/or catholyte into the corresponding chambers. The electricity generated from microscale MFCs is far less than that consumed by these pumps. As a result, in the future, self-driven or autonomous running needs to be studied. One example of autonomous-running MFCs is the macroscale MFC deployed to power meteorological buoy, presented by Tender *et al.* in 2008 [36].

#### 16.4.3

##### Elucidating the EET Mechanism

To date, researchers debate the mechanism of EET for *Geobacter sulfurreducens*, the exoelectrogen with a record high current/power density. The debate is whether *Geobacter sulfurreducens* relies on bacterial conductive nanowire or electron hopping. Unveiling the EET mechanism is critical as researchers understand the limitations and plan how to mitigate the limitations and consequently improve the performance of MEMS MFCs.

## References

1. Madou, M.J. (2011) *Fundamentals of Microfabrication and Nanotechnology: Manufacturing Techniques for Microfabrication and Nanotechnology*, vol. 2, CRC Press.
2. Cook-Chennault, K.A., Thambi, N., and Sastry, A.M. (2008) Powering MEMS portable devices—a review of non-regenerative and regenerative power supply systems with special emphasis on piezoelectric energy harvesting systems. *Smart Mater. Struct.*, **17** (4), 043001.
3. Huesgen, T., Woias, P., and Kockmann, N. (2008) Design and fabrication of MEMS thermoelectric generators with high temperature efficiency. *Sens. Actuators, A*, **145**, 423–429.
4. Motokawa, S., Mohamedi, M., Momma, T., Shoji, S., and Osaka, T. (2004) MEMS-based design and fabrication of a new concept micro direct methanol fuel cell ( $\mu$ -DMFC). *Electrochem. Commun.*, **6** (6), 562–565.

5. Sorrel, S., Speirs, J., Bentley, R., Brandt, A., and Miller, R. (2009) *Global Oil Depletion: An Assessment of the Evidence for a Near-Term Peak in Global Oil Production*, UK Energy Research Centre, London. ISBN 1-903144-0-35.
6. Bentley, R.W. (2002) Global oil and gas depletion: an overview. *Energy Policy*, **30** (3), 189–205.
7. Sorrell, S., Speirs, J., Bentley, R., Brandt, A., and Miller, R. (2010) Global oil depletion: a review of the evidence. *Energy Policy*, **38** (9), 5290–5295.
8. Logan, B.E. and Rabaey, K. (2012) Conversion of wastes into bioelectricity and chemicals by using microbial electrochemical technologies. *Science*, **337** (6095), 686–690.
9. Chiao, M., Lam, K.B., Su, Y., and Lin, L. (2002) A miniaturized microbial fuel cell. Solid-State Sensor, Actuator and Microsystems Workshop, Hilton Head Island, South Carolina.
10. McCarty, P.L., Bae, J., and Kim, J. (2011) Domestic wastewater treatment as a net energy producer—can this be achieved? *Environ. Sci. Technol.*, **45** (17), 7100–7106.
11. Logan, B.E. (2004) Peer reviewed: extracting hydrogen and electricity from renewable resources. *Environ. Sci. Technol.*, **38** (9), 160A–167A.
12. Perlack, R.D., Wright, L.L., Turhollow, A.F., Graham, R.L., Stokes, B.J., and Erbach, D.C. (2005) Biomass as Feedstock for a Bioenergy and Bioproducts Industry: The Technical Feasibility of a Billion-Ton Annual Supply. DTIC Document.
13. Xie, X., Yu, G.H., Liu, N., Bao, Z.N., Criddle, C.S., and Cui, Y. (2012) Graphene-sponges as high-performance low-cost anodes for microbial fuel cells. *Energy Environ. Sci.*, **5** (5), 6862–6866.
14. Chiao, M., Lam, K.B., Su, Y.C., and Lin, L. (2002) A miniaturized microbial fuel cell. Paper Read at Technical Digest of the 2002 Solid-State Sensors and Actuators Workshop.
15. Choi, S. and Chae, J. (2012) An array of microliter-sized microbial fuel cells generating 100 $\mu$ W of power. *Sens. Actuators, A*, **177**, 10–15.
16. Choi, S., Lee, H.S., Yang, Y. *et al.* (2011) A  $\mu$ L-scale micromachined microbial fuel cell having high power density. *Lab Chip*, **11** (6), 1110–1117.
17. Choi, S. and Chae, J. (2013) Optimal biofilm formation and power generation in a micro-sized microbial fuel cell (MFC). *Sens. Actuators, A*, **195**, 206–212.
18. Inoue, S. (2012) Structural optimization of contact electrodes in microbial fuel cells for current density enhancements. *Sens. Actuators, A*, **177**, 7.
19. Mink, J.E., Rojas, J.P., Logan, B.E., and Hussain, M.M. (2012) Vertically grown multiwalled carbon nanotube anode and nickel silicide integrated high performance micro-sized (1.25  $\mu$ L) microbial fuel cell. *Nano Lett.*, **12** (2), 791–5.
20. Qian, F., Baum, M., Qian, G., and Morse, D.E. (2009) A 1.5 [small micro]L microbial fuel cell for on-chip bioelectricity generation. *Lab Chip*, **9** (21), 3076–3081.
21. Ren, H. and Chae, J. (2012) Scaling effect on mems-based microbial fuel cells toward a carbon-neutral miniaturized power source. In IEEE Solid-State Sensors and Actuators Workshop, Hilton Head, SC.
22. Ren, H., Lee, H.-S., and Chae, J. (2012) Miniaturizing microbial fuel cells for potential portable power sources: promises and challenges. *Microfluid. Nanofluid.*, **13** (3), 353–381.
23. Ren, H., Rangaswami, S., Lee, H.-S., and Chae, J. (2013) A micro-scale microbial fuel cell (MFC) having ultramicroelectrode (UME) anode. Paper read at 2013 IEEE 26th International Conference on Micro Electro Mechanical Systems (MEMS).
24. Chiao, M., Lam, K.B., and Lin, L. (2006) Micromachined microbial and photosynthetic fuel cells. *J. Micromech. Microeng.*, **16** (12), 2547.
25. Mink, Justine E., and Muhammad, Mustafa Hussain (2013) Sustainable Design of High-Performance Microsized Microbial Fuel Cell with Carbon Nanotube Anode and Air Cathode. *ACS nano* **7** (8) 6921–6927.
26. King, D., Zuo, Y., Cheng, S., Regan, J.M., and Logan, B.E. (2008) Electricity generation by *Rhodospseudomonas*



- palustris DX-1. *Environ. Sci. Technol.*, **42**, 4146–4151.
27. Potter, M.C. (1911) Electrical effects accompanying the decomposition of organic compounds. Royal Society (Formerly Proceedings of the Royal Society) **B 84**, 260–276.
  28. Siu, C.P.B. and Chiao, M. (2008) A microfabricated PDMS microbial fuel cell. *J. Microelectromech. Syst.*, **17** (6), 1329–1341, 1057–7157.
  29. Wendisch, V.F., Bott, M., and Eikmanns, B.J. (2006) Metabolic engineering of *Escherichia coli* and *Corynebacterium glutamicum* for biotechnological production of organic acids and amino acids. *Curr. Opin. Microbiol.*, **9**, 268–274.
  30. Qian, F., He, Z., Thelen, M.P., and Li, Y. (2011) A microfluidic microbial fuel cell fabricated by soft lithography. *Bioresour. Technol.*, **102** (10), 5836–5840.
  31. Davila, D., Esquivel, J.P., Sabate, N., and Mas, J. (2011) Silicon-based microfabricated microbial fuel cell toxicity sensor. *Biosens. Bioelectron.*, **26** (5), 2426–2430.
  32. Hou, H., Li, L., Cho, Y., de Figueiredo, P., and Han, A. (2009) Microfabricated microbial fuel cell arrays reveal electrochemically active microbes. *PLoS One*, **4** (8), e6570.
  33. Inoue, S., Parra, E.A., Higa A, Lin L (2011) Cell-to-Electrode contact structure for power density enhancements in microbial fuel cells. Proc. of 21st IEEE Int. Conf. on Micro Electro Mechanical Systems (MEMS) 1297–1300.
  34. Parra, E. and Lin, L. (2009) Microbial fuel cell based on electrode-exoelectrogenic bacteria interface. Proc. of 19th IEEE Int. Conf. on Micro Electro Mechanical Systems (MEMS) 31–34.
  35. Merkel, T.C., Bondar, V.I., Nagai, K., Freeman, B.D., and Pinnau, I. (2000) Gas sorption, diffusion, and permeation in poly(dimethylsiloxane). *Journal of polymer Science Part B: Polymer Physics*, **38** (3), 415–434.
  36. Tender, L.M., Gray, S.A., Groveman, E. *et al.* (2008) The first demonstration of a microbial fuel cell as a viable power supply: powering a meteorological buoy. *J. Power Sources*, **179** (2), 571–575, 0378-7753.



## 17

### Micro Photovoltaic Module Energy Harvesting

*Shunpu Li, Wensi Wang, Ningning Wang, Cian O'Mathuna, and Saibal Roy*

This chapter introduces several typical solar cells and their application with photovoltaic micro energy harvester. Although various techniques can be used to harvest energy from ambient environment, as can be seen from other chapters of this book, photo energy harvesting has its unique advantages, such as ubiquitous availability, predictable radiation, and DC current character, which simplifies power management circuits. We start from crystalline silicon (c-Si) solar cell as c-Si is a good example to illustrate the power conversion principle of p–n junction type solar cells, while basic solar cell parameters, characterization technique, and cell fabrication process are introduced. Other p–n junction type thin film solar cells such as copper indium gallium selenide (CIGS), cadmium telluride (CdTe), and amorphous silicon are detailed with their cell structures and fabrication process. Two types of organic molecule–based cells, polymer solar cells, and dye-sensitized solar cells (DSSC), are also briefly introduced for readers with broader interests in the area of energy harvesting. Integrated micro photovoltaic modules are illustrated by taking amorphous-Si and CIGS as examples owing to their excellent indoor efficiency and low-temperature manufacturing process. The second part of this chapter addresses the application-related issues in micro photovoltaic energy harvesting. The power management circuitry is introduced with a focus on ultra-low-power maximum power point tracking (MPPT). Wide input voltage range DC–DC converters are introduced as the output voltage regulators for supercapacitor type energy storage units.

#### 17.1

##### Introduction

##### 17.1.1

##### p-n Junction and Crystalline Si Solar Cells

Photovoltaic (PV), which generates electricity through the direct conversion of sunlight, has eventually become an important technology for clean energy after nearly two century's effort.

A French physicist Alexandre-Edmond Becquerel inadvertently observed the photovoltaic effect around 1839 while manipulating an electrode inside a conductive fluid exposed to light [1]. After several decades, an American inventor Charles Fritts fabricated the first photovoltaic cell with selenium around 1883 [2]. Later, in 1888 a Russian physicist Aleksandr Stoletov assembled a photoelectric cell based on a photoelectric effect discovered by Heinrich Hertz in 1887 [3]. In 1946, American engineer Russell Shoemaker Ohl patented the junction semiconductor solar cell, which triggered the research and development activity in this area. In 1954, Bell Laboratories developed the first efficient photovoltaic cell using a diffused silicon p–n junction [4].

Today the mainstream of solar cells is still p–n junction type, in which the electrical potential is fundamentally created by forming a p–n junction between p- and n-type semiconductors. We take crystalline silicon (c-Si) as an example to introduce p–n junction solar cells. When p-type and n-type materials are placed in contact with each other, the majority carriers of n-type semiconductor diffuse through the interface to combine with holes in p-type semiconductor to form negative ions. As a result, they leave behind positive ions at n-type side, thus an electrical field that points from n-type to p-type is generated between two charged layers. Because of such an internal built-in field, electrical current flows readily in one direction but not in the other, creating a diode. Such a diode operates various important functions, such as current rectification, light emitting diode, and solar cell. For solar cells, electron–hole pairs are generated in semiconductor by absorbing light, diffuse to p–n junction, and are separated by the built-in field, and they further diffuse to respective electrodes and form current in external circuit. Solar cells are characterized by several parameters, including short-circuit current density  $J_{SC}$ , open-circuit voltage  $V_{OC}$ , peak power  $P_{max}$ , and fill factor FF. They are normally obtained from solar cell  $I$ – $V$  curves measured under one sun condition, that is, air mass1.5 (AM1.5).

1) *Short-circuit current density:*

Short-circuit current is the current that flows through the external circuit when the electrodes of the solar cell are short circuited, and it is determined from experimental  $I$ – $V$  curve with zero applied voltage (Figure 17.1).

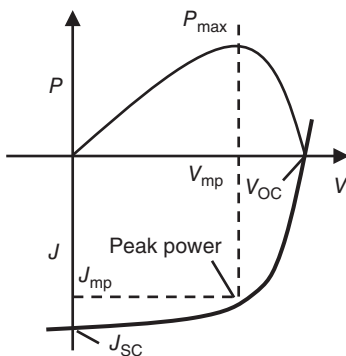


**Figure 17.1** Schematic representation of measured  $I$ – $V$  curve of solar cell where short-circuit current ( $J_{sc}$ ), open-circuit voltage ( $V_{oc}$ ), and maximum power ( $P_{max}$ ), voltage/current at which maximum power is generated ( $V_{mp}/J_{mp}$ ) are indicated.

2) *Open-circuit voltage:*

Open-circuit voltage is the voltage at which no current flows through the external circuit, which is the maximum voltage that the solar cell can deliver ( $V_{OC}$ ).

3) *Peak power:*

Peak power is the maximum power the solar cell can deliver, which equals the maximum area of rectangle found under  $I-V$  curve,  $P_{max} = J_{mp} \times V_{mp}$ .

4) *Fill factor:*

FF is the ratio between the maximum power  $P_{max}$  generated by the solar cell and the product of  $V_{OC}$  and  $J_{SC}$ , that is,  $FF = P_{max}/J_{SC} \times V_{OC}$ .

5) *Power conversion efficiency:*

Power conversion efficiency is a measure of effectiveness of a solar cell to generate electricity from light. It is generally measured by a ratio of peak power generated and incident light power ( $P_{in}$ ) under AM1.5.

$$\eta = \frac{J_{SC} \times V_{OC} \times FF}{P_{in}}$$

Crystalline Si solar cells are made from single-crystal Si or polycrystalline Si with large crystal domains. Silicon wafers are sliced from ingots using a circular saw and cut into rectangular or hexagonal wafers for solar cell production as such shapes can be fitted together perfectly, thereby utilizing all available space of solar panels. The wafers are normally doped (p-type for most silicon solar cells) during crystal growth by introducing a small amount of boron (for p-doping) or phosphorus (for n-doping).

A commonly used c-Si solar cell architecture is shown in Figure 17.2a. After polishing Si wafers, a doping process is carried out for creating p-n junction. P-doped wafers are sealed back to back and placed in a furnace heated to proper temperature in the presence of phosphorus gas. The phosphorous atoms diffuse into the surface of originally p-doped silicon to form p-n junction. Another way of doping silicon is ion implantation in which a particle accelerator is used to shoot phosphorus ions into the wafers. By controlling the speed of the ions, it is possible to control their penetrating depth. Absorption of c-Si is relatively weak with comparison

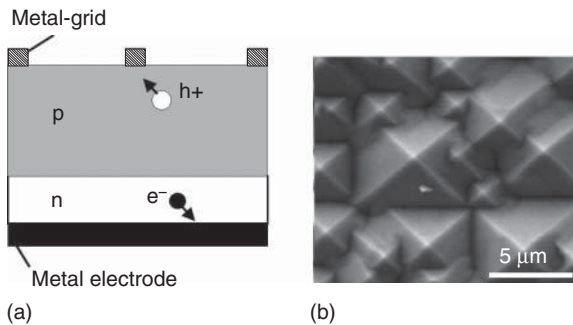


**Figure 17.2** Schematic illustration of crystalline silicon solar cell (a) and surface texture for antireflection (b). (Courtesy of IEEE (Ref [5]).)

of other solar cell absorbers, and a thicker c-Si wafer is used (300–700 nm). The photogenerated charges have to be collected quickly as recombination may occur between the photogenerated holes and electrons owing to their random motion and attraction between holes and electrons. Electrical contacts are deposited by evaporation (thermal evaporation or sputtering) or printing for the charge collection and wiring between cells. Because silicon is shiny, it can reflect up to one-third of sunlight. To reduce the amount of sunlight loss, an antireflective coating is applied on the silicon wafer. The commonly used coating materials are titanium dioxide, silicon oxide, silicon nitride. Sometimes, a combination of etched texture [5] (Figure 17.2b) and reflection coating is used to maximize light trapping property.

### 17.1.2

#### Amorphous Silicon Solar Cell

Crystalline silicon has been and remains the traditional solar cell material and it requires energy-intensive process to purify and crystallize. Furthermore, the rigid, thick silicon films are not compatible with fast production process, like roll to roll. Recently, commercial interest is beginning to shift toward thin-film solar cells such as amorphous silicon and  $\text{CuInSe}_2$ -based cells.

The invention of chemical vapor deposition has greatly advanced amorphous semiconductor technology [6]. Amorphous silicon (a-Si), an alloy of silicon and hydrogen, has drawn a wide interest for applications [7]. In 1976, Carlson and Wronski demonstrated the first a-Si solar cell with an efficiency of more than 2% [8]. After several decades, the a-Si-based solar cell became a mature technology for large-scale manufacturing. The technology has been evolved from single to double and triple junction cells for a much wide light spectrum response. The basic structure of amorphous silicon cell is shown in Figure 17.3. Different from the c-Si solar cell, amorphous silicon is a p–i–n junction structure instead of a p–n junction diode. As amorphous Si has a much higher light absorption compared with c-Si, films can be much thinner ( $< \mu\text{m}$ ) and they are entirely immersed in the field defined by n–i and i–p junctions. The separation of photogenerated e–h pairs generated in the intrinsic a-Si layer is realized by charge drifting in the established internal field between the n- and p-type a-Si layers. Light passes through the top transparent conductive oxide (TCO) film and is absorbed by the intrinsic  $\alpha$ -Si layer

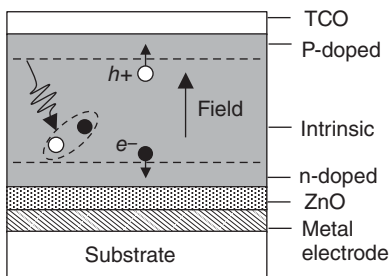


**Figure 17.3** Schematic illustration of basic architecture of amorphous silicon cell.

to generate e–h pairs. The generated charges are separated and drifted to corresponding electrodes. The bottom metal electrode also acts as reflector to improve light harvesting, and the higher refractive index of  $\alpha$ -Si ( $n \sim 4$ ) compared to TCO and ZnO ( $n \sim 2$ ) can further assist light harvesting. The effective cell structure allows the film thickness of amorphous Si to be less than 0.5  $\mu\text{m}$ . The n- and p-Si layers are normally less than 40 nm to minimize light absorption inside them because there is more likely a recombination of e–h pairs generated there is more likely. The standard cell fabrication process can be briefly described by the following steps [9]. First, metal reflection layer (like  $\sim 100$  nm of Ag) and ZnO:Al ( $\sim 100$  nm) are deposited by sputtering techniques. Second, n-doped, intrinsic, and p-doped layers are sequentially deposited by the radio-frequency plasma-enhanced chemical vapor deposition (RF-PECVD) system. Finally,  $\sim 100$  nm thick TCO (normally ITO) is deposited in sputtering system as top electrode. Although several methods can be used to deposit amorphous Si, however, the PECVD is a well-developed technique for solar cell production. It works at various frequencies with hot-wire chemical vapor deposition.

### 17.1.3

#### CIGS and CdTe Solar Cell Development

At present, CIGS [ $\text{Cu}(\text{In}_{1-x}\text{Ga}_x)\text{Se}_2$ ] semiconductor has become one of the hot points in solar cell field for its excellent performances, such as direct band gap, high light absorption coefficient, high photoelectric conversion efficiency, and long-term stability. Energy conversion efficiency of such cells is more than 20%. The first chalcopyrite-based solar cell was reported in 1974, and the cell was prepared from a p-type  $\text{CuInSe}_2$  crystal, and CdS film was evaporated in vacuum [10]. Glass is the most commonly used substrate, and now efforts are being made to develop flexible solar cells on polyamide and metal foil [11, 12]. Efficiency of 20.4% has been reported for CIGS cells on flexible substrates [13]. CIGS is a very good light absorption material, and its band gap varies from 1.1 to 1.7 eV depending on the Ga content. CIGS cell preparation starts with the deposition of back contact, usually Mo, on glass followed by p-type CIGS absorber, CdS, or other n-type buffer layer, undoped ZnO, transparent conductor (usually doped ZnO or  $\text{In}_2\text{O}_3$ ), metal charge collection grid, and antireflection coating. Mo is emerged as dominant back contact material owing to its high stability at process temperature, resistance of alloying with In and Cu of the absorber, and low contact resistance. Molybdenum is normally deposited by e-beam evaporation and sputtering on soda lime glass, which is low cost, and its Na content is favorable for enhancement of cell efficiency [14]. During the processing of absorber film, Na ions diffuse from the substrate through the Mo layer into the semiconductor. Figure 17.4 shows typical SEM image of CIGS solar cell.

A variety of thin film deposition methods has been used to deposit CIGS films. There two important deposition techniques that have been demonstrated to be suitable for large manufacturing with high device efficiency. The first approach is

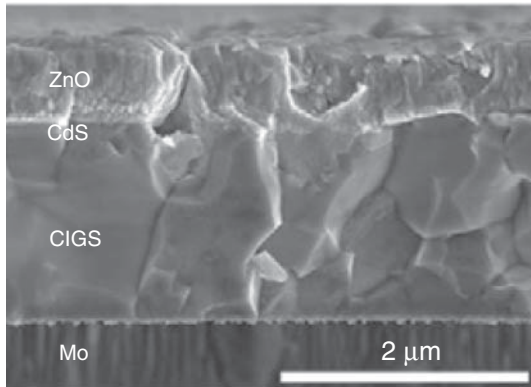


**Figure 17.4** SEM image of CIGS solar cell. (Courtesy of AIP (Ref [14]).)

vacuum co-evaporation in which all constituents (Cu, In, Ga, Se) can be simultaneously delivered to a substrate heated at 400–600 °C and the absorber film is formed in single deposition. Another approach is a two-step sequential process in which Cu, In, and Ga are deposited by low-cost methods and the films are annealed in a Se atmosphere (from 400 to 600 °C). For co-evaporation, Cu, In, Ga, Se are simultaneously evaporated from Knudsen-type effusion cells or open boat sources to a substrate that is heated at proper temperature. The flux of each element is controlled to form various composition profiles to optimize the material properties. For instance, a Cu-rich stage in the growth process end up with In-rich composition in order to combine the large grains of Cu-rich stage with favorable electronic property of In-rich composition. This deposition procedure is called “bilayer process.” Such a bilayer process yields large grain sizes, which is attributed to the formation of a  $\text{Cu}_x\text{Se}$  phase during the Cu-rich first stage, which improves the mobility of In(Ga) atoms during growth [15]. Another composition profile is deposited by a “inverted” process in which  $(\text{In, Ga})_2\text{Se}_3$  is deposited first at around 300 °C and Cu and Se are evaporated at higher temperatures [16]. This process is called three-stage process and up to now it offers most efficient solar cells. For a two-step sequential process, metal films are formed by vacuum deposition (evaporation or sputtering of Cu(In, Ga) alloy or multilayers) and subsequent selenization or sulfurization to form CuInGaSe or CuInGaS [17]. Selenization is done by reaction of the predeposited metal film in  $\text{H}_2\text{Se}$  or Se vapor at 400–500 °C for 30–60 min [18].

To reduce production cost, nonvacuum process of CIGS deposition has been developed, including (i) electrochemical process, (ii) particulate process, and (iii) solution-based process. Electrodeposition of absorber or metal precursors followed by selenization can be used to fabricate CIGS solar cell [19]. Absorbers have also been fabricated by preparing pastes of Cu, In, Ga, and Se [20] and spin-coating film from precursor solution followed by heat treatment [21].

CdS is widely used in CIGS cells as n-type buffer layer as it has continuously yielded cells with high efficiency. CdS films (40–100 nm) are generally deposited



by chemical bath deposition (CBD). The high efficiency of cells with CdS buffer is explained by optimizing the band alignment of the device, and a sufficiently wide depletion layer is built and this minimizes tunneling and establishes a high contact potential that allows a higher open-circuit voltage. The top contact electrode requires high light transparency and good electrical conductivity. Conductive transparent oxide is used for this purpose, and it can be sputter-deposited ITO or Al-doped ZnO.

Cadmium telluride (CdTe)-based thin film solar cells are studied since 1950. In 1972, 6% power efficiency was achieved by Bonnet and Rabenhorst [22]. More than 16% record efficiency had been reported [23]. EMPA lab also showed 13.5% efficiency on flexible polyimide substrates. Industry scale production already exists, like First Solar. CdTe is a II-VI compound semiconductor with a direct optical band gap, which is optimally matched to the solar spectrum for photovoltaic energy conversion. It has an energy band gap of  $E_g = 1.5$  eV and high absorption coefficient, which means that high quantum yield can be expected over a wide spectrum range from ultraviolet to the infrared corresponding material band gap ( $\lambda \sim 825$  nm). The architecture of CdTe solar cell is similar to that of CIGS cell, but a superstrate configuration is used (Figure 17.5). A typical process adopted is  $\sim 100$  nm CdS is first deposited on TCO carried on glass substrate. Then, a CdTe layer with several micrometer thickness and back electrode (like Mo) is deposited. CdTe can be deposited by various techniques such as close spaced sublimation (CSS) [24], vapor transport deposition (VTD) [25], electrodeposition [26], and other deposition techniques [27]. For close spaced sublimation, the source material, typically CdTe powder, is placed in a silicon carbide-coated graphite boat. The substrate is kept in proximity to the source material (several millimeters). A gas inlet and evacuation port is used to evacuate the chamber to introduce appropriate amount of gasses. The controlled parameters are substrate temperature ( $\sim 500^\circ\text{C}$ ) and source temperature, source-substrate separation, pressure, ambient. The ambient for deposition typically contains a nonreactive gas such as  $\text{N}_2$ , Ar, or He. VTD allows high-rate deposition. It works by transferring the saturated Cd and Te vapor stream to the substrate, where supersaturation of the vapor results in condensation and reaction to form CdTe. High-speed process can be used for industry manufacturing where the CdTe source is formed from a heated chamber containing CdTe in which the carrier gas mixes with the vapor and is exhausted through a slit and

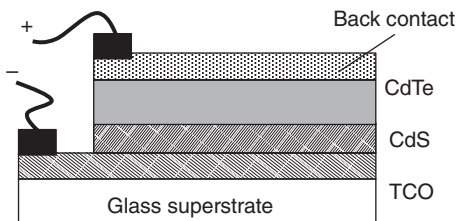


Figure 17.5 Schematic illustration of architecture of CdTe solar cell.

deposited onto a moving substrate. Electrodeposition of CdTe film is normally done by reduction of Cd and Te from  $\text{Cd}^{+2}$  and  $\text{HTeO}_2^+$  ions in low pH aqueous solution through reaction.

#### 17.1.4

##### Polymer Solar Cell

Another approach for low-cost manufacture of solar cells is to use conjugated polymers and molecules that contain alternative single and double bonds. The discovery of organic conductor/semiconductor leads, subsequently, to invention of polymer electroluminescence devices [28], thin film transistors [29], and solar cells [30]. Conjugated polymers and molecules have an immense advantage of facile, chemical tailoring to alter their properties, such as band gap, solubility, stability. Conjugated polymers combine the electronic properties known from the traditional semiconductor/conductor with its ease of processing, lightweight, and mechanical flexibility. Therefore, organic solar cells have attracted a considerable attention owing to its potential, providing environmentally safe, lightweight, inexpensive electronics. Because the physical properties of inorganic and organic semiconductors are significantly different, organic photovoltaic cells differ from inorganic semiconductor-based cells. Inorganic semiconductors generally have a high dielectric constant and a low excitation binding energy. The thermal energy at room temperature  $K_B T \sim 0.025 \text{ eV}$  is sufficient to dissociate the exciton created by absorption of a photon into a positive and negative charge carrier. The formed electrons and holes are easily transported as a result of high mobility of the charge carriers and the internal field of the p-n junction. In contrast, organic materials have a lower dielectric constant, the excitation binding energy is much larger than that of inorganic semiconductors, and dissociation into free charge carriers does not occur at room temperature. To dissociate the bonded electrons and holes, organic solar cells commonly utilize two different materials that differ in electron donating and accepting properties, that is, donor and acceptor. On interfaces of the donor and acceptor, the photogenerated e-h pairs are dissociated and free charges are created. To make organic solar cells with high efficiency, four processes need to be optimized: (i) absorption of light, (ii) dissociation of excitons, (iii) charge transport, and (iv) charge collection. For effective harvesting light, the active layer needs to be thick enough. However, a very thick film will negatively impact the charge transport to the corresponding electrodes caused by recombination. Thus, materials with a large overlap with solar spectrum and high absorption coefficient, which allows absorbing a large portion of incident light with film thickness  $\sim 100 \text{ nm}$ , are desirable.

Figure 17.6 shows a schematic of working principle of organic solar cells. Double layers of donor and acceptor are sandwiched between two electrodes (Figure 17.6a). Illumination of the donor through a transparent electrode, such as ITO, results in the photoexcited state of the donor and an electron is promoted from the highest occupied molecular orbital (HOMO) to the lowest unoccupied molecular orbital (LUMO) of the donor (Figure 17.6b). Subsequently, the excited

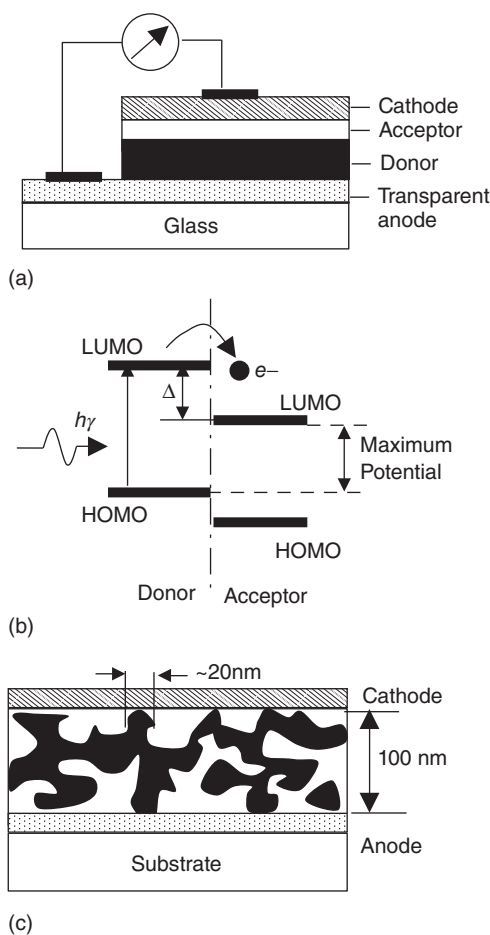


**Figure 17.6** Schematic illustration of organic polymer cell with double-layer structure (a), band alignment between donor and acceptor (b), and BHJ (c).

electron is transferred to the LUMO of the acceptor, resulting in an extra electron on the acceptor and leaving a hole on the donor. The photogenerated charges are then transported and collected at opposite electrodes. A similar process can occur when the acceptor is photoexcited instead of the donor. For effective withdrawal of the photogenerated charges, the two electrodes have to be dissimilar with work function, that is, the anode with higher work function and the cathode with lower work function. The first organic solar cell with double-layer structure was demonstrated with small organic molecules by Tang, in which copper phthalocyanine and perylene tetracarboxylic derivatives were used as donor and acceptor [31]. ITO and Ag were used as electrodes to collect positive and negative charges. The photogenerated e–h pairs are bonded together and need to diffuse toward the donor–acceptor interface in order to dissociate into free

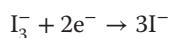
charges. The charge diffusing length is generally limited to  $\sim 10$  nm, above which the exciton will recombine. This greatly limits the film thickness and absorption property of device. To solve this problem, a bulk heterojunction (BHJ) strategy is applied to reduce the exciton diffusion length [30]. The BHJ devices can be prepared by simply mixing the p- and n-type materials in solvent, and phase separation in nanometer dimension ( $\sim 20$  nm) occurs during solvent evaporation (Figure 17.6c).

Suitable organic solar cell materials need to be optimized in many aspects, such as large absorption coefficient, low band gap, high charge mobility, favorable blend morphology, environmental stability, suitable HOMO/LUMO level, and solubility. A low-band gap material is favorable for light absorption. For a typical conjugated polymer with an energy gap of  $E_g \sim 2.0$  eV, it can only absorb photons with wavelength up to 600 nm, which covers  $\sim 25\%$  of solar energy. By decreasing the energy gap to  $E_g \sim 1.2$  eV, approximately 70 and 80% of solar energy will be covered theoretically. However, the problem faced is that once a polymer absorbs at a longer wavelength an absorption drop often exists at the shorter wavelength range, leading to a decreased energy conversion efficiency at that wavelength range. One approach to address this issue is to fabricate a tandem solar cell with both large and narrow band gap polymers utilized simultaneously for solar photon capture [32]. High charge mobility increases the diffusion length of electrons or holes generated by incident light and reduce chances of charge recombination. This charge transport property of the active layer is reflected by charge transporting behavior of both the donor and acceptor. Currently, typical material for BHJ solar cell is a benchmark n-type phenyl-C61-butyric acid methyl ester (PCBM) with combination of p-type polymer with high charge mobility such as P3HT, PTB7, and power conversion efficiency is achieved to 8–9% [33]. Controlled solvent evaporation and film annealing are normally used to optimize nanostructure of the BHJ film. A slow evaporation process assists in self-organization of polymer chains into a more ordered structure, which results in an enhanced conjugation length and a bathochromic shift of the absorption spectrum to a longer wavelength region. At controlled annealing, the p-type polymer and PCBM in the blend network tend to diffuse and form a better mixed network favorable for charge separation and diffusion in the photoactive layer. The air stability of solar cell devices is mainly caused by polymer degradation in air, oxidation of low-work-function electrode, and degradation of the morphology of active layer. To avoid oxidation and achieve long time span of polymer solar cells, the HOMO energy level should be less than the air oxidation threshold [34]. LUMO energy level also needs to be optimized. The maximum open-circuit voltage ( $V_{oc}$ ) is correlated with the difference between the LUMO level of acceptor and HOMO level of the donor (Figure 17.6b) [35]. To facilitate exciton dissociation and charge transfer in the BHJ blend, the LUMO level of the donor needs to be positioned above the LUMO level of the acceptor by 0.2–0.3 eV ( $\Delta = 0.2-0.3$ , Figure 17.6b).

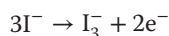
## 17.1.5

**Dye-Sensitized Solar Cells (DSSC)**

The study of DSSCs can be traced to 1972 when chlorophyll-sensitized ZnO electrode was used for photoelectron investigation, where photons were converted into electric current by charge injection from excited dye molecules into a wide band-gap semiconductor [36]. The efficiency could, during the following two decades, be improved by optimizing the porosity of electrodes prepared from fine oxide particles, but the instability remained a problem [37]. A modern DSSC, proposed by Brian O'Regan and Michael Grätzel [38], is mainly formed by a working electrode, counter electrode, and electrolyte introduced in between them (Figure 17.7). The working electrode is composed from a transparent electrode, porous layer of titanium dioxide nanoparticles covered with a molecular dye that absorbs sunlight, like chlorophyll in green leaves. The titanium dioxide and coated dye are immersed in the electrolyte solution. When light impinges onto the cell, the dye, which is typically a metal–organic Ru complex, absorbs photon where electrons are excited from the HOMO to LUMO and subsequently injected into conduction band of n-type semiconductor  $\text{TiO}_2$ . The electrons diffuse through the  $\text{TiO}_2$  network to the transparent electrode and pass through external circuits to the counter electrode. The counter electrode is coated with catalyst, such as Pt, where the electrons are delivered to triiodide in the electrolyte through reduction reaction:



The produced iodine ions ( $\text{I}^-$ ) diffuse toward dye molecules to supplement the iodine ions, which are consumed for reduction of the oxidized dye, and the reduction process is expressed as follows:



The sensitized dye has traditionally been made from ruthenium-based complexes (for example, N719 and Z907) [39, 40], which have fairly broad absorption spectra but low-molar extinction coefficients. Organic dyes have also been developed with substantially higher molar extinction but narrow spectral bandwidths. Co-sensitization of oxide particles by dyes with complimentary absorption spectra has been demonstrated to enhance light absorption and broaden the spectral

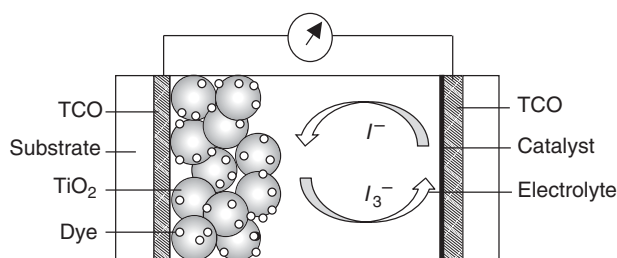


**Figure 17.7** Schematic illustration of working principle of DSSC.

response of DSSC [41]. In another technique called “energy relay”, a unattached luminescent chromophores dispersed in electrolyte absorb high-energy photon and subsequently transfer the energy by “Förster resonant energy transfer” mechanism to the anchored dye that is sensitive to long-wavelength light to achieve complementary absorption [42]. Up to now,  $\text{TiO}_2$  is the best material used for nanoporous thin films owing to its appropriate energy levels, dye adsorption ability, low cost, and easy preparation. Extensive research on other oxide materials has been carried out, and various materials have been developed such as ZnO [43].

Despite relatively high efficiencies for solar energy conversion, typical DSSC suffers from durability problem that results from their use of organic liquid electrolytes containing the iodide/triiodide redox couple, which causes serious problems such as electrode corrosion and electrolyte leakage. Replacements for iodine-based liquid electrolytes have been extensively studied, but the efficiencies of the resulting devices remain low [44]. Polymer hole-transport materials, such as 2,2',7,7'-tetrakis(*N,N*-di-*p*-methoxyphenyl-amine)9,9'-spirobifluorene (OMeTAD), P3HT, can be used to transport the holes generated on the dye molecules by photoexcitation to the counter electrode. Inorganic hole-transport materials have also been used to improve the cell stability, and more than 10% efficiency was reported recently by using  $\text{CsSnI}_3$  as hole-transport material loaded in N719-sensitized  $\text{TiO}_2$  porous material [45].

Table 17.1 summarizes the characteristics and performances of above-described solar cells. The crystalline cells have the highest efficiency, and the integration can only be done by a hybrid assembly. Thin film solar cells can be fabricated by a relatively low-temperature process, which is suitable for monolithic integration. Although the current effort of integration with IC/devices is mainly focused on inorganic solar cells ( $\alpha$ -Si, CIGS, etc.), organic solar cells are more promising because the potential of low-cost integration (like printing at room temperature) and their good indoor efficiency. CIGS and CdTe films can be deposited by electroplating; however, this process requires many additional steps, such as vacuum metallization, photolithography, encapsulation to protect IC/devices from attack of chemical bath.

**Table 17.1** Summary of performances of solar cells.

Solar cells	Lab efficiency (%), power density ( $\text{mW cm}^{-2}$ , AM1.5)	Panel efficiency(%), power density ( $\text{mW cm}^{-2}$ , AM1.5)	Hybrid assembly integration	Monolithic integration
c-Si	~24	13–18	Yes	Hard
$\alpha$ -Si	~14	5–10	Yes	Yes
CIGS	~20	10–12	Yes	Yes
CdTe	~18	~10	Yes	Yes
OPV	~9	~5	Yes	Yes
DSSC	~12 (liquid) ~10 (solid)	~9	Yes	Yes

## 17.2

## Monolithically Integration of Solar Cells with IC

As described earlier, solar cell is a competitive candidate as an energy harvester. There are two approaches to realize solar cell-based energy harvesting devices: hybrid assembly and monolithic. Hybrid assembly is off-the-shelf and offers freedom of using different sizes and types of energy generating and consuming components. Monolithically integrated devices, where solar cells are created above an IC, hold promise for small size and reduced manufacturing cost of microsystems [46]. The conversion efficiency is higher than that of hybrid assembly owing to the minimized wiring. Smaller cell sizes can lead to 3–5% efficiency boost [47]. Figure 17.8 shows the schematic of monolithic integration of a solar cell on an IC chip. Solar cells convert light into electricity, and the generated power is supplied to the underneath IC chip via conducting leads. The chip electronics consist of functional circuits, energy storage, and management modules. The energy storage can be done by capacitor or solid state battery. A stack of layers is deposited before solar cell fabrication, which functions as isolator, diffusion barrier (to avoid impurity contamination), and adhesion.

$\alpha$ -Si solar cell is a good candidate for monolithic integration as  $\alpha$ -Si materials can be processed at lower temperatures ( $\sim 200^\circ\text{C}$ ) and well-developed microfabrication technology exists owing to its wide application in flat-panel display industry. One embodiment of the fabrication process is first multilayers  $\text{SiO}_2/\text{Si}_3\text{N}_4/\text{SiO}_2$  are deposited in sequence by PECVD as passivation layer. Then, a metal layer, like Al, is deposited as bottom electrode of the solar cell. Ag, ZnO:Al, n-i-p  $\alpha$ -Si, ITO layers are deposited to complete the solar cells as described in Section 17.1.2. Similarly, other types of solar cells can be integrated on chips and processes are modified accordingly. CIGS is another good option for integrated energy harvester as the energy density of such solar cells is high [48]. However, the CIGS cell integration faces more challenges, such as high-temperature process ( $\sim 500^\circ\text{C}$ ) and Na ions contained in the active layer may cause negative impact

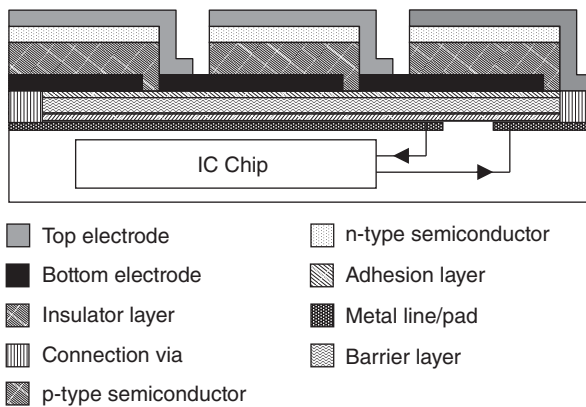


Figure 17.8 Schematic illustration of monolithically integration of solar cell with IC.

on the IC by diffusing through dielectric layers. Lu *et al.* introduced a CIGS–IC integration process with a maximum process temperature of 425 °C [46], where a stack of layers of  $\text{SiO}_2(250 \text{ nm})/\text{Si}_3\text{N}_4(300 \text{ nm})/\text{SiO}_2(250 \text{ nm})/\text{TiW}(100 \text{ nm})$  was deposited by PECVD on the IC chip surface. TiW was first deposited as adhesion layer between the IC and passivation layer stack. Then,  $\sim 1 \mu\text{m}$  Mo bottom electrode was sputter-deposited with 10 nm Ti as adhesion layer. 20–30 nm NaF was thermally evaporated for Na supply. CIGS (2  $\mu\text{m}$ ) absorption layer was deposited by three-stage co-evaporation [49]. CdS(50 nm) and i-ZnO(50 nm)/ZnO:Al(300 nm) were sequentially deposited by chemical bath and sputtering. Finally, the NiAl grid was thermally evaporated through shadow mask. They integrated both  $\alpha$ -Si and CIGS solar cells on Timepix CMOS chips using the aforementioned process. The efficiency of amorphous silicon solar cells reached 5.2%, and CIGS cells reached 7.1%. Energy of 70  $\mu\text{W}$  at one sun condition and 1  $\mu\text{W}$  at indoor condition has been generated with active area at approximately square millimeter scale, which is sufficient to power complicated CMOS circuits. After the integration process, the functionality of Timepix-CMOS chips remains unaffected [50].

### 17.3

#### Low-Power Micro Photovoltaic Systems

A typical low-power photovoltaic system has both input-end power management circuit, which interfaces the solar cell to the energy storage unit, and the output-end power management circuit, which connects the energy storage unit to the wireless sensor network (WSN) load as shown in Figure 17.9. The input-end power management often consists of the MPPT circuit. The output-end power management consists of the output voltage regulation.

##### 17.3.1

#### Maximum Power Point Tracking

Photovoltaic panels have  $I$ – $V$  (current–voltage) characteristics similar to the voltage-controlled current source [51]. The  $I$ – $V$  curve and related  $P$ – $V$  (power–voltage) curve showing the maximum power point (MPP) have been illustrated in Figure 17.1. The term “efficiency” of photovoltaic panels is referred

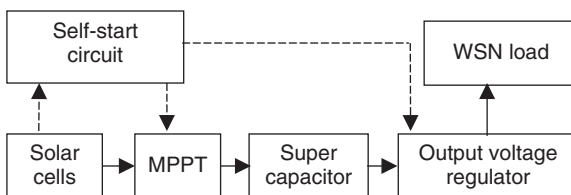


Figure 17.9 Low-power micro photovoltaic system architecture.



to as the conversion efficiency when the PV cell is operating at the MPP. However, MPP is not a fixed value. Factors such as irradiation level and temperature will impact the MPP. The process of tracking the MPP is called maximum power point tracking.

The typical MPPT circuit is illustrated in Figure 17.10. It consists of two parts: (i) DC–DC switching regulator with controllable switch frequency and duty cycle and (ii) MPPT control logic and algorithm. The MPPT control logic monitors the  $I-V$  characteristics of the PV cell and adjusts the switching regulator based on the control algorithm in order to achieve the MPPT. For conventional high-power applications, the main criterion of MPPT is the tracking accuracy. However, for MPPT design in energy harvesting applications, the primary difficulty resides in its small power budget. For PV cells with milliwatt or sub-milliwatt output power, microwatt power consumption MPPT circuit is required. Conventional methods such as perturb and observe (P&O) technique and incremental conductance (INC) technique are widely used for Watt level PV cells [52]. However, for energy harvesting applications, power consumptions of 10–100s milliwatts in these conventional MPPT systems are of several orders of magnitude higher than the power budget of micropower PV cells.

Recently, new P&O MPPT method using microcontroller and low-power boost converter has been proposed as shown in Figure 17.11 [53]. This method periodically samples the voltage of the PV cell using a Texas Instruments MSP430F microcontroller and generates a pulse width modulation (PWM) signal based on a programmed P&O MPPT algorithm. The low-frequency (100 Hz) PWM signal will then control the PWM signal generator to produce 10 KHz frequency PWM signal to boost low-position switch control. This frequency is adopted for two reasons: (i) it limits the inductor current to milliamp level in order to reduce the conduction loss and (ii) the form factor of the inductor is relatively small.

The main drawbacks of the P&O MPPT are (i) the P&O method needs a microcontroller or other digital signal processing (DSP) device to operate the control algorithm. This factor increases the cost of the MPPT controller. (ii) The needs to periodically disconnect the PV cells to monitor the open-circuit voltage reduce the harvested power and the overall conversion efficiency.

In addition to the P&O MPPT method, a technique called “fractional open-circuit voltage” MPPT has been introduced for energy harvesting applications [54]. The fractional open-circuit voltage technique is based on the nearly linear

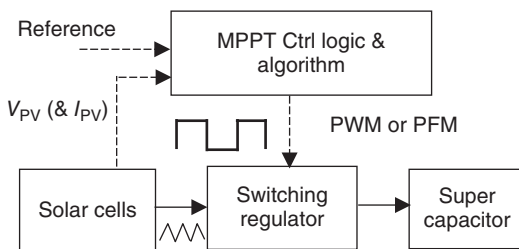
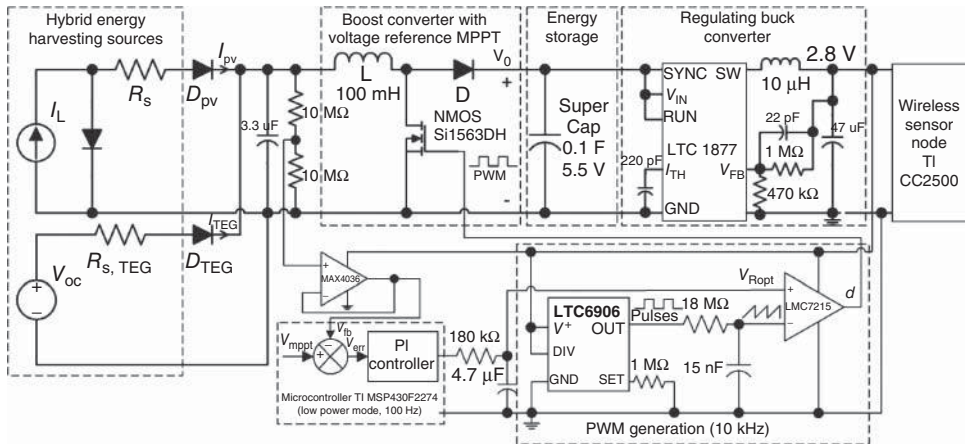
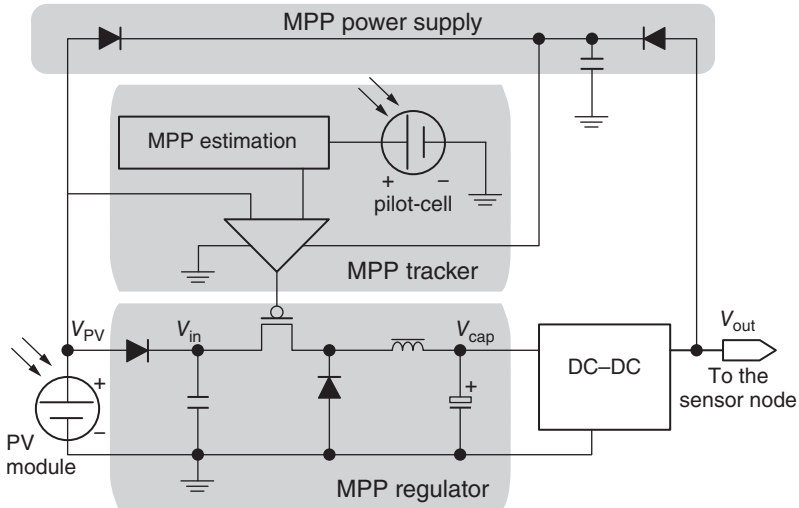


Figure 17.10 Switching regulator based maximum power point tracking.



**Figure 17.11** Low-power perturb and observe MPPT for low-power micro photovoltaic system. (Courtesy of IEEE.)

relationship between the MPP voltage ( $V_{MPP}$ ) and the open-circuit voltage ( $V_{OC}$ ) at certain light intensity. This relationship between  $V_{MPP}$  and  $V_{OC}$  leads to a simplified control mechanism. The MPPT control no longer requires a complicated microcontroller, but an analog comparator can fulfill the task as shown in Figure 17.12. The MPP estimation is performed using resistor voltage divider to set the 0.76 ratio ( $V_{MPP}/V_{OC}$ ) in this case [54]. The comparator is then used to generate the PWM signal for converter. This implementation takes the advantages of its simple structure and demonstrates its ultra-low-power



**Figure 17.12** Low-power fractional open-circuit voltage MPPT for low-power micro photovoltaic system. (Courtesy of IEEE.)

consumption capability. The disadvantage of slow response to changing light intensity (compared to P&O MPPT) is not a significant factor in this case because its applications are most likely for indoor environment with smaller irradiance changes.

### 17.3.2

#### Output Voltage Regulation

As discussed in the previous chapters, the electrical storage units for energy harvesting applications are mainly supercapacitors and rechargeable batteries. For WSN modules, the operating voltage is commonly between 1.8 and 5.0 V. Both supercapacitors and rechargeable batteries will require output voltage regulation circuits to provide a constant voltage to the load. The needs of output voltage regulation circuits are particularly important for supercapacitors, because its voltage varies, which is dependent on the state of charge (SoC).

For supercapacitors such as the ones reported in reference [55], the voltage rating is between 2.5 and 5.0 V. The supercapacitor voltage fluctuates between 0 V and its voltage rating. For conventional switching regulator targeted for applications with fixed input and output voltages in mind, for example, fixed 3–5 V boost converter for AA battery to USB applications, the voltage range is too small and not suitable for this application. Wide input voltage range boost converters or buck-boost converters are able to “extract” more power from supercapacitors than conventional fixed voltage converters.

In recent years, commercial off-the-shelf switching regulators with high efficiency at small input power have been developed for energy harvesting applications. Devices such as Texas Instruments boost converter TPS6122x series demonstrate >90% efficiency and a wide 0.9–3.3 V input voltage range as shown in Figure 17.13. Compared to linear drop-out regulator (LDO), the higher efficiency and smaller (microwatt) quiescent current improve the energy

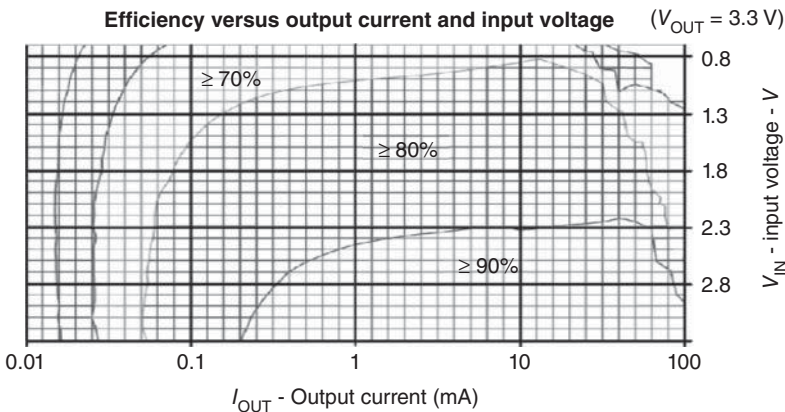


Figure 17.13 Texas instruments boost converter TPS61221 efficiency chart.

utilization from the stored energy in supercapacitors. However, for battery type of energy storage, owing to its smaller voltage difference between the battery (e.g., 3.7 V Li-ion battery) and the load (e.g., 3.5 V WSN module), the power loss is not significantly increased when the LDO is used. The low cost of the LDO device and no requirement for inductor make LDO a more suitable solution in the case of battery energy storage.

In summary, boost or buck-boost converters are essential for the output voltage regulation when the supercapacitor type of energy storage unit is used. The recent developments of the commercial off-the-shelf solutions provide suitable devices for energy harvesting applications. For a battery energy storage unit, linear regulators can be used for their low cost and small bill of material. The efficiency of linear regulators is not significantly lower than switching regulators and can be tolerated by choosing the battery voltage close to the load voltage.

### 17.3.3

#### Indoor-Light-Powered Wireless Sensor Networks – a Case Study

A case study in this chapter discusses the system level design details. Wireless sensor modules for machine health monitoring applications had been developed. An example of the proposed wireless sensor system is the Tyndall mote with its system architecture shown in Figure 17.14. The mote is implemented by using a Texas Instruments MSP430 series microcontroller. This solution includes an IEEE802.15.4 standard 2.4 GHz radio and also a series of I/Os in order to communicate with analog and digital sensors. Interintegrated circuit (I<sup>2</sup>C) ports have also

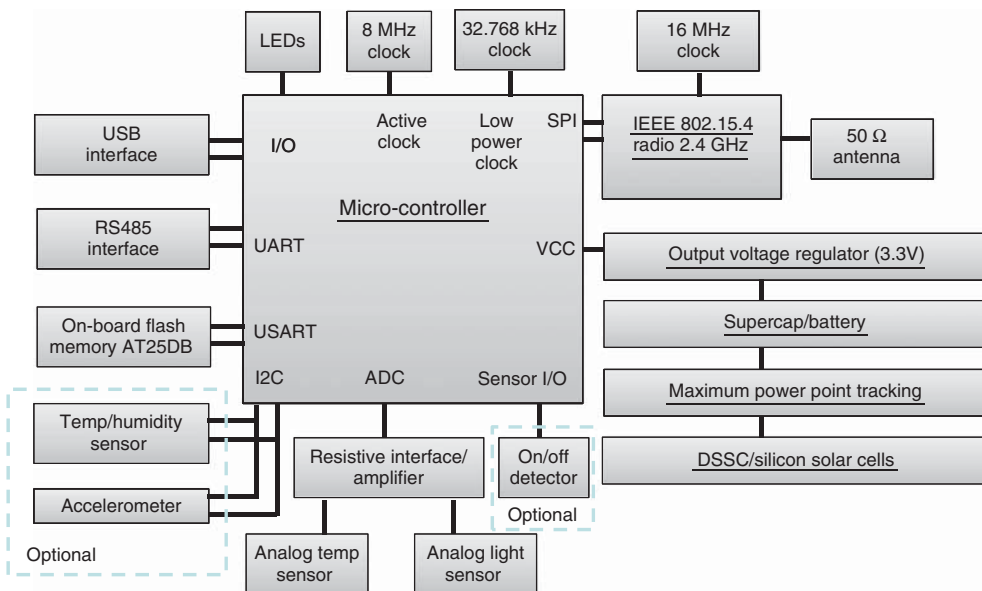
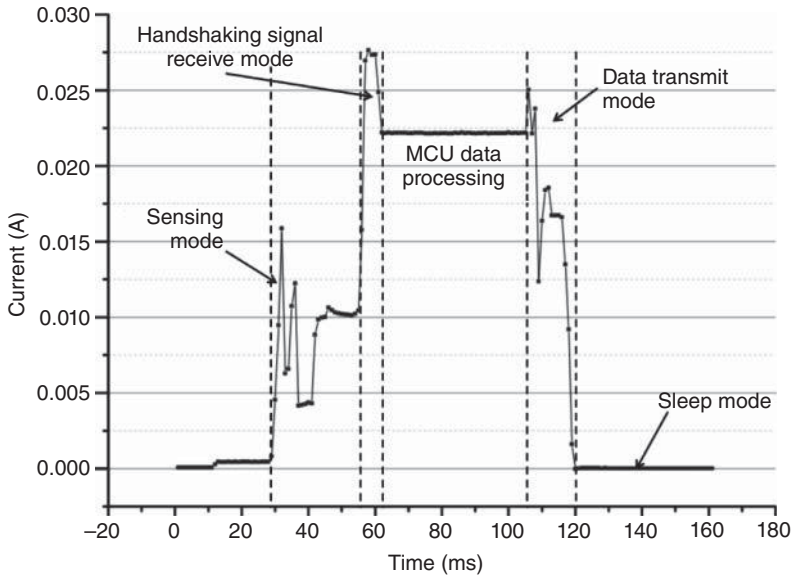


Figure 17.14 Tyndall National Institute Wireless Sensor Node System Architecture.



**Figure 17.15** Tyndall National Institute Wireless Sensor Node Power Consumption.

been utilized to connect the microcontroller to accelerometer and temperature and relative humidity sensors. An internal analog-to-digital converter (8 channels and 12 bits) is used to collect analog sensor data. For the machine health monitoring application, the main parameters need to be monitored are (i) temperature; (ii) vibration; and (iii) on/off condition of the machine. The sensing and transmission are repeated every 1 min. The power consumption of the mote is shown in Figure 17.15. The average active mode power consumption is approximately 20 mA, and the active mode lasts for 100 ms. The sleep mode lasts for 59.9 s and consumes 0.01 mA. The average current consumption of the mote is 0.045 mA. The average power consumption is 0.145 mW when the supply voltage is 3.3 V.

The vibration data is processed using fast Fourier transform to analyze the frequency domain signal. The accumulated data provide important indicators of the machine health. These data have been used to perform preventive maintenance for high-cost machinery in order to reduce downtime cost and repair cost.

Indoor-light energy harvesters have been used to supply power to the advanced machine health monitoring network. Amorphous silicon solar cell Sanyo AM series has been used as the main cell. The dimension of the cell is 58 mm × 48 mm. A reference solar cell from the same amorphous silicon solar cell family is used to detect the open-circuit voltage. The form factor of the secondary cell is only 20 mm × 9 mm. The MPPT circuit is a buck-converter-based fractional open-circuit voltage tracker similar to the design shown in Figure 17.12. The energy storage unit is a supercapacitor with 5F capacitance (62.5 J energy when fully charged). The output voltage regulator circuit is based on a Texas Instruments TPS61220 series boost converter. The complete system is shown in Figure 17.15.

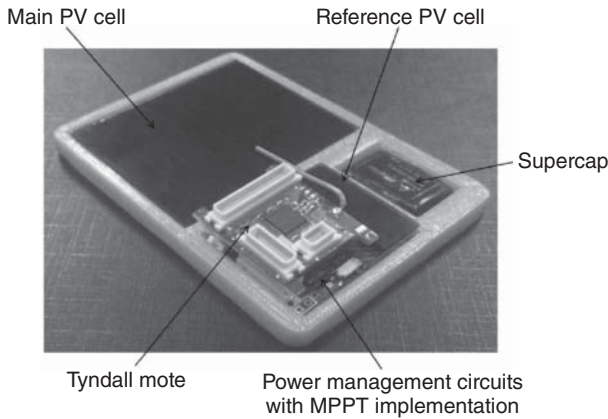


**Figure 17.16** Indoor-light-powered wireless sensor node.

The size of the complete self-powered sensor node is  $88\text{ mm} \times 60\text{ mm}$ , which is similar to the size of a credit card. The experimental results demonstrated a 70% end-to-end conversion efficiency of the power management circuit. In typical indoor conditions, the light intensity is between 300 and 500 lux. The harvested power is between 0.3 and 0.5 mW. The harvested energy is sufficient to continuously power the wireless sensor node. Once the supercapacitor is fully charged, the stored energy can supply the mote for more than 100 h when ambient light is not available (Figure 17.16).

## 17.4

### Summary

In this chapter, we have described several types of solar cells based on p–n junction and organic molecules. We have started from crystalline silicon solar cells that enable us to get familiar with p–n junction type solar cells. Based on this an other p–n-junction-based solar cells, which include amorphous silicon cells, CIGS, cadmium telluride (CdTe) cells have been introduced. Organic-molecule-based solar cells, DSSC and polymer solar cells, which are based on different working principles and can be fabricated by very low cost process, like printing, have also been illustrated. Solar cell architecture, material optimization, fabrication process were addressed. Although other types of solar cells, such as GaAs, nanowires, quantum dot solar cells, have not been mentioned because of the space limitation, one can understand them easily after reading this chapter. Monolithic integration of solar cells with functional devices/IC was briefly described by citing  $\alpha$ -Si and CIGS cells as examples. Power management circuitry was introduced with a focus on ultra-low-power MPPT. Micro photovoltaic power management circuits were illustrated showing the state-of-the art in this energy harvesting research area.

## References

1. Williams, R. (1960) *J. Chem. Phys.*, **32**, 1505.
2. Rezende, L. (2006) *Chronology of Science*, Infobase Publishing, p. 227.
3. Stoletow, M.A. (1888) *Philos. Mag. Ser.*, **5**, **26**, 317.
4. André, N. (2008) *History of Solar Flight*, Swiss Federal Institute of Technology, Zürich, July, 1–7.
5. Fesquet, L. *et al.* (2009) Modification of textured silicon wafer surface morphology for fabrication of heterojunction solar cell with open circuit voltage over 700 mV *34th IEEE Photovoltaic Specialists Conference (PVSC)*, p. 754–758, *IEEE, Philadelphia, PA*.
6. Sterling, H.F. and Swann, R.C.G. (1965) *Solid State Electron.*, **8**, 653.
7. Spear, W.E. and Le Comber, P.G. (1975) *Solid State Commun.*, **17**, 1193.
8. Carlson, D.E. and Wronski, C.R. (1976) *Appl. Phys. Lett.*, **28**, 671.
9. van Veen, M.K. and Schropp, R.E.I. (2002) *Thin Solid Films*, **403–404**, 135.
10. Wagner, S., Shay, J.L., Migliorato, P., and Kasper, H.M. (1974) *Appl. Phys. Lett.*, **25**, 434.
11. Basol, B.M. *et al.* (1996) *Sol. Energy Mater. Sol. Cells*, **43**, 93.
12. Herz, K. *et al.* (2002) *Thin Solid Films*, **403–404**, 384.
13. Chirila, A. *et al.* (2011) *Nat. Mater.*, **10**, 857.
14. Ishizuka, S. *et al.* (2008) *Appl. Phys. Lett.*, **93**, 124105.
15. Klenk, R., Walter, T., Schock, H.-W., and Cahen, D. (1993) *Adv. Mater.*, **5**, 114.
16. Gabor, A., Tuttle, J., Albin, D., Tennant, A., Contreras, M.A., Noufi, R., and Hermann, A.M. (1993) High efficiency polycrystalline Cu(In,Ga)Se<sub>2</sub>-based solar cells. *12th NREL Photovoltaic Program Review, Denver*, P59–66.
17. Chu, T.L., Chu, S.S., Lin, S.C., and Yue, J. (1984) *J. Electrochem. Soc.*, **131**, 2182.
18. Chen, G.S., Yang, J.C., Chan, Y.C., Yang, L.C., and Huang, W. (2009) *Sol. Energy Mater. Sol. Cells*, **93**, 1351.
19. Kang, F., Ao, J., Sun, G., He, Q., and Sun, Y. (2010) *Curr. Appl. Phys.*, **10**, 886.
20. Park, J.W. *et al.* (2009) *J. Cryst. Growth*, **311**, 2621.
21. Liu, W. *et al.* (2010) *Chem. Mater.*, **22**, 1010.
22. Bonnet, D. and Rabenhorst, H. (1972) New results on the development of a thin-film p-Cde-n-CdS heterojunction solar cell. *Proceedings of the 9th IEEE Photovoltaic Specialists Conference*, p. 129.
23. Ferekides, C. and Britt, J. (1993) *Appl. Phys. Lett.*, **62**, 2851.
24. Ferekides, C.S. *et al.* (2000) *Thin Solid Films*, **361–362**, 520.
25. Kestner, J.M. *et al.* (2004) *Sol. Energy Mater. Sol. Cells*, **83**, 55.
26. Bhattacharya, R.N. and Rajeshwar, K. (1984) *J. Electrochem. Soc.*, **131**, 2032.
27. Chu, T. and Chu, S. (1993) *Prog. Photovoltaics*, **1**, 31.
28. Burroughes, J.H. *et al.* (1990) *Nature*, **347**, 539.
29. Ebisawa, F., Kurokawa, T., and Nara, S. (1983) *J. Appl. Phys.*, **54**, 3255.
30. Yu, G. *et al.* (1995) *Science*, **270**, 1789.
31. Tang, C.W. (1986) *Appl. Phys. Lett.*, **48**, 183.
32. Kim, J.Y. (2007) *Science*, **317**, 222.
33. Zhou, H. *et al.* (2013) *Adv. Mater.*, **25**, 1646.
34. de Leeuw, D.M., Simenon, M.M.J., Brown, A.R., and Einerhard, R.E.F. (1997) *Synth. Met.*, **87**, 53.
35. Brabec, C.J. (2001) *Adv. Funct. Mater.*, **11**, 374.
36. Tributsch, H. (1972) *Photochem. Photobiol.*, **16**, 261.
37. Matsumura, M. (1980) *Ind. Eng. Chem. Prod. Res. Dev.*, **19**, 415.
38. O'Regan, B. and Grätzel, M. (1991) *Nature*, **353**, 737.
39. Nazeeruddin, M.K. *et al.* (2005) *J. Am. Chem. Soc.*, **127**, 16835.
40. Wang, P. *et al.* (2003) *Nat. Mater.*, **2**, 402.
41. Cid, J.-J. *et al.* (2007) *Angew. Chem.*, **119**, 8510.
42. Hardin, B.E. *et al.* (2009) *Nat. Photonics*, **3**, 406.
43. Zhang, Q., Dandeneau, C.S., Zhou, X., and Cao, G. (2009) *Adv. Mater.*, **21**, 4087.
44. Bach, U. *et al.* (1998) *Nature*, **395**, 583.
45. I Chung *et al.* *Nature* **485**, 486 (2012).

46. Lu, J. (2011) Solar cell on CMOS chips as energy harvesters – integration and CMOS compatibility, PhD thesis. University of Twente.
47. Green, M.A. *et al.* (2011) *Prog. Photovoltaics Res. Appl.*, **19**, 84.
48. Matsushima, O. *et al.* (2008) A high-sensitivity broadband image sensor using CuInGaSe<sub>2</sub> thin films, Electron Devices Meeting, IEDM. IEEE International.
49. Kohara, N. *et al.* (1995) *Jpn. J. Appl. Phys.*, **34**, L1141.
50. Lu, J. *et al.*, Above-CMOS a-Si and CIGS Solar Cells for Powering Autonomous Microsystems, Proceedings of the 2010 IEEE International Electron Devices Meeting (IEDM), p. 3131–3134, 6–8 Dec 2010, San Francisco, USA.
51. Castaner, L. and Silvestre, S. (2002) *Modelling Photovoltaic Systems Using PSpice*, John Wiley & Sons, Ltd, Chichester.
52. Femia, N., Petrone, G., Spagnuolo, G., and Vitelli, M. (2005) *IEEE Trans. Power Electron.*, **20**, 963.
53. Tan, Y.K. and Panda, S.K. (2011) *IEEE Trans. Ind. Electron.*, **58**, 4424.
54. Brunelli, D., Moser, C., Thiele, L., and Benini, L. (2009) *IEEE Trans. Circuits Syst.*, **56**, 2519.
55. Devillers, N. *et al.* (2014) *J. Power Sources*, **246**, 596.



## 18

# Power Conditioning for Energy Harvesting – Case Studies and Commercial Products

*Paul D. Mitcheson and Stephen G. Burrow*

### 18.1

#### Introduction

Many of the ideas presented in Chapter 4 are inspired by similar techniques already employed in larger-scale power electronics and the intention here therefore is to apply them to miniature energy harvesting systems. Some of the techniques are not utilized in more traditional power electronic systems, however, and have emerged as a result of the specific requirements that harvester systems bring. Irrespective of the background to each specific technique, all types of harvester interface circuits have several common considerations when designing a practical implementation:

- Real semiconductor switches are imperfect and at the low power output levels of a harvester, the leakage currents, parasitic capacitances, and the need to supply gate drive power can significantly reduce the efficiency of the power processing circuits.
- Control overhead (i.e., switch timing, duty cycle control, regulation, etc.) can typically be achieved using only a small fraction of the processed power in regular power electronics applications (e.g., a laptop power supply), but in the case of harvesters, the power levels are so low that maintaining the control power level to be a small fraction of the processed power can be very challenging.
- Components, both passive and active, may still need to handle relatively high peak currents, even if the root mean square (RMS) values are low. This means that semiconductor switches need a greater cross-sectional area than may originally be expected, and passives (particular inductors) may consume more volume than would be attractive in an energy harvesting system.

As we will see in this chapter, which discusses several case studies of prototype harvester systems which feature nontrivial power processing interfaces, the techniques utilized and solutions presented must work to mitigate these effects. Two examples of interface circuits for electromagnetic harvesters are presented, one which performs real-time maximum power point tracking, rectification, and voltage boost [1] and one which is able to frequency-tune the harvester, widening

the bandwidth [2]. An implementation of a single-supply pre-biasing circuit for piezoelectric harvesters is described, with particular emphasis on the design of the switches and low-power timing control [3]. A simple yet practical demonstration of an interface circuit for an electrostatic electret-based harvester is also presented. Then, moving away from kinetic harvesters, a thermal harvester system in which a low-power rectifier and interface circuit for use on an aircraft application is presented. Finally, some commercial power electronic interface integrated circuits are discussed.

## 18.2

### Submilliwatt Electromagnetic Harvester Circuit Example

The authors of [4] describe a self-contained power conditioning system for electromagnetic vibration harvesters based upon a boost rectifier power stage, and incorporating start-up and auxiliary circuitry. The system is designed for power levels in the 0.1–1 mW range and the system, realized from micro-power discrete components, achieves efficiencies of 65% at 0.9 mW and 51% at 200  $\mu$ W, including quiescent losses. The power circuit can extract 84% of the available power from the harvester: the ability of the power conditioning circuits to extract power from the harvester is quite distinct from efficiency, and is dependent upon the circuit providing optimal load impedance to the harvester, that is, an impedance match to the transducer and mechanical system.

The system is designed to power a wireless sensor node which consumes 40 mW in active mode, with operation duty cycled so that the average load power matches the average generated power. Matching the temporal power output is achieved by a supercapacitor and under-voltage lock-out which only connects the load when sufficient power is available for a cycle of operation.

The boost rectifier power stage topology, illustrated in Figure 18.1, has the advantage that the inductor is on the AC input side of the converter, and thus the parasitic inductance of the harvester can be used in place of a separate wound component (however, it should be noted that this parasitic inductor may have higher losses than could be achieved with a discrete component and so a careful design trade-off is required). Similar power stage topologies for energy harvesting have also been described by other authors, for example, by Dwari and Parsa [5]. In [4], the boost rectifier is operated as a resistance emulator with a fixed duty cycle pulse width modulation (PWM), similar to the concept described in Ref. [6].

As with all low-power, power switching circuits, the choice of the active devices is critical to achieving high performance. However, the optimum balance of switching and conduction losses for a particular device tends to occur at a particular power level and hence it is difficult to design the converter to operate efficiently over a wide power range.

The main boost rectifier [4] is unable to “cold start” as it requires gate drive signals from the control circuits and so a passive diode multiplier arrangement is employed. This is illustrated along with the other auxiliary circuits in Figure 18.2.

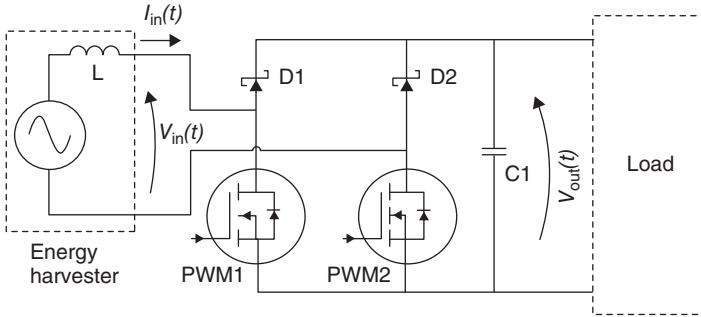


**Figure 18.1** Boost rectifier circuit from Ref. [4], exploiting inductance of the harvester coil to perform the boost function.

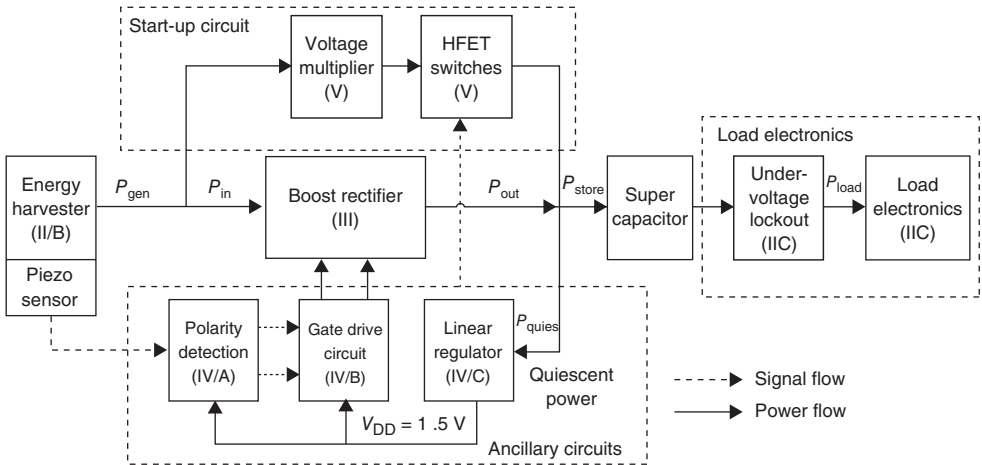


**Figure 18.2** Complete power conditioning system topology including start-up and auxiliary circuits. Redrawn from Ref. [4].

An advantage of the separated start-up and main power circuits is that the charge pump can quickly establish a supply to support the modest requirements of the auxiliary circuitry, enabling the boost rectifier to optimally load the harvester and charge the supercapacitor. If the supercapacitor and auxiliary circuits shared a common rail, the start-up time would drastically increase as the boost converter would be unable to operate as a resistance emulator until the supercapacitor is charged by the charge multiplier. The power extracted by the multiplier is affected by the number of stages, capacitance, and the output rail voltage, all of which have to be carefully chosen to produce the fastest possible start up. This is normally achieved when the multiplier's maximum power point occurs at an output voltage slightly below the final desired level.

All auxiliary circuits of Figure 18.1 consume just 21  $\mu\text{W}$ , and are realized from various discrete and micro-power components. This illustrates the potential to develop power conditioning circuits for low-power harvesters without the cost

implications of dedicated integrated manufacture, and keeping alive the possibility of small volume applications.

In a subsequent publication [1], the authors add an active control loop around the boost rectifier which implements an MPTT (maximum power transfer tracking) algorithm. The MPTT algorithm attempts to locate the loading point of the harvester (by altering the converter input resistance) which results in maximum power being developed in the load, or in this case, energy stored in the supercapacitor. By considering the output power, MPTT takes into account losses and thus the peak may occur at a differing point to peak input power (on which a standard MPPT scheme works). The MPTT algorithm was implemented on a Texas Instruments (TI) MSP430 digital signal processor (DSP) for an additional quiescent overhead of just 23  $\mu\text{W}$ ; however, although this device has enough capability to implement other control functions, it is not power efficient to do so. This is especially true for the PWM generation where the high clock frequencies required to synthesize even modest resolution variable duty cycles consume far too much power for ultra-low-power applications.

When energy harvesting first emerged in the research literature in the late 1990s/early 2000s, this level of functionality for such a low power level was unimaginable. However, rather ironically, the significant attention that has been given to power consumption by component and integrated circuit (IC) designers due to the ever increasing use of battery-operated mobile devices has drastically reduced the power consumption of key circuit building blocks, such as embedded microprocessors and comparators.

### 18.3

#### Single-Supply Pre-biasing for Piezoelectric Harvesters

Moving on to piezoelectric harvester interface circuits, the basic principle of single-supply pre-biasing as a method to provide increased electrical damping to a piezoelectric cantilever was described in Chapter 4. The method can be thought of as a low-power method of performing power-factor correction on a piezoelectric transducer (necessary because the piezoelectric element presents capacitive, rather than resistive, output impedance). The main requirements for implementation, therefore, are that the system is able to chop the otherwise sinusoidal voltage waveform output of the piezoelectric transducer into the characteristic shape that all the charge-modification circuits of this type perform, as shown in Figure 18.3 [7]. In order for the circuit to be beneficial (i.e., to collect more useful energy than a passive rectifier), the control and timing circuits must be very low power and the timing of the switching must be accurately timed to the peaks of the transducer displacement. In Chapter 4, the circuit operation was discussed in terms of perfect switches; however, a real system must use semiconductor switches and hence the limitations of Metal Oxide Semiconductor Field Effect Transistor (MOSFET)s, including leakage, parasitic capacitance, and

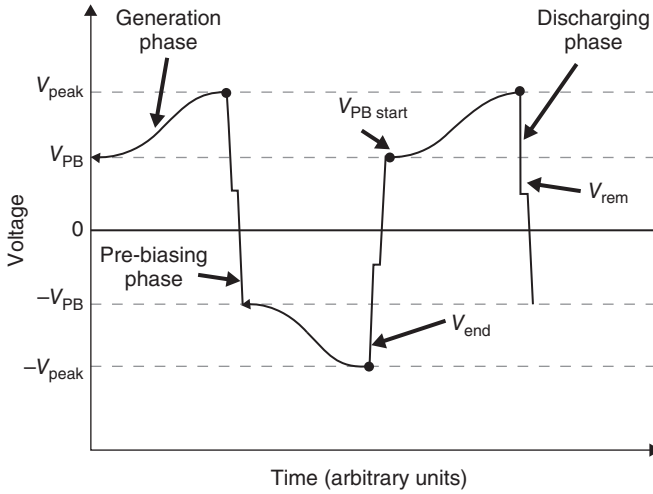


**Figure 18.3** Single supply pre biasing (SSPB) waveform consisting of a sine wave with polarity reversal twice per cycle. Redrawn from Ref. [7].

the ability only to block voltage in one direction can become significant barriers to successful implementations of this circuit.

A practical implementation of the SSPB circuit is shown in Figure 18.4. The most obvious difference between the idealized circuit discussed in Chapter 4 and the embodiment presented here is that it is not possible to simply replace each of the four switches with only one MOSFET, with two devices being used to form

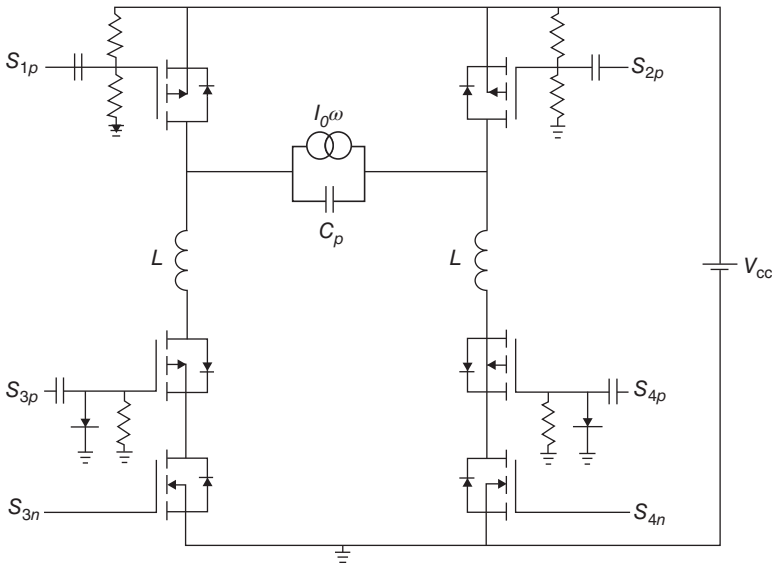


**Figure 18.4** Practical embodiment of SSPB circuit. Redrawn from Ref. [8].

each of the lower switches [8]. The low-side switches must each be constructed of two series-connected MOSFETs so that as the voltage across the piezoelectric element rises, the voltage is not constrained to have a magnitude the same value, or less, than the supply rails. If only a single MOSFET is used as a switch, if the voltage on the piezoelectric material exceeds the power supply, the drain-body diodes of the MOSFETs come into conduction and short-circuit the piezoelectric capacitance. Two series MOSFETs, however, are able to block voltage between source and drain with either polarity and hence the double arrangement allows SSPB operation.

As was mentioned in the discussion of the boost rectifier, the choice of MOSFETs is crucial so minimize the sum of the switching, conduction, leakage, and gate-drive losses. In this circuit, as the piezoelectric capacitance is charged using a resonant pulse of current through an inductor, the peak currents through the MOSFETs can be relatively large and care must be taken to ensure that the peak resonant current does not drive the MOSFETs into saturation, as this will significantly degrade the Q-factor of the resonant path.

An additional practical aspect is realizing this circuit is biasing the gates of the MOSFETs in such a way that the gate signals can be realized in a low-power way and easily generated from low-power digital control circuit. In order to achieve ultra-low-power operation of the gate drives, traditional gate drives, which include level-shifting circuitry and in some cases a large isolation barrier, cannot be used. However, simple level shifting of the gate control signals using capacitors, diodes, and resistors allows the MOSFET gates to be easily interfaced to a digital controller. These biasing circuits are also shown in Figure 18.4.

The final part of the SSPB system is the timing circuitry which determines when, and for how long, the MOSFETs should be turned on for. Sensing the peaks of the piezoelectric voltage waveform is complicated under the SSPB scheme because of the modifications that are made to the waveform during circuit operation. As it is easier to detect the peaks of a simple sinusoid than the SSPB-modified waveform, a sense piezo, mechanically linked to the power generation piezo, is used to drive the peak detect circuits. Figure 18.5 shows the low-power peak detect circuit that was used. The capacitor on the DC side of the bridge rectifier stores a copy of

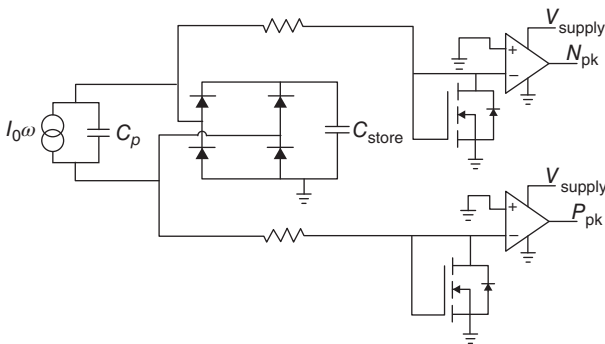


**Figure 18.5** Ultra-low-power peak detection circuit. Redrawn from Ref. [8].

the peak value of the piezoelectric device voltage which is then used to level shift the piezo voltage and the peaks and troughs of the level-shifted waveform pass through zero, causing the comparators to change state. This peak detector design consumes only  $2.8 \mu\text{W}$ , using Microchip MCP6542 comparators.

The positive and negative peak detect signals are then passed to a low-power field programmable gate array (FPGA) (commercial brand name (IGLOO)<sup>®</sup> nano by Microsemi) which controls the order in which the switches are fired and, through the use of a simple resistor capacitor (RC) time constant, the length for which the switches are held on (which is half a cycle of the resonant period of the series inductor and piezoelectric capacitance).

The power output from this implementation of SSPB has been measured and compared to other piezoelectric interface schemes. This comparison is shown in Figure 18.6. The  $x$ -axis shows the peak open circuit value of piezoelectric voltage and the  $y$ -axis the output power. As can be seen, the SSPB circuit outperforms all other known circuit interfaces across a wide range of power levels and achieves effectiveness (i.e., power output divided by maximum possible power output) of around 50%. As can be seen, for these tests, the lowest SSPB circuit overhead was  $126 \mu\text{W}$ , although later versions of the control scheme have consumed less than  $35 \mu\text{W}$ .

While SSPB, and other piezoelectric interfaces such as synchronised switch harvesting on inductor (SSHI) are able to extract significantly more power from a piezoelectric harvester than a simple bridge rectifier, challenges still remain, especially in determining when to switch the system if the input

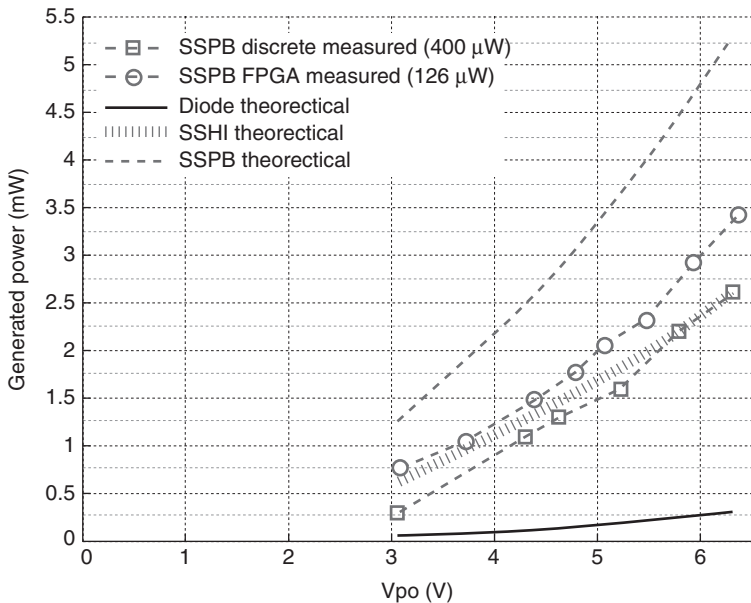


Figure 18.6 Power output from SSPB compared to other schemes. Replotted from Ref. [8].

motion is non-sinusoidal. However, this problem is more than just one of a circuit implementation, because the switching strategy is not necessarily straightforward.

#### 18.4

##### Ultra-Low-Power Rectifier and MPPT for Thermoelectric Harvesters

Thermoelectric harvesters have been recently prototyped as power supplies for strain gages on aircraft [9]. The strain gage and power supply are situated outside the cabin and thus are subjected to large temperature variations during the course of a flight cycle, from upward of 20 °C when the aircraft is on the ground in warm weather to below –50 °C at altitude. As thermoelectric harvesters require a spatial thermal gradient, and the outside airframe of the aircraft only exhibits temporal thermal gradients, a mechanism must be found to convert temporal thermal gradients to spatial thermal gradients. This is accomplished via the use of a heat storage unit, essentially a sealed container of water that will undergo a phase change when passing through 0 °C when freezing (as the aircraft climbs) and when melting (as the aircraft descends). This means that a spatial thermal gradient can be achieved between the atmosphere (i.e., the part of the airframe to which the harvester is fastened) and the heat storage unit.

In order for the system to convert as much of the latent heat energy of the phase change material as possible into an electrical form, the thermoelectric generators are connected to a switch-mode circuit capable of performing maximum power point tracking [10]. In this case, a Texas Instruments bq25504 MPPT boost converter is used. This circuit has a cold-start capability from around 300 mV, which means that the thermo electric generator (TEG) must be designed so that under normal operating conditions the transducer produces at least this voltage.

A critical aspect of this type of harvester is the reversal of polarity of the electrical output of the TEG between the ascent and descent of the airplane (as the hot side of the TEG changes) requires a rectifier to be used in the system. The rectifier must be of the full-wave variety or half the possible converted energy from the flight cycle will be lost. In addition, it cannot be a passive rectifier because the voltage needed to effectively overcome the diode on-state voltage is not feasible for the TEG under these thermal gradients. Therefore, the rectifier must be an active one using MOSFETs. In addition, if the system is truly cold starting (i.e., no energy is present in a local capacitor or battery), the active rectifier must be capable of self-starting, that is, the MOSFETs must be arranged in such a way that two of them are in the on-state and two are in the off-state to allow energy to be extracted from the TEG. The active rectifier arrangement is shown in Figure 18.7.

This is achieved by making devices  $M_2$  and  $M_4$  depletion-mode devices, so that they are normally on, allowing cold start of the aircraft has been on the ground for long periods. When the aircraft descends, these depletion mode devices need to be turned off and the normally off enhancement devices ( $M_1$  and  $M_3$ ) must be turned on. In order to turn off the depletion-mode devices,



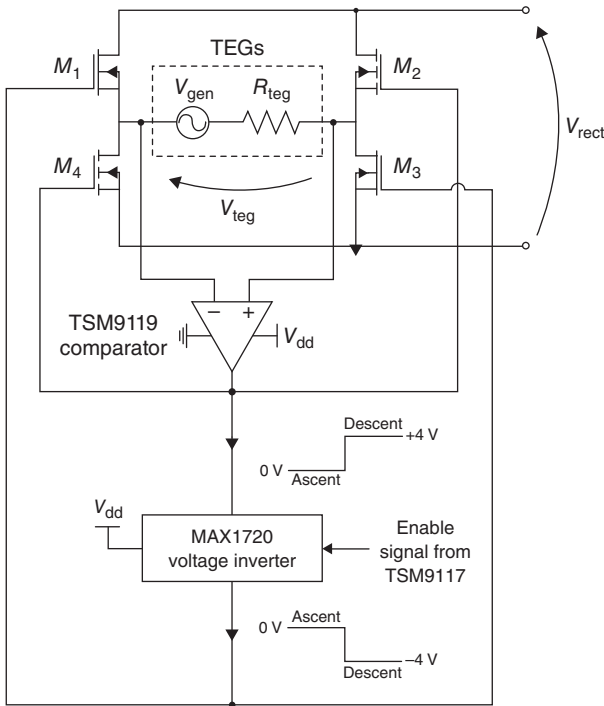


**Figure 18.7** Ultra-low-power rectifier for thermoelectric harvester in aircraft applications. Redrawn from Ref. [10].

a negative rail must be generated, and this is achieved with a MAX 1720 switch mode device. The MAX 1720 consumes a quiescent current of  $57 \mu\text{A}$  which is a significant overhead on current draw over half of the aircraft flight cycle. Therefore, when the negative voltage rail is needed, the MAX 1720 is duty cycled and only turned on when the voltage on its output capacitor goes above  $-2.5 \text{ V}$ .

The system has been shown to be capable of harvesting a total of  $126 \text{ J}$  from the TEG during one flight cycle, of which  $81 \text{ J}$  was delivered to the battery.

## 18.5

### Frequency Tuning of an Electromagnetic Harvester

As described in Chapter 4, the possibility of frequency tuning a mass-spring-damper system is attractive because the bandwidth of a motion-driven harvester can be maximized without compromising the peak available power – that is, the system can exhibit both the properties of a high  $Q$ -factor and large bandwidth at the same time. Mechanical tuning mechanisms add weight, volume, and mechanical complexity, whereas a mechanism which allows tuning using the power electronic interface adds little complexity other than a marginal increase

in sophistication of the control overhead. The mechanism for tuning involves providing a reactive load element which can tune out any residual reactance of either the mass or spring (which is present when the mechanical system is not operating at resonance), hence allowing a conjugate impedance match between the mechanical system and the electrical load even when the system operates away from the resonant frequency set by the mass and the spring.

Several circuits are capable of exchanging real and reactive power between a battery and the mechanical system and the example of a half-bridge used for this purpose was given in Chapter 4. A full bridge, or H-bridge, has the advantage of being able to allow the transducer to produce open circuit voltages of twice those that can be used with the half-bridge, while still operating correctly, for a given voltage on the storage element. An H-bridge-based frequency tuning mechanism, as deployed in conjunction with a large pendulum-based energy harvester [11], is shown in Figure 18.8. The pendulum-based harvester was deployed in a kayak and the objective was to modify the resonant frequency of the pendulum to equal the frequency of waves striking the kayak.

As can be seen in Figure 18.8, the pendulum is mechanically connected to two DC generators which are then electrically connected in series. The power interface circuit and control are shown in Figure 18.9. As was mentioned previously with the boost rectifier connected to an electromagnetic harvester, the transducer itself provides the necessary input inductance for the converter.

The control scheme is relatively simple: the electro-magnetic force (emf) generated by the transducers cannot be directly sensed, because when current is drawn from them their impedance causes the transducer terminal voltage to differ from the generated emf [2]. Consequently, a separate tachometer is used to measure a scaled copy of the transducer emf. The required current into the converter is then calculated by dividing the emf by the required load impedance that provides the

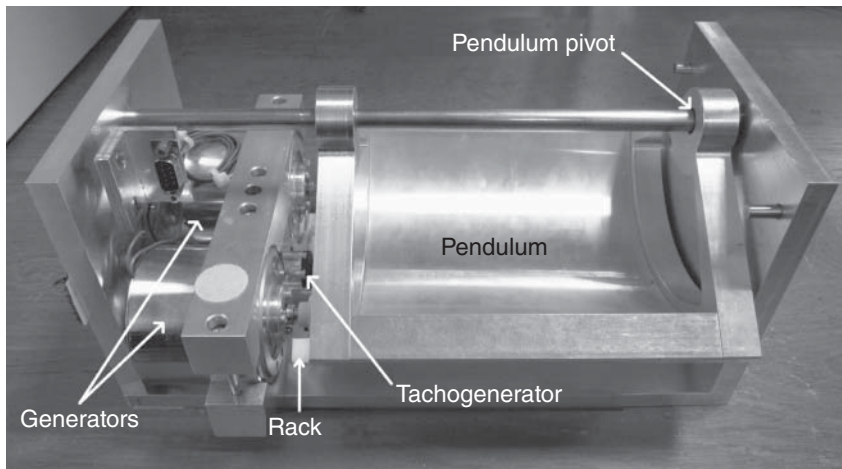


**Figure 18.8** Pendulum energy harvester used in a system with electronic frequency tuning. Redrawn from Ref. [2].

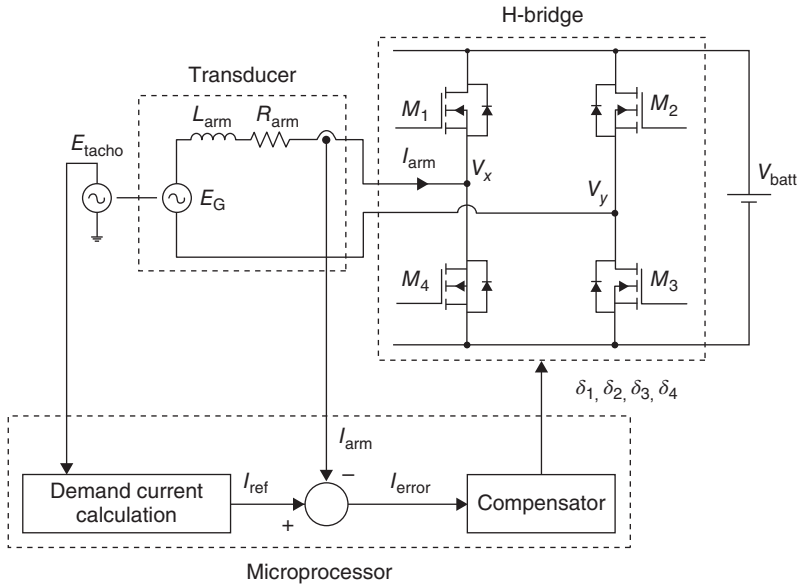


Figure 18.9 Electronic frequency tuning scheme. Redrawn from Ref. [2].

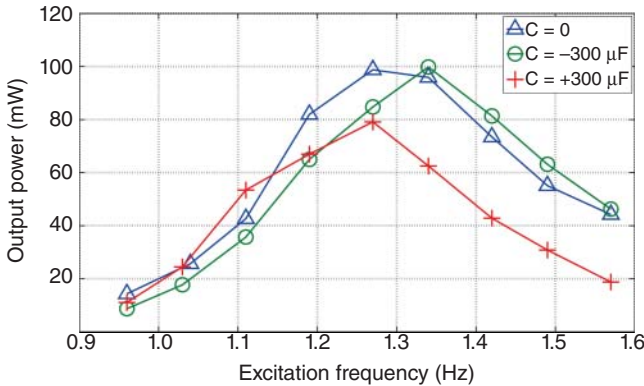


Figure 18.10 Performance of electronic tuning. Replotted from Ref. [2].

conjugate match. A proportional integral (PI) controller then ensures the transducer current follows the demand current.

The performance of the system is shown in Figure 18.10. The resonant frequency of the system clearly changes as reactive electrical loads are added, widening the effective system bandwidth. In this example, the controller is implemented on a Microchip PIC18F2431. The power consumption of the control scheme is several milliwatts, which in many cases is greater than the power improvement that the scheme can generate. Hence, a lower power control scheme should be implemented in this system.

## 18.6

## Examples of Converters for Ultra-Low-Output Transducers

A key frontier in the development of energy harvesting systems is the reduction in the operating power level. As greater attention has been paid to reducing quiescent overheads and improving efficiency the power levels at which a usable supply can be produced has reduced. Today, milliwatt level systems are common place and several systems have been reported below  $100 \mu\text{W}$ . At these very lowest powers, the circuits are fabricated using integrated processes.

In Ref. [12], the authors describe a variation on the pre-charging or pre-biasing techniques discussed in Chapter 4, describing it as “reinvestment” the circuit is shown in Figure 18.11. This energy flow backward from the output store to the harvesting device is achieved with a combination of timed switches and inductors, and the reader will appreciate that this is equivalent to reactive energy flow. The reinvestment approach is implemented in an integrated form for a piezoelectric transducer, and working in the sub- $100 \mu\text{W}$  region, achieves a doubling of the harvestable power compared to a standard rectifier.

While the majority of work on interface electronics for harvester systems has concentrated on motion-driven and thermal devices, harvesting from the low light intensity of indoor environments can also be challenging for power conditioning circuits, with output powers falling as low as just a few  $10 \mu\text{W cm}^{-2}$ . Although the DC output of the photo voltaic (PV) cell alleviates the need for a rectifier, typically a boost converter, and maximum power controller are needed to maximize harvested power. In Ref. [13] a switched capacitor converter and

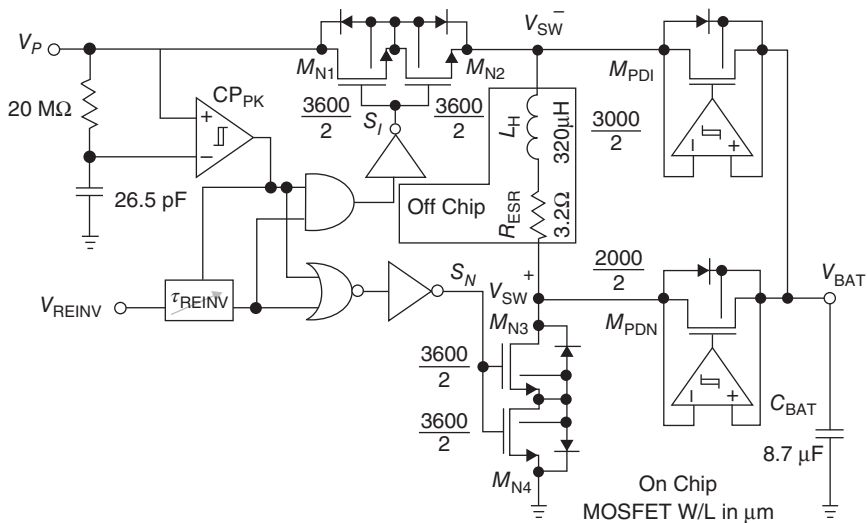


**Figure 18.11** Schematic of a power conditioning circuit for piezoelectric transducers. Redrawn from Ref. [12].

control is described which has a control overhead of just 850 nW and achieves 86% efficiency at 35  $\mu$ W output.

## 18.7

### Power Processing for Electrostatic Devices

In comparison to other forms of motion-driven harvesting transducer type, there have been very few examples of successful power electronics for electrostatic energy harvesters. This is largely because of the relative lack of popularity of electrostatic harvesters as presented in the research literature (even though some of the first work in the area was on electrostatic devices) and historical lack of commercial products, as well as the genuine difficulty of demonstrating the power output of these devices using off-the-shelf circuits or using readily available processes for integrated circuits. However, Yuji Suzuki's group has demonstrated an electrostatic harvester system with a power processing interface using an electret generator [14], as shown in Figure 18.12.

As can be seen, the system uses a conventional passive rectifier, which is possible because the transducer itself contains an electret, meaning that as the transducer capacitance changes, charge can be pumped back and forth through the rectifier, producing a DC voltage on the output.

## 18.8

### Commercial Products

In many energy harvesting-powered systems, the system integrator will likely wish to use off-the-shelf silicon for the power processing interfaces instead of constructing their own from discrete components or designing an application specific Integrated circuit (ASIC). Several off-the-shelf ASICs which provide harvesters interfaces are now available and so it is worth comparing them briefly in order to understand the potential constraints that these place on the system in terms of input and output capability. The three most widely available are families by Linear Technologies, Texas Instruments, and Maxim IC. These devices are essentially

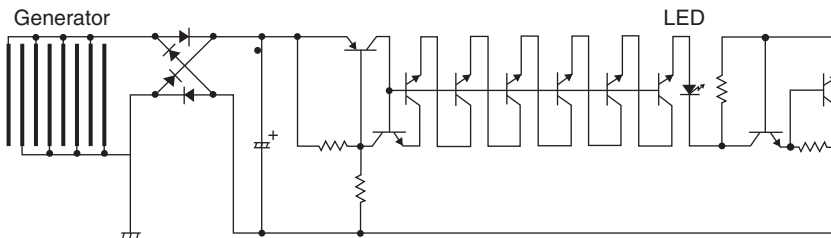


Figure 18.12 Electrostatic harvester and power processing output. Redrawn from Ref. [14].

DC–DC converters which operate either directly from a DC harvester source, or expect and external rectifier to be used allowing a battery to be charged. None of these circuits provide domain-specific harvester functions. However, they are all implemented to operate at low voltage with very low quiescent power consumption and some of these devices include basic maximum power-point tracking capability. None of these devices include circuitry to optimize output power from piezoelectric harvesters or any method of frequency tuning, and few of the commercial products include any rectification capability, with the expectation being that an external rectifier will be used when connecting these circuits to systems such as motion-driven harvesters. Consequently, these integrated circuits are more suitable for connection to solar cells or thermoelectric generators. Some of these circuits have the capability to charge secondary cells (including a suitable charge controller). The most common families of commercially available harvester interface are as follows:

- *Linear – LTC3 series of products (currently around 20 available)* [15]: Linear Technologies have a wide range of solutions which different applications and storage elements cater for. As an example, the LT3652 supports energy storage element voltages of between 3.3 and 14.4 V, can be cold started from the harvesting transducer output and therefore be used with both batteries and capacitors. It includes a maximum power point tracking function.
- *Texas Instruments – BQ25504* [16]: Designed to work with multiple different battery chemistries (including Li-ion, NiCad, etc.) or supercapacitors. The limits on the voltage of the storage elements are between 2.2 and 5.25 V and the system includes a programmable MPPT function where the user sets the fraction of the transducer open circuit voltage at the input terminals of the circuit when current is being drawn (usually 50% means a perfect impedance match).
- *Maxim – MAX17710* [17]: Designed to work with a Li-ion battery as the storage element, with references in the datasheet to the Infinite Power Solutions Thiner<sup>®</sup> cells. The voltage limits on the energy storage element are therefore relatively narrow, given the chemistry. The boost converter does not include MPPT.

Thus, while these devices have functionalities which include MPPT and low-input cold start, they lack the specific methods that have been discussed in this chapter that have proven a success in the literature primarily with regard to motion-driven harvesters. Therefore, while they are currently suitable for most solar or thermoelectric applications, the community would benefit from increased domain-specific circuits for kinetic-harvester applications.

## 18.9 Conclusions

As we have seen, many of the basic techniques described in Chapter 4 have been implemented in harvester systems, with some success. Issues arise at these power

levels in implementing these concepts, largely due to the low overhead power that can be tolerated in the control of the converters, the need for ideal switches, and the difficulties in obtaining passive components with large enough values and small enough volumes. Commercially available solutions for harvester interface integrated circuits are available, capable of cold start at a few hundred millivolts. However, the functionality of these systems is somewhat limited because they try to be generic and hence are not tailored for specific transducer types. Hence, although it is possible to purchase a low-power interface on an integrated circuit with an MPPT feature, it is not possible to tune the resonant frequency or maximize the power extracted from a piezoelectric element. Future development of these ICs must become more domain specific to improve power density and practicality of harvester systems.

## References

1. Szarka, G.D. *et al.* (2014) Maximum power transfer tracking for ultralow-power electromagnetic energy harvesters. *IEEE Trans. Power Electron.*, **29** (1), 201–212.
2. Mitcheson, P.D. *et al.* (2011) Tuning the resonant frequency and damping of an electromagnetic energy harvester using power electronics. *IEEE Trans. Circuits Syst. Express Briefs*, **58** (12), 792–796.
3. Elliott, A.D.T. and Mitcheson, P.D. (2012) Power density improvement of a piezoelectric energy harvester through use of a micropower switch-mode interface, in *11th IEEE Sensors Conference, 2012*, IEEE.
4. Szarka, G.D., Burrow, S.G., and Stark, B.H. (2013) Ultralow power, fully autonomous boost rectifier for electromagnetic energy harvesters. *IEEE Trans. Power Electron.*, **28** (7), 3353–3362.
5. Dwari, S. and Parsa, L. (2010) An efficient AC-DC step-up converter for low-voltage energy harvesting. *IEEE Trans. Power Electron.*, **25** (8), 2188–2199.
6. Burrow, S.G. and Clare, L.R. (2009) Open-loop power conditioning for vibration energy harvesters. *Electron. Lett.*, **45** (19), 999–1000.
7. Dicken, J. *et al.* (2012) Power-extraction circuits for piezoelectric energy harvesters in miniature and low-power applications. *IEEE Trans. Power Electron.*, **27** (11), 4514–4529.
8. Elliott, A.D.T. and Mitcheson, P.D. (2012) Implementation of a single supply pre-biasing circuit for piezoelectric energy harvesters. *Procedia Eng.*, **47**, 1311–1314.
9. Kiziroglou, M.E. *et al.* (2014) Design and fabrication of heat storage thermoelectric harvesting devices. *IEEE Trans. Ind. Electron.*, **61** (1), 302–309.
10. Toh, T.T. *et al.* (2014) A dual polarity, cold-starting interface circuit for heat storage energy harvesters. *Sens. Actuators, A*, **211**, 38–44.
11. Toh, T.T. *et al.* (2011) Electronic frequency tuning of a marine energy harvester. *PowerMEMS, 2011*, Seoul, Korea, pp. 383–386.
12. Prabha, R.D. *et al.* (2011) Increasing electrical damping in energy-harnessing transducers. *IEEE Trans. Circuits Syst. Express Briefs*, **58** (12), 787–791.
13. Jungmoon, K., Jihwan, K., and Chulwoo, K. (2011) A regulated charge pump with a low-power integrated optimum power point tracking algorithm for indoor solar energy harvesting. *IEEE Trans. Circuits Syst. Express Briefs*, **58** (12), 802–806.
14. Suzuki, Y. *et al.* (2008) Micro electret energy harvesting device with analogue impedance conversion circuit. *PowerMEMS, 2008*, Sendai, Japan, pp. 7–10.
15. LT (2014) Energy Harvesting, [http://www.linear.com/products/energy\\_harvesting](http://www.linear.com/products/energy_harvesting) (accessed 6 July 2014).

16. TI (2014) BQ25504, <http://www.ti.com/product/bq25504> (accessed 6 July 2014).
17. Maximintegrated (2014) MAX17710 Energy-Harvesting Charger and Protector, <http://www.maximintegrated.com/en/products/power/battery-management/MAX17710.html> (accessed 6 July 2014).



## 19 Micro Energy Storage: Considerations

Dan Steingart

### 19.1

#### Introduction

Moore's law does not apply to energy storage. While a transistor of equivalent functionality has become cheaper and smaller by a factor of 2 roughly every 18 months, the energy density of secondary batteries has doubled roughly every 50 years. This is because transistors get better as they become smaller. Electrochemical energy storage devices, however, have been accessing the fundamental limit of storage from their inception (i.e., the single bond and/or redox couple). As electrochemical engineering and materials science improved in the two centuries from the demonstration of the Volta pile, the accessibility, distribution, and reliability of the bond forming and breaking process (i.e., charging and discharging) has improved tremendously, but the dimension of the bond has not changed.

In this chapter, we will examine the fundamental reasons of this challenge, and determine the limit of energy that may be practically stored in small applications, as well as the limits of power that may be transferred.

### 19.2

#### Boundary Conditions

“Batteries” refer to electrochemical devices that store and release energy through forming and breaking chemical bonds. Two complementary bonds must be acted upon, a bond that is oxidizing with respect to the reducing bond (referred to as the *positive* or *cathode*) and a bond that is reducing with respect to the oxidizing bond (referred to as the *negative* or *anode*). The relative tendency to oxidize or reduce is quantified as the electrochemical potential.

The positive and negative electrodes are separated internally by a layer which prohibits electron migration but enables ion migration. This is the *electrolyte*. The anode and cathode are attached to the external circuit via *current collectors* that prohibit ion migration but enable electron migration. Media in which ions can

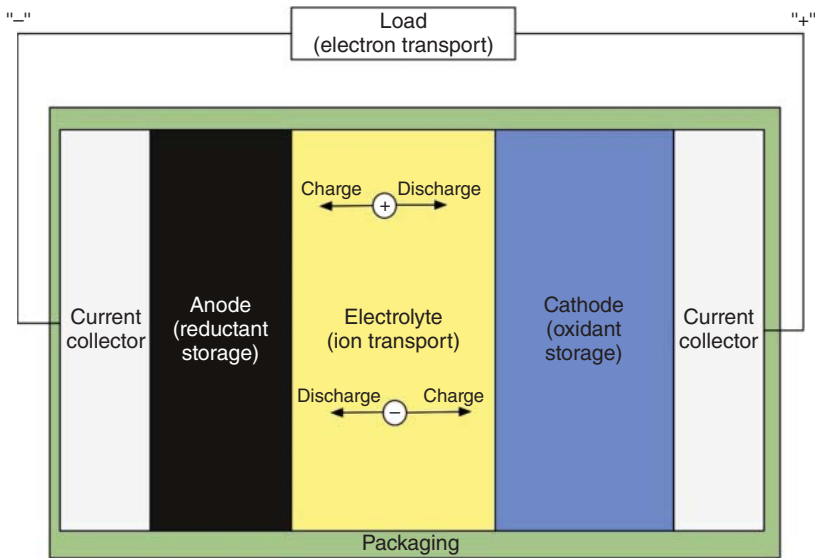


**Figure 19.1** Basic structure of an electrochemical energy storage device.

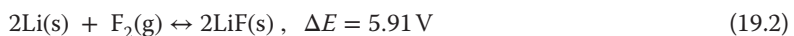
flow readily are the optimum choice for electrolytes; these tend to be liquid solvent with a dissociated salt. The electrolyte can be a liquid, a semi-solid gel, a solid polymer, or a solid crystalline material. As the electrolyte becomes “more solid,” it tends to become less ionically conductive, but there are exceptions to this rule that research is currently trying to exploit. Moreover, the stiffer an electrolyte is, the thinner it needs to be to provide structure support for the battery (Figure 19.1).

The maximum energy which can be stored within a volume/mass is determined by the number of active bonds within the anode and cathode multiplied by the electrochemical potential, subtracting the material required for the current collectors, electrolyte/separator, and packaging.

Let us examine the conditions for the ideal battery (one that would be exceptionally difficult to realize). The energy available is determined by

$$\Delta G = -nF\Delta E \quad (19.1)$$

where  $\Delta E$  is the potential between the anode and the cathode,  $n$  is the number of electrons to be transferred, and  $F$  is Faraday’s constant ( $96\,487\text{ F mol}^{-1}$ ). An initial guess would be to maximize the potential per mass, which means finding elements with low atomic numbers with high potential differences. A cursory examination of the periodic table would indicate that a battery containing a lithium anode and a fluorine cathode would be a good candidate. Indeed, the electrochemical potential between lithium and fluorine is



Assuming the battery was entirely lithium and fluorine, this would mean a potential energy of

$$5.91 \text{ V} \times 2 \times \frac{(96\,487 \text{ C mol}^{-1})}{(2 \times (6.94 + 18.99) \text{ g mol}^{-1})} = 21.9 \text{ kJ g}^{-1} = 6.1 \text{ Wh g}^{-1} \quad (19.3)$$

Assuming the electrolyte, packaging, and current collectors of the battery are near zero mass, the maximum energy possible from electrochemical storage is  $6.1 \text{ Wh g}^{-1}$ . Of course, fluorine is a gas at most useful temperatures and lithium is too reactive to handle in habitable atmosphere, so we must bind the oxidant and reductant to make them safe. Thus, the dream of a  $6.1 \text{ Wh g}^{-1}$  battery is tempered by reality, and the best we can do now, practically at a cell level is on the order of  $0.5 \text{ Wh g}^{-1}$ . In such a cell, lithium is not present in bulk form but as a guest that lives between a negative host (typically graphite, but silicon or titanate anodes are becoming commercially relevant) and a positive host (typically a blend of nickel, manganese, and cobalt oxide, but there are many commercially available options including sulfur, manganese dioxide, cobalt dioxide, vanadium pentoxide, etc.). In fact, significant research efforts are being applied to an “air breathing” cathode that would enable a  $\text{LiO}_2$  battery (significant challenges remain [1]).

For the researcher interested in this book, the construction and packaging of the battery will likely dominate her efforts: we must accept the best we can hope for looks like  $\sim 0.5 \text{ Wh g}^{-1}$ , and it will likely be less. The reason: as batteries get smaller, their surface to volume ( $S/V$ ) ratio becomes larger: as their  $S/V$  ratio becomes larger, a larger fraction of the battery must be dedicated to creating an impermeable barrier between the inside of the battery and the rest of the circuit. As the battery approaches volumes under  $1 \text{ cm}^3$ , this becomes a dominant concern.

The same general design principle applies to supercapacitors, which are (ideally) nonreactive devices that leverage the electrochemical double-layer capacitor (EDLC) to store ionic charge on a surface. Supercapacitors can exploit high-surface-area foams to store charge, but are limited in potential to the dissociation potential of the electrolyte in question. As a result, supercapacitor electrodes can approach  $\sim 500 \text{ F g}^{-1}$  capacitance values but are device limited to operating potentials below  $4 \text{ V}$  (typically, below  $3 \text{ V}$ ). Accounting for the mass of all components, most supercapacitor capacitance values are on the order of  $\sim 3 \text{ F g}^{-1}$ . Thus, assuming a  $3\text{-V}$  supercapacitor,

$$\text{Energy Density} = \frac{1}{2} C(\Delta V)^2 = 13.5 \text{ J g}^{-1} = 0.004 \text{ Wh g}^{-1}$$

Supercapacitors, however, are not kinetically limited, and provide their full capacity within seconds for millions of cycles. Batteries optimized for energy density and utilizing chemical reactions have tightly coupled depth of discharge to cycle life to discharge rate considerations, and a competitive commercial lithium ion battery can provide 1000 cycles over 80% of its rated capacity on a 2 h (or  $C/2$ ) discharge basis in 2014. The reader is directed to [2, 3] for a thorough analysis of the symbiosis of batteries and capacitors.

Finally, the reader is cautioned: many fundamental research efforts are underway to improve all aspects of batteries and capacitors listed above. With any luck,

this data will be outdated sooner rather than later, but if history is a reference, the above guidelines will be relevant for many years to come.

### 19.2.1

#### Microbatteries

Among the most mature attempts at “on-chip” micropower are the efforts of those using thin-film approaches [4]. These batteries use microfabrication-compatible processes such as chemical vapor deposition (CVD), physical vapor deposition, and sputtering. Beyond the process compatibility, these systems are attractive because per battery they can approach the highest active mass possible. Through CVD and sputtering, complex oxides can be deposited in crystallographically and compositionally optimized configurations directly on a device, *without* the need for binding elements, and at high packing density. The same is true of solid-state electrolytes: lithium phosphorus oxynitride (LIPON) and lithium zinc germanate (LISICON), lithium lanthanum titanate (LLTO) and high-molecular-weight ethylene oxide structures of various compositions and heterogeneity [5–8] can be deposited conformably and with minimal thickness. Recently, such batteries have been used to study fundamentals of electrochemical interactions [9] (Figure 19.2).

These promising properties have led to a number of commercialization efforts of this type of battery. Unforeseen challenges, largely unpublished, have limited the realizable energy density of these batteries, as such, in 2014, the best off the shelf structures can reach  $\sim 0.2 \text{ Wh g}^{-1}$ , and because of their small sizes and package requirements, the best volumetric energy density being on the order of  $800 \mu\text{Wh cm}^{-3}$ . Many efforts are underway to improve the *packaged* capacity of solid-state batteries, as of this writing none have been demonstrated effective in market.

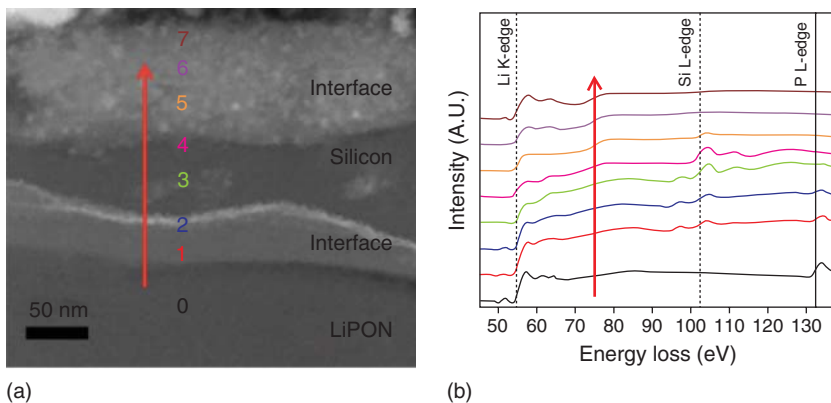


**Figure 19.2** TEM micrograph and map from Meng *et al.* [9] of a full solid-state battery reacting, imaged with TEM. (Adapted and reproduced with permission from Qian *et al.* [9]. Reproduced with permission of the American Chemical Society.)

**Table 19.1** A brief selection of microbatteries sorted by electrolyte.

Technology	Purpose/notes	Attributions
Lithium/lithium inorganic solid-state (LIPON/LISICON) electrolytes	Thin film-based approaches based on microfabrication technology. High rate capability (10 C) demonstrated high cycle life. To date, thickness and process limitations limit capacity to $<1 \text{ mW h cm}^{-2}$ and overall device capacity to $<5 \text{ mW h}$	[4, 5, 8, 10]
Lithium/lithium ion organic polymer electrolyte	Thin- and thick-film approaches, higher capacity, and energy density $>5 \text{ mW h cm}^{-2}$ and packages realized $>1 \text{ W h}$ . To date, lower power/longer duration systems, typically $C/10$ to $2C$ . Polymer electrolytes may be completely solid state (low rate, easier packaging) or gel/polymer composite (high rate, package limited)	[6, 11–13]
Aqueous polymer electrolyte batteries	Lower operating potential. Water stability allow simpler packaging	[14, 15]
Nonaqueous nonlithium approaches	A newer class of materials operating at lower potential than lithium ion but slightly higher than typical aqueous batteries. Advantages include lower evaporation losses (if ionic liquids are used) and less prone to off gassing electrolysis by-products ( $\text{H}_2/\text{O}_2$ )	[16–19]

Printed microbatteries are an engineering compromise. While they lack the ideal properties of the aforementioned solid-state cells, they have been realized in practical forms with energy density and power densities comparable to 18 650 type batteries. Table 19.1 indicates a few examples of such efforts: this is not a complete list but a representation of the various approaches possible. These batteries tend to require binders, liquid components that may leak, and are often volatile.

### 19.2.2

#### Supercapacitors

For applications where energy harvesting is feasible for the average power required but not sufficient for peak power, EDLCs, or supercapacitors have been demonstrated to be effective short-term storage devices with effectively infinite cycle life. Table 19.2 lists references that indicate implementation and uses of capacitors including supercapacitors.

## 19.3

### Primary Energy Storage Approaches

There exist efforts that may indicate “infinite power” as for small devices. Beta-voltaic sources [26, 27] or more generally, sources that leverage isotopic decay

**Table 19.2** Capacitor approaches.

Technology	Purpose/notes	Attributions
Solid-state dielectrics	Comparatively high potential, low capacitance, long cycle life, and highest power density. Ubiquitous	[20, 21]
Electrolytic capacitors	Used for millisecond to second energy storage, higher capacitance than solid state dielectric but lower operating potential and limited lifetime due to corrosion and/or evaporation of requisite liquid components	[22]
Electrochemical double-layer capacitors (EDLC)	Low potential (<5 V), high capacitance (>5 F g <sup>-1</sup> ), seconds to hours energy storage	[23–25]

of radioactive materials can potentially provide over 100 years of power for a sub-centimeter, square size sensor running at an average power of  $\sim 50 \mu\text{W}$ . The reader is reminded that challenges beyond thermodynamics exist when energy density becomes this high. These approaches have existed for over 50 years and face a number of external challenges, including public perception and regulatory hurdles [28, 29]. This said, the overall energy required for many applications to the reader of this book will be under 10 W h for the *lifetime* of their applications, so the absolute energy requirement of a nuclear decay source is well worth exploring if long life, environmentally isolated, touch free implementations are a priority.

Inspired by living organisms, some efforts exploiting electrochemical fuel cells which use atmospheric oxygen as an oxidant and hydrogen and/or hydrocarbons as a reductant have been demonstrated [30, 31]. Some approaches leverage bacterial digestion of fuels [32]: these are promising in the correct context (e.g., wastewater treatment, agricultural applications). Nature provides the complete refueling process through generational replacement of processing organisms and delivery of organic matter for the organisms to process. Although the power density of these approaches is thought to be limited to roughly  $15 \text{ W m}^{-2}$ , if stationary sensors or “free-riding” devices (e.g., tagged animals, secretly marked automobiles) can harvest local reducing agents, feed these living power plants, and only need average power draws on the order of  $1–10 \mu\text{W}$ , these approaches may be worthwhile.

A counterpoint to the microbial fuel cell is the enzymatic fuel cells. Enzymatic fuel cells effectively extract the functional conversion pathways from a microbial fuel cell, without the overhead and sensitivity of a living cell [33]. Enzymatic fuel cells can operate at much higher power density  $>(1 \text{ kW m}^{-2})$  but suffer from stability issues, and without the living cell, the enzymes cannot be replaced. At this time, research is underway to study the possibility of microbial fuel cells

which excrete/externalize enzymes, perhaps creating a system with the best of both methods. Newer digestion-emulating fuel cells seek to disregard biology and biological inspired pathways altogether. Sugar–air fuel cells utilizing various electrolytes [30, 31] have been demonstrated. The rough goal of these systems is to create a workable electrochemical storage solution from “a trip to the grocery store,” and it is left to the reader to infer the utility of such approaches.

Primary batteries utilizing metal anodes (Li [34, 35], Zn [36–38], Mg [39], and Al [40–42]) and high-energy-density cathodes of (e.g.,  $\text{MnO}_2$  [43–45],  $\text{ThNCl}$  [46–48], and S [49–51]) range from the ubiquitous to the specialized. In the author’s experience, many times these cells are sufficient for applications on the order of 5–10 years if the duty cycle and application parameters are well specified. While the overall package size may increase in this case, there are advantages in touch-free operation and installation and complete decoupling from environment for power.

There are edge cases, however, where energy harvesting is the *only possible* solution, cases where electrochemical batteries (primary or secondary), would not operate for a substantial duration. Any installation environment outside of the batteries stability window would necessitate this. For example, when monitoring the exhaust gas and current distribution of aluminum smelters [52, 53], the area of installation would experience temperatures in excess of  $100^\circ\text{C}$  for hours at a time. Few batteries can withstand such temperatures at all, fewer still for prolonged exposure over lifetime. But the exploitation of the thermal gradient associated with the installation temperature led to the use of thermoelectric harvesting for this application, and to date, the thermoelectric harvesters have been running for over 5 years. In this particular application, the sensor was specified to be within 1 ft of the sense location and exposed wires were unacceptable.

Thus, when designing energy storage systems for volume-constrained applications, it is best to first ask, “Will a primary source be sufficient for my application?” If after sufficient deliberation, energy harvesting has quantifiable benefits to application reliability and return on investment, one should examine the previous array of solutions (Table 19.3).

**Table 19.3** A brief selection of primary approaches sorted by fuel source.

Technology	Types/notes	Attributions
Micro nuclear decay	Energy source is a controlled low-power decay, typically beta particles	[26–29, 54]
Micro fuel cells	Typically organic feedstock, may or may not require biological processing	[30, 32]
Metal–air cells	High-energy plate metal, diffusion control membrane to typically decorated carbon cathode	[55–57]

## 19.3.1

## Volume-Constrained versus Conformally Demanding Approaches

Wearable electronics and folding devices [58–63] are substantial drivers of low-power device research, and the power requirements for these systems is similar to the constrained volume energy storage cases above, but not completely analogous. The highest volumetric energy density microbatteries to date [64, 65] utilize thick, dense structures of electrode material. In applications where absolute footprint and volume must be minimized [66, 67], this is an optimized solution. Figure 19.3 indicates a stretchable battery design from Ref. [15].

However, thin films have far higher strain compliance than thick films and many [58, 61, 68] wearable/conformal applications have large relatively high working areas (e.g., garments, bandages) and reinforced mesh design can provide up to  $10 \text{ mW cm}^{-2}$  for primary devices and  $3 \text{ mW cm}^{-2}$  for secondary devices, per layer [14, 15]. Novel designs in completely foldable and 1-D formats are also feasible, albeit with lower energy density (Table 19.4).

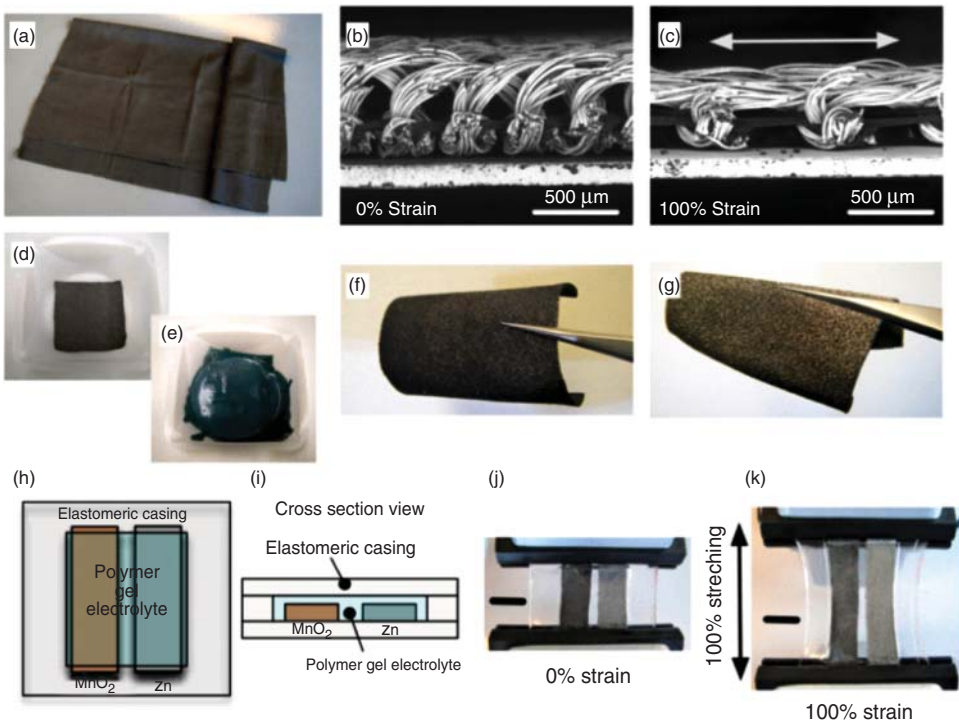


**Figure 19.3** Image of a flexible battery in conductive spandex from [15]. (a) Conductive substrate, (b,c) representative strain states of electrode, (d–g) examples of electrode

fabrication, and (h–k) battery architecture (Adapted and reproduced with permission from Gaikwad *et al.* [15]. Reproduced with permission of Wiley-VCH.).



**Table 19.4** A brief selection of flexible battery approaches.

Technology	Types/notes	Attributions
Thin-film, flexible	Sputter/CVD-friendly, limited areal capacity, can have 10C or greater rate capability	[69]
Thick-film, flexible	High areal capacity, lower power density (<2C). Readily solution processed	[14, 15]
Wire/cable batteries	Quasi 1D form factor, useful for semi-wired/short wire run applications to overload structures (e.g., sensor lead to a node)	[70]

## 19.3.2

**Caveat Emptor**

As mentioned in the introduction, energy storage improvements have been far outpaced by transistor-driven improvement (more computing capability with lower energy costs per operation). The reader is reminded that any energy storage solution is a compromise. The trend is thus: energy density, power density, and cycle life – pick two out of three. For reasons of entropy driven restructuring of well-defined spaces, we are currently limited to considering (i) high rates with high cycle life but low energy density (capacitors), (ii) moderates rates with high cycle life and moderate energy density (secondary chemistries), or (iii) high rates with high energy density but low cycle life (primary chemistries/fuel cells).

Certain solutions seem eternally poised to break this trend, but upon inspection limits become apparent. Air electrodes, for example, seem like a natural solution to improving energy density as atmospheric oxygen replaces the structural stored oxidant. But (i) surface needs to exist to facilitate the reaction, (ii) atmospheric concentrations of oxygen, paired with the density of gas, indicates that there is actually far *more* oxidant volumetrically in an oxide, and (iii) opening the battery to atmosphere provides entry ways for poisons to the desired reactions.

Air electrodes are an exciting area and deserve attention: this note is intended to remind the reader that all energy storage requires systematic interaction above and beyond material improvement.

## 19.3.3

**Future Work and First-Order Problems**

We have briefly covered the boundary conditions which determine the maximum energy that may be stored in a defined volume, and provided examples of the systematic design and compromise. For volumetrically constrained systems, any improvement to a standard battery can be generally applied to a smaller system. One improvement is perhaps more important to smaller systems than larger, and that is the continued development of a stable, low-cost, and high-conductivity solid-state electrolyte.

In volume-constrained systems, the volumetric packaging cost is significant and most structure of the packaging is dedicated to encapsulating sensitive electrolytes, aqueous, or aprotic. Over the past two decades, we have seen significant advances in inorganic [5, 71] and organic [11–13, 72–75] solid electrolytes, and it will be further improvements in the process cost and stability of these systems that creates disruptions in energy density beyond those in “large” energy storage materials development. In particular, a field ripe for research is the development of solid-state electrolyte capable of coping with massive structural reconfigurations required in next-generation electrodes such as silicon [76–80], SnO<sub>2</sub> [81–84], and sulfur [49, 85, 86].

## References

- McCloskey, B.D., Bethune, D.S., Shelby, R.M., Mori, T., Scheffler, R., Speidel, A., Sherwood, M., and Luntz, A.C. (2012) Limitations in rechargeability of Li-O<sub>2</sub> batteries and possible origins, *the* limitations in rechargeability of Li-O<sub>2</sub> batteries and possible origins. *J. Phys. Chem. Lett.*, **3** (20), 3043–3047.
- Otis, B., Gambini, S., Shah, R., Steingart, D., Quévy, E., Rabaey, J., Sangiovanni-Vincentelli, A., and Wright, P. (2007) Modelling and simulation techniques for highly integrated, low-power wireless sensor networks. *IET Comput. Digital Tech.*, **1** (5), 528.
- Cook-Chennaul, K.A., Thambi, N. and Sastry, A.M. (2008) Powering MEMS portable devices – a review of non-regenerative and regenerative power supply systems with special emphasis on piezoelectric energy harvesting systems. Review Article, **17** (4).
- Bates, J., Gruzalski, G., Dudney, N., Luck, C., and Yu, X. (1994) Rechargeable thin-film lithium batteries. *Solid State Ionics*, **70**, 619–628.
- Dudney, N.J. and Neudecker, B.J. (1999) Solid state thin-film lithium battery systems. *Curr. Opin. Solid State Mater. Sci.*, **4** (5), 479–482.
- Yuan, R., Teran, A.A., Gurevitch, I., Mullin, S.A., Wanakule, N.S., and Balsara, N.P. (2013) Ionic conductivity of low molecular weight block copolymer electrolytes. *Macromolecules*, **46** (3), 914–921.
- Stramare, S., Thangadurai, A.V., and Weppner, W. (2003) Lithium lanthanum titanates: a review. *Chem. Mater.*, **15** (21), 3974–3990.
- Robertson, A.D., West, A.R., and Ritchie, A.G. (1997) Review of crystalline lithium-ion conductors suitable for high temperature battery applications. *Solid State Ionics*, **104**, 1–11.
- Santhanagopalan, D., Qian, D., McGilvray, T., Wang, Z., Wang, F., Camino, F., Graetz, J., Dudney, N., and Meng, Y.S. (2014) Interface limited lithium transport in solid-state batteries. *J. Phys. Chem. Lett.*, **5**, 298.
- Sakamoto, J., Thompson, T., Wolfenstine, J., and Allen, J.L. (2013) Cycling stability, interfacial impedance, and ionic transport characterization of garnet ceramic electrolyte membranes. Meeting Abstracts, 2013.
- Kerr, J.B., Han, Y.B., Liu, G., Reeder, C., Xie, J., and Sun, X. (2004) Interfacial behavior of polymer electrolytes. *Electrochim. Acta*, **50** (2), 235–242.
- Wiers, B.M., Foo, M.-L., Balsara, N.P., and Long, J.R. (2011) A solid lithium electrolyte via addition of lithium isopropoxide to a metal–organic framework with open metal sites. *J. Am. Chem. Soc.*, **133** (37), 14522–14525.
- Downing, K.H., Borodin, O., Smith, G.D., and Balsara, N.P. (2009) Effect of ion distribution on conductivity of block copolymer electrolytes. *Nano Lett.*, **9**, 1212.
- Gaikwad, A.M., Whiting, G.L., Steingart, D.A., and Arias, A.C. (2011) Highly flexible, printed alkaline batteries based on

- mesh-embedded electrodes. *Adv. Mater.*, **23** (29), 3251–3255.
15. Gaikwad, A.M., Zamarayeva, A.M., Rousseau, J., Chu, H., Derin, I., and Steingart, D.A. (2012) Highly stretchable alkaline batteries based on an embedded conductive fabric. *Adv. Mater.*, **24** (37), 5071–5076.
  16. Ho, C.C., Evans, J.W., and Wright, P.K. (2010) Direct write dispenser printing of a zinc microbattery with an ionic liquid gel electrolyte. *J. Micromech. Microeng.*, **20**, 104009.
  17. Kim, J., Kim, H., Kim, I., Yoo, H.I., and Kang, K. (2013) A new high-energy cathode for a Na-ion battery with ultrahigh stability. *J. Am. Chem. Soc.*, **135** (37), 13870–13878.
  18. Kim, B.H., Song, S.H., Kwon, J., Kong, B.S., and Kang, K. (2012) Exfoliation of non-oxidized graphene flakes for scalable conductive film. *Nano Lett.*, **12** (6), 2871–2876.
  19. Kim, H., Park, I., Hong, J., Park, K.Y., and Kang, K. (2012) Multicomponent effects on the crystal structures and electrochemical properties of spinel-structured  $M_3O_4$  ( $M=Fe, Mn, Co$ ) anodes in lithium rechargeable batteries. *Chem. Mater.*, **24** (4), 720–725.
  20. Jia, Z., Kymissis, I., and O'Brien, S. (2010) High K capacitors and OFET gate dielectrics from self-assembled  $BaTiO_3$  and (Ba, Sr)  $TiO_3$  nanocrystals in the superparaelectric limit. *Adv. Funct. Mater.*, **20**, 554–560.
  21. Yang, S., Tull, B.R., Pervez, N.K., Huang, L., Leland, E.S., Steigart, D.A., O'Brien, S., and Kymissis, I. (2013) Asymmetric leakage in (Ba, Sr)  $TiO_3$  nanoparticle/parylene-C composite capacitors. *J. Polym. Sci., Part B: Polym. Phys.*, **51** (1), 35–38.
  22. Nishino, A. (1996) Capacitors: operating principles, current market and technical trends. *J. Power Sources*, **60**, 137.
  23. Jost, K., Dion, G., and Gogotsi, Y. (2014) Textile energy storage in perspective, review article in issue on flexible energy storage and conversion. *J. Mater. Chem. A*, **2**, 10776–10787.
  24. Ho, C.C., Steingart, D., Evans, J., and Wright, P. (2008) Tailoring electrochemical capacitor energy storage using direct write dispenser printing. *ECS Trans.*, **16** (1), 35–47.
  25. Simon, P. and Gogotsi, Y. (2008) Materials for electrochemical capacitors. *Nat. Mater.*, **7** (11), 845–854.
  26. Lal, A., Li, H., and Guo, H. (2004) *Integrated Radioactive Thin Films for Sensing Systems*, vol. 5, IEEE, pp. V–596–V–599.
  27. Guo, H. and Lal, A. (2003) *Nanopower Betavoltaic Microbatteries*, vol. 1, IEEE, pp. 36–39.
  28. Marquis, F., Paulo, G., and Engineering, S. (2013) Feasibility Study and System Architecture of Radioisotope Thermo-electric Generation Power Systems for Usmc Forward Operating Bases, June 2013.
  29. Olsen, L.C., Cabauy, P., and Elkind, B.J. (2012) Betavoltaic power sources. *Phys. Today*, **65**, 35–38.
  30. Scott, D.M., Tsang, T.H., Chetty, L., Aloji, S., and Liaw, B.Y. (2011) Mechanistic understanding of monosaccharide-air flow battery electrochemistry. *J. Power Sources*, **196**, 10328.
  31. Zhang, Y. (2009) A sweet out-of-the-box solution to the hydrogen economy: is the sugar-powered car science fiction? *Energy Environ. Sci.*, **2**, 272–282.
  32. Logan, B.E., Hamelers, B., and Rozendal, R. (2006) Microbial fuel cells: methodology and technology. *J. Environ. Sci. Technol.*, **40** (17), 5206–5211.
  33. Brozik, S., Barton, S.C., Cooney, M., and Liaw, B.Y. (2007) Enzymatic biofuel cells. *Electrochem. Soc. Interface*, **16**, 28–31.
  34. Crowther, O. and West, A. (2008) Effect of electrolyte composition on lithium dendrite growth. *J. Electrochem. Soc.*, **155**, A806.
  35. Monroe, C. and Newman, J. (2003) Dendrite growth in lithium/polymer systems a propagation model for liquid electrolytes under galvanostatic conditions. *J. Electrochem. Soc.*, **150** (10), A1377–A1384.
  36. Gallaway, J.W., Desai, D., Gaikwad, A., Corredor, C., Banerjee, S., and Steingart, D. (2010) A lateral microfluidic cell for imaging electrodeposited zinc near the shorting condition. *J. Electrochem. Soc.*, **157** (12), A1279–A1286.

37. Gallaway, J.W., Gaikwad, A.M., Hertzberg, B., Erdonmez, C.K., Chen-Wiegart, Y.-C.K., Sviridov, L.A., Evans-Lutterodt, K., Wang, J., Banerjee, S., and Steingart, D.A. (2014) An in situ synchrotron study of zinc anode planarization by a bismuth additive. *J. Electrochem. Soc.*, **161** (3), A275–A284.
38. Gallaway, J.W., Erdonmez, C.K., Zhong, Z., Croft, M., Sviridov, L.A., Shoklapper, T.Z., Turney, D.E., Banerjee, S., and Steingart, D.A. (2014) Real-time materials evolution visualized within intact cycling alkaline batteries. *J. Mater. Chem. A*, **2**, 2757–2764.
39. Vestfrid, Y., Chusid, O., Gofer, Y., and Aurbach, D. (2007) Progress in non-aqueous magnesium electrochemistry. *J. Power Sources*, **174**, 1234–1240.
40. Pradhan, D. and Reddy, R.G. (2012) Dendrite-free aluminum electrodeposition from AlCl<sub>3</sub>-1-ethyl-3-methylimidazolium chloride ionic liquid electrolytes. *Metall. Mater. Trans. B*, **43** (3), 519–531.
41. Zhang, M., Kamavaram, V., and Reddy, R.G. (2005) Aluminum electrowinning in ionic liquids at low temperature. *Light Metals*, **2**, 583–588.
42. Pradhan, D., Mantha, D., and Reddy, R.G. (2009) The effect of electrode surface modification and cathode overpotential on deposit characteristics in aluminum electrorefining using EMIC–AlCl<sub>3</sub> ionic liquid electrolyte. *Electrochim. Acta*, **54** (26), 6661–6667.
43. Kozawa, A. and Powers, R.A. (1972) Electrochemical reactions in batteries. Emphasizing the MnO<sub>2</sub> cathode of dry cells. *J. Chem. Educ.*, **49**, 587.
44. Kozawa, A. (1987) Lithium-MnO<sub>2</sub> cells containing CF<sub>x</sub> or C 2 F in the cathode. *J. Electrochem. Soc.*, **134** (4), 780–782.
45. Ruetschi, P. (1984) Cation-vacancy model for MnO<sub>2</sub>. *J. Electrochem. Soc.*, **131**, 2737–2744.
46. Brodd, R.J., Kozawa, A., and Kordesch, K.V. (1978) Primary Batteries 1951–1976. *J. Electrochem. Soc.*, **125**, 271C.
47. Istone, W.K. and Brodd, R.J. (1982) On the mechanism of thionyl chloride reduction. *J. Electrochem. Soc.*, **129**, 1853.
48. Istone, W.K. and Brodd, R.J. (1984) The mechanisms of thionyl chloride reduction at solid electrodes. *J. Electrochem. Soc.*, **131** (11), 2467–2470.
49. Shim, J., Striebel, K.A., and Cairns, E.J. (2002) The lithium/sulfur rechargeable cell effects of electrode composition and solvent on cell performance. *J. Electrochem. Soc.*, **149**, A574.
50. Lee, J.T., Zhao, Y., Kim, H., Cho, W.I., and Yushin, G. (2014) Sulfur infiltrated activated carbon cathodes for lithium sulfur cells: The combined effects of pore size distribution and electrolyte molarity. *J. Power Sources*, **248**, 752–761.
51. Wu, F., Magasinski, A., and Yushin, G. (2014) Nanoporous Li<sub>2</sub>S and MWCNT-linked Li<sub>2</sub>S powder cathodes for lithium-sulfur and lithium-ion battery chemistries. *J. Mater. Chem. A*, **2**, 6064–6070.
52. Steingart, D., Evans, J., Wright, P., and Ziegler, D. (2008) Experiments on wireless measurement of anode currents in hall cells. TMS Light Metals 2008, p. 6.
53. D. Steingart, J. Evans, A. Redfern, P. Wright, N. Dando, W. Xu, M. Gershenzon, and H. V. D. Meyden (2008) Wireless measurement of duct temperatures on aluminum smelting pots: correlation to roofline Hf concentration. TMS Light Metals 2008, pp. 1–5.
54. Adams, T.E. (2011) Status of Beta-voltaic Power Sources for Nano and Micro Power Applications, Research and Development.
55. Xiao, J., Mei, D., Li, X., Xu, W., Wang, D., and Graff, G.L. (2011) Hierarchically porous graphene as a lithium–air battery electrode. *Nano Lett.*, **11** (11), 5071–5078.
56. Thapa, A.K. and Ishihara, T. (2011) Mesoporous  $\alpha$ -MnO<sub>2</sub>/Pd catalyst air electrode for rechargeable lithium–air battery. *J. Power Sources*, **196**, 7016.
57. Cao, R., Lee, J.S., Liu, M., and Cho, J. (2012) Recent progress in non-precious catalysts for metal–air batteries. *Adv. Energy Mater.*, **2**, 816–829.
58. Rogers, J.A., Someya, T., and Huang, Y. (2010) Materials and mechanics for stretchable electronics. *Science*, **325**, 977–981.

59. Rogers, J.A., Bao, Z., Baldwin, K., Dodabalapur, A., Crone, B., Raju, V.R., Kuck, V., Katz, H., Amundson, K., Ewing, J., and Drzaic, P. (2001) Paper-like electronic displays: large-area rubber-stamped plastic sheets of electronics and microencapsulated electrophoretic inks. *Proc. Natl. Acad. Sci. U.S.A.*, **98** (9), 4835–4840 (Presented at the Proceedings of the, 2001).
60. Baca, A.J., Ahn, J., Sun, Y., Meitl, M.A., Menard, E. *et al.* (2008) Semiconductor wires and ribbons for high-performance flexible electronics. *Angew. Chem. Int. Ed.*, **47**, 5524–5542.
61. Arias, A.C., Ready, S.E., Lujan, R., and Wong, W.S. (2004) All jet-printed polymer thin-film transistor active-matrix backplanes. *Appl. Phys. Lett.*, **85** (15), 3304.
62. Wong, W.S., Ready, S.E., Chabinyc, M.L., and Arias, A.C. (2006) Jet printing flexible displays. *Mater. Today*, **9**, 32–37.
63. Shim, B.S., Chen, W., Doty, C., Xu, C., and Kotov, N.A. (2008) Smart electronic yarns and wearable fabrics for human biomonitoring made by carbon nanotube coating with polyelectrolytes. *Nano Lett.*, **8**, 4151–4157.
64. Erdonmez, C.K., Halloran, J.W., and Chiang, Y.M. (2013) Design of battery electrodes with dual-scale porosity to minimize tortuosity and maximize performance. *Adv. Mater.*, **25** (9), 1254–8.
65. Wang, Y., Erdo, C.K., Lai, W., and Chiang, Y.M. (2010) Ultrahigh energy density lithium microbatteries. Meeting Abstracts.
66. Warneke, B. and Pister, K. (2002) Exploring the limits of system integration with smart dust. Proceedings of ASME International Mechanical Engineering Congress and Exposition, 2002.
67. Kahn, J.M., Katz, R.H., and Pister, K. (2000) Emerging challenges: mobile networking for 'smart dust'. *J. Commun. Networks*, **2** (3), 188–196.
68. Kim, H.S., Huang, Y.Y., Hwang, K.C., and Rogers, J.A. (2009) Ultrathin silicon circuits with strain-isolation layers and mesh layouts for high-performance electronics on fabric, vinyl, leather, and paper. *Adv. Mater.*, **21**, 3703–3707.
69. Wang, X., Krishnaraju, D., Panat, R., and Chan, C.K. (2014) Origami lithium-ion batteries. *Nature*, **5**, 3140.
70. Kwon, Y.H., Woo, S.W., Jung, H.R., Yu, H.K., Kim, K., Oh, B.H., Ahn, S., Lee, S.Y., Song, S.W., Cho, J., Shin, H.C., and Kim, J.Y. (2012) Cable-type flexible lithium ion battery based on hollow multi-helix electrodes. *Adv. Mater.*, **24** (38), 5192–5197.
71. Thangadurai, V., Narayanan, S., and Pinzaru, D. (2014) Garnet-type solid-state fast Li ion conductors for Li batteries: critical review. *Chem. Soc. Rev.*, **43** (13), 4714–4727.
72. Buriez, O., Han, Y.B., Hou, J., Kerr, J.B., and Qiao, J. (2000) Performance limitations of polymer electrolytes based on ethylene oxide polymers. *J. Power Sources*, **89** (2), 149–155.
73. Doeff, M.M., Edman, L., Sloop, S.E., and Kerr, J. (2000) Transport properties of binary salt polymer electrolytes. *J. Power Sources*, **89** (2), 227–231.
74. Edman, L., Doeff, M.M., Ferry, A., Kerr, J., and De Jonghe, L.C. (2000) Transport properties of the solid polymer electrolyte System P(EO) nLiTFSI. *J. Phys. Chem. B*, **104** (15), 3476–3480.
75. Al, C.C.H.E. (2009) A super ink jet printed zinc-silver 3D microbattery. *J. Micromech. Microeng.*, **19** (9), 094013.
76. Cui, L.F., Yang, Y., Hsu, C.M., and Cui, Y. (2009) Carbon-silicon core-shell nanowires as high capacity electrode for lithium ion batteries. *Nano Lett.*, **113** (26), 11390–11398.
77. Wu, H. and Cui, Y. (2012) Designing nanostructured Si anodes for high energy lithium ion batteries. *Nano Today*, **7**, 414–429.
78. Park, M.-H., Kim, M.G., Joo, J., Kim, K., Kim, J., Ahn, S., Cui, Y., and Cho, J. (2009) Silicon nanotube battery anodes. *Nano Lett.*, **9** (11), 3844–3847.
79. Hertzberg, B., Alexeev, A., and Yushin, G. (2010) Deformations in Si-Li anodes upon electrochemical alloying in nanoconfined space. *J. Am. Chem. Soc.*, **132** (25), 8548.
80. Hertzberg, B., Benson, J., and Yushin, G. (2011) Ex-situ depth-sensing indentation measurements of electrochemically

- produced Si–Li alloy films. *Electrochem. Commun.*, **13**, 818.
81. Lin, Y.-M., Nagarale, R.K., Klavetter, K.C., Heller, A., and Mullins, C.B. (2012) SnO<sub>2</sub> and TiO<sub>2</sub>-supported-SnO<sub>2</sub> lithium battery anodes with improved electrochemical performance. *J. Mater. Chem.*, **22** (22), 11134–11139.
  82. WANG, C., Zhou, Y., Ge, M., Xu, X., and Zhang, Z. (2009) Large-scale synthesis of SnO<sub>2</sub> nanosheets with high lithium storage capacity. *J. Am. Chem. Soc.*, **132** (1), 46–47.
  83. Lou, X.W., Wang, Y., Yuan, C., Lee, J.Y., and Archer, L.A. (2006) Template-free synthesis of SnO<sub>2</sub> hollow nanostructures with high lithium storage capacity. *Adv. Mater.*, **18** (17), 2325–2329.
  84. Courtney, I.A. and Dahn, J.R. (1997) Key factors controlling the reversibility of the reaction of lithium with SnO<sub>2</sub> and Sn<sub>2</sub>BPO 6 glass. *J. Electrochem. Soc.*, **144** (9), 2943–2948.
  85. Wang, J.Z., Lu, L., Choucair, M., Stride, J.A., and Xu, X. (2011) Sulfur-graphene composite for rechargeable lithium batteries. *J. Power Sources*, **196**, 7030–7034.
  86. Yamin, H. and Peled, E. (1983) Electrochemistry of a nonaqueous lithium/sulfur cell. *J. Power Sources*, **9**, 281–287.

## 20

# Thermoelectric Energy Harvesting in Aircraft

*Thomas Becker, Alexandros Elefsiniotis, and Michail E. Kiziroglou*

### 20.1

#### Introduction

Energy harvesting is an umbrella term used to describe methods to generate electrical energy from ambient energy sources. These principles have been explained in detail in the previous chapters; this chapter reviews thermoelectric energy harvesting for aeronautical applications. Decentralized electrical energy generation from the environment is a key enabler for creating fully autonomous sensor systems or wireless systems in the aeronautic industry. It allows flexible system installation without extensive cabling effort and improves system modularity in order to enable local system functionalities. Furthermore, it is a maintenance-free solution for the perpetual operation of the device to be powered. Last but not least, it allows for rapid provision of new functionalities for retrofits in existing aircraft programs.

With reference to the aviation industry, energy harvesting can potentially provide cost reduction not only for manufacturers but also for the airline companies [1, 2]. On the one hand, it may decrease production costs by reducing cabling and aircraft customization costs. On the other hand, it offers weight reduction opportunities in the case of autonomous wireless sensor networks, compared to entirely wired or wireless data transmission only solutions. In turn, such weight reductions result in lower fuel consumption and operational costs.

The reason for integrating sensor networks in aircraft is to reduce maintenance costs by shifting paradigm from scheduled maintenance to unscheduled or even predictive maintenance. As stated in the previous paragraph, the advantage of wireless and autonomous solutions in terms of weight has been established. Therefore, the wireless sensor technology in general, and more specifically, energy harvesting technology, has been proved as the key enabler for aircraft wireless networks such as health monitoring systems.

This chapter begins with a review of aircraft standardization, describing the aircraft environment, followed by an architectural introduction to autonomous wireless sensor nodes and their key features. Next, recently introduced analytical and theoretical models for thermoelectric harvesting devices are presented in detail.

A review of the reported thermoelectric harvesting prototypes for aircraft applications is given in Section 20.5. Finally, an outlook of the future of thermoelectric harvesting for aircraft applications is presented in Section 20.6.

## 20.2

### Aircraft Standardization

The aviation industry has to comply with a lot of specifications and regulations in order to introduce a new technology in aircraft. Additionally, rigorous testing must be conducted, ensuring that any new technology is robust, reliable, and safe for in-service use. What is more, aircrafts are divided into fixed-wing and rotary-wing and, of course, in many other subcategories. Standardization can vary for different aircraft types. However, this section shows the minimum requirements that energy harvesting technologies should fulfill in fixed-wing aircraft in terms of research and technology considerations. A list with the most important standards is presented in Table 20.1.

A description of temperature and altitude conditions, temperature variations, humidity, and mechanical vibrations are briefly outlined according to the standard DO-160G. In any case, airworthiness has to be proved by complying with all relevant aspects.

An energy harvester might be installed in either a temperature-controlled or a non-temperature-controlled, pressurized or nonpressurized area, respectively.

**Table 20.1** Radio Technical Commission of Aeronautics (RTCA) publishes the standardizations used in aircraft.

Standard	Title
DO-160G	Environmental Conditions and Test Procedures for Airborne Equipment
DO-167	Airborne Electronics and Electrical Equipment Reliability
DO-171	Recommendations on Policies and Procedures for Off-the-Shelf Electronic Test Equipment Acquisition and Support
DO-178C	Software Considerations in Airborne Systems and Equipment Certification
DO-227	Minimum Operational Performance Standards for Lithium Batteries
DO-254	Design Assurance Guidance for Airborne Electronic Hardware
DO-293A	Minimum Operational Performance Standards for Nickel–Cadmium and Lead Acid Batteries
DO-311	Minimum Operational Performance Standards for Rechargeable Lithium Battery Systems
DO-313	Certification Guidance for Installation of Non-Essential, Non-Required Aircraft Cabin Systems and Equipment
DO-347	Certification Test Guidance for Small and Medium Sized Rechargeable Lithium Batteries and Battery Systems

This table summarizes the most important standards, which to be fulfilled when introducing a new technology in aircraft.



The temperature range for testing energy harvesting devices should be from  $-55$  to  $85^{\circ}\text{C}$ . Pressure tests should be performed from  $16\,973\text{ kPa}$  (corresponding to  $-4572\text{ m}/-15\,000\text{ ft.}$  altitude) to  $4.44\text{ kPa}$  (corresponding to  $21\,336\text{ m}/70\,000\text{ ft.}$  altitude). Temperature variation is not always consistent, and therefore, specifications should allow for some flexibility. A minimum rate of  $2^{\circ}\text{C}$  per min is defined in the standardization (DO-160G).

Another important factor is humidity, which can impact energy harvesting devices in different ways. It can cause corrosion and can influence the physical (e.g., electrical and mechanical) and chemical properties of the device. The energy harvester should be able to withstand harsh temperature and humidity environments, ranging, for example, from a relative humidity (RH) of 85% at  $40^{\circ}\text{C}$  to 95% at  $65^{\circ}\text{C}$ .

Mechanical vibrations, on the one hand, might be an energy source for a harvester. In this case, the transducer has to be carefully investigated for the expected number of cycles and the calculated lifetime. On the other hand, mechanical vibrations might affect the operational lifetime of a device. Mechanical loads ranging from shock to long-lasting vibrations may lead to fatigue in devices. Vibration tests depend strongly on the aircraft type, installation area, and test scenario. Owing to the large variety of the resulting test procedures, a simple strategy cannot be suggested. As a consequence, an extensive study on standards should be done before designing and introducing a new technology in aircraft.

### 20.3

#### Autonomous Wireless Sensor Systems

Each autonomous sensor or actuator system, wirelessly connected to a network, requires a very application-specific powering solution. Application-specific requirements have to be analyzed in detail for the design of an energy harvesting device and for the layout of a wireless sensor node. An autonomous sensor or actuator system or wireless sensor node consists typically, as shown in Figure 20.1, of sensors acquiring measurement signals or actuators and a power supply; in this case, the energy harvesting device consists of an energy storage unit, a power management module with a processor (usually a microcontroller), a data storage medium, and finally, a transceiver module for communication with a wireless network.

Application scenarios can typically be subdivided into two classes: monitoring tasks and powering small devices. Monitoring tasks are related to aircraft health assessment so as to decrease maintenance costs. The structural health of an aircraft can be assessed by detecting loads, strain, delamination, de-bonding, or cracks. The status of systems and components can be measured with temperature, pressure, humidity, or other chemical or physical sensors. The powering of small devices may vary from temporary illumination tasks to small motor operation or to small switches. For the synthesis of an autonomous sensor/actuator system, the selection of the sensor or actuator, the related measurement procedure,

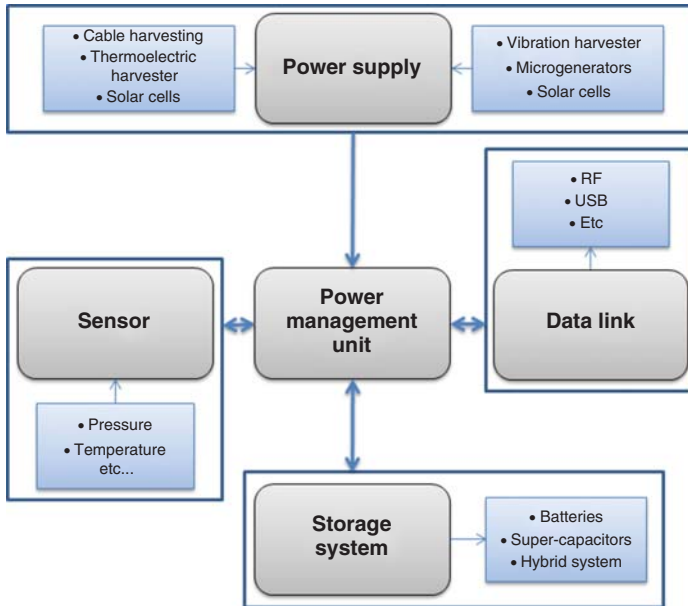


**Figure 20.1** A typical layout of an autonomous sensor (actuator) system or wireless sensor node.

and the operation scheme need to be analyzed in detail. New sensing technologies and measurement strategies should be used to reduce the power and energy needed.

The environmental conditions a harvesting module experiences determine its energy output. A study on the possible environmental sources has been conducted [3], and one of the most promising candidates is the different heat fluxes in aircraft structures. These heat fluxes can be converted into electrical energy using thermoelectric generators (TEGs), which make use of the Seebeck effect in order to generate electrical power from the temperature difference.

The selection of TEGs should be made very carefully, because their Seebeck coefficient and their internal thermal and electrical resistance determine the design of the power management unit. The Seebeck coefficient determines the open circuit voltage (at a specific  $\Delta T$ ) and plays an important role against the required startup voltage of the power management circuit. In order to maximize the power output, the internal electrical resistance of the TEG should be matched by the equivalent input resistance of the power management. Accordingly, maximum power point tracking (MPPT) algorithms have been developed recently [4]. The power management module is very important for the operation of an autonomous wireless sensor network (WSN). It is tasked with bringing the output voltages of the harvester to a specified input voltage threshold for a particular load (e.g., sensors, microcontrollers). In addition, it is responsible

for storing the surplus electrical energy in a medium (e.g., batteries and/or supercapacitors).

Energy storage is a challenge in itself because batteries and supercapacitors present both advantages and disadvantages. A typical trade-off is that batteries have higher energy densities, whereas supercapacitors offer higher power densities [5]. Batteries, in contrast to supercapacitors, have typically a shorter lifetime, a lower number of charging and discharging cycles, and a relatively limited operational temperature range. Although supercapacitors might be a possible solution, extended periods of downtime of an aircraft are not always possible due to their high self-discharge rate. Hybrid systems in which batteries and supercapacitors are combined are under research, and the advantages are described in detail in Refs. [5, 6].

Finally, the wireless sensor node includes the selection of a transceiver and a communication protocol. This part is subject to regulation and certification issues, and the selection of frequencies for communication is, for example, part of the wireless avionics intracommunication project WAIC [7].

## 20.4

### Thermoelectric Energy Harvesting in Aircraft

Thermoelectric energy harvesting refers to the conversion of environmental heat flow to electrical energy. A TEG is typically used for energy transduction through the Seebeck effect. The achievable electrical power depends strongly on the available temperature difference ( $\Delta T$ ) because it determines the heat flow power and the TEG conversion efficiency. TEGs are solid-state devices (no moving parts), which makes them reliable and hence, usable in any location where a temperature difference is present [8]. In the aircraft environment, temperature differences can be found in various locations such as near turbines and other engines or between the interior and exterior during flights. More particularly, such devices can be thermally connected to the inner part of the hull of the aircraft. The aircraft's fuselage serves as an "infinite" thermal energy source. From here on, two approaches to harnessing this energy and creating a heat flux are investigated.

One approach relies on creating a "quasi-static" state, where only passive components such as heat pipes and/or heat sinks are used in addition to the TEGs. The heat pipes and heat sinks need to conduct and absorb energy from a higher temperature source such as the space between the fuselage and the cabin lining, and conduct it toward and through the TEGs to the fuselage.

The second approach relies on creating a "dynamic" state, where a thermal mass (also referred to in the text as heat storage unit (HSU)) is used to temporarily create an artificial temperature difference between the two sides of the TEGs, caused by the significant temperature fluctuation during takeoff and landing. By using a thermal mass with high heat capacity on the surface of the TEG not facing the fuselage, the time needed to reach thermal equilibrium is increased, thus increasing electrical energy production. In order to maximize the heat capacity of the thermal

mass, a phase change material (PCM) is used. PCMs, while undergoing a phase change, absorb or release energy called latent heat, which boosts the amount of energy they can store. However, the phase change temperature is specific to each PCM and slightly affects their operational temperature ranges, making it therefore a crucial factor in device flexibility.

#### 20.4.1

##### Efficiency of a Thermoelectric Energy Harvesting Device

The thermoelectric phenomena present in a TEG are the Seebeck, Peltier, Thomson, and Joule effects. The Thomson effect is neglected in this analysis, and the Joule effect is assumed to be equally distributed between the cold and the hot sides [9]. Apart from that, the TEGs are placed between a heat source, in this case the fuselage, and a heat sink (either a heat spreader or an HSU), which introduce a thermal resistance to the system.

The TEG efficiency is defined as electrical output power,  $P_{el}$ , over thermal input power  $Q_h(I^2 \cdot R_L / \dot{Q}_h)$ , with  $R_L$  being the resistive load connected to the TEG. Defining the resistance ratio as  $\mu = R_L / R_i$ , where  $R_i$  is internal resistance of the TEG, the general expression for  $\eta_{TEG}$  can be written as follows [10]:

$$\eta_{TEG} = \frac{\Delta T}{T_h} \cdot \frac{\mu}{\frac{(\mu+1)^2}{ZT_h} + (\mu+1) - \frac{\Delta T}{2T_h}} \quad (20.1)$$

The maximum efficiency is obtained when  $\mu = \sqrt{1 + ZT_h}$ , yielding the usual TEG efficiency expression as derived in Chapter 10:

$$\eta_{TEG}(\Delta T) = \frac{\Delta T}{T_h} \frac{\sqrt{1 + ZT} - 1}{\sqrt{1 + ZT} + \frac{T_c}{T_h}} \quad (20.2)$$

This optimum point is different from the maximum power delivery point for a TEG, which is obtained for  $\mu = 1$ . Physically this means that at maximum power delivery, the TEG allows more heat flow through and, overall, it operates less efficiently. In direct (static) thermoelectric harvesting, this is not important as an infinite heat flow source can be assumed, so the desirable operation point is  $\mu = 1$ : maximum power delivery, and not maximum TEG conversion efficiency. Nevertheless, in heat storage (dynamic) thermoelectric harvesting, the desirable operation point is theoretically  $\mu = \sqrt{1 + ZT_h}$ ; maximum TEG conversion efficiency at the expense of a lower power delivery. In other words,  $R_L$  slightly greater than  $R_i$  is used, reducing the current and thereby partially saving thermal energy for conversion at the maximum overall efficiency. In practice, the low  $ZT$  values of state-of-the-art TEGs translate to smaller corresponding efficiency difference (e.g., 6% for  $ZT = 1$  at  $\Delta T = 30^\circ\text{C}$ ). In addition, a slow change in temperature over the harvester results in more heat leakage through insulation. It is concluded that at least in current TEG technologies, a matching load condition is advisable for characterization and operation of direct or heat storage harvesting. As a result, a more suitable TEG efficiency expression for thermoelectric harvesting

applications is that of a matched load condition, that is, Eq. (20.1) with  $\mu = 1$ , as derived in the thermoelectric maximum power analysis of Chapter 19:

$$\eta_{\text{TEG}} = \frac{\Delta T}{T_h} \frac{1}{2 + \frac{4}{ZT_h} - \frac{\Delta T}{2T_h}} \quad (20.3)$$

When  $ZT_h$  values are small and high accuracy is not critical, matched load efficiency can be written as follows:

$$\eta_{\text{TEG}} = \frac{Z\Delta T}{4} = \frac{\alpha^2 \Delta T}{4R_e K} = \frac{\frac{V_{oc}^2}{4R_e}}{\frac{\Delta T}{R}} \quad (20.4)$$

As expected, the last term of Eq. (20.4) is the ratio of load power to heat flow, with the Ohm and Peltier effects still neglected.

### 20.4.2

#### Static Thermoelectric Energy Harvester

A static harvester consists of a TEG with one of its sides attached to a heat source, usually the fuselage, and the other side attached to a heat spreader or to a heat sink. The basic equations of an ideal thermoelectric harvester should then be modified such that they include the thermal resistances in contact with the TEG. This includes the thermal resistances of the heat source or the fuselage and the heat sink. A schematic of a static harvester with the equivalent thermal and electrical circuits is illustrated in Figure 20.2.

For the equivalent (lumped) electrical circuit, the current flowing through the load resistance is

$$I = \frac{U}{R} = \frac{\alpha(T)\Delta T_{\text{TEG}}}{R_i + R_L} \quad (20.5)$$

where the Seebeck voltage is equal to  $U = \alpha(T) \cdot \Delta T_{\text{TEG}}$ . Consequently, the electrical power output of the equivalent electrical circuit can be written as

$$P_{\text{el}} = U \cdot I = I^2 R_L = \frac{\alpha^2(T)\Delta T_{\text{TEG}}^2}{(R_i + R_L)^2} R_L \quad (20.6)$$

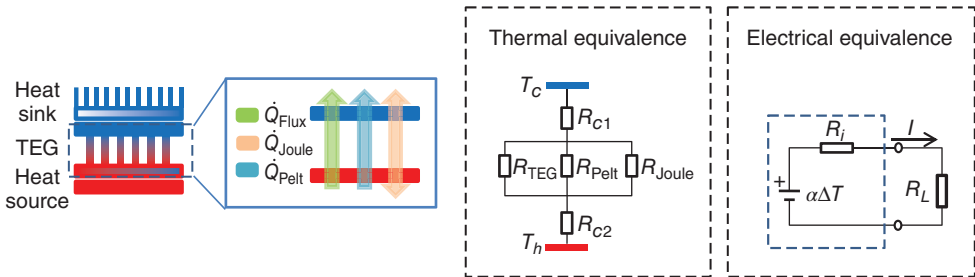


**Figure 20.2** A schematic of a static harvester with the equivalent thermal and electrical circuits.

where  $\Delta T_{\text{TEG}} = T_h^{\text{TEG}} - T_c^{\text{TEG}}$  (as shown in Figure 20.2). On a static harvester, the electrical power output depends on the thermal resistances, since the temperature difference across the TEG is not equal to the temperature difference applied. Using the Fourier heat equation, the heat flow on the cold and on the hot sides is equal to [11, 12],

$$q_h = \alpha(T_h)T_h I - \frac{1}{2}I^2 R_i + \frac{\Delta T_{\text{TEG}}}{\mathcal{R}_{\text{TEG}}} \quad (20.7)$$

$$q_c = \alpha(T_c)T_c I + \frac{1}{2}I^2 R_i + \frac{\Delta T_{\text{TEG}}}{\mathcal{R}_{\text{TEG}}} \quad (20.8)$$

where  $\mathcal{R}_{\text{TEG}}$  is the thermal resistance of the TEG. The first term shows the Peltier, the second the Joule, and the third the Seebeck effect. The temperature difference that is applied to the system, in comparison with the temperature difference applied on the TEG can be written as

$$\Delta T = \Delta T_{\text{TEG}} + \mathcal{R}_c q_c + \mathcal{R}_h q_h \quad (20.9)$$

Taking into account only the first-order terms of the  $\Delta T_{\text{TEG}}$  and a constant Seebeck coefficient for the given temperature range, the temperature difference applied on the TEG, using the Fourier heat equation, can be written as [11]

$$\begin{aligned} \Delta T_{\text{TEG}} &= \frac{\Delta T}{1 + \frac{\mathcal{R}_c}{\mathcal{R}_{\text{TEG}}} + \frac{\mathcal{R}_h}{\mathcal{R}_{\text{TEG}}} + \frac{\alpha^2(T_h)T_h \mathcal{R}_h + \alpha^2(T_c)T_c \mathcal{R}_c}{R_i + L}} \\ \Rightarrow \Delta T_{\text{TEG}} &\approx \frac{\Delta T}{1 + (\mathcal{R}_c + \mathcal{R}_h) \left( \frac{1}{\mathcal{R}_{\text{TEG}}} + \frac{\alpha^2 T_c}{R_i + R_L} \right)} \end{aligned} \quad (20.10)$$

The last term can be used to determine the power output of a static generator, which by math simplification can be written as [11]

$$P_{\text{el}} = (\alpha \Delta T)^2 \left( \frac{\mathcal{R}_{\text{TEG}}}{\mathcal{R}_c + \mathcal{R}_h + \mathcal{R}_{\text{TEG}}} \right)^2 \frac{R_i}{(R_L + R_i^{\text{eff}})^2} \quad (20.11)$$

where the effective internal resistance of the TEG is equal to [11]

$$R_i^{\text{eff}} = R_i + \alpha^2 T_c (\mathcal{R}_c + \mathcal{R}_h) \frac{\mathcal{R}_{\text{TEG}}}{\mathcal{R}_c + \mathcal{R}_h + \mathcal{R}_{\text{TEG}}} \quad (20.12)$$

The maximum power generation of a static harvester can be found by setting  $\frac{d}{dR_i} P_{\text{el}} \stackrel{\text{def}}{=} 0$ , and the result is that the load resistance should match the effective internal resistance.

$$R_L = R_i^{\text{eff}} \quad (20.13)$$

If the load resistance matches the effective internal resistance, by substituting the figure of merit  $Z = \frac{\alpha \mathcal{R}_{\text{TEG}}}{R_i}$  for the power output, the power is maximized when  $\frac{d}{d\mathcal{R}_{\text{TEG}}} P_{\text{el}}(R_L = R_i^{\text{eff}}) \stackrel{\text{def}}{=} 0$ . This corresponds to a TEG thermal resistance of

$$\mathcal{R}_{\text{TEG}} = (\mathcal{R}_c + \mathcal{R}_h) \sqrt{Z T_c + 1}. \quad (20.14)$$

Assuming that the internal electrical resistance is almost equal to the electrical load resistance, the above equation can identify the possible operating ranges. If the internal thermal resistance of the TEG is much smaller than the sum of the thermal resistances of the hot and cold sides, the Peltier effect is very big due to the large heat flow. If the internal thermal resistance of the TEG is much greater than the sum of thermal resistance of the hot and cold sides, then the Peltier effect is almost not present due to small heat flow. Nonetheless, the system should be designed in order for the thermal resistance of the TEG to match the sum of the thermal resistance of hot and cold sides of the contacts, achieving the optimal combination of heat flow and  $\Delta T$  across the TEG.

### 20.4.3

#### Dynamic Thermoelectric Energy Harvester

The operating principle of dynamic thermoelectric harvesting is illustrated in Figure 20.3. The HSU comprises a PCM inside a container, which provides thermal contact to a TEG. The HSU is otherwise thermally insulated from the environment. A uniform temperature distribution inside the HSU is desirable in order to maximize the  $\Delta T$  across the TEG. For this reason, an internal thermal bridge structure is used, which improves the temperature uniformity within the PCM. An insulation layer prevents heat leakage to the environment through the rest of the HSU surface. The outside surface of the TEG is in thermal contact with the aircraft structure through an appropriate thermally conducting interface. When the temperature of the aircraft structure fluctuates, heat flows in and out of the HSU through the TEGs, resulting in the generation of electrical energy. The energy output of the harvesting device can be collected, stored, and distributed by a power management system.

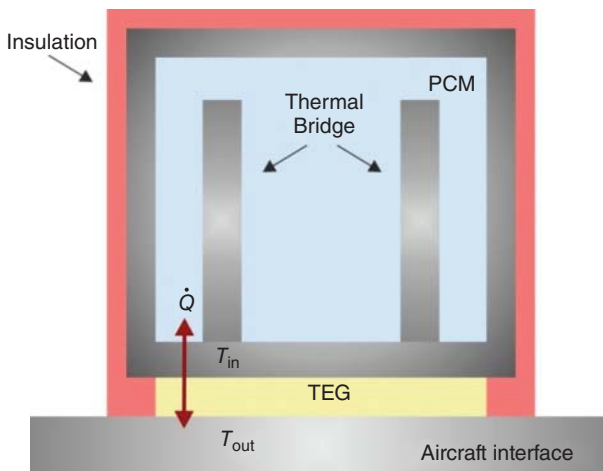


Figure 20.3 A schematic of the device structure.

The theoretical model for heat storage thermoelectric harvesters is summarized, as originally developed in Refs. [13, 14]. For simplicity, it is assumed that thermal conductivities are independent of temperature. It is also assumed that the PCM has a uniform temperature; temperature gradients in the HSU are negligible and phase change occurs uniformly.

If  $\mathfrak{R}$  is the thermal resistance between the environment and a HSU with heat capacity  $C$  and latent heat  $L$ , then during non-phase change (NPC) operation, the heat inside the HSU  $Q$  and the heat flow  $\dot{Q}$  will be

$$Q = C \cdot T_{\text{in}} \quad (20.15)$$

$$\dot{Q} = \frac{\Delta T}{\mathfrak{R}} \quad (20.16)$$

where  $\Delta T = T_{\text{out}} - T_{\text{in}}$  is the difference between outside and inside temperatures. Combining Eq. (20.15) with Eq. (20.16), one obtains a differential equation for  $\Delta T$ , for NPC operation:

$$\Delta \dot{T} + \frac{\Delta T}{\mathfrak{R}C} = \dot{T}_{\text{out}} \quad (20.17)$$

For the linear time variation of  $T_{\text{out}}$ , that is,  $T_{\text{out}}(t) = b \cdot t + T_{\text{out}}(0)$ , an analytical equation for  $\Delta T$  during NPC operation can be derived:

$$\Delta T(t)_{\text{NPC}} = \Delta T(0) \cdot e^{-\frac{t}{\mathfrak{R}C}} + b \cdot \mathfrak{R}C \cdot \left(1 - e^{-\frac{t}{\mathfrak{R}C}}\right) \quad (20.18)$$

The first term on the right side of Eq. (20.18) corresponds to the exponentially decaying  $\Delta T$  that would stem from an initial temperature difference; the second originates from the  $T_{\text{out}}$  change and approaches the limit  $b \cdot \mathfrak{R}C$  when  $t \gg \mathfrak{R}C$ . Hence, the value  $b \cdot \mathfrak{R}C$  physically represents the constant temperature difference that is established if  $T_{\text{out}}$  keeps changing linearly after time  $t \gg \mathfrak{R}C$ . As an example, a  $1 \text{ cm}^2$  TEG with  $\mathfrak{R} = 33 \text{ K W}^{-1}$  and  $1 \text{ cm}^3$  of water with  $C = 4.2 \text{ J}^{-1} \text{ K}^{-1}$  has an  $\mathfrak{R}C = 138 \text{ s}$ . At a temperature sweep of  $b = 4 \text{ K min}^{-1}$ , this device will yield a constant  $\Delta T = b \cdot \mathfrak{R}C = 9 \text{ K}$  after around 10 min of NPC operation.

During phase change operation,  $T_{\text{in}}$  is constant, and therefore  $\Delta T$  is the sum of any initial condition  $\Delta T(0)$  and the variations in  $T_{\text{out}}$ :

$$\Delta T(t)_{\text{PC}} = b \cdot t + \Delta T(0) \quad (20.19)$$

From the above equations, analytical expressions for heat, heat flow, and HSU temperature can be derived. To find the total electrical energy  $E_{\text{out}}$  produced by the TEG, heat leakage must be taken into account. If  $\delta \cdot \dot{Q}$  is the portion of  $\dot{Q}$  that flows through the TEG, then

$$E_{\text{out}} = \int \delta \cdot Q \cdot \eta_{\text{TEG}} dt = \frac{\delta}{\mathfrak{R}} \int \Delta T(t) \cdot \eta_{\text{TEG}} dt \quad (20.20)$$

A formulation for the maximum energy that can be harvested by a heat storage thermoelectric harvester of heat capacity  $C$  and latent heat  $L$ , from an ambient temperature cycle of change  $\Theta$ , has been shown in [13]. The resulting expression is



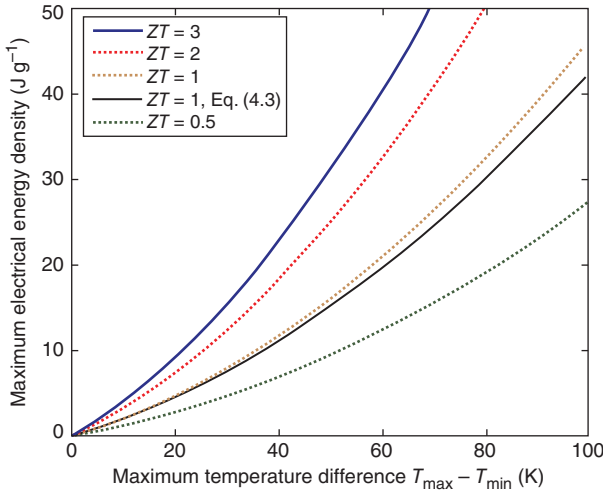


**Figure 20.4** Electrical energy per PCM mass versus ambient temperature variation, for TEGs with various figures of merit  $ZT$ .

$$E_{MAX} = 2 \cdot (\Theta \cdot C + L) \cdot \eta_{TEG} \left( \frac{\Theta}{2} \right) \quad (20.21)$$

where  $\eta_{TEG}(\Theta/2)$  is the TEG efficiency at the temperature difference  $\Delta T = \Theta/2$ . This means that the overall maximum efficiency is simply the TEG efficiency for  $\Theta/2$ . From Eqs. (20.20) and (20.21), one can calculate the maximum electrical energy per unit mass of heat storage material available from a TEG. Indicative simulation results are plotted in Figure 20.4 as a function of ambient temperature variation, for different TEG figures of merit, using  $L/m = 334 \text{ kJ kg}^{-1}$  and  $C/m = 4.2 \text{ kJ K}^{-1} \text{ kg}^{-1}$ , where  $m$  is the PCM mass. Water was chosen as the PCM because its heat storage properties are superior to other heat storage materials, which are typically salt-based or organic solutions.

## 20.5

### Design Considerations

In this section, the static and the dynamic thermoelectric harvesting design rules as introduced in [13] are summarized.

For designing a static harvester, and using commercially available heat sinks, an equation that relates the temperature difference obtained on the thermoelectric module in comparison with the temperature applied on system with thermal resistance and the figure of merit is written as [15]

$$\frac{\Delta T_{TEG}}{\Delta T} = \frac{\mathfrak{R}_{TEG}}{2 \left( 1 + Z \frac{(T_h + T_c)}{2} \right) (\mathfrak{R}_h + \mathfrak{R}_c)}. \quad (20.22)$$

**Table 20.2** Thermal resistance values for different convection types.

		Convection type	Thermal resistance ( $W K^{-1}$ )		
Complexity ↓		Natural	0.5 ... 2.0	↑	Thermal resistance
		Forced	0.02 ... 0.5		
		Liquid	0.005 ... 0.02		

These thermal resistances reflect the values that can be achieved by heat sinking structures and should be taken into account when designing a static harvester [15].

The factor 2 in the equation above shows the limit of what can be achieved with commercially available thermoelectric modules [12]. The thermal resistance values of commercially available heat exchangers depending on the convection type are provided in Table 20.2.

In order to design a dynamic thermoelectric harvesting device for a particular application, a number of key parameters must be considered. The nature of the application will determine the characteristics of the temperature cycle, such as the temperature range, rate of change, and cycle period.

To select a PCM, phase change within the available temperature range must be ensured. Maximum heat capacity  $c_p$  and latent heat with an abrupt phase change are desirable. High thermal conductivity  $k$  is required to minimize temperature gradients within the PCM. Additives to enhance  $k$  or thermal bridge structures may be used for  $k$  enhancement.

The HSU structure must provide good thermal contact between the PCM and the TEG while providing good thermal insulation at non-TEG heat paths. Minimization of the HSU surface area that is not covered by TEGs and the use of highly insulating materials such as polyurethane foam or polystyrene are required. Depending on the temperature profile of a particular application, control of supercooling and nonuniform phase changes may also be desirable.

Lastly, a TEG with high thermal resistance is desirable in order to increase the thermal time constant of the system and delay heat flow, such that the maximum possible  $\Delta T$  is achieved. This is also important for minimization of  $\Delta T$  loss in the PCM. As is explained in detail in Section 20.7, this is in contrast to the static thermoelectric harvesting case where heat resistance matching is required for maximum power harvesting. However, the thermal resistance of the TEG should be substantially smaller than that of the insulation used to minimize the heat leakage and also small enough to ensure a complete phase change cycle within the application-given temperature cycle period. These considerations are important for both the choice of materials and the design of geometry of a dynamic thermoelectric harvester. The desirable characteristics of each constituent part of the device are summarized in Table 20.3.

**Table 20.3** Desirable characteristics used to design a heat storage thermoelectric harvester.

	Phase change material	Heat storage unit	Thermo-electric generator
Desirable characteristics	High heat capacity $c_p$	Low thermal resistance of PCM–TEG interface	High efficiency at low $\Delta T$
	High latent heat $E_{PC}$	Low <i>thermal resistance</i> insulation	$k_{TEG} \ll k_{PCM}$ , $k_{Heat\ Contacts}$
	Phase change within temperature range	Low insulation area to TEG area ratio	$k_{TEG} \gg k_{HSU}$ insulation
	High thermal conductivity	Thermal bridge for $k_{PCM}$ enhancement	$k_{TEG}$ small, to maximize $T_{PCM}$ delay
	Minimized supercooling		$k_{TEG}$ high enough for full phase change

In this table,  $k$  generally represents thermal conductivity.

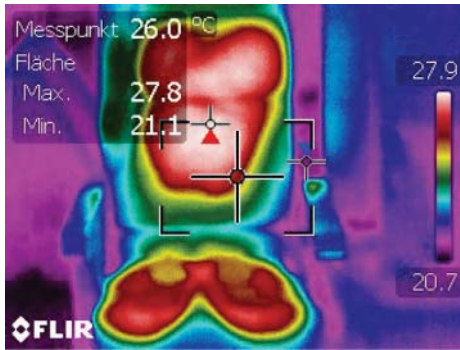
## 20.6 Applications

Thermoelectric energy harvesting has shown great potential on different application scenarios. Depending on the environmental conditions, heat dissipation, and sensor requirements, the static or the dynamic energy harvesting approach can be applied in order to build energy autonomous sensor systems. In this section, three different implementations are discussed: a static thermoelectric harvester for aircraft seat sensors, the first dynamic thermoelectric harvesting prototype, and a recently reported dynamic device designed for powering aircraft structural monitoring sensor nodes.

### 20.6.1

#### Static Thermoelectric Harvester for Aircraft Seat Sensors

In this application, wireless monitoring of aircraft seats is desirable, mostly for acquisition of seat state information such as occupancy, tray position, and seat-belt status [16]. The heat dissipation from the human body (around 100 W in total [17]) is used as the power source. The equilibrium body-to-seat temperature difference achieved is around 6 K. By matching the heat sink thermal resistance to that of the TEG, a steady-state temperature difference of 3 K across a  $10 \times 10$  mm TEG with a thermal resistance of around  $20 \text{ K W}^{-1}$  was achieved. The TEG was a Eureka TEG1-9.1-9.9-0.8/200. An electrical power output of 0.17 mW was demonstrated, and six such devices were used to achieve the 1 mW goal of the sensor application scenario. A custom power management unit was used for regulating the output voltage at 2.7 or 3.3 V from an input voltage of 0.2–0.5 V, in order to operate the microcontroller (MSP430), the radio frequency (RF) transceiver (Texas Instruments CC2420), and the sensors (a belt sensor, a tray sensor, and



(a)



(b)

**Figure 20.5** Infrared image (a) and installed demonstrator (b) of a static thermoelectric harvester for aircraft seat sensors [16].

right up position of the passenger seat sensor). An infrared image and the installed system are shown in Figure 20.5. Further information for this implementation may be found in Ref. [16]. Different sensors can be powered by energy harvesting and an overall profit on the aviation infrastructure could be established.

#### 20.6.2

##### The Dynamic Thermoelectric Harvesting Prototype

A dynamic thermoelectric harvester prototype was developed by EADS Innovation Works in 2009 [18]. This prototype consisted of a hemispherical stainless steel HSU with an internal thermal bridge, water as the PCM, and four EURECA TEG1-9.1-9.9-0.2\_200 TEGs. A schematic and image of this implementation are shown in Figure 20.6. A polyurethane layer was used for thermal insulation. A total output energy of 35 J from an outside temperature sweep corresponding to a typical flight, using 10 ml of PCM, was achieved. This device was tested under real flight conditions and for various flight cases demonstrating energy outputs up to 24 J [19]. More information regarding this implementation can be found in Refs. [18, 19]. This prototype was used to power up a wireless sensor node for more than 5 h, and different sensors ranging from temperature to strain gage can be adapted and installed in harsh environments.

#### 20.6.3

##### Heat Storage Thermoelectric Harvester for Aircraft Strain Sensors

The implementation presented in Refs. [13] was based on an aluminum HSU with 23 g of water as PCM and a 2 mm thick polystyrene thermal insulation layer.

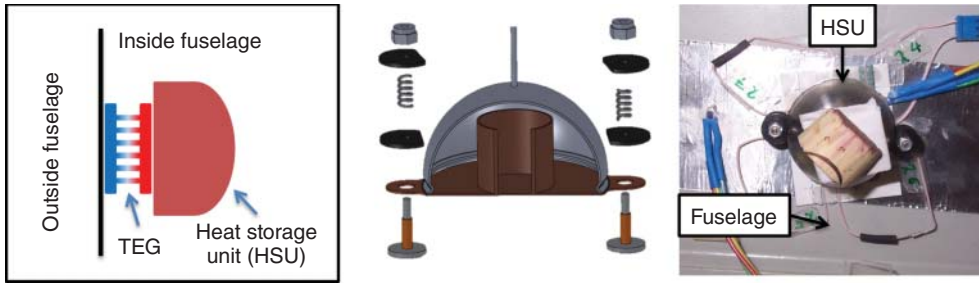


**Figure 20.6** A schematic of the EADS 2008 dynamic harvester implementation from concept to prototype [9].

The outer dimensions of the metal container were  $60\text{ mm} \times 30\text{ mm} \times 30\text{ mm}$  with  $2\text{ mm}$  thick walls and the container included two internal thermal bridges. Its mass was  $65\text{ g}$  with an internal volume of  $30\text{ cm}^3$ . Two Marlow TG12-2-5 TEGs were used, each measuring  $30\text{ mm} \times 34\text{ mm} \times 4\text{ mm}$ , and the thermal resistance was  $3.6\text{ K W}^{-1}$ . The figure of merit  $ZT$  and series resistance of each TEG were  $0.72$  and  $5\ \Omega$  ( $\pm 10\%$ ), respectively. The main design benefit of this implementation is the quality of insulation as it does not have heat bridges between the interior and the exterior other than TEGs, and the extruded polystyrene has an extremely low thermal conductivity ( $0.03\text{ W m}^{-1}\text{ K}^{-1}$ ). Photographs of the container and the assembled device are shown in Figure 20.7. Output energy of  $105\text{ J}$  into a  $10\ \Omega$  matched resistive load was demonstrated from a temperature sweep from  $+20\text{ }^\circ\text{C}$  to  $-21\text{ }^\circ\text{C}$ , and then to  $+25\text{ }^\circ\text{C}$ . Indicative output power results are shown in Figure 20.8. This corresponds to an energy-to-PCM volume density of  $4.6\text{ J ml}^{-1}$  and an energy-to-overall volume density of  $1.3\text{ J ml}^{-1}$ . Flight tests have been scheduled by Airbus for a strain sensor system powered by this implementation. A photograph of the device is shown in Figure 20.7 [14].

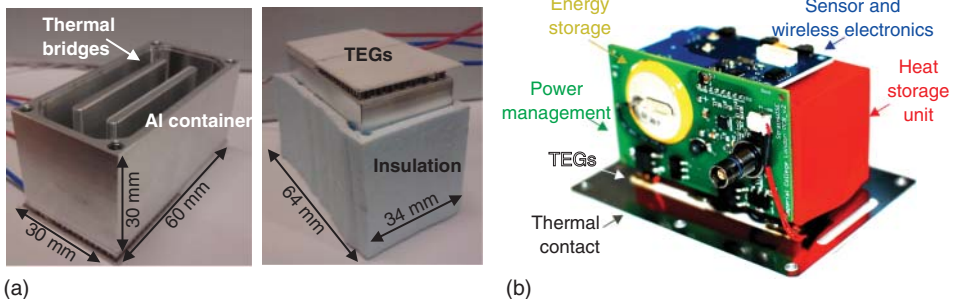


**Figure 20.7** (a) Photographs of the Imperial 2014 dynamic harvester implementation. Left: metal container with lid removed, showing two thermal bridges. Right: assembled

generator. The metal container is partially raised for visibility. (b) Photograph of the sensor node (unboxed) [14].

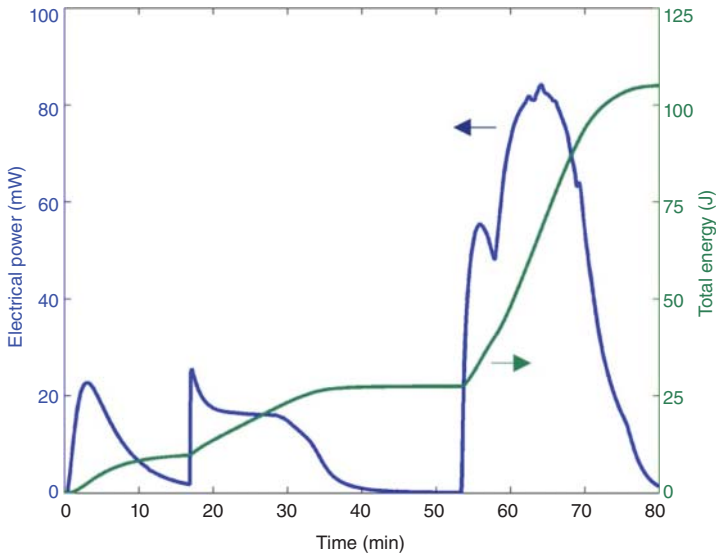


**Figure 20.8** Instantaneous electrical power output and energy of the Imperial 2014 device shown in Figure 20.7.

#### 20.6.4

#### Outlook

While the three application cases described in Section 20.5 are indicative, other implementations have also been reported, such as the dynamic harvester implementation of Baily *et al.* [20] intended for aircraft strain sensors. The reported prototype demonstrated an output energy of 34 J from a typical flight temperature cycle. A comparative summary of the reported dynamic energy harvesting devices is presented in Table 20.4.

Overall, both static and dynamic thermoelectric harvesting appear to be promising options for powering aircraft sensors. The choice between operation

**Table 20.4** Overview of dynamic thermoelectric harvesting device implementations.

Organization/ year	Size (ml)	TEG	Energy (J)	Energy density (J ml <sup>-1</sup> ) (PCM)	Energy density (J ml <sup>-1</sup> ) (device)	Comments
EADS/2008 [18]	24 plus insulation	4× Eureka TEG1-9.1- 9.9-0.8/200	35	3.5	1.5 (no insulation)	Flight tested
LAAS- CNRS/2008 [20]	—	Micropelt MPGD602	34	2.8	—	—
Imperial/ 2014 [21]	78	2× Marlow TG12-2-5	105	4.6	1.3	Flight tests scheduled

**Table 20.5** Physical properties of the most used phase change materials for thermoelectric applications.

Material name	Physical properties					
	$T_m$ (°C)	$C_p$ (kJ kg <sup>-1</sup> K <sup>-1</sup> )	$k$ (W m <sup>-1</sup> K <sup>-1</sup> )	$\rho$ (kg m <sup>-3</sup> )	$\Delta H$ (kJ kg <sup>-1</sup> )	
Water (solid)	0	4.2	2.18	917	334	
Water (liquid)		2	0.58	1000		
PCM inorganic	E-11 (PCM products)	-11.6	3.55	0.57	1090	301
	E-15 (PCM products)	-15	3.87	0.53	1060	303
	E-19 (PCM products)	-18.7	3.29	0.58	1125	282
	H120 (PCM products)	120	1.51	0.506	2220	120
	H355 (PCM products)	353	1.52	0.556	2060	230
PCM organic	RT10-HCG (Rubitherm)	+10 to +9	2	>0.2	770	152
	RT10-HC (Rubitherm)	+10 to +4	2	0.2	770	195
	RT-9-HCG (Rubitherm)	-9 to -10	2	>0.2	770	260
	A118 (PCM products)	118	2.7	nd	1450	340

In brackets the manufacturer of each PCM is given. On the “normal” temperature range (-50 to 80 °C) water has one of the best thermal properties.

principles and among designs depends on the sensor location, size and installation restrictions, and power requirements. In parallel with the considerable research on modern thermoelectric devices, such as super-lattice-based devices, current research efforts focus on the identification of application scenarios and associated locations. In addition, different PCM materials (salt-based, organic, eutectic, etc.) are considered in order to expand the applicability of applications [14]. Table 20.5 shows a selection of the commercially available PCMs and their thermal properties.

Finally, the use of multiple PCMs to improve the operational continuity of dynamic harvesting has been investigated [22]. Owing to a large variety of advancement potentials of the devices reviewed here, the development of a device – application combination assessment tool is desirable, to be used as a compass tool toward future implementations. In this direction, a set of design rules have been proposed in [13] and are outlined in the next section.

The performance of a thermoelectric energy harvesting device hinges, more than on anything else, on the efficiency of the TEG used. Current state-of-the-art TEGs only provide a very small efficiency margin (2–5%), which in turn limits the overall efficiency of the device to  $\approx 0.5\%$ . Performance figures are even worse for smaller device sizes or small  $\Delta T$ s. It becomes obvious that more efficient and scalable TEGs are crucial for challenging thermoelectric energy harvesting applications, not only in aircraft but potentially in other application sectors as well.

20.7

Conclusions

The development of reliable and adaptable energy harvesting solutions is critical for the success of autonomous wireless sensor nodes. A successful example can be found in dynamic thermoelectric harvesting sensors, which have recently been demonstrated in real flight environments, showing that harvesting can provide enough energy to power sensors and wireless transceivers for an adequate period of time [19].

In comparison with conventional, also referred to in this chapter as static, thermoelectric harvesters, optimization of performance has a critical difference. As discussed in Section 20.4.2, in cases where a TEG is used to exploit a local temperature difference directly, the energy source can typically be approximated as a limitless supply of heat at constant temperature, with the input temperature to the TEG affected only by the finite thermal conductance of the source structure, and not by the loss of energy through the TEG. Consequently, maximization of energy output requires maximization of the product of heat flow and TEG efficiency as shown in Figure 20.9a. Taking into consideration the approximately linear variation of  $\eta_{TEG}$  with  $\Delta T$ , simple calculations show that the thermal resistance of

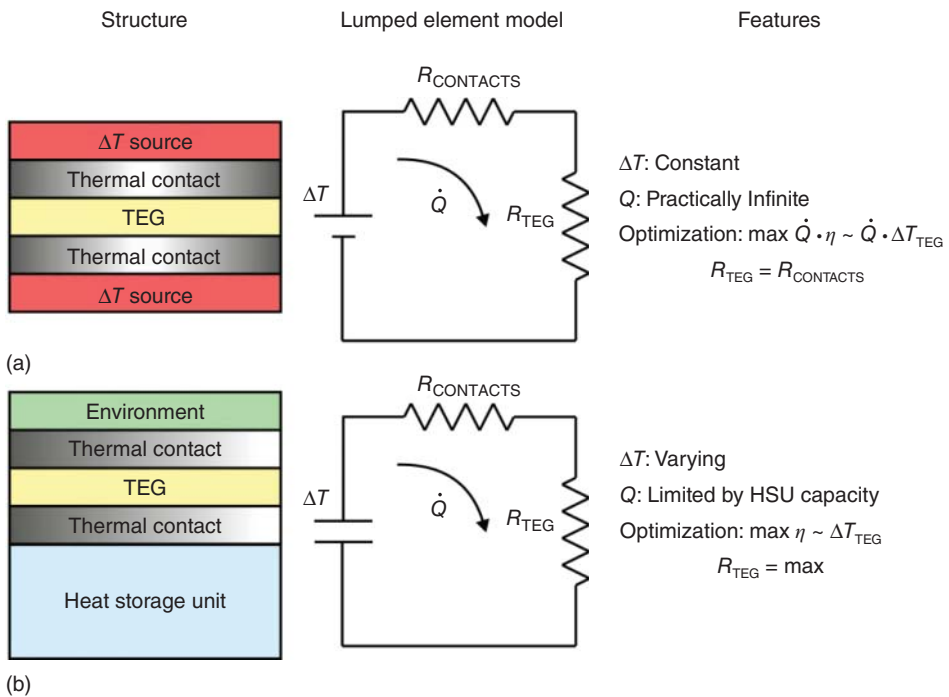


**Figure 20.9** (a) Direct thermoelectric harvesting. Heat availability is practically unlimited and optimum operation requires thermal resistance matching. (b) Architecture of heat storage thermoelectric harvesting. Maximum thermal resistance is required.



the TEG should match that of the rest of the thermal path between the high-temperature source and the ambient. This is why optimum operation in direct thermoelectric harvesters occurs when the temperature difference across the TEG is  $\Delta T/2$ , in analogy with load matching in electrical power transfer.

On the contrary, in heat storage thermoelectric harvesting, the total available heat energy is limited, and hence maximization of conversion efficiency, rather than output power, is required. By virtue of that, a TEG with as large a thermal resistance as possible is desirable. An electrical analogy of this effect can be found in the discharge of a capacitor into a resistive load, through its own series resistance, as shown in Figure 20.9b. As opposed to the case of power transfer from a voltage source where resistance matching is required, in the case of a capacitor discharge, maximization of the load resistance is required.

The theoretical background, design considerations, and implemented prototypes illustrate the great potential of thermoelectric energy harvesting deployed in aircraft wireless sensor networks. Harsh environments or difficult-to-access areas can be monitored using thermoelectric harvesters as supply sources. These sources may reduce maintenance costs, weight, and hence reduce fuel consumption, and finally operational costs.

## References

1. Kowalewski, P. (2012) Cost-benefit-analysis of wireless sensor networks and energy harvesting. Master thesis. Fachhochschule Wedel.
2. González, C. and Homero, J. (2013) Conduction of profitability analyses in research and development projects. Master thesis. Technical University of Hamburg.
3. Becker, T., Kluge, M., Schalk, J., Tiplady, K., Paget, C., Hilleringmann, U., and Otterpohl, T. (2009) Autonomous sensor nodes for aircraft structural health monitoring. *IEEE Sens. J.*, **9** (11), 1589–1595.
4. Weddell, A.S, Merrett, G.V., and Al-Hashimi, B.M. (2011) Ultra low-power photovoltaic MPPT technique for indoor and outdoor wireless sensor nodes. Design, Automation and Test in Europe Conference and Exhibition (DATE), 2011, IEEE, pp. 1-4.
5. Thangaraj, K., Elefsiniotis, A., Becker, T., Schmid, U., Lees, J., Featherston, C.A., and Pullin, R. (2013) Energy storage options for wireless sensors powered by aircraft specific thermoelectric energy harvester. *J. Microsyst. Technol.* doi: 10.1007/s00542-013-2009-3
6. Penella, M.T. and Gasulla, M. (2010) Runtime extension of low-power wireless sensor nodes using hybrid-storage units. *IEEE Trans. Instrum. Meas.*, **59** (4), 857–865.
7. ITU (2011) Technical Characteristics and Operational Objectives for Wireless Avionics Intra-Communications (WAIC). Report ITU-R M.2197, ITU.
8. Snyder, G.J. and Toberer, E.S. (2008) Complex thermoelectric materials'. *Nat. Mater.*, **7** (2), 105–114.
9. Strasser, M., Aigner, R., Franosch, M., and Wachutka, G. (2002) Miniaturized thermoelectric generators based on poly-Si and poly-SiGe surface micromachining. *Sens. Actuators, A: Phys.*, **97**, 535–542.
10. Rowe, D.M. (1995) *CRC Handbook of Thermoelectrics*, CRC Press.
11. Freunek, M., Müller, M., Urgan, T., Walker, W., and Reindl, L.M. (2009) New physical model for thermoelectric generators. *J. Electron. Mater.*, **38** (7), 1214–1220.
12. Min, G. and Yatim, N.M. (2008) Variable thermal resistor based on self-powered

- Peltier effect. *J. Phys. D Appl. Phys.*, **41**, 222001.
13. Kiziroglou, M.E., Wright, S.W., Toh, T.T., Mitcheson, P.D., Becker, T., and Yeatman, E.M. (2014) Design and fabrication of heat storage thermoelectric harvesting devices. *IEEE Trans. Ind. Electron.*, **61**, 302–309.
  14. Kiziroglou, M.E., Elefsiniotis, A., Wright, S.W., Toh, T.T., Mitcheson, P.D., Becker, T., and Yeatman, E.M. (2013) Performance of phase change materials for heat storage thermoelectric harvesting. *Appl. Phys. Lett.*, **103**, 193902–193902-5.
  15. Beeby, S. and White, N.M. (2010) *Energy Harvesting for Autonomous Systems*, Artech House.
  16. Samson, D., Kluge, M., Becker, T., and Schmid, U. (2010) Energy harvesting for remote monitoring of aircraft seats. *Sens. Lett.*, **8** (2), 328–335.
  17. Starner, T. (1996) Human-powered wearable computing. *IBM Syst. J.*, **35** (3-4), 618–629.
  18. Samson, D., Otterpohl, T., Kluge, M., Schmid, U., and Becker, T. (2009) Aircraft-specific thermoelectric generator module. *J. Electron. Mater.*, **39** (9), 2092–2095.
  19. Elefsiniotis, A., Samson, D., Becker, T., and Schmid, U. (2013) Investigation of the performance of thermoelectric energy harvesters under real flight conditions. *J. Electron. Mater.*, **42** (7), 2301–2305.
  20. Baily, N., Dilhac, J.M., Escriba, C., Vanhecke, C., Mauran, N., and Baffleur, M. (2008) Energy scavenging based on transient thermal gradients: application to structural health monitoring of aircrafts. Conference Proceedings of PowerMEMs 2008, Sendai, Japan.
  21. Toh, T.T., Wright, S.W., Kiziroglou, M.E., Mitcheson, P.D., and Yeatman, E.M. (2014) A dual polarity, cold-starting interface circuit for heat storage energy harvesters. *Sens. Actuators, A: Physical*, **211**, p. 38–44.
  22. Elefsiniotis, A., Kokorakis, N., Becker, T., and Schmid, U. (2013) A thermoelectric-based energy harvesting module with extended operational temperature range for powering autonomous wireless sensor nodes in aircraft. *Sens. Actuators, A: Phys.*, **206**, 159–164.

## 21

# Powering Pacemakers with Heartbeat Vibrations

*M. Amin Karami and Daniel J. Inman*

### 21.1

#### Introduction

One of the applications of energy harvesters is powering implantable biomedical devices. Romero *et al.* [1] performed a detailed survey on energy harvesting devices designed for this purpose. The majority of vibrational energy harvesters that extract energy from human motion are attached to the limbs. Arms and legs have a large range of motion and therefore provide abundant vibrational energy. However, it is not feasible to connect a biomedical device inside the torso to an energy harvester in arms or legs. If the biomedical device is intended to be implanted in the torso, it is preferred to include the energy harvesting device in the same package. The amount of vibrations inside the torso is limited. The human motion gait is in a way that keeps the torso steady. Human locomotion, therefore, does not induce significant vibrations inside the torso. There are three configurations for in vivo energy harvesting devices that can be used inside the torso. Microbial fuel cells use the oxidation of glucose for generating power [2–4]. For more information on microbial fuel cells, refer to Chapter 7. The second method is by harvesting energy from expansions of artery by wrapping a piezoelectric film around them [5]. The third solution is by printing piezoelectric ribbons onto rubber [6] and using the expansion of the lungs in respiration. We use the vibrations inside the chest area to power pacemakers and implantable cardioverter defibrillators (ICDs). Because pacemakers are implanted inside the chest area (typically below the collar bone), energy harvesters should use the energy inside the torso. The most significant vibrations inside the chest area are those caused by heartbeats. We investigate recharging power-efficient pacemakers with heartbeat-induced vibrations.

The power requirement of pacemakers has significantly reduced over the past years and  $1 \mu\text{W}$  is assumed a safe upper estimate of the required power of modern pacemakers [7]. Currently, more than 60% of the volume of pacemakers is dedicated to the battery. Still patients have to go through a surgical operation every

5–12 years to replace the batteries of their pacemakers [8]. Here, we introduce linear and nonlinear energy harvesters that can constantly recharge the battery of a pacemaker and significantly extend its lifetime.

Piezoelectric transduction was tried in the past for development of power sources for implantable medical devices [9–11]. The proposed devices were significantly less efficient than modern energy harvesters. As a result, to provide the required power, they suggested very intrusive approaches that were not acceptable.

This chapter starts with specifying the power expectations from a heartbeat harvester. The target maximum size of the harvester is also identified. Heartbeat-induced oscillations in the chest area are extracted from ultrasonic measurements in the literature and animal tests. The feasibility of using linear energy harvesting technologies at regular and microscales is investigated next. To increase the frequency bandwidth of the energy harvester and to reduce its sensitivity to heart rate, nonlinear energy harvesting devices are investigated. Both monostable and bistable energy harvesting technologies have been used. The performance of bistable energy harvesters is compared against monostable and linear designs. The modeling results have been verified with *in vitro* experiments. The device is subjected to vibration waveforms measured during the animal tests. The relation between the power generation and the location of the device and the relation between power output and heart rate have been experimentally investigated.

## 21.2

### Design Specifications

In this section, the acceptable size of the vibrational energy harvester and the power output requirement of the pacemaker are identified. It is desirable to have an energy harvester that is smaller than the battery of the current pacemakers. If such a vibrational energy harvester is realized, we succeed in both reducing the size of the pacemaker and significantly extending its lifetime. Currently, the size of a typical pacemaker is about 42 mm by 51 mm by 6 mm [12]. Typically, the battery takes about two-thirds of the size of the pacemaker. We target at reducing the power source area by 50% and therefore set the maximum size of the vibrational energy harvester as 27 mm by 27 mm by 6 mm.

Ohm and Danilovic [7] performed an extensive survey on changes in power consumption of pacemakers from 1965 to 1995. They stated that power requirement for pacemakers in 1995 was already below  $1 \mu\text{W}$ . Although the power demand should have significantly reduced since 1995, we take a conservative estimate and assume that the power consumption of pacemakers is still  $1 \mu\text{W}$ .

The choice of biocompatible materials can be a major issue in designing biomedical devices. The most commonly used piezoelectric materials (PZT) are composed of lead, which is toxic. Fortunately, the packaging of conventional pacemakers removes the need for using biocompatible materials for the energy harvesters. The batteries and circuits of pacemakers are encapsulated in a titanium

case. Titanium is a biocompatible material. The sealed casing ensures that there is no contact between the interior of the body and the pacemaker batteries or circuits. We plan to place the pacemaker inside the same titanium casing. It must be mentioned that the batteries currently used for pacemakers are lithium ion batteries [12]. Lithium is a toxic material, but it is incorporated due to the casing of the pacemakers.

### 21.3

#### Estimation of Heartbeat Oscillations

An energy harvester must not impede the heart beat. Attaching the energy harvester unit to the exterior of the heart mass loads the heart and is therefore unacceptable. The energy harvester should instead be placed in the vicinity of the heart. To get an initial estimate of the heartbeat vibrations, we use the ultrasonic velocity measurements performed by Kanai *et al.* [13]. They measure the velocity at two points on the sides of the interventricular septum (the wall separating the left and right ventricles of the heart). The interventricular septum is not the most movable part of the heart. The bottom of the heart is supported by the diaphragm and is almost fixed. Heartbeat therefore results in significant motion of the top of the heart (the base) [14]. Since the measurement points in [13] are close to the bottom of the heart, the velocity data is a good average of the motion of the heart and consecutively the vibration of the part of the body close to the heart area. We therefore design the energy harvester based on the sample acceleration profile in [13] (Figure 21.1). In this chapter, the waveform in Ref. [13] is referred to as the Kanai's waveform.

To accurately interpret the data presented in Ref. [13], the following steps are followed. In the first step, the period of the heartbeat is estimated. We consider the heart velocity profile over approximately six periods. The Fourier transform of the velocity profile is calculated. The Fourier transform of a periodic signal takes the form of a Fourier series and has only nonzero values at multiples of the fundamental frequency of the signal. The spacing between the dominant peaks in the Fourier transform of the velocity profile of the six beats accurately identifies the period of beatings.

The velocity profile over one period is illustrated in Figure 21.1a. The second step is to estimate the acceleration profile from the given velocity profile. To this end, we fit a not-a-knot spline to the velocity data from Ref. [13] and take the derivative of the resulting spline. This gives a smooth function representing the acceleration profile of heartbeats (Figure 21.1b). The third step is to extract the frequency spectrum of heartbeat vibrations. The Fourier series of the velocity and acceleration profile of heartbeats are illustrated in Figure 21.1c,d.

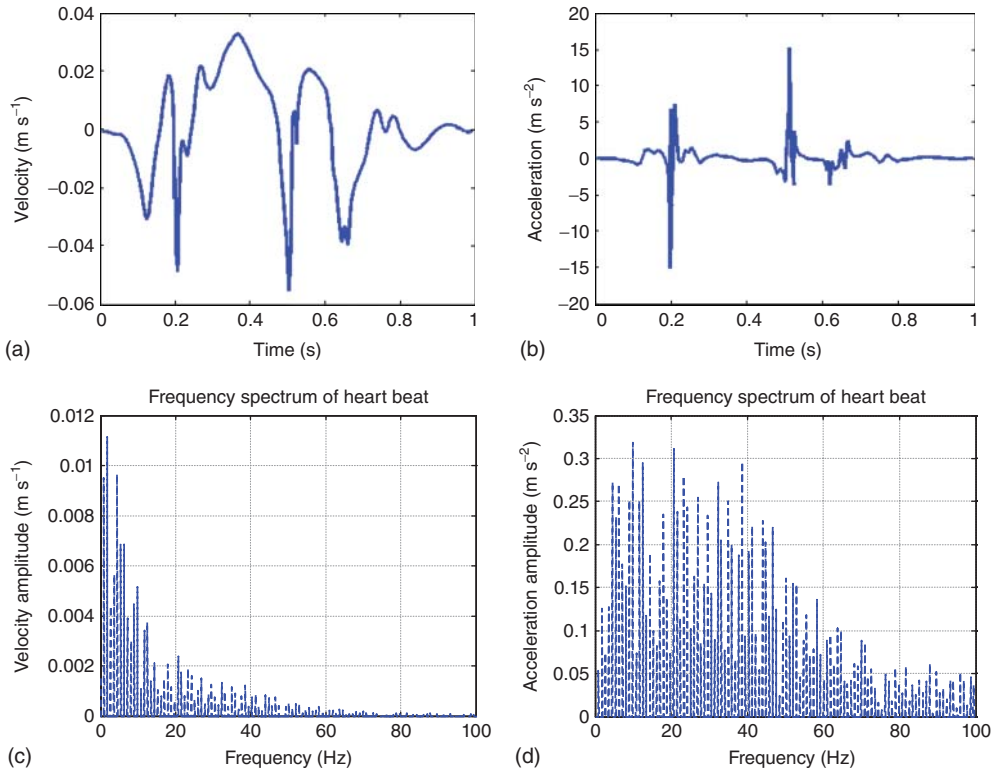


**Figure 21.1** Sample acceleration profiles of heart vibrations based on Ref. [13]: time domain representation of (a) velocity, (b) acceleration profiles and frequency domain representation of (c) velocity, and (d) acceleration profiles.

## 21.4

### Linear Energy Harvesters

This section investigates if linear vibrational energy harvesters can be used for powering pacemakers. Because the size of the energy harvester is relatively small, we use the unimorph zigzag geometry (Figure 21.2), which was analyzed in Ref. [15–17]. As illustrated in Figure 21.1d, heartbeat vibrations contain many frequency components. Linear energy harvesters have a small bandwidth. We design the linear energy harvester to generate energy mostly from the 39 Hz frequency component of the heartbeat oscillation. This is because the amplitude of the 39 Hz frequency component is relatively high. In addition, 39 Hz is a relatively high frequency and results in better power production.

We optimize every aspect of the zigzag harvester for better power generation. The length of the beams is specified by the size constraint. The width of each beam is 1/10 of its length. The thickness of the piezoelectric layer is prescribed by the fabrication method and is discussed shortly. For each value of the thickness of the

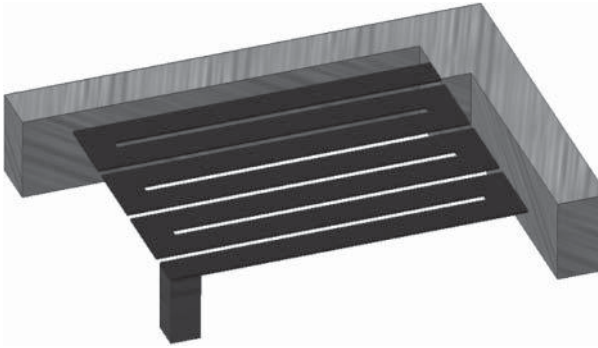


Figure 21.2 The zigzag structure.

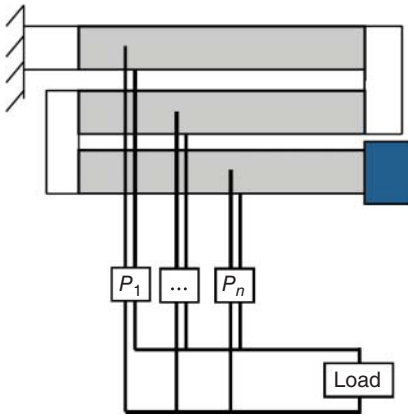
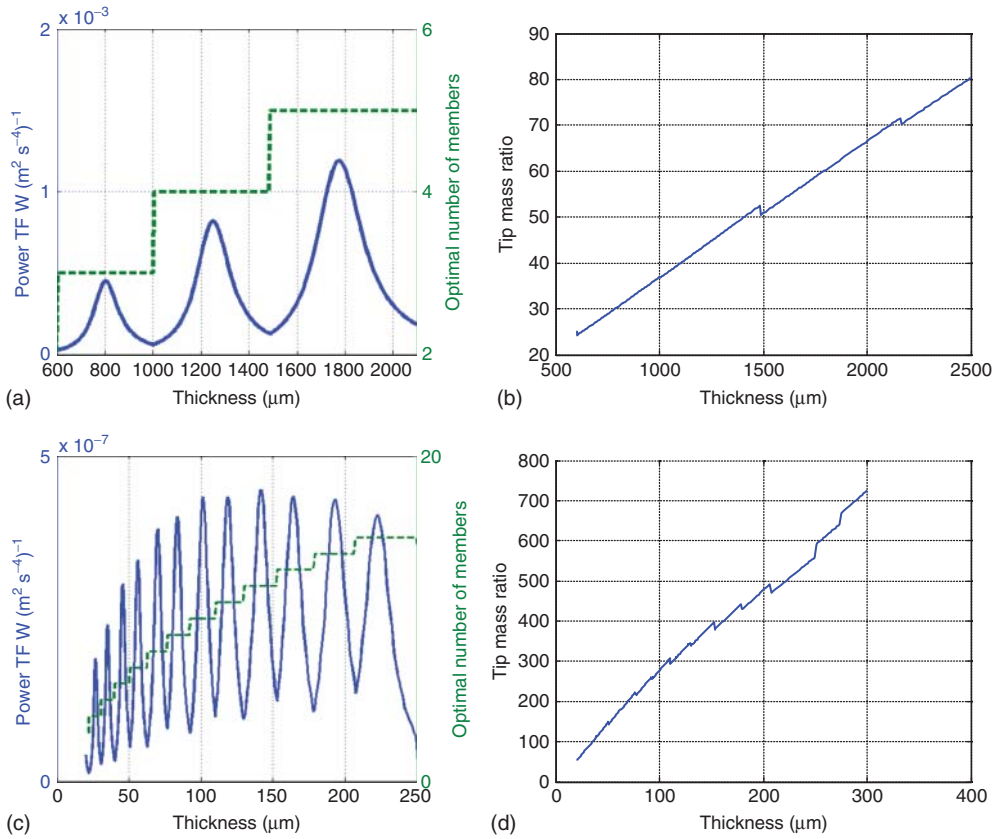


Figure 21.3 Electrical connections.

substrate, we optimize the tip mass, the polarity of connecting individual piezoelectric members (Figure 21.3), and the shunt resistance for maximum power. We then plot maximum power as a function of substrate thickness and identify the optimal value for the thickness of the substrate.

For the first linear energy harvesting design, we use the maximum space and consider zigzag energy harvesters with 27 mm long beams. Brass is chosen as the substrate material due to its large density and relatively large Young's modulus. The piezoelectric layer is attached to the substrate using epoxy (polyepoxide). The thickness of the commercial PZT-5A ceramics selected for the device is 0.01 inch (254  $\mu\text{m}$ ). The optimization procedure, briefly described above, results in the relation between the power and the substrate thickness (Figure 21.4a). The maximum power corresponds to 1700  $\mu\text{m}$  substrate thickness. The power output from such a structure is calculated to be  $1.2 \times 10^{-4} (\text{W}/(\text{m}^2\text{s}^{-4})) \times 0.3^2 (\text{m}^2\text{s}^{-4}) = 10 \mu\text{W}$ . The linear mesoscale device can therefore generate 10 times the power requirement of a pacemaker if excited at nominal heart rate.

The next step is to investigate whether we can meet the power requirement of pacemakers by microscale vibrational energy harvesters. To this end, the device has to be fabricated using microfabrication techniques. Silicon is



**Figure 21.4** Optimal power transfer function, number of members, and tip mass/mass of a single beam ratio for zigzag structures as a function of the thickness of the substrate: (a,b) mesoscale and (c,d) microscale.

accordingly considered the substrate material. The fundamental difference between millimeter-scale and micro-electro-mechanical-system (MEMS) energy harvesters is the thickness of the piezoelectric layer. In MEMS harvesters, the piezoelectric layer has to be deposited using chemical deposition methods. This limits the thickness of the piezoelectric layer to only  $3\ \mu\text{m}$  [18]. As shown in Figure 21.4c, the power generation of a 5 mm long MEMS structure is limited to  $4.3 \times 10^{-7} (\text{W}/(\text{m}^2 \text{s}^{-4})) \times 0.3^2 (\text{m}^2 \text{s}^{-4}) = 39\ \text{nW}$ . The significant difference between the power generation of the millimeter scale and MEMS devices is mainly attributed to the pronounced difference between the thickness of the piezoelectric layers of the two structures [19, 20]. The case study demonstrates that deposition-based MEMS piezoelectric energy harvesters are not suitable for powering pacemakers from heartbeats.



The millimeter-scale linear energy harvester meets the power requirement of a pacemaker, but it is very sensitive to the frequency of heart beating vibrations. This implies that there is an optimal heart rate for power production. If the heart rate deviates from the nominal value, power generation can drop by orders of magnitude. In reality, heart rate varies from moment to moment. In the next sections, nonlinear energy harvesting designs are investigated. Nonlinear energy harvesting devices are significantly less sensitive to heart rate compared to linear energy scavengers.

## 21.5

### Monostable Nonlinear Harvesters

The proposed configuration for monostable and bistable nonlinear energy harvesting is illustrated in Figure 21.5. The beam is a bimorph and has a brass substrate. The repelling force between the tip magnet and the magnets attached to the frame opposes the elastic restoring force of the composite beam. The designs are performed based on analytical models and experimental investigations presented in [21, 22].

In monostable configuration, the repelling magnetic force is always smaller than the restoring elastic force of the beam. The study in the previous section showed the significant advantage of millimeter-scale energy harvesters over the microscale counterparts. We therefore take advantage of the entire 27 mm by 27 mm area targeted. We assume that the length and the width of the beam are both 27 mm. We look into using off-the-shelf rare earth magnets for the nonlinear harvesters. The dimensions of the base and tip magnets are 25.4 mm

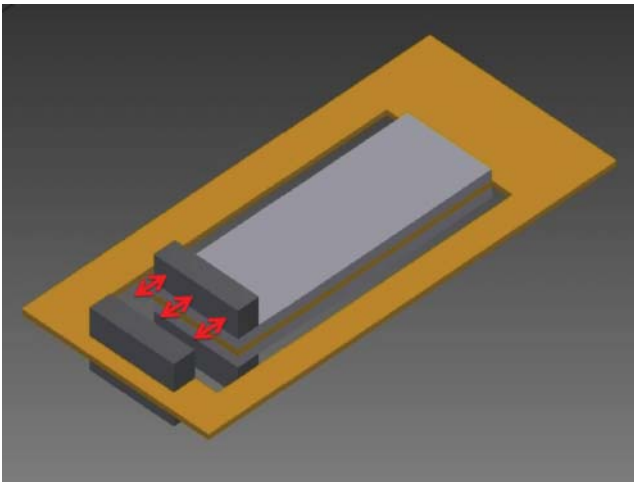


Figure 21.5 Nonlinear energy harvesting configuration.

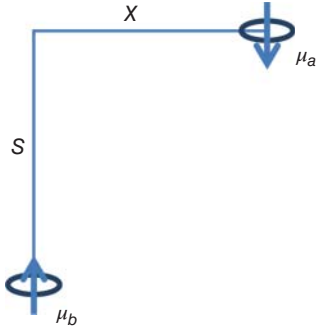


Figure 21.6 Schematic of magnetic dipoles.

by 3.18 mm by 3.18 mm. The residual flux densities of the magnets are derived during optimization.

Optimization of design variables has been performed using two different methods. The first optimization method uses the perturbation solution of the response of bistable energy harvesting systems to harmonic base excitations. Although the perturbation solution is fast, it lacks accuracy. This is because perturbation solutions are specifically valid for harmonic base accelerations. In contrast, excitations of heartbeat harvesters are not harmonic. The second optimization method is based on numerical simulation of the response of a monostable harvester to heartbeat waveforms.

To estimate the magnetic repulsive force between the two magnets, we follow the approach outlined in Ref. [23]. Force calculations are based on magnetic moment vectors. The magnetic moment vector of each magnet ( $\mu$ ) is related to the residual flux density of the magnet ( $B$ ), permeability of air ( $\mu_0$ ), and the volume of the magnet ( $V$ ) as (Figure 21.6)

$$\mu = \frac{B}{\mu_0} V \quad (21.1)$$

If  $\vec{r}_{ab}$  denotes the position vector from magnet  $a$  to magnet  $b$ , the magnetic field generated between the magnets is

$$\vec{B}_{ab} = -\frac{\mu_0}{4\pi} \frac{\vec{\nabla}(\mu_a \cdot \vec{r}_{ab})}{\|\vec{r}_{ab}\|^3} \quad (21.2)$$

where  $\|\cdot\|$  denotes the Euclidean norm, the dot is for the inner product, and  $\vec{\nabla}$  stands for the gradient. The magnetic potential energy between the two magnets is

$$U_m = -\vec{B}_{ab} \cdot \vec{\mu}_b = -\frac{\mu_0 \mu_a \mu_b}{4\pi} \left( \frac{x^2 - 2s^2}{(s^2 + x^2)^{\frac{5}{2}}} \right) \quad (21.3)$$

The electromagnetic force is derived by differentiation of the magnetic energy with respect to the  $x$ -coordinate:

$$f_x = \frac{\partial U_m}{\partial x} = \frac{3\mu_0 \mu_a \mu_b}{4\pi} \left( \frac{x^3 - 4s^2 x}{(s^2 + x^2)^{\frac{7}{2}}} \right) \quad (21.4)$$

Since the lateral displacement is small, binomial expansion can be used to simplify Eq. (21.4) to

$$f_x = \frac{\mu_0 \mu_a \mu_b}{4\pi} \left( -\frac{12}{s^5} x + \frac{45}{s^7} x^3 \right) \quad (21.5)$$

Equation (21.5) gives the linear and nonlinear coefficients of the magnetic force.

In the first optimization approach, we change the design parameters of the system, estimate the power production based on the perturbation solution in Ref. [21], and choose the best design configuration that results in the maximum amount of power. The broadband characteristics of the bistable energy harvester are used in the following manner. The frequency spectrum of the acceleration Figure 21.1d shows that the high-power frequency range is between 10 and 40 Hz. By adjusting the distance between the magnets, the linear resonance frequency of the structure is tuned to 10 Hz. The type of nonlinearity of the system is hardening, so that the frequency response function (FRF) starts from linear resonance frequency but peaks at a higher frequency. We make sure that the FRF peak occurs above 40 Hz. This approach utilizes the most of the base excitations energy from 10 to 40 Hz. The extent of nonlinearity of the system depends on the stiffness of the beam and the strength of the residual magnetic field. For a certain beam stiffness, if the magnetic field is weak, and we want the linear resonance at 10 Hz, we naturally have to set the magnet gap small to be able to get sufficient magnetic force. A small magnetic gap corresponds to large nonlinear forces. This indicates that the smaller the magnetic flux density, the more nonlinear the system.

The results of the optimization of a monostable harvester with 0.001 inch. thickness of the piezoelectric layer have been illustrated in Figure 21.7. The dynamic safety factor is calculated from the mode shapes and amplitude of the FRF at 39 Hz. It can be seen from Figure 21.7a that all of the structures can easily sustain the base vibrations. The best structure is selected on the basis of the amount of power it generates from  $0.3 \text{ m s}^{-2}$  base accelerations at 39 Hz. This is the best frequency component of the heartbeat oscillations, which is also considered for the design of linear systems.

The mechanical and power production FRF of the optimal harvester is illustrated in Figure 21.8. The power generation FRF (Figure 21.8b) suggests that the monostable harvester should generate about  $50 \mu\text{W}$  from heartbeats.

Perturbation solutions cannot be entirely relied on for this specific problem, because they are based on an unrealistic assumption. In perturbation solutions, excitations are assumed to be harmonic. Heartbeat vibrations are not harmonic and have more than one frequency component (Figure 21.1b). Since the system is nonlinear and the principle of superposition does not hold, we investigate the response of the system to the actual heartbeat waveform. Exciting the optimal monostable energy harvester (Figure 21.8) with Kanai's waveform has a surprising outcome. The monostable system undergoes a chaotic vibration in response to the periodic (but not harmonic) heartbeat waveform. The chaotic vibration of monostable systems in response to harmonic input is possible but very uncommon [24]. The strange attractor of the chaotic motion of the harvester is illustrated

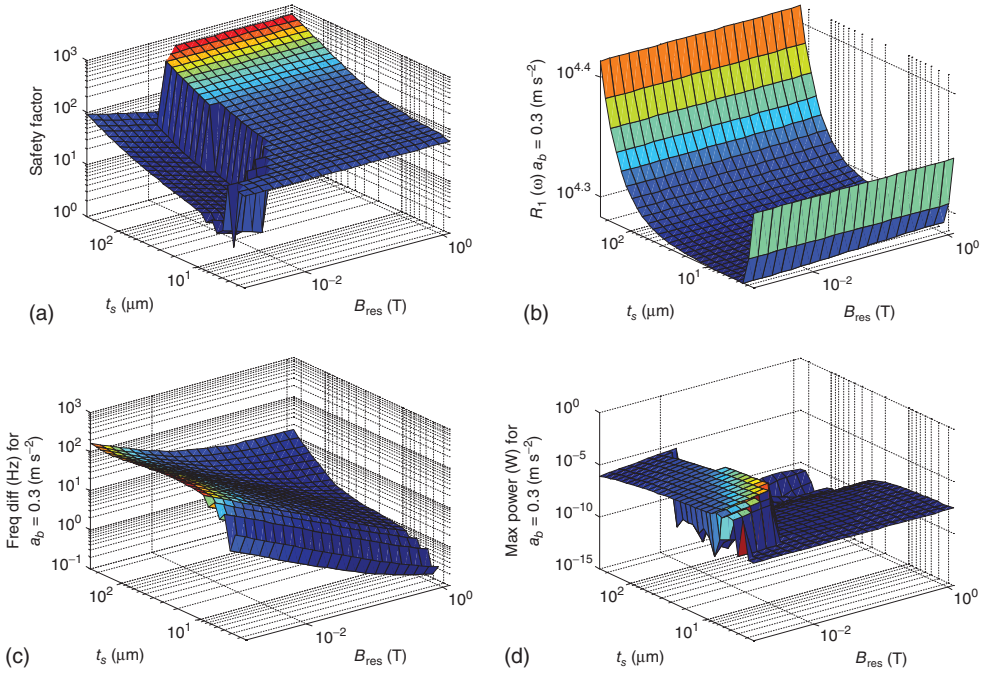


**Figure 21.7** Optimization results for monostable harvesters: (a) dynamic safety factor, (b) optimal resistance, (c) the frequency bandwidth of a nonlinear harvester, and (d) power at 39 Hz and  $0.3 \text{ m s}^{-2}$ .

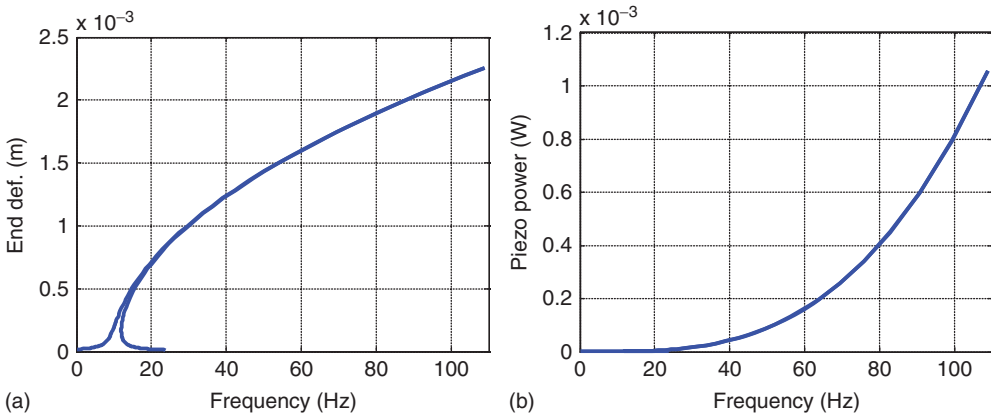


**Figure 21.8** FRF of the optimal design: (a) tip deflection FRF and (b) power generation FRF.

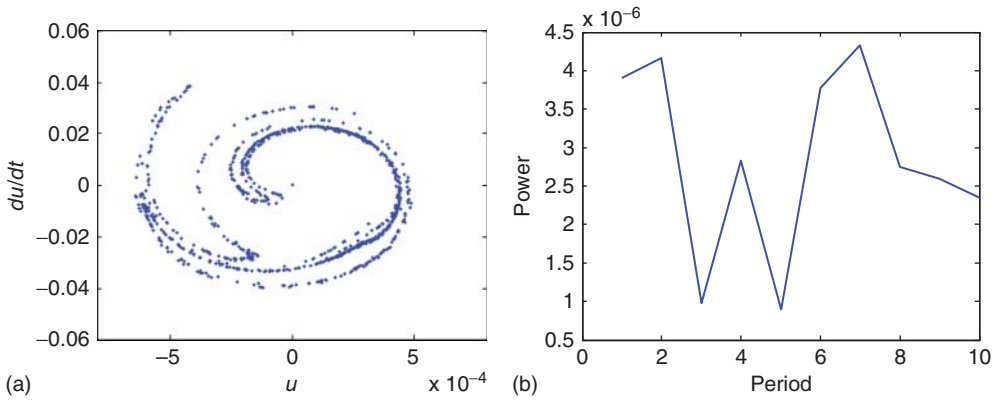


**Figure 21.9** Chaos in response to heartbeat waveforms: (a) strange attractor and (b) power variations among cycles of heartbeats.

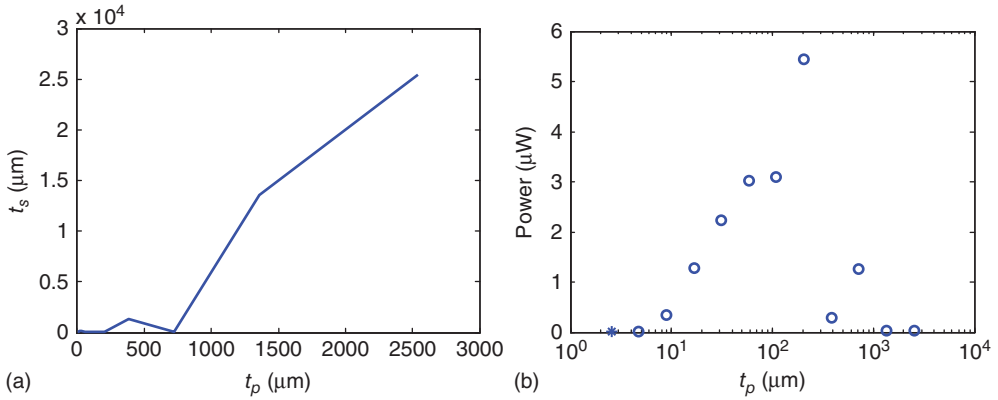


**Figure 21.10** Optimization of a softly nonlinear energy harvesting system: (a) optimal substrate thickness and (b) optimal piezoelectric thickness: circles represent periodic response and the star represents a chaotic response.

in Figure 21.9a. As the systems perform chaotic vibrations, the power output of the harvesters varies from cycle to cycle (Figure 21.9b).

Since the response to a heartbeat waveform is fundamentally different from the response to harmonic excitation, we determine the optimal nonlinear monostable harvester on the basis of its response to the former. For each value of the thickness of the piezoelectric layer, we optimize the thickness of the substrate, the residual magnetic flux density, and the magnetic gap. The relation between the thickness of the substrate and the piezoelectric layers has been illustrated in Figure 21.10a. The power output of the harvester is evaluated on the basis of the numerical integration of the governing equations (Figure 21.10b). If the response of the nonlinear harvester is periodic, we use a circle to illustrate the power output level. If the response is chaotic, a star is used in the power curve.

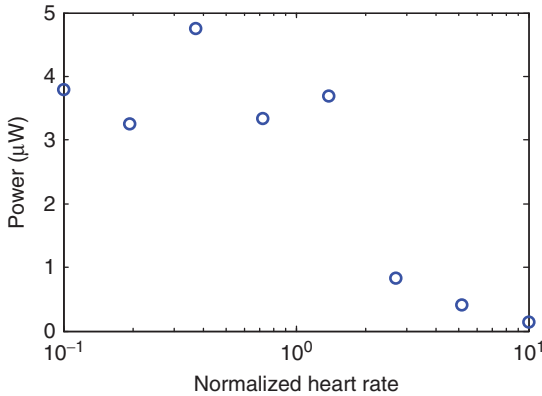


**Figure 21.11** Frequency sensitivity of a nonlinear harvester.

The power output results (Figure 21.10b) indicate that the nonlinear harvester can generate about  $7 \mu\text{W}$ . The robustness of the nonlinear harvester to the variations of heart rate is illustrated in Figure 21.11. For this study, we consider the optimal design determined from Figure 21.10b. The brass substrate is  $25 \mu\text{m}$  thick, and the thickness of each of its piezoelectric layers is  $200 \mu\text{m}$ . Normalized heart rate is defined as the ratio of the heart rate to the typical heart rate in Ref. [13]. A normalized heart rate of 10 corresponds to a heart beating 10 times faster than average. It is demonstrated that a softly nonlinear system maintains the level of output in response to slow heart rates. If the heart rate gets more than two times faster than normal, the power rating of the harvester becomes less than the requirement. In the next section, we overcome this shortcoming by using a bistable energy harvester.

## 21.6

### Bistable Harvesters

When the repulsive magnetic force between the tip and base magnets overcomes the restoring elastic force, the zero deflection position becomes unstable. There will be two equilibriums for the deflection of the beam on the two sides of the center. The studies in Refs. [21, 22] revealed that the power generation of bistable energy harvesters can be orders of magnitude larger than that of monostable harvesters. In Ref. [21, 22], the inputs to the shaker were assumed harmonic. Heartbeat oscillations are periodic but are not harmonic. We saw that this difference fundamentally changed the response of the monostable system. This section examines the nature of response of the bistable system to heartbeat oscillations and also investigates if the bistable configuration has a larger power output compared to the monostable arrangement.

The type of response of the nonlinear energy harvesting systems depends on the form of base excitations. A case study is examined to reveal the qualitative

differences between the response of the nonlinear bistable energy harvester to harmonic excitations and its response to heartbeat waveforms. The substrate in the case study is 25  $\mu\text{m}$  thick, and the thickness of the piezoelectric layers is 50  $\mu\text{m}$  each. In this case study, we subject the nonlinear bistable energy harvester to different levels of base excitations. The trend observed in Refs. [21, 22] was that low-intensity excitations induced small-amplitude periodic vibrations, medium-level base oscillations gave rise to chaotic motion, and large excitations resulted in large limit cycle oscillations of the nonlinear energy harvester. We subject the nonlinear bistable energy harvester to base excitations of 1/10, 1, and 10 times the intensity of typical heartbeat vibrations.

If the amplitude of the excitation is only 1/10 of the typical heartbeat vibrations, the bistable system performs small-amplitude periodic motion (Figure 21.12a). This is qualitatively similar to the response of the system to harmonic oscillations. If the bistable harvester is excited by heartbeat waveforms, it displays intra-well chaos (Figure 21.12b). The main distinction between intra-well chaos and ordinary chaos in Duffing systems is that in the former the tip stays in the vicinity of one of the equilibriums. Although this performance has been observed in the response of bistable harvesters to harmonic inputs [23], its occurrence for harmonic base excitations is a rare phenomenon. In contrast, when base excitations have the form of heartbeat accelerations, intra-well chaos commonly occurs. Extreme heartbeats (i.e., those 10 times more intense than normal beats) induce chaotic motion of the energy harvester (Figure 21.12c,d). Poincaré maps show that in this situation the tip of the energy harvester travels between the two equilibriums. The shape of the strange attractor is different from the form of the strange attractor of the harvester in response to harmonic motion. At the first glance, it appears that the Poincaré map resembles many concentric quasi periodic orbits. However, as we plot fewer number of points in the Poincaré map it becomes clear that the motion is in fact chaotic. No matter how large the base excitations are, the response of the energy harvesters never gets organized into limit cycle oscillations. This is qualitatively distinct from the response of the system to periodic excitations.

The optimal design parameters are identified through numerical simulations. The size of the piezoelectric beam is assumed to be the maximum targeted size (27 mm  $\times$  27 mm). The piezoelectric beam is assumed to have a bimorph configuration. The substrate is selected out of brass to have a large density. PZT-5A is selected as the piezoelectric material. The thickness of the substrate is assumed to be 100  $\mu\text{m}$ . The piezoelectric thickness is varied, and in the end the thickness that corresponds to the most amount of power is selected as optimal. For each of the piezoelectric thicknesses considered, the magnetic gap is adjusted. The energy harvester is tuned to heart beat excitations by adjusting the distance between the tip and the base magnets. The adjustment is done such that the fundamental frequency of the bistable harvester matches the heart rate. The fundamental frequency,  $\omega_0$ , equals  $\sqrt{-k}$ , where  $k$  is the negative linear restoring coefficient. The shunt resistance matches with the capacitive impedance of the piezoelectric layer.

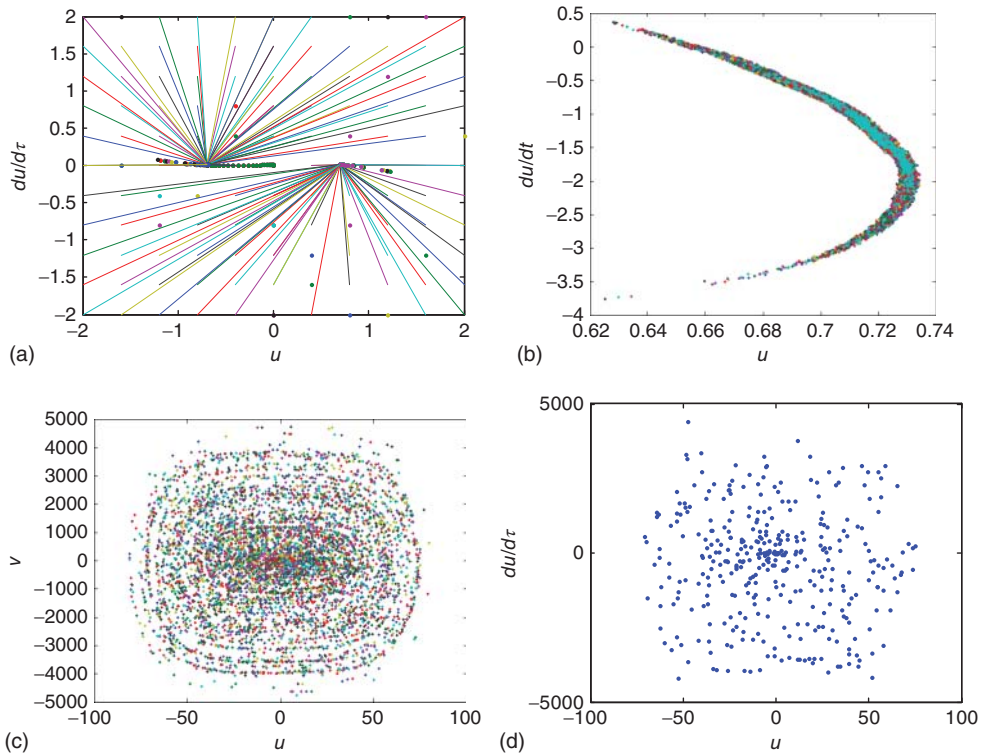


**Figure 21.12** Poincaré maps of a bistable harvester in response to different levels of heartbeat oscillations: (a) 1/10 of normal heartbeat intensity, (b) normal heartbeat intensity, (c) 10 times heartbeat intensity, and (d) 10 times heartbeat intensity sparse Poincaré map.

To evaluate the power, we run the system for numerous periods and allow it to reach steady state. Steady state vibrations can be periodic or chaotic. The power output is averaged over a few excitation periods to give the power metric. If the oscillations of the energy harvesting system are periodic, we use a circle to illustrate the power in graphs. If the response of the system to heartbeat excitations is chaotic, we represent the power output by a star in the power plots.

Figure 21.13a,b illustrates the variation of the power output with the thickness of the piezoelectric layer. It also shows that a nonlinear hybrid energy harvester with  $80\ \mu\text{m}$  piezoelectric thickness can generate about  $8\ \mu\text{W}$  from heartbeat oscillations. This amount of power is about eight times the power requirement of pacemakers. The frequency robustness of the harvester was examined in two different ways. In the first method, we examine the response of different designs to the typical heartbeat. In addition to the optimal design, where the fundamental frequency ( $\omega_0$ ) matches the heart rate, we look into “undertuned” and “overtuned” devices. The fundamental frequency of an undertuned design is tuned to half of the heart rate, while the fundamental frequency of an overtuned device is set to 40 times



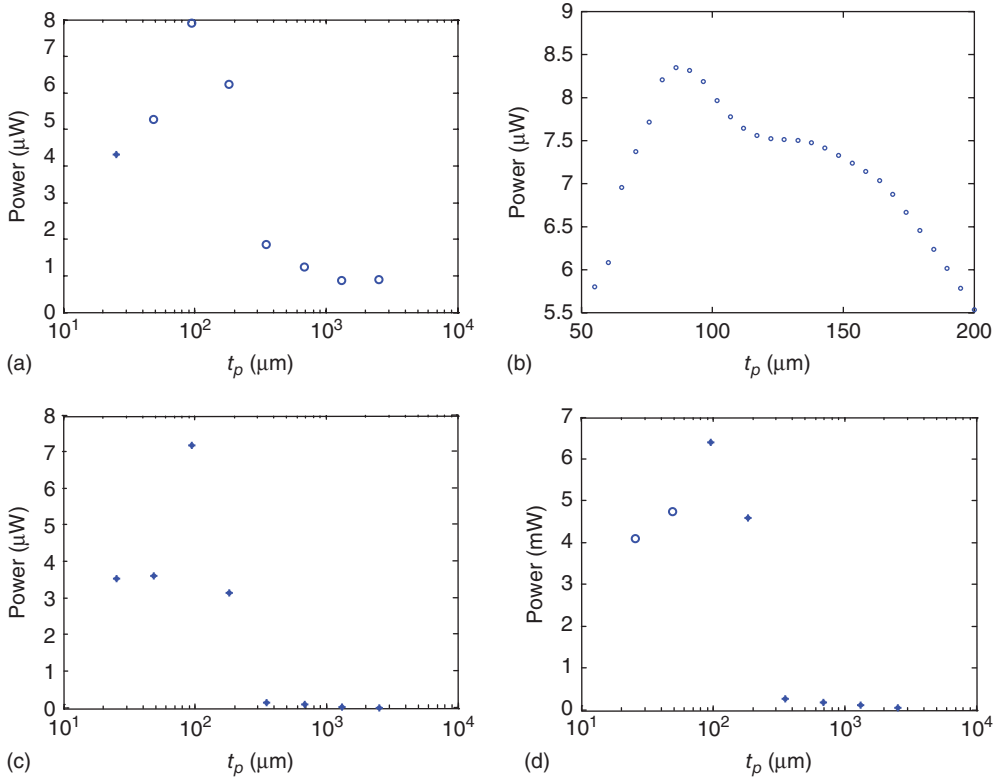


**Figure 21.13** Power output of a nonlinear bistable energy harvester: (a,b) system designed for regular heartbeats, (c) system designed for half frequency, and (d) system designed for 40 times regular beating frequency.

the heart rate. Figure 21.13c,d illustrates that the power generation of mistuned devices is close to that of the optimally tuned device. This suggests high robustness of the proposed device to variations in heart rate.

The second method to investigate the frequency sensitivity of the bistable hybrid device is to examine the relation between the power output of the optimal design from Figure 21.13b and the heart rate. Figure 21.14 illustrates that although both the type of vibrations and the output power change with the heart rate, the bistable energy harvester always generates more than  $3 \mu\text{W}$  of power. It must be mentioned that the heart rate range considered is immense. It includes variations of heart rate from 7 to 700 beats per min. The performance of the harvester is satisfactory over the entire range of heart rate. In comparison with the monostable harvester, the bistable energy harvester generates more power. This is in spite of the fact that the thickness of the PZT layers in bistable harvesters is one half of that in monostable harvesters. Bistable harvesters are also more robust to variations of heart rate.

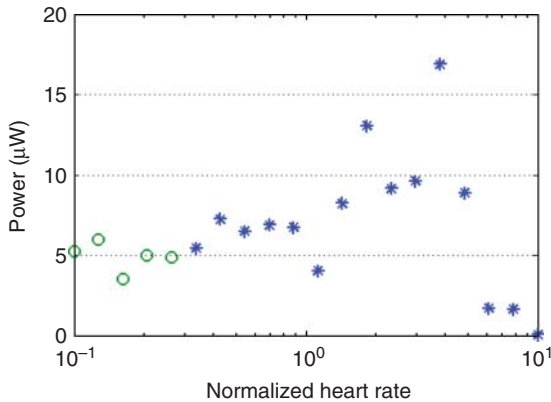


**Figure 21.14** Variations of power output of a bistable harvesting device with the heart rate.

## 21.7

### Experimental Investigations

To verify our predictions, we first measured heartbeat-induced vibrations through animal studies. We then fabricated a prototype of the optimized energy harvester and subjected the prototype to vibration waveforms from animal tests and measured the power output.

## 21.8

### Heart Motion Characterization

Two pigs and one sheep were examined (Figure 21.15). Animal tests were done at the Extracorporeal Life Support Research Laboratory at University of Michigan. The animals were used for research on artificial organs and heart pressure sensors, and they were to be sacrificed. Before each animal was sacrificed, we got the opportunity to measure the vibrations inside the chest area of each animal. During the examination, the chest area was opened and the heart was exposed. To measure the intrathoracic vibrations, we used a Polytec<sup>®</sup> laser Doppler vibrometer (LDV). The LDV uses a visible low-power laser (similar to the beam in laser pointers) to measure the velocity of a moving surface (Figure 21.16). The method is a noncontact method, so it does not interfere with the motion of the organs. In this chapter, we present the results from one of the pigs. The vibration samples were taken from the apex of the heart, the base of the heart, the lung, and at one point beneath the diaphragm on the liver.

Using the LDV during each motion sample, we measured and saved the velocity and displacement of the heart surface over approximately 10 s. To study the variations of heart motion with the heart rate, the pig's heart rate was



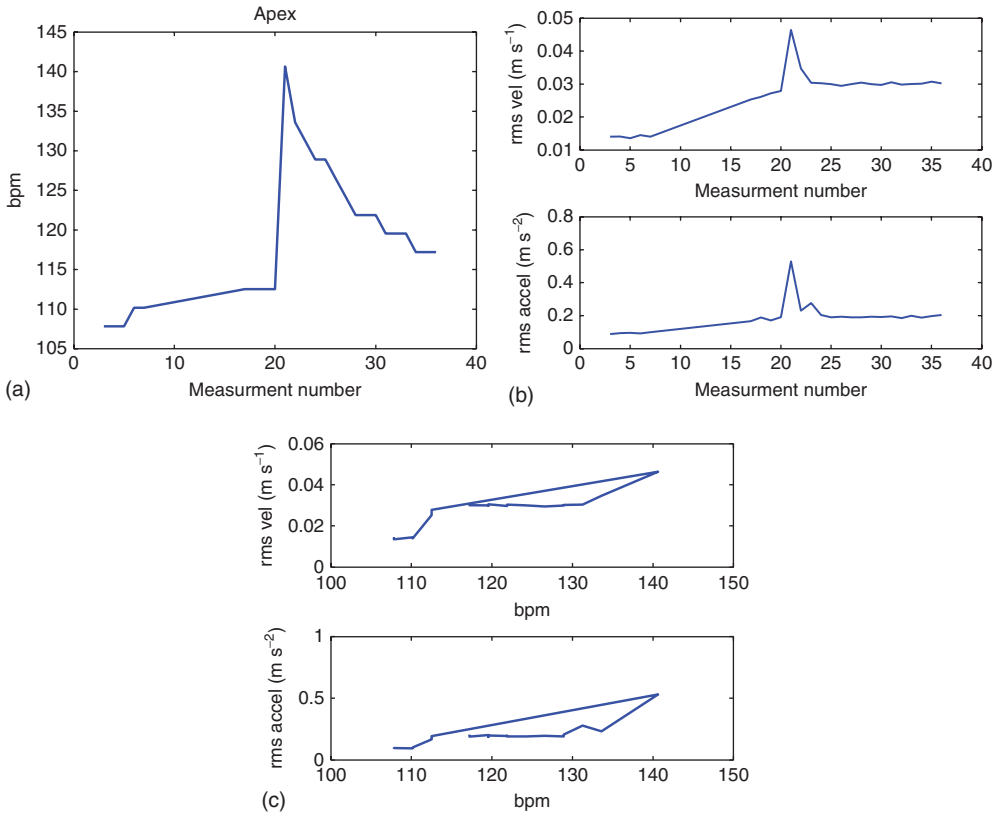
Figure 21.15 Animal tests.



Figure 21.16 Heartbeat vibration measurements.

changed by a single injection of epinephrine. As illustrated in Figure 21.17a, the epinephrine injection occurs between motion samples 20 and 21. The heart rate almost instantly rises from 112 to 142 bpm and then gradually drops over time. Figure 21.17b illustrates that both root mean square (rms) heart apex velocity and apex acceleration increase with the injection of epinephrine and then gradually decay. The rms heart velocity and rms heart acceleration have been calculated over the entire 10 s measurement period. Figure 21.17c shows that both apex velocity and acceleration increase with heart rate, but the relation is not one to one. At the same heart rate, the heart contractility is larger before injection of the epinephrine compared to after the injection. The heart could have become “tired” during the fast beating period, or the health of the animal could have deteriorated due to bleeding and having its chest area open for the duration.

Besides the amplitude of the heart motion, the waveforms of the heart vibrations are studied. To this end, the apex velocity waveforms are normalized to have the same rms value as the Kanai’s waveform. The waveforms are compared to the Kanai’s waveform because the Kanai measurement location is closest to the apex. The figure depicts the velocity waveform before the injection of epinephrine



**Figure 21.17** Apex motions: (a) heart rate at each sample, (b) rms velocity and acceleration of the apex, and (c) relation between velocity and acceleration and the heart rate.

(Figure 21.18a), immediately after the injection (Figure 21.18b), and long after the injection when the effects of epinephrine have subsided (Figure 21.18c).

Our LDV measurements of the heart-induced vibrations at the base of the heart, at liver closest to the diaphragm, and at the lung closest to the base of the heart are summarized in Table 21.1. The best location in terms of the strength of the vibrations is the base of the heart, followed by the lung. The vibrations at the liver are very small because the diaphragm acts as a barrier and blocks the transmission of heart vibrations. The waveforms of the velocity of the tissue at the base of the heart, the lung, and the liver are depicted in Figure 21.19. In all of the plots in Figure 21.19, the waveforms have been scaled to have the same rms as the Kanai's waveform. It can be seen that sharp features are present more in the velocity waveform of the base of the heart than in the waveform at the lung and over the liver. This is expected because the tissues act as low-pass vibration filters. This low-pass filtering reduces the strength of the acceleration waveform the farther we get from the heart.

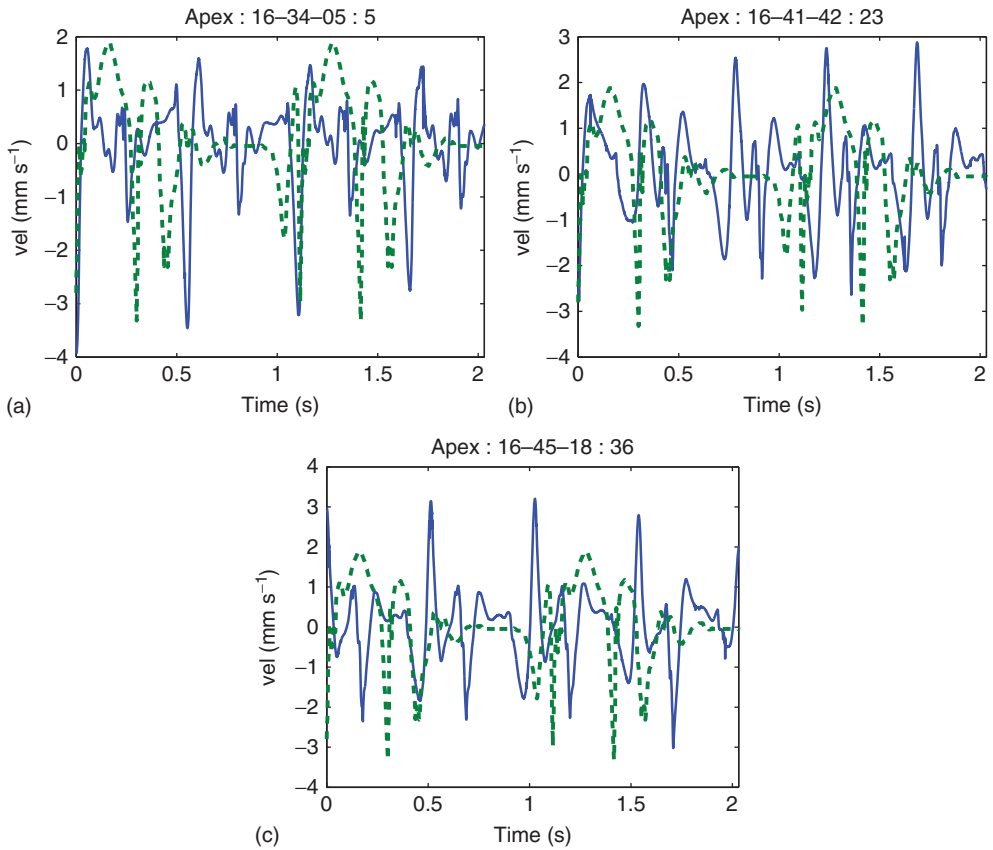


**Figure 21.18** Apex motion waveforms: (a) sample 5, (b) sample 23, and (c) sample 36: the dotted line is Kanai's waveform and the solid blue line is the normalized velocity waveform.

**Table 21.1** LDV measurements.

Location of the measurement	rms velocity (m s)	rms acceleration ( $\text{m s}^{-2}$ )	Heart rate (bpm)
Base of the heart	0.02	0.2	112
Lung adjacent to the heart	0.007	0.075	115
Liver	0.003	0.03	113

The energy harvester prototype is half the size of the batteries in ICDs and is about the same size as the batteries of the pacemakers (Figure 21.20). To examine how much power the piezoelectric energy harvester (PEH) generates, we subjected the PEH to the vibration waveforms, measured through the animal tests. An electromagnetic shaker was used to generate the heartbeat vibrations (Figure 21.20). To measure the vibration of the beam in the energy harvester, we

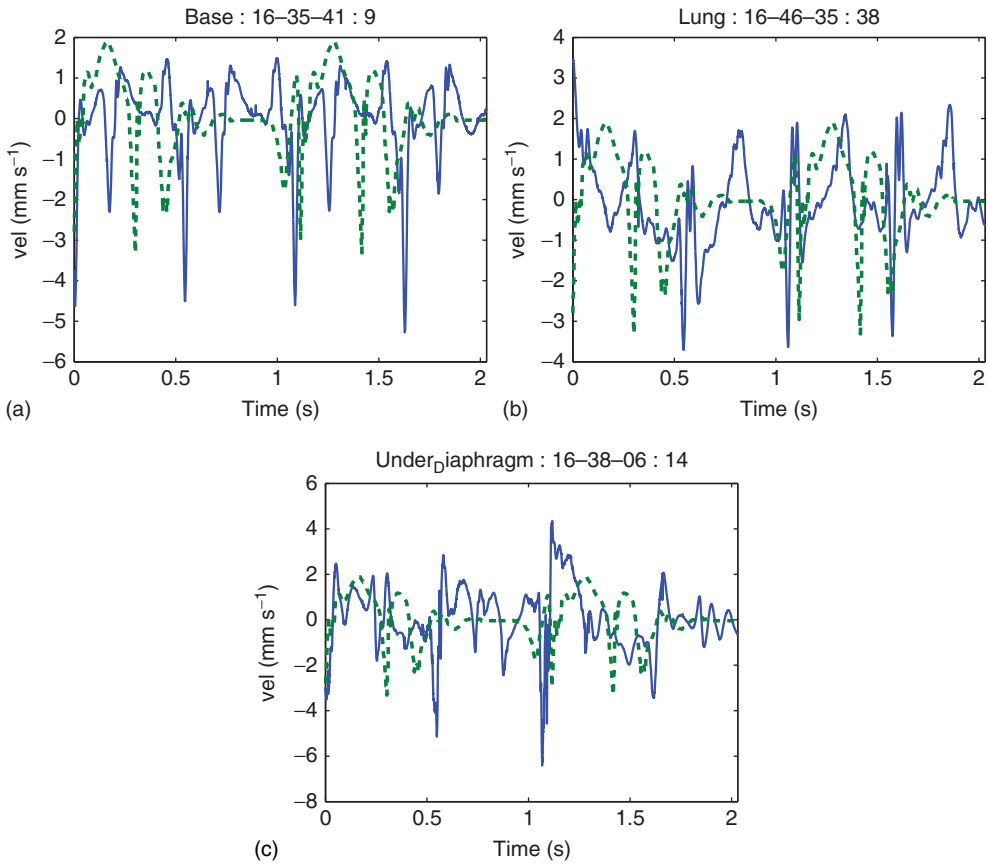


**Figure 21.19** Tissue vibration waveforms: (a) base of the heart, (b) lung, and (c) diaphragm: the dotted line is Kanai's waveform and the solid blue line is the normalized velocity waveform.

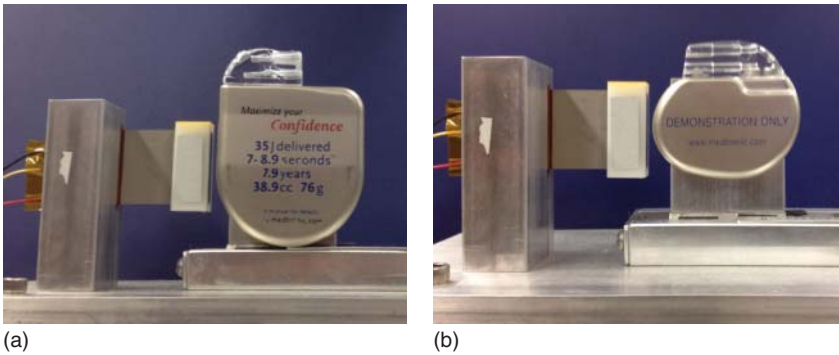


**Figure 21.20** Comparison of energy harvesting device with (a) an ICD and (b) a defibrillator.

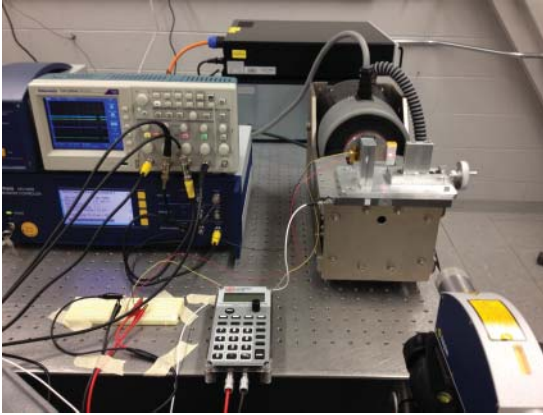
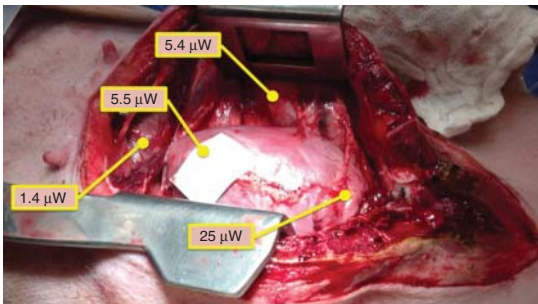
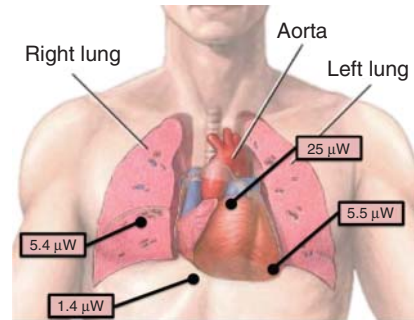


Figure 21.21 Shaker, velocity sensor, and power circuits.



(a)



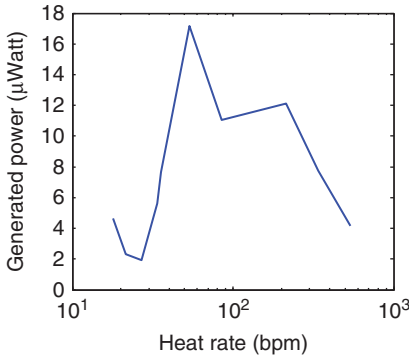
(b)

Figure 21.22 Experimentally measured power output of the harvester in response to vibrations at different points: (a) point on the pig's thorax and (b) corresponding points on human chest.

used the LDV. The piezoelectric element was connected to a variable resistor box. To accurately generate the vibration waveforms, measured in the animal tests, we used a closed-loop controller for the shaker (Figure 21.21). The shaker acceleration is measured by an accelerometer. The closed-loop control assures that there is almost no difference between the acceleration profile we measured in the animal tests and the acceleration profiles the energy harvester was subjected to.

The power generated by the PEH in response to vibration waveforms from the pig thorax has been illustrated in Figure 21.22 [25]. At the normal heart rate, the device can generate  $25 \mu\text{W}$  if mounted at the base of the heart; the power values corresponding to other locations are  $5.5 \mu\text{W}$  at apex,  $5.4 \mu\text{W}$  at the lung, and  $1.4 \mu\text{W}$  below the diaphragm.

In the next step, the performance of the PEH was examined over a much larger range of heart rate. By using the Kanai's waveform, we simulated heartbeat vibrations at heart rates ranging from 20 to 600 bpm. We used the simulated waveform



**Figure 21.23** Heart rate variation results based on Kanai's waveform.

in our experimental setup and measured the vibration output from the energy harvester. During the tests, the time axis of the acceleration waveform was scaled to simulate different heart rates. This means that the rms acceleration is equal for all heart rates. This is a conservative assumption at higher beats per minute. It was shown in Figure 21.17 that the heart acceleration increases with the heart rate.

As illustrated in Figure 21.23, the PEH generates  $18 \mu\text{W}$  at normal heart rate. This is 18 times the estimate for the power requirement of pacemakers in [7]. Even more impressive is the fact that over the entire range of heart rate considered the PEH can generate at least twice the estimated power requirement of a pacemaker.

## 21.9

### Conclusions

A feasibility study was conducted on using three different energy harvesting configurations for powering pacemakers from heartbeat vibrations. An approximate waveform of heartbeat vibrations was extracted based on ultrasonic measurements in the literature. It was shown that millimeter-scale zigzag linear structures can provide sufficient power to the pacemakers. The power from microscale zigzag harvesters was not sufficient for the application. Nonlinear monostable harvesters were designed so that they could meet the power demand. The best performance was by bistable nonlinear harvesters, which produced large amounts of power and was also functional over an extra wide range of heart rate.

It was shown that the special form of heartbeat excitations makes the nonlinear problem distinct from harmonic input cases. The heartbeat waveform is periodic but not harmonic. The response of nonlinear harvesters to the heartbeat waveform can be fundamentally different from their response to harmonic oscillations of the same level. For example, a monostable energy harvesting device became chaotic when excited by the heartbeat waveform. Harmonic excitations can very rarely result in the chaotic vibration of a monostable Duffing system.

The vibrations inside the chest area were measured through animal tests. The chest of two pigs and a sheep were opened, and the motions of the heart and



the surrounding tissues were measured by an LDV. The vibrations were reproduced in the laboratory by a closed-loop shaker. The energy harvester prototype was mounted on the shaker, and its performance was characterized. At normal heart rate, the device could generate  $25 \mu\text{W}$  if mounted at the base of the heart; the power values corresponding to other locations were  $5.5 \mu\text{W}$  at apex,  $5.4 \mu\text{W}$  at the lung, and  $1.4 \mu\text{W}$  below the diaphragm. In addition, the experiments showed that the nonlinear piezoelectric energy harvester produces sufficient power if the human heart rate is between 20 and 700 bpm.

### Acknowledgment

The authors would like to thank Dr. David J. Bradley for his consultations and help. The animal tests were conducted in collaboration with Prof. R. Bartlett, Dr. A. Rojas, and Dr. D. Demos from Extracorporeal Life Support Research Lab at University of Michigan. This work was performed in part under the support of the US Department of Commerce, National Institute of Standards and Technology, Technology Innovation Program, Cooperative Agreement Number 70NANB9H9007". This work was supported in part by the Institute for Critical Technology and Applied Science (ICTAS) at Virginia Tech. Research reported in this publication was supported in part by the National Center for Advancing Translational Sciences of the National Institutes of Health under Award Number 2UL1TR000433-06. The content is solely the responsibility of the authors and does not necessarily represent the official views of the National Institutes of Health.

### References

- Romero, E., Warrington, R., and Neuman, M. (2009) Energy scavenging sources for biomedical sensors. *Physiol. Meas.*, **30**, R35.
- Franks, A.E. and Nevin, K.P. (2010) Microbial fuel cells, a current review. *Energies*, **3**, 899–919.
- Rinaldi, A., Mecheri, B., Garavaglia, V., Licoccia, S., Di Nardo, P., and Traversa, E. (2008) Engineering materials and biology to boost performance of microbial fuel cells: a critical review. *Energy Environ. Sci.*, **1**, 417–429.
- Oncescu, V. and Erickson, D. (2011) A microfabricated low cost enzyme-free glucose fuel cell for powering low-power implantable devices. *J. Power Sources*, **196**, 9169–9175.
- Potkay, J.A. and Brooks, K. (2008) An arterial cuff energy scavenger for implanted microsystems. The 2nd International Conference on Bioinformatics and Biomedical Engineering, 2008. ICBBE 2008, 2008, pp. 1580–1583.
- Qi, Y., Jafferis, N.T., Lyons, K. Jr., Lee, C.M., Ahmad, H., and McAlpine, M.C. (2010) Piezoelectric ribbons printed onto rubber for flexible energy conversion. *Nano Lett.*, **10**, 524–528.
- Ohm, O.L.E.J. and Danilovic, D. (1997) Improvements in pacemaker energy consumption and functional capability: four decades of progress. *Pacing Clin. Electrophysiol.*, **20**, 2–9.
- Romero, E., Warrington, R.O., and Neuman, M.R. (2009) Body motion for powering biomedical devices. Annual International Conference of the IEEE

- Engineering in Medicine and Biology Society, 2009. EMBC 2009, pp. 2752–2755.
9. Parsonnet, V., Myers, G., Zucker, I.R., and Lotman, H. (1964) The potentiality of the use of biologic energy as a power source for implantable pacemakers. *Ann. N.Y. Acad. Sci.*, **111**, 915–921.
  10. Schroepfel, E.A. (1987) Pacing Lead With Piezoelectric Power Generating Means.
  11. Kennedy, J.H., Enger, C.C., and Michel, A.G. (1965) A subminiature implantable self-powered cardiac pacemaker: circuit design. *Ann. Thoracic Surg.*, **2**, 576.
  12. Biotronik (2000) *Actros + Programmable Family of Implantable Pulse Generators*, BIOTRONIK Inc., Berlin.
  13. Kanai, H., Sato, M., Koiwa, Y., and Chubachi, N. (1996) Transcutaneous measurement and spectrum analysis of heart wall vibrations. *IEEE Trans. Ultrason. Ferroelectr. Freq. Control*, **43**, 791–810.
  14. Starling, E.H. and Hartridge, H. (1920) *Principles of Human Physiology*, Lea & Febiger.
  15. Karami, M.A. and Inman, D.J. (2011) Analytical modeling and experimental verification of the vibrations of the zigzag micro-structure for energy harvesting. *J. Vib. Acoust.*, **133**, 011002-1–011002-10.
  16. Karami, M.A. and Inman, D.J. (2011) Electromechanical modeling of the low frequency zigzag micro energy harvester. *J. Intell. Mater. Syst. Struct.*, **22**, 1838–1849.
  17. Karami, M.A. and Inman, D.J. (2012) Parametric study of zigzag micro-structure for vibrational energy harvesting. *J. Microelectromech. Syst.*, **21**, 145–160.
  18. Miller, L., Halvorsen, E., Dong, T., and Wright, P. (2011) Modeling and experimental verification of low-frequency MEMS energy harvesting from ambient vibrations. *J. Micromech. Microeng.*, **21**, 045029.
  19. Mo, C., Kim, S., and Clark, W.W. (2009) Theoretical analysis of energy harvesting performance for unimorph piezoelectric benders with interdigitated electrodes. *Smart Mater. Struct.*, **18**, 055017.
  20. Karami, M.A., Bilgen, O., Inman, D.J., and Friswell, M.I. (2011) Experimental and analytical parametric study of single crystal unimorph beams for vibration energy harvesting. *IEEE Trans. Ultrason. Ferroelectr. Freq. Control*, **58**, 1508–1520.
  21. Karami, M.A. and Inman, D.J. (2011) Equivalent damping and frequency change for linear and nonlinear hybrid vibrational energy harvesting systems. *J. Sound Vib.*, **330**, 5583–5597.
  22. Karami, M.A., Varoto, P.S., and Inman, D.J. (2011) Experimental study of the of the nonlinear hybrid energy harvesting system. SEM International Modal Analysis Conference, IMAC-XXIII, Jacksonville, FL, 2011.
  23. Stanton, S., McGehee, C., and Mann, B. (2010) Nonlinear dynamics for broadband energy harvesting: Investigation of a bistable piezoelectric inertial generator. *Physica D*, **239**, 640–653.
  24. Moon, F. (1987) *Chaotic Vibrations*, John Wiley & Sons, Inc., New York.
  25. N. I. H. U.S National Library of Medicine (2011) <http://www.nlm.nih.gov/medlineplus/ency/images/ency/fullsize/19566.jpg> (accessed 8 November 2014).

## Index

### a

- $\alpha$ -Si solar cell 375
- acoustic energy harvesters 271
  - brief history 272–274
  - challenges 277
  - electroacoustic transduction 277–278
    - impedance matching and energy focusing 281
    - modeling 278–281
    - transduction methods 281–283
    - transduction structures 284–288
  - fabrication methods 288
    - materials 288
    - processes 289
  - fundamentals 276, 277
  - principles and concepts 276
  - reported performance survey 274–276
  - testing and characterization 289–290
- active system 224,
- actuator disc 298, 300
- aluminum nitride (AlN) 205, 207, 210, 217
  - electromechanical properties 207
- ambient vibrations stochastic character 14
- amorphous silicon solar cell 366–367
- anode and cathode potential and total cell potential 350–351
- antenna–rectifier matching 326–327
  - antenna matched to rectifier 328–329
  - antenna not matched to rectifier/multiplier 329–330
  - design consequences 330
  - voltage boosting technique 327–328
- areal and volumetric current density and areal and volumetric power density 351
- areal resistivity reduction 355
  - application of materials with high surface-area-to-volume ratio 355, 358
  - oxygen intrusion mitigation 358–359

- autonomous wireless sensor systems 417–419
- axial-flux permanent magnet (AFPM) generator 301, 302
- axial force 227–229
- axial induction factor 298

### b

- beams 288
- Betz limit 298, 300
- bimorph cantilever 134
- bistable harvesters 446–450
- bistable oscillators
  - buckled beam 21–23
  - cantilevers 19–21
- blackbody 66, 71, 74, 75
- blade element momentum (BEM) 303, 304
- bluff body 307
- body heat 251, 257, 259
- Boltzmann transport equation (BTE) 61, 62, 63
- breakdown voltage 53
- buckled beam 21–23
- bulk heterojunction (BHJ) 371, 372
- bulk single crystals
  - energy harvesting with perovskites 135
  - perovskites 135
- bypass heat flow domination 113

### c

- canonical resonant-type electrodynamic energy harvester 176
- cantilevers 19–21
- cantilever-shaped out-of-plane generator 168
- capacitive voltage boost converter 340
- cation exchange membrane (CEM) 350
- ceramics
  - energy harvesting examples 134

- ceramics (*contd.*)
  - fabrication process 132, 133–134
  - chalcogenides properties (group 16) 106
- chamber 350
- chemical bath deposition (CBD) 369
- CMOS-MEMS technology 254–255
- cold start 97
- commercialized micro technologies
  - Micropelt technology 257–258
  - Nextreme/Laird technology 258–259
  - Thermogen technology 259–260
- composite and piezoelectricity 134
- conjugate power variables 185, 279, 280
- converters for ultra-low-output transducers and examples 396–397
- copper indium gallium selenide (CIGS) 363, 375, 376
  - and CdTe solar cell development 367–370
- corona charging 162–163
- Coulombic efficiency 353
- coupling strength 191
- cross-plane configuration (CPC) 247, 249, 250
- crystallogens properties (group 14) 106, 107
- current status and trends 3–4
  
- d**
- deep reactive-ion etching (DRIE) 208, 209–210, 214, 289
- diaphragms 286–287
- dielectric polymers 54
- die-level hermetic packaging 210, 213
- direct transduction 280–281
- dry etching 208, 209
- dyadic Green's functions (DGFs) 68, 69, 73
- dye-sensitized solar cells (DSSCs) 373–374
- dynamic models 12–13
  - ambient vibrations stochastic character 14
  - electromagnetic generator 15
  - piezoelectric cantilever generator 14, 15
  - transfer function 15–16
- dynamic thermoelectric harvesting prototype 428
  
- e**
- eddy current damping 192
- effective damping coefficient 312
- effective isotropic radiated power (EIRP) 325
- effective radiated power (ERP) 325
- electrets *see under* electrostatic/electret-based harvesters
- electrical contact resistances domination 112–113
- electrical damping 203, 204
- electrical interface 34
- electroacoustic transduction 277–278
  - impedance matching and energy focusing 281
  - modeling 278–281
  - transduction methods 281–283
  - transduction structures 284–288
- electrochemical deposition *See* electrodeposition
- electrodeposition 253
- electrodes 350
- electrodynamics physics 179
  - Faraday's law 179–180
  - Lorentz force 180
  - simplified equations 180–181
- electrodynamics transduction coefficient 181
- electrodynamics vibrational energy harvesting 175–178
  - fabrication of harvesters 194–196
  - harvester architectures 181–183, 184
  - harvesters design 192–194
  - modeling and optimization 183
    - modeling 184–190
    - optimization 190–191
  - theoretical background 178
  - electrodynamic physics 179–181
    - energy storage, dissipation, and conversion 178
- electrolyte 401
- electromagnetic generator 15
- electromagnetic harvester 10–11
- electromagnetic induction 177
- electromagnetic transducers 27–28
  - basic principle 27–28
    - induced voltage 28
    - mechanical aspect 29–30
    - self-induction 28–29
  - energy extraction cycle 33
    - figures of merit and limitations 36–37
    - rectification cycle 35
    - resistive cycle 34
    - self-inductance cancelation 34–35
    - Synchronized Magnetic Flux Extraction (SMFE) 36
      - typical architectures 30, 31
      - case study 30, 32–33
      - general case 33
- electromagnetic transduction 282
- electromechanical coupling factor and piezoelectric materials 126–128
  - special considerations for energy harvesting 128–129
- electromechanical transducers 27
  - electromagnetic transducers 27–28

- – basic principle 27–30
  - – energy extraction cycle 33–37
  - – typical architectures 30–33
  - electrostatic transducers 45
    - – capacitance 45, 46
    - – design parameters for capacitor 47–48
    - – electric potential 46
    - – energy extraction cycles 48–51
    - – energy 46–47
    - – force 47
    - – Gauss’s law 45
    - – limits 51, 52–53
    - electrostrictive materials 53
      - – energy harvesting strategies 54, 55
      - – physical origin and constitutive equations 53–54
    - magnetostrictive materials 55
      - – constitutive equations 56
      - – physical origin 55
    - piezoelectric transducers 37
      - – constitutive equations 38
    - – energy extraction cycles 41–44
    - – maximal power density and figure of merit 44–45
    - – physical origin in ceramics and crystals 37–38
    - – typical architectures for energy harvesting 39–41
  - vibration energy harvester mechanical structure effect 56–58
  - electromotive force 28
  - electronic loads 86
  - electroplating, electrophoresis, and dielectrophoresis 117–118
  - electroquasistatic (EQS) regime 279
  - electrostatic/electret-based harvesters 149
    - conversion cycle 149–151
    - electrets 160–161
      - – charging technologies 162–163
      - – generator model 163–168
      - – generators 168–171
      - – materials 161–162
    - electrostatic generators
      - – design and fabrication methods 156–158
      - – examples 158–159
    - generator models
      - – configuration 151–153
      - – electrode design 153–156
  - electrostatic harvester 11
  - electrostatic pull-in 282–283
  - electrostatic transducers
    - basic principles 45
    - – capacitance 45, 46
    - – electric potential 46
    - – energy 46–47
    - – force 47
    - – Gauss’s law 45
    - design parameters for capacitor 47
      - – architecture 47–48
      - – dielectric 48
    - energy extraction cycles 48–49
      - – charge-constrained cycle 49–50
      - – electret cycle 51
      - – voltage-constrained cycle 50–51
    - limits 51
      - – breakdown voltage 53
      - – parasitic capacitors 51, 52
      - – pull-in force 53
  - electrostatic transduction 282–283
  - electrostrictive materials 53
    - energy harvesting strategies 54, 55
    - physical origin and constitutive equations 53–54
  - energy-autonomous sensors for air flow temperature 261
  - energy conversion efficiency 354
  - energy harvesting, meaning and definition of 1–2
  - EnOcean 261
  - equivalent circuits 279–280
  - evanescent modes 67, 71, 72, 73, 74, 76, 79
  - exoelectrogen 350
  - external tuning 16
  - extracellular electron transfer (EET) mechanism, elucidating 359
- f**
- Faraday’s law 175, 176, 179–180, 186
  - far-field radio frequency (RF) energy transfer and harvesting 321
    - examples and future perspectives 341–344
    - harvesting versus transfer 324–325, 326
    - nonradiative transfer 322, 323
    - radiative transfer 323, 324
    - rectifier 330–331
      - – 50- $\Omega$  antenna 335
      - – antenna 334–335
      - – complex conjugately matched antenna 335, 336
      - – DC output voltage 332–334
      - – rectenna results 336, 337–338, 339
      - – RF input impedance 331–332
      - – voltage up-conversion 339, 340
    - rectifying antenna 326
      - – antenna–rectifier matching 326–330
      - – transmission 340–341

- Fermi–Dirac and Bose–Einstein distributions 62
  - ferroelectricity, in perovskites 129, 130–131
  - figure of merit 66, 104, 207, 425
    - material 126–129
    - and maximal power density 44–45
  - fill factor 365
  - finite element method 185, 188–189
    - combination with lumped element method 189–190
  - finite element modeling (FEM) 278, 287
  - flame spraying *See* thermal spray
  - fluctuation-dissipation theorem 69
  - fluid flows and energy harvesting 297–298
    - energy harvesters based on flow instability 306
      - – devices based on galloping and flutter 310, 311–316
      - – vortex shedding devices 307–310
      - fundamental and practical limits 298–300
      - miniature wind turbines 301–302
      - – scaling effects 302–306
      - performance comparison 316–317
  - flutter *See* galloping and flutter
  - foil 248, 249, 259, 260
  - Fourier heat equation 422
  - fractional open-circuit voltage technique 377, 378
  - frequency response function (FRF) 443, 444
  - frequency tuning 16
    - of electromagnetic harvester 393–395
  - friction damping 193
  - Friss equation 340
- g**
- galloping and flutter 310, 311–316
  - gap-closing electrostatic/electrets generators 152, 153, 154, 155, 156, 157
  - Gauss's law 45, 160
  - Gibbs energy 125–126
  - gyrators 89
- h**
- Halbach array 183, 184
  - Harman method 114
  - head actuator, in hard drives 183, 184
  - heartbeat oscillations estimation 437–438
  - heart motion characterization 450–456
  - heat flow 245, 247, 249, 251, 257
  - heat sink 249, 250, 261, 263
  - heat storage thermoelectric harvester for aircraft strain sensors 428, 429–430
  - Helmholtz resonators 272, 284–285, 286
  - high-temperature flux technique 135
  - horns 285
- i**
- impedance matching
    - energy focusing 281
    - structures 284–285
  - incremental conductance (INC) technique 377
  - indirect transduction 281
  - indoor-light-powered wireless sensor networks 380–382
  - inductively coupled plasma (ICP) dry etching 209
  - inertial vibration energy harvester 57–58
  - Infinite Power Solutions Thinergy® cells 398
  - in-plane configuration (IPC) 247, 249, 250
  - in-plane electrets generator 168
    - and equivalent circuit 163–164
    - fabricated with precision machining 169
    - one-dimensional model 165
    - with parylene high-aspect-ratio spring 169
    - with shared electrodes 170
    - soft-X-ray charged 170–171
    - two-plate 167
  - in-plane gap closing 48
  - in-plane generator with comb drive 153–154
  - in-plane strain 124
  - intelligent thermostatic radiator valve (iTRV) 262–263
  - internal resistance and areal resistivity 352–353
  - ion exchange membrane 350
  - ionic electrostrictive polymers 53–54
- j**
- jacket-integrated wireless temperature sensor 263, 264
  - Joule effect 420, 422
- k**
- Kanai's waveform 451, 452, 453, 455–456
  - Kirchhoff's law 13, 160, 165
- l**
- Langevin equation set 14
  - laser Doppler vibrometer (LDV) 450, 452, 453, 455, 457
  - laser vibrometry 290
  - lead-free perovskites 138–139
    - energy harvesting 139
  - lead zirconate titanate (PZT) 204–205, 207, 216, 217

- electromechanical properties 207
- Lenz's law 29
- linear energy harvesters 438–444
- Linear Technologies 398
- Lorentz force 175, 177, 180
- low-power micro photovoltaic systems 376
  - indoor-light-powered wireless sensor networks 380–382
  - maximum power point (MPP) tracking 376, 377–379
  - output voltage regulation 379–380
- lumped element method 184–188
  - combination with finite element method 189–190
- lumped element modeling (LEM) 278–279
- m**
- magnetostrictive materials 55
  - constitutive equations 56
  - physical origin 55
- material hysteresis damping 193
- Maxim Instruments 398
- maximum power point (MPP) tracking 376, 377–379
  - *see also* power conditioning
- maximum power transfer tracking (MPTT) 96
- Maxwell's equations 67, 72
- mean flow acoustic engine (MFAE) 274
- mechanics and dynamics 7–8
  - dynamic models 12–13
    - – ambient vibrations stochastic character 14
    - – electromagnetic generator 15
    - – piezoelectric cantilever generator 14, 15
    - – transfer function 15–16
  - beyond linear micro-vibration harvesting 16
    - – frequency tuning 16
    - – multimodal harvesting 17
    - – up-conversion techniques 17, 18
  - micro vibration energy harvesting strategies 8–9
    - – electromagnetic 10–11
    - – electrostatic 11
    - – from macro to micro to nano 11–12
    - – piezoelectric 9–10
  - nonlinear micro-vibration energy harvesting 18–19
    - – bistable oscillators 19–23
    - – monostable oscillators 23
- metal oxide semiconductor field effect Transistor (MOSFET) 388, 389, 390, 392
- microbatteries 404–405
- microbial fuel cell (MFC) 347–348
  - future work 355
    - – areal resistivity reduction 355–359
    - – autonomous running 359
    - – extracellular electron transfer (EET) mechanism elucidation 359
  - MEMS, fundamentals of
    - – critical parameters for testing 350–354
    - – materials 350
    - – prior art MEMS MFCS 354–355
    - – structure 348–349
- micro device technologies 252–253
  - research and development 255, 257
    - – CMOS-MEMS technology 254–255
    - – electrodeposition 253
    - – silicon-MEMS technology 253–254
- micro-electro-mechanical-system (MEMS) 153, 156, 157, 158, 161, 168
  - CMOS-MEMS technology 254–255
  - silicon-MEMS technology 253–254
    - *see also* microbial fuel cell (MFC); piezoelectric MEMS energy harvesters
- micro energy storage 401
  - boundary conditions 401–404
    - – microbatteries 404–405
    - – supercapacitors 405, 406
  - primary energy storage approaches 405, 406–407
    - – caveat emptor 409
    - – future work and first-order problems 409–410
    - – volume-constrained versus conformally demanding approaches 408–409
- micromachined acoustic energy harvesters *See* acoustic energy harvesters
- micromachining 208, 213
- Micropelt technology 257–258
- micro photovoltaic module energy harvesting 363
  - amorphous silicon solar cell 366–367
  - CIGS and CdTe solar cell development 367–370
    - dye-sensitized solar cells (DSSCs) 373–374
  - low-power micro photovoltaic systems 376
    - – indoor-light-powered wireless sensor networks 380–382
    - – maximum power point (MPP) tracking 376, 377–379
    - – output voltage regulation 379–380
  - monolithically integration of solar cells with IC 375–376
  - p–n junction and crystalline Si solar cells 363–366

- micro photovoltaic module energy harvesting (*contd.*)
    - polymer solar cell 370–372
  - micro thermoelectric generators 245–247
    - classification 247–250
    - complete systems applications 260
      - energy-autonomous sensors for air flow temperature 261
      - intelligent thermostatic radiator valve (iTRV) 262–263
      - jacket-integrated wireless temperature sensor 263, 264
      - wireless power generator evaluation kit 263
      - wireless pulse oximeter SpO<sub>2</sub> sensor 261–262
    - general considerations 250–252
    - micro device technologies 252–253
      - commercialized micro technologies 257–260
      - research and development 253–257
  - miniature wind turbines 301–302
    - scaling effects 302
      - generator and bearing losses 305–306
      - turbine performance 302–305
  - monolithically integration of solar cells with IC 375–376
  - monostable nonlinear harvesters 441–446
  - monostable oscillators 23
  - motion-based energy harvesting 3
  - multilayer ceramic capacitors (MLCCs) 134
  - multimodal harvesting 17
- n**
- nanomaterials 143–144
  - nanoscale-gap thermophotovoltaic power generation 76–80
  - nanoscale heat conduction and Seebeck effect 62–64
  - nano-TPV power generators 71
  - nanowires 113, 114
  - near-field thermal radiation and thermophotovoltaic power generation 66–67
    - fluctuational electrodynamics 67–70
    - heat transfer between two bulk materials separated by subwavelength vacuum gap 70–76
    - nanoscale-gap thermophotovoltaic power generation 76–80
  - negative springs 229
  - Nernst equation 350–351
  - Newton's law 13
  - Nextreme/Laird technology 258–259
  - nonlinear input impedance circuits 90
  - nonradiative transfer 322, 323
  - numerical approaches, for acoustic energy harvesters 281
- o**
- Ohm's law 351
  - on-board tuning 16
  - open-circuit voltage 365
  - out-of-plane finger type *See* in-plane gap closing
  - out-of-plane gap closing 48
  - out-of-plane strain 124
  - overlapping-area-change electrostatic/electrets generators 152, 153, 154–155, 156, 157
- p**
- pacemakers powering with heartbeat vibrations 435–436
    - bistable harvesters 446–450
    - design specifications 436–437
    - experimental investigations 450
    - heart motion characterization 450–456
    - heartbeat oscillations estimation 437–438
    - linear energy harvesters 438–444
    - monostable nonlinear harvesters 441–446
  - parallel SSHI (Synchronized Switch Harvesting on Inductor) 43
  - parasitic capacitance 86, 163, 164, 165, 166, 167, 168
  - parasitic capacitors 51, 52
  - passive system 224,
  - peak power 365
  - peak rectifiers 90–92
  - Peltier effect 422, 423
  - permittivity change electrostatic/electrets generators 152, 153
  - perovskite materials 129
    - bulk single crystals 135
    - ceramics 132–134
    - lead-free 138–139
    - phase diagram 131–132
    - polycrystalline perovskites thin films 136–137
    - single-crystal thin films 137–138
    - structure 129–131
  - Perpetua Power Source Technologies 259, 260, 263, 264, 265
  - perturb and observe (P&O) technique 377
  - phase change material (PCM) 420, 426, 431
  - photoionization 163
  - photovoltaic (PV) cells 3
  - piezoelectric cantilever generator 14, 15
  - piezoelectric effect 9–10



- piezoelectric energy harvester (PEH) 453, 455, 456
- piezoelectric materials 123–125
  - electromechanical coupling factor 126–128
  - – special considerations for energy harvesting 128–129
  - nanomaterials 143–144
  - perovskite materials 129
  - – bulk single crystals 135
  - – ceramics 132–134
  - – lead-free 138–139
  - – phase diagram 131–132
  - – polycrystalline perovskites thin films 136–137
  - – single-crystal thin films 137–138
  - – structure 129–131
  - PVDFs 141
    - – energy harvesters 143
    - – structure 141–142
    - – synthesis 143
  - thermodynamics 125–126
  - typical values 144–145
  - wurtzites
    - – doping 141
    - – structure 139–140
    - – thin films and energy harvesting 140–141
- piezoelectric MEMS energy harvesters 201–202
  - challenging issues 213
    - – frequency response 215–216
    - – output power 213–215
  - piezoelectric material 217–218
  - development 204–205
    - – characterization 211–213
    - – fabrication technologies 205, 207–210
  - general governing equation 202–203
    - – design consideration 203–204
- piezoelectric pre-biasing 92–94
- piezoelectric transducers 37
  - constitutive equations 38
  - energy extraction cycles 41
    - – active cycles 43
    - – comparison 43–44
    - – rectification cycles 43
    - – resistive cycles 41–42
  - maximal power density and figure of merit 44–45
  - physical origin in ceramics and crystals 37–38
  - typical architectures for energy harvesting 39
    - – application to typical configurations 40–41
    - – modeling 39, 40
- piezoelectric transduction 281–282
- piston/spring arrangements 288
- Planck's blackbody distribution *See* blackbody
- pnictides properties (group 15) 107, 108
- p-n junction and crystalline Si solar cells 363–366
- Poincaré maps 447, 448
- Pointing vector 68
- polycrystalline perovskites thin films
  - energy harvesting with poly-PZT films 136, 137
  - fabrication process 136
- polydimethylsiloxane (PDMS) 350, 358
- polymer solar cell 370–372
- Polytec<sup>®</sup> laser Doppler vibrometer 450
- polyvinylidene fluoride (PVDFs) 141, 234
  - energy harvesters 143
  - structure 141–142
  - synthesis 143
- potassium hydroxide (KOH) etching 289
- power conditioning 85, 385–386
  - commercial products 397, 398
  - converters for ultra-low-output transducers and examples 396–397
  - frequency tuning of electromagnetic harvester 393–395
  - function of 85–86
    - – circuits with nonlinear input impedance 90
    - – circuits with reactive input impedance 89–90
    - – circuits with resistive input impedance 87–89
    - – highly dynamic load power 98–99
    - – interface to harvester 86–87
    - – peak power controllers 96–97
    - – peak rectifiers 90–92
    - – piezoelectric pre-biasing 92–94
    - – system architectures 97–98
    - – voltage regulation 94–96
  - power processing for electrostatic devices 397
  - single-supply pre-biasing for piezoelectric harvesters 388–392
  - submilliwatt electromagnetic harvester circuit example 386–388
  - ultra-low-power rectifier and MPPT for thermoelectric harvesters 392–393
- power conversion efficiency 365
- power processing for electrostatic devices 397

propagating modes 71, 72, 73, 76, 79  
pull-in force 53

**q**

quasi-static state 419

**r**

radiative transfer 323, 324  
radial flux 183, 184  
Radio Technical Commission of Aeronautics (RCTA) 416  
reactive input impedance circuits 89–90  
reactive-ion etching (RIE) 208, 210  
rectifier 330–331  
– 50- $\Omega$  antenna 335  
– antenna 334–335  
– complex conjugately matched antenna 335, 336  
– DC output voltage 332–334  
– rectenna results 336, 337–338, 339  
– RF input impedance 331–332  
– voltage up-conversion 339, 340  
rectifying antenna, receiving 326,  
– antenna–rectifier matching 326–330  
reduced damping *See* Scruton number  
resonance frequency 211  
resonant coupling RF energy transfer system 322  
resonant-type harvesters 89  
resonator tubes 285  
Reynolds number 302–303, 307  
Ritz–Galerkin averaging method 332

**s**

Scruton number 309  
Seebeck coefficient 418  
Seebeck effect 250, 422  
– and nanoscale heat conduction 62–64  
self-tuning system 224, 233–234, 241  
shake-powered flashlight 176  
short-circuit current density 364  
silicon-MEMS technology 253–254  
single-crystal thin films 137  
– energy harvesting with SC perovskite films 137–138  
– fabrication process 137  
single degree of freedom (SDOF) 215, 216  
single-supply pre-biasing 92, 94  
single-supply pre-biasing for piezoelectric harvesters 388–392  
skutterudites properties 108, 109–110  
Snell's law 71  
soft-X-ray charged in-plane electrets generator 170–171

sol–gel method 208, 209  
sputtering 140  
stall flutter 315  
static thermoelectric harvester for aircraft seat sensors 427–428  
stiffness modification, for frequency tuning 226–227  
– using axial force 227–229  
– using electrical external spring 231–232  
– using external spring 229–231  
Strouhal number 307  
submilliwatt electromagnetic harvester circuit example 386–388  
supercapacitors 405, 406  
surface polaritons 72, 73  
synchronized switch harvesting on inductor (SSHI) 273  
synchronous switched harvesting on inductor (SSHI) 92, 93  
system architecture 2  
system damping 192–193

**t**

tachometer 394  
tape casting 134  
TEGwear<sup>TM</sup> 263, 264, 265  
temperature difference 247, 249, 250, 251, 255, 261, 262, 263, 265  
temperature gradient 247, 258, 259, 260, 261  
Texas Instruments 398  
thermal conductance mismatch 111, 112  
thermal conductivity 247, 251  
thermalization 79  
thermal resistance 251, 252, 257  
thermal spray 118  
Thermobility<sup>TM</sup> 263, 264  
thermoelastic damping 193  
thermoelectric devices 3  
thermoelectric energy harvesting in aircraft 415–416, 419–420  
– aircraft standardization 416–417  
– applications 427  
– – dynamic thermoelectric harvesting prototype 428  
– – heat storage thermoelectric harvester for aircraft strain sensors 428, 429–430  
– – outlook 430–431  
– – static thermoelectric harvester for aircraft seat sensors 427–428  
– autonomous wireless sensor systems 417–419  
– design considerations 425–427  
– dynamic thermoelectric energy harvester 423–425

- static thermoelectric energy harvester 421–423
  - thermoelectric energy harvesting device efficiency 420–421
  - thermoelectric generators (TEGs) 392, 393
    - *see also* micro thermoelectric generators; thermoelectric energy harvesting in aircraft
  - thermoelectric materials 103
    - internal micro/nanostructure and related approaches 114–115
      - – thermal expansion and role in materials selection 115–116
    - material synthesis with relevance to micro energy harvesting 116, 117
      - – electroplating, electrophoresis, and dielectrophoresis 117–118
      - – thin and thick film deposition 118
    - performance considerations in materials selection 103–105
      - – chalcogenides properties (group 16) 106
      - – crystallogens properties (group 14) 106, 107
      - – pnictides properties (group 15) 107, 108
      - – skutterudites properties 108, 109–110
    - raw material cost considerations 116
    - scale influence on material selection and synthesis 110, 111
      - – bypass heat flow domination 113
      - – electrical contact resistances domination 112–113
      - – thermal conductance mismatch 111, 112
      - – thermoelectric property measurement challenges 113–114
  - thermoelectric power generation
    - heat transfer analysis 64–66
    - nanoscale heat conduction and Seebeck effect 62–64
  - Thermogen technology 259–260
  - thermopile 250, 251
  - thin film 245, 246, 247, 249, 252, 255, 257, 258, 259, 264
    - and thick film deposition 118
  - Thomson effect 420
  - transduction and acoustic energy harvesters 280–281
    - methods 281
      - – comparative analysis 283
      - – electromagnetic transduction 282
      - – electrostatic transduction 282–283
      - – piezoelectric transduction 281–282
    - structures 284
      - – for acoustical to mechanical transduction 286–288
      - – impedance matching 284–285
  - transfer function 15–16
  - tunable resonant systems 224, 225, 240
    - active schemes 225–226
      - – mass modification for frequency tuning 232
      - – stiffness modification for frequency tuning 226–232
    - passive schemes 232–233
      - – modification by coupling axial force with centrifugal force from rotation 234
      - – modification by coupling mass position with beam excitation 233–234
      - – modification using centrifugal force to toggle beam clamp position 234–235
- u**
- ultra-low-power rectifier and MPPT for thermoelectric harvesters 392–393
  - up-conversion techniques 17, 18
- v**
- variable capacitance 11
  - velocity-damped resonance generator (VDRG) 156, 167
  - vibration-driven electrets generators 166
  - vibration energy harvesting, from wideband and time-varying frequencies 223, 225, 240–241
    - active schemes for tunable resonant devices 225–226
      - – mass modification for frequency tuning 232
      - – stiffness modification for frequency tuning 226–232
    - device classification 223–225
    - future research directions
      - – system size considerations 242
      - – tuning range and resolution 241–242
      - – tuning sensitivity to driving vibrations 242
    - passive schemes for tunable resonant devices 232–233
      - – modification by coupling axial force with centrifugal force from rotation 234
      - – modification by coupling mass position with beam excitation 233–234
      - – modification using centrifugal force to toggle beam clamp position 234–235
    - wideband devices 235–236
      - – multimodal designs 236–237
      - – nonlinear designs 237–239
  - Villard cascaded multiplier 333
  - Villari effect 55

- viscid damping 192
  - voice-coil architecture 183, 184
  - vortex shedding devices 307–310
- W**
- wake galloping 313
  - wearable electronics 245, 247, 251, 260, 264, 408
  - wet etching 208, 209
  - wideband systems 224, 225, 235–236, 241
    - multimodal designs 236–237
    - nonlinear designs 237–239
  - windbelt energy harvester 315–316
  - wireless power generator evaluation kit 263
  - wireless pulse oximeter SpO<sub>2</sub> sensor 261–262
  - wireless sensor network, made by
    - vibration-driven wireless nodes 8
  - wireless sensor node (WSN) 86, 99
  - wurtzites
    - doping 141
    - structure 139–140
    - thin films and energy harvesting 140–141
- Z**
- zinc oxide (ZnO) 207
    - electromechanical properties 207
  - ZT meter *See* Harman method

# **WILEY END USER LICENSE AGREEMENT**

Go to [www.wiley.com/go/eula](http://www.wiley.com/go/eula) to access Wiley's ebook EULA.